AIRFLOW DISTRIBUTION AND TURBULENCE ANALYSIS IN THE LONGITUDINAL DIRECTION OF A BOEING 767 MOCKUP CABIN

by

MAHER SHEHADI

B.E., Beirut Arab University, 2007
M.S., Kansas State University, 2010

AN ABSTRACT OF A DISSERTATION

submitted in partial fulfillment of the requirements for the degree

DOCTOR OF PHILOSOPHY

Department of Mechanical and Nuclear Engineering
College of Engineering

KANSAS STATE UNIVERSITY
Manhattan, Kansas

2015

Abstract

This dissertation focuses on airflow distribution in the longitudinal direction of a wide-body mockup aircraft cabin, turbulence energy and dissipation rates, and the effect of thermal plumes, generated by passengers, on airflow distribution within the cabin.

The mockup cabin utilized for this study mimics a Boeing 767 passenger cabin and includes 11 rows in the longitudinal direction with each row consisting of seven seats. Each seat is occupied by an inflatable manikin which is instrumented with a 10 meters long wire heater generating approximately 100 Watts of distributed sensible heat, representing heat load from a sedentary human being.

In order to investigate the fluid dynamics characteristics of the airflow within the cabin, different experimental techniques were implemented. Smoke visualization was used to qualitatively visualize the general airflow pattern inside the cabin. A tracer gas composed mainly of carbon dioxide was used to track the airflow distribution inside the cabin. The tracer gas was released in several locations and then sampled at various locations throughout the mockup cabin. The release and sampling of the tracer gas allowed tracing the airflow inside the cabin using non dispersive infrared sensors. Combining results from different release-sampling scenarios gave better understanding of the chaotic and three-dimensional nature of the airflow behavior inside the cabin. Air speed and turbulence parameters were evaluated using omni-directional probes. Finally, the effect of the heat generated by the thermal manikins on the airflow behavior was investigated.

The results from the airflow visualization and the tracer gas were complementary and showed that there were multiple air circulations along the length of the cabin. The dimension of the circulations were controlled by the minimum physical distance inside the cabin. The

identified-isotropic turbulence were spread over the full width of the cabin in the front and middle sections of the cabin, whereas, multiple-smaller circulations were identified in the rear section. Cabin sections identified with high speed fluctuations were associated with higher turbulence kinetic energy levels and lower local dissipation rates. These sections served as driving forces to create the circulations identified in the tracer gas experiments. Furthermore, the heat generated by the thermal manikins was shown to significantly impact the behavior of the gaseous flow inside the cabin, the turbulence parameters, and speed fluctuations.

Detailed uncertainty analysis was conducted to estimate the uncertainty limits for the measurements taken. The uncertainty estimates obtained for the tracer gas results ranged from ±14% for the test cases with the heated manikins to ±17% with the corresponding unheated manikins cases. The data uncertainty limits for the turbulence parameters were of higher levels due to limitations associated with the omni-directional probes used to measure the speed. With flow repeatability phenomena in same locations inside the mockup cabin during different days reaching up to ±10%, the uncertainty estimates were considered acceptable for these chaotic and highly random airflow conditions within the cabin.

AIRFLOW DISTRIBUTION AND TURBULENCE ANALYSIS IN THE LONGITUDINAL DIRECTION OF A BOEING 767 MOCKUP CABIN

by

MAHER SHEHADI

B.E., Beirut Arab University, 2007
M.S., Kansas State University, 2010

A DISSERTATION

submitted in partial fulfillment of the requirements for the degree

DOCTOR OF PHILOSOPHY

Department of Mechanical and Nuclear Engineering
College of Engineering

KANSAS STATE UNIVERSITY
Manhattan, Kansas

2015

Approved by

Co-Major Professor
B. W. Jones

Approved by

Co-Major Professor
M.H. Hosni

Copyright

MAHER SHEHADI

2015

Abstract

This dissertation focuses on airflow distribution in the longitudinal direction of a wide-body mockup aircraft cabin, turbulence energy and dissipation rates, and the effect of thermal plumes, generated by passengers, on airflow distribution within the cabin.

The mockup cabin utilized for this study mimics a Boeing 767 passenger cabin and includes 11 rows in the longitudinal direction with each row consisting of seven seats. Each seat is occupied by an inflatable manikin which is instrumented with a 10 meters long wire heater generating approximately 100 Watts of distributed sensible heat, representing heat load from a sedentary human being.

In order to investigate the fluid dynamics characteristics of the airflow within the cabin, different experimental techniques were implemented. Smoke visualization was used to qualitatively visualize the general airflow pattern inside the cabin. A tracer gas composed mainly of carbon dioxide was used to track the airflow distribution inside the cabin. The tracer gas was released in several locations and then sampled at various locations throughout the mockup cabin. The release and sampling of the tracer gas allowed tracing the airflow inside the cabin using non dispersive infrared sensors. Combining results from different release-sampling scenarios gave better understanding of the chaotic and three-dimensional nature of the airflow behavior inside the cabin. Air speed and turbulence parameters were evaluated using omni-directional probes. Finally, the effect of the heat generated by the thermal manikins on the airflow behavior was investigated.

The results from the airflow visualization and the tracer gas were complementary and showed that there were multiple air circulations along the length of the cabin. The dimension of the circulations were controlled by the minimum physical distance inside the cabin. The

identified-isotropic turbulence were spread over the full width of the cabin in the front and middle sections of the cabin, whereas, multiple-smaller circulations were identified in the rear section. Cabin sections identified with high speed fluctuations were associated with higher turbulence kinetic energy levels and lower local dissipation rates. These sections served as driving forces to create the circulations identified in the tracer gas experiments. Furthermore, the heat generated by the thermal manikins was shown to significantly impact the behavior of the gaseous flow inside the cabin, the turbulence parameters, and speed fluctuations.

Detailed uncertainty analysis was conducted to estimate the uncertainty limits for the measurements taken. The uncertainty estimates obtained for the tracer gas results ranged from ±14% for the test cases with the heated manikins to ±17% with the corresponding unheated manikins cases. The data uncertainty limits for the turbulence parameters were of higher levels due to limitations associated with the omni-directional probes used to measure the speed. With flow repeatability phenomena in same locations inside the mockup cabin during different days reaching up to ±10%, the uncertainty estimates were considered acceptable for these chaotic and highly random airflow conditions within the cabin.

Table of Contents

List of Figures

List of Tables

Acknowledgements

I would like to express my extreme gratitude to Dr. Mohammad Hosni and Dr. Byron Jones for their guidance and help in my research during my PhD studies. I would like to thank Dr. Hosni for his continuous support and advice, not only on the academic side, but on the personal side, as well. Special thanks to Dr. Jones, as well, for his extraordinary advice and recommendations. Their assistance and guidance were as fuel for engines; It was vital for my PhD degree accomplishment.

I would like to thank Dr. Larry Glasgow and Dr. Terry Beck for being members on my supervisory committee and for providing suggestions and corrections to my thesis. In addition, I would like to thank Dr. Rys for serving as an outside chairperson on my committee.

The research was funded, in part, by the U.S. Federal Aviation Administration (FAA) Office of Aerospace Medicine through the National Air Transportation Center of Excellence for Research in the Intermodal Transport Environment under Cooperative Agreement 07-C-RITE-KSU. Although the FAA supported this project, it neither endorses nor rejects the findings of this research. The presentation of this information is in the interest of invoking technical community comment on the results and conclusions of the research.

The research was also funded, in part, by the Kansas State University Targeted Excellence Program.

Finally, I would like to thank my family for their continuous encouragement, help, and support.

Dedication

To my mom (Ibtisam) and dad (Farouk)

To my lovely wife (Heba) and daughter (Layan)

To the rest of my family .....

Chapter 1 - Introduction

The Bureau of Transportation Statistics (BTS, 2013) indicates that the number of passengers using commercial aircraft has doubled over the last two decades reaching to approximately 813 million passengers in 2012. Figure 1.1 shows a plot for the number of passengers using commercial aircraft within US over the period from 2002 to 2012. Eighty percent of passengers were domestic travelers who traveled inside the US, and twenty percent were international passengers who flew to or from the US via international flights. Biological and chemical incidents have been detected on various flights such as SARS (Severe Acute Respiratory Syndrome) and H1N1 (swine flu). Ebola was the latest virus threat on board flights. Chemical incidents that were reported can be related to smoke and fumes detected inside passengers' cabins. The smoke and fumes are thought to be a result of oil that can be thermally degraded under high temperature and pressure inside the jet propulsion engines of the aircraft and leak into the passengers fresh air supply duct system. With such high numbers of passengers spending from 1 to 20 hours in flights, such odors, fumes, viruses, and bacteria can result in serious health hazards to cabin crew and passengers.

The health and comfort of air travelers depend on various factors such as the ventilation system that controls quality of air supplied into the cabin, concentration of contaminants, temperature, and relative humidity (O'Donnell et al, 1991). Crew members around the world have reported neurological illness after reports of exposure to oil fumes, but there were no exposure data (Michaelis, 2007). According to Murawski and Supplee (2008), in 2007 the International Transport Workers' Federation Civil Aviation section in London indicated that

crew members around the world are reporting chronic health effects consistent with exposure to tricresyl phosphates “TCPs”, oil aerosols, and carbon monoxide.

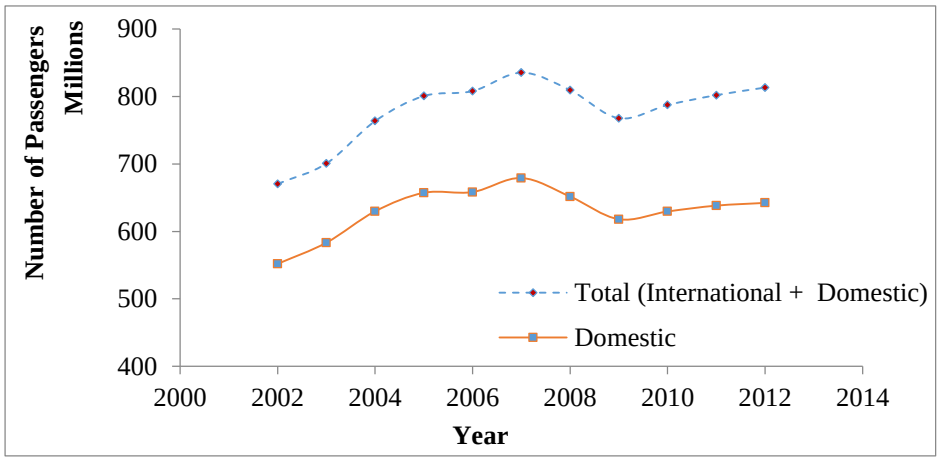

Figure 1.1 - Number of passengers on board flights within the United States

Ventilation air systems and the quality of air supplied into passengers in aircraft cabins have been an interest to many researchers and industries such as Airliner Cabin Environment Research (ACER), Federal Aviation Administration (FAA), Boeing, and many other affiliates. Various experimental and computational efforts have been done so far to understand the airflow distribution and behavior inside passenger cabins in aircraft for many reasons.

To help in monitoring and controlling the disease transport and chemical particulates dispersion inside aircraft cabins, it was essential to understand airflow behavior inside these enclosed environments.

The objective of the study is to understand the airflow distribution, gaseous transport phenomena, and turbulence levels inside a mockup aircraft cabin. Various approaches were used from smoke visualization, to tracer gas sampling, to speed measurements in order to understand the above proposed topics that were thought of being significant in order to control infectious disease, chemical contaminants, and particulates dispersion inside aircraft passenger cabins.

Testing conditions and gaseous flow repeatability conditions over the period of the study were investigated and documented to validate the results and to check for any experimental flaws or errors. The accuracy of the results was examined by conducting uncertainty analyses for all the experimental measurements, instrumentations, and equipment used.

Chapter 2 - Literature Review

2.1 Historical review of air quality incidents and bleed air events inside commercial aircraft cabins

This section discusses some interests and purposes behind the intention to conduct this study. Engine oil and hydraulic fluids used in aircraft engines is a synthetic fluid that contains various hazardous constituents such as organophosphates "OP", tricresyl phosphates "TCPs", and tributyl phosphates "TBP". The OP-isomers are neurotoxic and likely immunotoxic and are thought to be mixed with the supply air of aircraft cabins. Lubricating oil or hydraulic fluids used in the propulsion engines of the aircraft are exposed to high temperatures and pressures that can cause their thermal degradation (Michaelis, 2007). TCPs are added to all major commercial aviation engine oil. The presence of those chemicals at ambient and elevated temperatures has been confirmed by chemical analysis (van Netten and Leung, 2001; van Netten, 2000). TCPs are added to jet engine oil and fluids primarily because of their anti-wear properties. The total concentration of TCPs varies between 1-5%.

The effects of inhalation of toxic aircraft engine oil during commercial flights is a subject that has received increasing attention in the past 20 years in the US, UK, Europe, Australia and other parts of the world, as well. Commercial aircraft industries tend to minimize the energy usage on aircraft and thus design the supplied air into aircraft cabins to have 30-55% recirculated air. The remaining air is supplied from outdoor air that is compressed in either the aircraft engines or in the auxiliary power unit "APU" engines. Part of the compressed air is "bled" off the engines and is routed to the aircraft environmental control systems "ECS" where it is cooled and conditioned and then mixed with the recirculated air exhausted from the aircraft cabin. Only the recirculated

air passes through a set of high efficiency particulate air “HEPA” filters before going into a mixing manifold where it is mixed with the outdoor air bled off from the engines compressors at different stages. HEPA filters were utilized to offer filtration solutions to filter out the recirculated air from any bacteria and viruses up to 99.99%, if properly fitted and maintained, and depending on the type of filters used. Bleed air extracted from the engines compressors is not filtered and is mixed directly with the filtered recirculated air in a mixing plenum before being supplied to different sections in the cabin. In some modes of operation, outside air may be supplied by an auxiliary power unit (APU) which is a small turbine engine typically used during gate and taxi operations and other times when the propulsion engines are not operating at sufficient power levels to generate adequate bleed air. Whether from the propulsion engines compressors or APU, the outside air would be at elevated temperatures due to the compression process inside the aircraft engine compressors and any oil or other contaminants maybe subject to thermal decomposition and the resulting products might be carried through the air ducting system and into the cabin and flight deck. The potential of contaminating the supplied air due to maintenance, operation, and design failures or deficiencies is an ongoing problem and has been documented by various parties within the aviation industry since 1950s when bleed air supply systems were introduced into aircraft systems (SAE 1997). As per Murawski and Supplee (2008), Kayser reported in 1953 that the Committee on Aviation Toxicology of the Aero Medical Association acknowledged, shortly after the introduction of bleed air system, the potential of toxic substances in aircraft cabins coming from oil and hydraulic fluids.

According to several years’ data, frequency estimates of bleed air contamination events are estimated between 0.09 to 3.88 incidents per 1,000 flight cycles (NRC, 2002). The total number of departures recorded in between 2007-2012 by different airlines within the US was

approximately 64,037,351 flights. This will give approximately 10 million domestic flights annually in the United States serving approximately 1,780,000 passengers per day (average of 650 million passengers per year – Figure 1.1). Thus, considering the lowest limit of incidents of about 0.09 events per 1000 flight cycles, there might be around 2.47 bleed-air events per day. A review of data from the Service Difficulty Reporting System "SDRS" of the Federal Aviation Administration (FAA) for the period between Jan. 1999 – Nov. 2008 indicated that there had been 252 events of air contaminants of which 33% were due to fuel leaks, 23% were due to engine oil leaks, 18% were due to APU oil leaks, 13% were due to hydraulic fluid leaks and the remaining 13% were due to air cycle machine oil leaks (ACER, 2012). The report also recommended installation of sensors in either the passengers cabin or along the bleed air supply path between the pre-cooler and the air conditioning packs or between the air conditioning packs cooling the bleed air and the mixing chamber where the bleed air is mixed with recirculated air. Murawski conducted a survey for incidents of air supply contaminants over the period January 2006 – June 2007. The reports were collected from Service Difficulty Reports (SDR), from Accident and Incident Data System (AIDS) that were collected by the Federal Aviation Administration (FAA), from incidents that cabin crew documented, and from newspaper clips identified in online searches (Murawski and Supplee, 2008). For this survey, 74% of contamination events were identified within the FAA database with 24% reported by the Association of Flight Attendant (AFA). Aircraft types that were included in the survey ranged from small turboprop aircraft to wide-body jets, such as, A300, A310, A319, A320, A321, Beech 400/407/1900, B717, B727-200, B737, B747, B767 and B777-200 aircraft. The results showed, after removing duplicate entries from multiple sources for a given event, that the dataset included 470 incidents over an 18 months period yielding an average of 0.86 incidents per day.

In 1992, Vasak (1992) investigated air filter samples from routine revenue flights on BAe146-aircraft operated by East-West Airlines (now part of Ansett Australia). The study reported oil mist levels in the cockpit with concentrations of 1.5 mg/m^3, and in the passengers cabin 1.3 mg/m^3. In 1995 Currie took air samples on ground from a BAe146-aircraft after landing due to vomiting incidents reported by passengers and the crew members. The sampling method used Tedlar bags and the duration of each sample was 15 minutes. The results found that oil mist concentrations were below the detectable levels (below 0.02 mg/m^3) (Winder, 2006). Another study on BAe146-aircraft was conducted by the Building Research Est. in 2003 and it included 7-flights using BAe146 and 6-flights using Boeing 737-300 under normal flying conditions. Over 50 volatile organic compounds (VOCs) were identified although some concentrations were lower during the cruise phase of the flight. The study noted that one source of the VOCs was from passengers and that another source was the bleed air system (BRE, 2003). A study conducted by Pierce et al. (1999) during routine flights yielded a mean of 1,469 ppm of CO_2, a mean of 7 ppm of CO, 0.9 ppm of VOCs, and a maximum 10 $\mu g/m^3$ of particulates. Nagda et al. (2001) conducted a study for ASHRAE that addressed bleed air quality and included measurements on 10 routine revenue flights using B737, B767, and B747 aircraft. The study examined bleed air quality under normal operating conditions and there were no fume/smoke events during any of the sampled flights. Measurements reported were a maximum of 4,238 ppm of CO_2, a maximum of 9 ppm of CO, a maximum of 380 $\mu g/m^3$ of particulates, and semivolatile organic compounds (SVOCs) were under normal detection limits. Given the difficulty for capturing bleed air contamination events in real time, Eckels et al. (2014) investigated the ability to assess incidents through chemical analysis of material captured on cabin recirculation filters. They first used a laboratory bleed air simulator to create oil

contaminated air which was then directed to a filter test stand to expose aircraft filter media to the contaminated air. Chemical analysis of the exposed filter media was used to establish a signature for oil contamination consisting of three isomers of TCP plus synthetic lubricant. Then, 107 filters that were removed from aircraft at routine service intervals were evaluated and 77 filters that were collected from aircraft that either had repeated air quality issues or after a reported incident. The 107 filters show widespread presence of TCP but only 3% had the oil contamination signature. For the 77 filters, 30% contained the oil contamination signature. No attempt was made to use the filter analysis to estimate exposure levels. This study showed that filter analysis is useful to determine if oil contamination of bleed air is the cause of an air quality incident but it does not provide a detailed assessment of the incident itself nor can it be used by itself to determine when an incident occurred.

There have been several additional studies not addressed specifically at bleed air contamination events but that do provide useful baseline information. Malmfors (1989) measured CO and CO_2 on 48 Scandinavian Airline System (SAS) routine revenue flights including DC-9 and MD-80 aircraft models. O'Donnel et al. (1991) conducted a study on 45 routine revenue flights from 7 identical aircraft. The study showed a maximum of 2,170 ppm for CO_2; 4 ppm for CO; less than 0.1 ppm for NO_2; 200 $\mu g/m^3$ for total particulates; and no VOCs were detected. Waters et al. (2002) conducted a study on 36 commercial transport routine revenue flight segments including 11 different aircraft. Average levels of carbon monoxide over the full-flight duration were generally less than 1 ppm and during 5-minutes sampling the average was as high as 9.4 ppm. The predominant VOC was ethanol with toluene and limonene also found. Toluene levels ranged from less than 0.3 to 130 ppb, limonene from 3 to 12 ppb, and ethanol from less than 0.8 to 2.4 ppm. Inhalable particulates had an average

of 120 μg/m^3 over the full flight time whereas total particulates had 86 μg/m^3. Carbon dioxide concentrations had an average during the entire flight period ranging between 874 ppm and 2,328 ppm. Some flights never had CO_2 concentrations less than 1,556 ppm. CO_2 levels were higher on aircraft with recirculation systems and were slightly higher on smaller aircraft and on short flights, as well. As far as can be determined, none of the flights sampled by these researchers had any kind of air quality incident.

Guan et al. (2014) conducted in-flight measurements on 107 commercial revenue flights operating between August 2010 and August 2012. Most samples were collected prior to take-off, during cruise, and upon landing phases of the flights. The selected aircraft included Boeing models B737, B747, B777, B757, B767, and Airbus models A319, A320, A321, A330, A340, and A380. On average, 59 volatile organic compounds were identified in each flight and were 41% alkanes and alkenes, 15% esters and alcohols, 11% ketones and aldehydes, 20% aromatics (mostly benzene), 6% halides, and 6% of other volatile organic compounds. It was concluded that, among the three investigated flight phases, landing showed to experience the lowest exposure limits compared to prior to take-off and cruise phases. The Institute of Environment and Health (IEH) at Cranfield University reported that the most abundant chemicals measured on 100 revenue flights in 2007, based on mean values, were toluene and limonene. The highest concentrations of tributyl phosphates, limonene, m+p-xylene, and undecane were detected during first engine start, while that for tetrachloroethylene (TCE) occurred at the instant when the sampling kits were opened. On the other hand, the highest levels of triorthocresyl phosphates (TOCP), tricresyl phosphates (TCP), and toluene occurred during climb, pre-landing, and take-off phases, respectively. Five flights experienced more than 500,000 particles per cubic centimeter (particle/cm^3) of ultrafine particles and 19 flights

experienced more than 10 ppm of volatile organic compounds with the majority being detected during taxi-out phase of the flights (IEH, 2011).

Limits for tricresyl phosphates (TCP), tributyl phosphate (TBP), and dibutylphenyl phosphate (DBPP) were set for enclosed environments in some countries and are tabulated in Table 2.1 as 8 hour and/or 15 minute time weighted averages (TWA). The limits for TCP have been set on the basis of its neurotoxic properties, whilst those for DBPP and TBP have been set because of their potential for irritation of the eyes and respiratory system (Lamb et al., 2012).

Table 2.1 - International occupational exposure limits for organophosphates (Lamb. et al, 2012)

Substance	TBP		TCP		DBPP	
Country	8 hr TWA mg/m^3	15 min TWA mg/m^3	8 hr TWA mg/m^3	15 min TWA mg/m^3	8 hr TWA mg/m^3	15 min TWA mg/m^3
Austria	2.5	5	0.1	0.2	3.5	-
Belgium	2.2	-	0.1	-	3.6	-
Canada	2.2	-	0.1	-	3.5	-
Denmark	2.5	5	0.1	0.2	3.5	7
France	2.5	-	0.1	-	-	-
Germany	11	22	-	-	-	-
Poland	-	-	0.1	0.3	-	-
Singapore	2.2	-	0.1	-	3.5	-
Spain	2.2	-	0.1	-	3.6	-
Sweden	-	-	-	-	-	-
Switzerland	2.5	10	0.1	-	-	-
USA-NIOSH	2.5	-	0.1	-	-	-
USA-OSHA	5	-	0.1	-	-	-
UK	5	5	0.1	0.3	-	-

Shehadi examined databases from the Federal Aviation Administration, NASA, and other governmental and non-governmental online databases in detail to determine the frequency and nature of air contamination events inside aircraft cabins (Shehadi et al., 2015). The analyses

presented bleed air incidents on board commercial aircraft, their impact on aircraft cabin environment, and focused on the financial losses incurred by airlines due to bleed air contamination related events. Reported incidents that were related to oil and smoke for a wide range of commercial aircraft models including Boeing, Airbus, McDonnell-Douglas, Canadian Royal Jets, Embraer Royal Jets EMB, and other aircraft models were examined. Thirty three aircraft models were included in the study. The list of included aircraft models is shown in Table 2.2. Figure 2.1 shows the frequency of the reported bleed air contamination incidents versus different aircraft models over the period from 2007 to 2012. The total number of reported incidents was approximately 8,000 non-duplicated reported incidents.

Table 2.2 – Aircraft models investigated by Shehadi (Shehadi et al., 2015)

Index	Aircraft Model		Index	Aircraft Model		Index	Aircraft Model
1	A300		12	B737-700		23	B777-200/200ER
2	A319-100		13	B737-800		24	DC-10
3	A320-100/200		14	B737-900		25	DC-9
4	A321-200		15	B747-100		26	MD-11
5	A330-300		16	B747-200		27	MD-83/88
6	B717-200		17	B747-400		28	EMB 135
7	B727-200		18	B757-200		29	EMB 170-100
8	B737-100/200		19	B757-300		30	EMB 190-100
9	B737-300		20	B767-200/200ER		31	CRJ 900
10	B737-400		21	B767-300/300ER		32	CRJ 200
11	B737-500		22	B767-400/400ER		33	CRJ 700

A: Airbus – B: Boeing – DC: Douglas Commercial – MD: McDonnell Douglas – EMB: Embraer – CRJ: Canadair Regional Jet

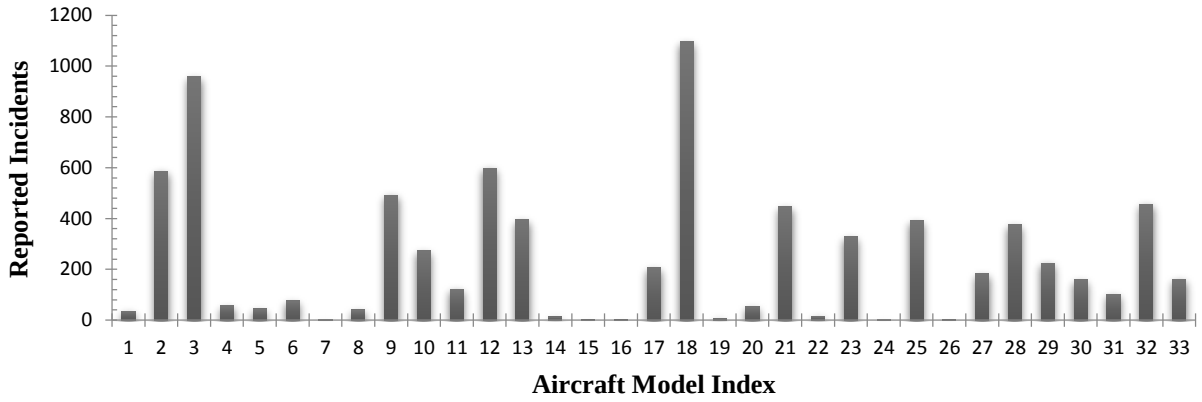

Figure 2.1 - Total reported incidents for different commercial aircraft models over the period 2007-2012 (Shehadi et al., 2015)

Table 2.3 shows a breakdown of reported incidents on flights in 2012 with the associated financial costs (Appendix K – Paper submitted to SAE – Journal of Aerospace). Two cases were considered for the cost estimation. Lower limit costs were based on the fact that when an incident occurred, the aircraft would land without having to burn or dispose the remaining fuel in the fuel storage tanks and with minimal maintenance cost. On the other side, the upper limit cost or the worst case scenario was based on disposing of the whole fuel tank and having higher maintenance fees associated with it. Other costs included leasing an alternative aircraft to transfer passengers, landing fees, parking fees, overtime or additional working hours for the cabin crew or requesting additional crew to serve on the additional flight, luggage loading and unloading fees, and costs for replacing meals. Table 2.3 shows that the total financial losses, due to the reported incidents in 2012, ranged between $32,000 to $47,000 per aviation incident totaling approximately 4.5M to 6.5M US dollars in 2012. With the highest estimates for both the reported incidents (2.7) and the cost loss ($47,000), there was approximately $127,000 paid on a daily basis as a result of such incidents. This figure could even be doubled when knowing that the reported incidents are being under reported (Murawski and Supplee, 2008). Muraswki and

Supplee (2008) found that incidents are significantly under reported but the extent to which they are under reported is not clear. It is entirely possible that under reporting could vary considerably from airline to airline due to reporting policies and other factors.

Table 2.3 - Loss in US dollars per aircraft capacity during 2012 due to incident reporting

# of Passengers	# of events	Case 1 - Low Limit Loss		Case 2 - Upper Limit Loss	
		Total Loss ($)	Loss per event ($)	Total Loss ($)	Loss per event ($)
< 50	**24**	$271,454	$11,311	$326,703	$13,613
50-100	**15**	$369,138	$24,609	$445,306	$29,687
100-150	**38**	$1,008,564	$26,541	$1,447,470	$38,091
150-200	**37**	$1,501,221	$40,574	$2,105,472	$56,905
200-250	**17**	$713,533	$41,973	$967,449	$56,909
250-300	**6**	$600,975	$100,163	$1,044,550	$174,092
300-350	**6**	$222,722	$37,120	$400,203	$66,701
Total # Events	**143**	**$4,687,607**	**$32,780**	**$6,737,153**	**$47,113**

It is unknown what the chemical composition and what concentrations of these contaminants are present onboard flights due to the fact that no aircraft has any form of detection system installed with its system and there is not an appropriate air monitoring and warning system, as well. The concentration of airborne contaminants is expected to vary depending on the aircraft type, airline maintenance practices and whether the bleed air is extracted from the aircraft engines or the APU (NRC, 2002). No regulatory body has published regulations explicitly intended to prevent exposure to oil fumes on aircraft, such as mandating the use of air supply cleaners, air supply sensors, and less toxic engine oils, for example (Murawski and Hecker, 2011). Although, in 2007 the ASHRAE Standard 161 was published that recommended continuous monitoring of bleed air contaminants, exposure to data for crew and passengers who report symptoms related to oil fumes, and requested control measures to prevent contamination of the supply air, no airline

has implemented the standard (Murawski and Hecker, 2011). It is of interest to note that the aviation industry in Europe had proposed a standard for air quality that lists reference data for occupational exposure limits for various chemicals, including CO, and ultrafine particles on aircraft, however, the standard was withdrawn.

Harrison reported cases that were examined and reviewed after the submission of written reports due to exposure to airborne contaminants that were suspected to be from engine oil or hydraulic fluid. The cases are summarized in Table 2.4 as documented by Harrison et al. (2009).

Table 2.4 - Case series - acute health effects follows exposure to contaminated bleed air (NRC, 2002)

Case No.	Age	Exposure Document	Symptoms	Signs / Positive Tests
FA-2	26	Cabin Incident Report	muscle pain	PE: decreased plantar reflexes, memory loss
			chest pain	
			throat irritation	Psychiatric evaluation: Conversion disorder
			Dizziness	
			loss of balance	
FA-4	38	Cabin Incident Report	weakness	PE: tremor, nasal congestion, throat hyperemia and edema
			nausea	
			vomiting	
			dizziness	
FA-7	39	Employee Incident Report	myalgias	PE: poor serial 7s, memory loss
			eye irritation	
			headache	
			disorientation	
FA-10	38	Flew MD-80	nausea	PE: poor serial 7s, memory loss
			vomiting	
			throat irritation	
			headache	
			lightheadedness	

			slurred speech	
			anxiety	
			fatigue	
			insomnia	
			wheezing	
			cough	
FA-11	42	Mechanical Report	nausea	Laboratory: decreased plasma cholinesterase
			vomiting	
			diarrhea	
			headache	Neuropsychological testing: attention and information processing deficits, learning and memory impairments
			throat irritation	
			lightheadedness	
			slurred speech	
FA-12	39	Mechanical Report	Headache dizziness	PE: Right hand tremor Psychiatric evaluation: depression, anxiety
FA-14	49	Doctors First Report	nausea	PE: wheezing, rhonchi
			vomiting	
			Headache	
			chest tightness	
FA-15	36	Flew MD-80	headache	PE: truncal movement disorder
			confusion	
			extremity jerks	
FA-21	32	Flew MD-80	joint pain	PE: ataxia
			nausea	
			vomiting	
			confusion	
			loss of balance	
			anxiety	
FA-23	51	Mechanical	nausea	Laboratory: decreased plasma

		Report	vomiting	cholinesterase
			throat irritation	
			cough	
			SOB	
			chest tightness,	
			headache	
			lightheadedness,	
			memory loss	
FA-26	49	Pilot Report	eye burning throat	PE: mucous membrane erythema, abnormal Romberg, tandem gait
			irritation headache	
			nausea	

In 2011, a report by Murawski and Hecker included an incident when the captain and the first officer showed some symptoms during a flight on a Boeing 767 aircraft. Symptoms included burning chest pain and unusual fatigue. During the same flight, it was reported that cabin crew and some other passengers experienced headache, blurred vision, dry cough, and difficulty in taking a full breathe. The aircraft maintenance records confirmed that engine oil had leaked into the air supply system. The captain and the first officer licenses were revoked at a later time. The revoke came from FAA due to incompliance with medical certification requirements and were classified as being unable to operate any aircraft as a result of neurological symptoms caused by exposure to the fumes (Murawski and Hecker, 2011).

Crew members around the world have reported neurological illness after reports of exposure to oil fumes, but there were no exposure data. A recent sampling study funded by UK-Department for Transport reported low levels of airborne TCPs on 23 of 100 passenger flights and cargo flights, involving 4 aircraft types (Murawski and Michaelis, 2011). The study covered around 100 flights, although the call was for 10,000-15,000 flights. The project was to monitor the air

quality during all phases of the flight starting with the same time when the kit was immediately set in the plane, for the starting of each of the engines (left and right), taxi, takeoff, climb, top of climb, cruise, start of descent, pre-landing, taxi-back and during any reported air event. The sampling techniques included:

- Continuous measurements of total volatile organic compounds (TVOCs), CO, and ultrafine particles.
- Five minutes average exposure measurements of some specific VOC and SVOCs including TOCP, TCPs, and TBP. The sampling time was minimized in order to maximize the ability to capture transient air quality events, otherwise the concentration would be diluted.
- When an unusual odor was noted or when the sampling showed high level of TVOCs or particulates a 30 minute sampling was conducted.
- Aircraft covered included B757, BAe-146, A320 and A 319. The B757 included one cargo and one passenger aircraft flights.
- Samples were sent either to BRE or AES laboratories who had previous experiences with air quality analysis.
- A researcher travelled on each sampled flight.
- Samples were collected according to a predetermined phase of flight.
- SVOCs and TCPs were sampled near floor level.
- All samples collected for each phase and for each type of particulate were averaged over all flights sampled.
- The samples were taken into Tenax-sorbent tubes using a portable air sampling pump. In case of an event, a second pump was used.

- Photoionization detectors (PID) were used to detect total VOCs. It used a pump to collect the samples in the sorbent tubes.
- Electrochemical cell (gas monitor) was used to measure CO.
- A portable condensation particle counter (P-Track) was used to detect ultrafine particles.
- Data were sent to Cranfield University by email and/or CD.

Out of 552 crew members who completed a health survey at the end of each of the 100 flights, only 4 reported a headache/slight headache, but this does not mean that there is no health impact. A total of 38 flights had fumes or smells as reported by at least one crew member. The measured concentrations were compared to IAQ guidelines of occupational buildings. The results showed that CO concentrations did not exceed safety or health limits as set by the European Standard "Aircraft internal air BS EN 4618:2009 (Murawski and Michaelis, 2011). Regarding possible influence of aircraft type, no TCPs were detected on A320/321, whereas limonene concentrations were relatively high on these flights. The most abundant chemical among all 100 flights (mean-wise) were toluene and limonene, while TCPs were below the guidelines limits (BS EN 4618:2009). Some of the results concluded during the study in addition to the above were:

- The highest concentration of TBP, limonene, m+p-xylene and undecane occurred during first engine start, while TCE concentration was during immediate sampling (opening of the kit).
- Highest concentrations of TOCP, TCPs, and toluene occurred during climb, pre-landing and takeoff respectively. However, there was no detectable amount of TOCP or other TCPs in 95% of the air samples. TBP was detected more routinely.
- Out of 30 events claimed during 25-flights, the highest concentrations were recorded during engine start and takeoff.

- During all flights, five flights recorded a maximum of 500,000 particles/cm^3 of ultrafine particles and 19-flights recorded peak concentrations for total VOCs higher than 10 ppm of which 13 were recorded during immediate and taxi-out phases.
- Limonene, undecane, and TCE showed high levels on Airbus A320/A321 aircraft with no noticeable levels of TCPS. On the other hand, A319 aircraft experienced high levels of m+p+xylene.
- The report also concluded that concentrations of toluene, limonene, xylenes, undecane, and TCE found in the studied aircraft were of similar magnitude of concentrations present in homes in developed countries and that CO produced by gas cookers are often higher than those occurring in the aircraft cabins.

Two Airbus aircraft types were selected by Dechow (1996) to perform measurements to check the microbiological contaminants inside the aircraft and the types and amount of volatile organic compounds (VOC) and to have a clearer understanding of the air quality present in aircraft. The aircraft types were the Airbus A310 of Swissair and the Airbus A340 of Lufthansa. A310 aircraft filter efficiency can remove 90% of particles with diameters 0.51 μm and 99% of the air conditioning coarse test dust. The A340 has high efficiency particulate air "HEPA" filters. Eight particle sensors were used and a pressure transducer was installed to determine the flight phase. A central power unit for supply and data storage was used to log the recorded data. The above equipment were installed on the aircraft for 1 year and the data were collected during normal in-service flights. The sensor air intakes were located between ceiling sensors and floor sensors. Another air sensor was installed in the fresh air duct downstream of the air conditioning pack and one in the recirculating air duct downstream of the recirculation filter. The measuring principle of the particle sensors is based on a laser optic that counts the number of particles in the

air conducted through the sensor. Particles with more than 0.5 μm in diameter were detected. The data were separated according to the following phases of the flight: twenty-five minutes before takeoff, twenty five minutes after takeoff, cruise condition, 25 minutes before landing, and 25 minutes after landing. A slit impactor was selected for the measurements and 50 liters per minute were collected for 2 minutes. Many different types of measurement tubes and suction flows were used such as activated carbon tubes (NIOSH 30/15 mg), Tenax tubes, silica gel tubes, ADT-Tenax tubes and impregnated silica gel tubes. The usual bacteria size was found to be between 0.3 μm to 3.5 μm. Ventilation air had a very low contamination level due to the high efficiency of the recirculation filters and the contamination free conditions at high altitudes. Sixty-four different compounds were detected, many of them in concentrations too low for quantification. It was concluded that the main source of bacteria was the occupants. Some of the main compounds found were ethanol, acetone, toluene, formaldehyde, acetic acid, and nicotine (Dechow, 1996).

Another study was conducted by Lee et al. (1999) which included 16 flights on Cathay Pacific airlines from June 1996 to August 1997 of which 3 were smoking flights. One sampling location on each flight was used. Sampling methods and analysis were performed according to the standard methods described by the ASTM, American Conference Governmental Industrial Hygienists, American Public Health Association, and National Institute for Occupational Safety and Health. Electrochemical cell was used for 5 minutes during each flight for CO monitoring; Non-dispersive infrared NDIR sensors for 5 min for CO_2 detection; Airbag/Pulse Fluorescence SO_2 analyzer for Sulphur dioxide (twice per flight); Airbag/chemiluminescene NO_x analyzer for Nitrogen dioxide (used twice per flight); passive ozone badges or biocheck enzyme for ozone; flame ionization detectors for total hydrocarbon (twice per flight). The CO_2 level recorded

higher concentrations during boarding and deboarding than cruise due to low fresh air supply. The average concentrations of CO_2 ranged between 629 and 1,097 ppm. Ozone detectability ranged from null up to 90 ppb. The average particulate level in smoking flights was 138 $\mu g/m^3$, whereas on nonsmoking flights it was as low as 7.6 $\mu g/m^3$. The average temperature was 21.9 ^{0}C which was within the comfort temperature range. Carbon monoxide concentrations were below 1 ppm and the average was between 2 and 3 ppm. The impact of high and low modes of ventilation on indoor air quality was investigated on one of the flights for 30 minutes and CO_2 levels were reduced by 29%, temperature by 0.7%, and humidity by 27.6%. In-addition to the above analysis, a questionnaire was completed by the cabin crew evaluating the overall cabin air quality. 185-questionnaires were completed of which 32% responded as adequate air quality, 36% responded acceptable quality, 2% outstanding, 21% poor, and 9% with no opinion. In general, the cabin crew felt that the air quality was best in the first class, followed by business class and lastly economy class (Lee et al., 1999).

A passenger survey included 3,630 passengers on 71 flights with 3 different flight durations including 2-3 hours, 6-7 hours and 10-12 hours flights. Six types of aircraft were studied of which three were wide-body and three were of the standard-body. Results returned with 57% of the ratings scoring above 4 out of a 7 scale of which the cabin appearance was the highest rank. All standard body aircraft had lower average ratings than the wide body craft. The ratings for health during the flights were quite high. The symptoms experienced by the passengers were back/joint/muscle pain and dry or stuffy nose (Rankin et al., 2009).

In 1990, a request was made by the Association for Flight Attendants (AFA) for NIOSH to evaluate potential employee exposures to toxic gases and/or a lack of oxygen aboard Alaska Airlines flights on McDonnell Douglas MD-80 airplanes. This request came after many

incidents were reported during passenger flights on Alaska Airlines MD-80 airplanes, during which some of the flight attendants experienced illness symptoms (including headache, dizziness, blurred vision, mental confusion, and numbness). Three NIOSH site visits were made in association with the Health Hazardous Evaluation (HHE Report– NIOSH, 1993). In the first visit which was mainly a visual inspection of the ventilation system, data were collected from American Airlines, employee representatives, and the airplane which had the highest number of incidents was checked, as well. In the second visit, NIOSH investigators conducted environmental monitoring aboard three test flights on two Alaska Airlines MD-80 airplanes under flight conditions thought to represent "worst case" and "normal" for cabin air quality. The third visit was to conduct additional follow up for CO monitoring on three commercial flight segments using electrochemical cells. Testing locations included cockpit (left & right), first class galley, first class seats, main cabin galley, main cabin seats, main cabin flight attendants, and main cabin aft entry door. Aircraft models included were MD-80, B727 and B737 (models 700 and 900). Two CO dosimeters were used side-by-side at each sampling location and the CO was continuously monitored during the flight. Total particulates were continuously monitored as well using optical sensors. The samples were collected using battery-operated personal sampling pumps. Photoionizations detectors (PIDs) were used to detect total VOCs and toluene. Of the 56 airplane staffed by Alaskan Airlines, 66% of the flights were involved in at least one illness incident. B737 and MD-80 each had three incidents of which none had identifiable exposure. Seven B727 and three MD-80 each had two incidents. An odor was reported on 24% of all 83 incident flights. VOCs averaged in the 1.8-3.2 ppm range. Testing with magnetic resonance imaging of the head showed possible brain abnormalities for six passengers, and in three of these cases (all of whom had persistent neurologic symptoms), psychological testing indicated

cognitive or motor abnormalities. Carbon dioxide averaged between 550-1191 ppm, ozone between 0.005-0.017 ppm, temperature 23-24 C, and total particulates 3-26 μg/m3. Other neurologic and generalized symptoms were also common, such as, irritative and respiratory symptoms. The results indicated that cabin conditions commonly may not meet the ASHRAE comfort criterion (ASHRAE Standard 161, 2007) for temperature, relative humidity, and CO_2 particularly during gate time.

In 2007, 12 flights were evaluated on 7 aircraft with durations ranging from 4.5 to 6.5 hours. All flights phases were investigated during the study and sampling was conducted in the center of the first three rows, but not the bulk head row, and in the center of the last three rows, as well. Temperature, relative humidity, and CO_2 were collected using portable Q-Track instrument (TSI-8550). Bacteria were monitored using N-6 impactor, tryptic soy agar (TSA) media and a high flow pump. Three sequential 4-minutes samples were collected for each sampling phase. In addition to the above, surface sampling inside the aircraft for cultural bacteria was conducted using cotton wool tipped sticks wetted with a Stuart solution. Each sample covered an area of 5 cm x 5 cm surface area. The cotton samples were stored in a sterile tube for later analysis in the laboratory. This collection technique is documented with the American Industrial Hygiene Association Biosafety Committee. The bacterial samples were kept cool and shipped on blue ice within 24 hours after sample collection. A total of 513 airborne culturable bacterial samples were collected. Total airborne bacterial concentrations did not differ between the front and back locations. Forty eight surface swab samples were collected from surfaces. Positive detections indicating the presence of bacteria was on 87.5% of the swab samples. The detected bacteria were analyzed and found to be coming from human skin surface or from dust and outdoor air. None were respiratory pathogens. Interestingly, it was concluded

that micrococeus luteus, m. roseus, and staphylococcus concentrations increase when passengers move within the aircraft which indicates that these are coming from humans (McKernan et al., 2008).

2.2 Background of airflow distribution studies inside enclosed spaces

Ventilation air systems and the quality of air supplied to passengers inside aircraft cabins have been an interest to many researchers and industries such as Airliner Cabin Environment Research (ACER), Federal Aviation Administration (FAA), Boeing, and many other affiliates. Various experimental and computational efforts have been done so far to understand the airflow distribution and behavior inside the cabins of aircraft for many reasons. Some of the major issues that are of concern are contaminant dispersion inside an aircraft due to airflow supplied by the ventilation system, the transport of viruses and bacteria, and oil leakage and its effect on passengers and crew that might be due to a leakage in the bleed air supplied through the compressors or the auxiliary power units of aircraft.

2.2.1 Air distribution studies

Airflow behavior inside most aircraft that have linear air supply diffusers installed longitudinally along the center of the cabin ceiling has been thought to be controlled only by two major circulations formed in the lateral direction of the cabin cross section as shown in Figure 2.2. However, this is partially accurate. Many studies have shown that the circulations in the transverse sides of the cabin are asymmetrical despite the fact that the supplied air through the diffusers is symmetrical. When the airflow hits the cabin side walls and the floor, part of the air will reflect back and causes mixing that can create tilted swirls and eddies that in turn might cause longitudinal airflow circulations in addition to the transverse circulations along the cabin's

cross section. Beneke (2010) showed that particulates dispersion, within an 11-row Boeing 767 mockup cabin, followed an exponential decay in the longitudinal direction as shown in Figure 2.3. In Figure 2.3, talcum powder was released in row 2 inside an 11-row mockup cabin and was sampled in each of the remaining 10 rows in the centerline seats.

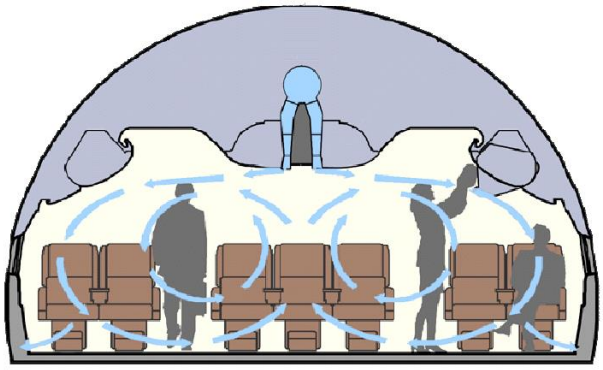

Figure 2.2 Airflow circulation in the cross section of an aircraft cabin

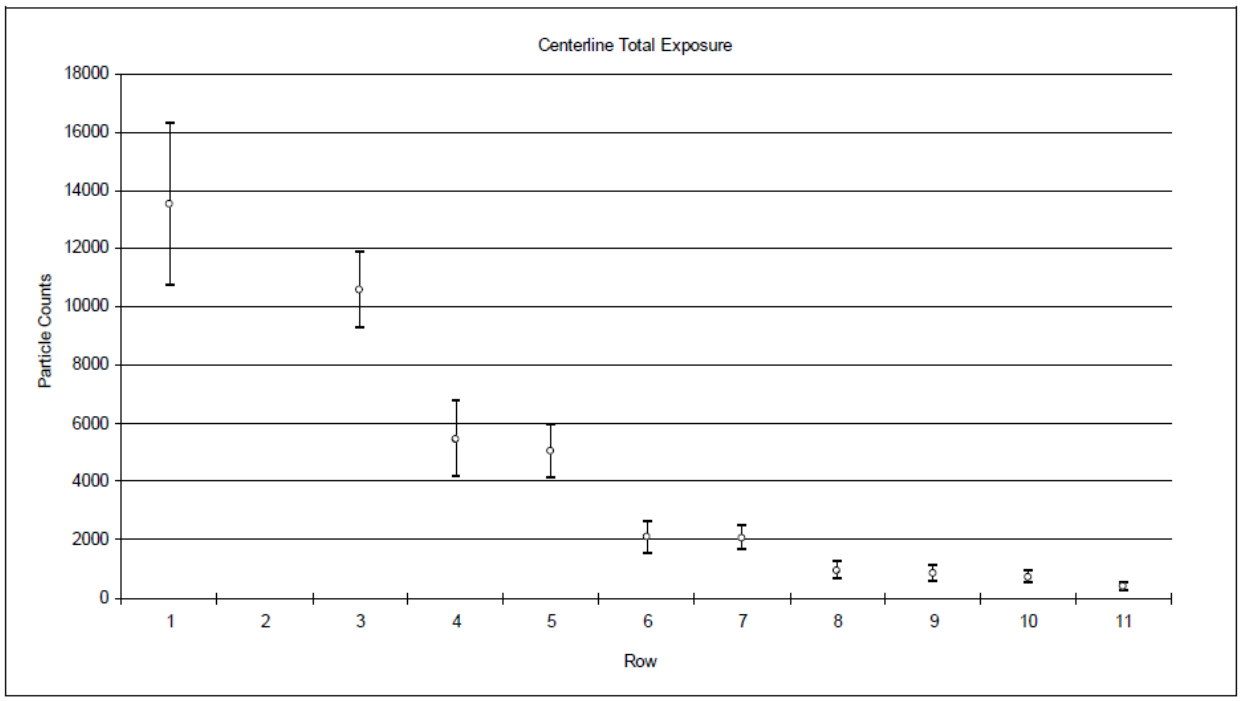

Figure 2.3 - Particulate dispersion in the longitudinal direction of an 11-row B767 mockup cabin (Beneke, 2010)

A numerical study by Gupta et al. (2011) investigated droplets transport from the middle of a seven-row, twin-aisle, fully-occupied aircraft cabin using CFD simulations. It was found that the bulk airflow pattern in the cabin played the most important role on droplet transport. In four minutes, the droplets were dispersed to all seven rows. The total airborne droplet fraction reduced to 48%, 32%, 20%, and 12% after they entered the cabin for 1, 2, 3 and 4 minutes, respectively, due to the ventilation from the environmental control system.

Various previous studies have indicated that there is a noticeable, but not well understood or documented circulation in the longitudinal direction inside aircraft cabins. The results of Trupka (2011), who investigated the airflow inside the same mockup cabin used by Shehadi et al. (2010) and Beneke et al. (2010), indicated that there were counter clockwise directed circulations in the fore and aft sections of the plan view of an 11-row Boeing 767 mockup cabin.

In 2010, Shehadi et al. investigated particles transport inside an 11-row B767 mockup cabin in both lateral and longitudinal directions. Investigations were conducted in the fore and middle sections of the mockup cabin. The middle section measurements included rows up to the third quarter of the longitudinal length of the cabin. Auxiliary observations that were not investigated in details, at that time, indicated that the right-front section of the mockup cabin had more particulates transported than into the left side, whereas, the opposite was true just after the middle section. A preliminary observation was concluded, but not investigated, which identified a counterclockwise swirl in the fore section of the cabin, similar to the results of Trupka (2011), and in the counter clockwise direction in the middle and aft sections of the cabin, as shown in Figure 2.4 (Shehadi et al., 2010).

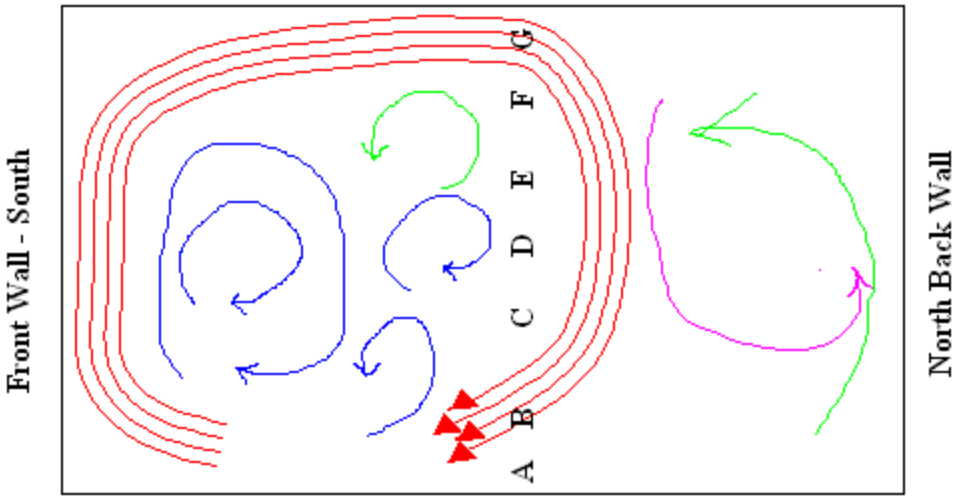

Figure 2.4 - Swirls in the plan view of 11-row B767 mockup cabin (Shehadi et al., 2010)

Another study on particle transport inside aircraft cabins was done by Beneke in 2010. No conclusions were made regarding any clockwise or counterclockwise directed eddies in the same mockup cabin used by Shehadi et al. in 2010. However, the results of particle dispersion in the lateral direction at different location in the fore and aft sections of the cabin, as shown in Figure 2.5, indicates that there was some asymmetrical particle distribution in the transverse section of the cabin at multiple locations of the cabin, as seen in row 3 and row 4. As in the previous studies, this phenomenon was not reported or documented, however, the results showed that there was a secondary circulation in the longitudinal direction controlling the transport of particles into either the right or left sections in the fore and aft sections of the cabin instead of being equally and symmetrically distributed. Lin et al. (2005) used LES (Large Eddy Simulation) to study airflow distribution inside a B767-300 aircraft and his results showed that the overall flow pattern was not symmetrical with respect to the cabin cross section even though the geometry and the boundary conditions were symmetrical. The study has proved that the airflow leaving the diffusers was symmetrical.

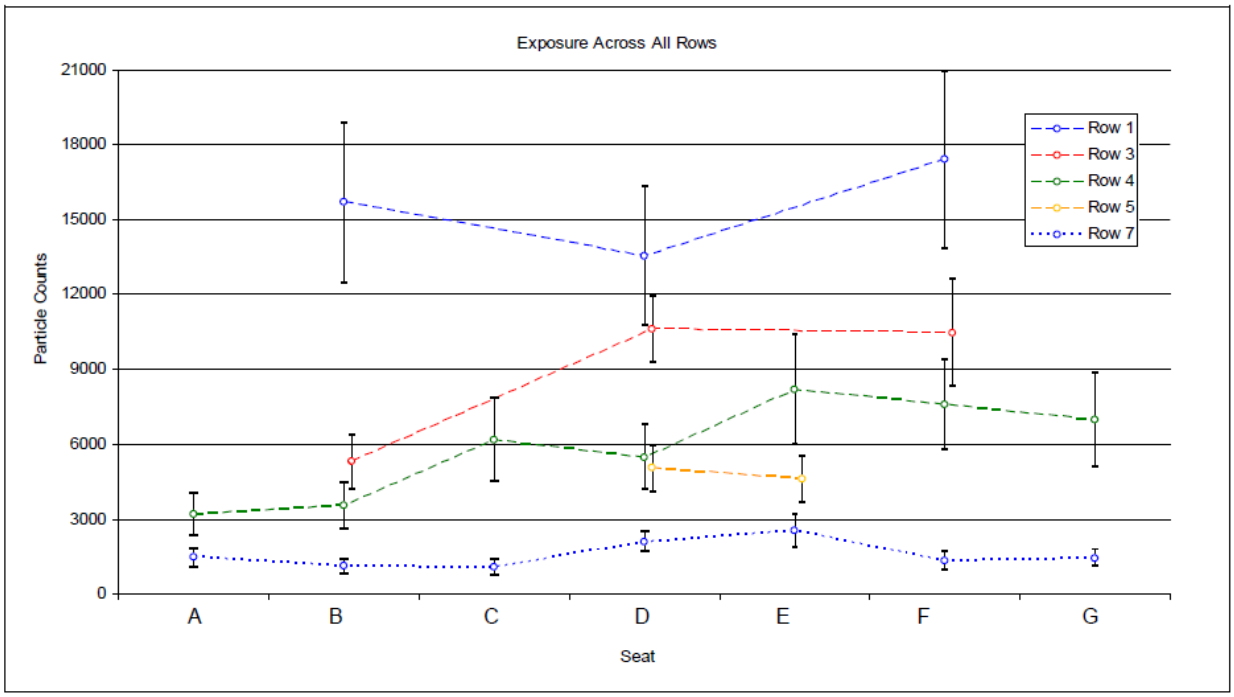

All Rows Total Exposure

Figure 2.5 - Particles transport in the lateral direction of an 11-row B767 mockup cabin (Beneke, 2010)

In 2013, three dimensional turbulent models were utilized by Ahmed et al. (2013) to simulate air distribution within enclosed spaces. The Realizable k-ε and SST k-ω models were utilized with the wall-function method. Simplified diffuser boundary conditions were used in the numerical models to simulate airflow in a room ventilated by grille diffuser, displacement diffuser, slot diffuser, and square diffuser. Four experimental tests were conducted in parallel with the simulation to check for the accuracy and the uncertainty of the suggested turbulence models. For experimental purposes, a room having a length, width, and height of 5.16 m, 3.65 m, and 2.43 m, respectively, was considered. Comparing the simulated results with experimental data, it was noted that the simplified methodology can predict indoor airflow and the change in temperature with acceptable accuracy (Ahmed et al., 2013).

Sarkar and Mandal (2008) investigated temperature and flow distribution inside enclosed spaces using experimental and numerical modeling. A rectangular enclosure made of glass having length of 1 m, width and height of 0.67 m was used. The prototype box had one single inlet and one single outlet with 0.0416 m diameter. Fluent software was used to simulate three dimensional CFD models. Comparing the experimental results with the numerical simulations, it turned out that k-ε and k-ω models give closer results for velocity and temperature distributions compared with Reynolds stress model. Gilani conducted another study implementing 3D steady Reynold's Averaged Navier Stokes (RANS) CFD models inside an enclosed space. The purpose of the work was to investigate temperature stratification in an indoor environment to help in the evaluation of displacement ventilation in buildings. Experimental temperature measurements were taken from another report published by the Heating and Ventilation Laboratory of the National Swedish Institute for Building Research. Steady RANS CFD simulations were performed for a one story building with a heat source and two ventilation openings. Gilani concluded that steady RANS model can accurately predict the temperature stratification in an indoor environment. The SST k-ω model showed better performance compared with other turbulence models (Gilani et al., 2013). For large enclosures, Buchmann recommended low Reynolds turbulence model which showed to predict better results than k-ε model (Buchmann et al., 1994).

2.2.2 Tracer gas studies

Tracer gas has been widely used in experimental studies to study ventilation effectiveness, airflow circulations, airflow velocities, and other parameters inside aircraft cabins, enclosed environments and structures, buildings, hospitals, and many other applications. Some

of the properties of the tracer gases to result in good simulation are reactivity and sensibility. The tracer gas used should be non-reactive. It should not react chemically or physically with any part of the system under study. The tracer gas should be insensibile so that it does not affect the processes that are under study. In other words, tracer gases should not affect airflow or air density of the system. In addition to that, the tracer gas used should have measurable criteria in order to be quantified. On top of all of the above properties, the tracer gas used should be safe and should be non-flammable, non-toxic, and non-allergenic. Some of the gases that have been used are carbon mono oxide, carbon dioxide, hydrogen, SF6 (sulfur hexafluoride), ethane, methane, and argon. Nitrous oxide (N_2O) has been used and was found to have a ±3% accuracy (Lidwell, 1960). Howard compared N_2O with hydrogen and oxygen using an infrared analyzer, a katharometer, and by absorption in aqueous chromous chloride for each gas, respectively (Howard, 1966).

Yan et al. (2009) conducted tracer gas experiments in a full-scale Boeing 767-300 mockup cabin to study air transport process within the mockup cabin. The mockup cabin consisted of five rows with 7 seats in each row. Ventilation air was provided through diffusers located around the central storage bin at rates of 816 m^3/hr (480 cfm), 1052 m^3/hr (618 cfm), and 1259 m^3/hr (740 cfm) corresponding to 80%, 100%, and 120% of the full ventilation load, respectively. Carbon-dioxide was used as tracer gas and it was injected at a rate of 4.5 lit/min for 5 minutes. Infrared sensors were used to collect and sample CO_2 for a duration of 1000 seconds after the release of tracer gas. Yan concluded that the ventilation system divided the cabin into two separate domains. Each side had a big swirl in the lateral cross sectional direction. The simulation also concluded that longitudinal airflow was inevitable, because of obstacles in the cabin. Tracer gas released beside sidewalls was exhausted out of the cabin faster than gas

released relatively away from the walls. It was concluded that there existed a longitudinal airflow from row to row. Yan also concluded that higher ventilation rates can dilute the tracer gas and improve its mixing which would yield lower concentrations. Upon applying the k-ε turbulence model, Yan was able to notice a significant difference in tracer gas concentrations between the left and the right sides of the cabin in the same cross sectional row as shown in Figure 2.6 (Yan et al., 2009).

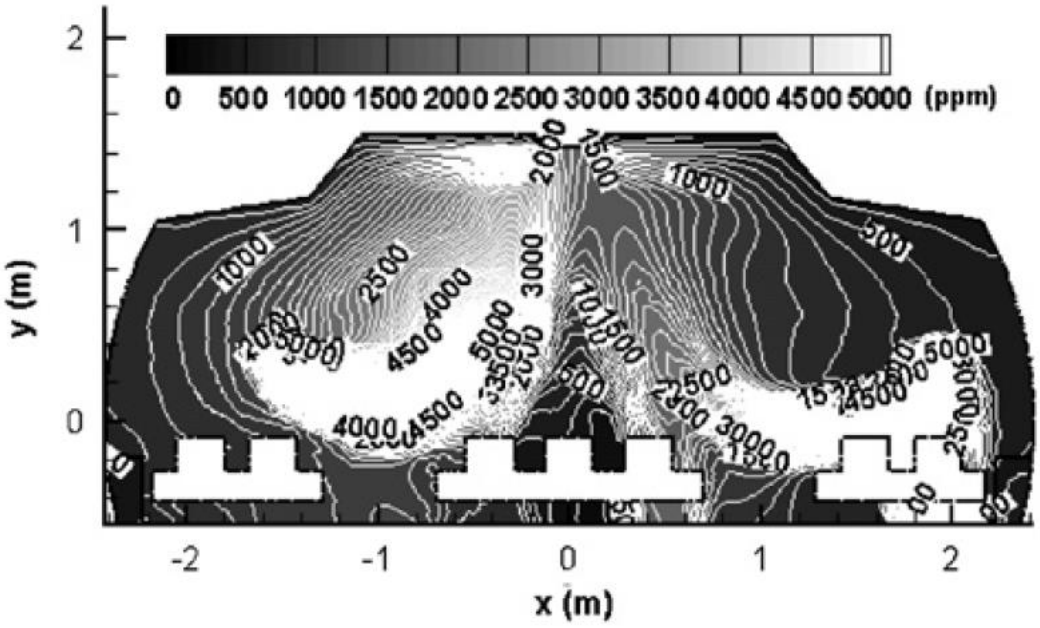

Figure 2.6 - Simulated iso-CO_2-concentration contour evolution in the vertical plane of a Boeing 767 cabin (Yan et al., 2009)

A group of scientists at Ernest Orlando Lawrence Berkeley National Laboratory conducted experiments using passive tracer gas techniques to measure and evaluate ventilation rates in residential homes. Ventilation rates and conditions were monitored and controlled during the experiments. Large numbers of samplers were used to collect and monitor the tracer gas. Active sampling methods were used by acquiring sampling bags with programmable samplers. The gas was not continuously sampled, but rather it was sampled over regular time

intervals. The resulting samples characterized the average concentration of the tracer over the sampling period. On the other side, passive samplers used stainless steel desorption tubes. However, passive samples required multiple day sampling. Different number of heated emitter blocks with active samplers and passive samplers were used in 3 different houses. Experiments were run from June to December with various ventilation conditions. The spatial variability of the tracer concentrations decreased with the use of a central ventilation system fan which indicated that there was more effective mixing when using a central ventilation system (Lunden et al., 2012).

Bosbach conducted an experimental and numerical study for the turbulent ventilation inside aircraft cabins (Bosbach et al, 2006). Reynolds Averaged Navier-Stokes (RANS) equations were used for numerical simulations, whereas PIV was used for the experimental testing. The model used half of an aircraft cabin modeling an Airbus A380 aircraft cabin. The cabin has been reduced to a box of height 1.35 m, length 3.43 m, and width 2.0 m. The airflow entered the modeled chamber through three slits on the side wall right above the windows at a rate of 40 lit/s and exited through same openings at the floor level. For experimental studies, tracer particles were added to the inlet air. The tracer particles were made up of 1 to 3 mm diameter soap bubbles filled with helium. Plexi-glass windows were used to allow the formation of a light sheet using pulses of laser combined with cylindrical and spherical lenses. The duration between two pulses was five nano-seconds. The sheet had a 30 mm thickness with a 45^{o} opening angle. Comparing the numerical results using RANS equations with the PIV results revealed that low Reynolds k-ε turbulence models should be used to describe turbulent velocity fields inside aircraft cabins. Other models over-predicted the jet diffusion. It was concluded that structured grids can increase the speed of the computation time.

Kuhn et al. (2009) conducted a PIV study similar to Bosbach to study forced and mixed convection inside aircraft cabins. Tracer gas was illuminated using 30-50 mm thick light sheet with a 40^{o} opening angle. However, the slit was made in the floor of the mockup cabin instead through the side wall windows. The study investigated the effect of interactions between thermal plumes and air jets inside the cabin. It concluded that cooling conditions favors more asymmetrical airflow distribution.

In 1990, Sherman classified concentration distribution analysis inside enclosed spaces into three main techniques: regression, integral, and averaged techniques. In the regression and integral analysis techniques, the ventilation rate was assumed to be constant, whereas, in the averaged techniques different ventilation rates could be applied. Other analysis techniques fell under either steady state conditions or transient ones. Concentration accumulation was assumed to be negligible in the steady state techniques (Sherman, 1990). Applying the regression techniques, equation (2.1) represented the concentration decay inside a single zone if there was no source generation.

$$C(t) = C_R e^{-\lambda_R t} \tag{2.1}$$

where λ is the air change rate (hr^{-1}), C_R and λ_R are parameters to be fit.

Equation (2.2) and equation (2.3) were suggested by Sherman to represent the integral decay and average decay, respectively.

$$\lambda = \frac{C_{initial} - C_{final}}{T.C_{avg}} \tag{2.2}$$

$$Q_{avg} = \frac{V}{T}\ln\left(\frac{C_{initial}}{C_{final}}\right) \tag{2.3}$$

where C represents the tracer gas concentration in mol-tracer gas per mol of air, V is the volume in m^3, Q is the ventilation flow in (m^3/hr), and T is the length of measurement period in hour (Sherman, 1990).

Horstman investigated numerically the transport of carbon dioxide in a half aircraft cabin model. The aim of the study was to model breathing behavior inside aircraft cabins. It was found that tracer gas, which was mainly composed of carbon dioxide, dispersed in three minutes into half of the cabin after its release. The maximum CO_2 concentrations remained near the source (Horstman, 1988).

Zhao conducted a particle image velocimetry (PIV) measurement to predict indoor airflow fields and air velocity distribution to validate numerical simulation models in a step to analyze ventilation effectiveness. The results showed that the PIV technique can be an effective method to quantitatively measure the room air velocities, especially for those regions with very low velocities (Zhao et al., 2001).

In 2005, Sun conducted a study in an aircraft cabin representing a Boeing 767 aircraft cabin. The cabin consisted of 5-rows in the longitudinal direction with 7 seats in each row. Each seat was occupied with a heated manikin by providing the manikins with electrical wire heaters around their waist. The inlet flow was approximately 37.8 lit/min (80 cfm). Velocities ranged between 0 and 0.3 m/s with an average of approximately 0.2 m/s. It was also concluded that an increase in the number of heated manikins can lead to a decrease in velocity variations in the cabin (Sun et al., 2005).

2.2.3 Velocity Analysis studies

There are relatively few studies conducted to study the airflow speed inside aircraft compartments and cabins.

A full scale section of a Boeing 767 aircraft cabin, consisted of 5 rows with 7 seats in each row, was used by Wang et *al*. (2008) to evaluate the ventilation effectiveness inside aircraft cabins. All seats were equipped with heated manikins to simulate human bodies. Heat was created by placing heating pads around the neck of the mannequins. Carbon dioxide was released in each seat of the 35 seats inside the mockup cabin at a height equivalent to the passengers' breathing zone. Non-dispersive infrared sensors were used to sample the collected CO_2 in every seat to reflect the effectiveness of the ventilation inside aircraft cabins. Air was supplied at a rate of 1052 m^3/h (619 cfm) which would be equal to approximately 30 m^3/h (17.5 cfm) per passenger. To study the effect of ventilation on particulates transport, other rates were considered which were 70%, 80%, 90%, and 120% of the above supply flow rate. It was concluded that there were two circulations controlling the flow in the lateral cross section of the mock-up cabin. Velocity distribution showed an asymmetrical behavior in the lateral cross section of the cabin, as shown Figure 2.7.

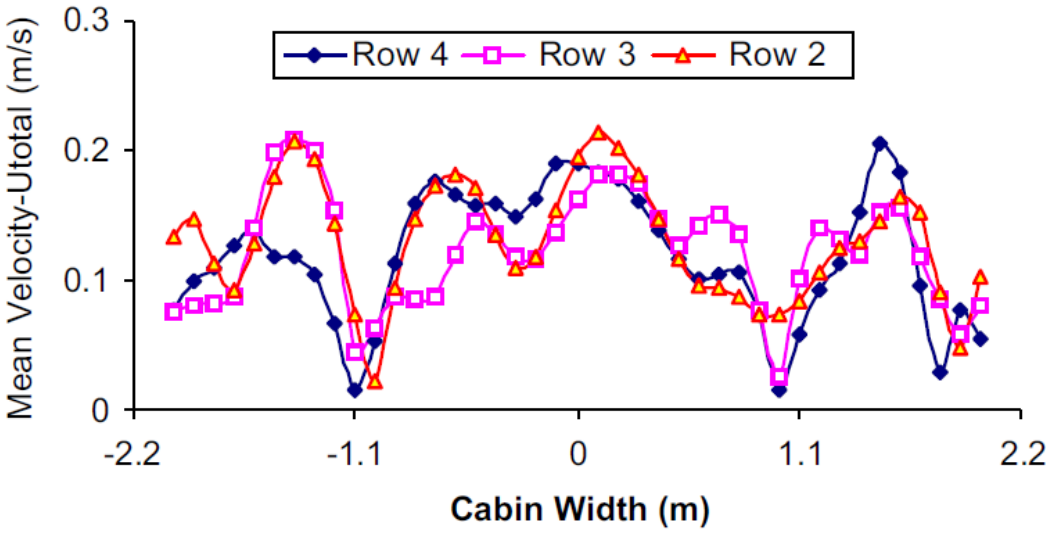

Figure 2.7 - Air velocity distribution in the lateral direction of a Boeing 767 Mock-up Cabin (Wang et al., 2008)

In 1997, Muller et al. applied particle tracking velocimetry over one half of a cabin representing an Airbus A300 aircraft model. Helium filled soap bubbles were used as seeding particles with a 0.7 mm thick light sheet (Muller et al., 1997). Later on in 2000, Muller used an improved helium bubble generator to conduct PIV measurements. Halogen lamps were used to create the light sheet that spanned over one half of the cabin section. However, halogen lamps can add extra heat source to the cabin (Muller et al., 2000). In both studies, there was an agreement between the PIV or PTV and the CFD simulations.

In 1998, Emmerich and McGrattan conducted a detailed literature review summarizing the state of the art CFD research in building ventilation and indoor air quality (IAQ) fields. The review included studies related to airflow distribution, ventilation effectiveness, temperature distribution and stratification, and thermal comfort for various ventilation systems and room configurations. The review covered various turbulence modeling techniques such as k-ω, k-ε eddy viscosity, the algebraic stress model (ASM), and the differential stress model (DSM) to predict the flow in a room. The ASM adds a consideration of anisotropy of Reynolds stresses to

the k-ε model by adding additional algebraic equations. The DSM or the Reynolds stress model (RSM) uses Time-Averaged –Navier-Stokes equations with differential equations to consider anisotropy of Reynolds stresses. For velocity determination the DSM model served best, whereas, for temperature predictions, both the DSS and the ASM were better than k-ε model. Large Eddy Simulation (LES) has been shown to predict airflow patterns better than the typical k-ε model. LES model with Smagorinsky subgrid-scale model was applied to simulate and test the ventilation effectiveness in a room. Experimental measurements agreed with the predicted results in the main core of the room, but was not as good near the floor and the ceiling where no empirical near-wall model was implemented (Emmerich and McGrattan, 1998).

2.3 Turbulence length scale

With turbulent conditions, there are various parameters that should be investigated in order to have a full understanding of the flow behavior. Some of these parameters are the turbulence time scale, turbulence length scale, and turbulence velocity scale.

The rate at which momentum is transferred inside a tube of radius "R" to its wall is proportional to the average velocity V in laminar flow and to V^2 in turbulent flow. Thus, it was important to investigate some other parameters in turbulent flow that are different than in laminar flow. Starting with time scales, equation (2.4) defines the time scale with laminar flow inside a tube, whereas equation (2.5) defines that with turbulent conditions. Equation (2.5) is the Kolmogorov characteristic time scale for dissipative eddies where τ is the time scale, ν is the kinematic viscosity, and ε is the dissipate rate.

$$\tau_L = \frac{R^2}{\nu} \tag{2.4}$$

$$\tau_K = \left(\frac{\nu}{\varepsilon}\right)^{\frac{1}{2}} \tag{2.5}$$

Ludwig Prandtl was the first one to use one-equation turbulence models in which an equation for the turbulence kinetic energy is solved with the turbulence length scale known. However, Kantha reported that it was Kolmogorov, who was the first to propose the use of two-equation models in which equations for both the turbulence kinetic energy and the length scale were solved. There are many ways to prescribe the turbulence macro-length-scale " l ". The simplest and the most arbitrary method has been to simply prescribe it arbitrarily by an algebraic equation. The first method to evaluate the macro- turbulent length scale in a boundary layer on a solid surface is to assume that it is proportional to the distance from the surface (Kantha, 2004).

$$l(y) = l_0 \left(\frac{k.y}{k.y + l_0}\right) \tag{2.6}$$

where "k" is the von Karman constant (k=0.4), y is the distance from the surface, and l_0 is the asymptotic value of l toward the edge of the boundary layer. l_0 can be defined either as part of the turbulent boundary layer thickness or might be calculated using equation (2.7) (Kantha, 2004 cited from Mellor and Durbin, 1975; Martin, 1985, 1986).

$$l_0 = \alpha \left(\frac{\int_0^\infty q.y.dy}{\int_0^\infty q.dy}\right) \tag{2.7}$$

where α is an empirical constant and

$$q = \left(\frac{\varepsilon}{B_1.l}\right) \tag{2.8}$$

B1 = 16.6 (Kantha, 2004 cited from Mellor and Yamada, 1982)

While the influence of the rotation of the reference frame on small scale turbulence is negligible in geophysical flow situations, this is not true for many engineering devices (Kantha, 2004 cited from Johnson et al., 1972; Watmuff et al., 1985). The maximum eddy size appears to be much smaller in rotating boundary layers such as the neutral atmospheric boundary layer (ABL) compared to nonrotating boundary layers in the laboratory. The length scale "l" is about 0.09 times the boundary layer thickness in laboratory boundary layers, while a more appropriate value is 0.03 for the neutral (ABL) (Kantha, 2004). In many other applications, it may be necessary to carry out calculations on mixing all the way to the boundary. Sediment transport in an oceanic bottom boundary layer is a typical example. Also, it is important to integrate to the wall in the case when the turbulence includes separation of flow.

Thus, in turbulent boundary layer

$l \sim y$ where y is the distance from the wall including the viscous effects.

The largest eddies in the flow account for most of the transport of momentum and energy. The size of these eddies is only constrained by the physical boundaries of the flow. The size of the largest eddy is the "Integral Length Scale" and the smallest eddies is micro-scale length scale. For example, the upper bound or the integral length scale inside pipes is of the order of magnitude of the flow, thus

$l_{pipe} \sim 2D$ where D is the pipe diameter and

$l_{pipe} \sim \delta$ where δ is the boundary layer thickness

Rodi (1974) gave different values for the

$\frac{l}{\delta} =$ 0.07 (mixing layer)

0.09 (plane jet)

0.075 (round jet)

0.16 (plane wake)

As mentioned earlier the integral length scale is constrained by the physical boundaries of the domain. The integral time scale is the time needed for the largest possible distance within a given domain, defined as integral length scale, to be convected. If we define the velocity fluctuation, within a convection field, as u(t) where t is the time, then the correlation for the convection is

$$\rho(\tau) = \frac{\overline{u(t).u(t+\tau)}}{\overline{u(t)^2}} \tag{2.9}$$

where τ is the Kolomogorv time scale. The integral time scale can then be defined as

$$T = \int_0^\infty \rho(\tau) d\tau \tag{2.10}$$

The lower bound or the micro length scale is set by the influence of viscosity. Kolmogorov first similarity hypothesis stated that the only factors influencing the behavior of the small scale motions are the overall turbulence kinetic energy production rate, which equals the dissipation rate, and the viscosity. The dissipation rate will be independent of viscosity, but the scales at which the kinetic energy is dissipated will depend on both the dissipation rate and viscosity. Defining η as the micro length scale

$$\eta_K = \left(\frac{\nu^3}{\varepsilon}\right)^{\frac{1}{4}} \tag{2.11}$$

This small length scale is an indication of the scale where turbulent kinetic energy (TKE) is dissipated into heat. Combining equation (2.5) and (2.11) together, the Kolmogorov speed scale is defined in equation (2.12).

$$V_k = (\varepsilon.\nu)^{1/4} \tag{2.12}$$

An intermediate length scale was defined by Taylor (λ) and it falls in between the Kolmogorov length scale (η_K) and the integral length scale (L_o).

$$\eta_K << \lambda << Lo \tag{2.13}$$

Similarly, Taylor's time scale falls in between the integral time scale and the Kolmogorov time scale.

$$\tau_k << \lambda_t << T \tag{2.14}$$

2.3.1 Relation between Kolmogorov length scale and integral length scale

$$\frac{L_o}{\eta_K} = L_o.\varepsilon^{1/4}\nu^{-3/4}$$

$$= \frac{\varepsilon^{1/4}}{\left(V_o^3/L_o\right)^{1/4}} L_o.L_o^{1/4}V_o^{3/4}\nu^{-3/4}$$

$$= \left(\frac{\varepsilon}{V_o^3/L_o}\right)^{1/4}.\left(\frac{L_oV_o}{\nu}\right)^{3/4}$$

Using the definition that will be introduced later for the dissipation rate, where

$$\varepsilon = \frac{V^3}{L}$$

Thus,

$$\frac{L_o}{\eta_K} = \left(\frac{L_o V_o}{\nu}\right)^{3/4} = (Re_{Lo})^{3/4} \quad (2.15)$$

where, ε: dissipation rate; Lo is the integral length scale; Re is the Reynolds number; ν is the kinematic viscosity; η_K is the Kolmogorov length scale;

Therefore, the integral and micro-scale length scale are related with Reynolds number based on the integral length scale as shown in equation (2.15).

Chapter 3 - Experimental Setup

In order to meet the objective of the study that was summarized in the Introduction section, a testing chamber that mimics a Boeing 767 passenger cabin equipped with actual aircraft equipment, extracted from a salvaged Boeing 767, was utilized for this study. The mockup cabin external profile was made up of wooden structure. Eleven rows of seats with 7 seats in each row were equipped with thermal heated manikins.

This section gives more details about the experimental set up and experimental methodologies used to achieve the goals of the study. It also outlines the manner in which the instruments were setup.

3.1 Experimental facility description

3.1.1 Mockup cabin description

To understand the airflow behavior inside aircraft cabins in a realistic way that is close to actual conditions, a full-scale aircraft mockup cabin housed within the Airliner Cabin Environment Research (ACERL) laboratory at Kansas State University was utilized. The mockup cabin mimics a Boeing 767 aircraft and is one of the largest available research mockup cabins in its class. The geometric shape and the dimensions of the mockup cabin are the same as an actual 767 Boeing aircraft cabin. It has a length of 9.41 meters and a width of 4.72 meters. The overall dimensions of the cabin with two hallways located to the east and west sides of the mockup cabin are shown in Figure 3.1. The mockup cabin seats, the air supply duct, and the diffusers are parts from a salvaged Boeing 767 aircraft. Within the cabin, there are 11 rows of seats distributed longitudinally with 7 seats in each row. Each seat in the cabin is occupied by an inflatable manikin which is instrumented with 10 m wire heater elements to generate

approximately 100 Watts which is equivalent to the average heat gain from a resting adult (ASHRAE Fundamentals, 2009). There are two outboard and two centered simulated stowage bins installed along the length of the cabin. The air diffusers are located between the two centered stowage bins which are similar to the air outlets indicated in Figure 3.2. The data acquisition system and all equipment used for testing purposes were equipped in the east and west hallways shown in Figure 3.1. Figure 3.2 shows the interior of the mockup cabin with the diffuser outlets indicated. For further details about the cabin profile, seats location or geometry, the following report serves as a good asset for this purpose "Draft Final Technical Report, Contaminant Transport in Airliner Cabins Project, Kansas State University, 2009."

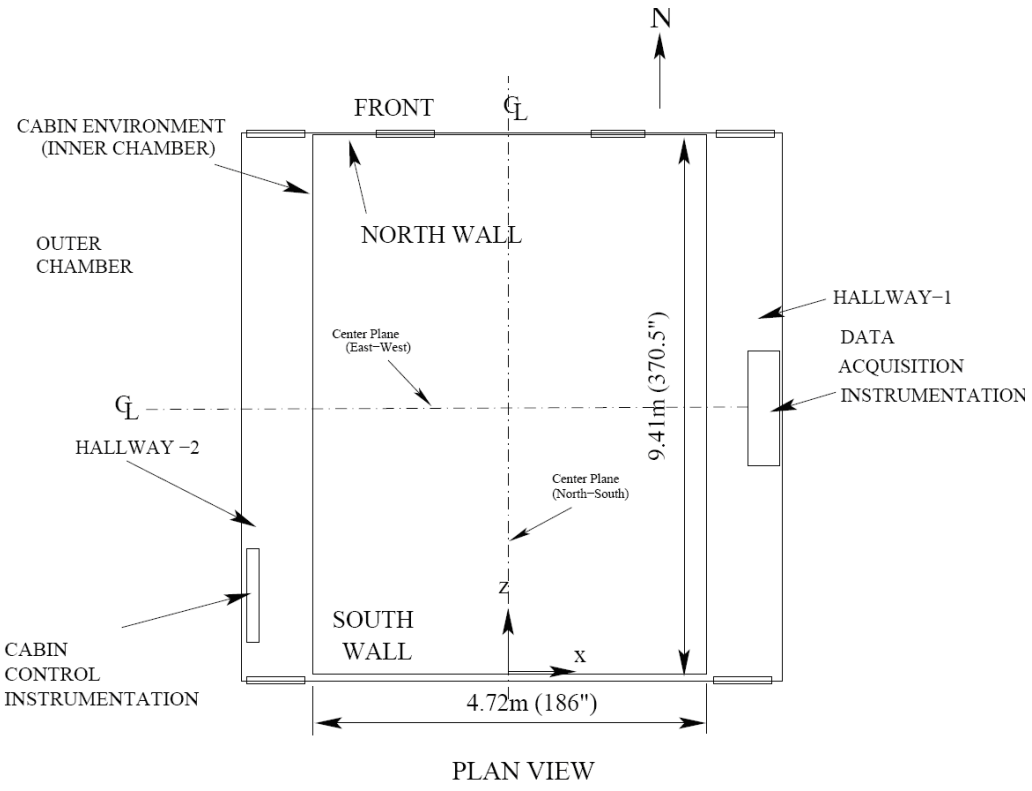

Figure 3.1 - Cabin chamber overall dimensions and sections

Figure 3.2 – Interior section of the Boeing 767 mockup cabin at ACER laboratory showing the seats, thermally heated manikins, and other sections of the cabin

3.1.2 Air supply system

The mockup cabin was supplied with 100% outside air, conditioned to 15.6 $^{\circ}$C (60 F) at the upstream of the cabin main supply duct with a flow rate of 0.661 m^3/sec (1400 cfm).

3.1.2.1 Heating, cooling, and dehumidifying cycles

The temperature of the supplied air was controlled by an electric water heater and a chiller system. The humidity was controlled by a Munter dehumidifier Figure 3.5. The heating and cooling system, used to control the temperature of the air, is shown in Figure 3.3 and Figure 3.4. The dehumidification system was installed upstream to the duct going into the heating and cooling cycles as shown Figure 3.3. Further details about the technical specifications for any component illustrated in Figure 3.3 can be found in Shehadi (2010).

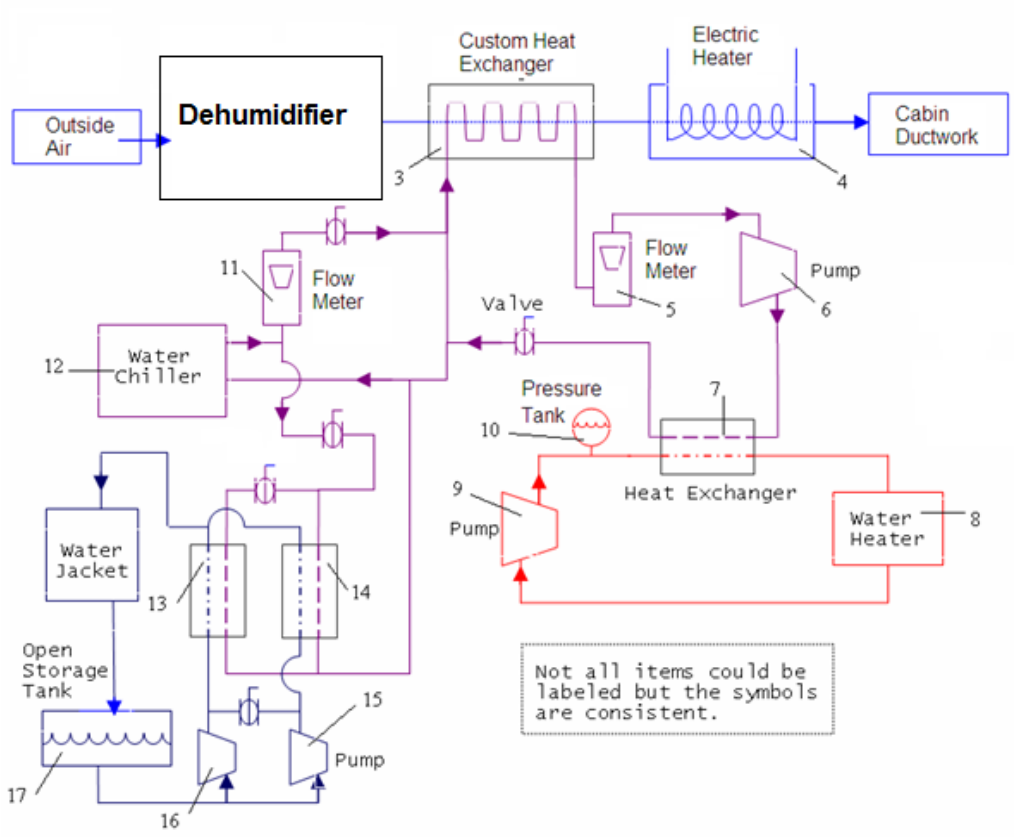

Figure 3.3 – Supplied air control system

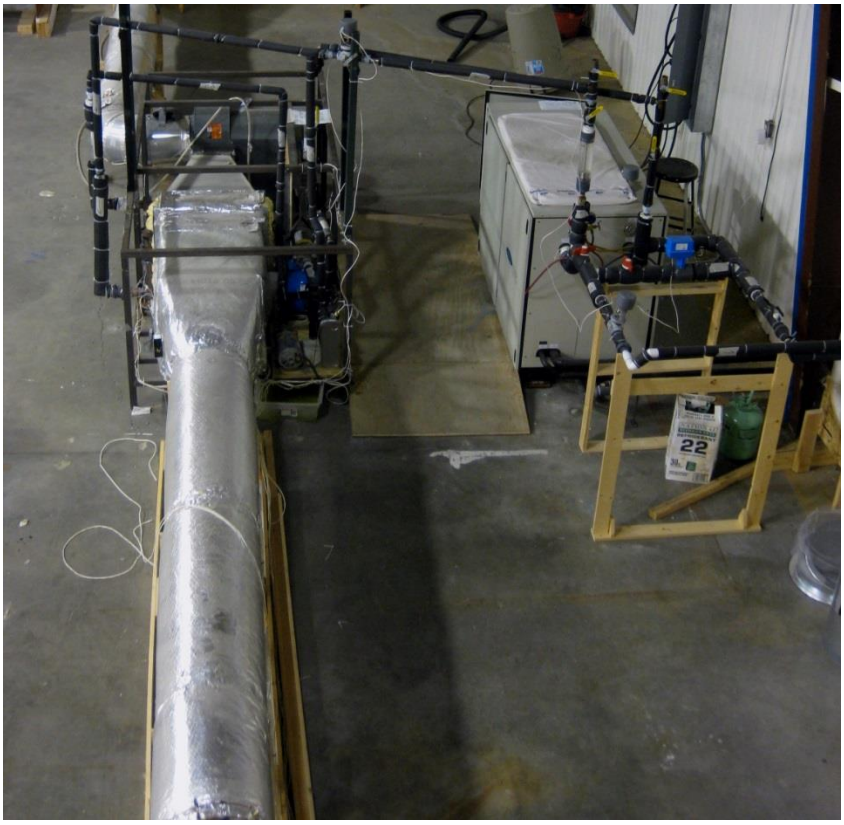

Figure 3.4 - Heating and cooling system

Figure 3.5 - Dehumidification system

3.1.2.2 Air distribution system

Figure 3.6 shows the external enclosure of the mockup cabin with the supply inlet and exhaust ports indicated. Inside the external enclosure, 17 pairs of clear and smooth-wall plastic hoses were attached to the main supply duct whose cross section was decreased along the length of the mockup cabin, as shown in Figure 3.7. The numbers below the diffusers in Figure 3.7 refer to the supply hose pairs. The hose connectors extend approximately 38 mm (1.5 inches) from the supply duct (Figure 3.8-B). Inside the duct, the connector is flush with the supply duct wall. The edge between the supply duct and the connector is sharp (Figure 3.8-C). Each hose connector is fitted with a round and thin orifice as shown in (Figure 3.8-D). These orifices presumably were to aid the balance of the flow along the length of the cabin.

Figure 3.2 shows the linear diffusers installed within the mockup cabin that were used to supply the fresh air into the cabin. The diffusers are built of 11 ft (3.35 meters) sections as shown in Figure 3.9-A. The diffuser section mounts to the back side of the centered overhead bin assembly. Air enters through the hoses connected shown in Figure 3.7 and Figure 3.8-E to the top of the diffuser assembly where it enters a plenum that extends the full length of the diffuser section. The diffuser is sealed to the back of the overhead bin assembly at the top. Air passes from the plenum through a narrow gap near the top of the assembly. This gap is established by small spacer buttons that are mounted on the edge of the lip (see Figure 3.9-C). The purpose of this narrow gap is to provide uniform flow over the full length of the diffuser section. This gap is approximately 3.2 mm (0.125 inches) wide. End caps plugged both ends of the diffuser assembly as shown in Figure 3.9-D. When mounted in the cabin, the diffusers form a single continuous unit from the front to the back end of the cabin as viewed from inside the cabin, as shown in Figure 3.2. However, there is no fluid path connection between the 11 ft

diffuser sections since flow is blocked from flowing between sections by the end caps. Figure 3.10 shows the locations of the joints between the diffuser sections in the cabin mockup. The two back-to-back end caps take up approximately 50.8 mm (2 inches) of space. Thus, there are approximately 50.8 mm at each joint between the sections where there was no airflow.

To test the homogeneity and uniformity of the mixed air temperature inside the cabin, measurements at different locations showed that the average air temperature inside the cabin ranged between 18.7 $^{\circ}$C at the tip of the diffuser to 24.2 $^{\circ}$C in regions close to the floor, as shown in Appendix A - Figure A.1 and Figure A.2. The east and west, shown in the legend of Figure A.1 and Figure A.2, indicate that the measurements were taken either in the east or the west sections of the mockup cabin. The minimum and maximum represent the minimum temperatures against the maximum temperatures recorded during each respective test. To check the validity of the differences in the recorded temperatures, the distributed sensors were run with no airflow inside the cabin. Two identical fans were used in each aisle of the cabin, east and west, to push the air and create airflow circulation inside the mockup cabin. The differences in the maximum recorded temperatures between the east and west aisles are shown in Figure A.3. As can be seen in Figure A.3, the maximum differences in temperature between the east and west aisles at different locations ranged from as low as 0.05 $^{\circ}$C to 0.45 $^{\circ}$C. This indicates that the sensors and the DAQ system were running accurately with minimal and acceptable differences.

Figure 3.6 - Aircraft mockup cabin external enclosure

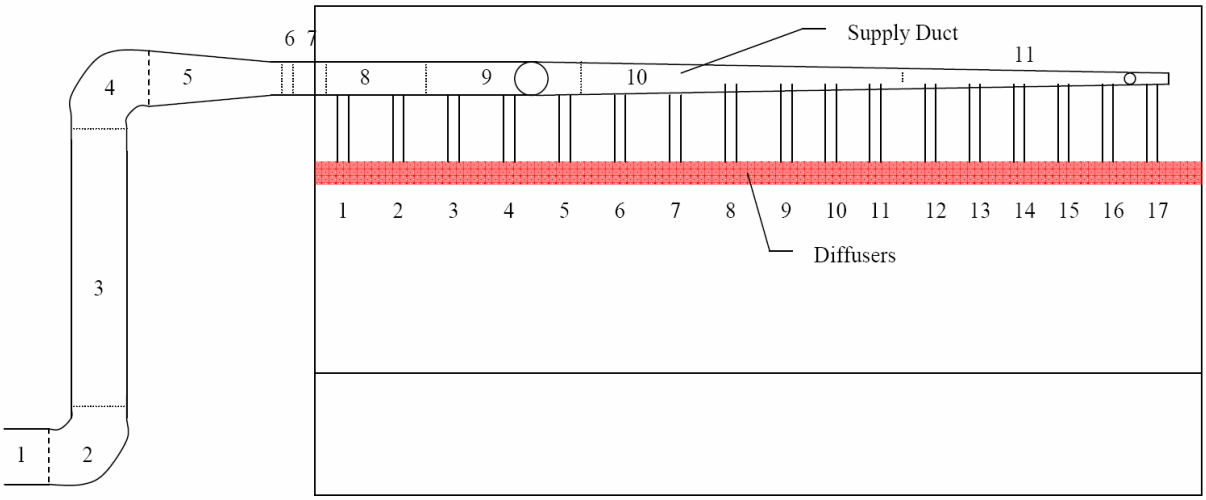

Figure 3.7 - Air supply ducting layout

A) Plastic Lines from Supply Duct to Diffusers

B) A Typical Section of Supply Duct

C) Interior of Supply Duct Showing Hose Connector Interface

D) Close Up View of Supply Hose Connectors and Flow Restrictors

E) Hose Connection to Supply Duct

F) Hose Connection to Diffuser

G) Supply Duct Joint

Figure 3.8 – Air supply duct details inside the enclosure located above the cabin profile

Figure 3.9 - Diffuser assembly

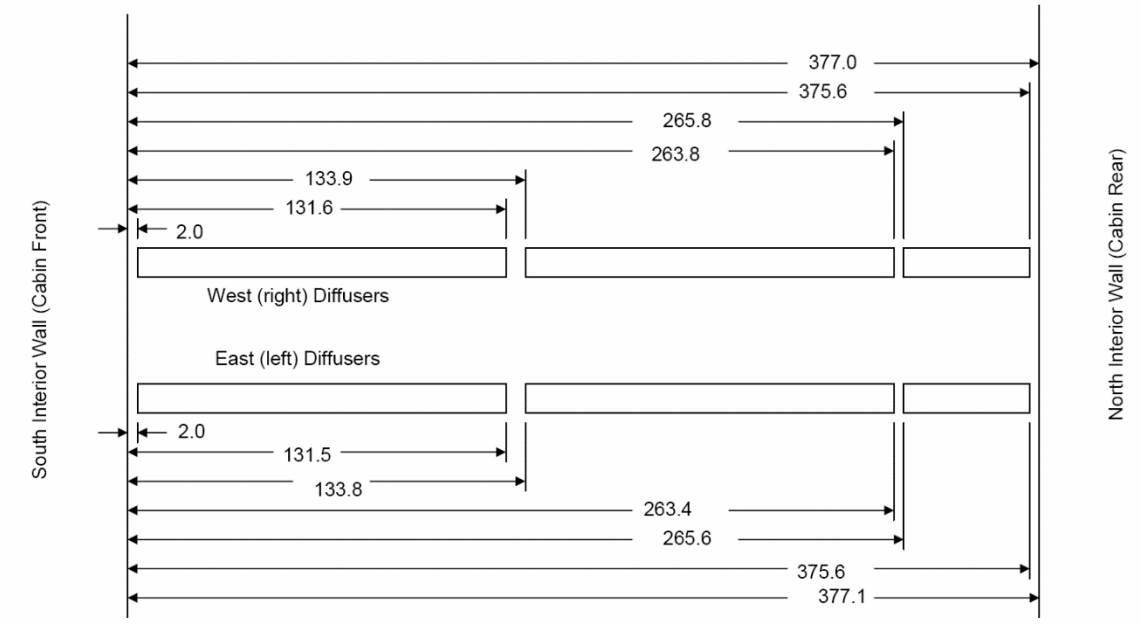

Figure 3.10 - Diffuser joint locations showing the diffuser plenum end caps (All dimensions are in inches and drawing is not to scale)

3.1.2.3 Air supply instrumentation and control

The control system operation was based on two key parameters:

1. Desirable flow rate

2. Supply air temperature

As shown in Figure 3.1, the cabin control and instrumentation board was located in the west hallway. Data from all the sensors was sent to this board and then from this board was transferred to the computer to perform the required analysis. Based on the received data from the sensors, new orders were sent to the controllers. Figure 3.11 shows the different parts of the control system in which the arrows indicate the flow of data signals.

Figure 3.11 – Schematic of the supplied air control system

3.1.3 Flow visualization experimental system setup

Two approaches were followed in investigating the airflow behavior inside the Boeing 767 11-row mockup cabin. The first approach was qualitative and it used theatrical smoke to visualize the airflow inside the mockup cabin. The second approach was quantitative and it used industrial carbon dioxide as tracer gas which was released and sampled at different locations inside the mockup cabin.

Theatrical smoke was utilized to visualize the airflow inside the mockup cabin to help in determining critical locations that might be of interest to be tackled when conducting the tracer gas sampling. Theatrical smoke generator was enclosed inside a sealed box that had an outlet

connected into the cabin using polycarbonate tubes. The tubes were used as release ports inside the cabin. All lights inside the cabin were turned off and a laser sheet was created at a height of 1.23 meters above the cabin floor by placing a cylindrical lens in front of a laser source. A digital camera was used to capture videos and snap shots of the detected smoke. A schematic showing the experimental setup is shown in Figure 3.12.

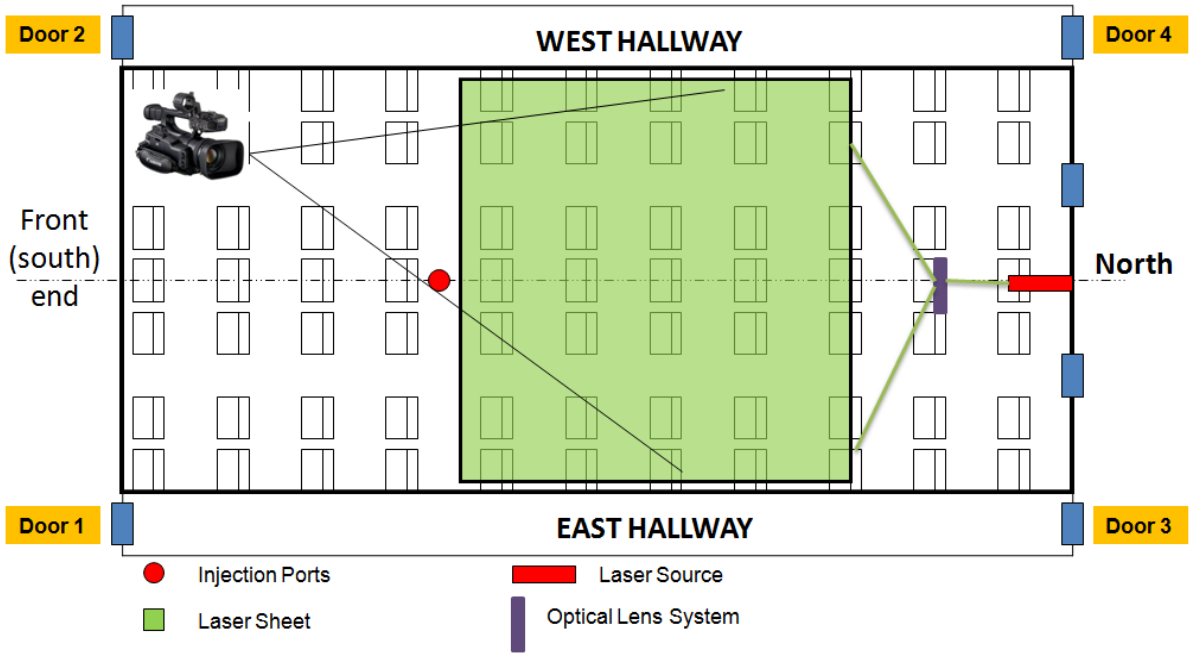

Figure 3.12 - Smoke visualization experimental setup

3.1.4 Tracer gas experimental system setup

Tracer gas has been widely used in experimental studies to study ventilation effectiveness, airflow circulations, airflow velocities, and other characteristics and parameters inside aircraft cabins, enclosed environments, buildings, hospitals, and many other applications. To track air movement throughout the cabin and to check for the swirling effect inside it, tracer gas was used. The gas was mainly composed of carbon dioxide. Carbon dioxide was sampled at different locations throughout the cabin.

3.1.4.1 Injection system

3.1.4.1.1 Tracer gas injection system description

A system was installed inside the mockup cabin to inject tracer gas. The mixture made up of CO_2 and helium was mixed and injected into the cabin through proper tubing connections. The flow of each gas was controlled by mass flow controllers. The flow controllers were controlled through an Agilent DAQ system and a 2-channel power supply unit. However, the values could be manually overridden by entering the intended values of the flow rates manually into the 2-channel power unit. Figure 3.13 gives a schematic illustration of the tracer gas injection system.

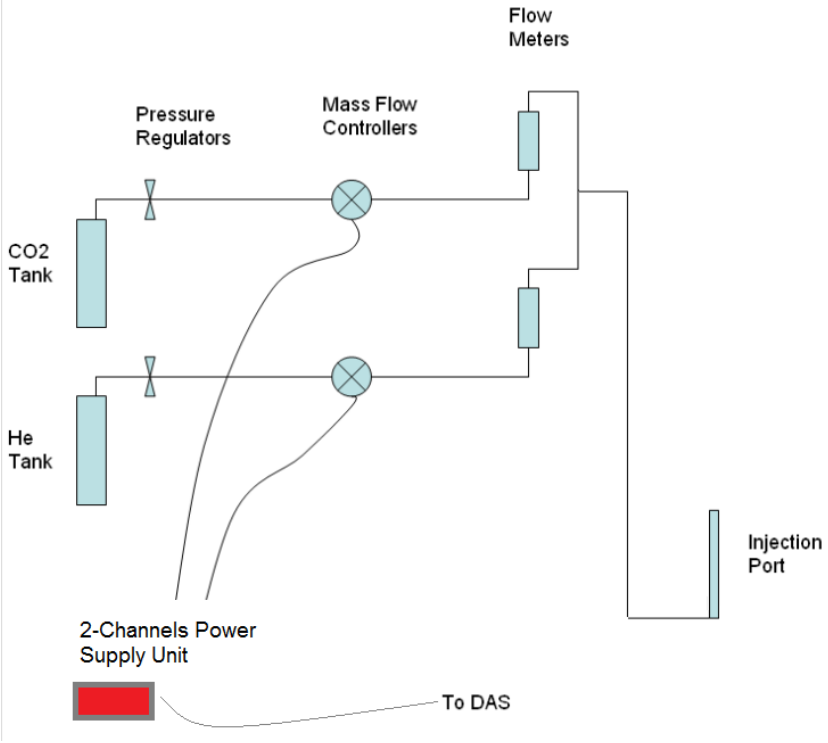

Figure 3.13 - Tracer gas injection system

3.1.4.1.2 CO_2 Helium equilibrium

The tracer gas was mainly composed of carbon dioxide. Since CO_2 is 1.5 denser than atmospheric air, Helium was mixed with CO_2 to maintain buoyancy between the injected tracer gas and the circulating air inside the cabin. Based on ideal gas principles, as shown below, it was found that the injected tracer gas should consist of 62.4% CO_2 and 37.6% He. A total of 7.1 lit/min of CO_2 and 4.28 lit/min of He were injected at a height of 1.25 m above the cabin floor. A copper tube having a 25.4 mm inner diameter was used as the injection port inside the cabin as shown in Figure 3.14.

Figure 3.14 - Tracer gas injection port

To maintain buoyancy with the air density inside the cabin, helium was mixed with CO_2 and the mixture of both gases was injected at different locations inside the cabin.

Ideal gas law:

$$P.V = m.R.T \tag{3.1}$$

where P is the pressure, V is the volume, m is the mass, R is the gas constant, and T is the temperature. Assuming that the pressure, volume, and temperature do not change, then the only variables are m and R, where

$$R = \frac{\bar{R}}{M} \tag{3.2}$$

$where\ \bar{R}\ is\ the\ universal\ gas\ contant$, and M is the gas molar mass

Now, to maintain buoyancy between air and the gas

$$\mathrm{mair} = \mathrm{x.mCO2} + \mathrm{y.mHe} \tag{3.3}$$

where x & y are percent fraction of CO_2 and He, respectively

Using the ideal gas law, as in equation (3.1), and substituting the values of R from equation (3.2) into equation (3.3),

$$\mathrm{M}_{air} = \mathrm{x.M}_{CO2} + \mathrm{y.M}_{He} \tag{3.4}$$

M_{air} = 28.96 g/mol ; M_{CO2} = 44.01 g/mol ; M_{He} = 4.003 g/mol

To meet the conditions of equation (3.4), it was found that x=0.624 and y=0.376. Therefore, the injected mixture was composed of 62.4% CO_2 and 37.6% of He. With 7.1 lit/min of CO_2, a total volumetric flow rate of 4.28 lit/min of Helium was needed to maintain this balance and to maintain buoyancy with air.

3.1.4.1.3 Mass flow controllers

The injection and mixing of carbon dioxide and helium were controlled with the aid of two mass flow controllers and a 2-channel power supply. The flow controllers were connected to the 2 channel power supply which in turn was connected to the main data acquisition system. This would allow automatic input of the required quantities of CO_2 and He. For CO_2 injection, an electric MKS 1559A-200L-SV-S controller was used. Similarly, a pneumatic MKS 2179A-00114-CS-18V controller was used for Helium. Both mass flow controllers, shown at the bottom of Figure 3.15, were operated by an MKS PR4000 power supply and RS-232 interface unit. Two flow meters were connected downstream of the flow controllers to verify the mass flow rates going into the injection point inside the cabin. The flow meters are shown at the top of the mass flow controllers in Figure 3.15. The 2 channel power supply unit is shown in Figure 3.16 along with an Agilent 34970A DAQ. The pressure of the supply cylinders, both CO_2 and He, were set to 200 kPa. Two pressure gauges were installed upstream of the mass flow controllers to make sure there was no leakage in the lines connecting the cylinders to the controllers. Two other pressure gauges were installed downstream of the controllers to verify that both CO_2 and He were supplied at the same pressure to ensure the mixing of the two gases is done at the same pressure. The pressures at the inlet of the controllers were almost around 200 kPa and the pressure at the exit lines of the controllers were zero PSI which is the atmospheric pressure since the outlet was opened to room atmospheric pressure inside the cabin. To check the pressure drop inside the flow controllers, the outlet line which was going to the cabin was blocked. The two pressure gauges, installed at upstream and downstream of the controllers, showed 200 kPa pressure readings.

Figure 3.15 - Mass flow controllers and flow meters used to control CO_2 and Helium

Figure 3.16 - Two channels power supply unit (top) used to control the mass flow controllers; Agilent DAQ system (bottom)

3.1.4.1.4 Speed of injected tracer gas through the injection port

The speed of the gas injected into the cabin was checked using a TSI omni-directional spherical probe. The probe was installed inside the injection tube for 20 minutes with 5 seconds between consecutive readings. The average over 20 minutes was found to be approximately 53

cm/s with ±1.2% random uncertainty in the measurement readings. However, the probe has a total bias uncertainty equal to ±1% of the readings as discussed in the uncertainty section in Chapter 5. Thus, the total relative uncertainty was approximately ±1.6% using a 95% confidence interval. The average speed is shown in Figure 3.17 along with 95% C.I. limits. It was noticed that it took the probe approximately 30 seconds, 115 seconds, and 300 seconds to achieve 90%, 95%, and 99% of the average speed, respectively. However, considering the limits within the confidence interval, 95% of the average speed was enough to be considered steady state. Thus, 120 seconds (2 minutes) was a good estimate to achieve steady state injection flow through the copper tube. Comparing this time limit to the time needed to achieve steady state when sampling tracer gas, as discussed in section 3.2.2.2, the five-minutes waiting period was quite reasonable to allow both the injection and the sampling procedures to achieve steady state.

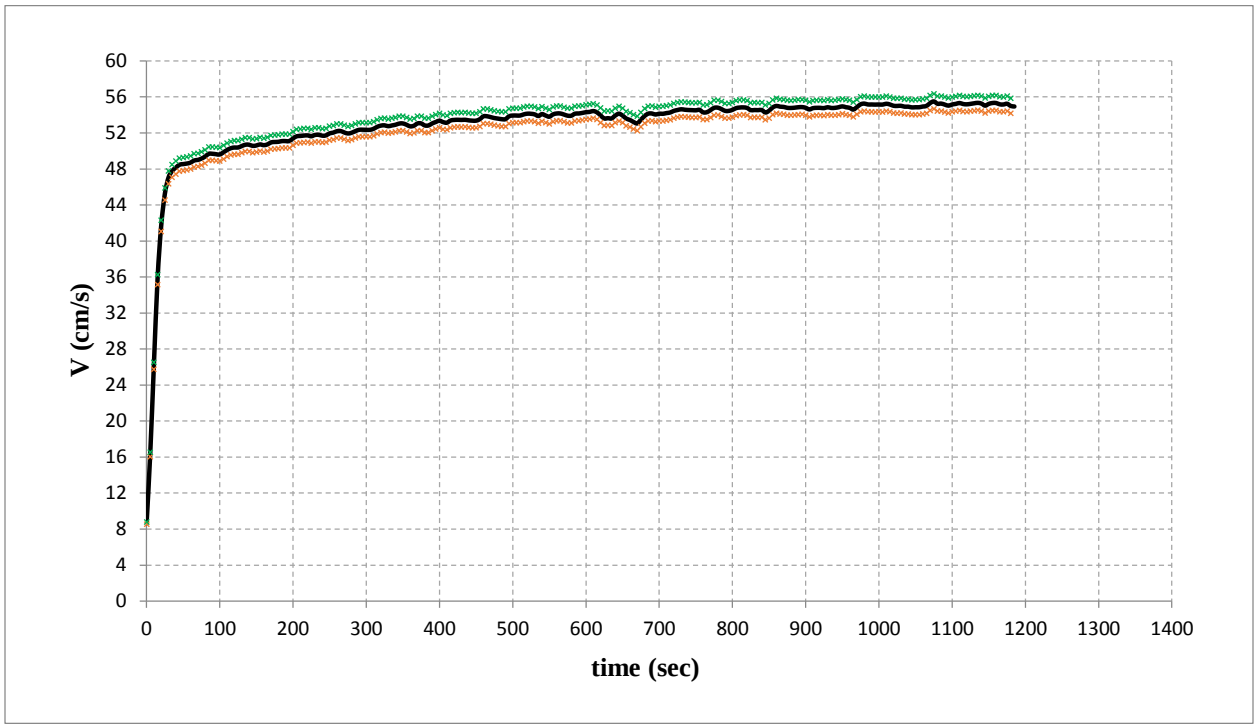

Figure 3.17 - Speed of tracer gas inside the injection port with 95% confidence interval

3.1.4.2 Sampling System

The transported tracer gas inside the cabin, the CO_2 concentration coming into the cabin with the supplied air, and the CO_2 concentration leaving the cabin with the exhausted air were sampled using CO_2 analyzers.

3.1.4.2.1 CO_2 analyzers

CO_2 analyzers use NDIR (Non-dispersive Infrared) sensors that are linearly dependent on the concentration of carbon-dioxide. The absorption of CO_2 by NDIR is governed by Lambert-Beer law which states that the absorption of a gas is directly proportional to its concentration (RAE Systems, 2005).

$$I = I_o . 10^{-A} \tag{3.5}$$

where A=ε.l.c

I_o is the lamp light intensity, I is the measured light intensity, ε is the molar extinction coefficient, l is the path length, and c in the concentration to be determined.

Infrared sensors usually use a heated filament to emit broadband IR radiation through the gas mixture to be analyzed. The radiation is then filtered to narrow bandwidth IR beam for measurement by an IR sensor. Figure 3.18 shows one configuration of an NDIR sensor that uses a single lamp. The measurement is independent of the gas mixtures and provides a reference signal for sensor compensation due to variations in lamp intensity and light scattering from particulates. The narrowly filtered bandwidth of these non-dispersive IR sensors does not create complete spectral fingerprints of gases but instead enables measurement of the absorption of the narrow beam at a specific wavelength. The principle disadvantages of NDIR sensors are in the sensitivity of the optical components to impact, vibration, and maintenance of the cleanliness of the sensor windows for reliable operation.

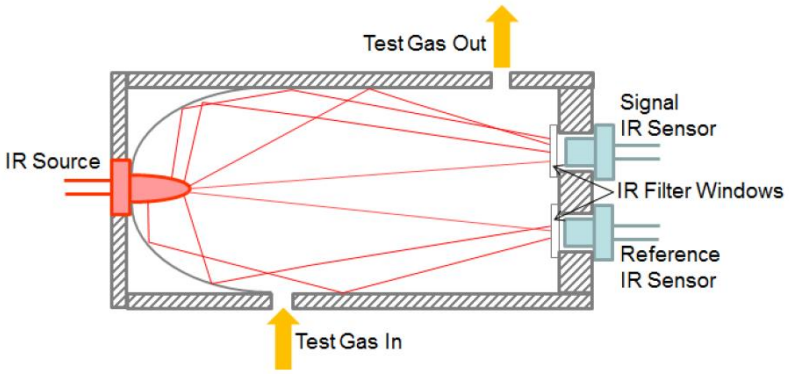

Figure 3.18 - NDIR sensor schematic

Two types of CO_2 analyzers were used: the first one is a PP Systems analyzer (model WMA-4), shown in Figure 3.19, and the other type is a custom made Edinburg Gascard sensors, shown in Figure 3.20. Accuracy and range for each unit are summarized in Table 3.1. The circulating pumps inside each analyzer that pull the samples through the inlet port of the analyzers and exhaust them out were of the diaphragm pump type. The diaphragm might have some leak and, thus, might lead to inaccurate results. As a result, all pumps were bypassed and the exhaust of each analyzer was connected to a common balance flow meter, shown in Figure 3.21, whose exit was connected to a common vacuum pump. The single vacuum pump and the balance flow meters box ensured that the same flow rate was running through the three analyzers. The flow meters were each set to 1 lit/min.

Figure 3.19 - P.P. systems CO_2 analyzer (model WMA-4)

Table 3.1 – CO_2 analyzers specifications

	Edinburg Gascard	**WMA-4**
Range (ppm)	0-3000	0-2000
Accuracy	2% of range	1% of range
Repeatability	1.50%	< 1%
Response Time	10 sec	1.6 sec

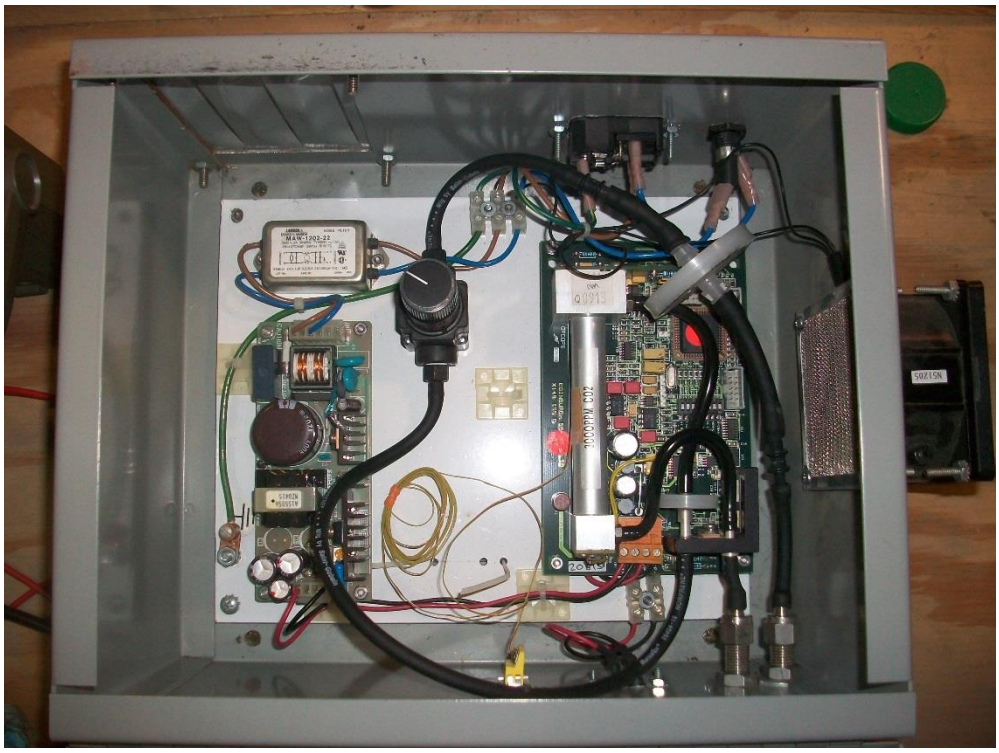

Figure 3.20 - Edinburg Gascard CO_2 analyzer

Figure 3.21 - Balance flow meters connected to the CO_2 analyzers at the inlet side and to a common vacuum pump at the exit side

3.1.4.2.2 Sampling tree

The location of the inlet port of the CO_2 analyzer needed to be changed throughout the cabin to allow sampling at different locations. Thus, the experimenter needed to access the mockup cabin each time the sampling location was to be changed. To reduce the effect of disturbance on the airflow and to prevent the addition of other potential CO_2 sources, upon accessing the mockup cabin, a 3.1 m long sampling tree composed of 4 equidistant sampling ports was constructed and used as shown in Figure 3.22. This allows four seat locations to be sampled without having to access the cabin. Each port was controlled with a normally closed (NC) SMC Pneumatics NVKF334V-3G 2-way solenoid valve connecting each of the 4-sampling lines to a common outlet port that was connected to the inlet of the CO_2 analyzer. Thus, the ports were opened sequentially, one at a time, permitting isolated sampling in each seat. Each sampling line was made of 304 stainless steel welded tubing with an inside diameter of 5 mm. A fifth solenoid valve was mounted to the manifold in reverse orientation so it was in normally open position. This valve was opened to the atmosphere, rather than connected to a sampling line. This allows the tube connected to the common rail of the manifold on one side and to the CO_2 analyzer on the other side to constantly be pulling a sample through to the CO_2 analyzer.

Figure 3.22 - Sampling tree showing the manifold containing the 5 solenoid valves and the exit tubing at the rear end of the manifold that was connected to the inlet of the CO_2 analyzer

When a test was run, the NO (Normally Opened) reversed valve would be closed and the valve corresponding to the sampling port would open. This would ensure that the air that was leaving the manifold and being analyzed by the CO_2 analyzer was the air being sampled through the corresponding port.

3.1.4.2.3 Tracer gas control system

To measure tracer gas movement throughout the different locations in the cabin, a measurement from each of the CO_2 analyzers was recorded every five seconds during experimentation. All measurements were controlled by commercial LabVIEW package. The data acquisition system was an Agilent 34970A DAQ. At each sampling interval, temperatures were also recorded inside the cabin at different locations. Fourteen temperature sensors were

used to measure the temperature in the vertical direction inside the cabin (can be moved around the cabin). Two other sets of sensors, each composed of twelve sensors, were attached to the cabin walls on each of the east and west cabin walls starting by the locations next to the air supply diffusers all the way down to the cabin floor. The supplied inlet air was also controlled through Agilent DAQ but the LabVIEW program used was separate from the tracer gas and the interior temperature control system. The tracer gas injection rate, duration, and timing were also controlled by the same LabVIEW program. A snapshot of the program interface is shown in Figure 3.23. The program could also control the sampling interval and selects which ports to sample on the sampling tree. This enabled all four ports of the sampling tree to be utilized in four separate seat locations during a single experiment as discussed in the previous section.

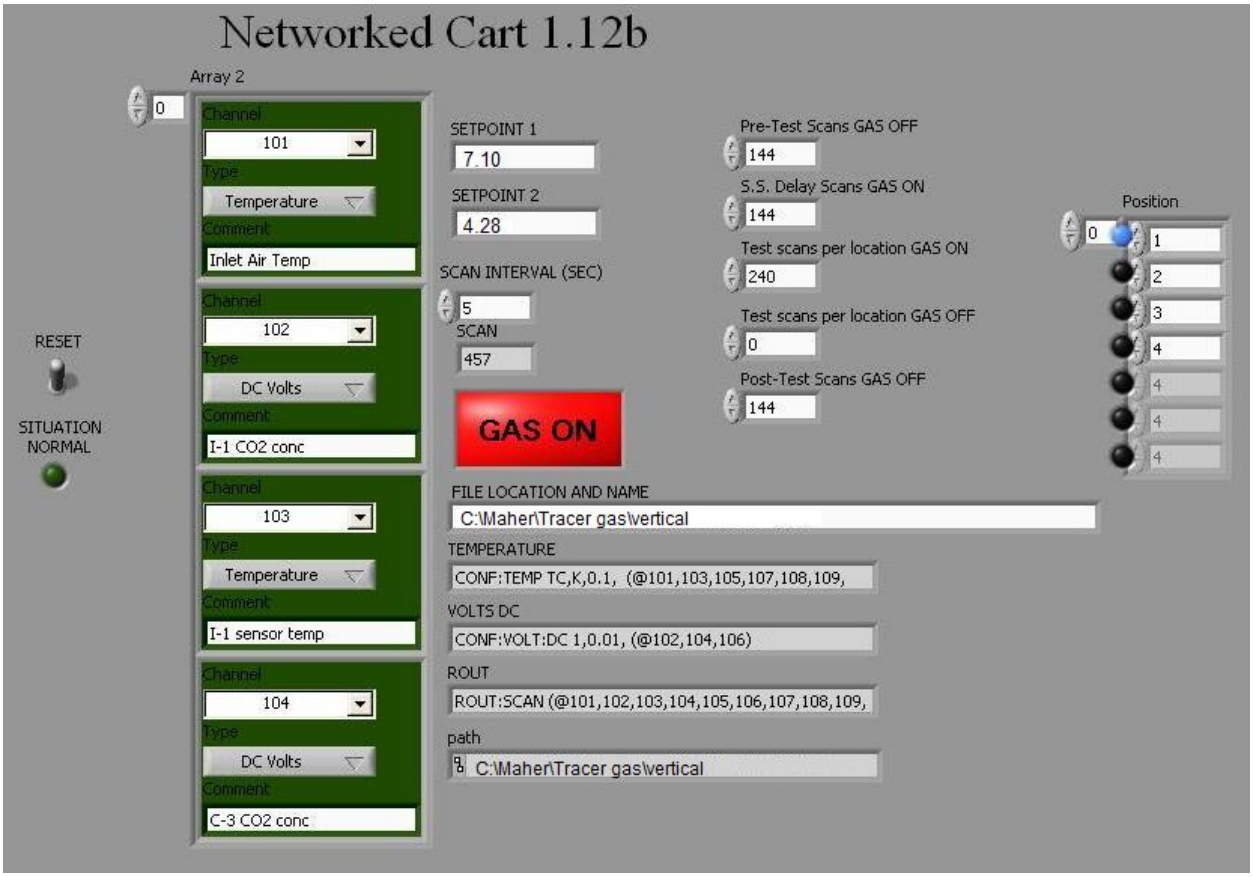

Figure 3.23 - Tracer gas injection control system (LabVIEW package)

3.1.5 Airflow speed measurements

In order to analyze the different airflow turbulence characteristics and parameters, the speed of the airflow at various locations inside the cabin was measured. A spherical omni-directional TSI velocity transducer (8475 series), having a ±3% uncertainty of the measured value and ±1% relative uncertainty of full scale, was used to measure the speed at different locations inside the cabin at the same elevation where the CO_2 was sampled. The probe is made up of a small heated sphere that maintains a constant temperature and an unheated sensor which is used to correct the air velocity measurement when the temperature differs from the calibration temperature. Lebbin (2006) recommended that such probes should not be used to measure velocities below 0.03 m/s (3 cm/s). In parallel to that, the 8475 manual recommends a range of speed between 5 to 245 cm/s. To be able to determine the turbulence parameters accurately, the measuring instrument should have a low time constant. Depending on the behavior of the response, the time constant can be defined as the time needed to achieve 63% of a step change in velocity, if it is of the first order. The hot wire anemometer has an approximately 0.1 second time constant, against 0.7 seconds for the omni-directional spherical anemometer (Lebbin, 2006). However, the large temperature differences associated with the hot-wire anemometer limits its use to velocities greater than 10 cm/s. Different probes were considered for the purpose of measuring the speed inside the cabin at the specified height. Table 3.2 summarizes three TSI probes along with their specifications. However, previous studies and some benchmark testing inside the mockup cabin, showed that the speed can be as low as 6 cm/s or even lower. For that it was decided to use TSI-8475 omni-directional transducer. The time constant for the TSI omni-directional transducer ranges between 0.05 to 10 seconds while the time response was approximately 5 seconds.

Table 3.2 - Comparison between different TSI omni-directional probes

Probe TSI Model #	Accuracy (-/+)	Full Scale accuracy	Response Time	Speed Range
8455	2%	0.5% of selected range	0.2 sec	0.127 to 50.8 m/s
8465	2%	0.5% of selected range	0.2 sec	0.127 to 50.8 m/s
8475	3%	1% of selected range	5 sec	0.05 to 2.54 m/s

The spherical probe was fixed at a height of 1.23 m above the cabin floor in the east, center, and west sides of the cabin in each row of the 11 rows of the cabin as shown in Figure 3.24 . The system was run for 20 minutes preceded by a 5 minute waiting period after all doors were closed to allow steady state conditions to be achieved. Data points were collected every 5 seconds. The measurements in each seat were repeated three times to check on the uncertainty in the repeatability of the data. The velocity measurements were taken under heated and unheated manikin conditions. In later sections for the analysis of the viscous energy dissipation rates (section 5.2.4.2), three speed probes were used instantaneously during the same test to measure the speed at three different locations that were close enough to each other to discretize and predict the spatial speed gradient with minimal errors. The averages of the three probes used in section 5.2.4.2.1 were compared to the results of these tests and good agreement was found with ±15% relative difference. Further details related to the three probes installation is given in Appendix G - where the three probes were installed in different directions inside the cabin: vertical, transverse, and longitudinal.

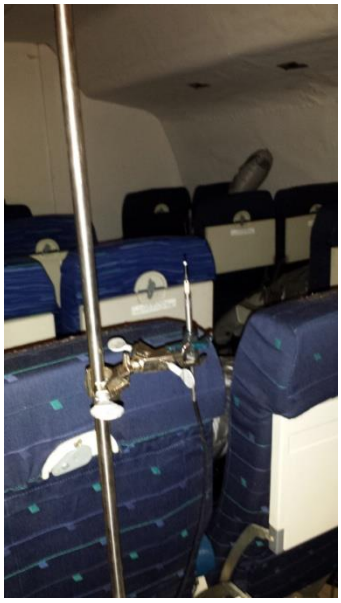

Figure 3.24 - Omni directional speed transducer used to measure airflow speed inside the mockup cabin

3.2 Experimental methodology

3.2.1 Airflow visualization methodology

Smoke was released in different scenarios, sometimes it was injected intermittently and other times it was injected continuously. Several trials were conducted to adjust the smoke flow to have an emerging speed that has minimal effects on the cabin airflow patterns. Figure 3.12 illustrates the experimental setup for smoke visualizing tests along with the main equipment used. Eighteen locations were selected to release the smoke into the cabin, one at a time, as shown in Figure 3.25 and Figure 3.26. The locations for smoke release were selected to cover as much of the airflow inside the mockup cabin as possible. Six release locations were selected in the east side of the cabin (seats A & B of each row) and other 6 release locations were selected in the west side (seat F). After visualizing the smoke in the above selected locations, other 6 locations were selected in the middle section of the cabin to clarify some of the results and

conclusions drawn from previous tests. So the middle seats locations were not selected to satisfy symmetrical release, but rather were selected to satisfy the needs of the previous tests and to better understand the airflow phenomena in a qualitative way. The smoke was injected at a height of 1.1 m above the cabin floor which was 130 mm below the laser sheet. During each test, videos were recorded from one or multiple locations to capture and trace the smoke flow in the region around the release point. Pictures were taken from the videos sometimes as standalone pictures that show a specific direction of the smoke or as time dependent pictures that track the smoke over a time interval after its release from the injection port.

The following list summarizes the release locations of the theatrical smoke inside the cabin during the visualization tests where seat A is the first seat next to the east wall of the cabin and seat G is the seat next to the west wall of the cabin as shown in Figure 3.25 and Figure 3.26.

- Row 1 – Seat D
- Row 2 – Seat B, Seat C and Seat F
- Row 3 – Seat A
- Row 4 – Seat C and Seat F
- Row 5 – Seat B and Seat F
- Row 6 – Seat B and Seat F
- Row 7 – Seat D
- Row 8 – Seat F
- Row 9 – Seat B and Seat C
- Row 10 – Seat F
- Row 11 – Seat A and Seat D

The airflow patterns were tracked by capturing consecutive pictures of the smoke dispersion after its release in different locations inside the cabin. Many cases for smoke flow were repeated and documented as will be discussed in the results and analysis sections.

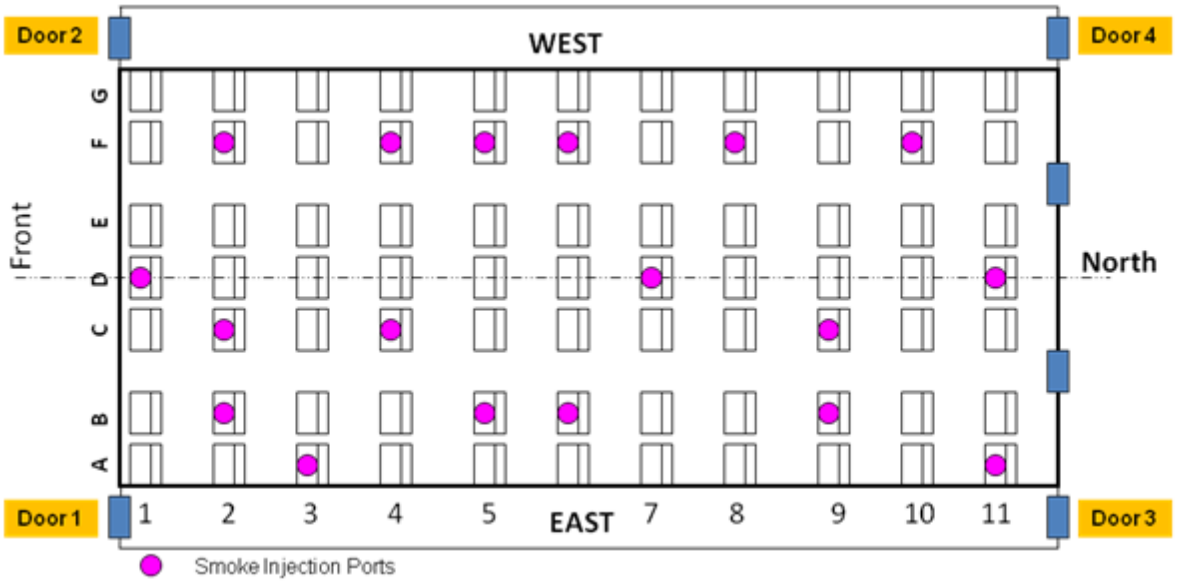

Figure 3.25 - Smoke visualization release points inside the mockup cabin

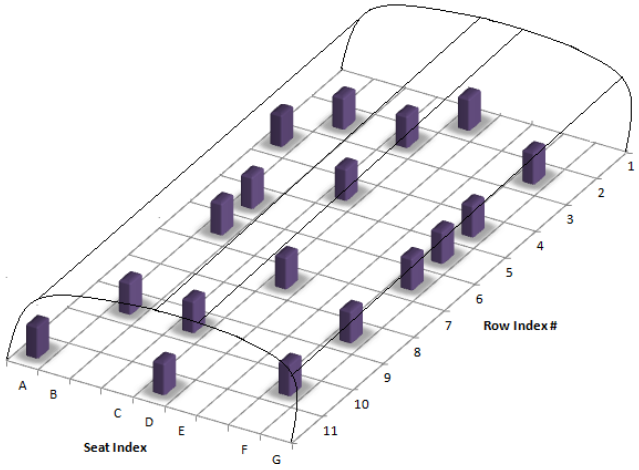

Figure 3.26 - Smoke release locations during smoke visualizing tests

3.2.2 Tracer gas tests

To capture the airflow behavior inside the mockup cabin in a quantitative way, tracer gas was released in different locations inside the cabin based on smoke visualization results shown in Figure 5.1. Eight release locations were selected with 4-locations in the centerline seats, 2-locations in the east side, and 2-locations in the west side of the cabin, as shown in Figure 3.27. Exact heights for the release locations are given along with the sampling location coordinates inside the cabin in section 3.2.2.1.1.

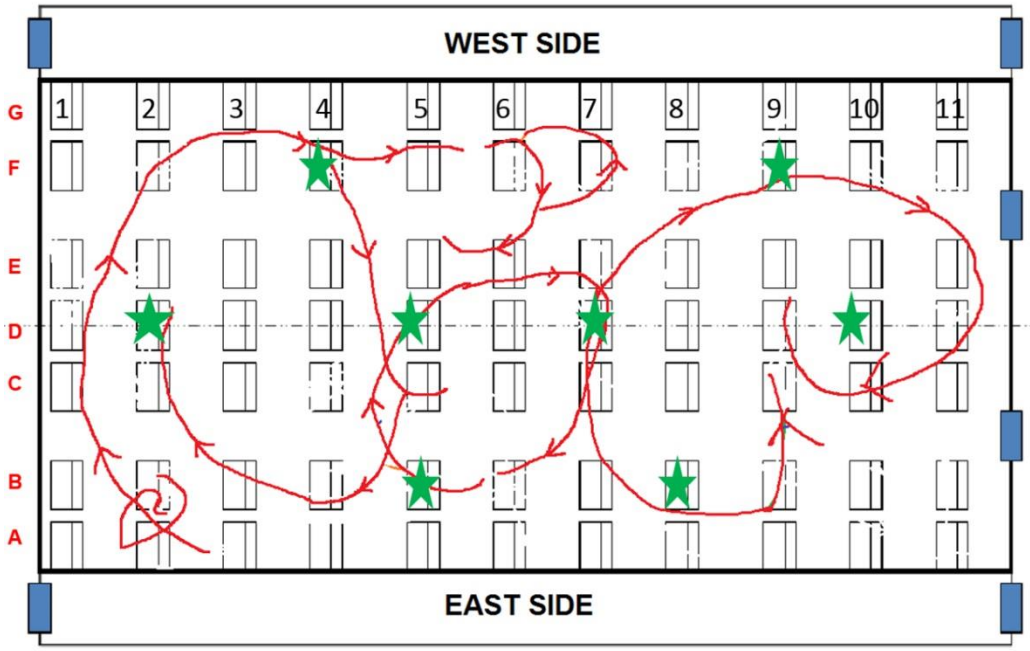

Figure 3.27 - Tracer gas release locations (green stars) - (red lines represent the airflow patterns based on visualization results in Figure 5.1)

3.2.2.1 Sampling methodology

The injected gas into the cabin was sampled at different locations within the cabin at a height of 1.23 m. This would be around the nasal region or the breathing zone of a seated passenger. The transported tracer gas was sampled using CO_2 analyzers shown in Figure 3.19 and Figure 3.20. One CO_2 analyzer was used inside the cabin to sample the tracer gas in

different locations. Analogue voltage signals were taken from each analyzer and were connected to the main data acquisition system. In order to have a meaningful interpretation of these signals, calibration was performed to relate the recorded voltage to CO_2 concentration (ppm). Section 3.2.2.1.2 summarizes the calibration procedures and results for the different analyzers used.

Tracer gas was sampled, in most cases, in the same row of gas release, three rows in front and three rows to the back except in the cases when the cabin walls were a restriction. Figure 3.28 to Figure 3.35 show the proposed sampling locations for each release location. Upon analyzing the sampled tracer gas and to have better understanding of the gaseous flow behavior, additional samples were collected, whenever necessary, in locations other than those shown in Figure 3.28 to Figure 3.35. In each seat/port, 240 samples were collected in each of the 4 ports, within the sampling tree, with 5 seconds between each scan/sample. The time needed to achieve steady state after releasing the CO_2-He mixture is estimated in section 3.2.2.2 and was added to each test prior to sampling. Also the time needed to exhaust all the gas out from the cabin after each test and before starting a new test was added, because when accessing the cabin to change the location of the sampling tree, additional carbon dioxide might have entered into the cabin from the experimenter, through the access door, and from the air surrounding the chamber closure.

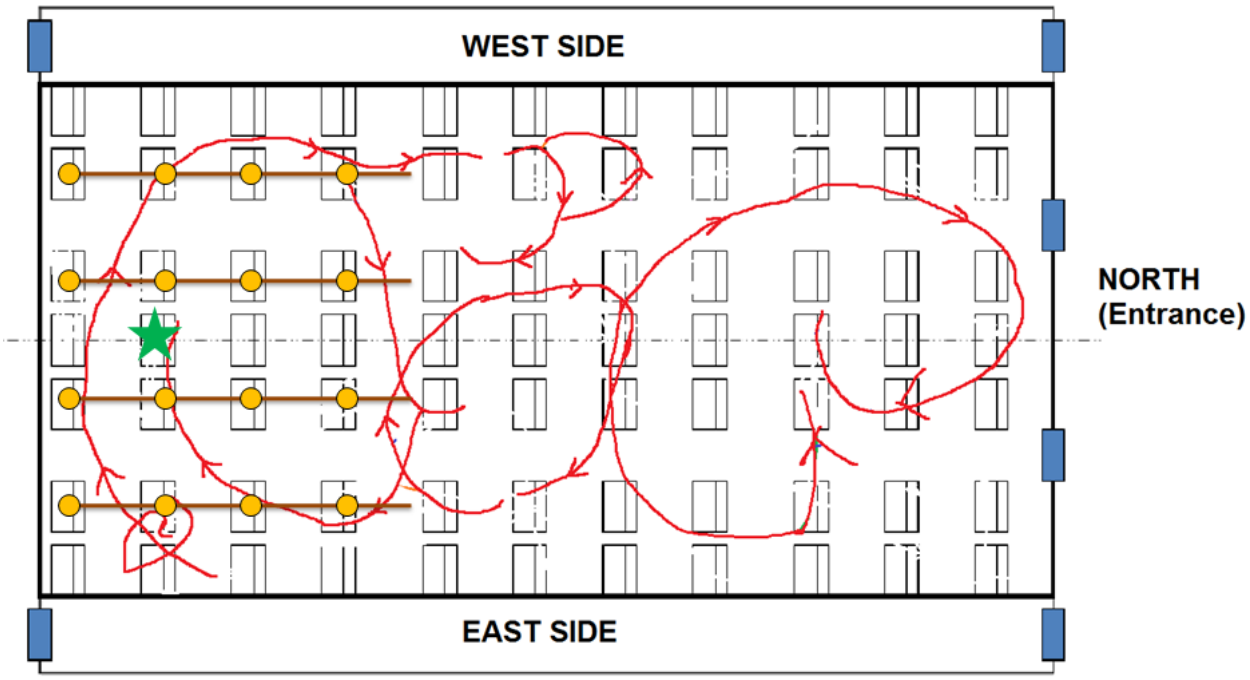

Figure 3.28 - Sampling locations when releasing in Seat 2D

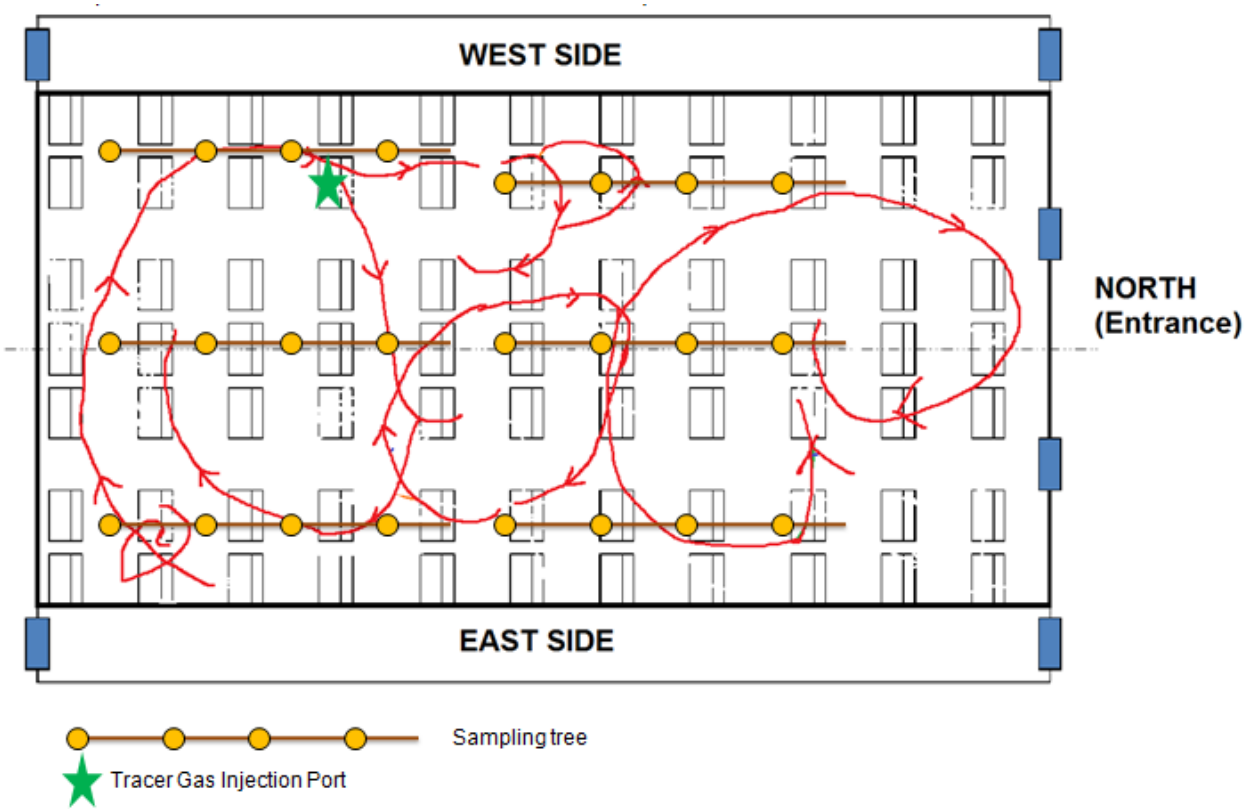

Figure 3.29 - Sampling locations when releasing in Seat 4F

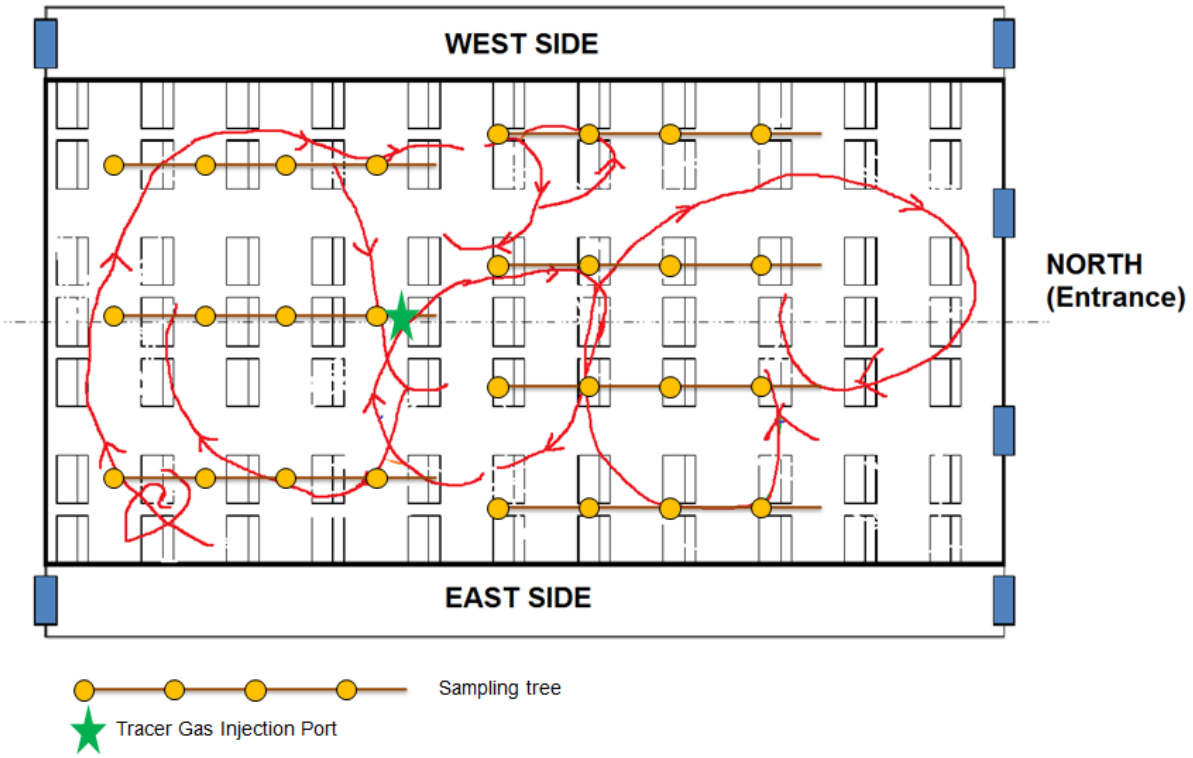

Figure 3.30 - Sampling locations when releasing in Seat 5D

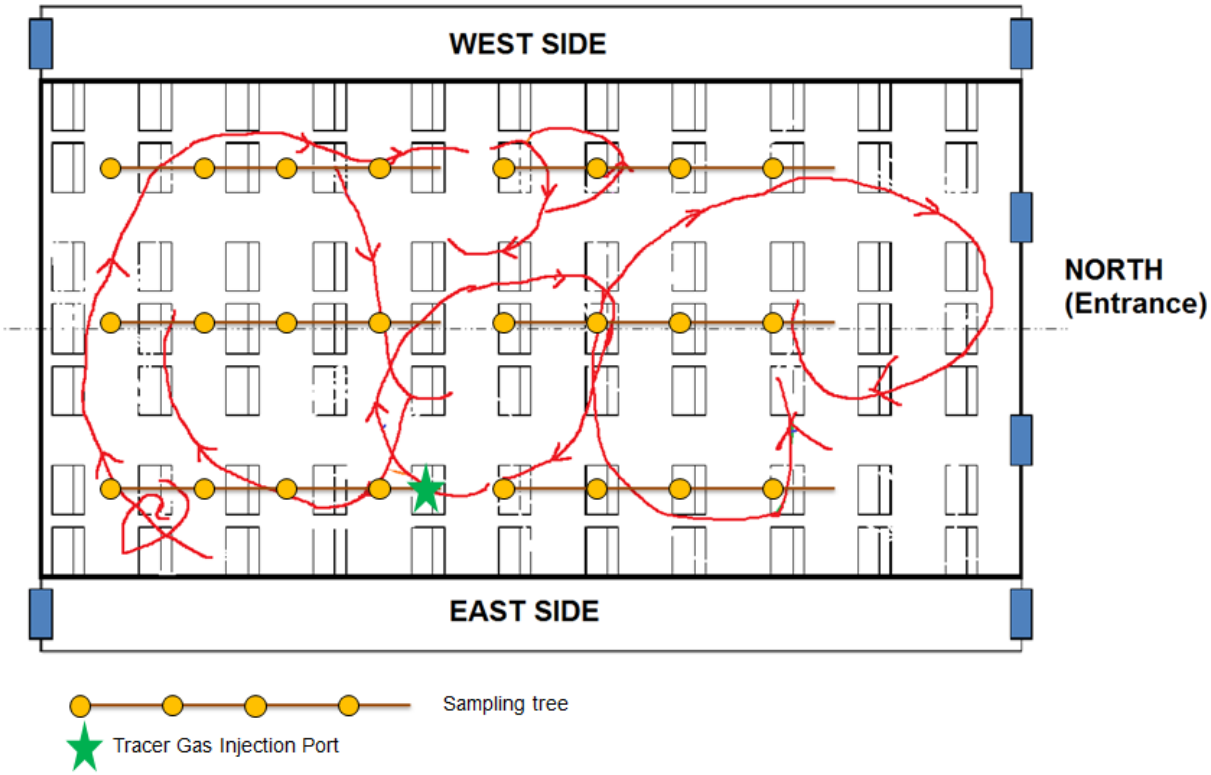

Figure 3.31 - Sampling location when releasing in Seat 5B

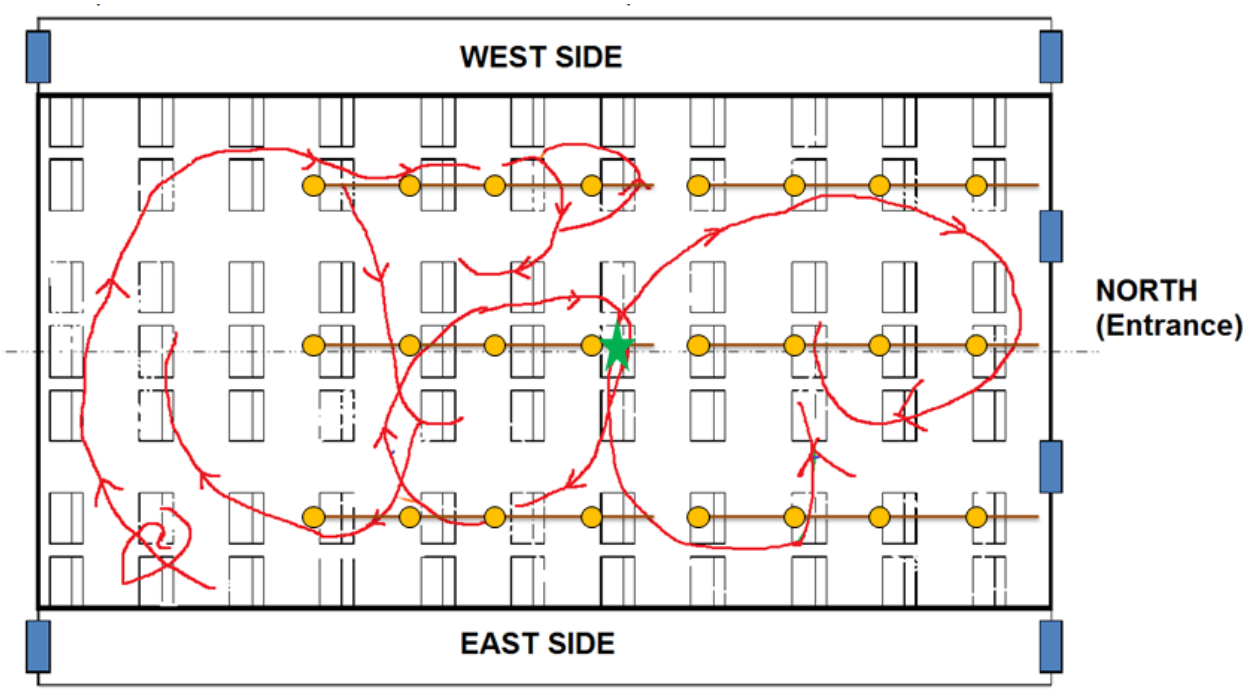

Figure 3.32 - Sampling locations when releasing in Seat 7D

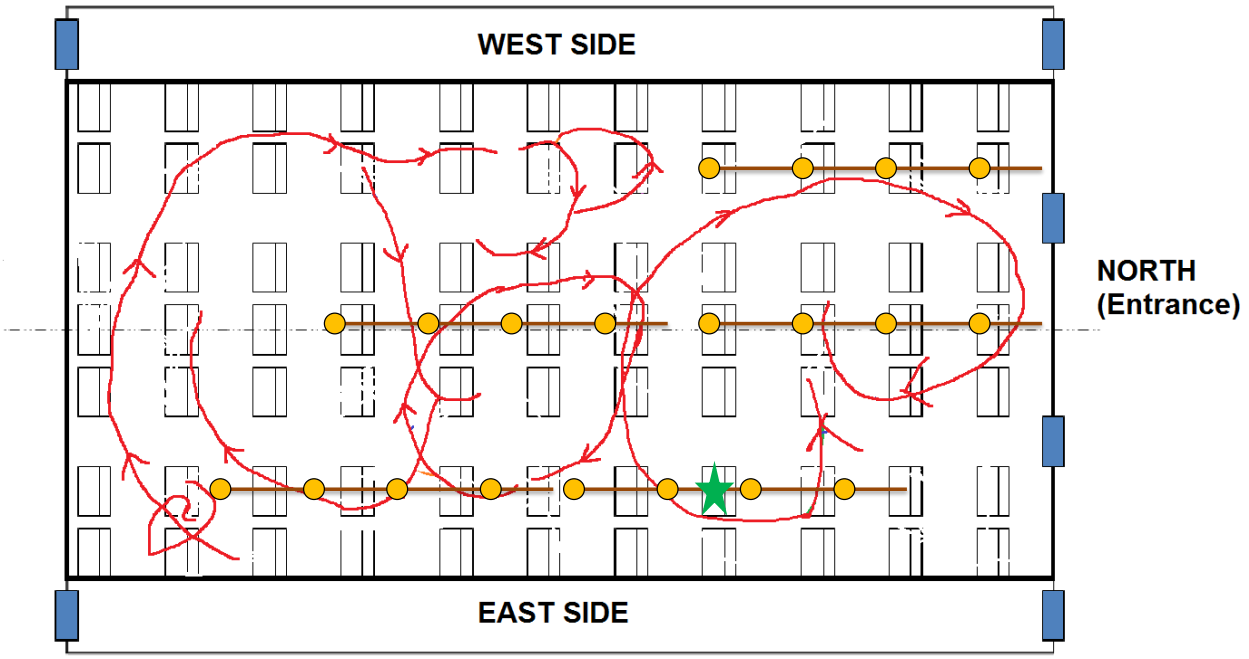

Figure 3.33 - Sampling locations when releasing in Seat 8B

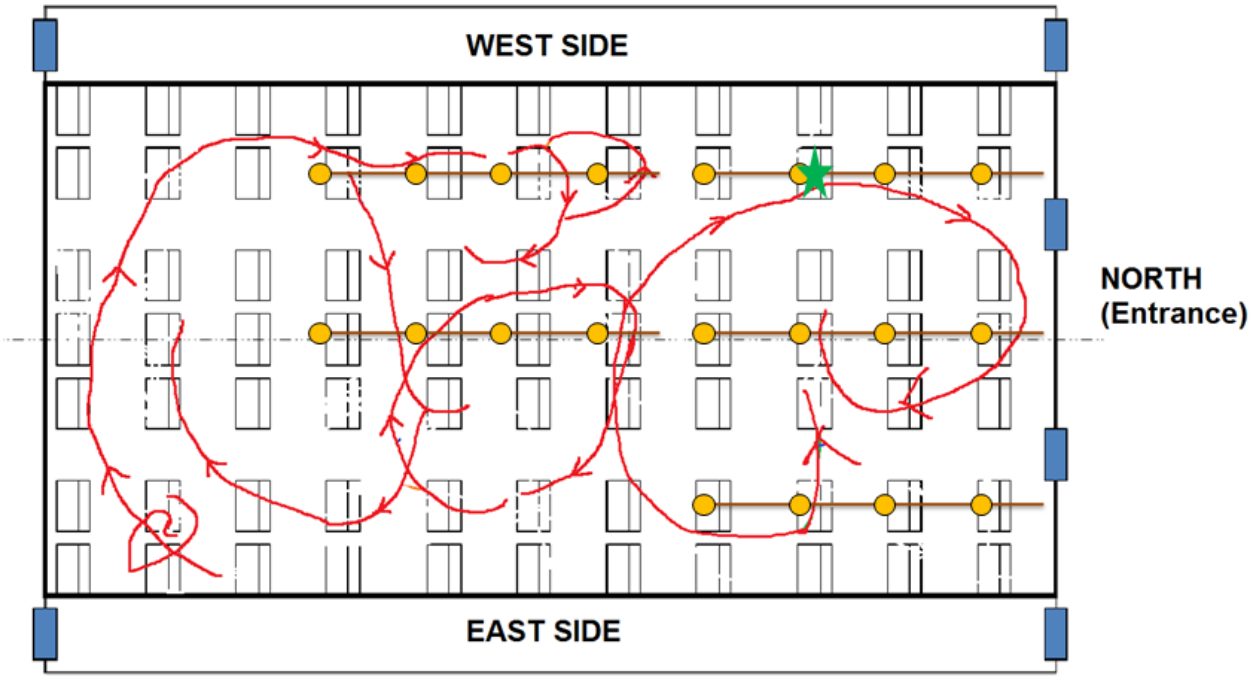

Figure 3.34 - Sampling locations when releasing in Seat 9F

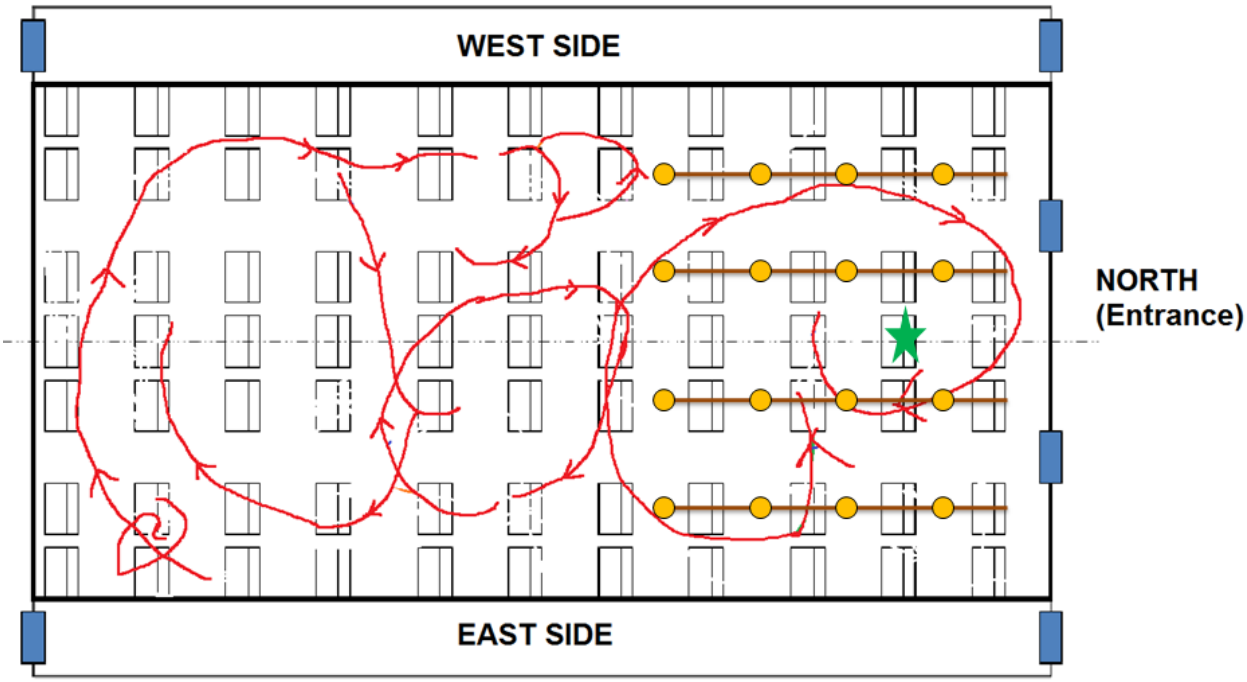

Figure 3.35 - Sampling locations when releasing in seat 10D

3.2.2.1.1 Sampling ports coordinates inside the mockup cabin

The exact locations of the sampling ports during all tests with respect to the front, back, east, and west walls of the cabin are shown in Table 3.3 through Table 3.10.

Table 3.3 - Sampling and release location coordinates when releasing in seat 2D

Sampling Location	Distance from front wall (mm)	Distance from West Wall (mm)		Sampling Location	Distance from front wall (mm)	Distance from East Wall (mm)
Seat 1F	660	711		**Seat 1B**	660	660
Seat 2F	1499	711		**Seat 2B**	1499	660
Seat 3F	2337	711		**Seat 3B**	2337	660
Seat 4F	3175	711		**Seat 4B**	3175	660
Seat 1E	368	1753		**Seat 1C**	597	1778
Seat 2E	1207	1753		**Seat 2C**	1435	1778
Seat 3E	2045	1753		**Seat 3C**	2273	1778
Seat 4E	2883	1753		**Seat 4C**	3112	1778
Seat 5D	4318	940		**Seat 2D**	1270	centerline
Seat 5E	4318	1778		**Release was in Seat 2D - 1.25 m above the cabin floor, 1448 mm from Front wall - on the centerline**		
Seat 5F	4318	2616				
Seat 5G	4318	3454				

Table 3.4 - Sampling and release location coordinates when releasing in seat 5D

Sampling Location	Distance from front wall (mm)	Distance from West Wall (mm)		Sampling Location	Distance from front wall (mm)	Distance from East Wall (mm)
Seat 2E	1524	1753		**Seat 5C**	3683	1778
Seat 3E	2362	1753		**Seat 6C**	4521	1778
Seat 4E	3200	1753		**Seat 7C**	5359	1778
Seat 5E	4039	1753		**Seat 8C**	6198	1778
Seat 6E	4521	1803		**Seat 5B**	3734	737
Seat 7E	5359	1803		**Seat 6B**	4572	737
Seat 8E	6198	1803		**Seat 7B**	5410	737
Seat 9E	7036	1803		**Seat 8B**	6248	737
				Release was in Seat 5D - 1.25 m above the cabin floor, 3760 mm from Front wall - on the centerline		
Seat 2F	1499	737				
Seat 3F	2337	737				
Seat 4F	3175	737				
Seat 5F	4013	737				

Seat 6F	4496	762		
Seat 7F	5334	762		
Seat 8F	6172	762		
Seat 9F	7010	762		
R3-Hall 1	3023	1397		
3D	3023	2235		
R3-Hall 2	3023	3073		
3B	3023	3912		
				Release was in Seat 5D - 1.25 m above the cabin floor, 3760 mm from Front wall - on the centerline
Row 3 - Row 4 Hall 1	2159	1448		
Row 3 - Row 4 - D	2159	2286		
Row 3 - Row 4 Hall 2	2159	3124		
Row 3 - Row 4 - B	2159	3962		

Table 3.5 - Sampling and release location coordinates when releasing in seat 7D

Sampling Location	Distance from front wall (mm)	Distance from West Wall (mm)		Sampling Location	Distance from back wall - North (mm)	Distance from West Wall (mm)
Seat 4F	2883	749		**Seat 8F**	3353	749
Seat 5F	3721	749		**Seat 9F**	2515	749
Seat 6F	4559	749		**Seat 10F**	1676	749
Seat 7F	5398	749		**Seat 11F**	838	749
Seat 4D	3124	Center line		**Seat 8D**	3099	Center line
Seat 5D	3962	Center line		**Seat 9D**	2261	Center line
Seat 6D	4801	Center line		**Seat 10D**	1422	Center line
Seat 7D	5639	Center line		**Seat 11D**	584	Center line
Sampling Location	**Distance from front wall (mm)**	**Distance from East Wall (mm)**		**Sampling Location**	**Distance from back wall - North (mm)**	**Distance from East Wall (mm)**
Seat 4B	3124	686		**Seat 8B**	3226	584
Seat 5B	3962	686		**Seat 9B**	2388	584
Seat 6B	4801	686		**Seat 10B**	1549	584
Seat 7B	5639	686		**Seat 11B**	711	584
Release was in Seat 7D - 1.25 m above the cabin floor, 5461 mm from Front wall - on the centerline						

Table 3.6 - Sampling and release location coordinates when releasing in seat 10D

Sampling Location	Distance from back wall (mm)	Distance from West Wall (mm)		Sampling Location	Distance from back wall (mm)	Distance from East Wall (mm)
Seat 8F	3073	711		**Seat 8B**	3264	749
Seat 9F	2235	711		**Seat 9B**	2426	749
Seat 10F	1397	711		**Seat 10B**	1588	749
Seat 11F	559	711		**Seat 11B**	749	749
Seat 8E	3073	1727		**Seat 8C**	3112	1753
Seat 9E	2235	1727		**Seat 9C**	2273	1753
Seat 10E	1397	1727		**Seat 10C**	1435	1753
Seat 11E	559	1727		**Seat 11C**	597	1753
Release was in Seat 10D - 1.25 m above the cabin floor, 1575 mm from back wall (North) - on the centerline						

Table 3.7 – Sampling and release location coordinates when releasing in seat 5B

Sampling Location	Distance from front wall (mm)	Distance from West Wall (mm)		Sampling Location	Distance from front wall (mm)	Distance from East Wall (mm)
Seat 2F	58	28		**Seat 2B**	48.5	27
Seat 3F	91	28		**Seat 3B**	81.5	27
Seat 4F	124	28		**Seat 4B**	114.5	27
Seat 5F	157	28		**Seat 5B**	147.5	27
Seat 2D	59	CENTERLINE		**Seat 6F**	200	56
Seat 3D	92	CENTERLINE		**Seat 6D**	200	89
Seat 4D	125	CENTERLINE		**Seat 6C**	200	122
Seat 5D	158	CENTERLINE		**Seat 6B**	200	155
Release was in Seat 5B - 1.25 m above the cabin floor, 3760 mm from Front wall, and 737 mm from east wall						

Table 3.8 - Sampling and release location coordinates when releasing in seat 8B

Sampling Location	Distance from front wall (mm)	Distance from West Wall (mm)		Sampling Location	Distance from front wall (mm)	Distance from East Wall (mm)
Seat 7F	5639	711.2		**Seat 7B**	5385	762
Seat 8F	6477	711.2		**Seat 8B**	6223	762
Seat 9F	7315	711.2		**Seat 9B**	7061	762
Seat 10F	8153	711.2		**Seat 10B**	7899	762
Seat 4D	3099	centerline		**Seat 8D**	6274	centerline
Seat 5D	3937	centerline		**Seat 9D**	7112	centerline
Seat 6D	4775	centerline		**Seat 10D**	7950	centerline
Seat 7D	5613	centerline		**Seat 11D**	8788	centerline
Release was in Seat 8B - 1.25 m above the cabin floor, 6300 mm from Front wall, and 660 mm from east wall						

Table 3.9 – Sampling and release location coordinates when releasing in seat 4F

Sampling Location	Distance from front wall (mm)	Distance from West Wall (mm)		Sampling Location	Distance from Front wall (mm)	
Seat 2F	1753	737		**Seat 1D**	635	Center line
Seat 3F	2337	737		**Seat 2D**	1473	Center line
Seat 4F	3175	737		**Seat 3D**	2311	Center line
Seat 5F	3937	813		**Seat 4D**	3150	Center line
Seat 6F	4775	813				
Seat 7F	5613	813		**Seat 5D**	3708	Center line
Seat 8F	6452	813		**Seat 6D**	4547	Center line
				Seat 7D	5385	Center line
				Seat 8D	6223	Center line
Sampling Location	**Distance from front wall (mm)**	**Distance from East Wall (mm)**		**Sampling Location**	**Distance from front wall (mm)**	**Distance from East Wall (mm)**
Seat 1B	660	660		**Seat 5B**	3708	737
Seat 2B	1499	660		**Seat 6B**	4547	737
Seat 3B	2337	660		**Seat 7B**	5385	737
Seat 4B	3175	660		**Seat 8B**	6223	737
Release was in Seat 4F - 1.25 m above the cabin floor, 2870 mm from Front wall, and 737 mm from west wall						

Table 3.10 - Sampling and release location coordinates when releasing in seat 9F

Sampling Location	Distance from back wall (mm)	Distance from West Wall (mm)		Sampling Location	Distance from back wall (mm)	Distance from East Wall (mm)
Seat 6F	5029	737		**Seat 8B**	2972	787
Seat 7F	4318	737		**Seat 9B**	2134	787
Seat 8F	3073	737		**Seat 10B**	1295	787
Seat 9F	2235	737		**Seat 11B**	457	787
Seat 10F	1397	737				
Seat 11F	559	737				
Seat 6D	4940	CENTERLINE		**Seat 9D**	2248	CENTERLINE
Seat 7D	4102	CENTERLINE		**Seat 10D**	1410	CENTERLINE
Seat 8D	3086	CENTERLINE		**Seat 11D**	572	CENTERLINE
Release was in Seat 9F - 1.25 m above the cabin floor, 2413 mm from back wall (North), 737 mm from West wall						

3.2.2.1.2 CO_2 analyzers calibration

Since the CO_2 analyzers work with NDIR (Non Dispersive Infrared) sensors that have deviation in the absorption of the concentration sampled, calibration was conducted on a regular basis every two weeks, when the soda lime used in the PP-System analyzers became brown, and when negative voltage readings were obtained. Since NDIR is linearly dependent on the concentration of carbon-dioxide, the output voltage should be linear with the concentration. Thus, a linear regression can be manipulated to relate the two variables together. To perform this calibration, standard and accurate CO_2 gases were run through the analyzers. Three standard concentrations were used: 500, 1000, and 2000 ppm. With each calibration gas, four tests were performed on each of the analyzers used (number of analyzers used will be discussed in the normalization section). During each test, 36 data points were collected with 5 seconds in between each sample. The 36 collected data points during each test were averaged. The averages of the 4 tests performed for each gas were then averaged. Thus, at the end of each

calibration, 144 (36×4) data points were collected for each standard gas. Figure 3.36, Figure 3.37, and Figure 3.38 show some of the calibration results for the cabin, exit, and inlet analyzers, respectively. The cabin and the exit were of the same type (PP-system WMA-4) and they showed less deviation than the Edinburg type that was used to measure the CO_2 in the inlet air.

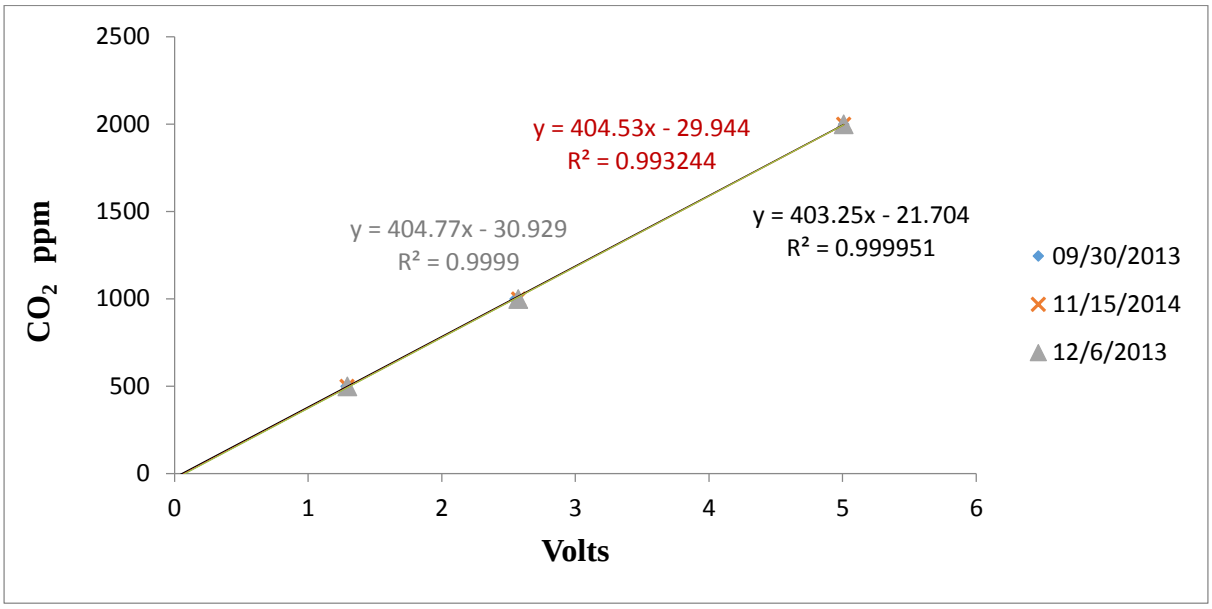

Figure 3.36 - Cabin CO_2 analyzer calibration curves

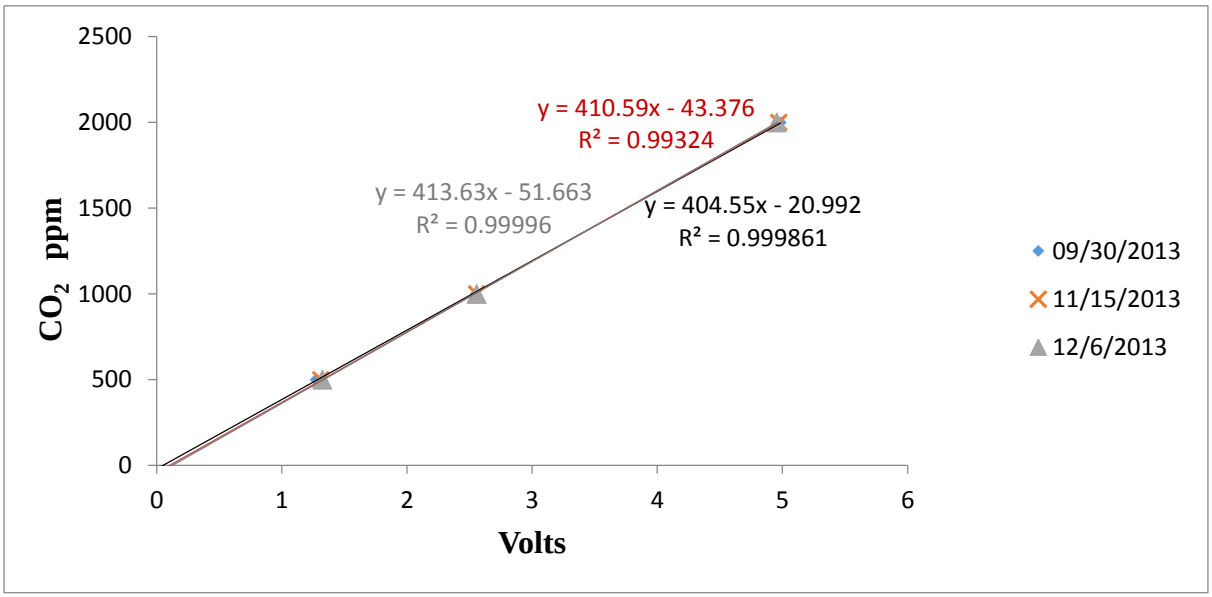

Figure 3.37 - Exit CO_2 analyzer calibration curves

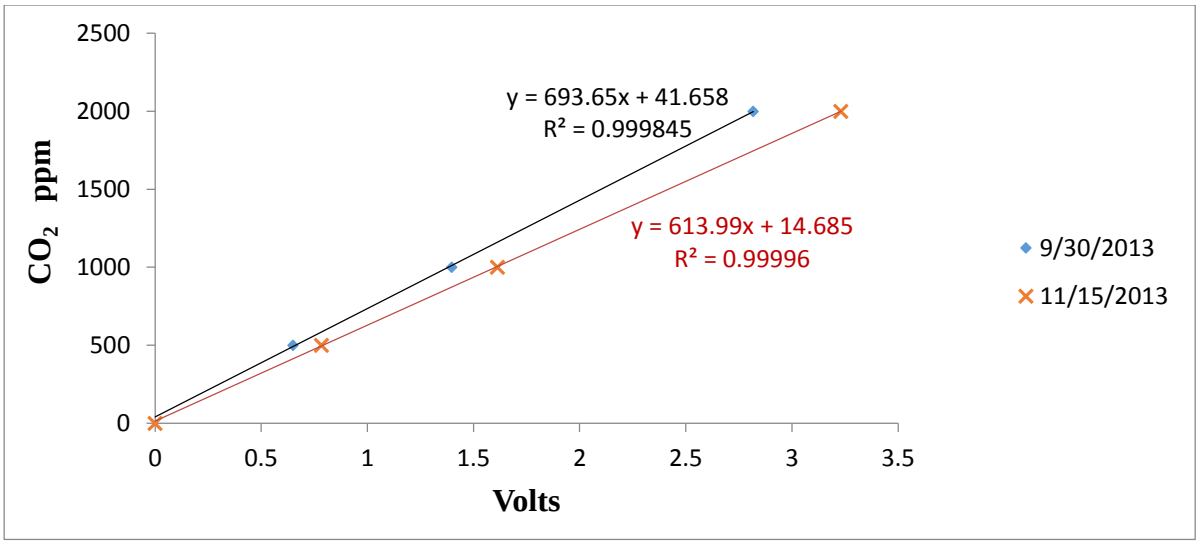

Figure 3.38 - Inlet CO_2 analyzer calibration curves

3.2.2.1.3 Sampling normalization

All of the data sets were normalized such that direct comparisons can be made independent of the carbon dioxide injection rate. The normalization is defined in equation (3.6). This normalization accommodates for the background CO_2 level that was present in the supplied air. Thus, to perform this normalization one analyzer was used to measure the CO_2 concentrations in the supplied air coming into the cabin and it was custom made using Edinburgh Instrument gas sampling cards and 24V power supplies with 60 Hz noise filters (Figure 3.20). Another analyzer was used to measure CO_2 concentrations of air leaving the cabin and was placed at the exit ports of the cabin. The exit analyzer was of the same model as the one used inside the cabin (Figure 3.19).

$$C_n = \frac{C_{cabin} - C_{inlet}}{C_{exit} - C_{inlet}} \tag{3.6}$$

where C_n is non-dimensional carbon dioxide concentration, C_{cabin} is the average concentration inside the cabin, C_{inlet} is the average CO_2 concentration measured at the inlet duct, and C_{exit} is the average CO_2 measured within the exhausted air.

3.2.2.2 Steady state determination

- Tracer gas was released in Seat 6D on the center line of the cabin at a height of 1.25m above the cabin floor and at a distance of 4.66 m from the Front (South) wall.
- The gas was sampled in Seat D of each of the following rows: 4, 5, 6, and 7 at a height of 1.25 m from the cabin floor, on the centerline of the cabin, and at a distance of 2.87 m, 3.71 m, 4.56 m, and 5.40 m from the front wall, respectively.
- The tests were repeated 2 times for the above seats and the average of the two was adopted as the time needed to achieve steady state.
- After that, four other locations were tested with the release location still in seat 6D. The new locations were Seats 5F, 6F, 7F, and 8F.
- The sampling duration in each seat was 600 seconds (20 minutes) with 1 scan every 5 seconds (i.e. 240 samples).
- After completing the above two sets, the release point was moved to seat 4F and 9A, respectively. In the case when releasing in seat 4F, the sampling was done in seats 5B, 6B, 7B, and 8B. On the other hand, the sampling was conducted in seats 5F, 6F, 7F, and 8F when releasing the gas in seat 9A. The time duration for each sampling location during the last two sets was 700 seconds. There was a 300 seconds gap between each release, when switching from port to another port in the sampling tree, to allow the gas inside the cabin to exhaust out.

- Table 3.11 and Table 3.12 show the time needed to achieve steady state conditions for each sampling seat when releasing CO_2-He mixture in seat 6D, 4F, and 9A, respectively.

Table 3.11 - Steady state time when releasing in seat 6D

Release in Seat 6D			
Collection in Seat	Steady State Time (sec)	Collection in Seat	Steady State Time (sec)
8F	158	7D	151
7F	260	6D	19
6F	253	5D	99
5F	154	4D	154

Table 3.12 - Steady state time when releasing in seats 4F and 9A

Release in Seat 4F		Release in Seat 9A	
Collection in Seat	Steady State Time (sec)	Collection in Seat	Steady State Time (sec)
8B	293	8F	192
7B	228	7F	212
6B	238	6F	222
5B	253	5F	177

Taking the largest possible transported distance into consideration, which is the diagonal distance from opposite corners of the mockup cabin, a 30 minutes test was run to check the maximum possible steady state time. To do so, the release point was installed in seat 11B, whereas, the sampling port was in seat 1F. The steady state time was around 100 seconds, but the signal (sampled concentration) was very weak/small which was not surprising as the transport in the longitudinal direction of the mockup cabin was not expected to be very strong especially when considering the distance from the front to the end back of the cabin. However, the transient concentration stabilized after approximately 100 seconds so an assumption of 300

seconds was a reasonable estimate for the steady state time based on the results shown in Table 3.11 and Table 3.12.

3.2.2.3 Carbon dioxide baseline determination

Since three different CO_2 analyzers were used in the cabin, at the exit, and at the inlet ports, baseline tests were needed to clear any instrumental differences. Each unit was placed in the location where it was used during normal testing (exit and inlet units were placed on the roof of the mockup cabin and the cabin analyzer was connected to the sampling tree to mimic the same conditions during the tracer gas sampling tests). The analyzers were run for 13 continuous hours without any CO_2 injection. The cabin doors were kept close during the testing and the supplied air temperature was maintained at 15.5 °C (60 F). The CO_2 concentration, in parts per millions (ppm), sampled during the 13 hours test by the three analyzers are plotted in Figure 3.39. Figure 3.40 plots the same data but averaged over 100 points of the actual sampled data.

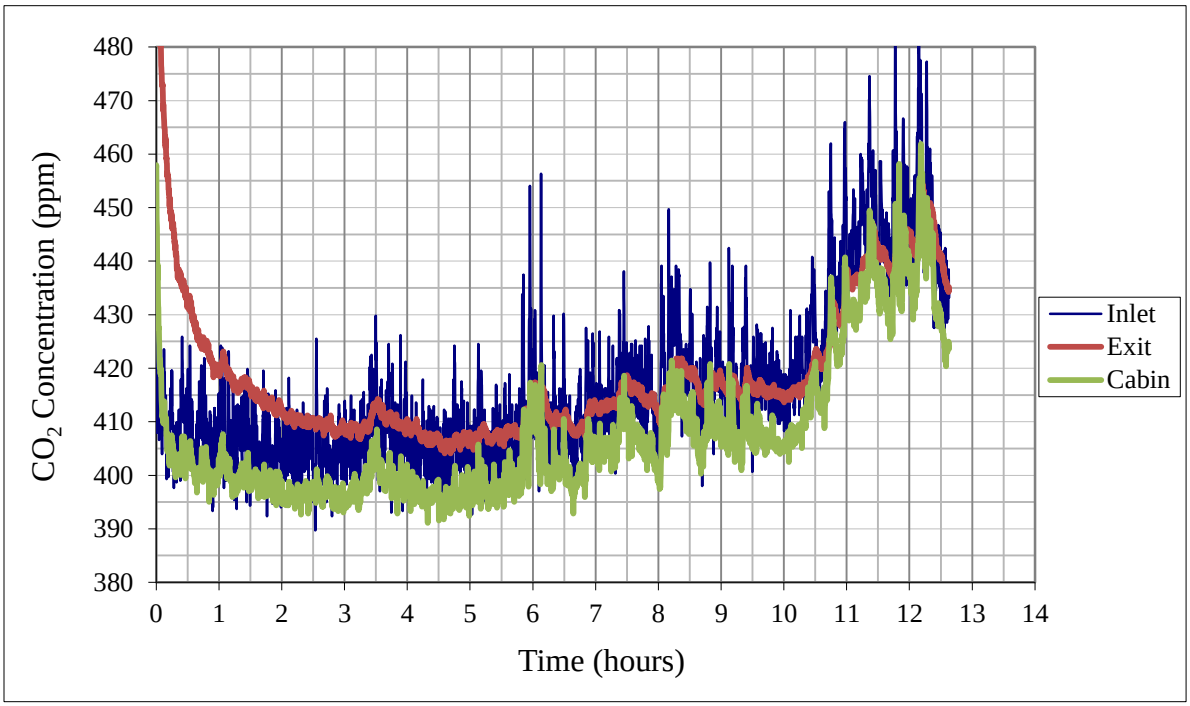

Figure 3.39 - Baseline test # 1 for the three CO_2 analyzers

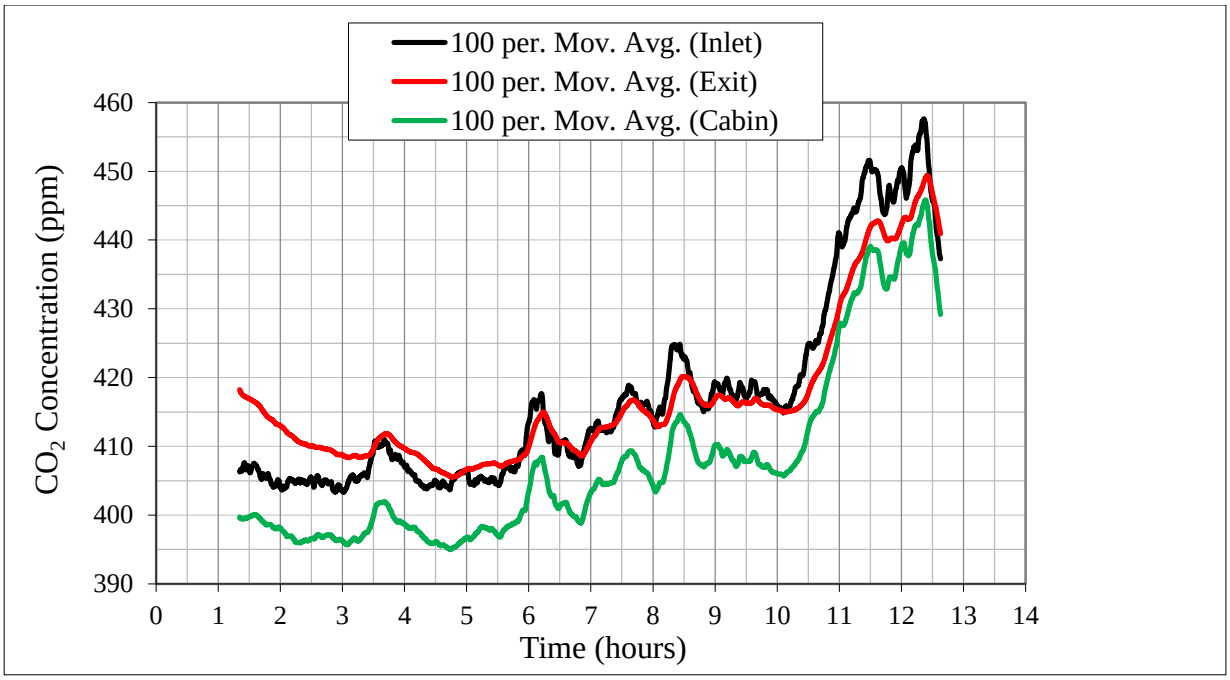

Figure 3.40- Baseline test # 1 for the three CO_2 analyzers averaged over 100 points

The inlet analyzer, the Edinburg analyzer, showed more noise than the other two units. However, the exit and the inlet analyzers seemed to be running with minimal differences as shown in Figure 3.39 or Figure 3.40. The cabin analyzer was offset by approximately 10 ppm.

As described before in the calibration tests, every time the soda lime used in the PP-System analyzers became brown the units were calibrated and baseline reference tests were repeated to ensure accurate data were collected. Another set of baseline tests is shown in Figure 3.41. Results of the two baseline tests concluded that the concentration sampled by the unit placed in the cabin were offset by a value of approximately 10 ppm. To accommodate for this shift between the analyzers and to ensure that the three analyzers were running with the same background reference, a value of 10 ppm was added to the concentration sampled by the cabin analyzer.

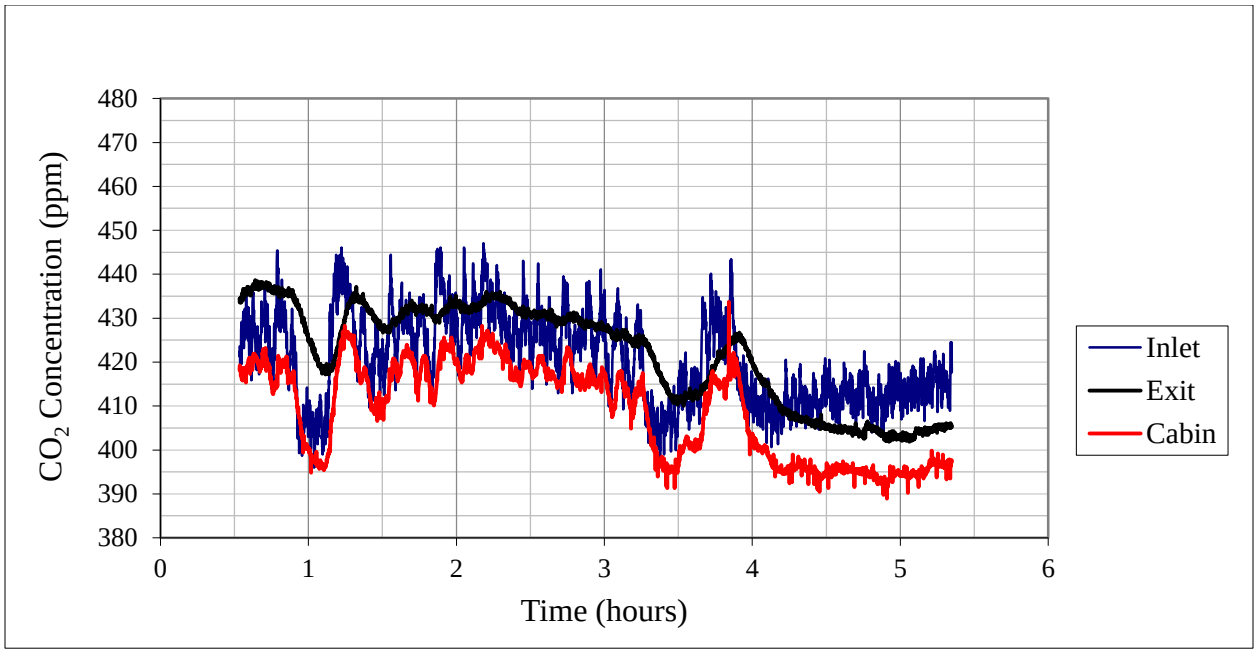

Figure 3.41 - Baseline test # 2

3.2.2.4 Investigating the effect of thermal plumes on airflow

Heat sources are very common in most indoor environments. They have an impact on indoor airflow as they generate thermal plumes – warm convective currents driven upwards by buoyancy forces. Thermal plumes can significantly influence air flow distribution indoors as well as indoor environment quality. Aircraft passenger cabins are occupied by humans. The sensible heat released by the human body can affect the temperature and humidity of the surrounding environment. This rise in temperature and humidity can affect the velocity and the airflow distribution inside aircraft cabin.

This section examined the effect of thermal plumes and energy generated by passengers occupying an aircraft cabin on airflow, temperature distribution, and turbulence parameters inside the mockup cabin. Tracer gas measurements and procedures described in previous sections were repeated, but with no heat generated by the thermal manikins.

3.2.2.5 Vertical investigation methodology

In the heated and unheated manikin cases, the tracer gas release point was fixed at a height of 1.25 m above the cabin floor, while the sampling ports where the tracer gas was sampled were fixed at a height of 1.23 m above the cabin floor. Since the airflow inside the cabin is highly mixed and chaotic, as was shown in the smoke visualization results, a three dimensional flow is thought to control the flow transport resulting from mixing the lateral and longitudinal circulations. To examine the difference in the exposure levels at different elevations, vertical sampling tests were conducted under heated and unheated manikins conditions. Tracer gas was released in seat 2D and in seat 5D and all procedures described in the previous sections were repeated. The only difference was that the sampling was done at different elevations at heights of 448, 896, 1344, and 1792 mm (448 mm vertical increments), as shown in Figure 3.42. When releasing in seat 2D, the east and west aisles of the cabin in row 2 were investigated. When releasing in seat 5D, CO_2 was sampled in the east and west aisles of row 4 and row 6. Equation (3.6) was used to perform normalization for the sampled tracer gas.

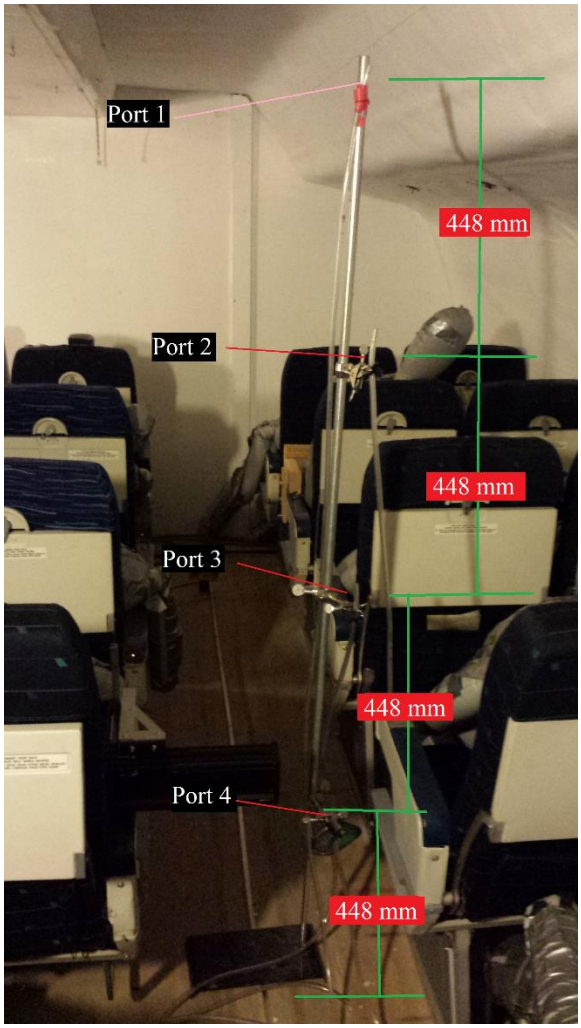

Figure 3.42 - Vertical sampling experimental setup

Chapter 4 - Results

4.1 Flow visualization results

Airflow patterns inside the mockup cabin were tracked by capturing consecutive timed series photos and video snapshots for the smoke dispersion after its release in different locations inside the cabin. Many cases of smoke flow were repeated and documented in Appendix B - . Figure 4.1 illustrates one timed series event captured in seat 1D with the camera being directed from top to bottom. More than one picture or incident were documented in Appendix B - for each location to ensure the repeatability of the observed smoke flow phenomena. Each event was represented in Figure 4.2 where the length of the arrows indicates an approximation of the limit at which smoke was observed in each specific release location and the arrow direction is the direction of the traced gas.

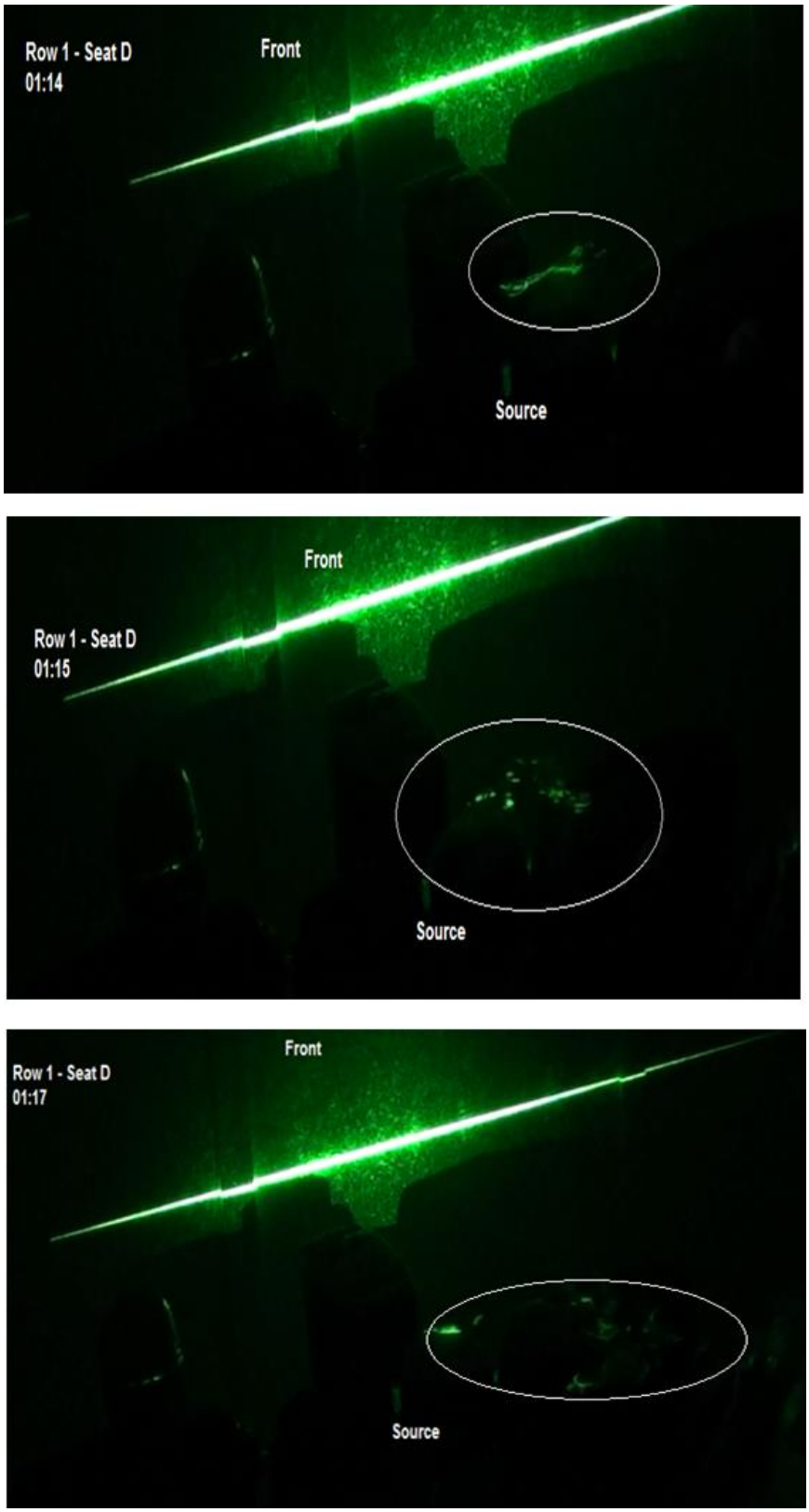

Figure 4.1 - Smoke visualization time series events for seat 1D

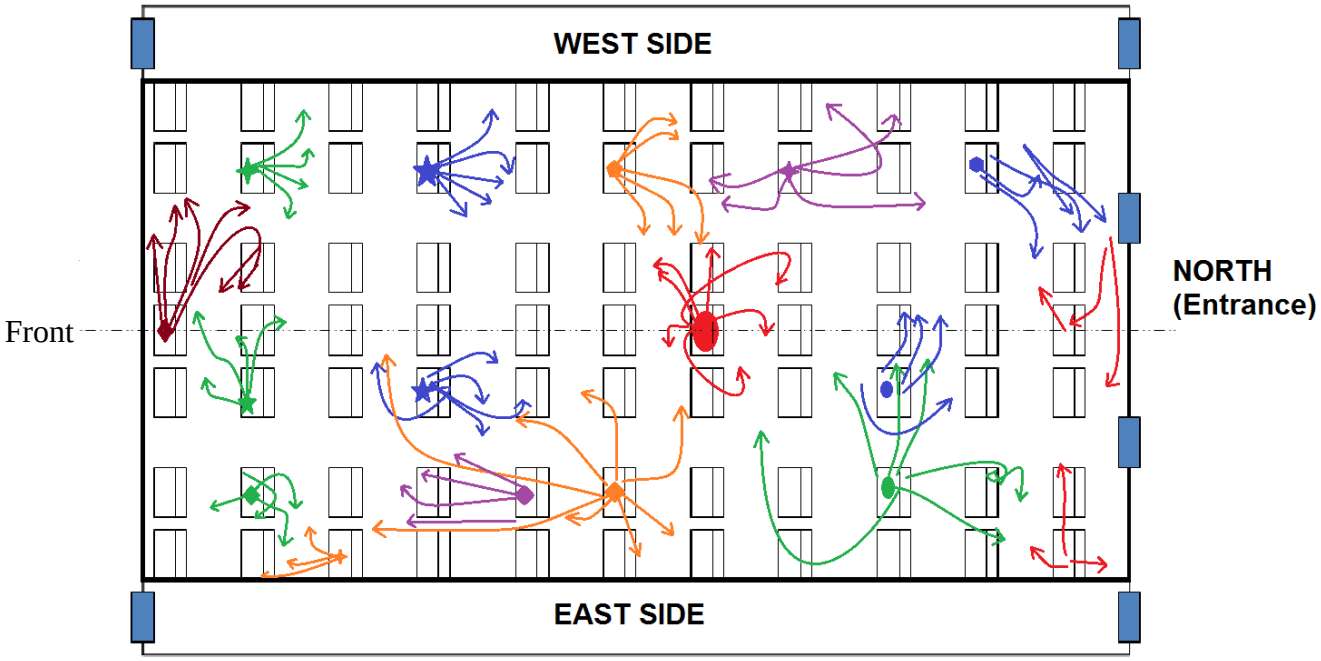

Figure 4.2 - Local smoke visualization results

4.2 Tracer gas results

The r esults for the tracer gas experiments for heated and unheated manikins as described in Chapter 3 - are shown in this section. Tracer gas was released in each scenario in seats: 2D, 5D, 7D, and 10D to investigate the airflow in the regions around the centerline seats of the cabin; in seats 4F and 9F in the west side and in seats 5B and 8B in the east side of the mockup cabin.

4.2.1 Heated manikins results

Tracer gas sampling was repeated 3 times in each sampling location. The individual test results along with the averages are documented in Appendix C - . The y-axis is the normalized CO_2 in parts per million (ppm), and the x-axis is the duration of the tests. The averages for each release location are summarized in Figure 4.3 through Figure 4.10 where the normalized CO_2 is on the vertical axis, seat index is on the transverse axis, and row index is on the longitudinal

index. The normalized values are plotted and colored as a percentage of the sampled CO_2 in the release location.

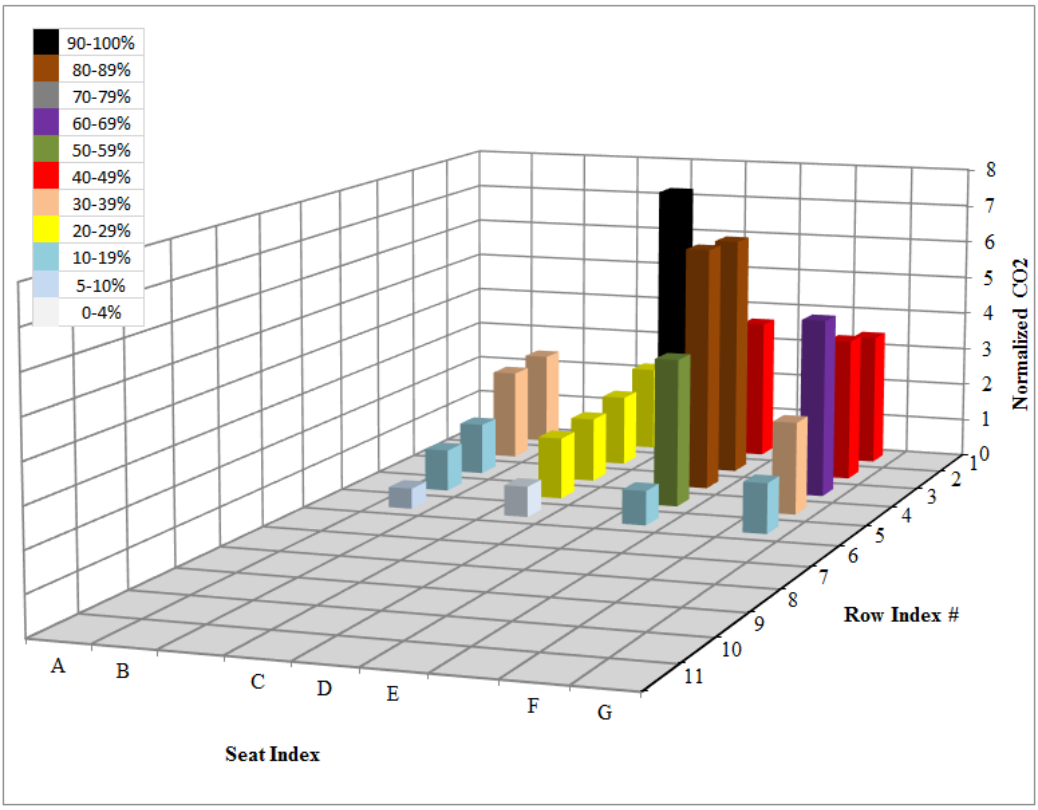

Figure 4.3 - Normalized CO_2 with a colored map percentage distribution with respect to the concentration sampled in the release seat in 2D (heated manikins)

As a preliminary observation, the majority of the tracer gas released in the front section of the mockup cabin was drifting towards the west side of the cabin, as can be seen in Figure 4.3 (seat 2D) and in Figure 4.9 (seat 5B). More quantitative analysis is presented in the analysis section. For the middle and the back sections of the cabin, it was more difficult to draw any conclusions based on the colored map charts presented in Figure 4.4 through Figure 4.10. More detailed and quantitative analysis had to be done before drawing out any conclusions. The exact average values of the sampled tracer gas were used in the analysis section instead of the charts

presented in this section as these charts present good visualized results but not the best tool for detailed quantitative comparisons. The results of more than one release location were combined together to conclude the behavior of the flow in specific sections inside the mockup cabin. For example, the results for seat 2D showed that the extent of the gaseous longitudinal dispersion were limited to the region between row 4 and row 5. However, this result was not certain. Analysis of the results for release in seat 4F (Figure 4.7) and in seat 5D (Figure 4.4), it was concluded that the gaseous transport around row 5 had a major drift from the west to the east side and beyond that region it was from east to west and moving backwards as was seen in results when releasing in seat 5D (Figure 4.4) and in 7D (Figure 4.5). Also, the results of sampling in the vertical direction were utilized to clarify and confirm some of the results.

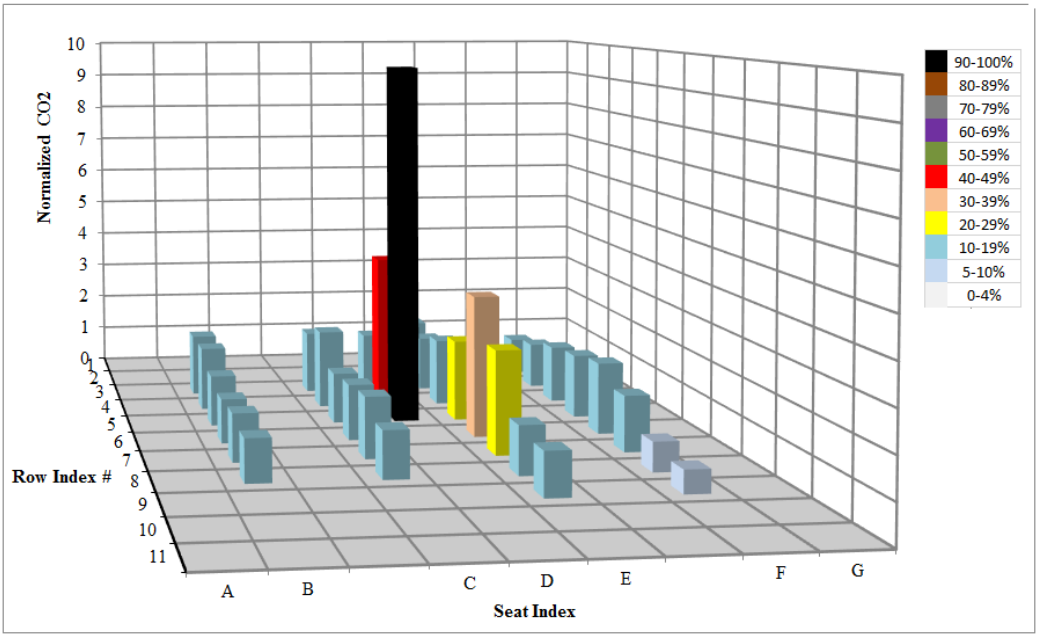

Figure 4.4 - Normalized CO_2 with a colored map percentage distribution with respect to the concentration sampled in the release seat in 5D (heated manikins)

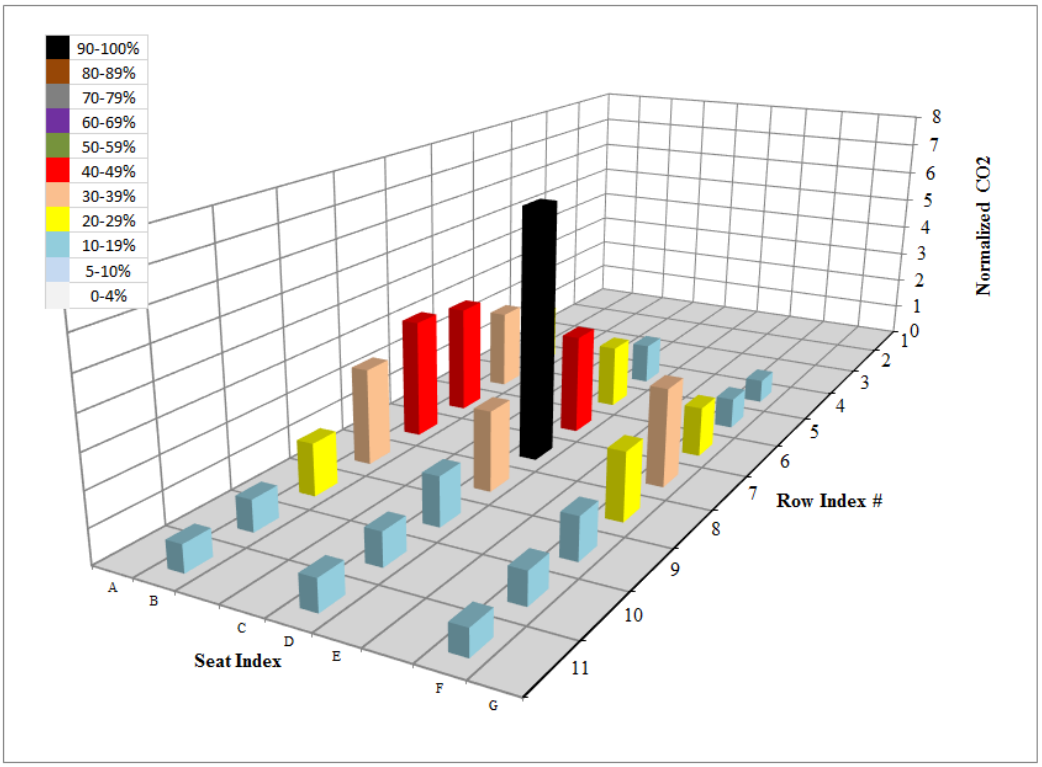

Figure 4.5 - Normalized CO_2 with a colored map percentage distribution with respect to the concentration sampled in the release seat in 7D (heated manikins)

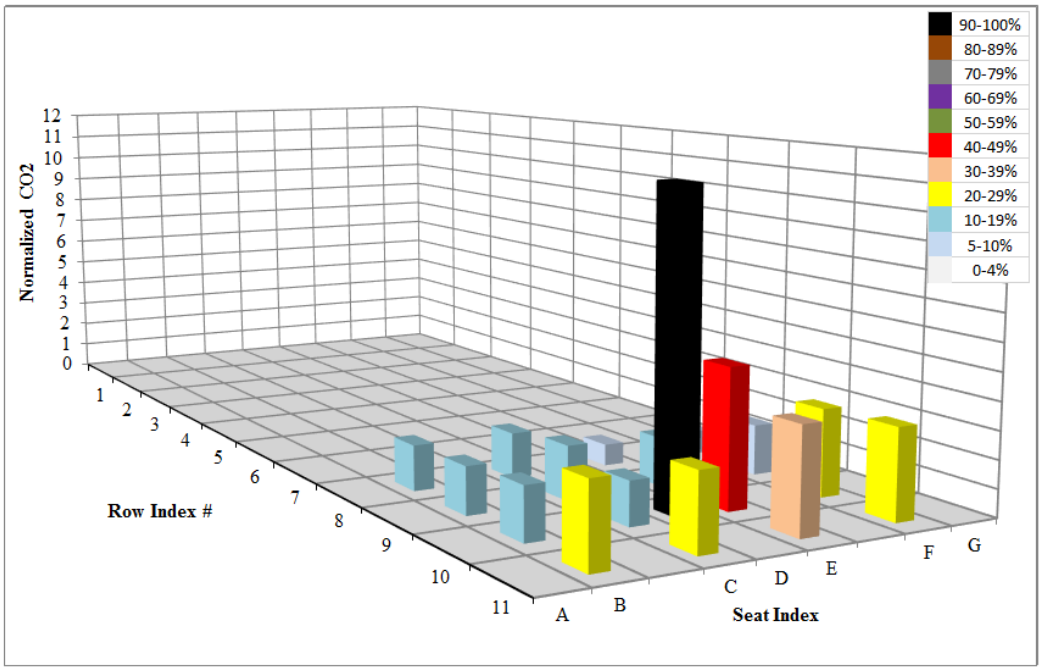

Figure 4.6 - Normalized CO_2 with a colored map percentage distribution with respect to the concentration sampled in the release seat in 10D (heated manikins)

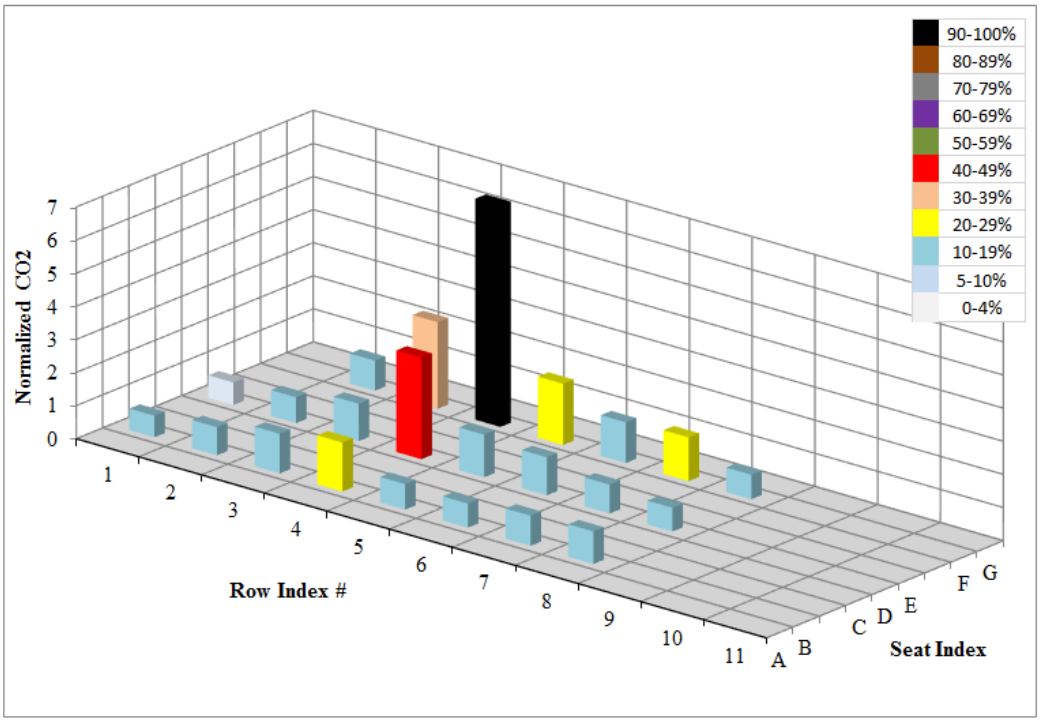

Figure 4.7 - Normalized CO_2 with a colored map percentage distribution with respect to the concentration sampled in the release seat in 4F (heated manikins)

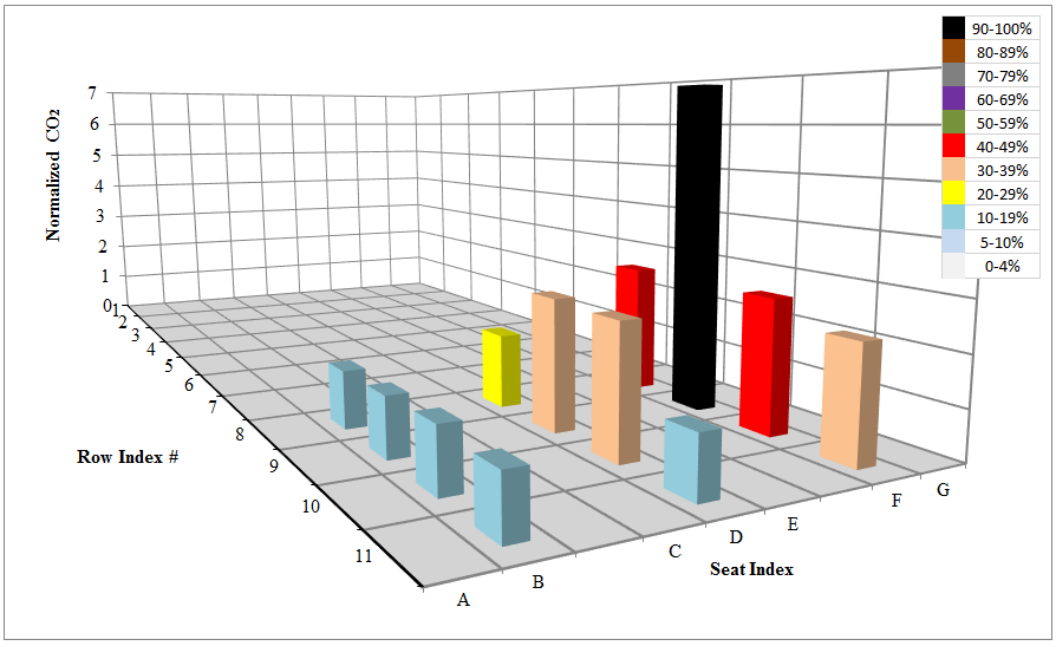

Figure 4.8 - Normalized CO_2 with a colored map percentage distribution with respect to the concentration sampled in the release seat in 9F (heated manikins)

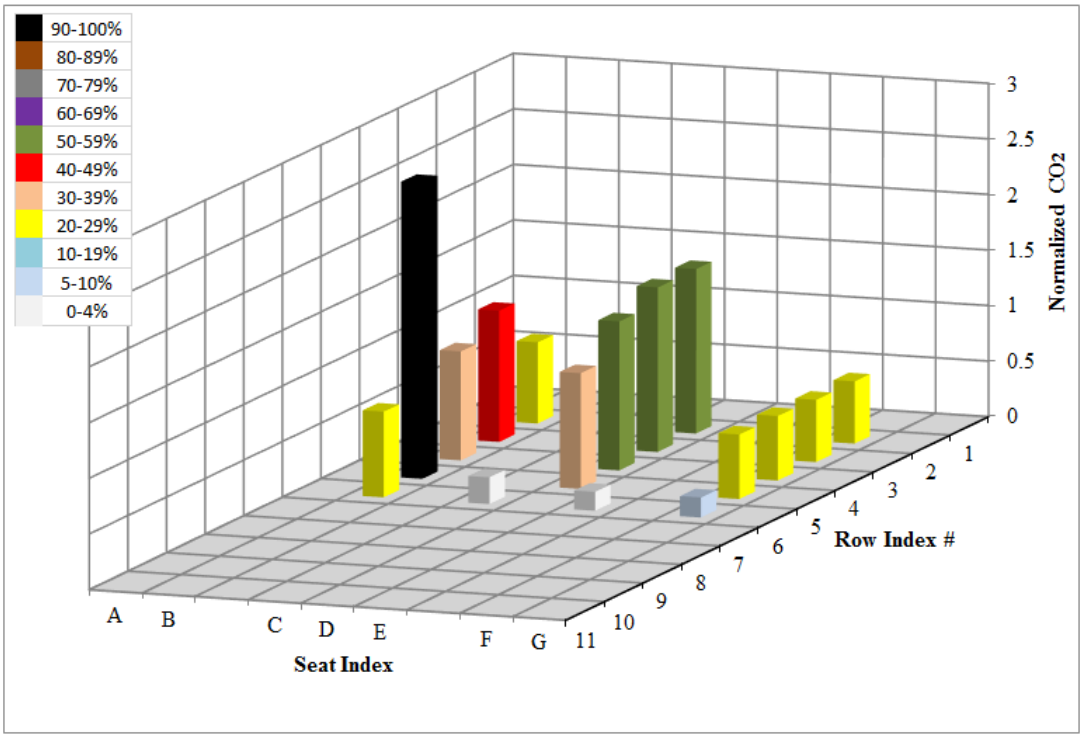

Figure 4.9 - Normalized CO_2 with a colored map percentage distribution with respect to the concentration sampled in the release seat in 5B (heated manikins)

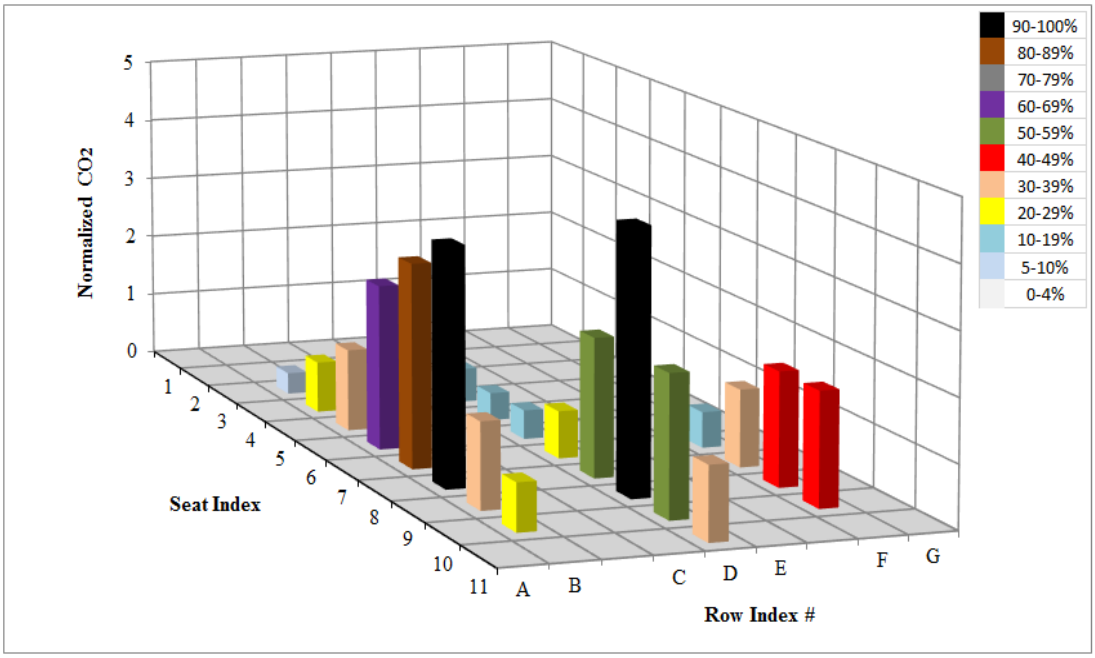

Figure 4.10 - Normalized CO_2 with a colored map percentage distribution with respect to the concentration sampled in the release seat in 8B (heated manikins)

4.2.2 Unheated manikins results

The individual test results for tracer gas sampling with unheated manikins are documented in Appendix D - . Similar to heated average results, presented in the previous section, colored percentage distribution charts are shown in Figure 4.11 through Figure 4.18.

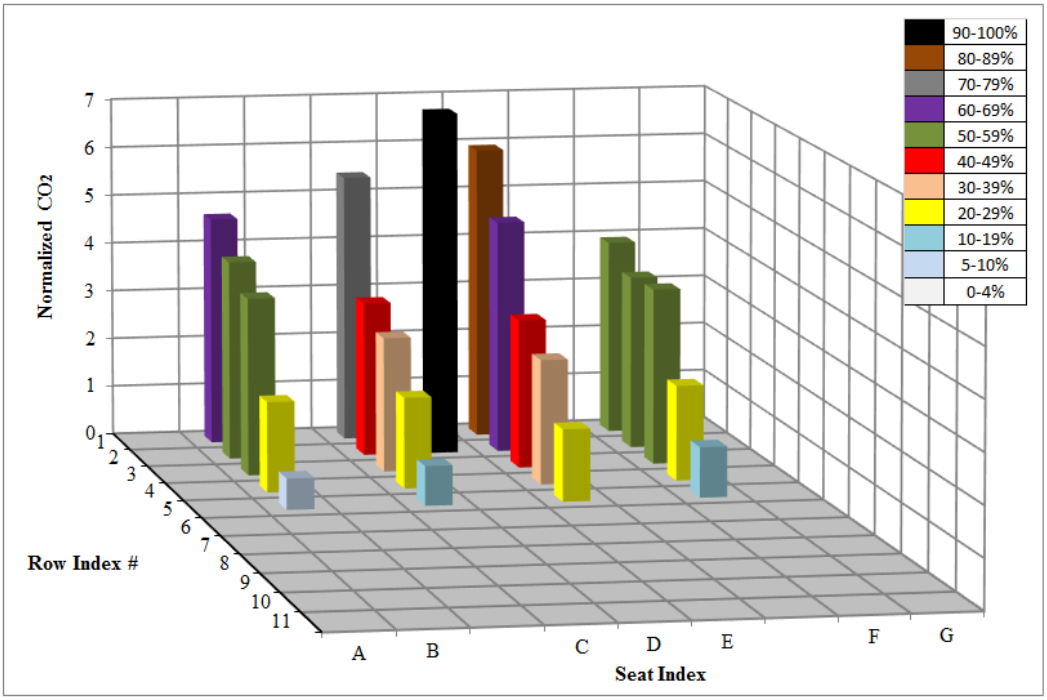

Figure 4.11 - Normalized CO_2 with a colored map percentage distribution with respect to the concentration sampled in the release seat in 2D (unheated manikins)

With unheated manikins, the data were scattered over more seats in the east and west sides of the cabin with similar exposure rather than into one side of the cabin only with higher exposures than the other. This can be seen by comparing results for seat 2D (Figure 4.3 and Figure 4.11), for seat 5D (Figure 4.4 and Figure 4.12), and for seat 7D (Figure 4.5 and Figure 4.13).

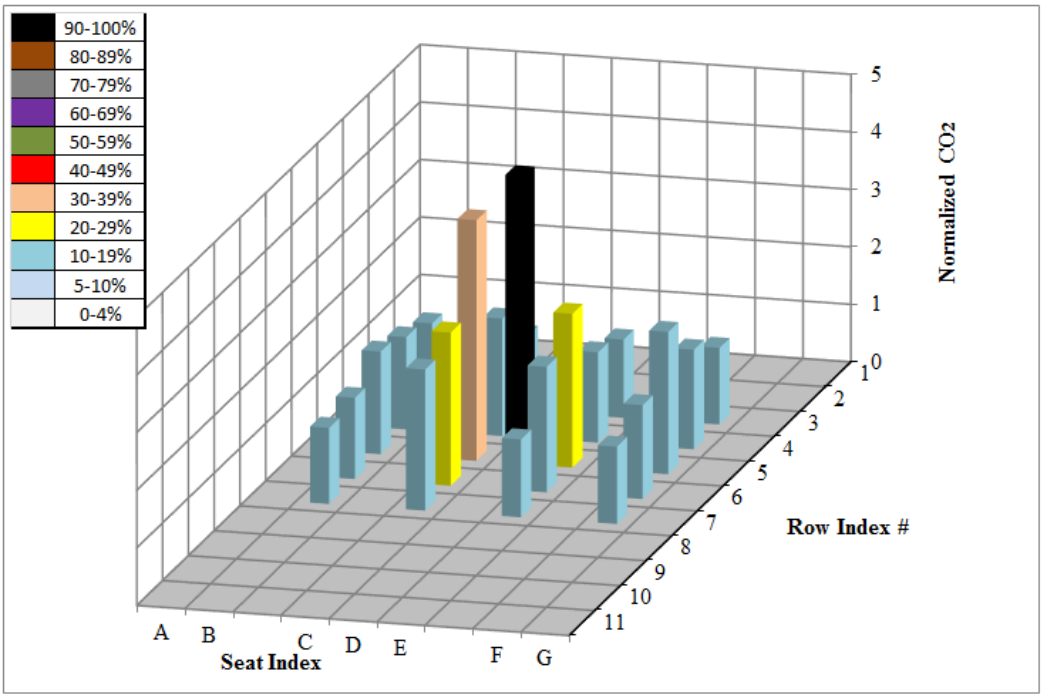

Figure 4.12 - Normalized CO_2 with a colored map percentage distribution with respect to the concentration sampled in the release seat in 5D (unheated manikins)

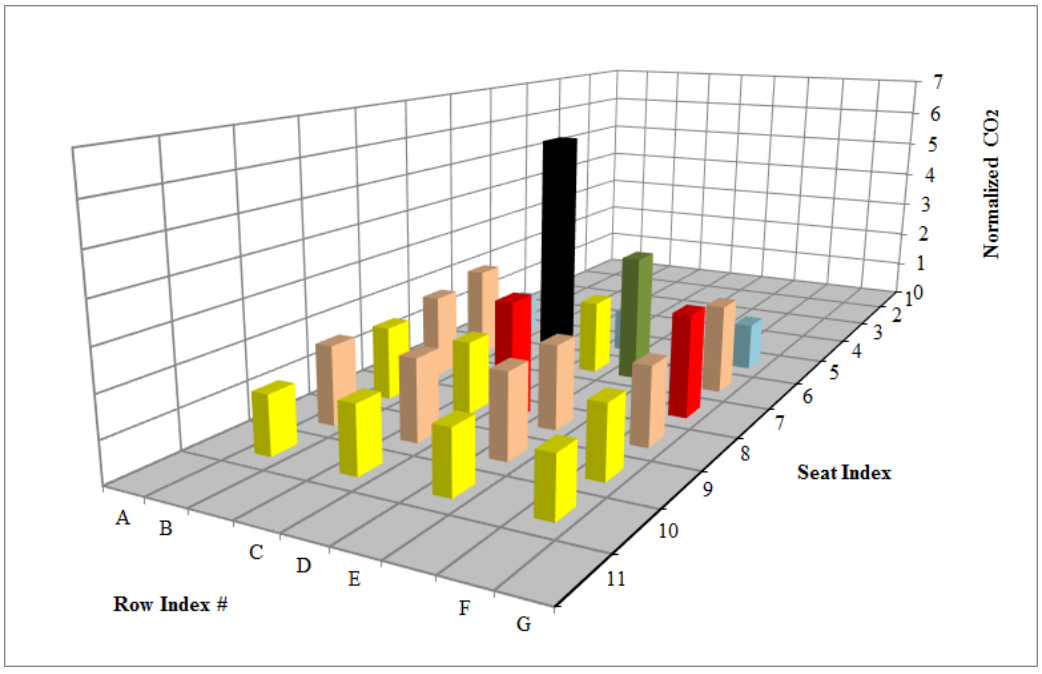

Figure 4.13 - Normalized CO_2 with a colored map percentage distribution with respect to the concentration sampled in the release seat in 7D (unheated manikins)

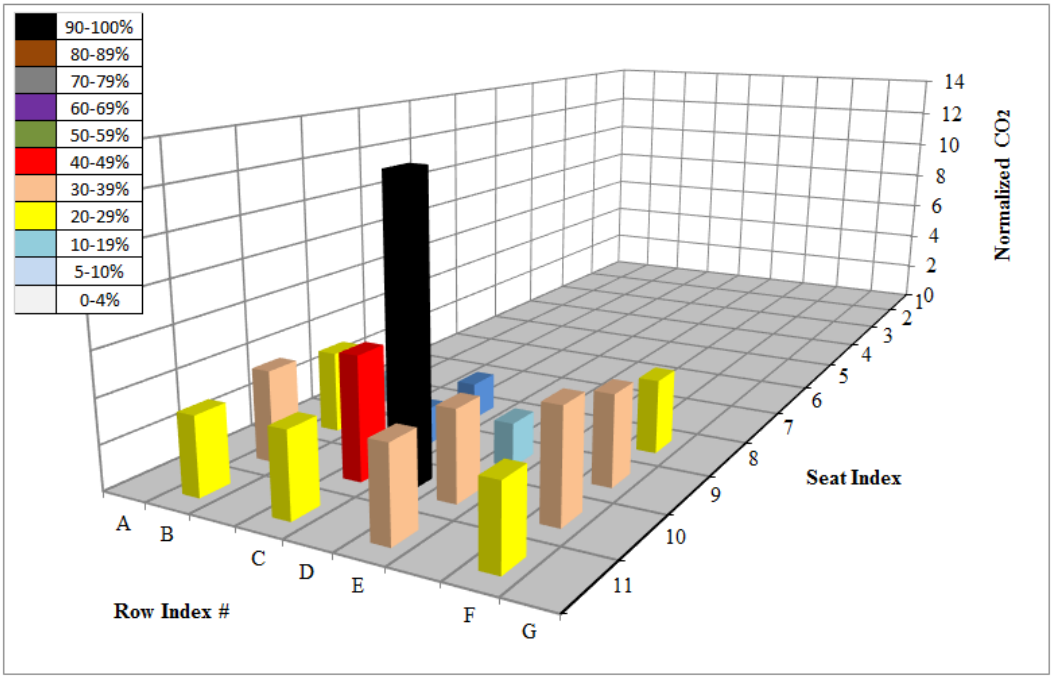

Figure 4.14 - Normalized CO_2 with a colored map percentage distribution with respect to the concentration sampled in the release seat in 10D (unheated manikins)

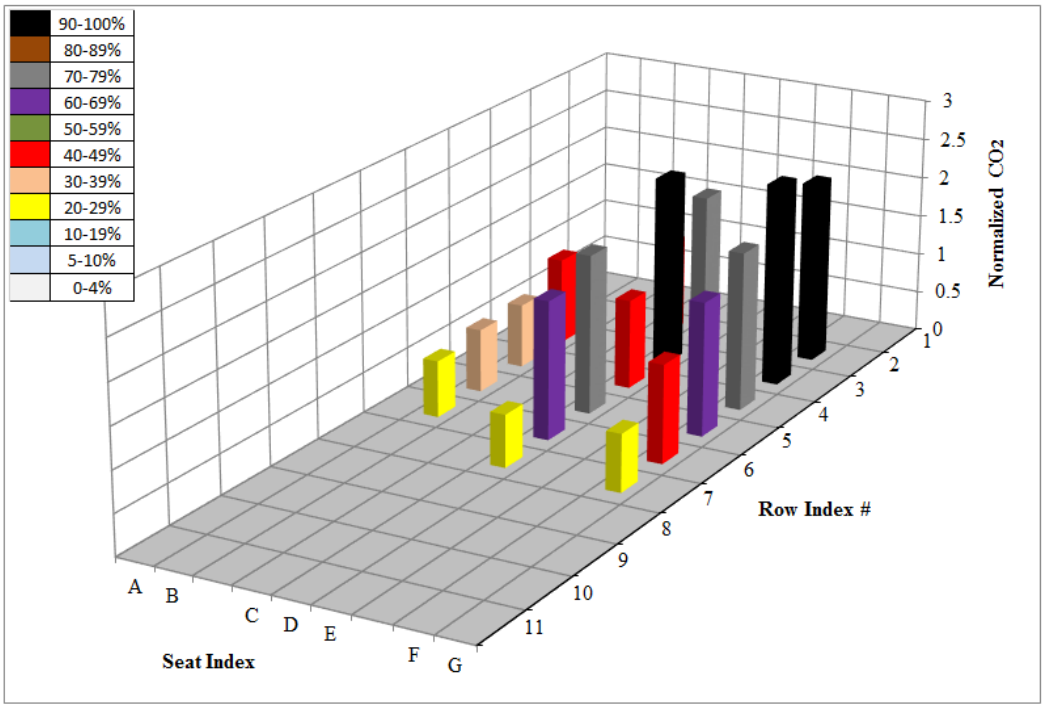

Figure 4.15 - Normalized CO_2 with a colored map percentage distribution with respect to the concentration sampled in the release seat in 4F (unheated manikins)

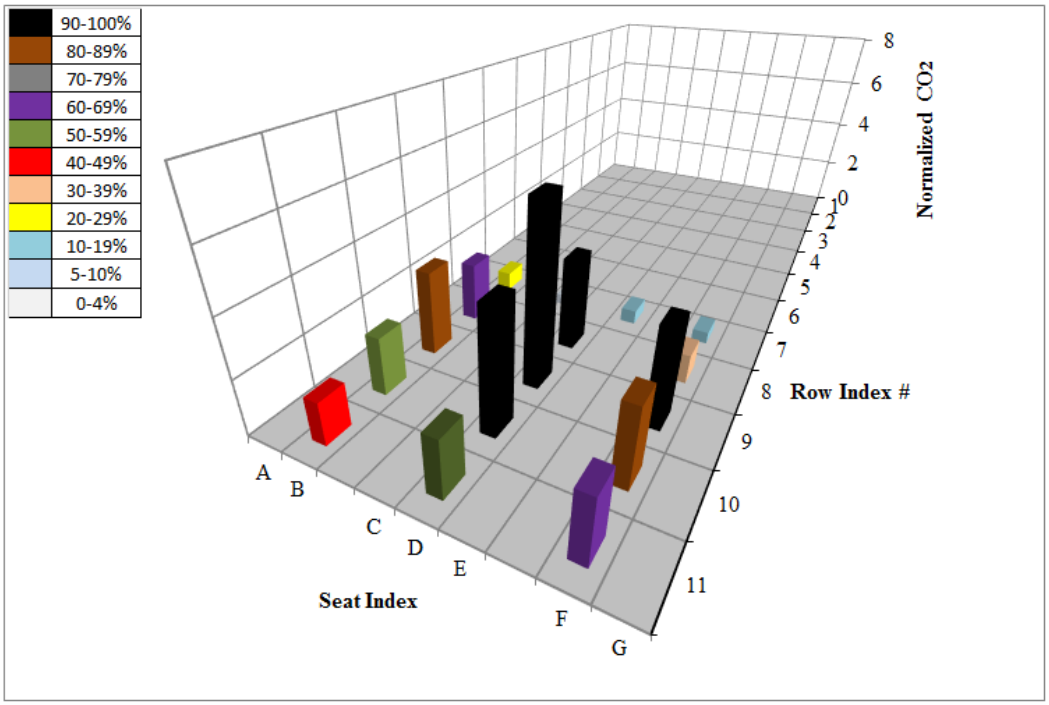

Figure 4.16 - Normalized CO_2 with a colored map percentage distribution with respect to the concentration sampled in the release seat in 9F (unheated manikins)

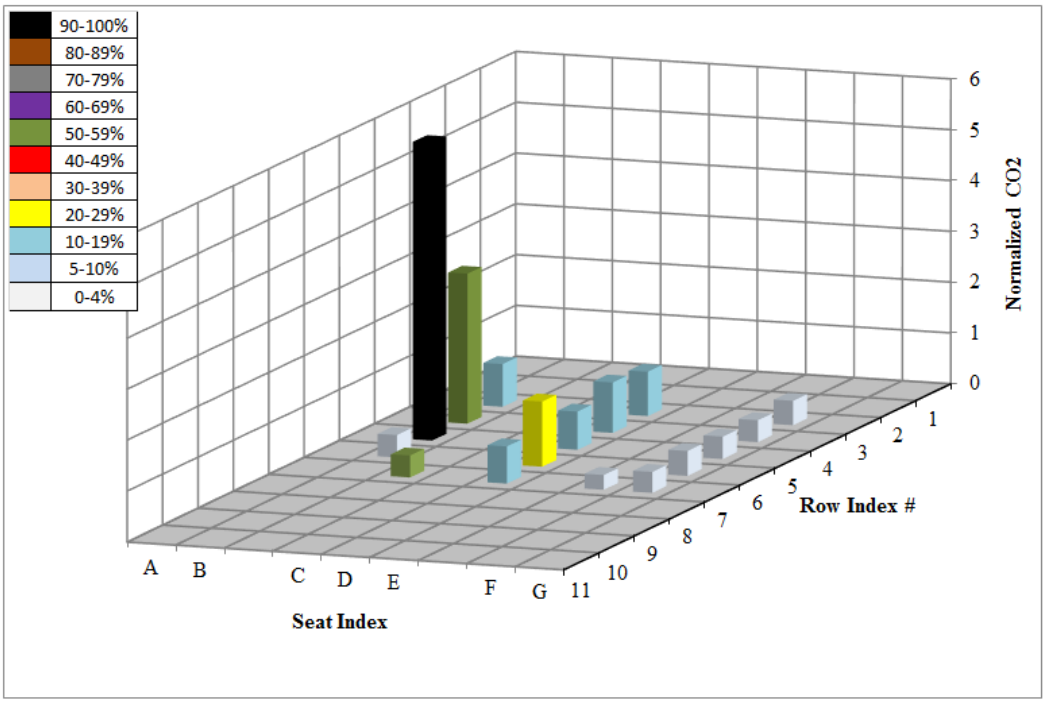

Figure 4.17 - Normalized CO_2 with a colored map percentage distribution with respect to the concentration sampled in the release seat in 5B (unheated manikins)

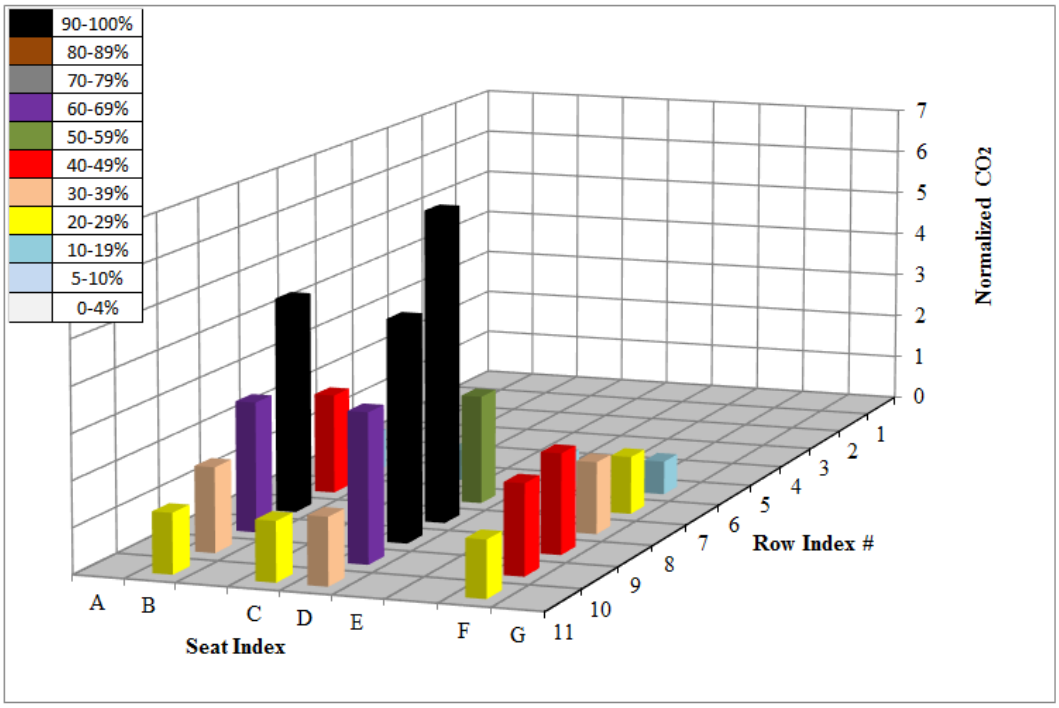

Figure 4.18 - Normalized CO_2 with a colored map percentage distribution with respect to the concentration sampled in the release seat in 8B (unheated manikins)

4.2.3 Vertical sampling results

As described in the experimental setup and methodology sections, it was important to check on the differences in the sampled tracer gas at various elevations to justify some of the results and analysis as will be discussed later in the analysis section. Tracer gas was released in seats 2D and 5D and was collected in the east and west aisles at a height of 448, 896, 1344, and 1792 mm above the cabin floor as shown in Figure 3.42. The results for release in seat 2D are shown in Figure 4.19 and Figure 4.20 for sampling in the east and west aisles of row 2, respectively. It was observed that in the front section of the cabin, the east side experienced lower exposures than the west side under both conditions heated and unheated manikins. With unheated manikin cases, the exposure increased in the east and decreased in the west. Despite the running conditions, heated or unheated, the lower levels in the west aisle of row 2 had the

highest exposures compared to all levels considered in the east and west aisles or row 2. Two other observations were concluded from the vertical exposure testing in the front part of the cabin. The first one was that the vertical exposure in the east aisle was almost the same at all elevations for each case taking into consideration the different individual tests (shown in the figures) and the statistical differences based on 95% confidence intervals (not shown) and that the heated cases had lower exposures than the unheated cases. The other observation was that the samples collected in the west aisle of row 2 for 1 m and above were almost the same with unheated manikins only.

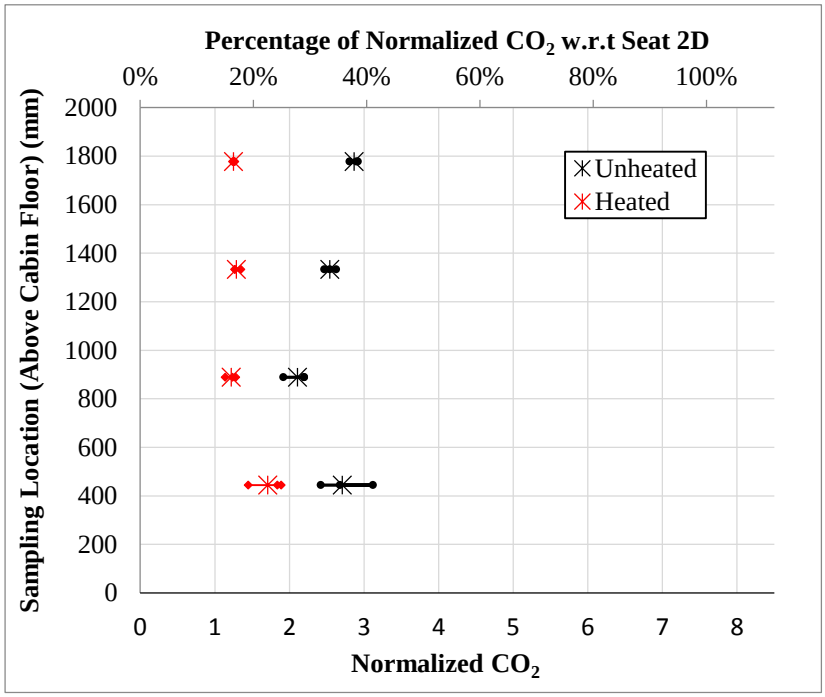

Figure 4.19 – Individual and average vertical exposures in the east aisle of row 2 when releasing in seat 2D

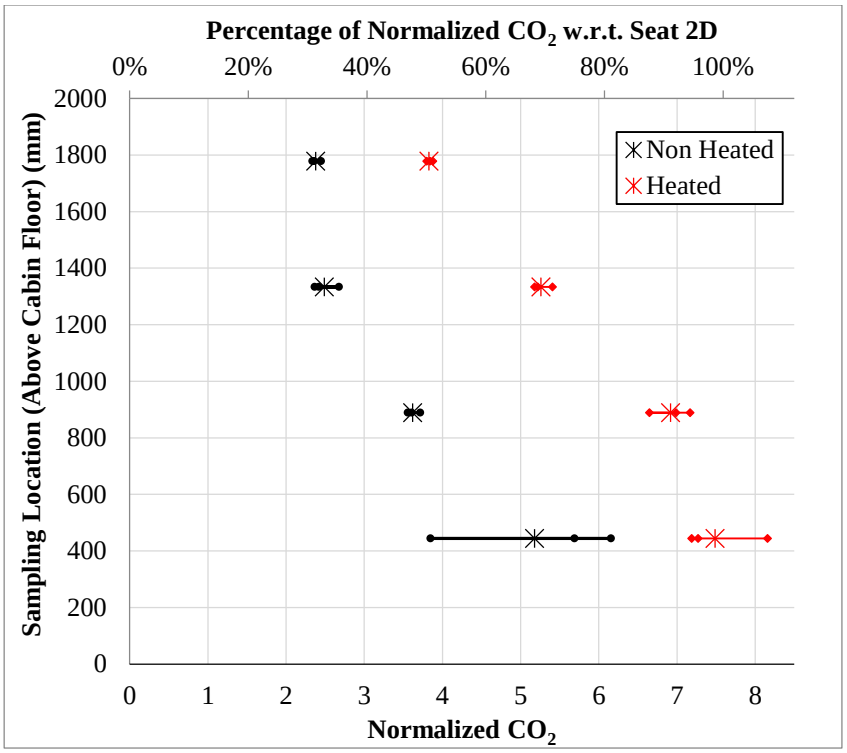

Figure 4.20 - Individual and average vertical exposures in the west aisle of row 2 when releasing in seat 2D

For the middle section of the cabin, Figure 4.21 shows the samples collected in the east and west aisles of each of row 4 and row 6, when releasing tracer gas in seat 5D, under normal operating conditions with heated manikins. Figure 4.22 shows the same results presented in Figure 4.21 but with unheated manikins. For the heated case, the samples collected at all elevations in the east side of row 4 were higher than those in the west side, whereas the opposite was true for row 6 where the west side experienced higher exposures than the east side at all elevations. The differences between the east and west sides were reduced with unheated manikins and it even overlapped in row 6.

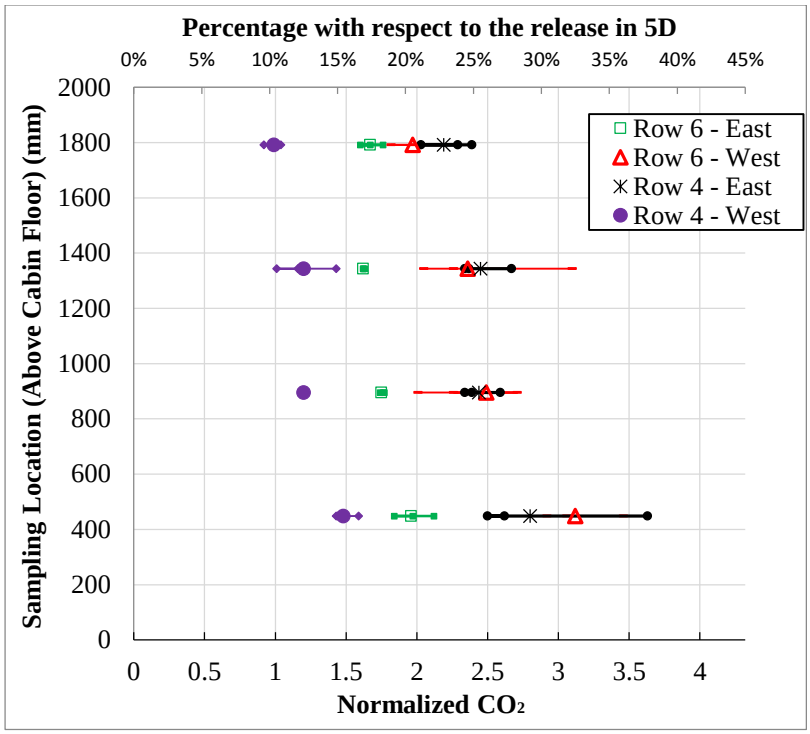

Figure 4.21 - Individual and average vertical exposures in the east and west aisles of row 4 and 6 when releasing in seat 5D (heated case)

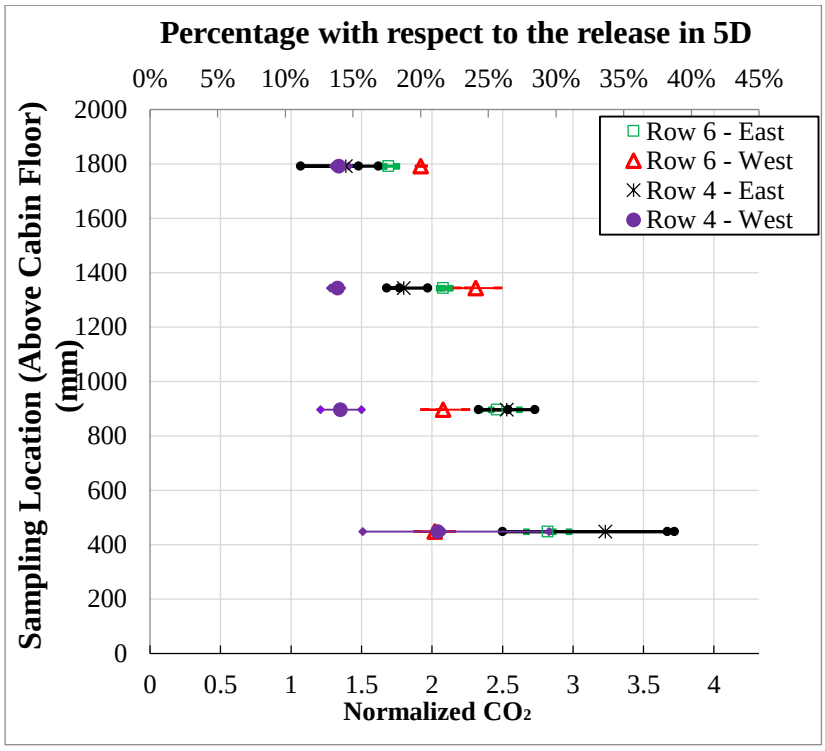

Figure 4.22 - Individual and average vertical exposures in the east and west aisles of row 4 and 6 when releasing in seat 5D (unheated case)

4.3 Airflow speed results

The speed was measured in 33 seats, as described in section 3.1.5, at a height of 1.23 m above the cabin floor which was the same level where the tracer gas was sampled. Measurements were taken in seat B of the east aisle seats, in seat D of the centerline seats, and in seat F of the west aisle seats in each of the 11-rows inside the cabin. The plots in Figure 4.23 through Figure 4.55 show the averages of the three measurements taken in each seat with heated manikins, whereas for unheated manikins it is shown in Figure 4.56 to Figure 4.88. The dashed line was the waiting period for the airflow to achieve steady state conditions inside the cabin which was the same as the time used during tracer gas sampling (300 seconds).

4.3.1 Airflow speed results with heated manikins

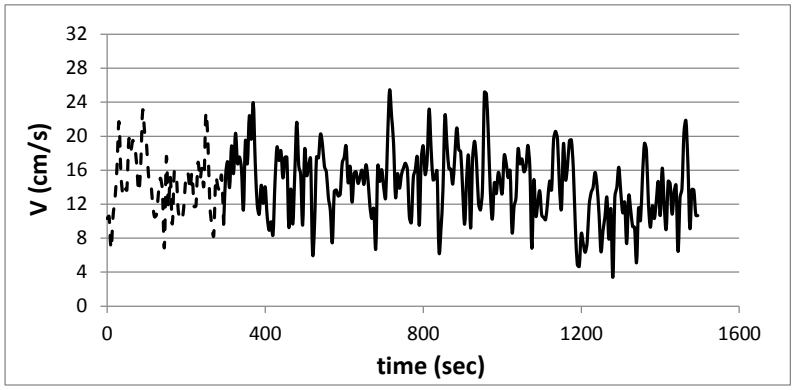

Figure 4.23 - Average speed in row 1 - seat B

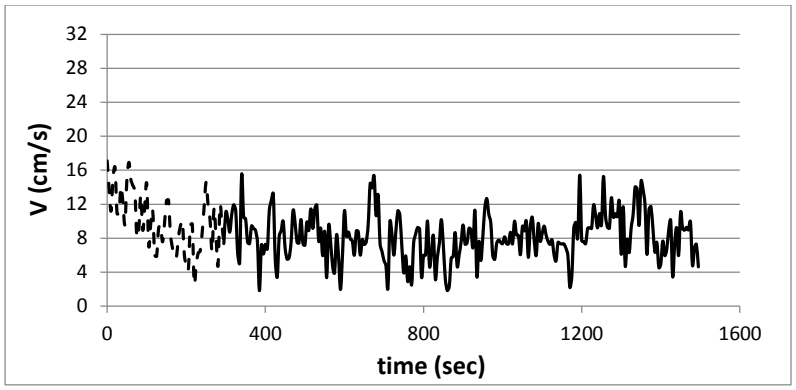

Figure 4.24 - Average speed in row 2 - seat B (heated)

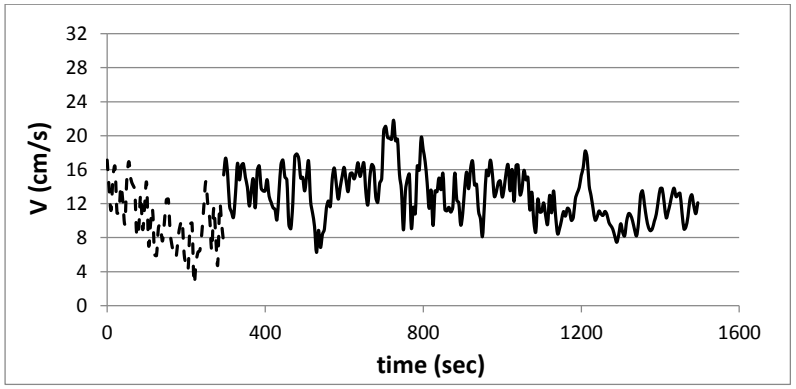

Figure 4.25 - Average speed in row 3 - seat B (heated)

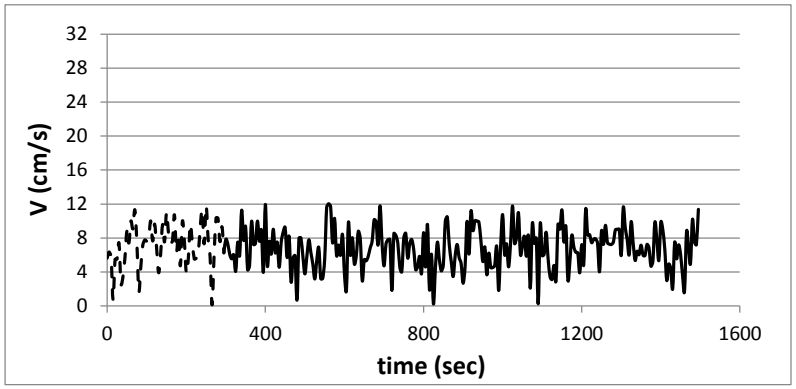

Figure 4.26 - Average speed in row 4 - seat B (heated)

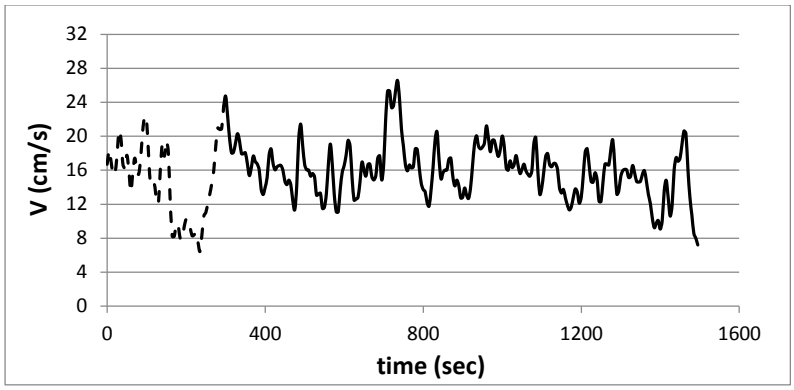

Figure 4.27 - Average speed in row 5 - seat B (heated)

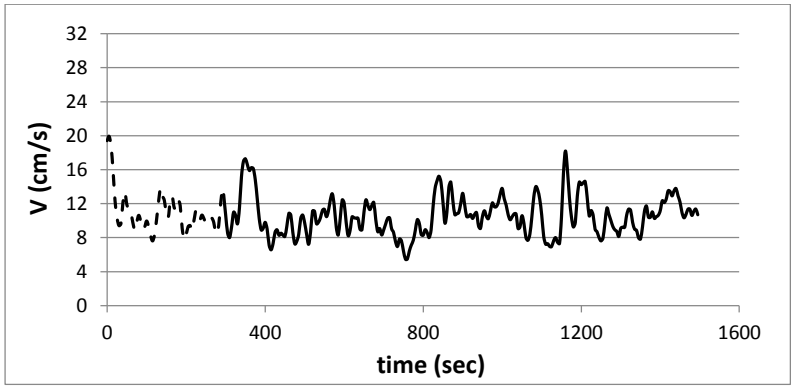

Figure 4.28 - Average speed in row 6 - seat B (heated)

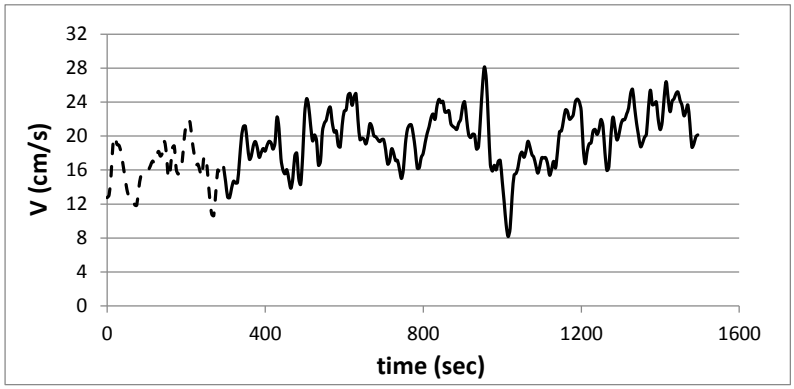

Figure 4.29 - Average speed in row 7 - seat B (heated)

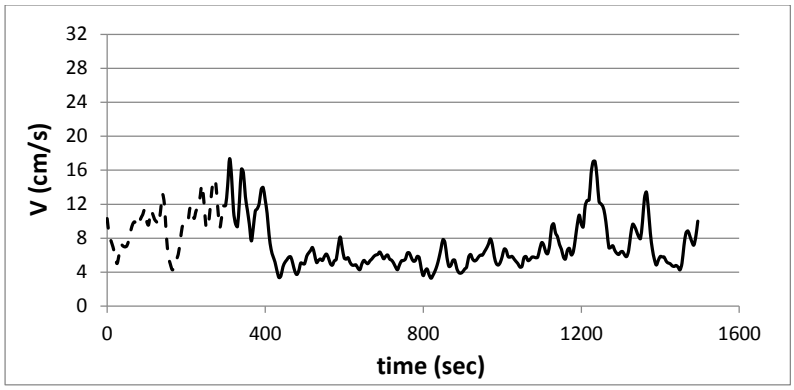

Figure 4.30 - Average speed in row 8 - seat B (heated)

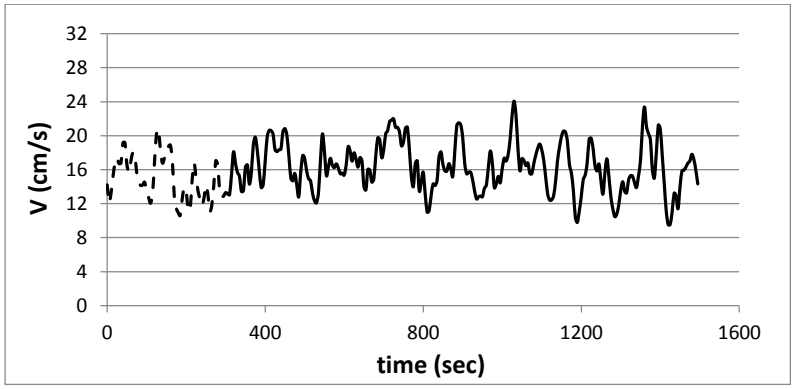

Figure 4.31 - Average speed in row 9 - seat B (heated)

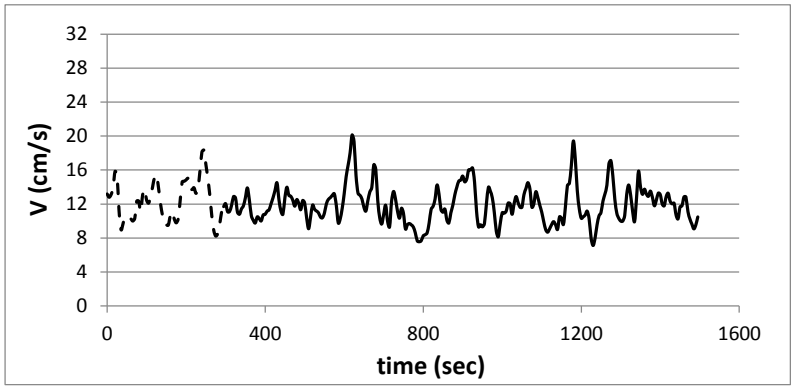

Figure 4.32 - Average speed in row 10 - seat B (heated)

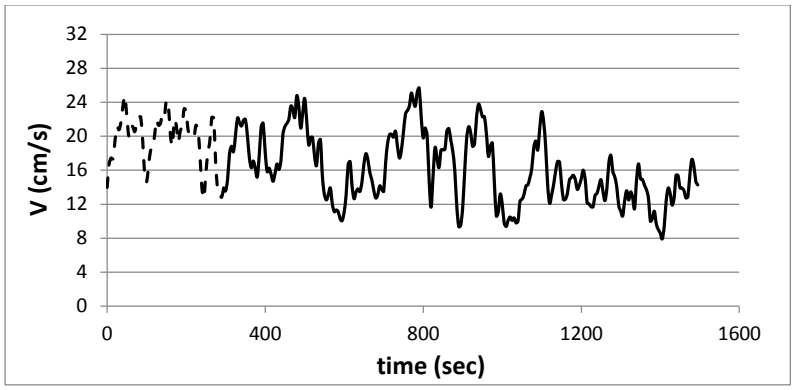

Figure 4.33 - Average speed in row 11 - seat B (heated)

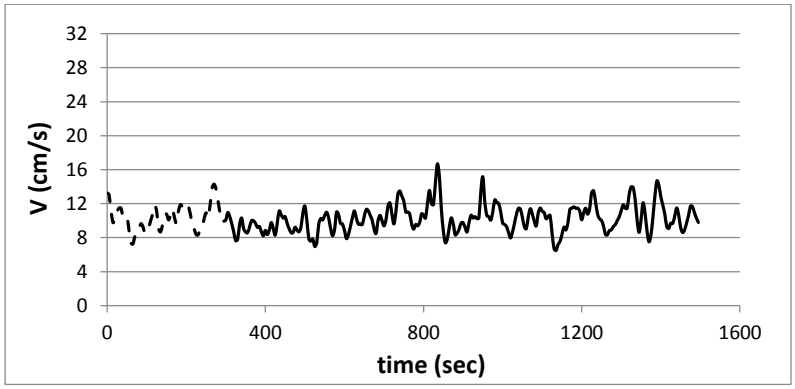

Figure 4.34 - Average speed in row 1 - seat D (heated)

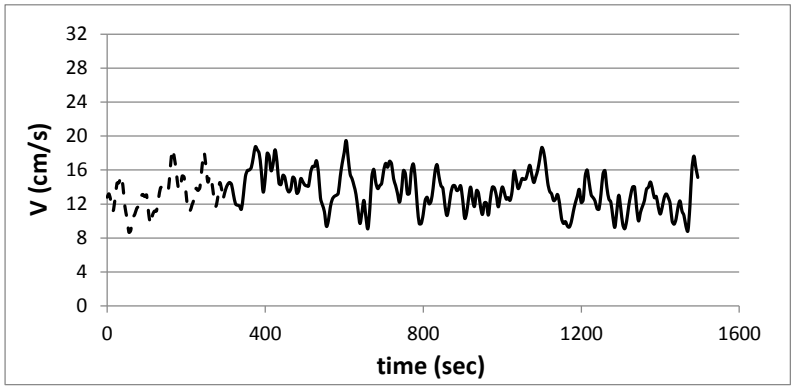

Figure 4.35 - Average speed in row 2 - seat D (heated)

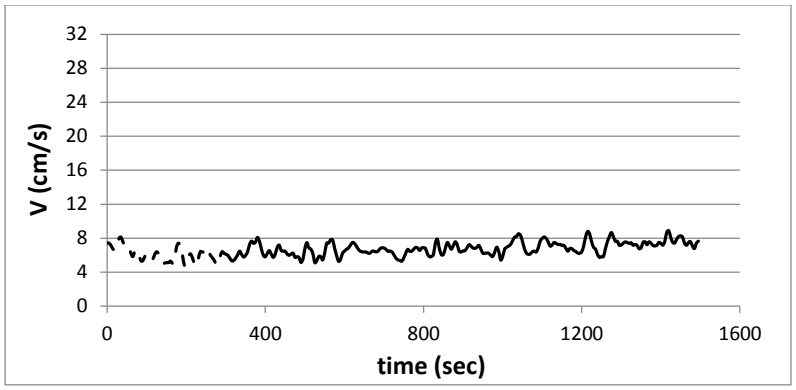

Figure 4.36 - Average speed in row 3 - seat D (heated)

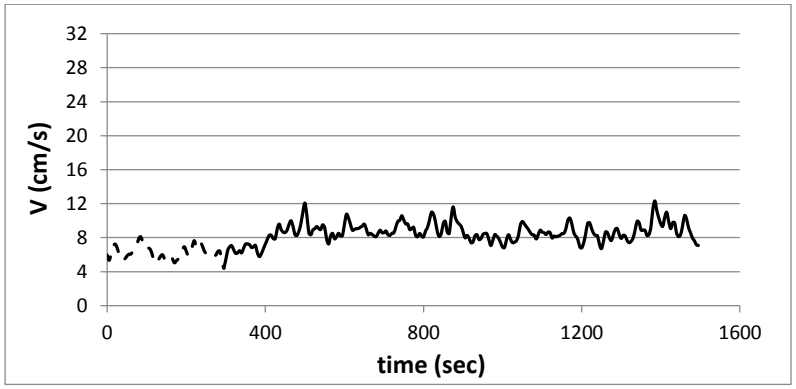

Figure 4.37 - Average speed in row 4 - seat D (heated)

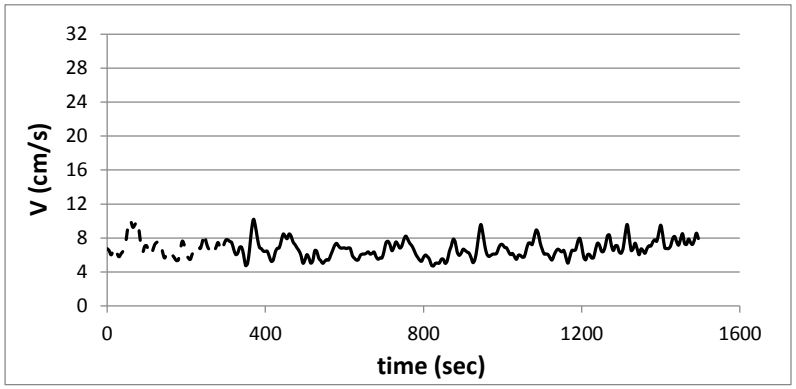

Figure 4.38 - Average speed in row 5 - seat D (heated)

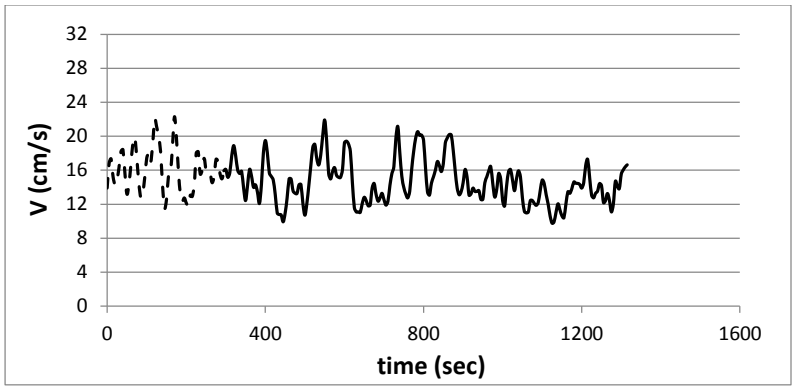

Figure 4.39 - Average speed in row 6 - seat D (heated)

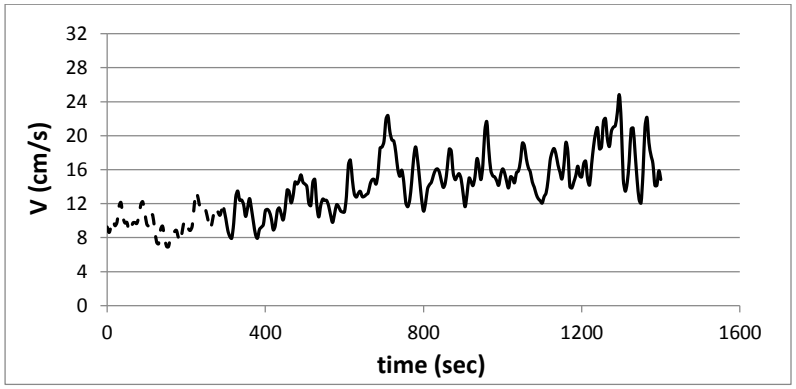

Figure 4.40 - Average speed in row 7 - seat D (heated)

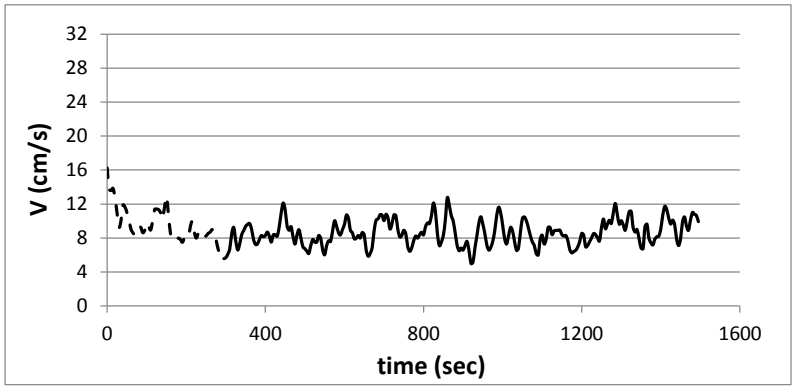

Figure 4.41 - Average speed in row 8 - seat D (heated)

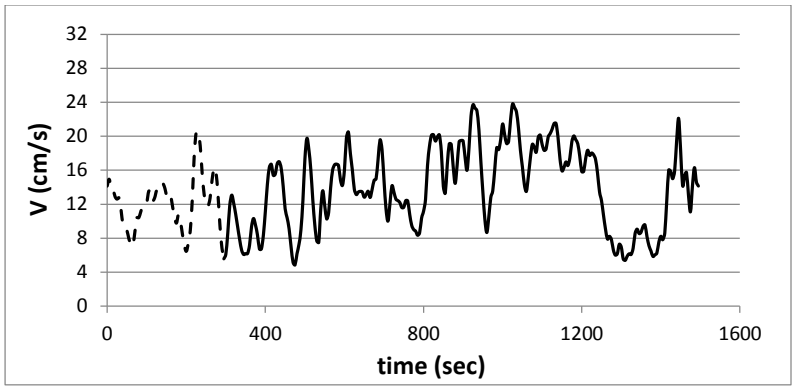

Figure 4.42 - Average speed in row 9 - seat D (heated)

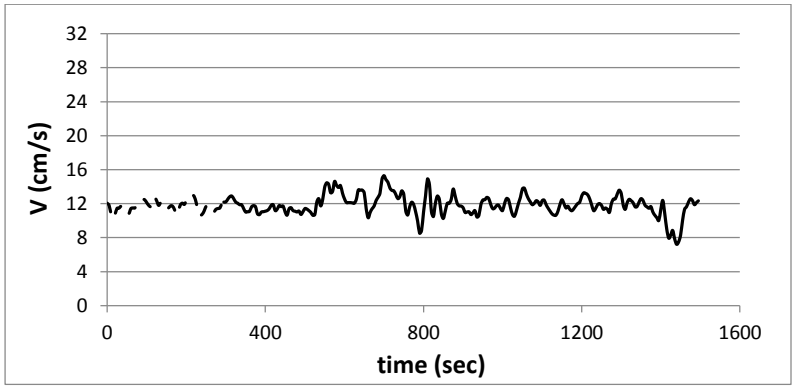

Figure 4.43 - Average speed in row 10 - seat D (heated)

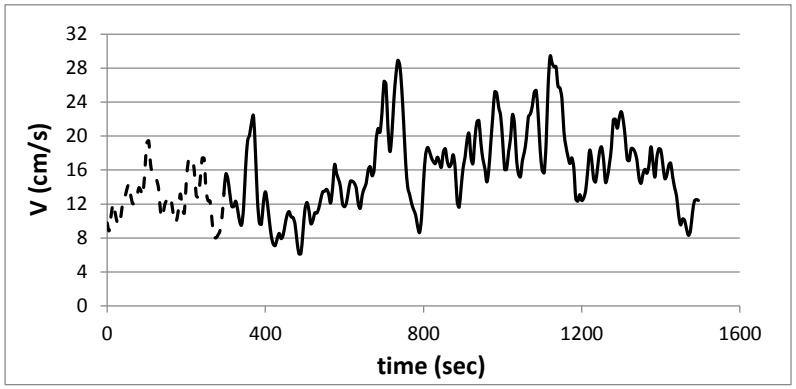

Figure 4.44 - Average speed in row 11 - seat D (heated)

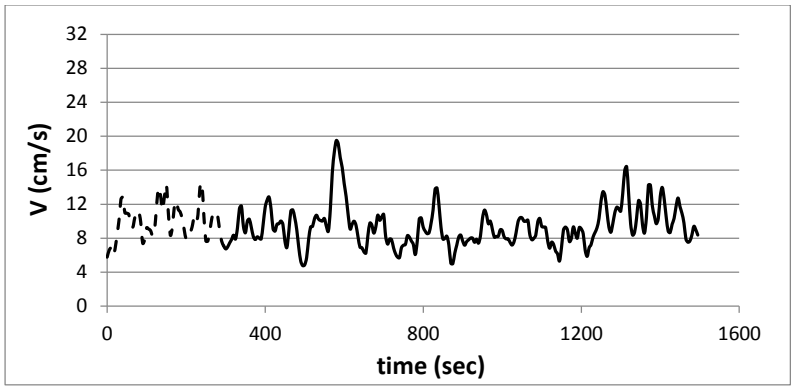

Figure 4.45 - Average speed in row 1 - seat F (heated)

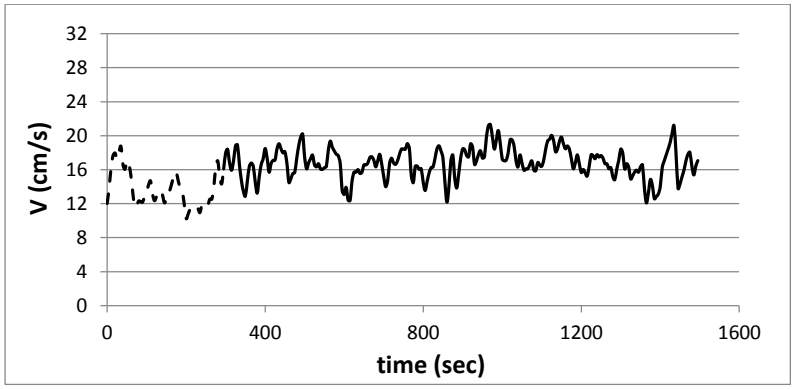

Figure 4.46 - Average speed in row 2 - seat F (heated)

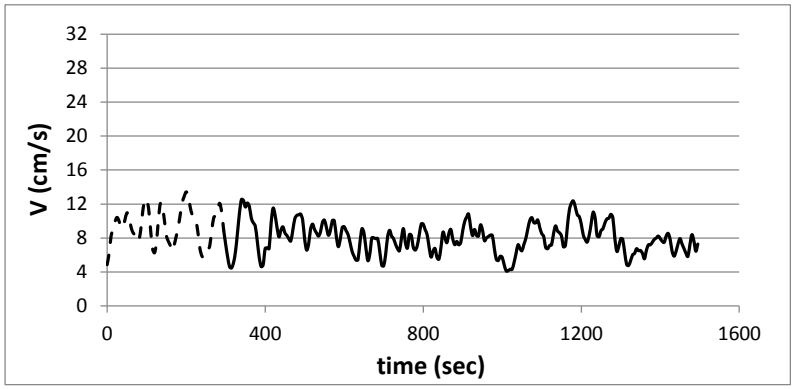

Figure 4.47 - Average speed in row 3 - seat F (heated)

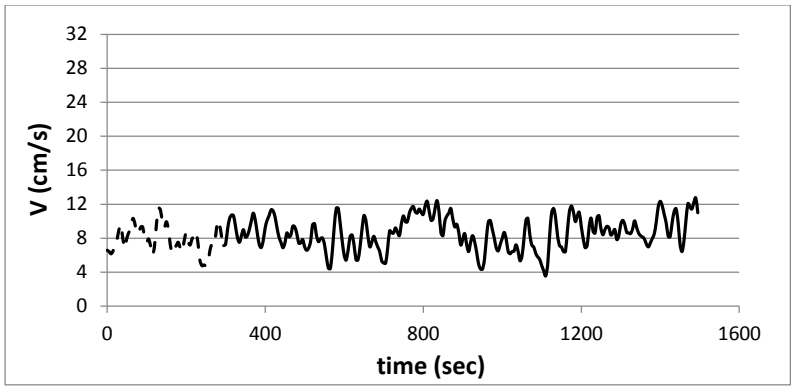

Figure 4.48 - Average speed in row 4 - seat F (heated)

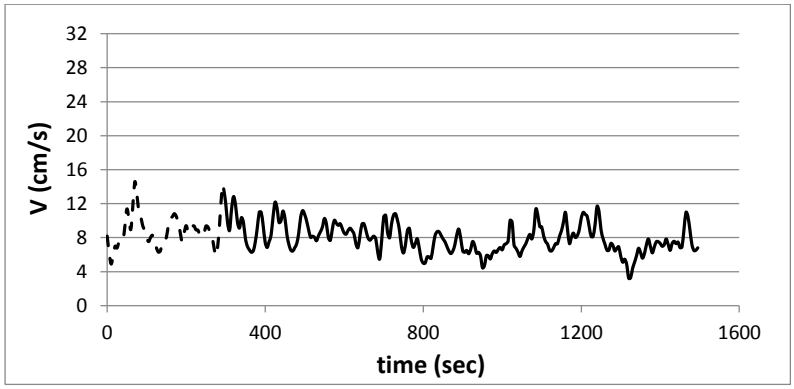

Figure 4.49 - Average speed in row 5 - seat F (heated)

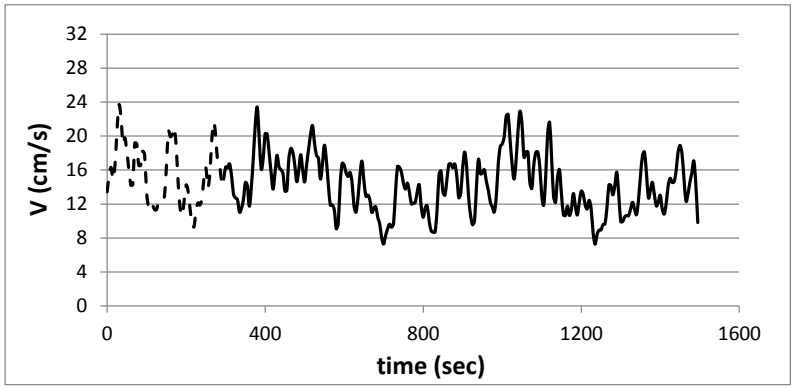

Figure 4.50 - Average speed in row 6 - seat F (heated)

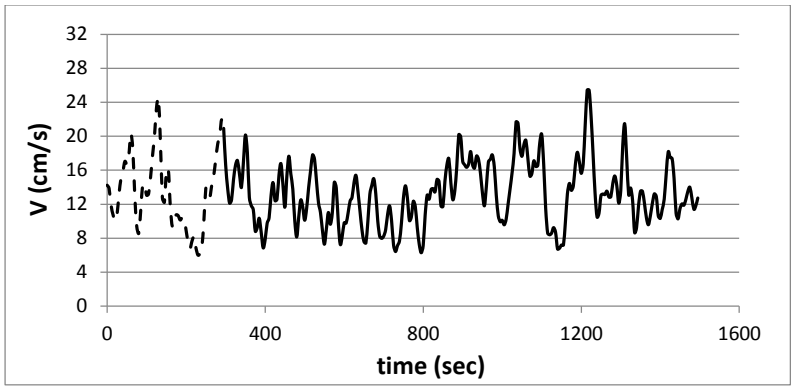

Figure 4.51 - Average speed in row 7 - seat F (heated)

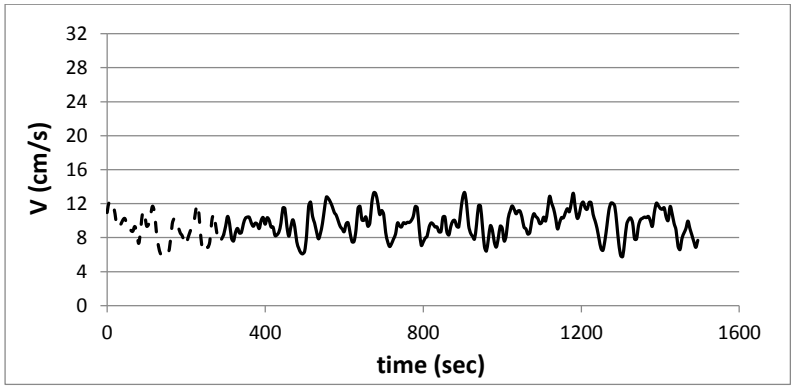

Figure 4.52 - Average speed in row 8 - seat F (heated)

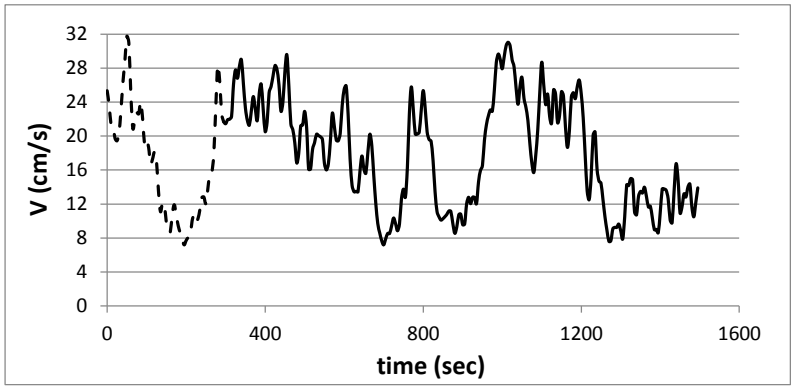

Figure 4.53 - Average speed in row 9 - seat F (heated)

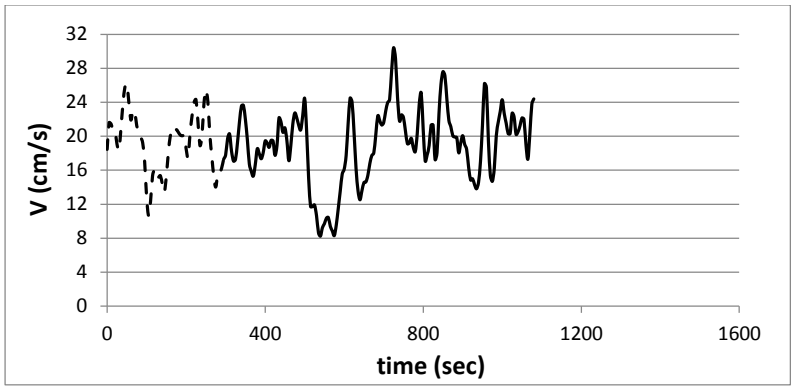

Figure 4.54 - Average speed in row 10 - seat F (heated)

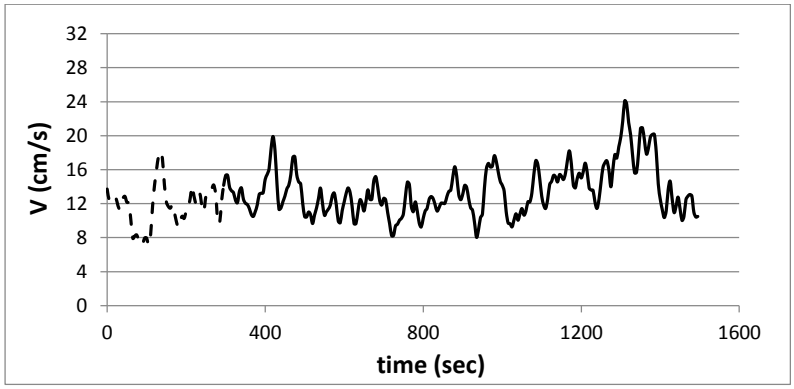

Figure 4.55 - Average speed in row 11 - seat F (heated)

4.3.2 Airflow speed results with unheated manikins

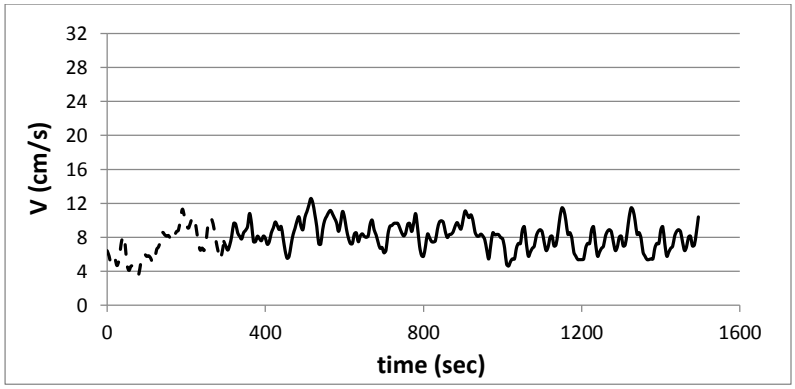

Figure 4.56 - Average speed in row 1 - seat B (unheated)

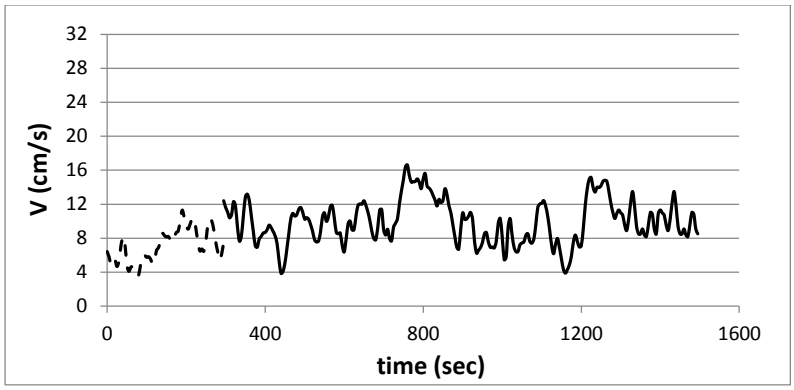

Figure 4.57 - Average speed in row 2 - seat B (unheated)

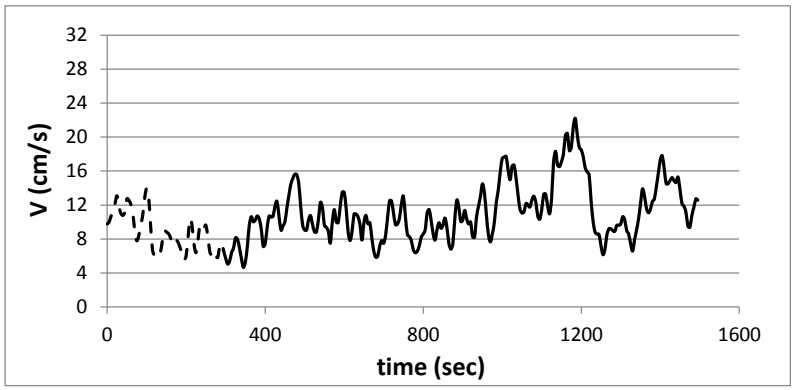

Figure 4.58 - Average speed in row 3 - seat B (unheated)

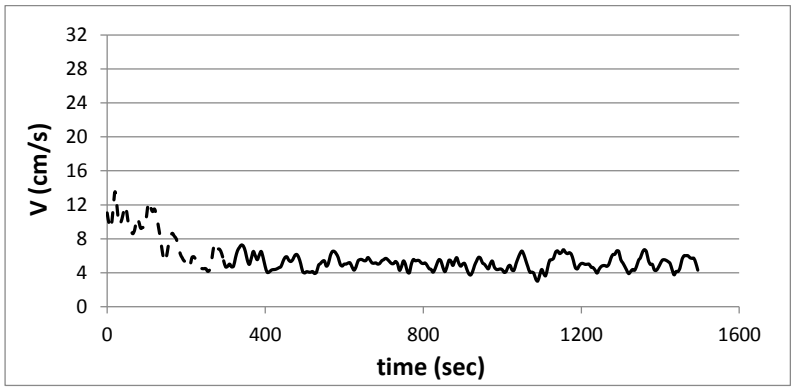

Figure 4.59 - Average speed in row 4 - seat B (unheated)

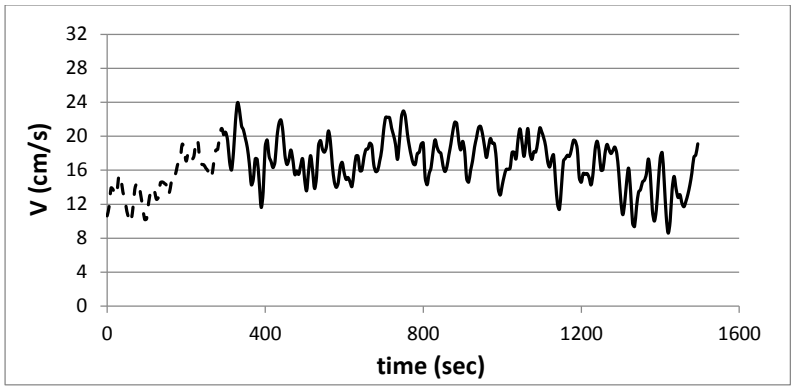

Figure 4.60 - Average speed in row 5 - seat B (unheated)

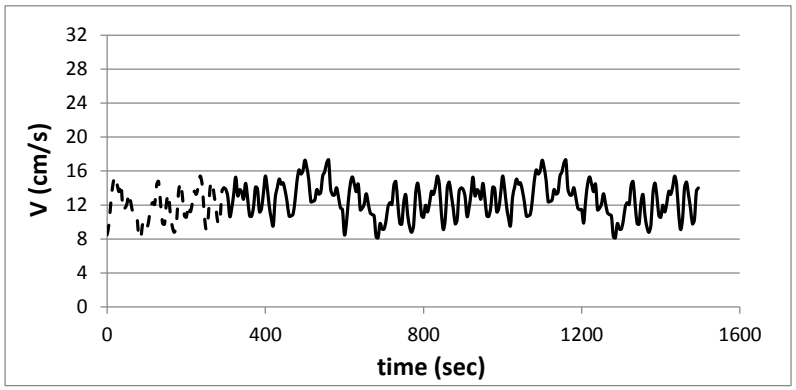

Figure 4.61 - Average speed in row 6 - seat B (unheated)

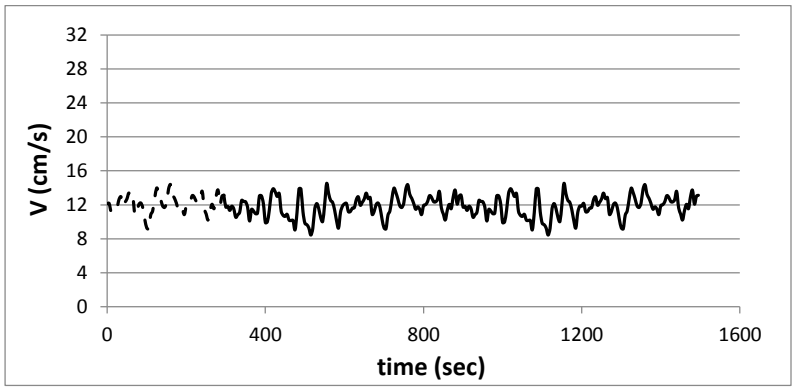

Figure 4.62 - Average speed in row 7 - seat B (unheated)

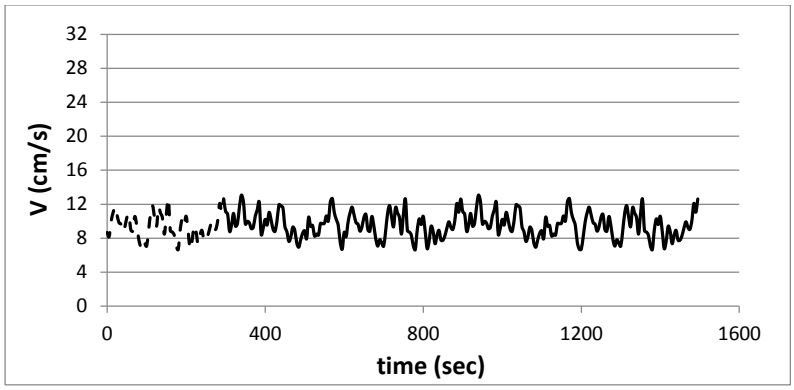

Figure 4.63 - Average speed in row 8 - seat B (unheated)

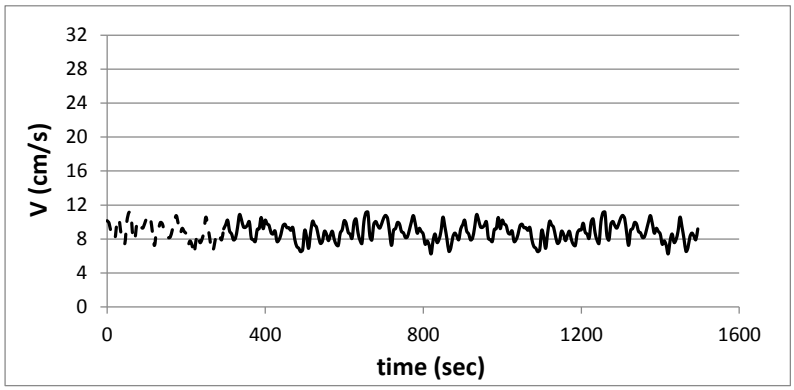

Figure 4.64 - Average speed in row 9 - seat B (unheated)

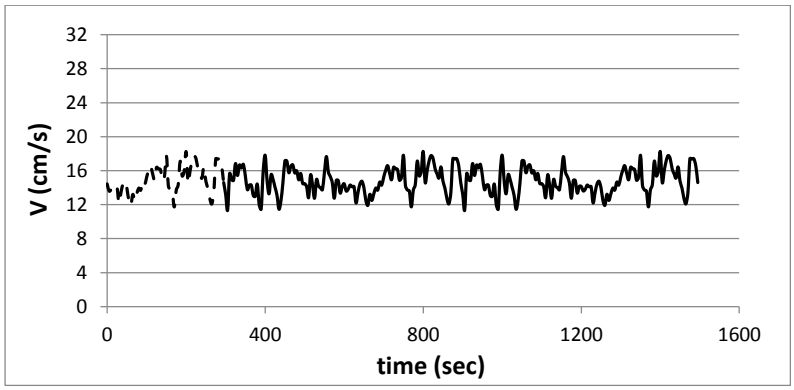

Figure 4.65 - Average speed in row 10 - seat B (unheated)

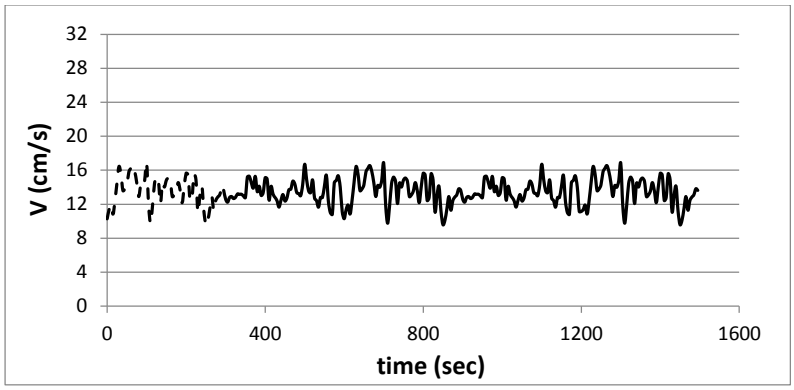

Figure 4.66 - Average speed in row 11 - seat B (unheated)

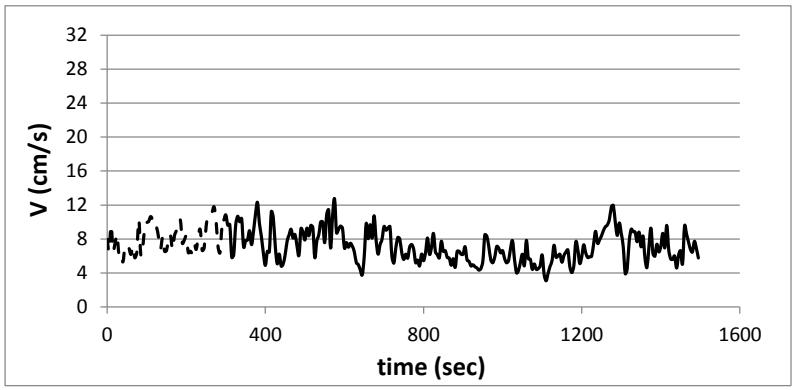

Figure 4.67 - Average speed in row 1 - seat D (unheated)

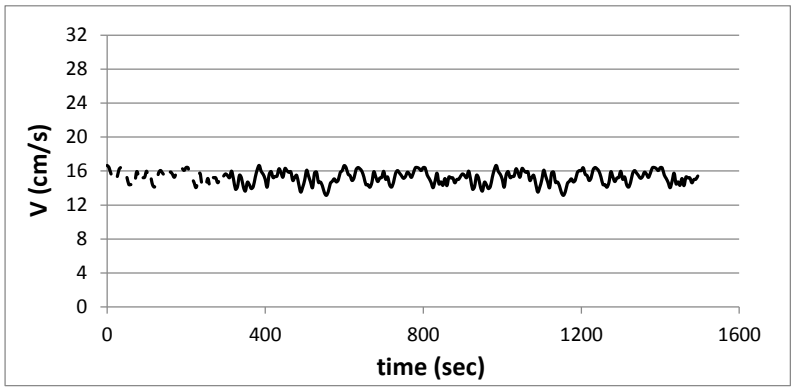

Figure 4.68 - Average speed in row 2 - seat D (unheated)

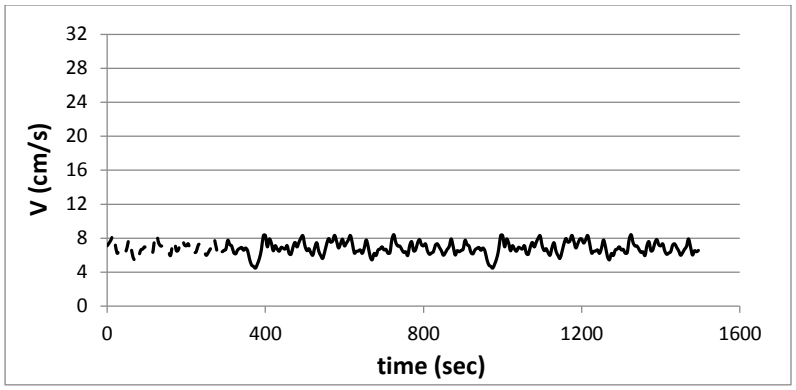

Figure 4.69 - Average speed in row 3 - seat D (unheated)

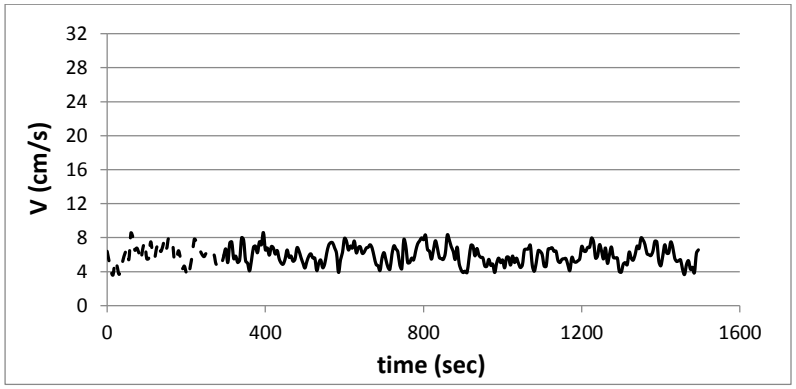

Figure 4.70 - Average speed in row 4 - seat D (unheated)

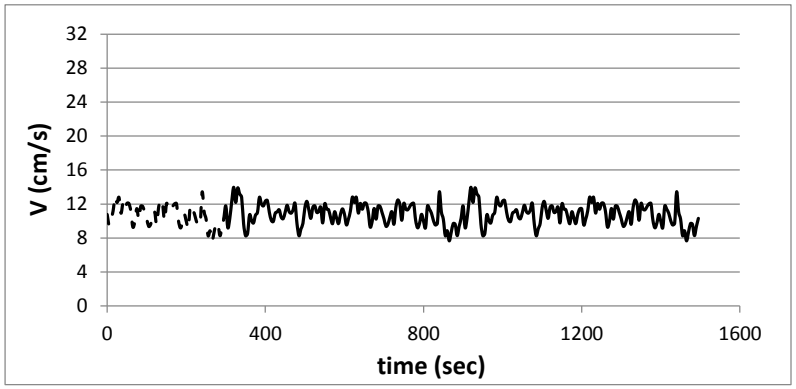

Figure 4.71 - Average speed in row 5 - seat D (unheated)

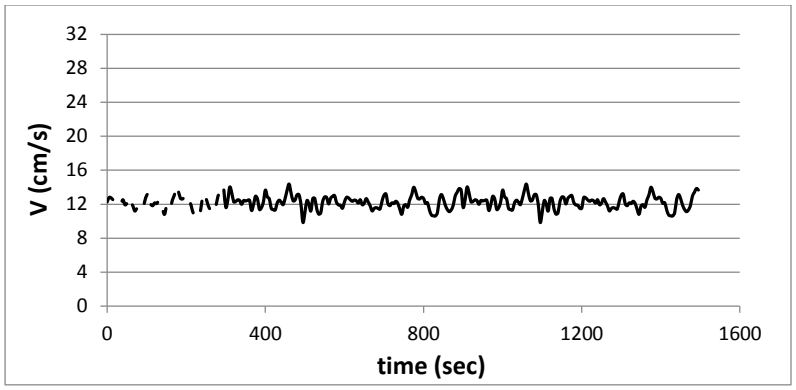

Figure 4.72 - Average speed in row 6 - seat D (unheated)

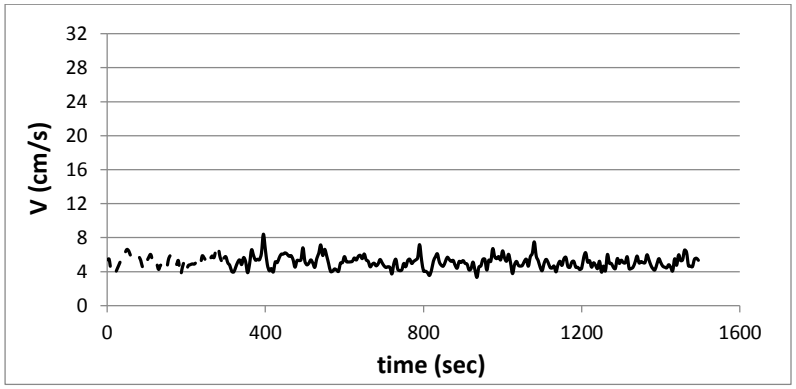

Figure 4.73 - Average speed in row 7 - seat D (unheated)

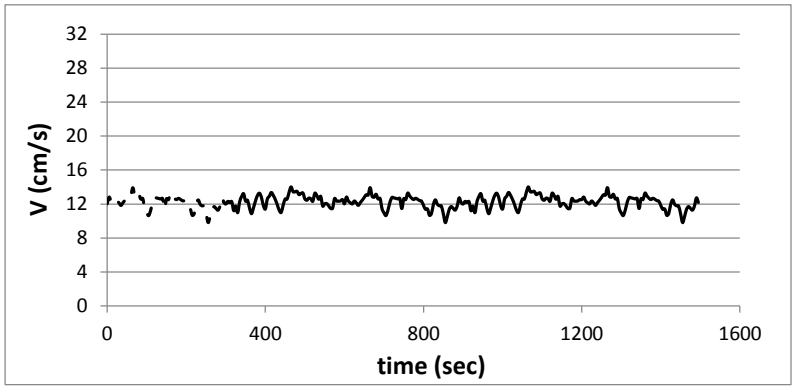

Figure 4.74 - Average speed in row 8 - seat D (unheated)

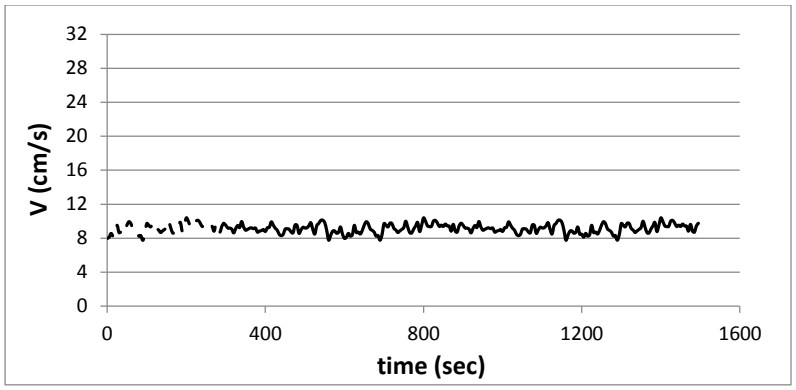

Figure 4.75 - Average speed in row 9 - seat D (unheated)

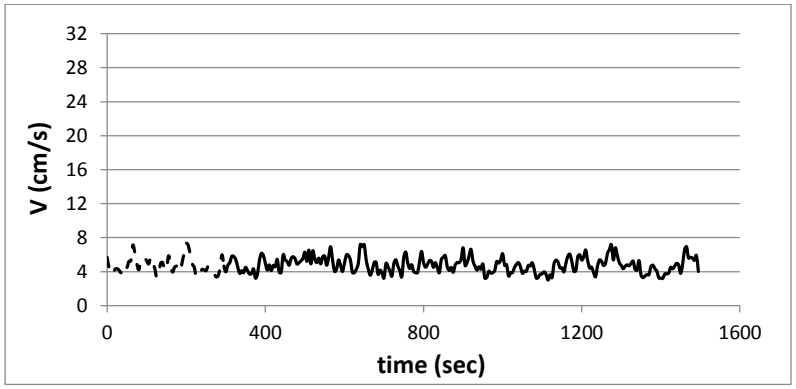

Figure 4.76 - Average speed in row 10 - seat D (unheated)

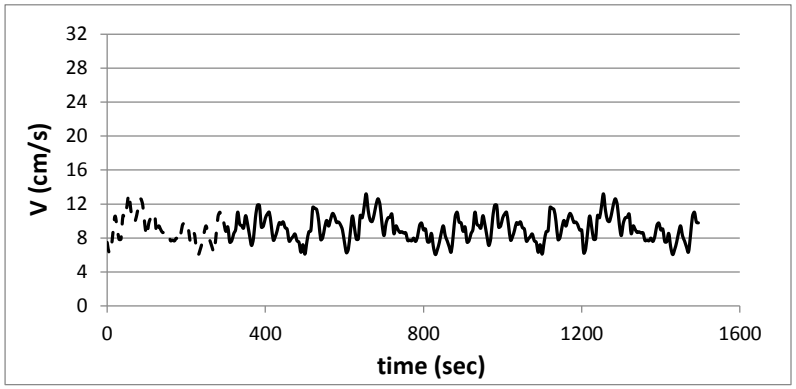

Figure 4.77 - Average speed in row 11 - seat D (unheated)

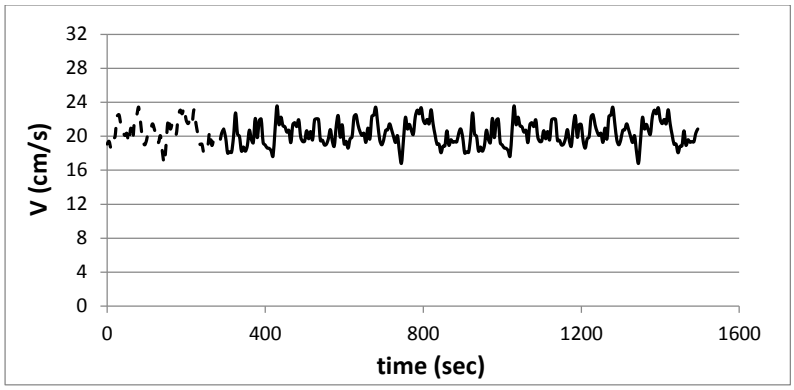

Figure 4.78 - Average speed in row 1 - seat F (unheated)

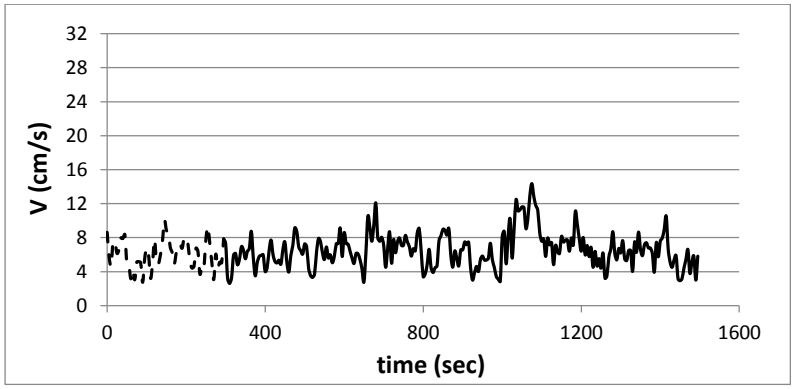

Figure 4.79 - Average speed in row 2 - seat F (unheated)

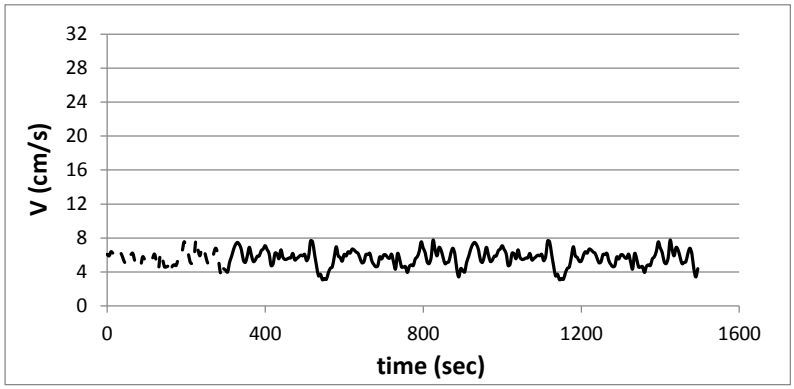

Figure 4.80 - Average speed in row 3 - seat F (unheated)

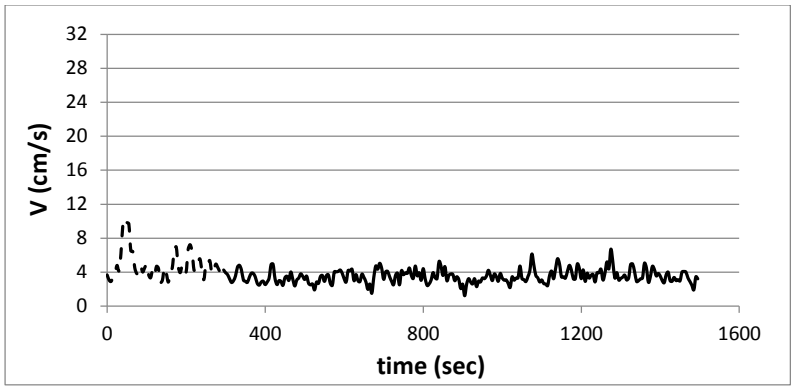

Figure 4.81 - Average speed in row 4 - seat F (unheated)

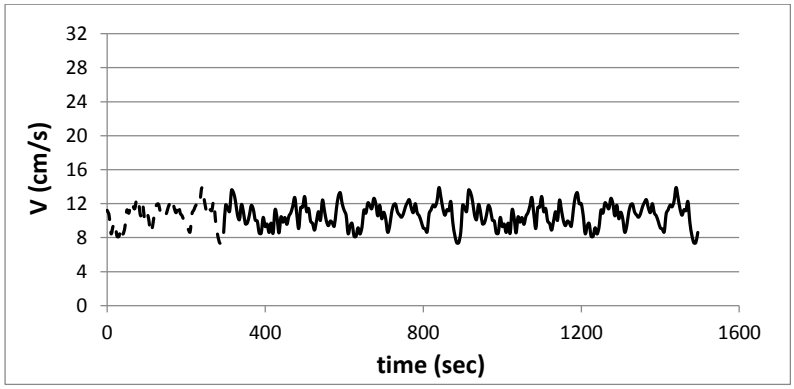

Figure 4.82 - Average speed in row 5 - seat F (unheated)

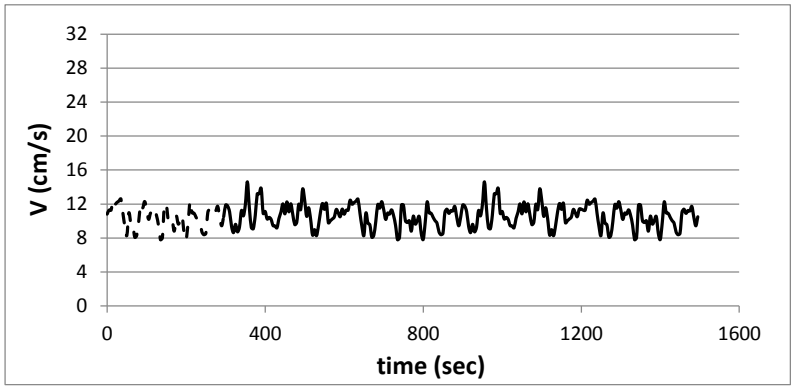

Figure 4.83 - Average speed in row 6 - seat F (unheated)

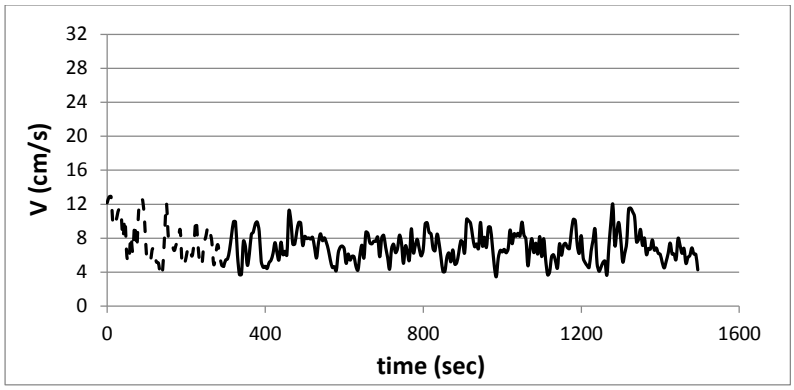

Figure 4.84 - Average speed in row 7 - seat F (unheated)

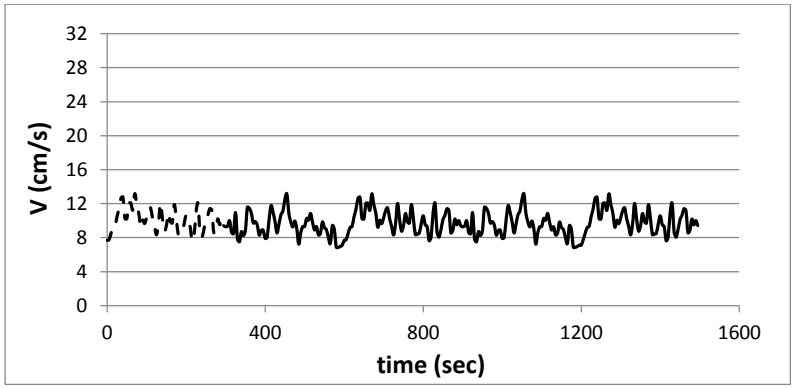

Figure 4.85 - Average speed in row 8 - seat F (unheated)

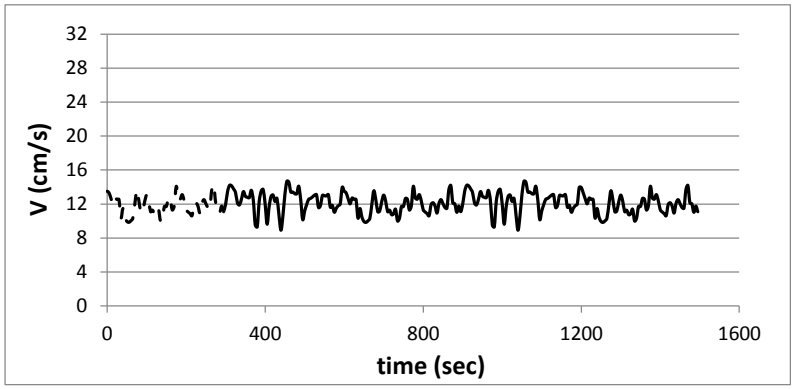

Figure 4.86 - Average speed in row 9 - seat F (unheated)

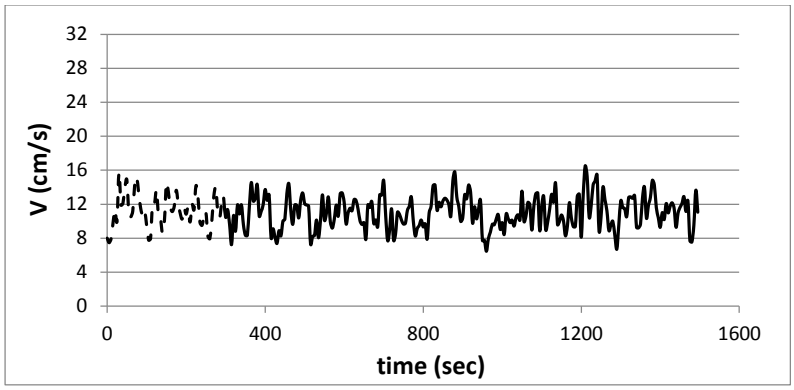

Figure 4.87 - Average speed in row 10 - seat F (unheated)

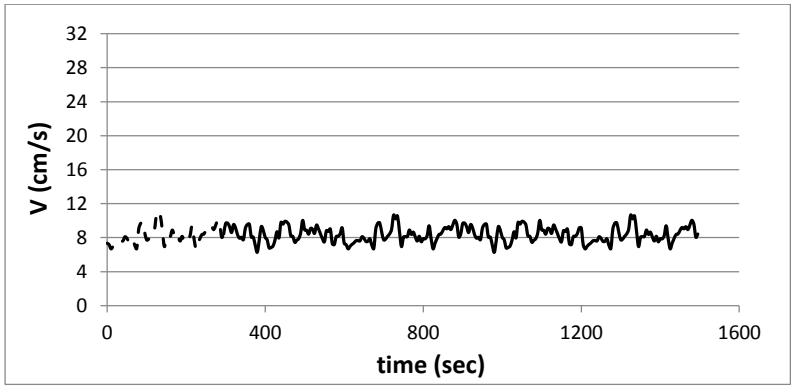

Figure 4.88 - Average speed in row 11 - seat F (unheated)

Chapter 5 - Analysis and Discussions

5.1 Airflow distribution in the plan view of the mockup cabin

5.1.1 Flow visualization analysis

It was noticed in Figure 4.2 that in the front east side of the cabin the majority of the smoke flow was directed towards the front wall, whereas in the front west side it was mainly moving backwards. For the middle seats release tests, no identifiable phenomena were detected except around the release seat. As can be seen in Figure 4.2 the smoke extent in the middle seats section was ±1 row to the front and to the back of the release row. In seat 1D the flow had a tendency to move mostly from the east to the west side of the cabin. However, the situation was different in seat 7D which is right in the middle section of the cabin where it was not very clear whether the flow migrated towards the west side or whether it deviated to the back section after being released. Figure 4.2 reflects the high degree of randomness in the flow and shows how chaotic it was which is a characteristic of 3-dimensional turbulent flow. General rough flow patterns were suggested based on the results shown in Figure 4.2. Those flow patterns are shown in Figure 5.1. Thus, based on the smoke visualizing results it can be concluded that there was a tendency for multiple airflow circulations throughout the cabin. The length of the circulations in the front and back sections were larger than those in the middle section of the cabin which implied that the airflow was more chaotic in the middle section that was preventing a uniform flow from being developed.

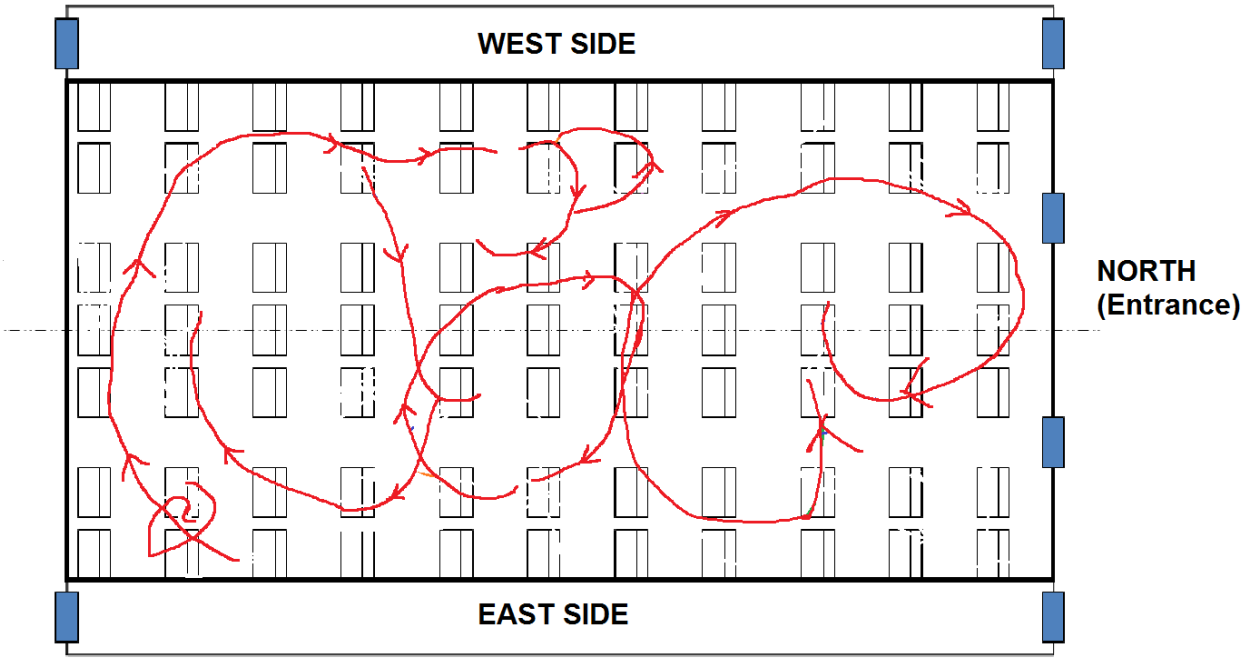

Figure 5.1 - Proposed flow patterns inside the cabin based on smoke visualization tests

5.1.2 Tracer gas analysis under normal operating conditions (heated manikins)

5.1.2.1 Gaseous transport analysis in the front section of the mockup cabin

Starting with the front part of the cabin by investigating the results when releasing the tracer gas in seat 2D, as shown in Figure 4.3 and in Figure 5.2, it was noticed that the gas moved from seat 2D to either 1E or 2E/3E based on the highest normalized values in Figure 5.2. The highest exposures were detected, in non-preferential order, in seats 2E, 3E, 3F then in seats 1E, 1F, 2F, and 4E. In either case, the flow showed a tendency to follow a counter clockwise circulation moving towards the west side of the cabin. The backward dispersion extent of this circulation decreased as approaching the region between row 4 and row 5. This break in the flow dispersion strength in the longitudinal direction was built on the samples collected in each sampling point considered in row 5 and also based on results sampled in seat 2B. The gas

exposure in row 5 was of relatively lower order of magnitude compared to those in each of row 1, 2, 3 and 4. Considering the front-west side only, which was thought to have a longitudinal backward dispersion, the percentage of gas sampled with respect to that in seat 2D dropped from 84% in row 3, to 51% in Row 4, to 17% in row 5. On the other hand, seat 2B showed higher exposure than seat 2C with the source being in the central seat of row 2. As the source was in seat 2D, this means that the tracer gas moved from seat 2D into seat 2B through a different path than through seat 2C. Results of vertical sampling in the east aisle of row 2 with the release port in seat 2D, as shown Figure 4.19 for heated manikins, revealed that the east aisle in the front part of the cabin had an average percent exposure ranging between 17% to 22% with respect to seat 2D at different elevations, whereas seat 2B had an average approximately 31%, as shown in Figure 5.2 and Figure 5.3. This confirmed that the tracer gas sampled in seat 2B did not come by lateral circulation only and it raised the chances that it was transported through a circulation in the longitudinal direction.

The data collected when releasing in seat 4F, as shown in Figure 5.4, confirmed the break in the flow direction of the circulation in the west side of the front section of the cabin. The release point in seat 4F was positioned 305 mm ahead from the sampling port in seat 4F and 533 mm to the back of the sampling port in seat 3F. Having a normalized exposure of 6.68 and 2.62 in seat 4F and seat 3F, respectively, confirmed the results drawn for release in seat 2D that a backward drifted flow was dominating over the airflow in the front-west side of the cabin. The majority of the tracer gas was collected in seat 4F followed by seat 4D. From there, the flow might have moved forward, backward, or continued its path to the east aisle of the cabin. Noticing that seat 4B had higher exposure that both seats 3D and 5D indicated that the flow favored continuing its path to the east side. Also observing that all of the seats 2B, 3B, and 4B had higher exposures

than in seat 5B confirmed that the flow tended to move forward in the front-east aisle. This result in the east aisle seats was confirmed by the results shown in Figure 5.5 for the release in seat 5B where it was clearly noticed that there existed a forward drifted circulation. Another observation, from Figure 5.5, was that the middle seats in the consecutive front rows (2D, 3D, and 4D) had relatively higher exposures than the seats in Column B (i.e. 4B, 3B, 2B). This meant that the flow was drifting from east to west while moving forward. Thus, the results of Figure 5.2, Figure 5.4, Figure 5.5, along with the results of vertical sampling in Figure 4.19 confirmed the existence of a clockwise directed flow moving forward in the east side that switched over to the west side, as illustrated in Figure 5.6.

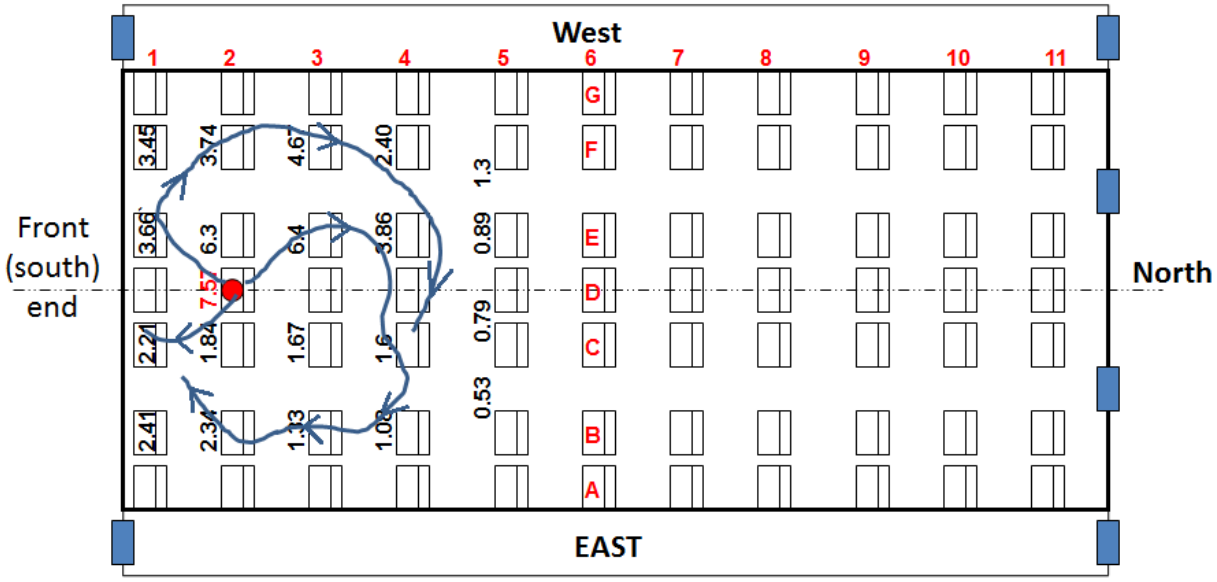

Figure 5.2 - Averages of the normalized sampled CO_2 when releasing in seat 2D (heated manikins)

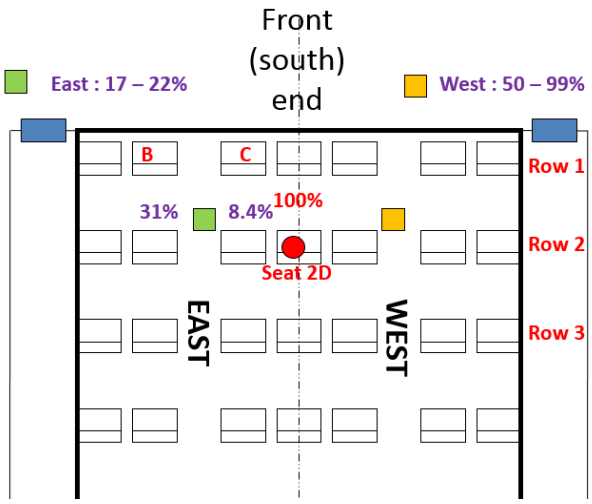

Figure 5.3 - Comparison between seat 2C, 2B, and various locations in the vertical direction of the front-east aisle

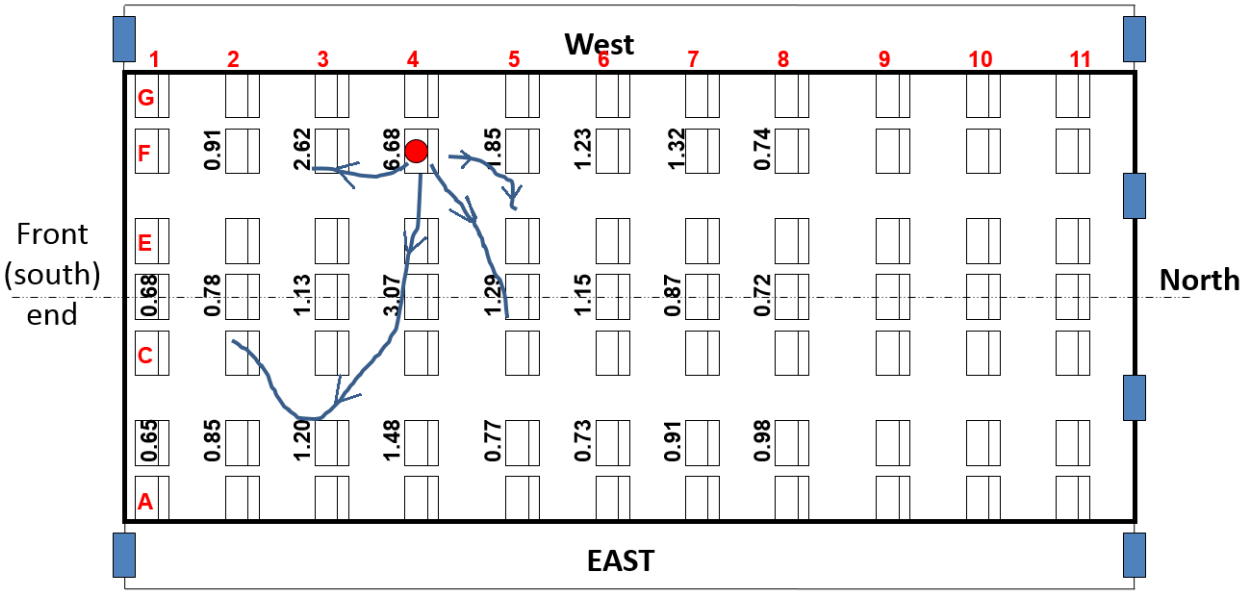

Figure 5.4 - Averages of the normalized sampled CO_2 when releasing in seat 4F (heated manikins)

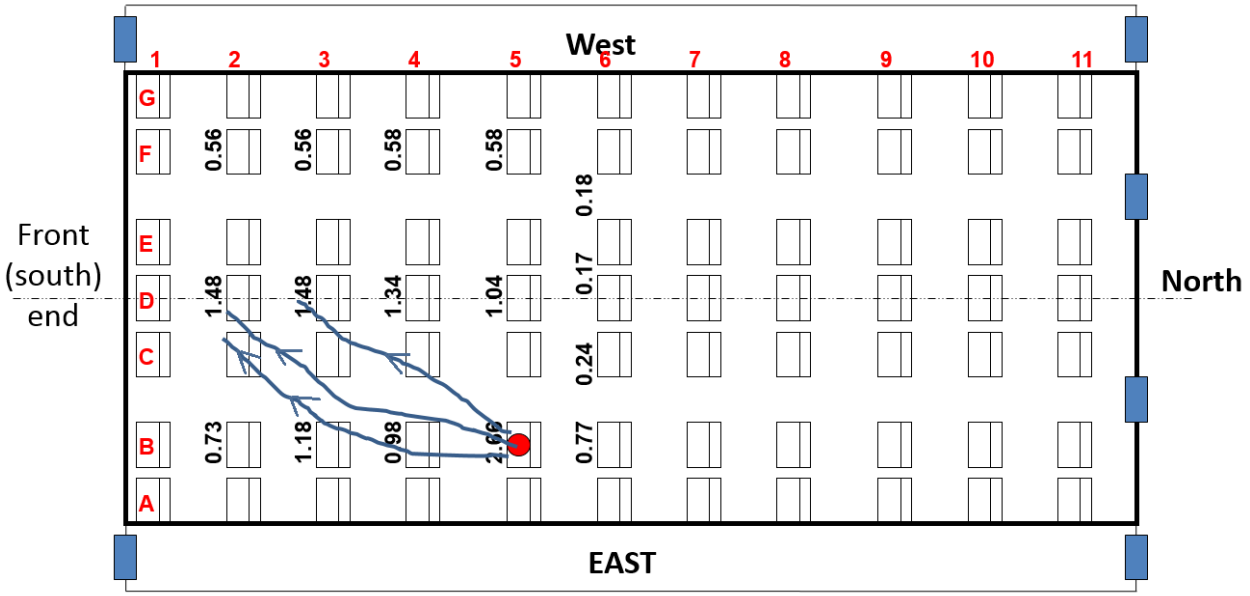

Figure 5.5 - Averages of the normalized sampled CO_2 when releasing in seat 5B (heated manikins)

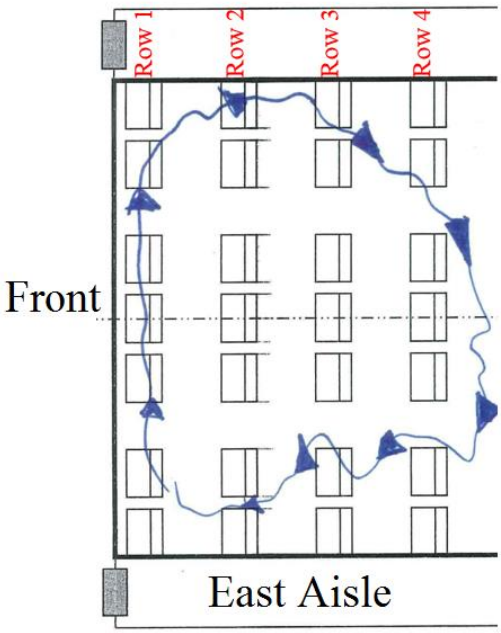

Figure 5.6 - Identified clockwise circulation in the front section of the mockup cabin

5.1.2.2 Gaseous transport analysis in the middle section of the mockup cabin

Results for release in the middle seats of the cabin in seat 5D, presented in Figure 4.4 and in Figure 5.7, showed that the tracer gas mainly circulated into the front-east side of the cabin and into the back-west side, as illustrated by the purple lines in Figure 5.7. The first observation was that there existed two clockwise circulations around row 5, represented by the purple path-lines in Figure 5.7, or there was a bigger clockwise swirl that moved forward through the east side and moved backwards through the west side as shown in red in Figure 5.7. However, since the gaseous exposure in seat 5E was 22% of that sampled around the release port in seat 5D, in seat 6E was 39%, and in seat 7E was 28%, which all were higher than those collected in seats 4E, 4F, and 5F, then it was certain that the sampled tracer gas in 5E, 6E, and 7E was coming from the source seat in 5D and not through the seats in the west aisle as indicated in the red path-line in Figure 5.7. Thus, it can be concluded that the assumption of two clockwise circulations, as illustrated in purple in Figure 5.7, was more reasonable than the second assumption. This observation was confirmed with results of seat 7D, shown in Figure 5.8, especially when comparing the sampled tracer gas in seats 10F to 5F where both had approximately 12% exposure of that in seat 7D. Since seat 10F is three rows to the back of seat 7D and it had the same exposure as in seat 5F, then it was concluded that the backward flow was more dominant than the forward one in the west side of this section. On the other side, since the exposure in seat 7B, 6B, and 5B was higher than that in seat 9B, 10B and 11B, a forward circulation was concluded to be controlling the flow in the east side of the same region. However, the results in the east side of seat 7D did not really show whether the flow migrated from seat 7D through 8D and then forward to the front section of the east side of the cabin or whether there was a direct lateral transport from seat 7D to the east side before flowing forwards and, thus, leaving the

exposure in the east side of row 8 in a vague situation. To illustrate more on this, the results collected when releasing in seat 8B were investigated. In Figure 5.9, the sampling port in seat 8B was placed 77 mm ahead and 77 mm to the right (west) side of the release point in seat 8B. Since more tracer gas was collected in seat 9D, approximately 111%, than it was in 8B and 7B, then the gaseous transport had two major paths, one moving forward towards the front seats in column B and the other moving backwards while drifting towards the west side. Thus, based on the results of seat 7D there were two main drifts in each aisle of the middle section of the cabin, a forward directed one over the east seats and a backward directed one over the west seats. The results concluded for seat 5D were complimentary to 7D and showed that the forward circulation in the east side was split into two streams, the first one merged with the front clockwise circulation that was identified in the fore section of the cabin, whereas the second one migrated into the west aisle based on the identified purple path-lines in Figure 5.7. Combining those results with that for seat 5D, 7D, and 8B it was concluded that the middle section of the cabin was controlled by a clockwise circulation that was dominating over most of the seats but there were some disturbances in the east around row 8. Figure 5.10 combines those results together where it was not clear till the moment how the flow was behaving around row 8 and 9.

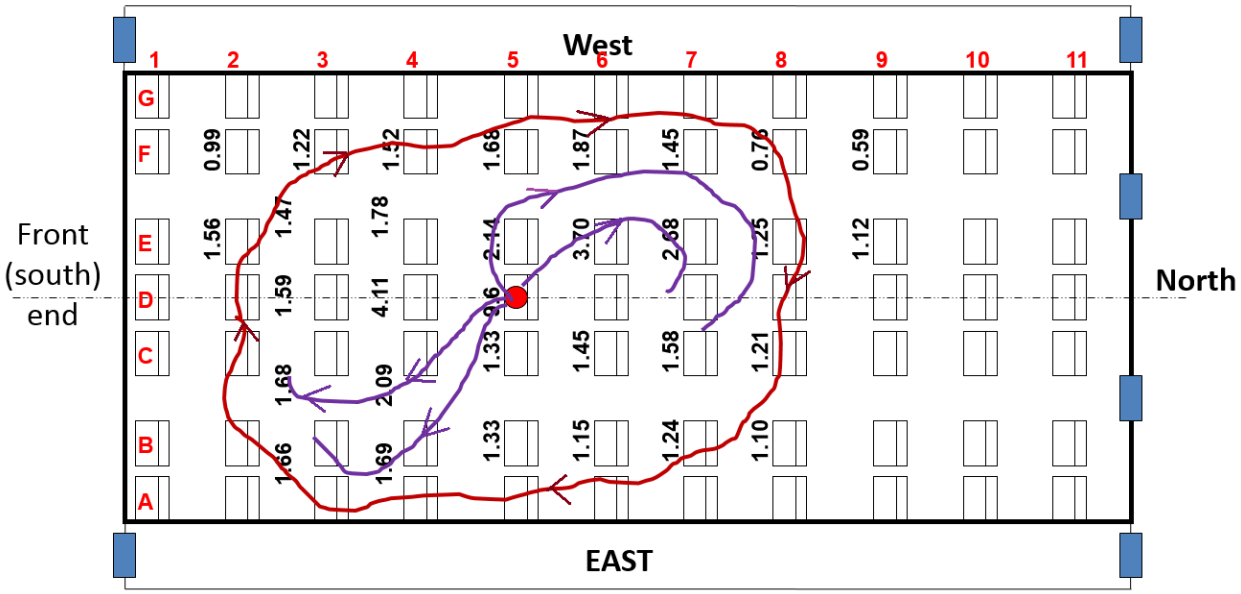

Figure 5.7 - Averages of the normalized sampled CO_2 when releasing in seat 5D (heated manikins)

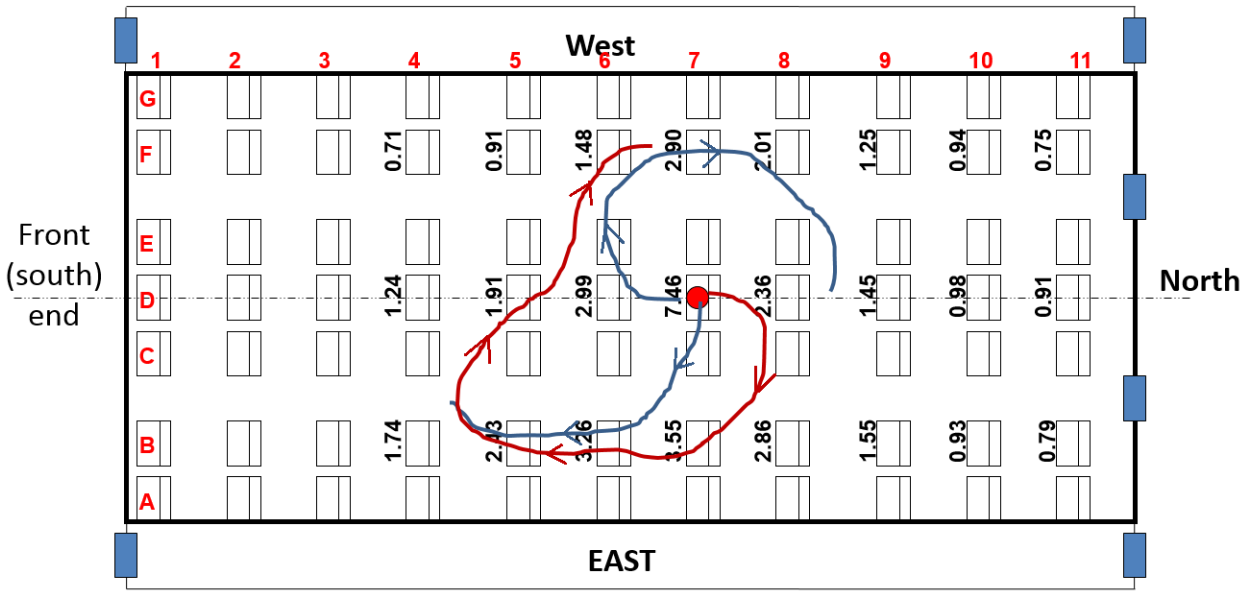

Figure 5.8 - Averages of the normalized sampled CO_2 when releasing in seat 7D (heated manikins)

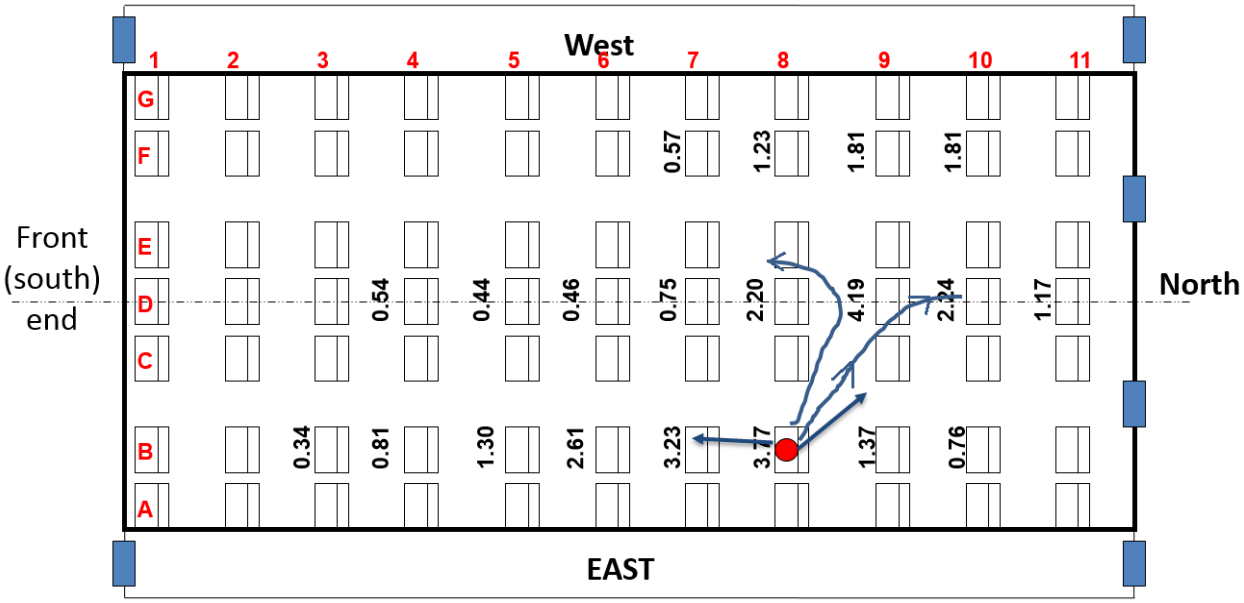

Figure 5.9 - Averages of the normalized sampled CO_2 when releasing in seat 8B (heated manikins)

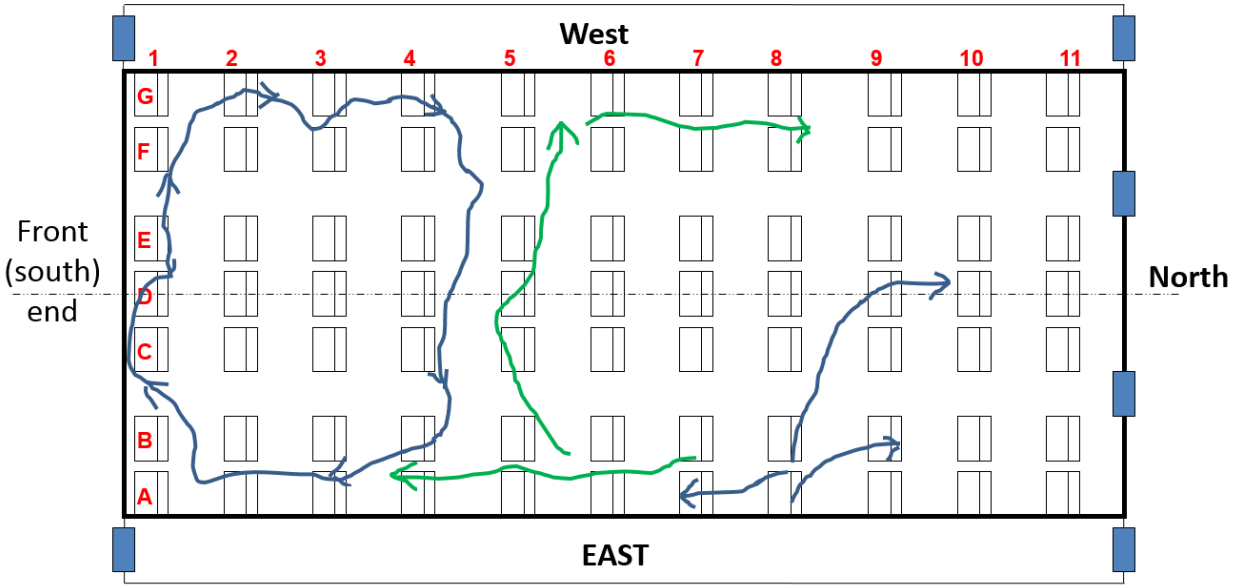

Figure 5.10 - Sketch for the flow in the front and middle sections of the cabin

5.1.2.3 Gaseous transport analysis in the aft section of the mockup cabin

Figure 5.11 shows that the airflow moved equally to the front and back sections of the release seat in 9F. The centerline seats in row 9 and row 10 had more tracer gas sampled than in

row 8. Also, noting that seats 10F and 11F had 34% to 40% exposure and that this exposure dropped to 17-19% in seat B in each of the last 4-rows of the cabin, a conclusion was made that there was a circulating airflow in the clockwise direction that went all the way to the back wall of the cabin. The strength of this circulation in the transverse direction dominated over the region from the west wall till the centerline seats in column D. Switching into the results of seat 10D in Figure 5.12, the asymmetrical distribution between the east and west sides of the back section of the cabin was clear. The longitudinal strength of the flow in this part of the cabin was weak as the sampled tracer gas in row 8 (7-14%) were much lower than that collected in row 10 and row 9. The exposure in row 9 dropped into 15-17% and then into 7% in the west seats of row 8 and 14% in the east seats of row 8. The majority of the flow had a tendency to move backwards towards the back wall of the mockup cabin through clockwise directed circulation, as shown in Figure 5.12.

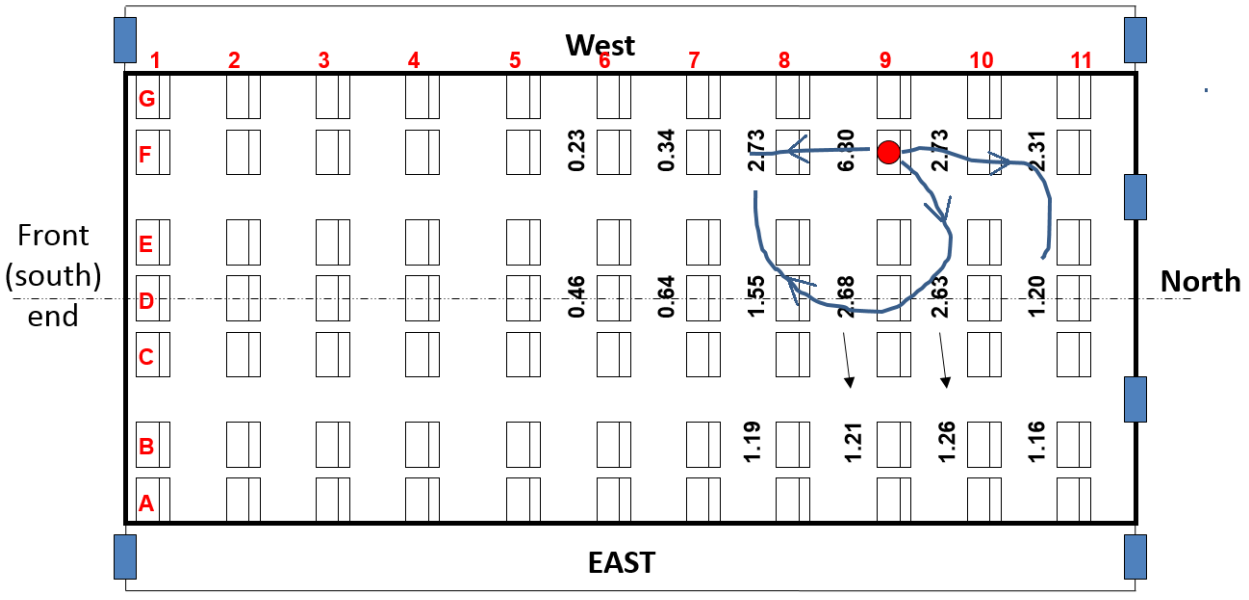

Figure 5.11 - Averages of the normalized sampled CO_2 when releasing in seat 9F (heated manikins)

No conclusions could be drawn whether there existed two swirls in each side of the cabin around seat 10D or only one swirl that was dominating over the entire cross section of the back section of the cabin. However, the results concluded for seat 9F indicated that the flow in the west-back section dominated over half the width of the cross section and the results for seat 8B showed a backward flow in the east-back side, as shown in Figure 5.9 and Figure 5.10. Upon combining the results of 8B and 9F with 10D, a conclusion was made that the back section of the cabin was controlled by two circulations that were smaller in size than in the front and middle section of the cabin. The combined results are shown in Figure 5.13.

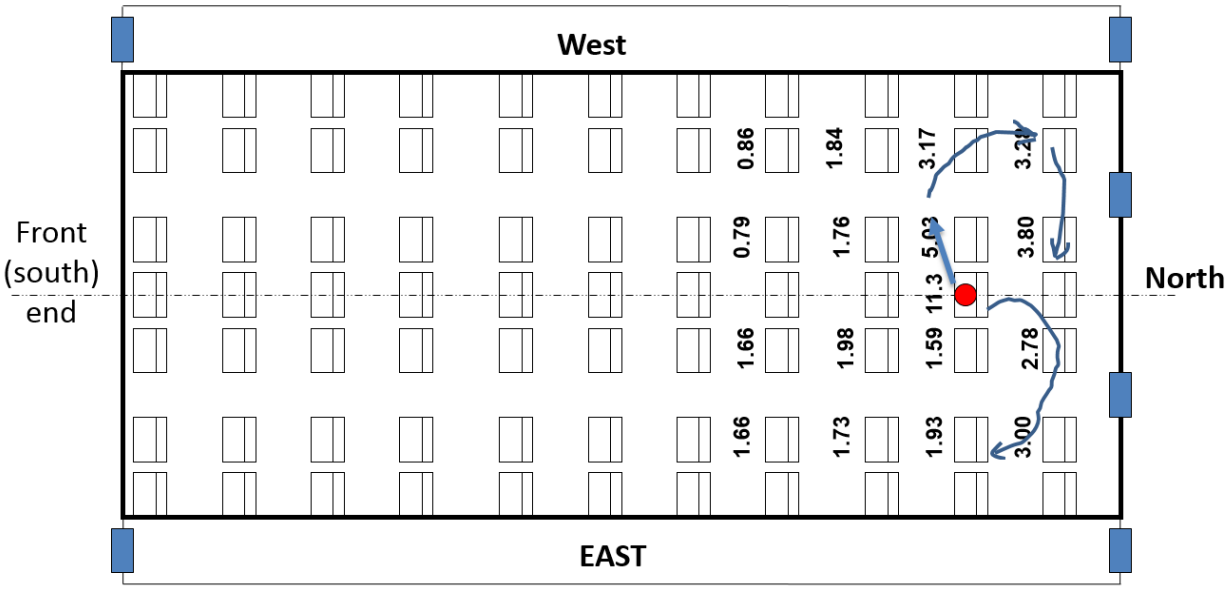

Figure 5.12 - Averages of the normalized sampled CO_2 when releasing in seat 10D (heated manikins)

5.1.2.4 Comparing the flow on the sides of the fore and aft sections of the cabin

Results drawn from tests conducted in seats 4F and 9F were used to understand the flow nature and behavior on the sides of the cabin. Both locations showed that the flow tended to move backward and forward away from the source. However, the dominant flow in the front and

back sections of the cabin moved forwards while drifting to the east side of the cabin. In the front section, the drifting in the lateral direction continued all the way from the west to the east wall, while in the aft part of the cabin it reached around the centerline seats only and then flipped forwards.

5.1.2.5 Overall gaseous transport behavior inside the mockup cabin

The results concluded for the fore, middle, and aft sections of the cabin were presented together on one layout in Figure 5.13 to illustrate the overall flow distribution phenomena in the B767 mockup cabin. Two main clockwise directed circulations were controlling the flow in the fore and mid sections of the mockup cabin. The rear section of the cabin, beyond row 7, was chaotic and had more discrepancies. Two smaller clockwise circulations were hardly identified in this section. Although, two circulations were concluded in the back section, but there might be smaller eddies inside these circulations. Another guess is the existence of a bigger clockwise circulation dominating over the region from row 5 all the way till the back wall of the cabin.

The front circulations controlling the flow in the front half of the cabin were spread over the whole lateral cross section of the cabin. The swirl at the very front part of the cabin controlled the flow from row 1 to 4 over a longitudinal distance approximately 3.5-4 m, whereas, the middle one controlled the region from row 5 to 7 with a longitudinal dispersion length of approximately 2.6 m. Circulations in the rear side were comparatively of smaller lengths either in the lateral or longitudinal directions. A refined layout illustrating the overall flow with associated lengths is shown in Figure 5.14.

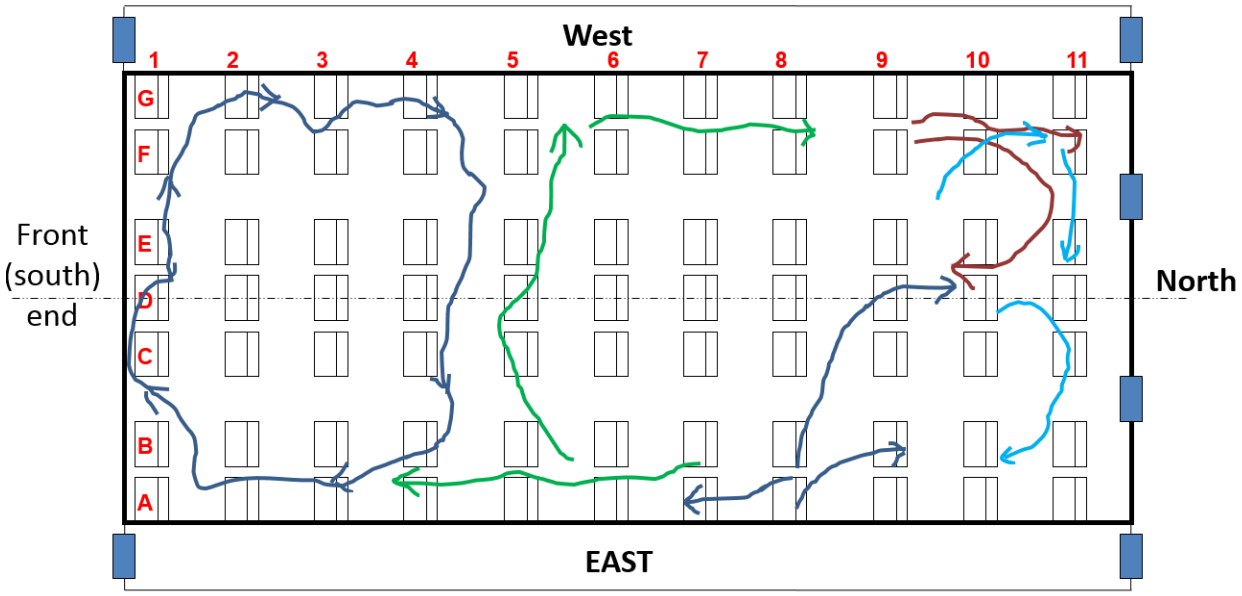

Figure 5.13 - Overall flow behavior inside the cabin based on tracer gas results with heated manikins

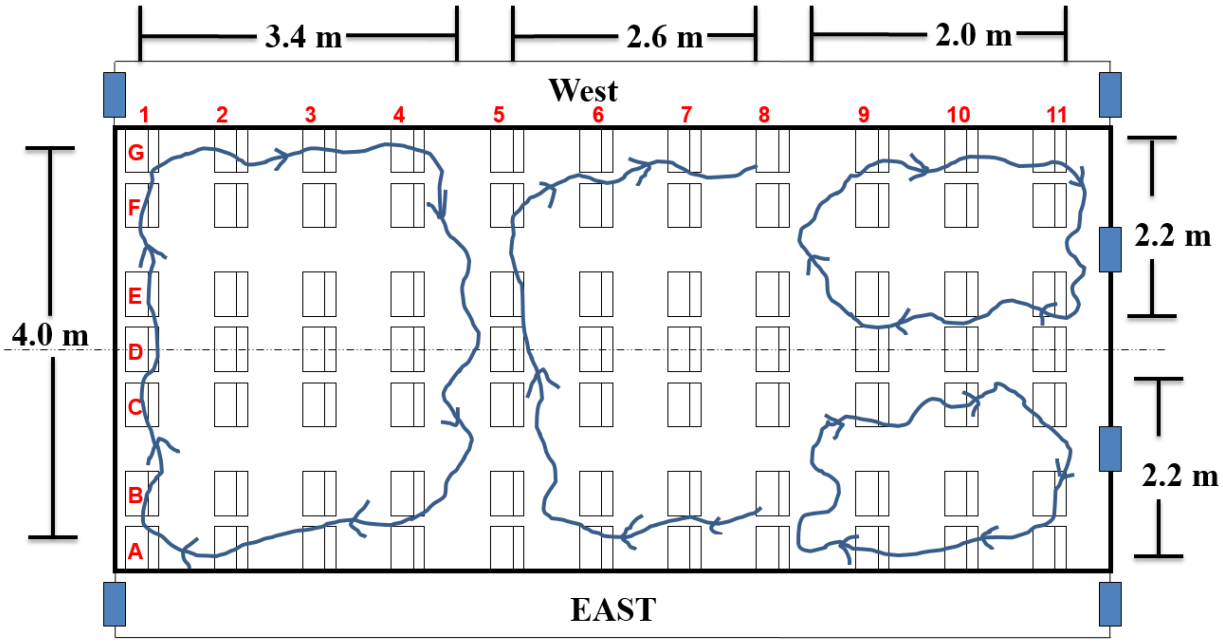

Figure 5.14 - Identified gaseous circulations inside the cabin with approximate dimensions (Dimensions of the cabin and the circulations are not to scale. The cabin seats are not exactly equidistant)

5.1.3 Comparing flow visualization results with the tracer gas results

Comparing Figure 5.14 with Figure 5.1, it was seen that there was a strong agreement between smoke visualizing tests and tracer gas experiments. Both approaches showed that there was a clockwise directed airflow in the fore section of the mockup cabin. For the middle section, the tracer gas results experienced a clockwise circulation over the section from row 5 to the back of row 7. This circulation extended over the entire transverse cross section of the cabin, whereas the smoke visualizing results showed that a clockwise directed circulation dominated over the same longitudinal length from row 5 to the region around row 7, but it did not control the west side of the middle section and was approximately dominating over the seats from A to E only. The west side of the middle section was shown to have small eddies or swirls in the clockwise and counterclockwise directions.

Two circulations were identified in the rear section of the cabin using smoke visualizing technique. The airflow moved backwards in the far back-west side and then reflected its direction as it hit the back wall of the mockup cabin. On the other hand, smaller circulations and eddies were controlling the back-east side. No conclusions were made, using the smoke visualizing, regarding the flow distribution in the rear-east corner as no observations were caught. The tracer gas results came into agreement with the above results from smoke visualizing and added another piece of the flow phenomena in the east-back corner.

5.1.4 Effect of thermal plumes created by the thermal manikins on airflow behavior inside the mockup cabin

The effect of the heat generated by the thermal manikins, which is equivalent to 100 W of sensible heat per manikin, over the airflow distribution inside the cabin is shown in Figure 4.11 through Figure 4.18 and in Figure 5.15 through Figure 5.22. The temperature difference between

heated and unheated environments due to the energy released by the manikins was approximately 6 ˚C. In general, when looking into the results for the centerline seats in 2D, 5D, 7D, and 10D, it was seen that the data was scattered more symmetrically between the east and west sides of the cabin. Starting with the front section of the cabin and examining the data for seat 2D and 5D, in Figure 5.15 and Figure 5.18, it was observed that the tracer gas dispersion did not favor any side of the cabin over the other with some exceptional seats. Figure 5.15 showed that in the front part of the cabin, when releasing in seat 2D, the flow was pushed towards the front wall of the cabin and was then circulated backwards with a symmetrical flow in both sides east and west. The vertical investigation in the fore-front part of the cabin in Figure 4.19 and Figure 4.20 showed that for the case of unheated manikins the exposure in the east and west aisles were of the same order of magnitude except for the lower elevations, approximately below 1 meter, in the west side that had higher average exposures. However, it should be noted that at these low levels the seats formed a blockage for the gaseous flow and since vertical sampling was conducted in the aisles between the seats where there were no flow constrictions, the tracer gas might have favored the transport through this zone to find its way to the exhaust ports located at the lower levels of each of the side walls. Despite that, it was also noticed that the level of discrepancies increased in the lower levels near the floor. Figure 4.20 shows that some individual samples in the lower levels were of the same order of magnitude as other data sampled at higher elevations. So, for the heated manikins case it was clear that more tracer gas moved to the west side than to the east side at all elevations. Table 5.2 shows that the exposure with heated manikins ranged between 16% and 23% in the east aisle against 51% to 99% in the west aisle. On the other hand for unheated manikins, it was observed that the east and west sides experienced almost the same exposure levels, approximately 35%, except for the lower-west

section below 1 m for the reasons argued previously. Taking the above observations into account, it can be concluded that the flow in the west and east sides of the fore section of the cabin were symmetrical at 1 m and above.

Comparing the results for seat 5D, under heated and unheated manikins, Figure 5.18 shows that the data was more evenly distributed in the transverse direction with unheated manikins, although there were some exceptions, such as in the seats around the release port. With unheated manikins, more samples were collected in seat 5F (west of the release point) than in seat 5B (east of the release point), but on the other side more samples were collected in seat 5C (east of the release point) than in seat 5E (west of the release point). So within the same row, some seats in the east had higher exposures and some had lower exposures than in the west side. This was not surprising due to the chaotic characteristics of the flow inside the cabin as was observed earlier. Considering the heated manikin case where seat 5E had (22% ±2%) exposure (with respect to the tracer gas sampled in the release location in 5D) against (14% ±1.5%) exposure in seat 5C; (18% ±0.45%) in seat 5F against (13% ±0.35%) in seat 5B; (39% ±2%) in seat 6E against (15% ±0.5%) in seat 6C, it can be seen that there were some differences in the samples collected in symmetrical seats with respect to seat 5D and that the west side seats had higher exposures than the corresponding east seats. On the other side, the exposures under unheated case were (17% ±0.44%) in seat 6E against (20% ±0.46%) in seat 6C; (12% ±%0.43) in seat 6B against (11% ±0.24%) in seat 6F; (18% ±0.49%) in seat 5F against (14% ±0.42%) in seat 5B. The margin indicated in the above figures was based on the total relative uncertainty of the results described in section 5.3 and summarized in Appendix E - Table 5.1 shows the differences between the upper and lower exposure limits for the indicated seats in the 2nd row of the table under heated and unheated cases. Basically, the comparison sets represent the difference

between symmetrical seats in the east and west sides of the cabin with respect to seat 5D. An example for the calculations shown is the difference between 5C and 5E under heated conditions: the lower limit in seat 5E under heated conditions was 20% (22% - 2%), whereas the upper limit of the symmetrical seat in 5C was 15.5%. Thus, the difference between 5C-5E under heated conditions was 4.5% as shown in the 5th column of the table. Four out of the six considered cases in Table 5.1 showed lower exposure differences between the symmetrical seats with unheated cases. The differences for the second set (4C-4E) was almost the same for both heated and unheated conditions, leaving one case only with the unheated having higher differences. Note that the latest case represented seats that were adjacent to the source seat.

Table 5.1 - Differences between the upper and lower exposures in different seats when releasing in seat 5D and taking into consideration the total relative uncertainty

	seat comparison sets					
	4B-4F	4C-4E	5B-5F	5C-5E	6C-6E	6B-6F
Heated	1.4%	1.2%	4.2%	4.50%	21.5%	7%
Unheated	0.25%	**1.5%**	3%	**6.50%**	2%	0.33%

Vertical sampling in the mid-section of the cabin showed that when tracer gas was released in seat 5D more tracer gas was sampled in the east aisle of row 4 than in the west aisle of the same row for both cases heated and unheated manikins, as shown in Figure 4.22 and in Table 5.2. However, above 1 m the differences in the same row between the east and west sides were less with unheated manikins as reflected in Figure 4.22 and Table 5.2. Looking into the figures in Table 5.2 above 1 meter under unheated conditions, the east side of row 4 experienced 20-26% against 19% in the west side of the same row; the east side of row 6 experienced 24-30% exposures against 26-33% exposure. For the heated case, row 4 had 29-34% in the east side against 13-16% in the west side, whereas row 6 had 22% in the east against 26-31% in the west.

Again, the differences in the exposure between the east and west sides of both row 4 and row 6 were lower with unheated conditions.

Similar observations were noted for results of release in 7D and 10D, Figure 5.19 and Figure 5.22, where the flow tended to be of equal order of magnitude between the east and west sides of the cabin.

The tracer gas release in the centerline seats of the mockup cabin under unheated manikins was followed by the release in the side seatss in the fore and aft sections of the cabin. Starting with the east side of the cabin, it was noticed that the flow behavior agreed in the back section of the east side with heated results. The majority of the gaseous flow moved from seat 8B to 8D, to 9D, 10D similar to the flow for heated case. It should be mentioned that the sampling port in seat 8B was 762 mm ahead from the source in 8B. Having a normalized value in 8B less than that detected in seats 8D and 9D, would support the conclusion that the dominating low was moving to the west side of the cabin while drifting more into the back side of the cabin. The analysis of the results in seat 9F (Figure 5.21) indicated that the flow moved to the east side with higher exposures in the back rows than in the front rows by comparing the sampled tracer gas in row 10 with row 8 and row 11 with row 7. Although it might be argued that there seemed to be some longitudinal circulations in this section as was argued with heated manikins, for example when considering 8D, 9D, and then 10D, but the high exposures in some other seats reduced the chances of such circulations, such as in seat 8D and 8B. It should be kept in mind, when analyzing such flow, the coherent transverse circulation effect might cause such lateral dispersion. Similar observations were made for seat 4F in Figure 5.16 where it might be concluded that the tracer gas moved to the front rows, but there were high exposures at the same time in the back rows that could not be ignored.

Concluding this section, the heat generated by the thermal manikins played a major rule over the gaseous flow dispersion. With unheated manikins, the gaseous flow tended to behave in a symmetrical way between the east and west sides of the cabin when releasing the tracer gas in the middle seats but showed different behaviors with side wall seats release.

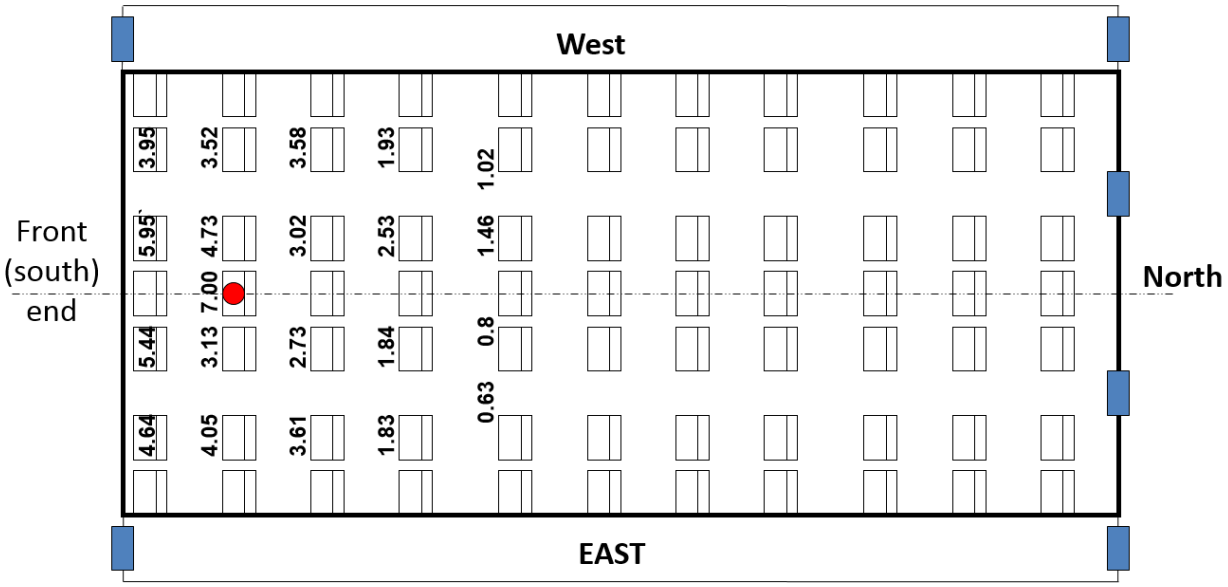

Figure 5.15 - Averages of the normalized sampled CO_2 when releasing in seat 2D (unheated manikins)

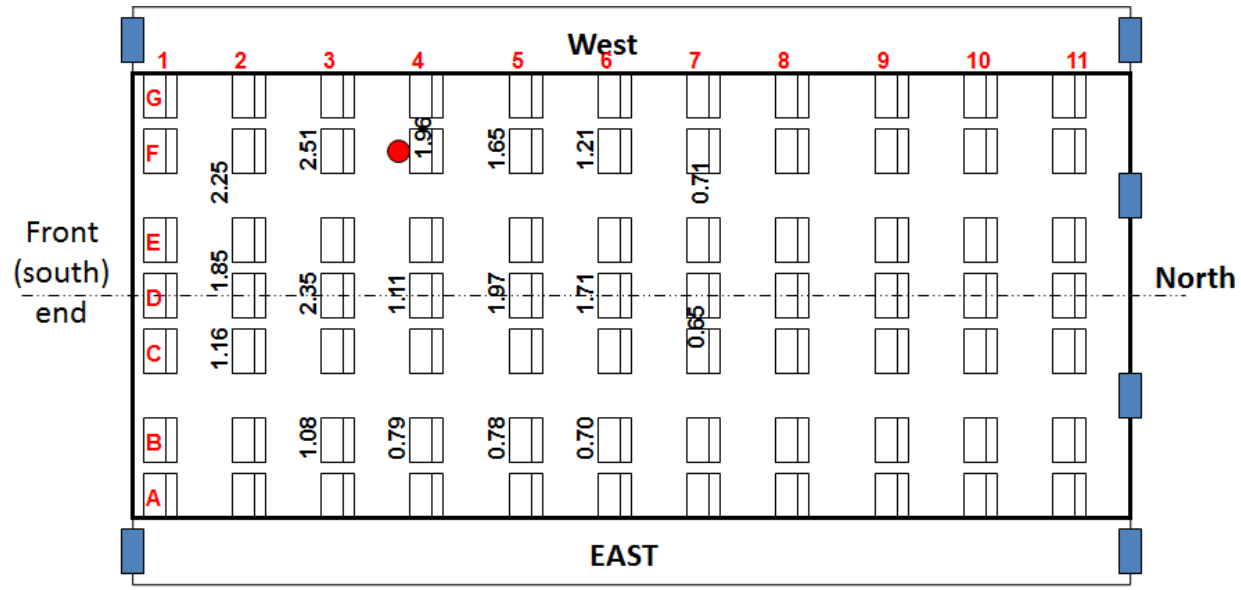

Figure 5.16 - Averages of the normalized sampled CO_2 when releasing in seat 4F (unheated manikins)

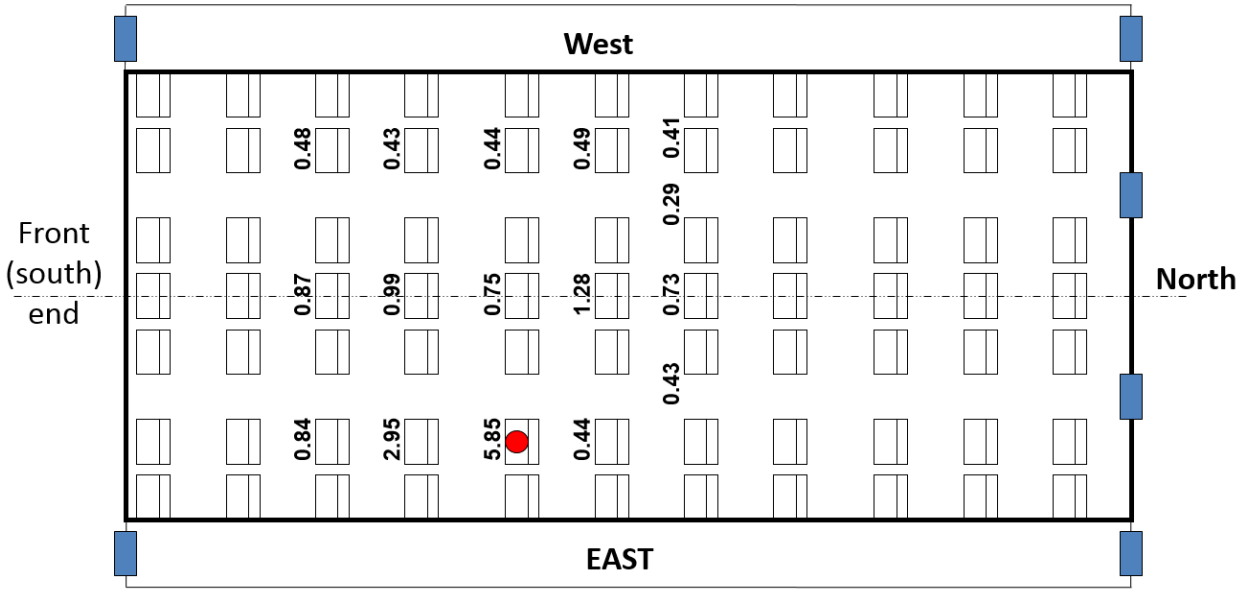

Figure 5.17 - Averages of the normalized sampled CO_2 when releasing in seat 5B (unheated manikins)

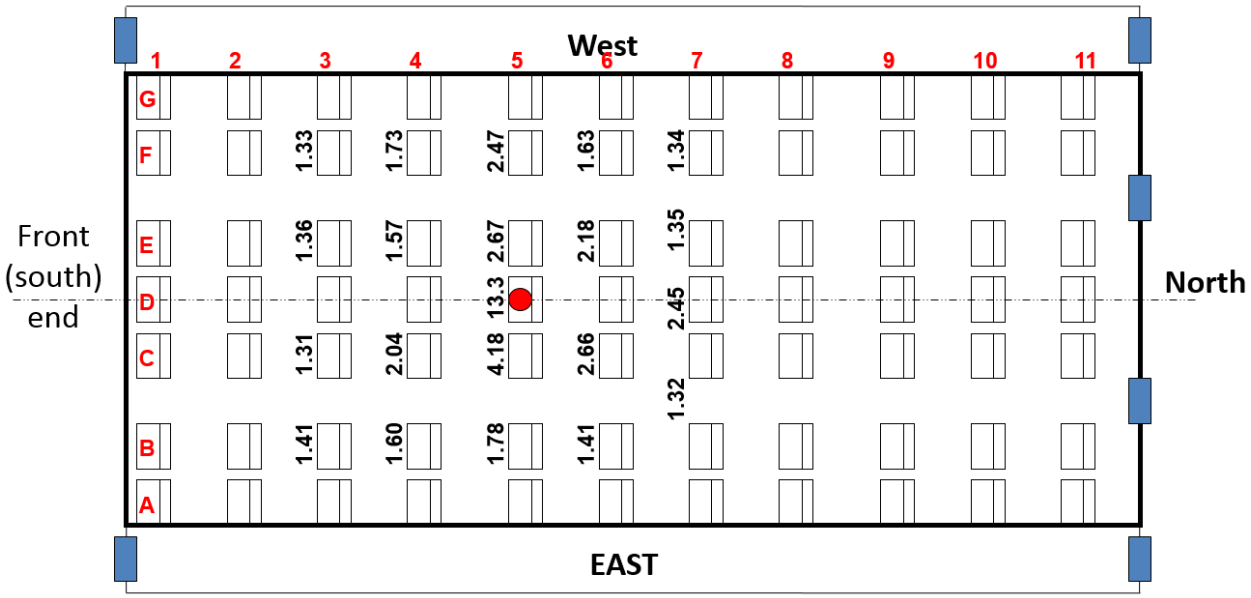

Figure 5.18 - Averages of the normalized sampled CO_2 when releasing in seat 5D (unheated manikins)

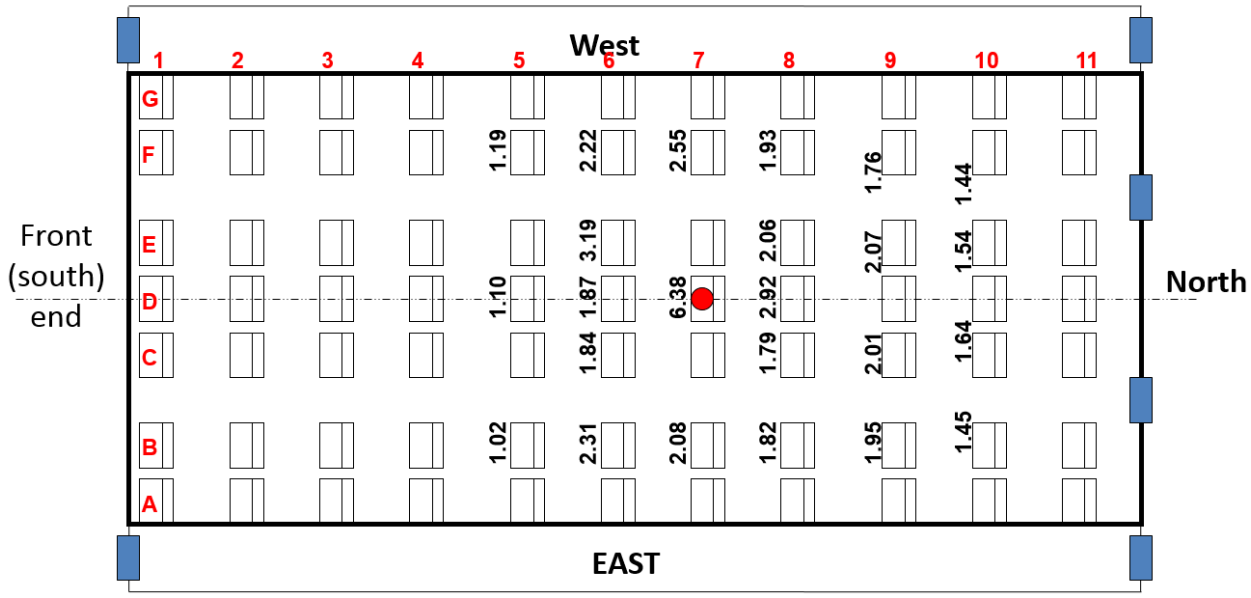

Figure 5.19 - Averages of the normalized sampled CO_2 when releasing in seat 7D (unheated manikins)

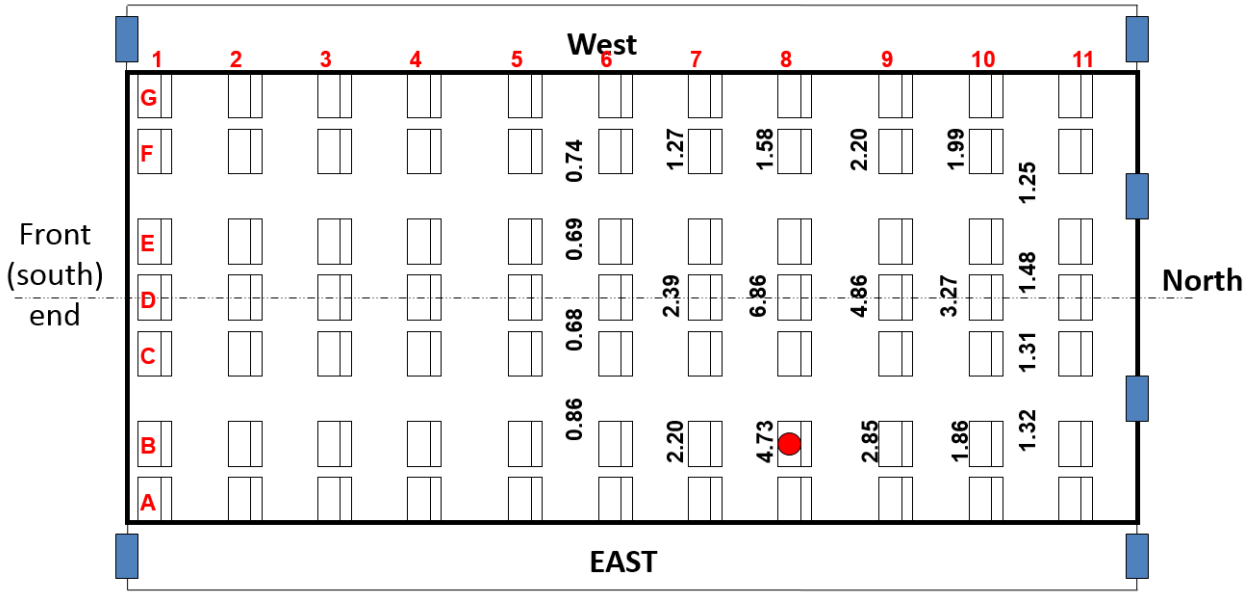

Figure 5.20 - Averages of the normalized sampled CO_2 when releasing in seat 8B (unheated manikins)

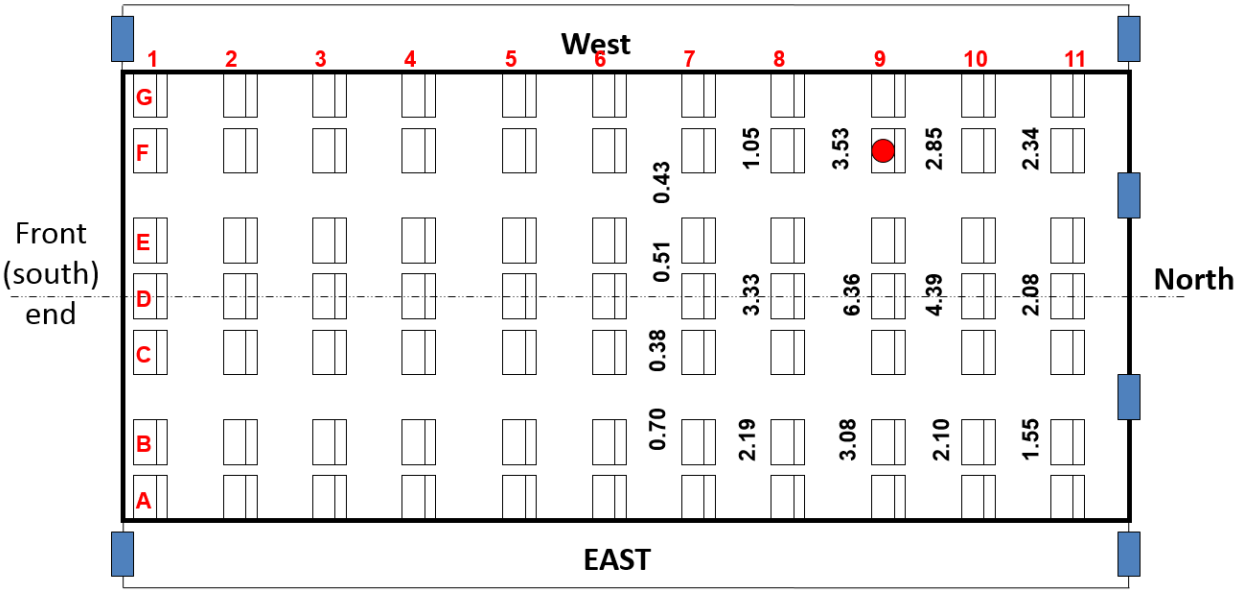

Figure 5.21 - Averages of the normalized sampled CO_2 when releasing in seat 9F (unheated manikins)

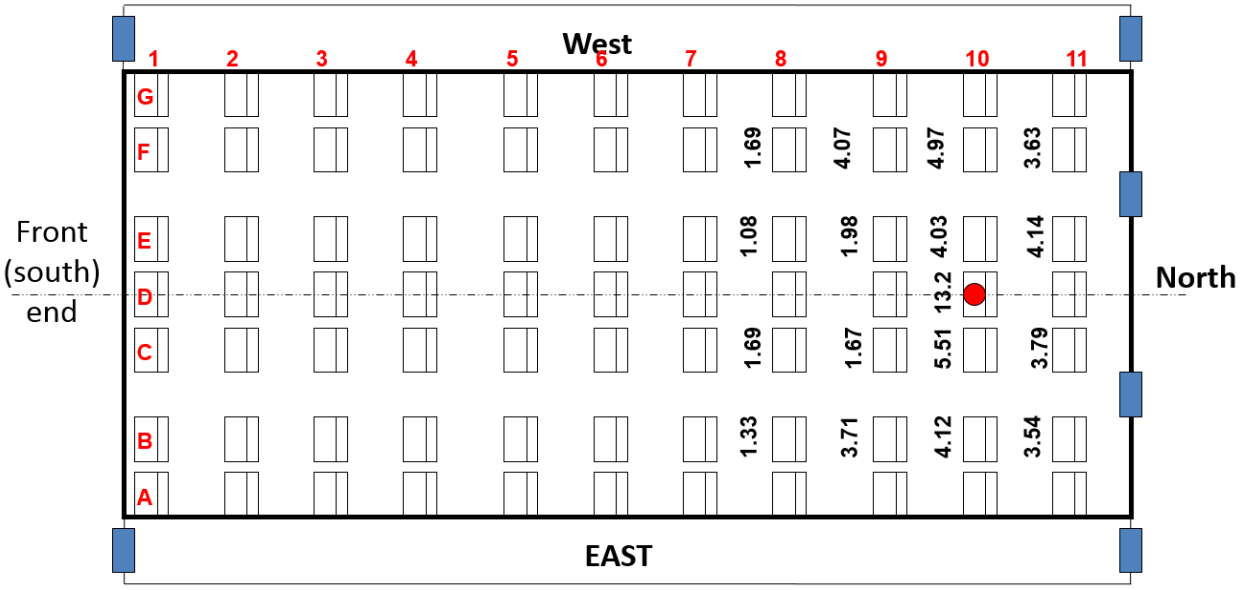

Figure 5.22 - Averages of the normalized sampled CO_2 when releasing in seat 10D (unheated manikins)

Table 5.2 - Vertical exposure percentages

		Location Above Floor	East Aisle		West Aisle	
			Heated	Unheated	Heated	Unheated
Release in Seat 2D	Row 2	1792 mm	16.5%	41%	51%	34%
		1344 mm	17%	36%	70.0%	35.5%
		896 mm	16%	30%	91%	52%
		448 mm	23%	39%	99%	74%
Release in Seat 5D	Row 4	1792 mm	29%	20%	13%	19%
		1344 mm	33.5%	26%	16%	19%
		896 mm	32%	36%	16%	19%
		448 mm	37%	46%	20%	29%
	Row 6	1792 mm	22%	24%	26%	26%
		1344 mm	21.4%	30%	31%	33%
		896 mm	23%	35%	33%	30%
		448 mm	26%	40%	41%	29%

5.2 Turbulence Analysis

The speed measurements were conducted using omni-directional speed probes. It should be noted that measurements conducted using omni-directional probes are less accurate than similar measurements using PIV or directional hot wire anemometers due to limitations with the omni-directional probes. However, the 3D chaotic airflow inside the cabin made it difficult to use the directional wire anemometers. Previous tests inside the mockup cabin using hot wire anemometers showed no significant differences between directional velocities due to the high intermingling phenomena. Also, the low airflow speed range inside the cabin limited the speed measurements to this speed transducer model (TSI-8475) although there are other omni-directional speed transducers with better accuracies, such as TSI-8455 and TSI-8465 shown in Table 3.2, but the minimum measured speed associated with these probes is limited to approximately 13 cm/s which is higher than the detected speed range inside the mockup cabin.

5.2.1 Speed analysis within the cabin

Section 4.3.1 presents the average airflow speed in the east, centerline, and west seats of the cabin with heated manikins. Figure 5.23 combines the average speed in all of the considered 33 seats and Figure 5.24 shows the average speed along with 95% confidence interval margins (analysis of the uncertainty is presented in section 5.3). With some exceptions in some seats but it can be observed that the east side of the cabin experienced higher speeds in the mid-section of the cabin, whereas the west side had higher speeds in the back section. Another observation was that the center-line seats had lower speeds in almost all rows compared to the west and east sides.

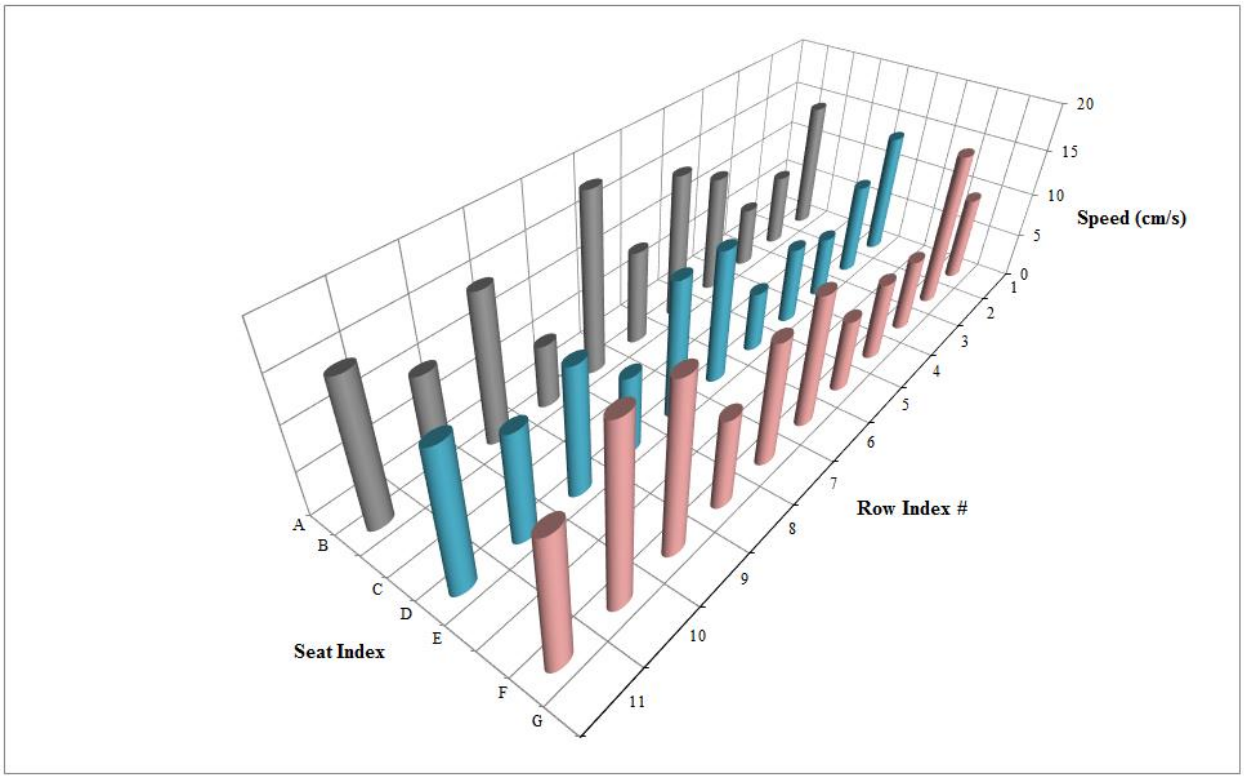

Figure 5.23 - Average airflow speed (heated manikins)

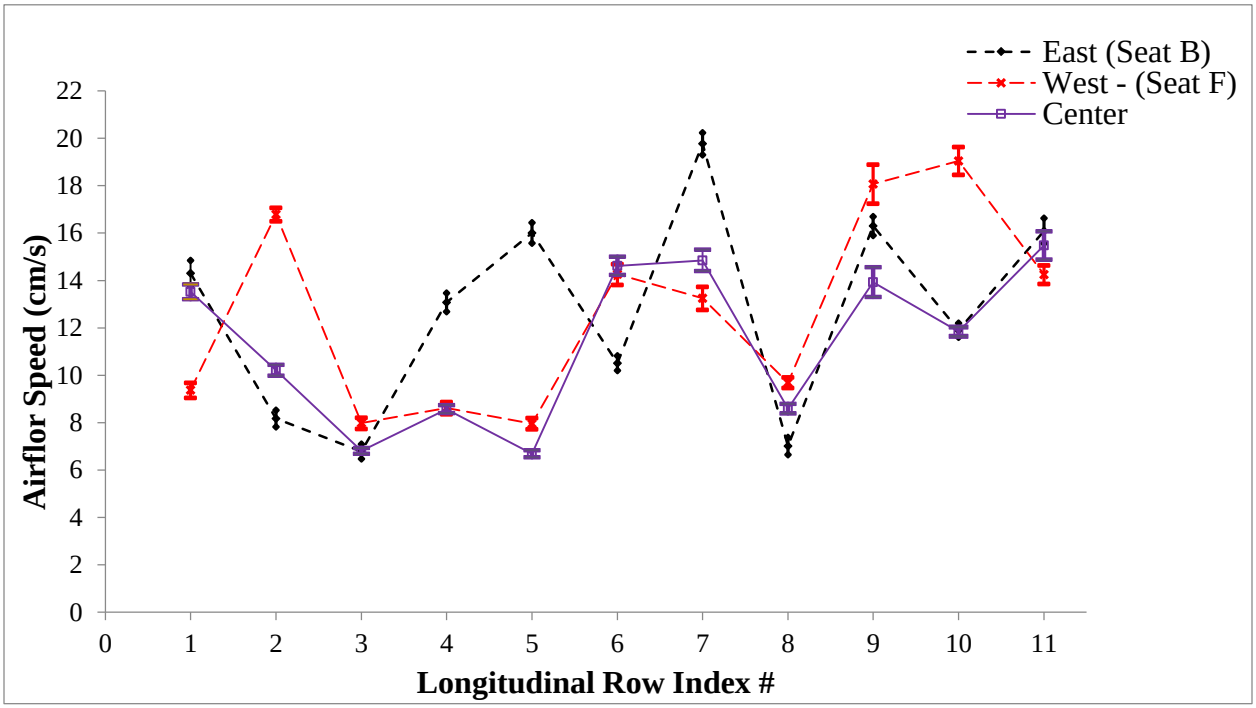

Figure 5.24 - Average airflow speed with 95% C.I. margins (heated manikins)

5.2.2 Turbulence kinetic energy (TKE) and turbulence intensity (TI) inside the mockup cabin

Phenomenology of turbulence involves use of dimensional analysis, a variety of scaling arguments, symmetries, invariant properties and various assumptions. In the broad sense, phenomenology of turbulence includes also most of the semi-empirical approaches and turbulence modeling when Reynold's averaged equations are used due to equation closure requirement. The Reynold's decomposition theory or the theory of small disturbances assumes that the instantaneous velocity is decomposed of a fluctuating component around a mean value. The same is assumed to apply to speed analysis as shown in equation (5.1).

$$v = \bar{V} + v' \tag{5.1}$$

where v is the instantaneous speed, $\bar{V}$ is the average speed, and v' is the fluctuating speed. Using the above equation for all measurements taken, the fluctuating speed can be used as an indication for the level of disturbance at any location and can be used to compare the relative disturbance level between different locations in the cabin. The fluctuating speeds in the east, center, and west sides of the cabin are shown in Figure 5.25 through Figure 5.35. The fluctuating speed plots revealed that the fluctuating speed in the east side of the cabin was dominating over the front section of the cabin from row 1 to row 5 as the amplitudes of the fluctuating speed in the east side were higher than those measured in the centerline and the west sides of the cabin for the same rows. The region from row 6 to row 8, shown in Figure 5.30 to Figure 5.32, experienced an increase in the amplitude of the fluctuating speed measured in the center and the west side of

the cabin. Hence, the three locations east, center, and west sides of the same row had almost the same order of magnitude in the middle and back sections of the cabin. This shows that the level of turbulence would be almost the same in these sections. Moving further to the back section of the cabin, although the east side was still experiencing large fluctuating speeds, but the centerline and west side seats had similar trends with the west side seats having even higher fluctuations, such as in row 10.

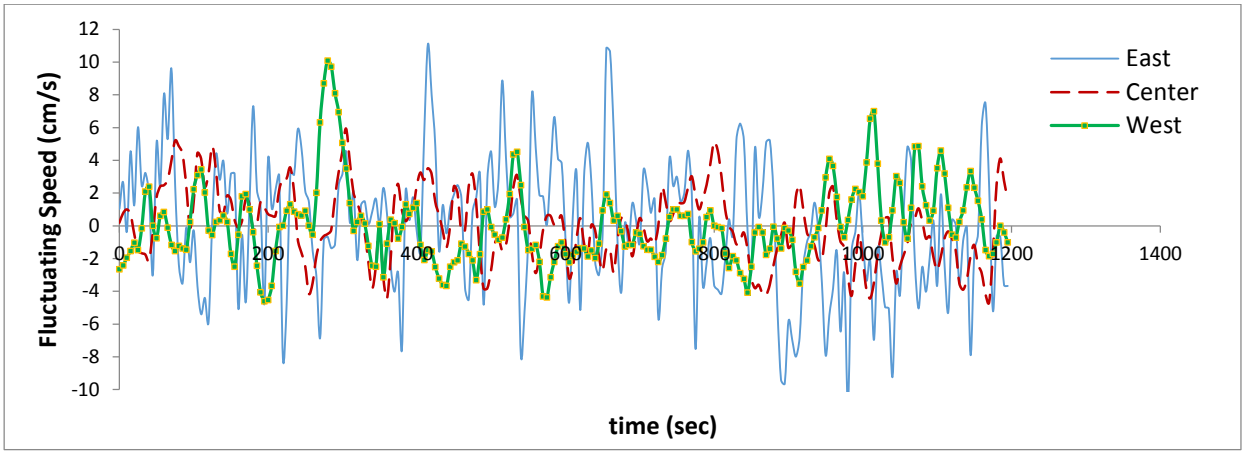

Figure 5.25 - Fluctuating speed in row 1 (heated manikins)

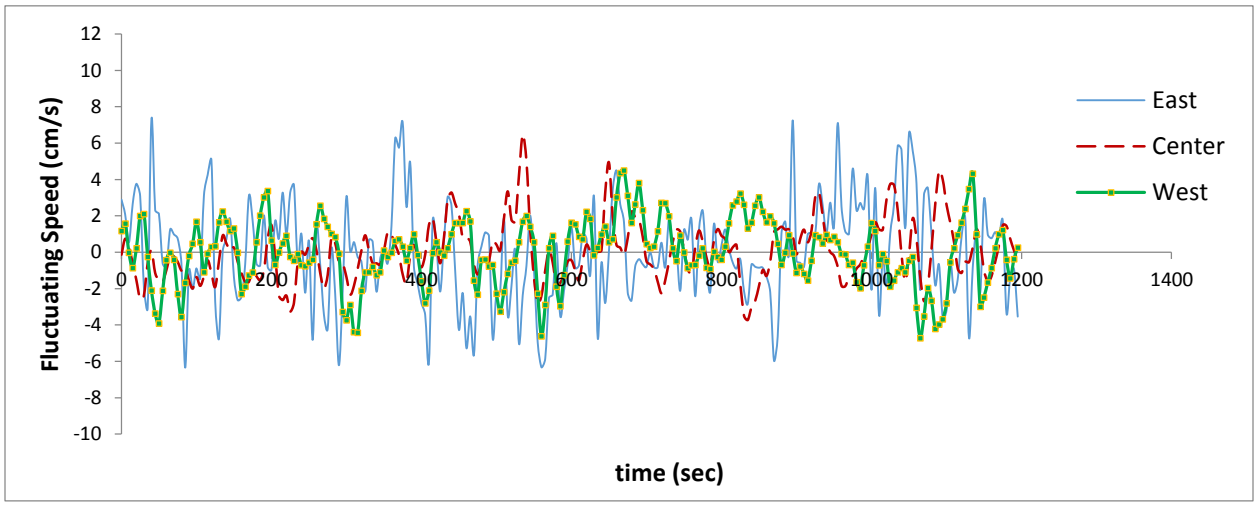

Figure 5.26 – Fluctuating speed in row 2 (heated manikins)

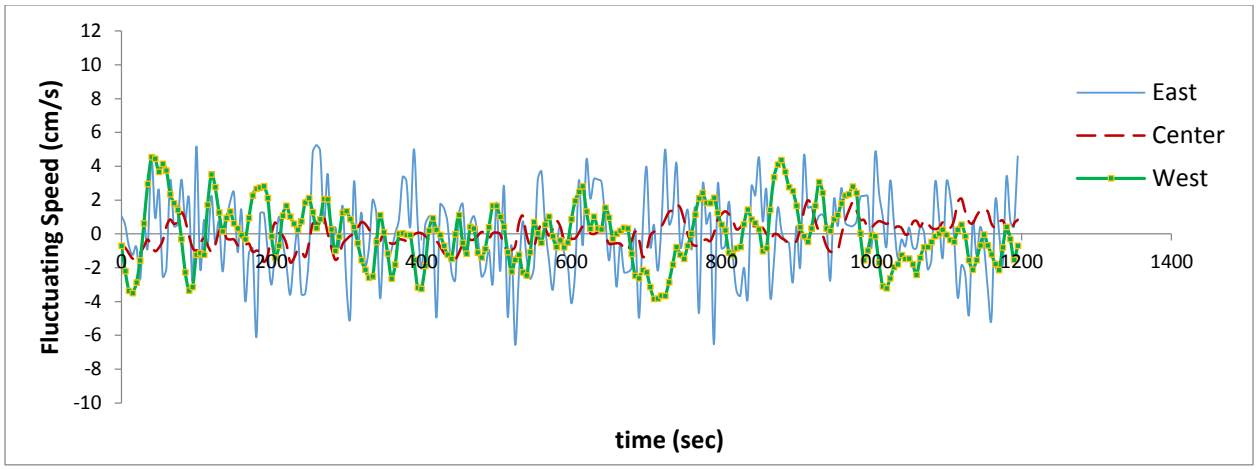

Figure 5.27 – Fluctuating speed in row 3 (heated manikins)

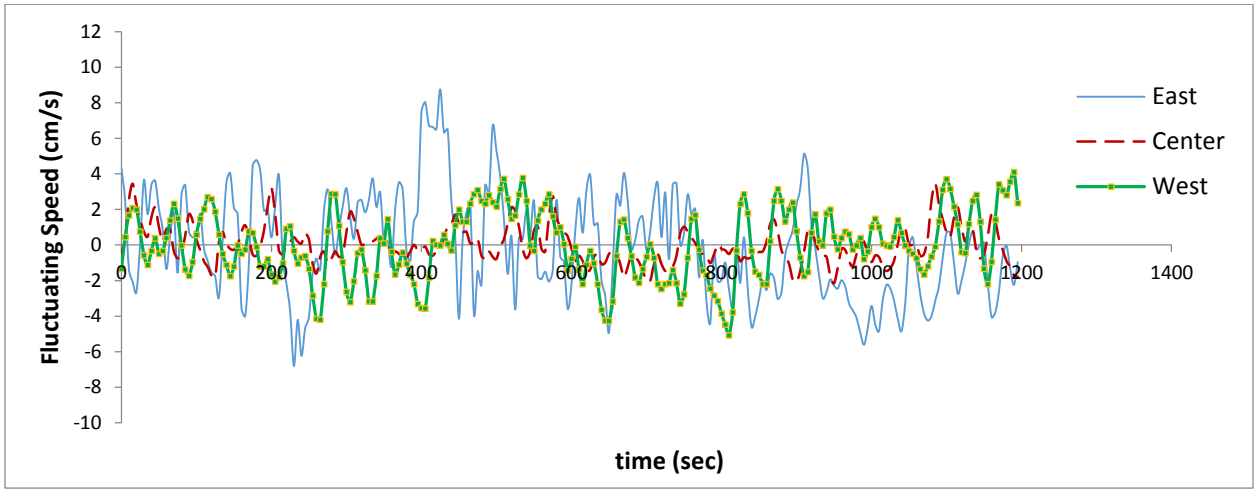

Figure 5.28 – Fluctuating speed in row 4 (heated manikins)

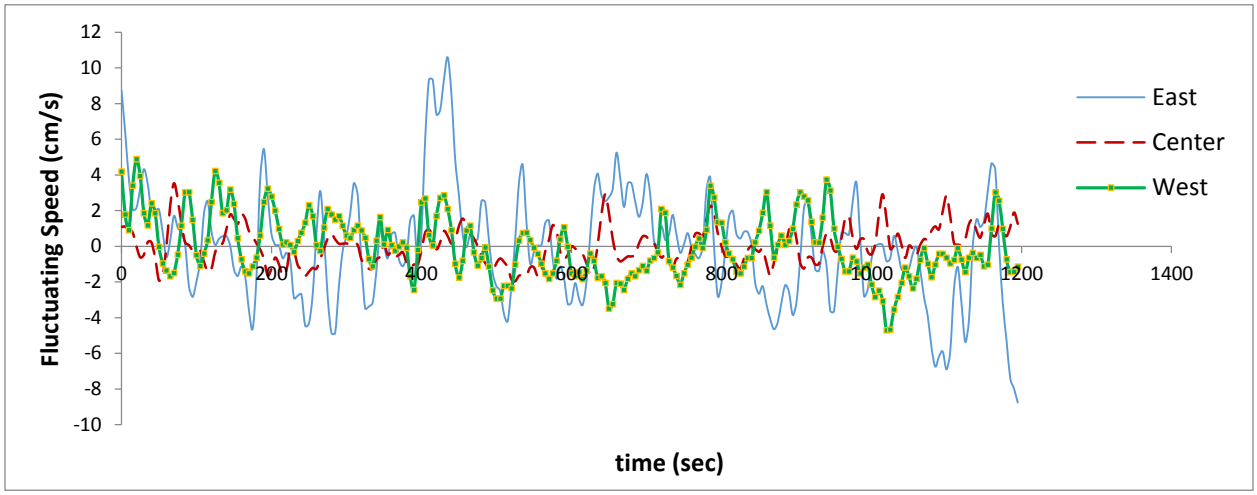

Figure 5.29 – Fluctuating speed in row 5 (heated manikins)

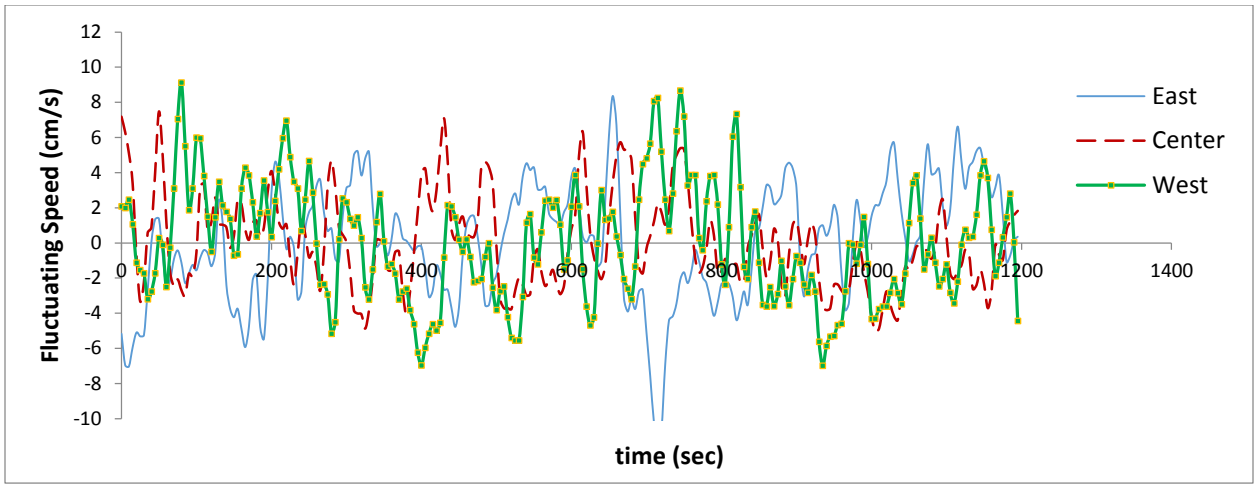

Figure 5.30 - Fluctuating speed in row 6 (heated manikins)

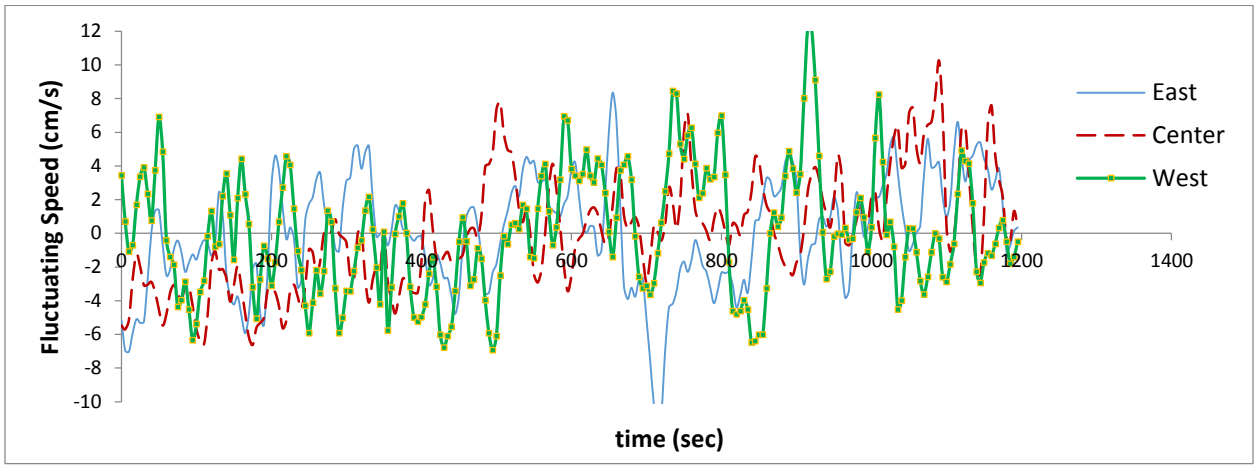

Figure 5.31 - Fluctuating speed in row 7 (heated manikins)

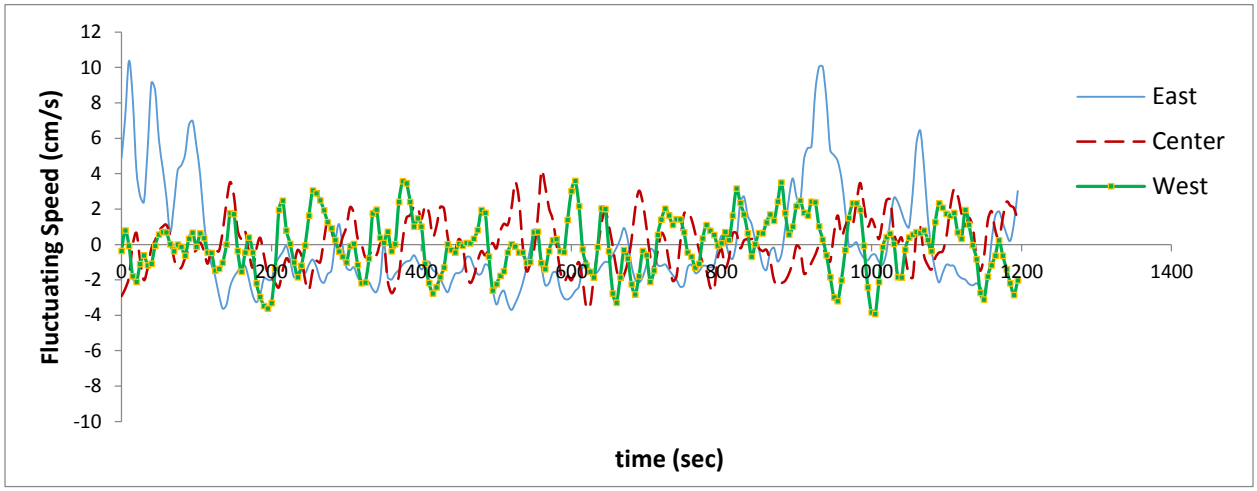

Figure 5.32 - Fluctuating speed in row 8 (heated manikins)

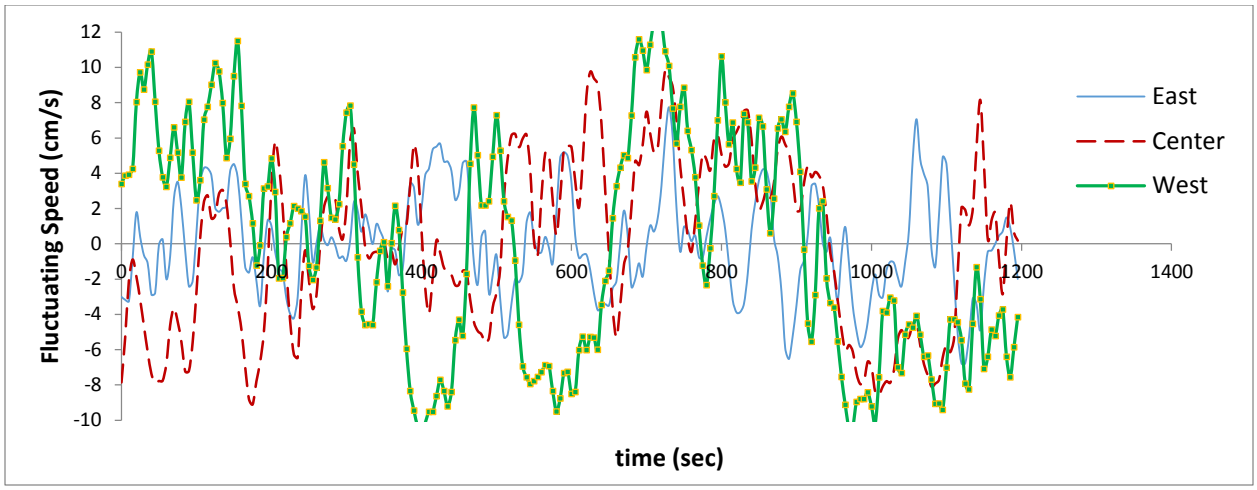

Figure 5.33 - Fluctuating speed in row 9 (heated manikins)

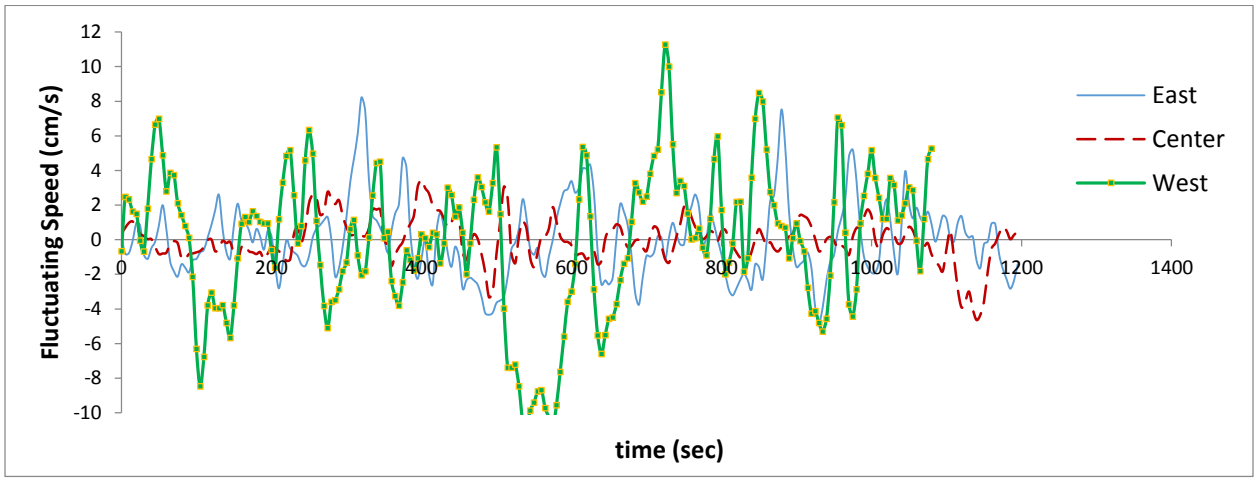

Figure 5.34 - Fluctuating speed in row 10 (heated manikins)

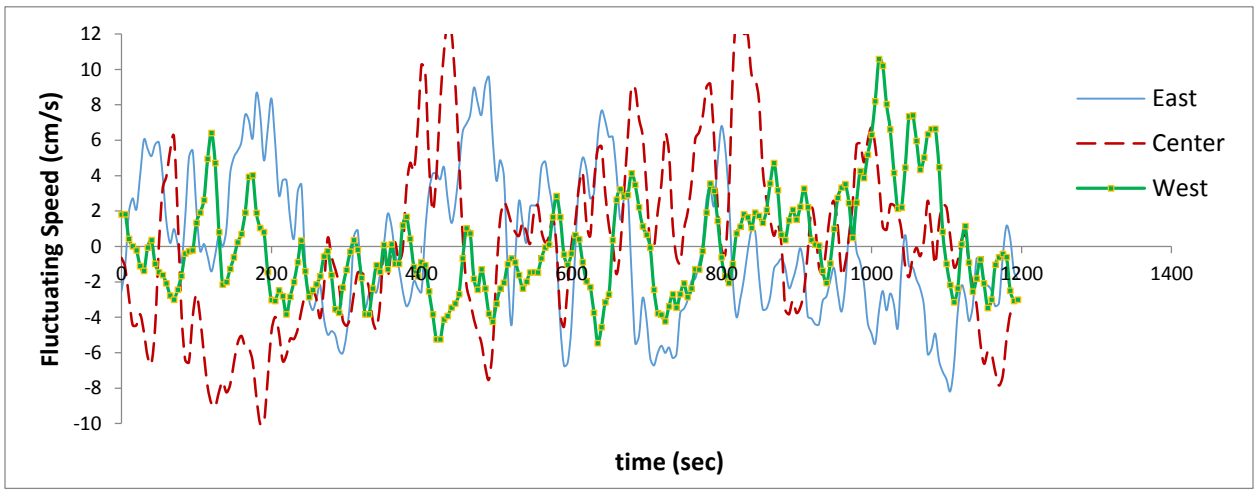

Figure 5.35 - Fluctuating speed in row 11 (heated manikins)

The turbulent kinetic energy can be defined in tensor format as

$$k = \frac{1}{2}\overline{u_\iota u_\iota} \tag{5.2}$$

Without going through the derivations, the widely used k-ε model is given in equation (5.3) and (5.4). The k-ε model is one of the most frequently used two-equation models. Equation (5.4) that represents the dissipation rate "ε" contains complex correlations whose behavior is little known and for which drastic assumptions must be introduced to make the equation tractable.

$$\frac{\partial}{\partial t}(\rho k) + \frac{\partial}{\partial x_i}\left(\rho k u_i - \Gamma^{(k)}\frac{\partial k}{\partial x_i}\right) = \rho(P^{(k)} - \varepsilon) \tag{5.3}$$

$$\frac{\partial}{\partial t}(\rho \varepsilon) + \frac{\partial}{\partial x_i}\left(\rho \varepsilon u_i - \Gamma^{(\varepsilon)}\frac{\partial \varepsilon}{\partial x_i}\right) = \rho(C_{\varepsilon 1}P^{(k)} - \varepsilon C_{\varepsilon 2})\frac{\varepsilon}{k} \tag{5.4}$$

Rate of change advection diffusion source

$$\Gamma^{(k)} = \mu + \frac{\mu^T}{\sigma_k} \quad ; \quad \Gamma^{(\varepsilon)} = \mu + \frac{\mu^T}{\sigma_\varepsilon}$$

μ^T is the turbulence dynamic viscosity, $P^{(k)}$ is the turbulence production rate, u_i is the velocity vector, ρ is the density.

Values for the different empirical constants were proposed by Launder and Spalding in 1974 and are given as

$C_{\varepsilon 1} = 1.44$; $C_{\varepsilon 2} = 1.92$; $\sigma_\epsilon = 1.3$; $\sigma_k = 1$

$$P^{(k)} = -\overline{u'v'}\frac{\partial u}{\partial y} = \frac{\mu^T}{\rho}\left(\frac{\partial u}{\partial y}\right)^2 \quad \text{or} \quad -\overline{u'_\iota u'_J}\frac{\partial u_i}{\partial x_j} \tag{5.5}$$

An important model that will be used for turbulent dissipation analysis is the modeling of the turbulent dissipation rate based on large scale eddies which is defined in equation (5.6).

$$\varepsilon = C_{\mu}^{3/4} . \frac{k^{3/2}}{l} \tag{5.6}$$

where l is the Taylor's inviscid turbulence length scale, k is the turbulence KE, and C_{μ} is defined as

$$C_{\mu} = \left(\frac{-\overline{u'v'}}{k} \right)^2 \tag{5.7}$$

Again C_{μ} was approximated by Launder and Spalding as having a value of 0.09.

These values were based on extensive examination of free turbulent flows, but they cannot be used for wall flows. Thus, this model is applicable only to flows or flow regions with high turbulence rates and cannot be applied near walls, where viscous effects become dominant. For such situations near wall function approach is usually used.

Assuming that the turbulence is isotropic, the turbulence kinetic energy can be estimated using equation (5.8)

$$k = \frac{3}{2} (v')^2 \tag{5.8}$$

where v' is the fluctuating speed component as was given in equation (5.1).

Another important parameter for turbulence analysis is the relative turbulence intensity and is given in equation (5.9)

$$TI = \frac{\sqrt{\overline{v'^2}}}{\bar{V}} \tag{5.9}$$

Using equations (5.8) and (5.9) along with the measured speeds as presented in previous sections, the turbulence kinetic energy (TKE) "k" and turbulence intensity (TI) at different

locations inside the mockup cabin were evaluated. The averages along with total relative uncertainties, as discussed in section 5.3, are presented in Figure 5.36 and Figure 5.37. The east side had higher TKE and higher turbulence intensities in the front section of the cabin than in the center and west sides. On the other hand, the west side had higher TKE in the back section of the cabin than in the east and the centerline seats, but that was associated with higher uncertainties, as well.

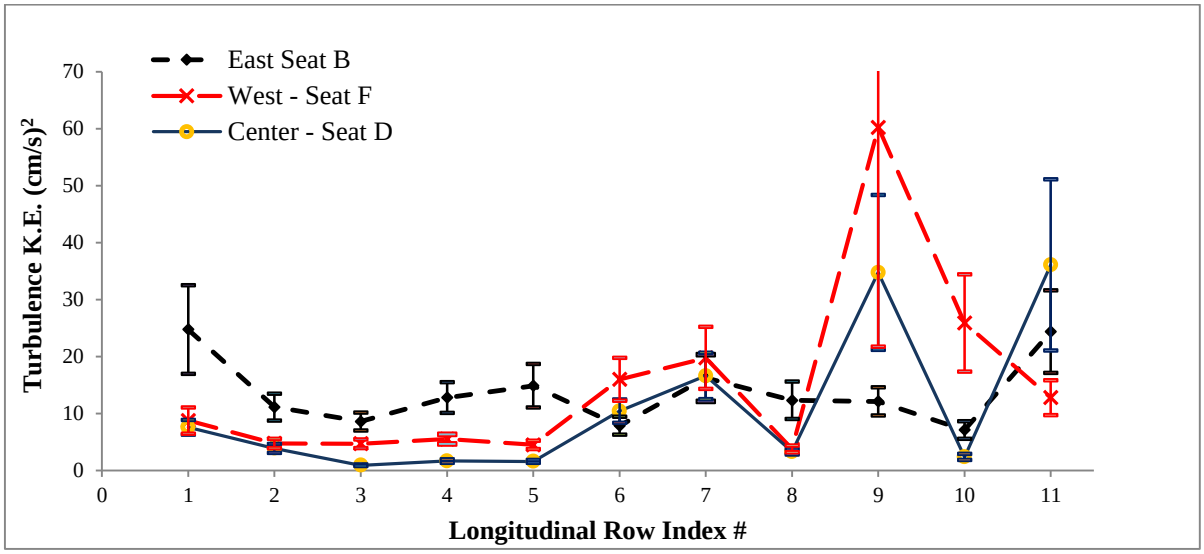

Figure 5.36 - Turbulence kinetic energy with heated manikins

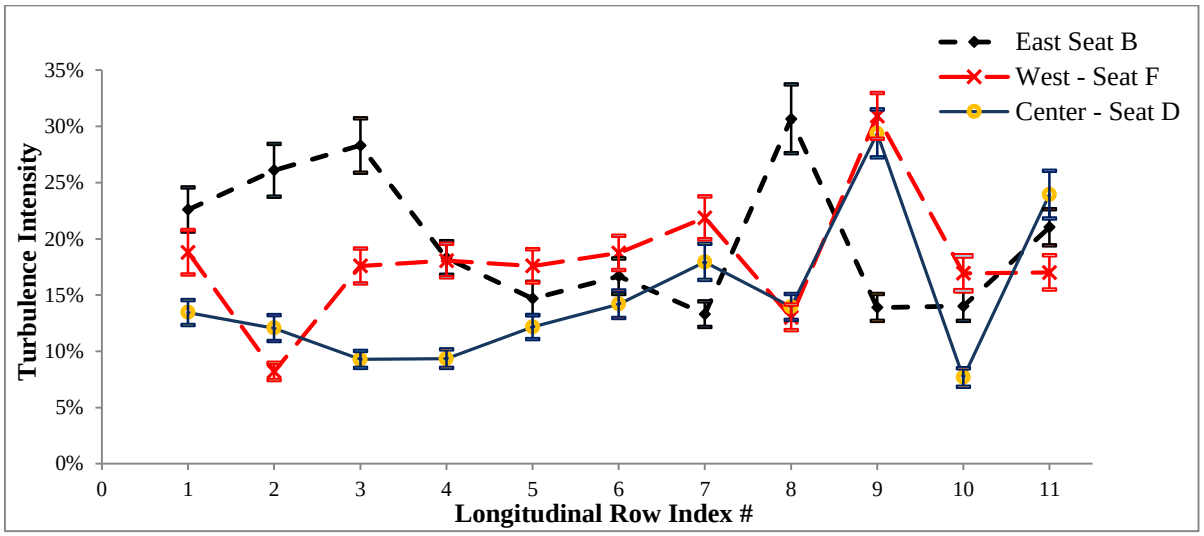

Figure 5.37 - Turbulence intensity with heated manikins

It was observed earlier that the speed in the back section of the cabin was higher in the west side of the cabin than in the east and the centerline seats. Figure 5.36 showed similar results in the back section where the west side had higher TKE than the east and centerline seats. However, it is not the speed that determines the level of turbulence in a region. Equation (5.8) shows that the TKE is controlled by the fluctuation part of the speed and not the average speed. For that, the east side seats had higher TKE levels in the front section of the cabin (row 1 to 5) which agrees with the conclusion pointed when analyzing the fluctuating speed. Similarly, it was concluded that the three transverse locations (east, center, and west) had almost the same speed fluctuation amplitudes in the region from row 6 to 8 and that the west side fluctuations were relatively higher in the back section of the cabin. Again the same argument discussed for the front section applies here where the TKE plots in Figure 5.36 showed overlapping results in the mid-section of the cabin and showed that the west side was dominating in the back section. To investigate how strong the fluctuating speed was with respect to the average speed, then the turbulence intensity should be checked. The east side seats had higher turbulence intensities in the front section of the cabin which means that the speed fluctuations were much higher than the average speed compared to those measured in the center and west side seats of the same section. The turbulence intensities from row 4 all the way to the cabin back wall were almost the same in the three transverse sides, which means that the fluctuating part of the speed with respect to the average was almost the same in each of the three transverse sides. Based on the TKE plots, it would be concluded that the local energy dissipation rate is higher in regions with low TKE that is being dissipated and transformed into heat. This was confirmed when looking into Taylor's viscous dissipation rates in Figure 5.44.

5.2.3 Turbulence length scale inside the mockup cabin

General review for turbulence length scaled was presented in section 2.3. For this study, the turbulence length scale was needed to evaluate the energy dissipation rate inside the mockup cabin. The kinetic energy dissipation rate is introduced in the following section (5.2.4). Equation (5.10) needed to be evaluated in order to investigate the inviscid energy dissipation rate inside the cabin.

$$\varepsilon = C_{\mu}^{3/4} . \frac{k^{3/2}}{l} \tag{5.10}$$

where Cμ is a constant, k is the TKE, and *l* is the macro turbulence length scale. The intent of this section was to evaluate the proper turbulence length scale that can be used in other sections when evaluating the energy dissipation rates.

3D-isotropic homogeneous turbulence is an idealization that is never encountered in nature. The challenge is then to understand what aspects of these theories apply to natural flow. A turbulent flow is said to be isotropic and homogeneous if,

- Rotation is not dependent on one specific direction
- Buoyancy is not important and can be neglected
- There is no mean flow

Since for isotropic turbulence the circulation is independent of the direction, in 3D isotropic turbulence flows there would be circulations that have the same dimensions in all three directions x, y, and z. Thus, in this study the size of the eddy was controlled by the minimum physical distance inside the mockup cabin. This can be justified by looking into the budget TKE equation:

$$\frac{Dk}{Dt} - \frac{\partial}{\partial x_j}\left[\frac{\gamma_t}{\sigma_k}\frac{\partial k}{\partial x_j}\right] = \overline{-u_j u_k}\frac{\partial U}{\partial x_k} - \beta g_j \overline{u_j}\theta - \varepsilon \quad (5.11)$$

where the terms in equation (5.11) (numbered left to right) are as follows:

(1): storage rate of the kinetic energy (can be neglected for steady state conditions)

(2): advection rate of turbulent kinetic energy and turbulent transport rate by eddies

(3): mechanical or shear production or loss term (can be neglected for isotropic turbulence since it was assumed that there is no mean flow)

(4): production rate or consumption term

(5): ε is the energy dissipation rate

Thus, with the first and third terms being neglected and forcing the production rate (4th term) to be zero, an estimate for the turbulent length scale can be obtained by comparing equation (5.10) and (5.11).

$$\varepsilon = C_\mu^{3/4}.\frac{k^{3/2}}{l} \sim \frac{\partial}{\partial x_j}\left[\frac{\gamma_t}{\sigma_k}\frac{\partial k}{\partial x_j}\right]$$

Therefore, $l \sim x_j$

With the assumption that for isotropic turbulence the dimensions of the circulation are the same in the x, y, and z directions, the minimum physical distance among the three directions should be controlling the circulation size. The geometry of the cabin has three major physical constraints: the height from the floor to the ceiling denoted by "H", the width from the east to the west wall "W", and the longitudinal length of mockup cabin "L_{long}". A schematic diagram for the plan view of the mockup cabin with dimensions showing the length and width is shown in Figure 3.1. The width is approximately 4.72 meters and the longitudinal length is 9.41 meters. Another schematic for the cross section of the mockup cabin is shown in Figure 5.38 with different

heights. The values of the heights shown in the figure are tabulated in Table 5.3. For simplicity, the largest H was used (H=2.1 meters). Thus, the integral length scale for air circulations inside the cabin was equivalent to the height "H". The turbulence length scale would then be l = 0.07H. (7% of the integral length scale). This result agrees with the results reported by Lin et. al (2005) where the turbulence length scale was between 0.15-0.3 m inside the same type of aircraft cabin used for this study.

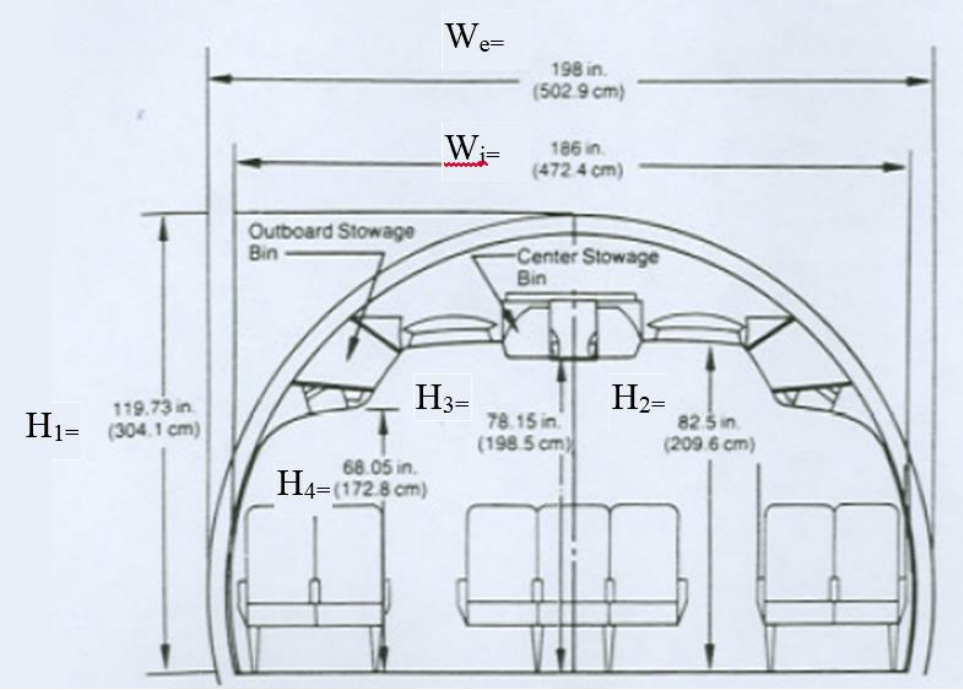

Figure 5.38- Boeing 767 Aircraft Cabin Cross Section

Table 5.3 - Dimension data for Boeing 767 Aircraft Cabin (as indicated in Fig. 5.38)

Dimension Description		cm	inch
Exterior Width (Maximum Width, We)		502.9	198
Interior Width (Wi)		472.4	186
Distance between floor and highest point on external surface of the aircraft (H1)		304.1	119.73
Heights of Different parts inside the aircraft cabin	H_2	209.6	82.5
	H_3	198.5	78.15
	H_4	172.8	68.05

With the integral length scale determined as L_o = H = 2.1 m, and the average speed inside the mockup cabin around 12 cm/s (evaluating the average of the speed in the 33 seats with heated manikins - Table 5.4) an order of magnitude for the Kolmogorov length scale can be evaluated using equation (2.15).

$$\frac{L_o}{\eta_K} = \left(\frac{L_o V_o}{\nu}\right)^{3/4} = (Re_{Lo})^{3/4}$$

$$Re_{Lo} = 25{,}200$$

$$\frac{L_o}{\eta_K} = 2{,}000$$

therefore, $\eta_K = 1.05\, mm$

This result agreed with results reported by Lin et al. (2005) who indicated that the Kolmogorov length scale inside a B767-300 aircraft was approximately 0.9 mm (0.003 ft).

In the local dissipation analysis (section 5.2.4.2), the square of the speed derivative needed to be evaluated. The term was discretized and it was important to determine the separation distance between two speed probes to evaluate the speed derivative with minimal errors. Section 5.2.4.2.1 investigates the separation distance. It was found based on the time constant of the speed transducer that the minimum distance needed was 300 mm. Based on experimental investigation, this distance was recommended to be approximately 127 mm. If this distance represents the Taylor length scale (λ), then when comparing it with the integral length scale L_o=2.1 meters and the micro-length scale $\eta_K = 1.05\, mm$, it is seen that $\eta_K << \lambda << Lo$ is satisfied.

5.2.4 Turbulence dissipation rate

Turbulence dissipation rate is an important parameter in addition to the energy production rate when analyzing turbulence of any module as it describes the rate at which the turbulence kinetic energy is being dissipated and transformed into heat.

The dissipation rate should follow the same behavior as the TKE since it was shown previously in equation (5.11) that

$$\varepsilon \sim \frac{\partial}{\partial x_j}\left[\frac{\gamma_t}{\sigma_k}\frac{\partial k}{\partial x_j}\right]$$

Thus,

$$\varepsilon \sim \frac{\partial(K.E.)}{\partial t} \tag{5.12}$$

However, it should be noted that at large scales, the energy dissipation rate becomes negligible. Thus, it is to be expected when using equation (5.10) to have the dissipation rate negligible and to be much smaller than the Taylor's viscous dissipation that was defined in equation (5.18).

In this section, two approaches were used to analyze the dissipation rate. The first approach dealt with the large scale inviscid model while the second one was more concerned with the local viscous dissipation rates.

5.2.4.1 Macro-scale dissipation rate (k-ε inviscid model)

For homogeneous isotropic turbulence, the rate of energy dissipation is assumed to be equal to the rate of energy production.

$$P_{K.E.} \sim U^2.\frac{U}{L} \tag{5.13}$$

where, $P_{K.E.}$ represents the kinetic energy production rate, U^2 is the kinetic energy rate, and U/L represent the strain rate due to vortex stretching. Thus,

$$P_{K.E.} \sim {U^3}/{L} \tag{5.14}$$

Therefore,

$$\varepsilon \sim {U^3}/{L} \tag{5.15}$$

The k-ε model defined an empirical correlation for the dissipation rate which was defined for homogenous fully turbulent flows in equation (5.10),

$$\varepsilon = C_{\mu}^{3/4} . \frac{k^{3/2}}{l}$$

where Cμ is a standard constant for the k-ε model and its value was recommended by Launder and Spalding in 1974 and is usually taken as 0.09; *l* is the turbulence length scale; and k is the turbulence kinetic energy. The turbulence length scale was estimated to be 0.07H, where H is the integral length scale inside the cabin (section 5.2.3).

Using the speed fluctuations and the TKE as was determined in the previous sections, the large scale dissipation rates were evaluated and presented in Figure 5.39. In this figure, it was observed that the large scale dissipation rate followed the same behavior as the TKE shown in Figure 5.36 since Cμ and *l* were held constant. However, since the dissipation rate is a measure for the dissipation of the turbulence energy, then regions with high kinetic energy levels should be accompanied with low dissipation rates, whereas regions with low kinetic energy levels should have high dissipation rates. For that, relating the large scale energy dissipation rates with local TKE was not the appropriate tool. Local dissipation rate seemed to be more reseanobale

approach to justify the local TKE analysis. The micro-scale (local) dissipation rates were investigated in the following section.

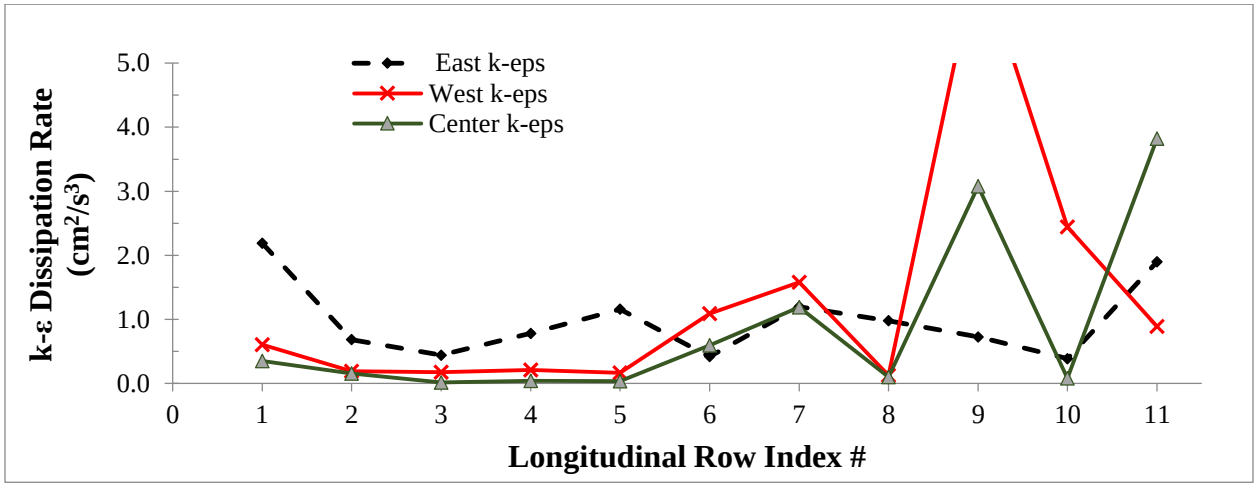

Figure 5.39 - Dissipation rates inside the cabin based on k-ε model given in equation (5.10) (heated manikins)

5.2.4.2 Micro-scale (local) dissipation rate (Taylors' viscous model)

Kolmogorov formulated the hypothesis of local isotropy based on definitions of local homogeneity and isotropy. This hypothesis postulates that at large Reynolds numbers all the symmetries of the Navier–Stokes equations are restored in the statistical sense. Kolmogorov presented some characteristics to his hypotheses. The first characteristic/similarity of his hypothesis states that for the locally-isotropic turbulence the distributions are uniquely determined by the quantities ν and ε (kinematic viscosity and turbulent dissipation rate). In other words, the only factors influencing the behavior of the small scale motions are the overall kinetic energy production rate and the viscosity. The second similarity of the hypothesis states that, if the separations between the points are large in comparison with $\eta = \left(\frac{\gamma^3}{\varepsilon}\right)^{1/4}$ [Kolmogorov microscale – equation (2.11)], then the distributions are uniquely determined by the quantity ε and do not depend on ν. Thus, the local dissipation rate can be defined as

$$\varepsilon = \gamma S_{ij} S_{ij} \tag{5.16}$$

Plugging the definition of the strain, the local dissipation rate becomes

$$\varepsilon = \gamma \left[\frac{1}{2} \left(\frac{\partial U_i}{\partial x_j} + \frac{\partial U_j}{\partial x_i} \right) \right]^2 \tag{5.17}$$

where $S_{ij} = \frac{1}{2}\left(\frac{\partial U_i}{\partial x_j} + \frac{\partial U_j}{\partial x_i} \right)$ is the local strain rate

In Taylor's hypothesis, which assumes isotropic turbulence, the local dissipation rate that depends on viscous stresses becomes as given in equation (5.18).

$$\varepsilon = A\gamma = 15\gamma \overline{\left(\frac{\partial v}{\partial x} \right)^2} \tag{5.18}$$

where A is an empirical constant, γ is the kinematic viscosity, and v is the velocity (speed in this study).

Using finite difference to discretize equation (5.18) and the above speed differential form, equation (5.19) was obtained using central difference discretization.

$$\varepsilon = 15\gamma \left(\frac{v_{i+1} - v_{i-1}}{2\Delta x} \right)^2 \tag{5.19}$$

Central difference discretization was used around the location "i" which represents the point of interest to evaluate the dissipation rate. In order to evaluate the above equation numerically with minimal errors, the separation distance Δx needs to be as small as possible. Section 5.2.4.2.1 investigates the optimum separation distance and it was found approximately 12.7 cm (5 inches).

5.2.4.2.1 Investigating the separation distance between two consecutive omni-speed probes

The TSI omni-directional speed transducers have time constants of 5 seconds (±uncertainty determined upon calibration by the manufacturer). For the aim of this investigation the absolute value of 5 seconds was used. Preliminary bench mark measurements were conducted to check for the minimum speed inside the cabin at the specified height (same height as that used for sampling tracer gas). Thirty three measurements were recorded. The minimum speed was found to be approximately 6 cm/s which was larger than the minimum range of the probe (5 cm/s) as given in Table 3.2. With a minimum recorded speed of 6 cm/s inside the mockup cabin, the smallest distance needed for a flow to be convected by two consecutive points would be 0.06 m/sec × 5 sec = 0.3 m = 300 mm (around 12 inches). To investigate the distance experimentally, three speed transducers (TSI-8475) were aligned in the longitudinal direction of the mockup cabin with different separating distances as shown in Figure 5.40. Two different locations inside the cabin were used to check the difference in the term $\overline{\left(\frac{\partial v}{\partial x}\right)^2}$ which was discretized in equation (5.19) to determine the local dissipation rate as shown in equation (5.18). Five different separation distances were examined: 5.08 cm (2 inches), 10.16 cm (4 inches), 15.24 cm (6 inches), 20.32 cm (8 inches), and 25.4 cm (10 inches). During each test, normal operating conditions inside the cabin were maintained as was described and used for tracer gas experiments with heated manikins. Each test was run for 20 minutes with 5 seconds between consecutive samplings. Each test was repeated 3 times for statistical consistency. It should be noted that the three tests were randomly repeated, sometimes 2 tests were run back to back, sometimes after some delayed time, and some other times on completely different days.

The averages of the 3 tests along with the relative uncertainties with 95% confidence intervals are shown in Figure 5.41 to Figure 5.43. The relative uncertainty included the bias uncertainty

for each probe and the random uncertainty encountered during each test. The equations used to calculate the relative uncertainties are similar to those presented in section 5.3.4.

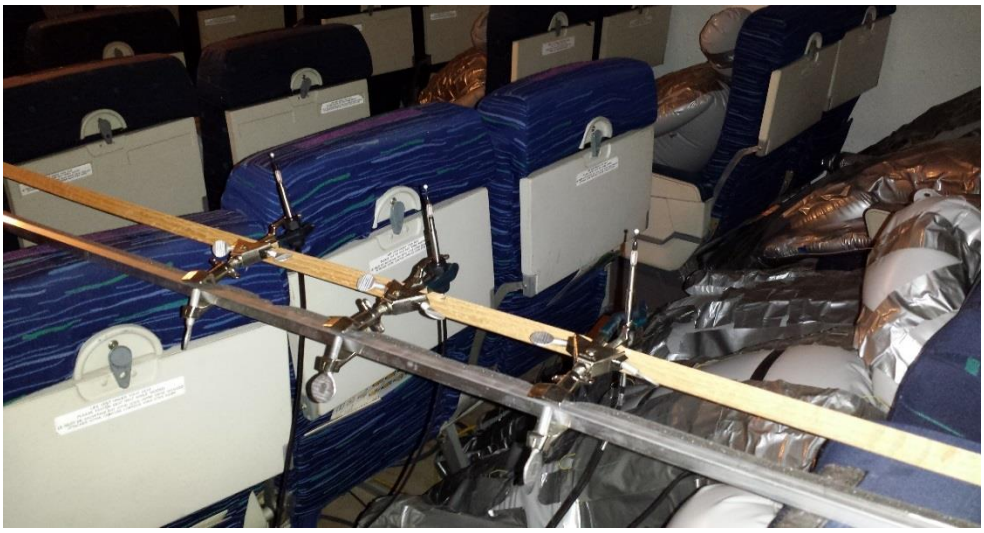

Figure 5.40 – Arrangement of the omni-directional TSI-8475 probes to investigate the separating distance between the sensors

The total relative uncertainty for the measurements taken in the east-back section of the mockup cabin (Figure 5.41 and Figure 5.42) were between 18-19% (including random and bias uncertainty), while those for the measurements taken in seat 5D (Figure 5.43) were between 15-17% (including both random and bias uncertainty). Note that the probes have ±3% accuracy and ±1% of full scale.

Comparing the results of both locations, it was observed that the results with different separation distances in seat 5D agreed more than in the east-back section of the mockup cabin. Thus, the debate for the rest of this section would be by analyzing the results in the east-back section. It was noticed that with a separation distance of approximately 5 cm, the values for the term $\overline{\left(\frac{\partial v}{\partial x}\right)^2}$ were much higher than those for other separation distances, as shown in Figure 5.41. Figure 5.42 shows the same results in the east-back section but with zoomed scale on the y-axis.

It was seen from this figure that the results for the separation distances of 15 cm and above were statistically the same (uncertainty bars are shown for all points, but those with lower values were not very clearly due to small values compared with the scale used on y-axis). With a smaller separation distance of 10 cm, the square of the spatial speed derivative started increasing. Based on the above results and to prevent any blockage effects from consecutive probes, and to accommodate for the radiation that might affect the cooling of the sensors by the probes stems a value of 12.7 cm (5 inches) was thought to be a reasonable separation distance. This distance is approximately 6% of the integral length scale (L_o = H = 2.1 m) which is in agreement with the value used for the turbulence length scale in the k-e model which has a value of 7% of the integral length scale.

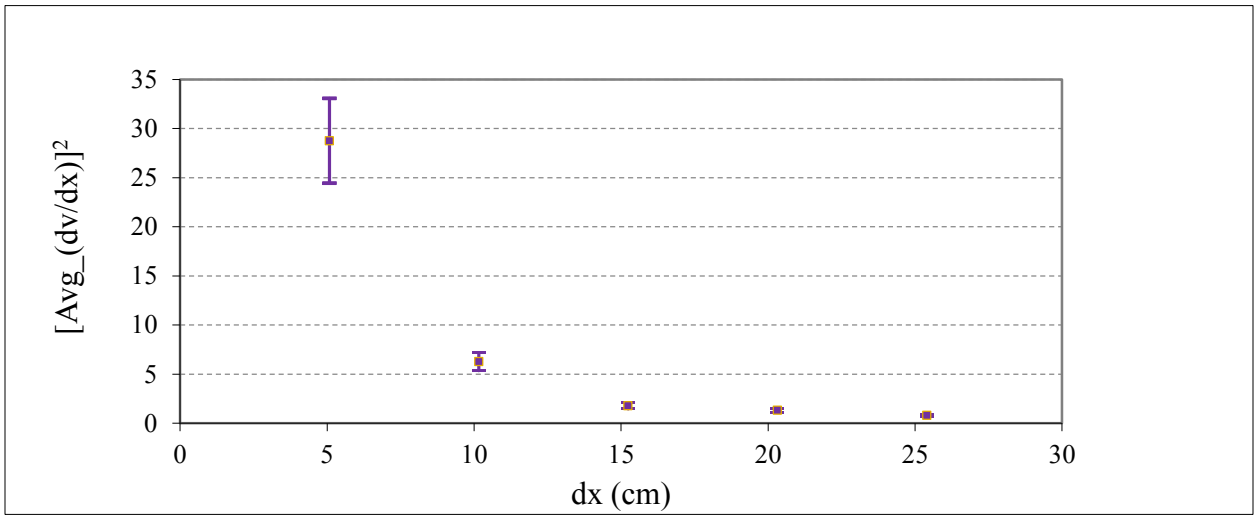

Figure 5.41 – Evaluating the square of the spatial speed derivative in the east back side of the cabin

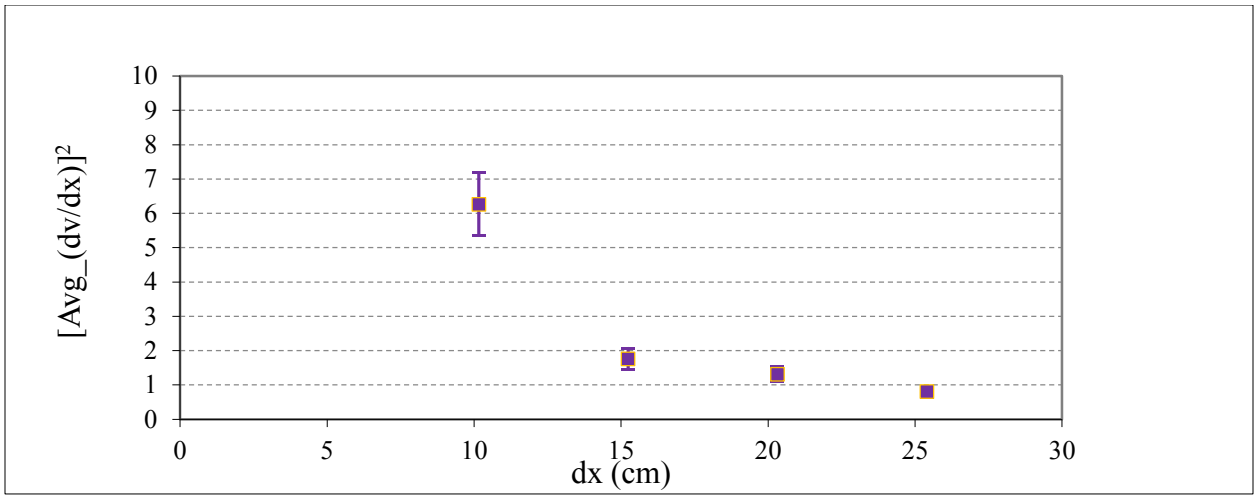

Figure 5.42 – Similar results to Figure 5.41 but with zoomed scale on y-axis

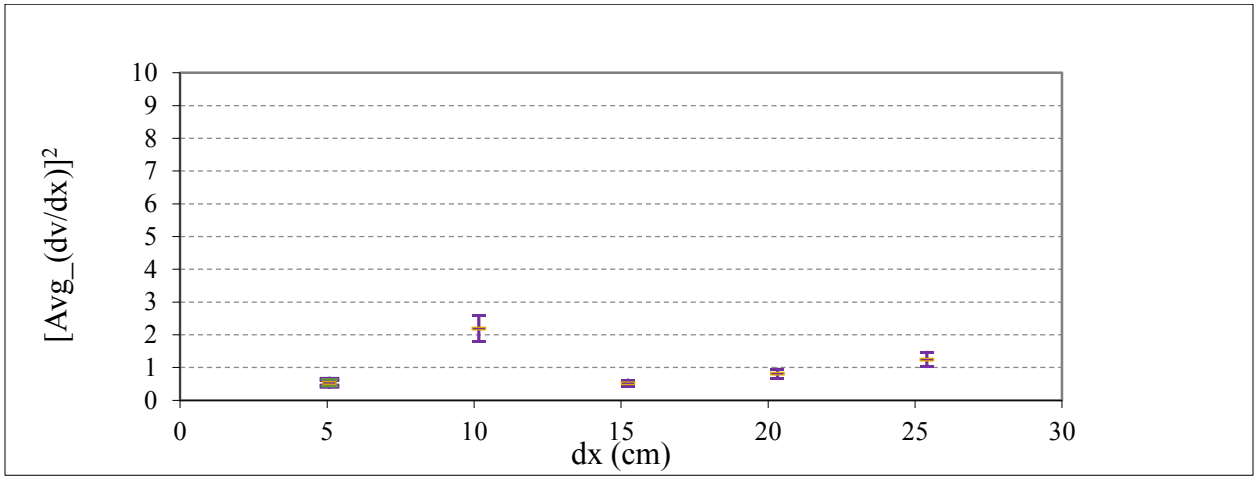

Figure 5.43 - Evaluating the square of the spatial speed derivative in seat 5D

Comparing this result to the 300 mm that was concluded previously, 127 mm was used as a separating distance between two consecutive probes. Comparing this value to the integral length scale (L_o=2.1 m) and to the Kolmogorov micro-length scale ($\eta_K \sim 1.05\ mm$), 127 mm is a good estimate to satisfy Taylor's length scale ($\lambda = 127$ mm).

$$\eta_K << \lambda << \text{Lo}$$

5.2.4.2.2 Taylors' local viscous dissipation rate results

Thus, the arrangement of the 3 speed probes, with a separation distance of $\lambda = 127$ mm between two consecutive probes, was used in 33-seats inside the cabin to evaluate the local dissipation rate in the east, west, and centerline seats. The results are shown in Figure 5.44.

The east side had higher dissipation rates in the back section of the cabin than in the centerline and west side seats. On the other side, the centerline seats had comparatively higher dissipation rates in the front section followed by the west then the east side seats. These two observations agreed with the concept that section s with low TKE levels are associated with high dissipation rates. This effect was reflected in the mid- section of the cabin, as well, with some exceptions. These exceptions might be due to the mixing effect caused by the coherent transverse circulations as shown in Figure 2.2.

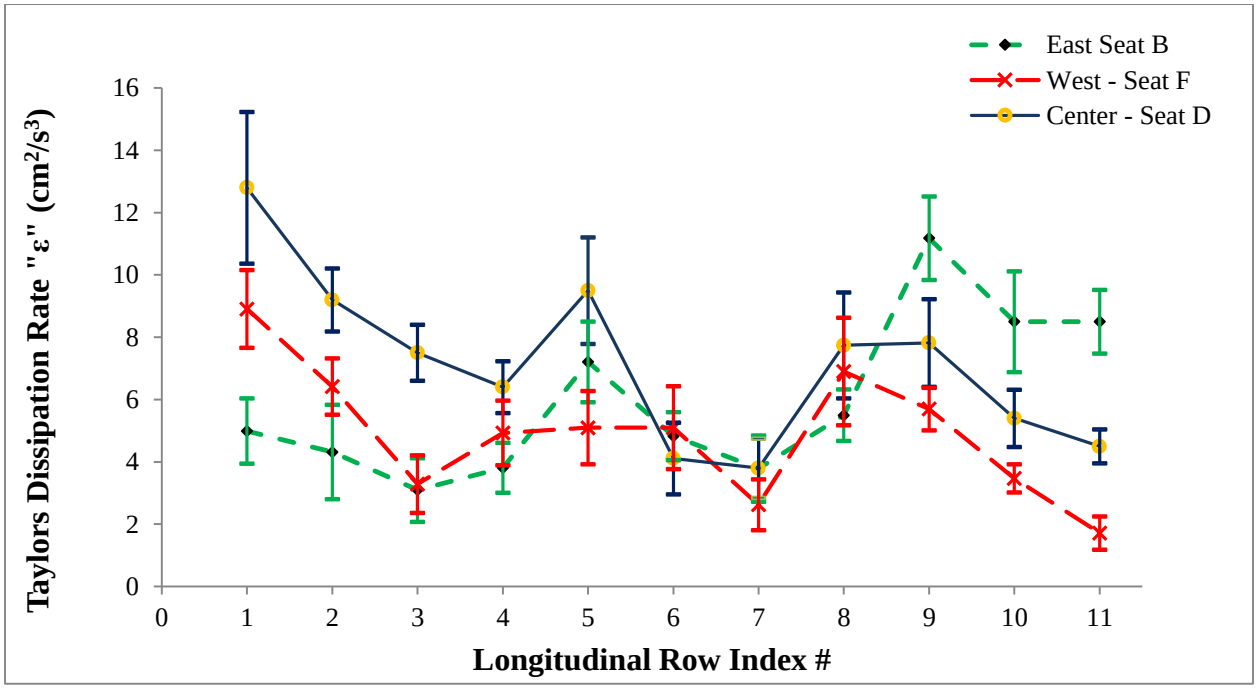

Figure 5.44 – Taylor's viscous dissipation rates inside the cabin (heated manikins)

5.2.4.3 Comparing the macro and micro scale dissipation rates

Although each of the two approaches used to evaluate the dissipation rate dealt with different parameters, but it was interesting to check on the order of magnitude between the macro- and micro- scale dissipation rates. Figure 5.45, Figure 5.46, and Figure 5.47 show comparisons between the k-ε and Taylors' dissipation rates in the east, center, and west sides of the cabin, respectively. It was clear that the large scale dissipation rates were much smaller than the local-viscous dissipation rate with approximately 1-order of magnitude. Lin et al. (2005) showed that the actual TKE measured experimentally and by LES inside a B767-300 aircraft was approximately eight times larger than the predicted values when using the standard k-ε model. So it would be expected that the actual dissipation rates would be larger than what was estimated by the k-ε model in equation (5.10).

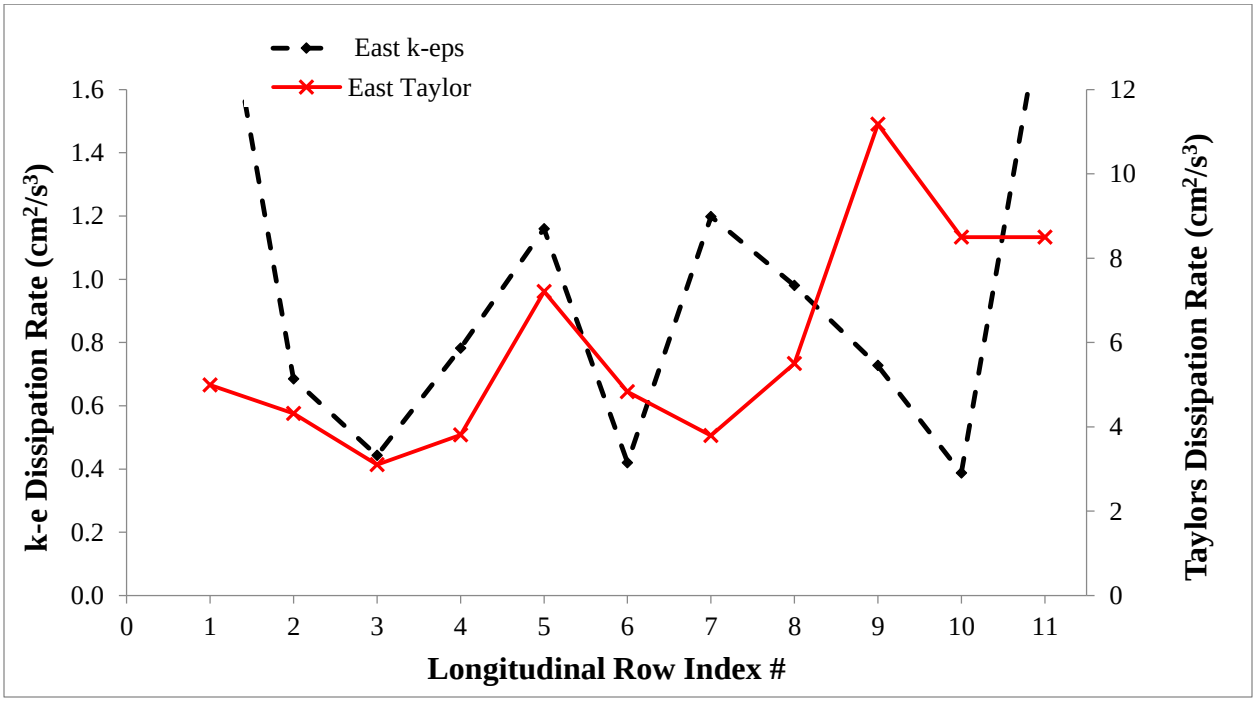

Figure 5.45 - Comparison between k-ε and Taylors dissipation rates in the east side seats (k-ε on left y-axis and Taylors on the right side y-axis) (heated manikins)

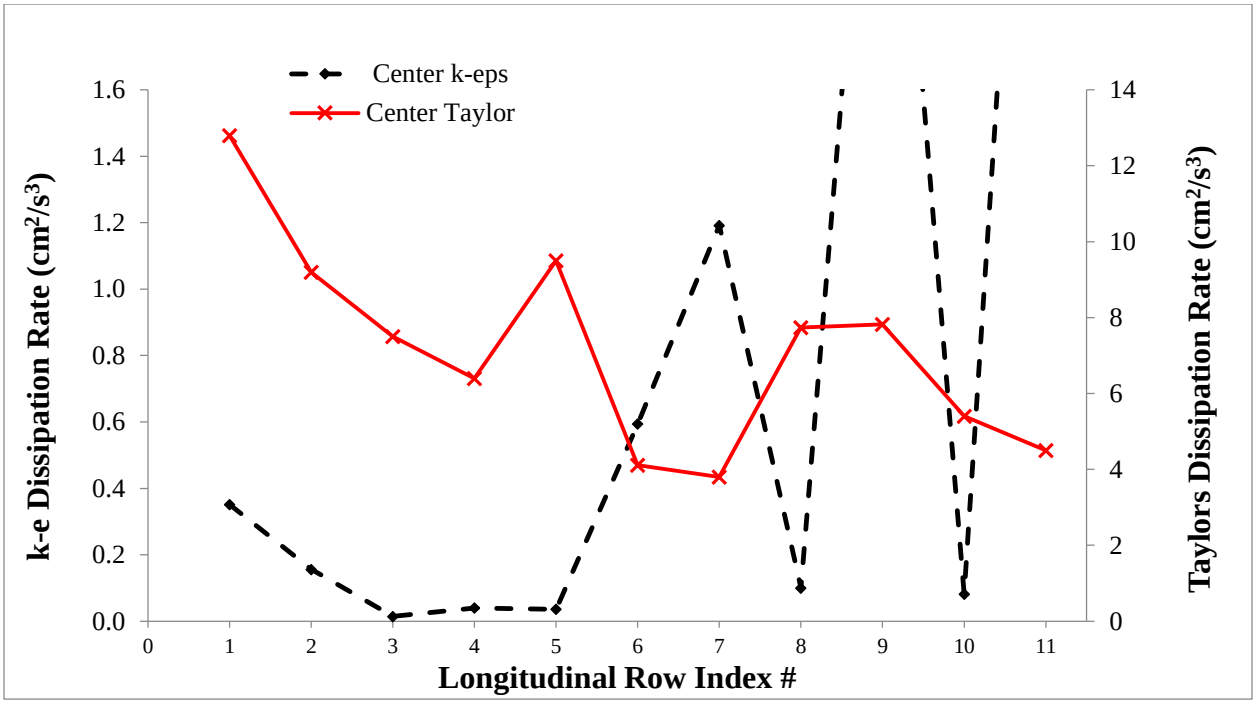

Figure 5.46 - Comparison between k-ε and Taylors dissipation rates in the centerline seats (heated manikins)

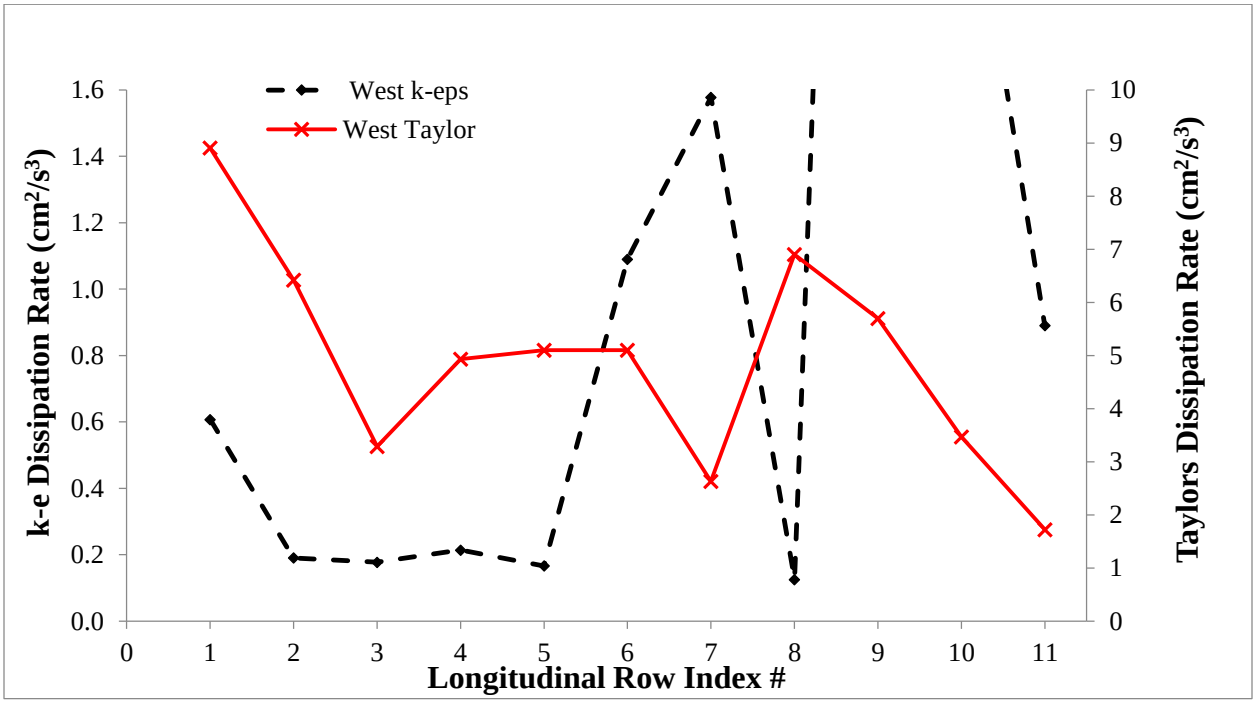

Figure 5.47 - Comparison between k-ε and Taylors dissipation rates in the west side seats (heated manikins)

5.2.5 Effect of thermal plumes on airflow speed and turbulence parameters inside the mockup cabin

The speed inside the mockup cabin with unheated manikins is reported with 95% C.I. margins in Figure 5.48. With heated manikins, as shown in Figure 5.24, the east side experienced higher speeds in the mid-section of the cabin compared to the west and centerline seats, whereas the west side experienced higher speeds in the back section of the cabin. With unheated manikins, these observations were changed with the east side having higher speeds in the front and back sections of the cabin, except near the cabin front wall. Another observation was that the mid-section of the cabin had almost the same speeds in the east, center, and west seats of row 5 to around row 8 beyond which the east side speeds dominated and the centerline seats speeds dropped down.

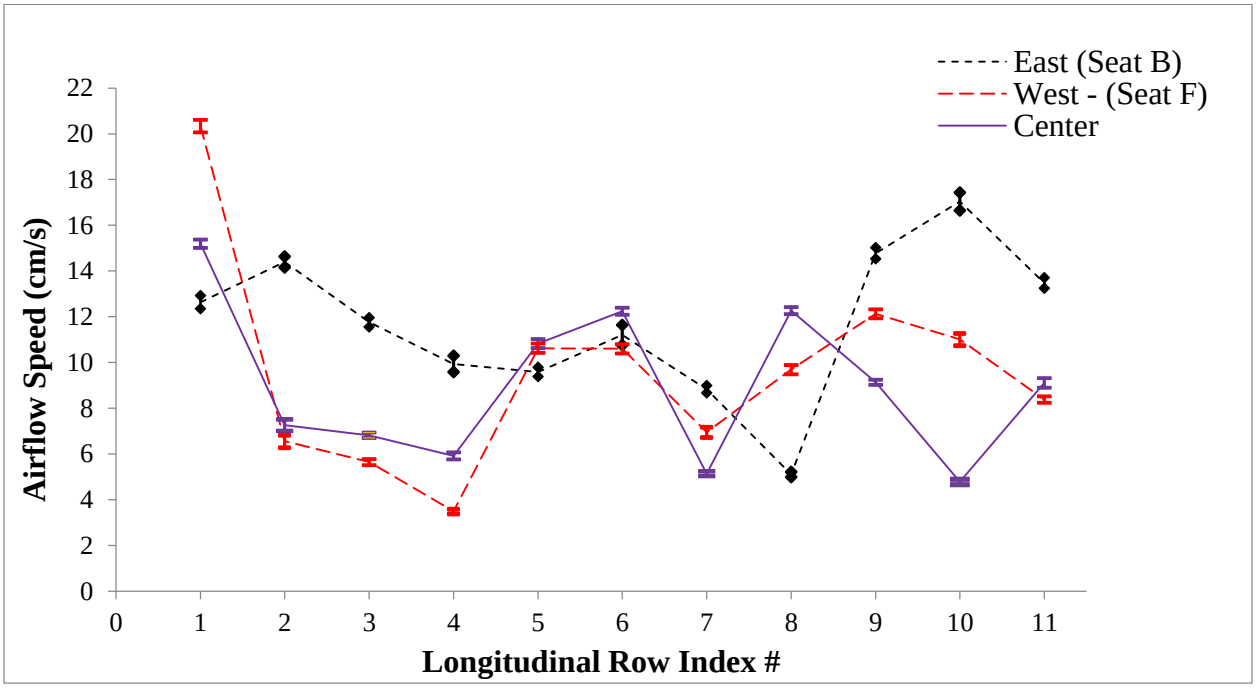

Figure 5.48 - Average airflow speed with 95% C.I. margins (unheated manikins)

In most seats, the heated case showed higher average speeds than with unheated manikins as shown in Figure 5.49, Figure 5.50, and Figure 5.51. However, the statistical speed margins showed that the values were of equal magnitude under both conditions heated and unheated manikins. Table 5.4 shows the averages for the measured speed over the 11-row in each side of the cabin. The third and fifth columns are the total errors that included the random and bias uncertainties. The speed fluctuation amplitudes were decayed with unheated manikins in most of the seats. Selected comparisons are shown in Figure 5.52 through Figure 5.56 with all plots showing higher amplitudes with heated manikins except in Figure 5.56 (seat 6B). The drop in the fluctuating speeds with unheated manikins was reflected on the TKE behavior shown in Figure 5.57 to Figure 5.59. Figure 5.60 and Figure 5.62 showed that the TI is proportional to heat. With unheated manikins, the values were decreased.

Table 5.4 - Average speed (cm/s) over the 11 rows in each side of the cabin with heated and unheated manikins

Side	Heated		Unheated	
	Average	Total Error	Average	Total Error
East	13	±2.6	12	±2.0
Center	11	±2.1	9	±2.1
West	13	±2.6	10	±2.7

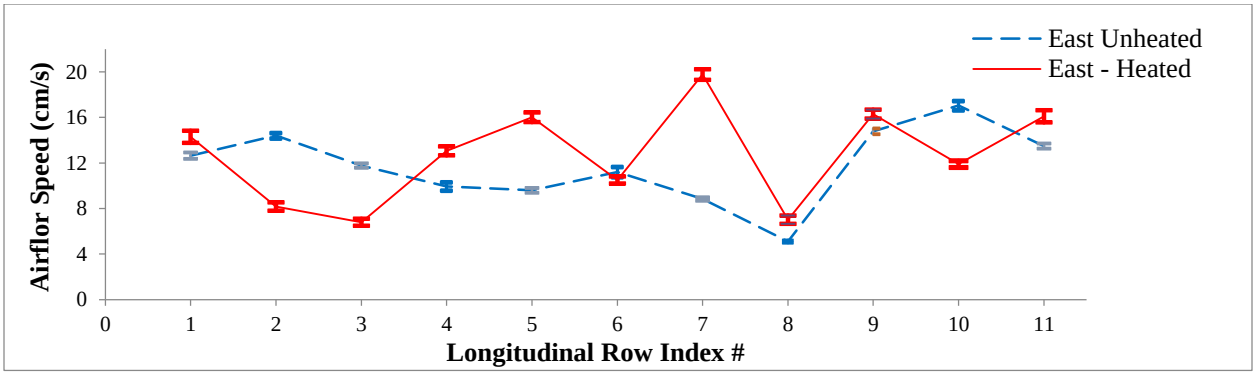

Figure 5.49 - Comparison of the east side speeds with heated and unheated manikins

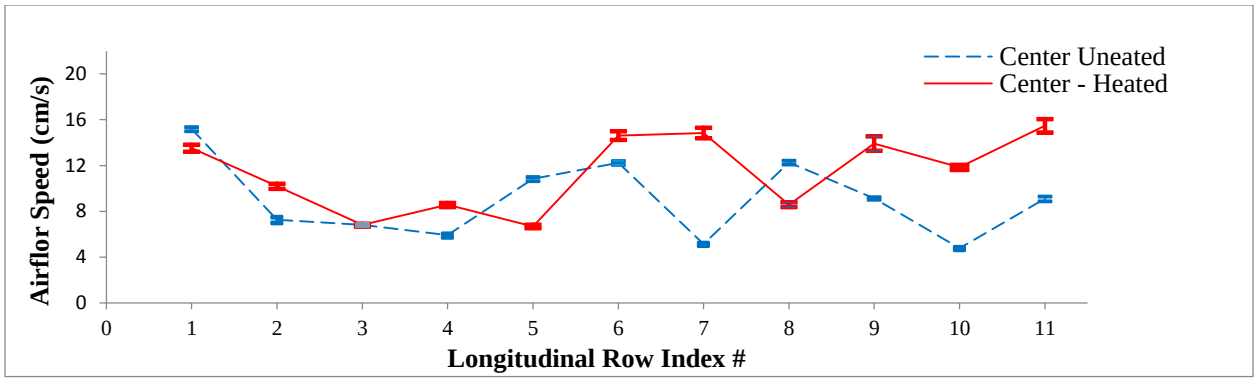

Figure 5.50 - Comparison of the centerline speed with heated and unheated manikins

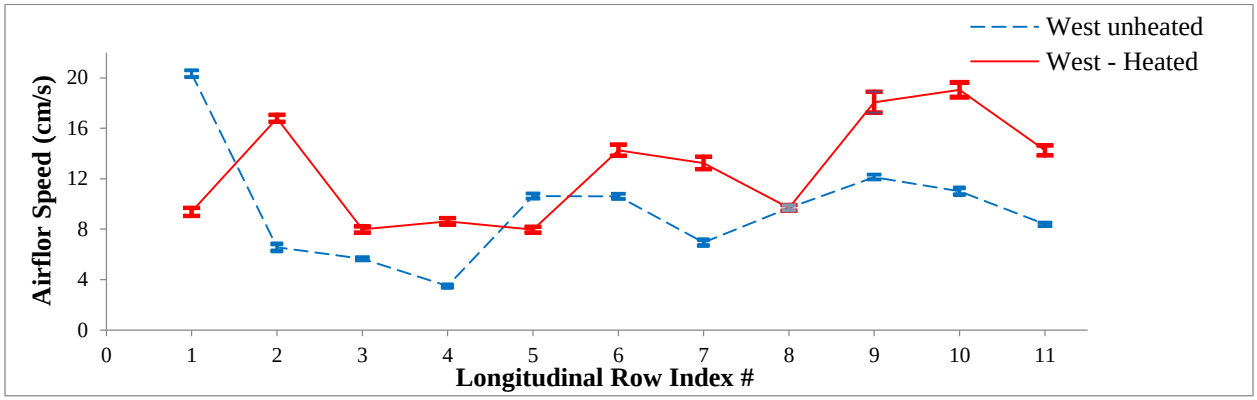

Figure 5.51 - Comparison of the west side speed with heated and unheated manikins

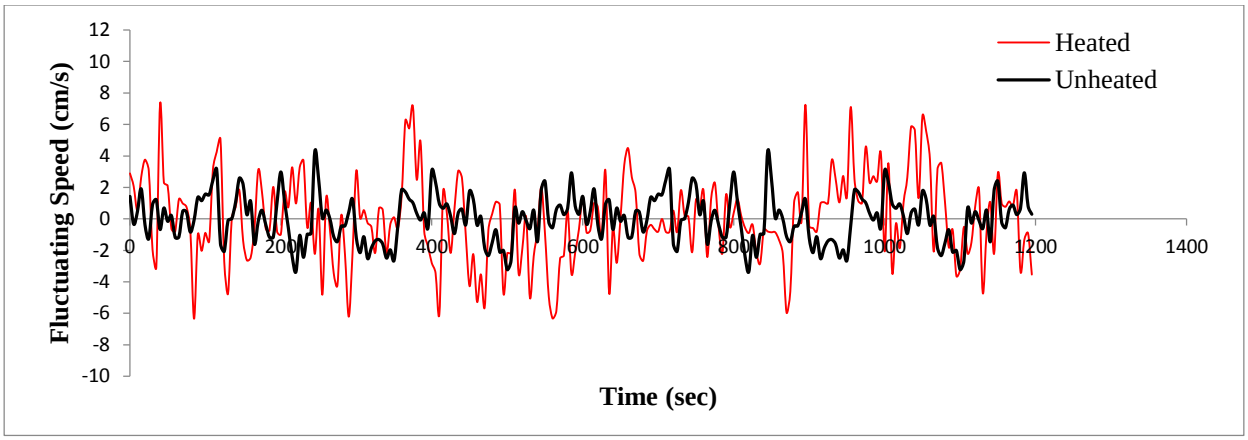

Figure 5.52 - Comparison of the fluctuating speed in seat 2B (east) with heated and unheated manikins

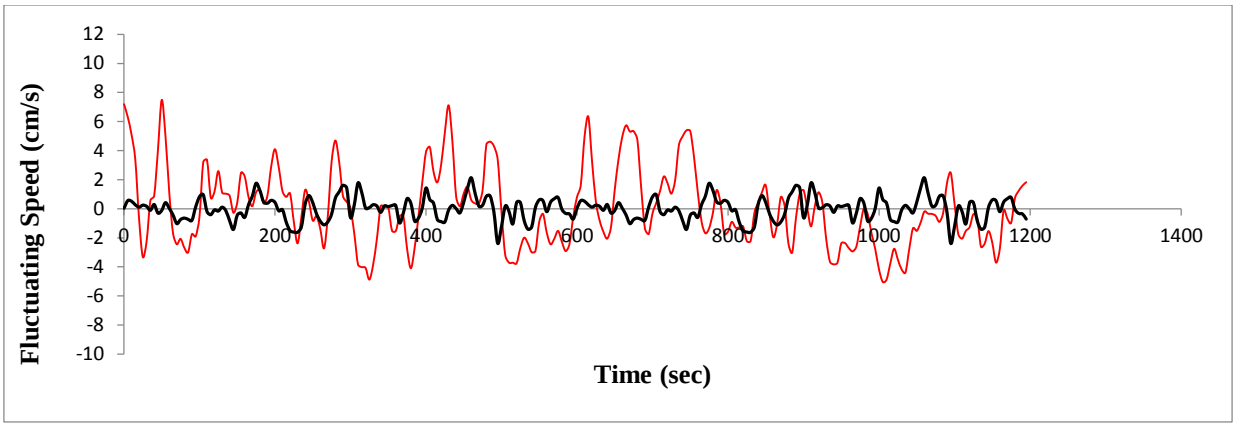

Figure 5.53 – Comparison of the fluctuating speed in seat 6D (centerline) with heated and unheated manikins

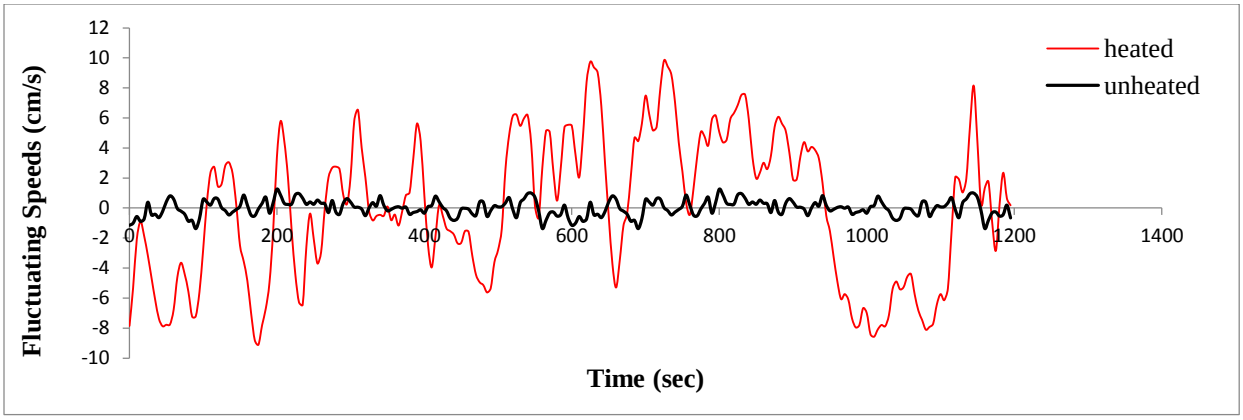

Figure 5.54 - Comparison of the fluctuating speed in seat 9D (centerline) with heated and unheated manikins

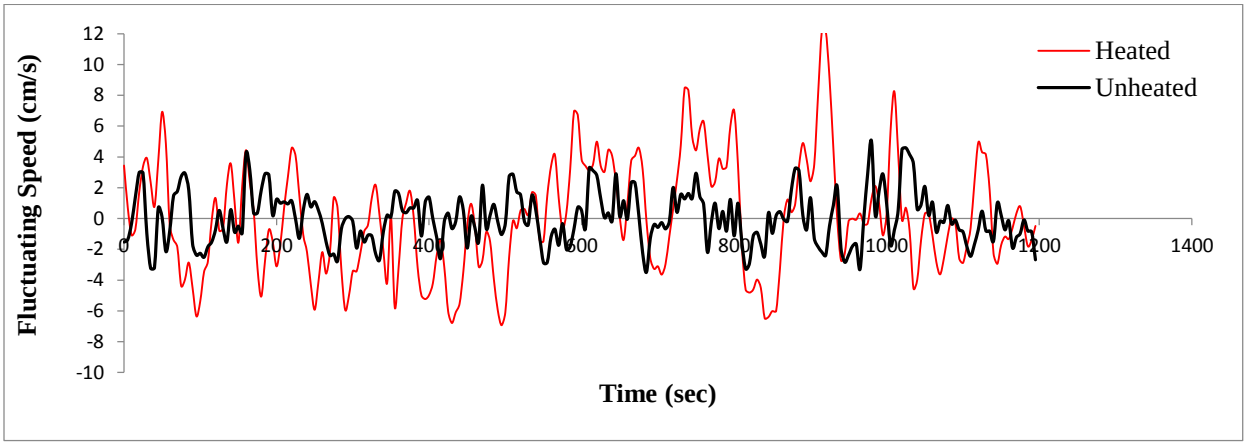

Figure 5.55 - Comparison of the fluctuating speed in seat 7W (west) with heated and unheated manikins

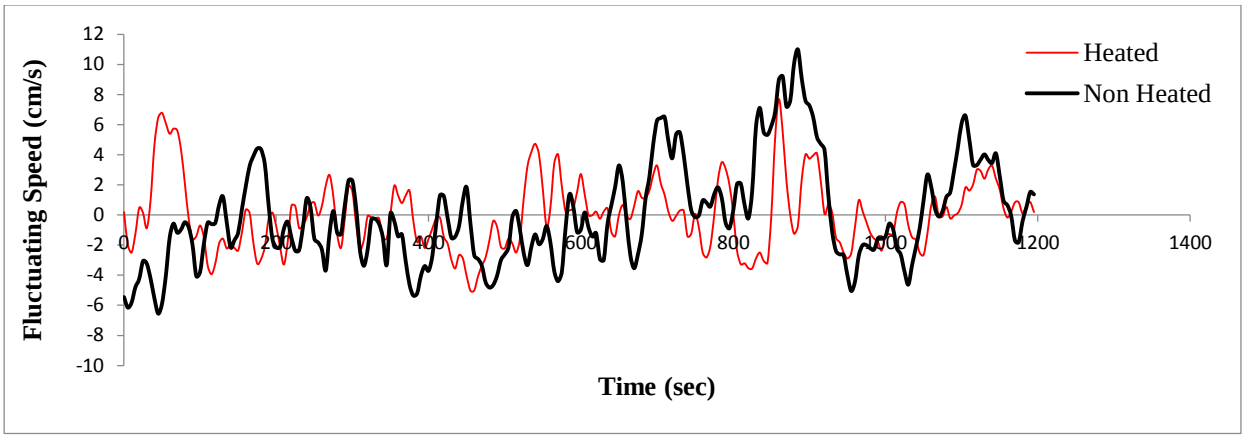

Figure 5.56 - Comparison of the fluctuating speed in seat 6B (east) with heated and unheated manikins

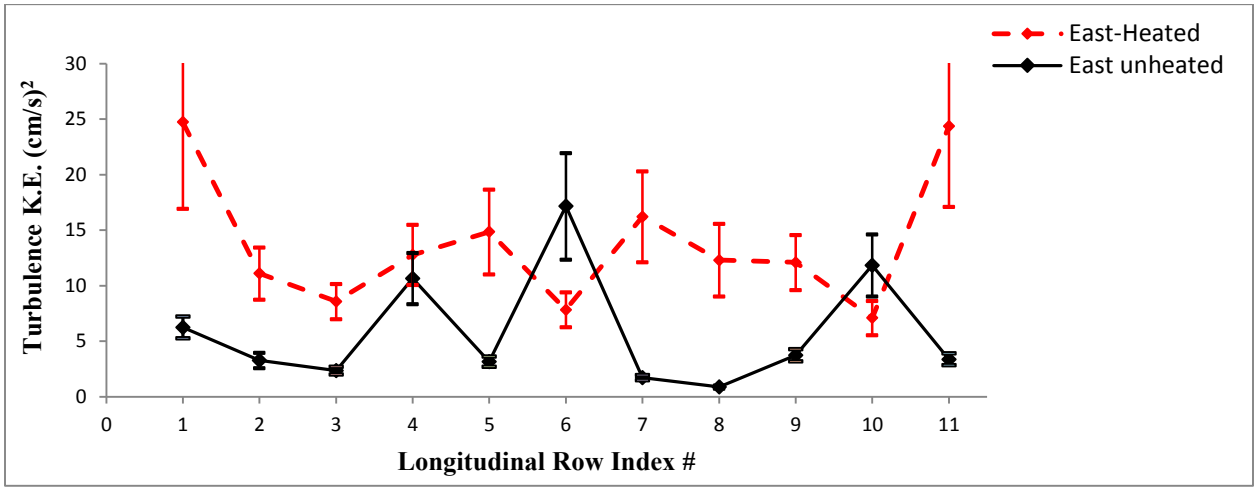

Figure 5.57 - Comparison of the east side TKE with heated and unheated manikins

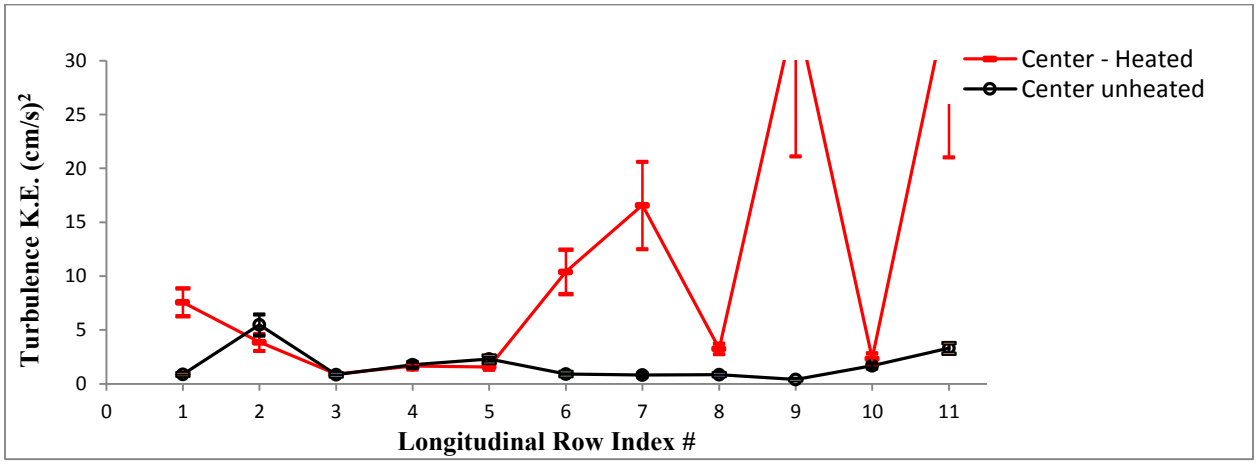

Figure 5.58 - Comparison of the centerline TKE with heated and unheated manikins

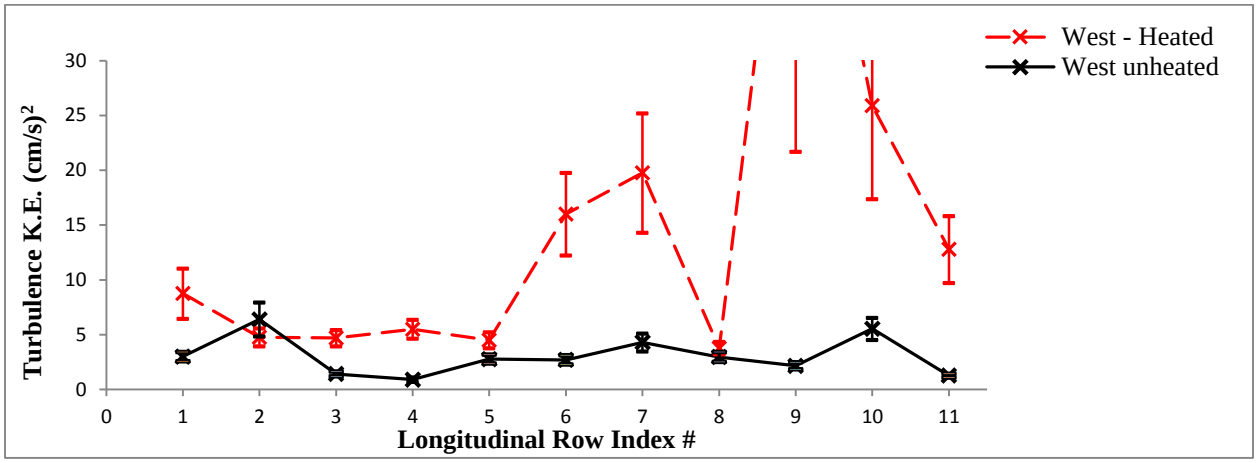

Figure 5.59 - Comparison of the west side TKE with heated and unheated manikins

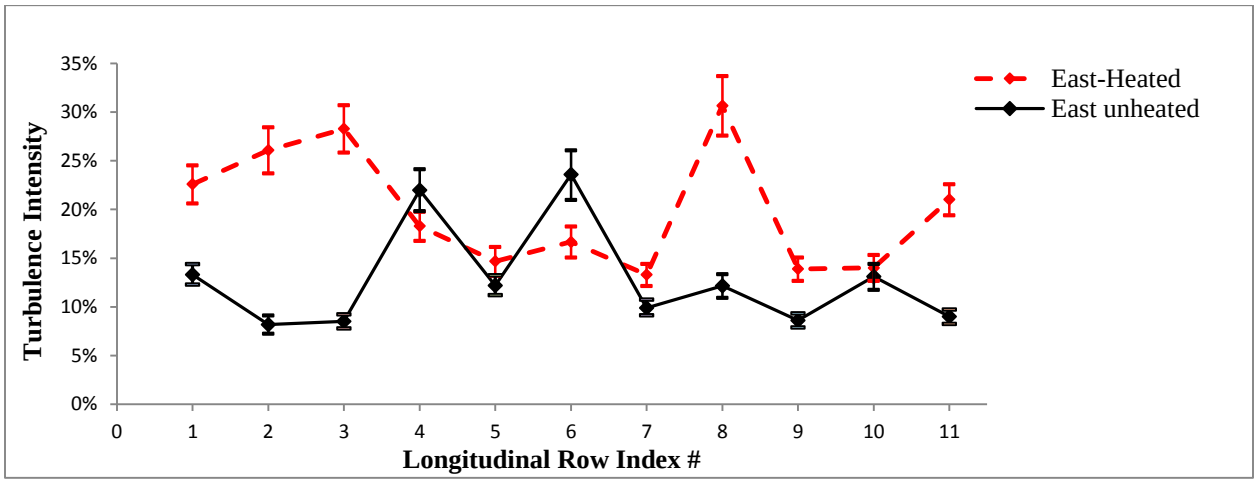

Figure 5.60 - Comparison of the east side TI with heated and unheated manikins

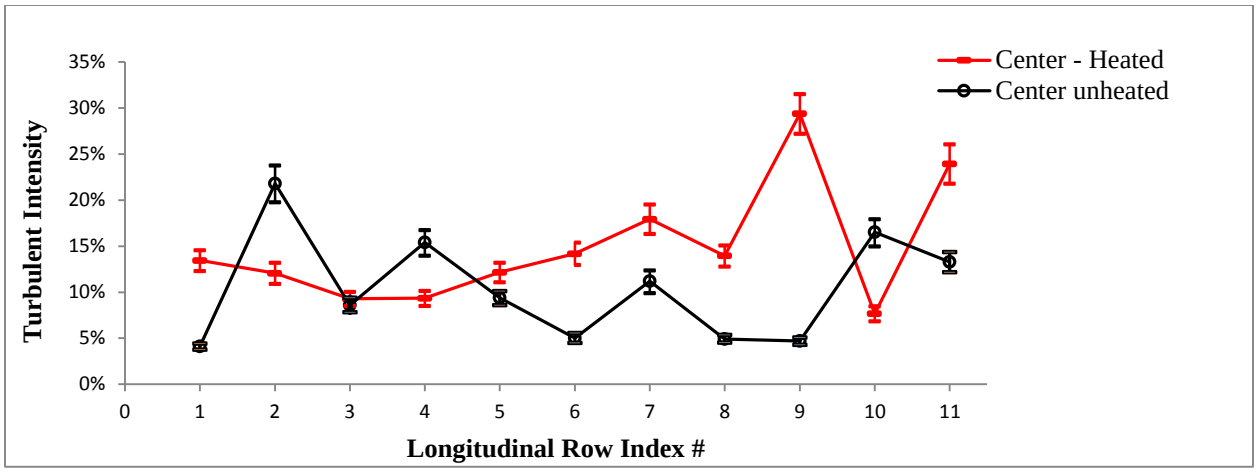

Figure 5.61 - Comparison of the centerline TI with heated and unheated manikins

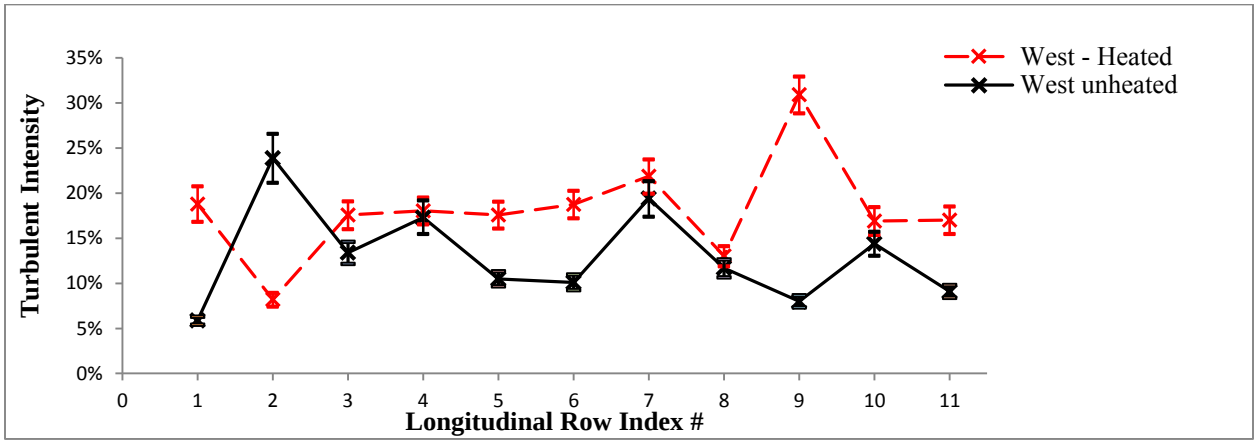

Figure 5.62 - Comparison of the west side TI with heated and unheated manikins

The relative change between heated and unheated results in TKE and TI were evaluated using

$$RELATIVE\_CHANGE = \frac{HEATED - UNHEATED}{HEATED} \tag{5.20}$$

The relative change in TKE and TI were plotted in Figure 5.63 and Figure 5.64, respectively. A negative value means that the unheated results were higher than the heated ones. Analyzing both figures, it was found that there were 6 points less than zero in each case. In the TKE plot in Figure 5.63, there were two negative peaks in row 6 and row 10 in the east side (6B and 10B).

However, from Figure 5.57 it was noted that the TKE in seat 10B was statistically close in both cases, which would leave one seat only having higher turbulence energy levels with unheated manikins. Although the effect of generated heat was obvious on the turbulence intensity from Figure 5.64 that had 6 negative values only, but, in-general, the turbulence intensity in the east and west sides of the cabin were less sensitive to heat than the turbulence kinetic energies were. This could be seen in Figure 5.60 through Figure 5.62 or by comparing Figure 5.63 to Figure 5.64 where 58% of the points in TKE relative change charts were spread between 0.5-1, whereas for TI it was mostly between 0-0.5 relative values.

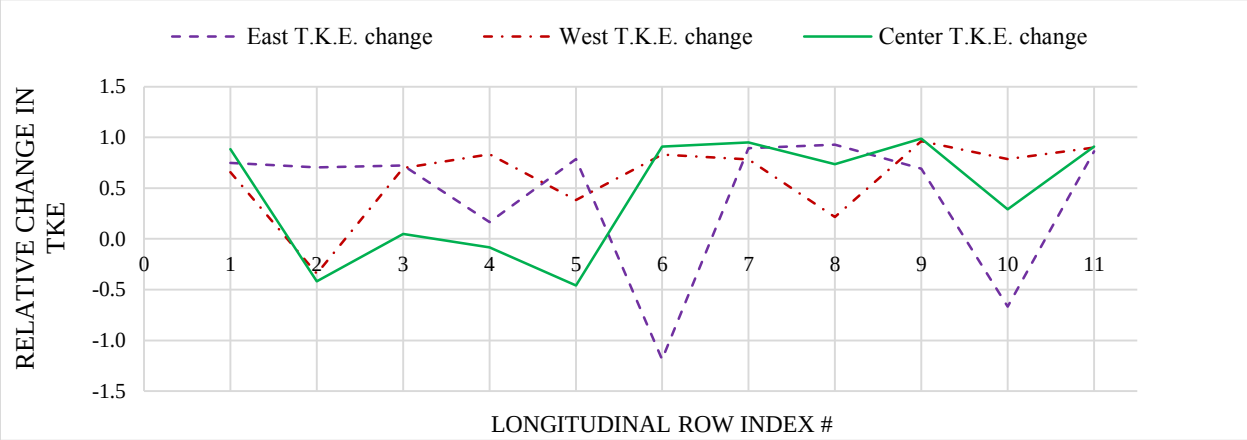

Figure 5.63 - Relative change in TKE between heated and unheated manikins

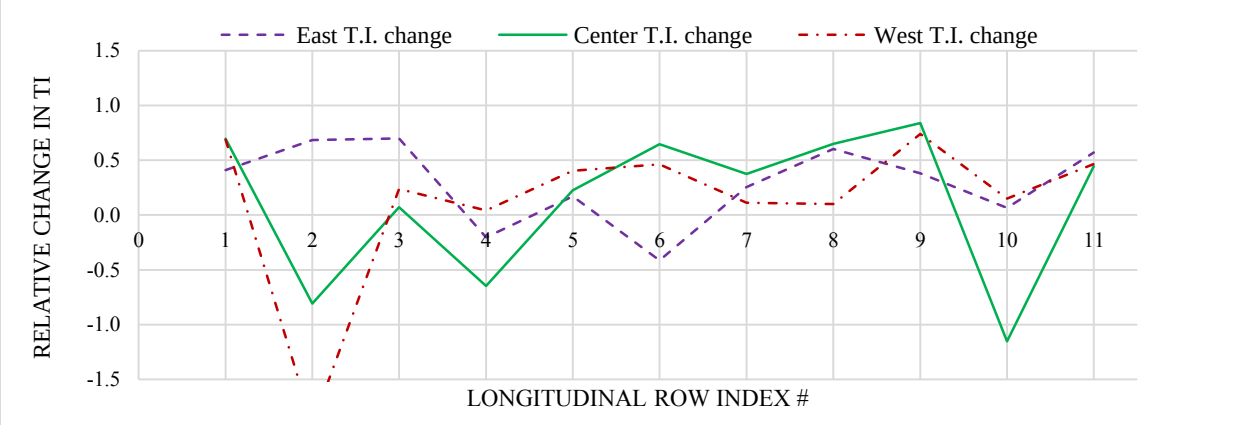

Figure 5.64 - Relative change in TI between heated and unheated manikins

Finally, the last part in investigating the effect of heat generated by the thermal manikins was to look into changes in the behavior of the turbulence dissipation rates. The k-**ε** dissipation rates with unheated manikins are shown in Figure 5.65 while those obtained by using Taylors' viscous model are shown in Figure 5.66. The relative change in the dissipation rates with unheated manikins over heated cases when using the k- ε model and when using Taylor's viscous model are shown in Figure 5.67 and Figure 5.68, respectively. Positive values would favor heated results over unheated ones. As can be seen from Figure 5.65 and Figure 5.67 the large scale dissipation rates, estimated by using the k-ε model, were reduced considerably with unheated environment. However, Taylors' viscous dissipation that evaluates the local dissipation rate did not show a drop in the dissipation rate values across the cabin, but it showed some changes as shown in Figure 5.66. Figure 5.68 shows that for Taylors model there were 40% of the 33 measurements between -0.25 and 0.25, 39% were above 0.25, and 21% were below -0.25. Thus, the relative change between heated and unheated when using Taylors' viscous form was scattered. It did not favor any environment over the other, but it showed some changes especially in the front section of the cabin where the centerline seats showed a drop in its values compared to the west and east side.

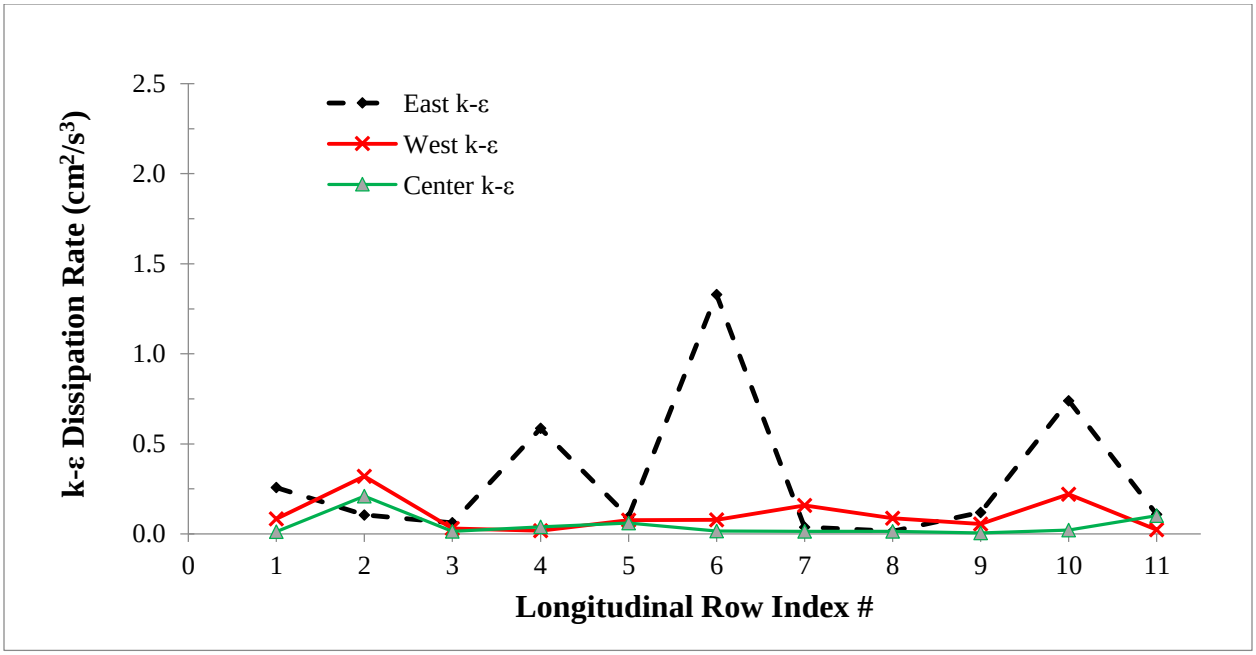

Figure 5.65 - k- ε dissipation rate with unheated manikins

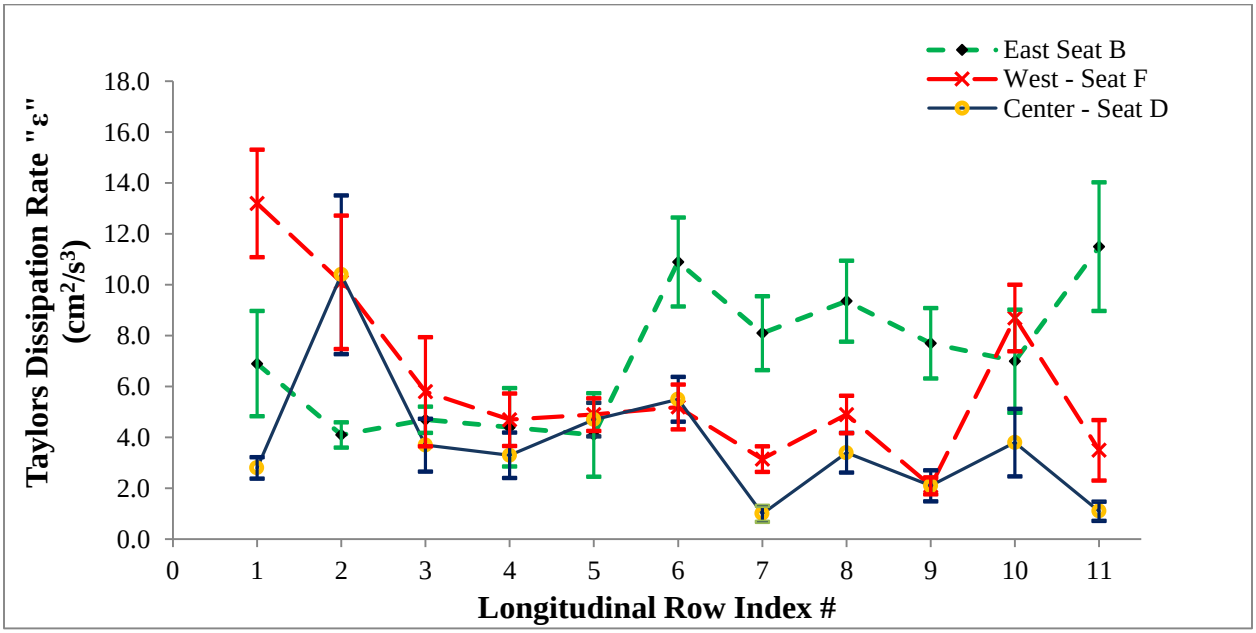

Figure 5.66 - Taylors' dissipation rates with unheated manikins

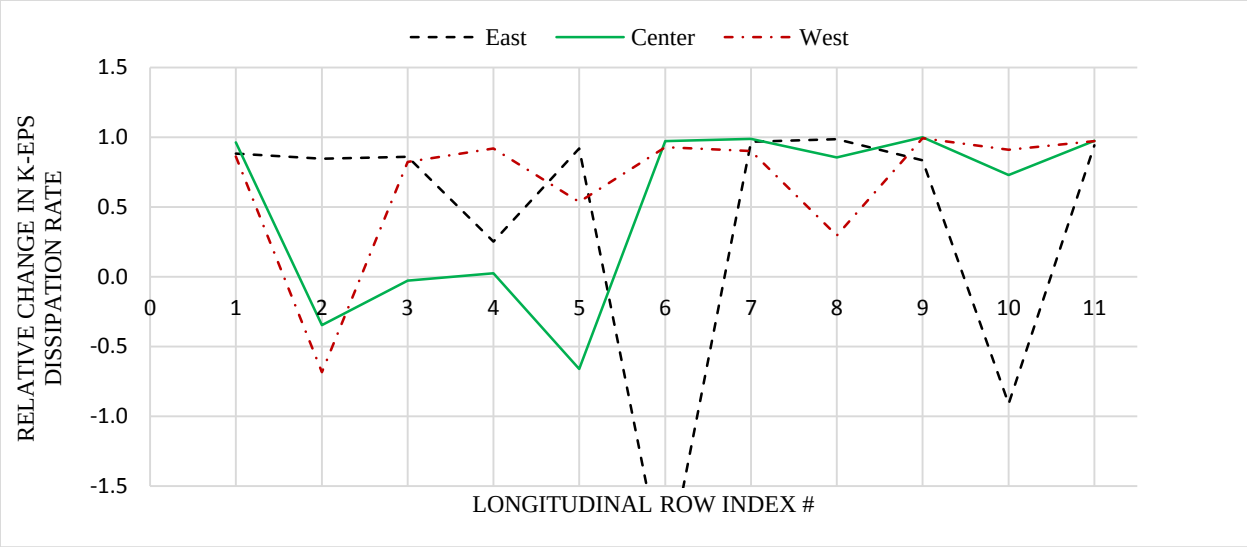

Figure 5.67 - Relative change in the k- ε model dissipation rate between heated and unheated case using equation (5.20)

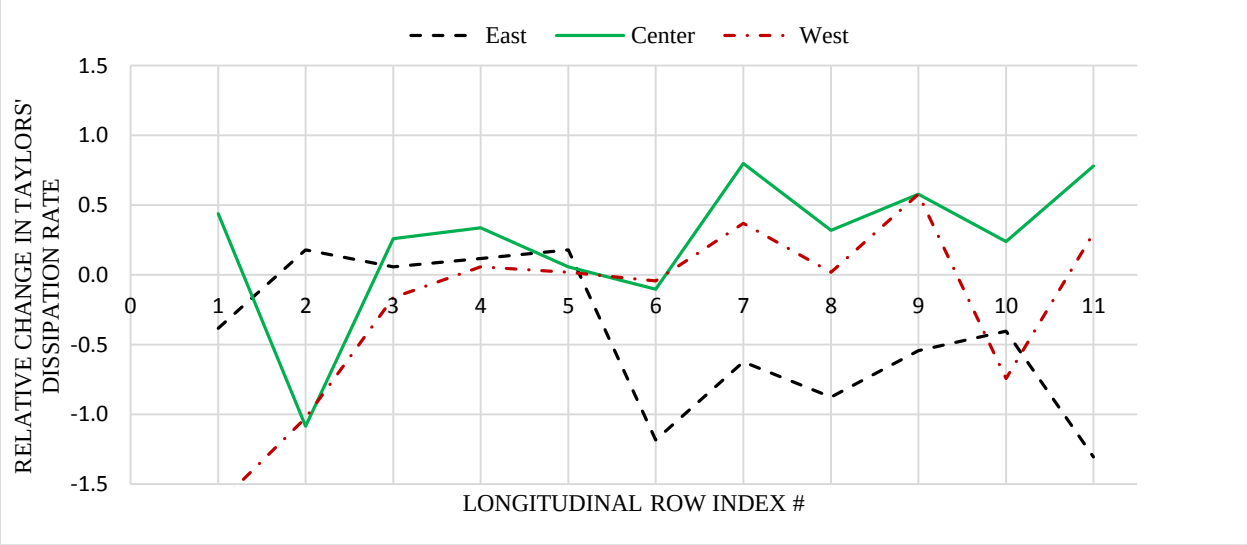

Figure 5.68 - Relative change in Taylors' dissipation rate between heated and unheated cases using equation (5.20)

5.3 Uncertainty analysis

This section deals with the uncertainty analysis of the measurements taken during the tracer gas tests and speed measurements. It also presents the uncertainty estimates for the parameters used for evaluation of the turbulence levels.. Uncertainty analyses necessarily involve assumptions related to measurement uncertainties associated with equipment items used, the type of the uncertainties (bias vs. precision), and propagation of elemental uncertainties into an experimental result. Two key assumptions used for these analyses are:

1) Random errors are assumed to be normally distributed.
2) Errors for individual measurements are independent of each other. So, for example, when computing the normalized concentration of tracer gas measurements, it is assumed that the errors in the gas injection system, the flow controller, and the gas analyzers are independent of each other. Thus, the uncertainties are uncorrelated, i.e., only uncorrelated measurement uncertainties were considered.

With the above two assumptions, the estimates for uncertainties of individual measurements can be combined to obtain an estimate for the overall uncertainty of aggregated measures such as normalized tracer gas concentrations. However, estimates of the uncertainties of individual measurements can also be challenging because measurement equipment manufacturers typically provide estimates for uncertainties of their instruments, but of course, the unit performance may deviate from the rated accuracy due to environmental factors, electric power fluctuations, poor installation, or improper usage. Consequently, these factors may further compromise the accuracy of measurement equipment used. On the other hand, it is easy to grossly overestimate the uncertainty by choosing the worst-case values for each individual measurement.

Confidence intervals used herein are based on the 95% level which increased the errors by approximately 2 times depending on the number of samples or repeated measurements. In most cases, the number of samples were more than 120, thus, a value of ±1.96 was used. If the number of samples was less than 120, then values provided in Ott and Longnecker (2004) were used.

The following nomenclatures and terminologies were used in this section:

$< i >$: average value of i

σ : standard deviation

$t_{95\%}$: 95% confidence interval coefficient

N : number of samples or number of measurements

Another concept used for evaluating the uncertainty of experimental results calculated from correlations containing independent variables was the propagation of elemental error into the result. Coleman and Steele (1999) used equation (5.21) to evaluate the absolute uncertainty for results determined from a group of independent measured variables. This equation determines the effects of errors in each variable on the total uncertainty of the result. If the result is defined as $f = fn\ (x_1, x_2, \ldots x_j)$, Coleman and Steele (1999) indicated that the total uncertainty of the result would be in the form

$$U_f{}^2 = \sum_{i=1}^{j} \left(\frac{\partial f}{\partial x_i}\right)^2 . \left(U_{x_i}\right)^2 \tag{5.21}$$

where j is the number of independent variables. Thus, the total relative uncertainty would be

$$u_f{}^2 = \frac{U_f{}^2}{f^2} = \sum_{i=1}^{j} \left(\frac{\partial f}{\partial x_i}\right)^2 . \left(\frac{U_{x_i}}{x_i}\right)^2 . \left(\frac{x_i}{f}\right)^2 \tag{5.22}$$

and consequently,

$$u_f{}^2 = \sum_{i=1}^{j} \left(\frac{x_i}{f}\frac{\partial f}{\partial x_i}\right)^2 . \left(u_{x_i}\right)^2 \quad (5.23)$$

The parameter $\left(\frac{x_i}{f}\frac{\partial f}{\partial x_i}\right)$ can be defined as *uncertainty magnification factor* (UMF) that compensates the effect of the uncertainty in a given variable over the uncertainty of the total result. The sign of the UMF for variables is of no significance since they are squared.

5.3.1 CO_2 analyzers uncertainties

Three analyzers were used during the tracer gas tests. Two were from PP-systems, model WMA-4 and were used to sample CO_2 in the cabin and at the exit port while the other one was custom made using Edinburgh Instrument gas sampling cards as described in section 3.1.4.2.1. PP-systems analyzers have ±1% uncertainty, whereas the Edinburg unit has ±2% as shown in Table 3.1. However, some other factors should be included with the uncertainty of each unit to have a total uncertainty that accounts for any changes during calibration, deviation over time, repeatability, etc. The factors that were included are the linearity deviation, calibration gas uncertainty, repeatability, and Data Acquisition (DAQ) System uncertainty.

- *Calibration Gas Uncertainty*

  The standard calibration gas had different uncertainties that were identified by the supplier and classified according to the gas purity. The 500 ppm standard CO_2 gas has ±2% uncertainty, whereas both the 1000 ppm and 2000 ppm have ±1%.

  So the total uncertainty for the calibration gas based on the RMS of the above uncertainties would be

$$u_{Gas,cal} = \sqrt{u_{500}{}^2 + u_{1000}{}^2 + u_{2000}{}^2} = \pm 2.45\% \quad (5.24)$$

- *DAQ Uncertainty*

The data acquisition system unit was an Agilent DAQ type. These units have different uncertainties according to the voltage range as shown in Table 5.5.

Table 5.5 - DAQ Agilent uncertainties

Volt Range	Uncertainty of the reading	Uncertainty of the voltage range
10 Volts	0.0035%	0.0005%
1 Volt	0.0040%	0.0007%

- *Linearity Uncertainty*

The linearity uncertainty determines the error in each unit from calibration to calibration. Table 5.6 shows the deviation in the linearity for each unit. It was based on R^2-coefficient of each calibration curve that gives an indication of how well the regression line approximates the real data points. The linearity was calculated using equation (5.25)

$$u_{linearity} = \frac{\pm t_{95\%}.\sigma_{R^2}}{\sqrt{N-1}.\langle R^2 \rangle} \quad (5.25)$$

- *Repeatability Uncertainty*

The repeatability for each analyzer was calculated based on the repeatability of the readings when calibrating with different standard CO_2 gases (500 ppm, 1000 ppm, and 2000 ppm). The repeatability of the unit when using each gas was evaluated using equation (5.26) and the total repeatability of the analyzers was evaluated using the repeatability with each gas as shown in equation (5.27).

$$u_{repeatability,std\_gas} = \pm t_{95\%}.\sigma_{Readings}.\sqrt{N} \quad (5.26)$$

$$u_{repeatability,analyzer} = \sqrt{\left(Repeatability_{500\ ppm}\right)^2 + \left(Repeatability_{1{,}000\ ppm}\right)^2 + \left(Repeatability_{2{,}000\ ppm}\right)^2} \quad (5.27)$$

Table 5.6 - Repeatability and linearity uncertainties for CO_2 analyzers

	R^2		
	Cabin	**Exit**	**Inlet**
	0.999951	0.999861	0.999845
	0.9999	0.99996	0.99996
	0.993244	0.99324	0.999976
Average "R^2"	**0.997698**	**0.997687**	**0.999927**
Average Linearity Rel. Uncertainty	**0.219%**	**0.219%**	**0.005%**
Repeatability Rel. Uncertainty	**0.09%**	**0.23%**	**1.44%**

The repeatability of each unit agreed with the specification given in Table 3.1. PP-system WMA-4 units, used inside the cabin and at the exit port, had repeatability less than 1% and the Edinburg unit (inlet port) had 1.44% repeatability which was less than 1.5%.

The analyzers' relative uncertainty was evaluated using equation (5.28) that accommodates for all of the above factors. The relative uncertainty for each analyzer is summarized in Table 5.7. For comparison reasons, two decimal digits are shown in the results, but in-general, the analyzers had almost the same relative uncertainty of approximately ±3%.

$$u_{Analyzer} = \sqrt{{u_{DAQ}}^2 + {u_{Gas,cal}}^2 + {u_{linearity}}^2 + {u_{repeatability}}^2} \quad (5.28)$$

Table 5.7 - Total uncertainty for each of the three CO_2 analyzers

Analyzer Location	Cabin	Exit	Inlet
Total Relative Uncertainty	2.46%	2.47%	2.84%

5.3.2 Injection system uncertainty

The flow exiting the mass flow controllers passed through flow meters before being mixed together as shown in Figure 3.15. After being mixed, the tracer gas was injected into the cabin through a 0.5 meter long copper tube having 25.4 mm (1 inch) inside diameter as shown in Figure 3.14. The speed of the gas injected into the cabin was checked using an omni-directional spherical probe as described in section 3.1.4.1.4. The average over 20 minutes was found to be approximately 53 cm/s with ±1.6% relative uncertainty (random and bias) as was shown in section 3.1.4.1.4.

The uncertainty of the injection system should take into account the uncertainty of the mass flow controllers, as well. The mass flow controllers have a ±1% relative uncertainty. Thus, the total uncertainty of the injection system was calculated using equation (5.29)

$$u_{injection,system} = \sqrt{u^2_{measurement} + u^2_{probe,bias} + u^2_{controllers}} \tag{5.29}$$

Therefore, the total relative uncertainty of the injection system was found to be ±1.9%. Since the injection tube diameter was fixed, its uncertainty was assumed negligible, thus, it can be concluded that the system provided a reasonable flow with a relative uncertainty of approximately ±2%.

5.3.3 Tracer gas results uncertainties

The normalized concentration was defined previously in equation (3.6) as

$$[CO_2]_{Normalized} = \frac{[CO_2]_{Cabin} - [CO_2]_{Inlet}}{[CO_2]_{Exit} - [CO_2]_{Inlet}}$$

Thus, to find the relative uncertainty of the normalized concentration, equation (5.23) was implemented for the above variables.

If we define $C_i=[CO_2]_i$, then

$$u_n{}^2 = \left[\frac{\bar{C}_{cabin}}{\bar{C}_n}\frac{\partial \bar{C}_n}{\partial \bar{C}_{cabin}}\right]^2 (u_{Cabin})^2 + \left[\frac{\bar{C}_{exit}}{\bar{C}_n}\frac{\partial \bar{C}_n}{\partial \bar{C}_{exit}}\right]^2 (u_{exit})^2 + \left[\frac{\bar{C}_{inlet}}{\bar{C}_n}\frac{\partial \bar{C}_n}{\partial \bar{C}_{inlet}}\right]^2 (u_{inlet})^2 \tag{5.30}$$

where $\bar{C}_i$ is the average of the concentration.

$$\frac{\partial \bar{C}_n}{\partial \bar{C}_{cabin}} = \frac{1}{(\bar{C}_{exit} - \bar{C}_{inlet})} \tag{5.31}$$

$$\frac{\partial \bar{C}_n}{\partial \bar{C}_{exit}} = \frac{-(\bar{C}_{cabin} - \bar{C}_{inlet})}{(\bar{C}_{exit} - \bar{C}_{inlet})^2} \tag{5.32}$$

$$\frac{\partial \bar{C}_n}{\partial \bar{C}_{inlet}} = \frac{-(\bar{C}_{exit} - \bar{C}_{inlet}) - [-(\bar{C}_{cabin} - \bar{C}_{inlet})]}{(\bar{C}_{exit} - \bar{C}_{inlet})^2} = \frac{\bar{C}_{cabin} - \bar{C}_{exit}}{(\bar{C}_{exit} - \bar{C}_{inlet})^2} \tag{5.33}$$

Combining (5.30), (5.31), (5.32), and (5.33)

$$u_n{}^2 = \left[\frac{\bar{C}_{cabin}}{\bar{C}_n}\frac{1}{(\bar{C}_{exit} - \bar{C}_{inlet})}\right]^2 (u_{Cabin})^2 + \left[\left(\frac{\bar{C}_{exit}}{\bar{C}_n}\right).\left(\frac{-(\bar{C}_{cabin} - \bar{C}_{inlet})}{(\bar{C}_{exit} - \bar{C}_{inlet})^2}\right)\right]^2 (u_{exit})^2 + \left[\left(\frac{\bar{C}_{inlet}}{\bar{C}_n}\right)\frac{(\bar{C}_{cabin} - \bar{C}_{exit})}{(\bar{C}_{exit} - \bar{C}_{inlet})^2}\right]^2 (u_{inlet})^2 \tag{5.34}$$

Thus,

$$u_n{}^2 = \left[\frac{\bar{C}_{cabin}}{\bar{C}_n(\bar{C}_{exit}-\bar{C}_{inlet})}u_{cabin}\right]^2 + \left[\frac{\bar{C}_{exit}(\bar{C}_{cabin}-\bar{C}_{inlet})}{\bar{C}_n(\bar{C}_{exit}-\bar{C}_{inlet})^2}u_{exit}\right]^2 + \left[\frac{\bar{C}_{inlet}(\bar{C}_{cabin}-\bar{C}_{exit})}{\bar{C}_n(\bar{C}_{exit}-\bar{C}_{inlet})^2}u_{inlet}\right]^2 \quad (5.35)$$

Equation (5.35) gives the propagation relative uncertainty in the normalized concentration due to the uncertainties in the variables included in equation (3.6). The random uncertainty about the true mean was evaluated using equation (5.36) and then added to the uncertainty obtained from equation (5.35). The addition was based on the RMS of the errors, as shown in equation (5.37), and yielded the total relative uncertainty of the tracer gas measurements.

$$u_{co2,random} = \frac{t_{95\%}.\sigma_n}{\sqrt{N-1}.\bar{C}_n} \quad (5.36)$$

$$u_{total,tracer\ gas} = \sqrt{(u_n)^2 + \left(u_{co2,random}\right)^2} \quad (5.37)$$

The detailed relative uncertainties for tracer gas results with both heated and unheated manikins are presented in Appendix E - (Part I and II). The minimum and maximum relative uncertainties for each tracer gas release location are summarized in Table 5.8 for heated and unheated manikins cases.

Table 5.8 – Total relative uncertainties for tracer gas measurements

	u-total (min-max)	
Release Location	**Heated**	**Unheated**
2D	1.3 - 5.2%	1.9 - 7.9%
5D	1.5 - 9.6%	2.2 - 8%
7D	1.2 - 7.9%	1.3 - 8.7%
10D	4 - 8.4%	2 - 8%
5B	2.7 - 35%	1.2 -10.5%
8B	1.5 - 13.3%	1.5 - 6.2%
4F	1.5 - 7.6%	1.6 - 8.6%
9F	1.5 - 12.8%	1.9 - 16.5%

The maximum relative uncertainty for tracer gas with heated manikins ranged between ±5-14%. However, it should be pointed out that when releasing the tracer gas in seat 5B and sampling in row 6, the relative uncertainty was approximately double the above values and ranged between ±30-35%. Further investigation for the average CO_2 concentrations sampled in row 6 showed that row 6 experienced lower exposures than other locations. With this low exposure, the potential to have high variations in the sampled concentrations is expected to be high and, thus, resulting in higher relative uncertainties. With unheated manikins, the relative uncertainties were of the same range as with heated and ranged between ±6-17%.

5.3.4 Speed measurements uncertainties

5.3.4.1 Omni-directional transducer accuracy

As mentioned earlier in section 3.1.4.1.4 and in Table 3.2, the TSI transducer has an accuracy of ±3% of the readings and ±1% of selected full range. However, these values represent upper bounds and would overestimate the bias uncertainty. A more reasonable value

for the bias uncertainty would be obtained by calculating the uncertainty of the probe and the data acquisition system used or in general the system which is used to record and store the data. Previous experience when calibrating similar probes and other transducers indicated that the total bias uncertainty was within the repeatability range of each probe. Therefore, a value of 1% of the average speed will be used as the nominal bias uncertainty.

5.3.4.2 Speed measurements uncertainties

To obtain the relative uncertainty, the bias uncertainty of the probe should be added to the random uncertainty of the measurements. The random and relative uncertainties are calculated as shown in equation (5.38) and equation (5.39), respectively.

$$u_{v,random} = \frac{t_{95\%}.\sigma_v}{\sqrt{N-1}.< V >} \tag{5.38}$$

$$u_{total,v} = \sqrt{\left(u_{probe,bias}\right)^2 + \left(u_{v,random}\right)^2} \tag{5.39}$$

where $u_{probe,bias}$ is ±1%.

The relative uncertainties for speed measurements with heated manikins, shown in Table 5.9, ranged between ±2-5%. With unheated manikins, the local uncertainties were lower than with heated manikins as shown in Table 5.9, Table 5.10, and in Figure 5.69 that revealed 5 negative points only. With two other values being approximately zero, as shown in Figure 5.69, there were 79% of the 33 seats having higher uncertainties with heated manikins.

Table 5.9 – Relative uncertainties for speed measurements with heated manikins

	East	Center	West
Row 1	4%	2%	3%
Row 2	4%	2%	2%
Row 3	5%	2%	3%
Row 4	3%	2%	3%
Row 5	3%	2%	3%
Row 6	3%	3%	3%
Row 7	2%	3%	4%
Row 8	5%	2%	2%
Row 9	2%	5%	5%
Row 10	3%	2%	3%
Row 11	3%	4%	3%

Table 5.10 - Relative uncertainties for speed measurements with unheated manikins

	East	Center	West
Row 1	2%	1%	1%
Row 2	2%	3%	4%
Row 3	2%	2%	2%
Row 4	4%	3%	3%
Row 5	2%	2%	2%
Row 6	4%	1%	2%
Row 7	2%	2%	3%
Row 8	2%	1%	2%
Row 9	2%	1%	2%
Row 10	2%	3%	2%
Row 11	2%	2%	2%

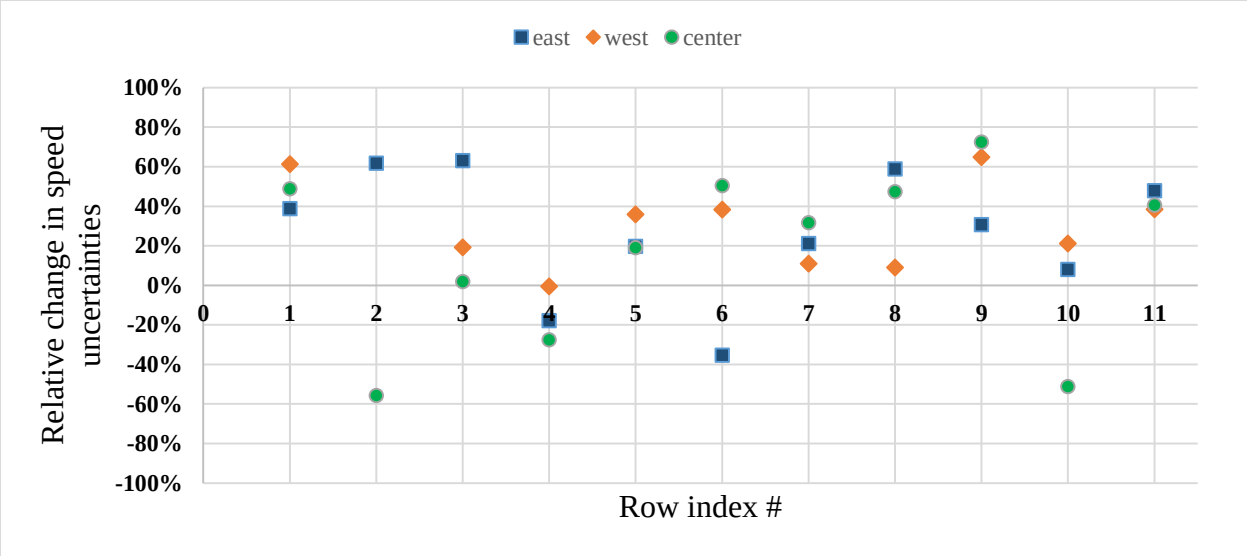

Figure 5.69- Relative change in speed uncertainties between heated and unheated manikins based on equation (5.20)

5.3.5 Uncertainties in turbulence analysis

5.3.5.1 Uncertainties in turbulence kinetic energies (TKE)

The turbulence kinetic energy was defined as

$$k = \frac{3}{2}(v')^2 = \frac{3}{2}(v - \bar{V})^2 \tag{5.40}$$

Using equation (5.21), the uncertainty in TKE is

$$\left(U_{k,bias}\right)^2 = \left[\frac{\partial k}{\partial v}\right]^2 (U_v)^2 + \left[\frac{\partial k}{\partial \bar{V}}\right]^2 (U_{\bar{V}})^2$$

$$\left(U_{k,bias}\right)^2 = [3(v - \bar{V})]^2\left(U_{v,bias}\right)^2 + [-3(v - \bar{V})]^2\left(U_{\bar{V},bias}\right)^2 \tag{5.41}$$

$$U_{v,bias} = u_v.\bar{V} = 1\%\bar{V} \tag{5.42}$$

$$U_{\bar{V},bias} = u_{\bar{V}}.\bar{V} = u_v.\bar{V} = 1\%\bar{V} = U_{v,bias} \tag{5.43}$$

Therefore,

$$\left(U_{k,bias}\right)^2 = 2 \times [3(v - \bar{V})]^2\left(U_{v,bias}\right)^2 \tag{5.44}$$

dividing by k^2 or $\left[\frac{3}{2}\ (v-\ \bar{V})^2\right]^2$

$$\left(u_{k,bias}\right)^2 = \left(\frac{U_{k,bias}}{k}\right)^2 = \frac{2\times[3(v-\ \bar{V})]^2}{\left(\frac{3}{2}(v-\ \bar{V})^2\right)^2}.\left(U_{v,bias}\right)^2 = \frac{8}{(v-\ \bar{V})^2}.\left(U_{v,bias}\right)^2$$
$$= 8\left(\frac{U_{v,bias}}{v'}\right)^2 \tag{5.45}$$

where U_v is the total bias uncertainty for the omni-directional TSI probe.

Thus, the relative uncertainty for the TKE would be

$$u_{TKE,total} = \sqrt{{u_{k,bias}}^2 + {u_{k,random}}^2} \tag{5.46}$$

where, $u_{k,random} = \frac{t_{95\%}.\sigma_{TKE}}{\sqrt{N-1}.<TKE,readings>}$ (5.47)

5.3.5.2 Uncertainties in turbulence intensities (TI)

The turbulence intensity was defined in equation (5.9) as the quotient of the speed root mean square to the average speed. To simplify the analysis of the uncertainty, the form defined in equation (5.48) was used.

$$TI = \frac{\sqrt{\overline{v'^2}}}{\bar{V}} = \frac{v'}{\bar{V}} = \frac{v-\bar{V}}{\bar{V}} \tag{5.48}$$

$$\left(U_{TI,bias}\right)^2 = \left[\frac{\partial(TI)}{\partial v}\right]^2\left(U_{v,bias}\right)^2 + \left[\frac{\partial(TI)}{\partial \bar{V}}\right]^2\left(U_{\bar{V},bias}\right)^2 \tag{5.49}$$

$$\left(U_{TI,bias}\right)^2 = \left(\frac{1}{\bar{V}}\right)^2\left(U_{v,bias}\right)^2 + \left(\frac{-\bar{V}-v+\ \bar{V}}{\bar{V}^2}\right)^2\left(U_{\bar{V},bias}\right)^2$$

but $U_{\bar{V},bias} = U_{v,bias}$ as shown in equation (5.43)

$$\left(U_{TI,bias}\right)^2 = \left(\frac{U_{v,bias}}{\bar{V}}\right)^2\left[1+\ \left(\frac{v}{\bar{V}}\right)^2\right] \tag{5.50}$$

Dividing both sides by $(TI)^2 = \left(\frac{v'}{\bar{V}}\right)^2$

$$\left(U_{TI,bias}\right)^2 \Big/ (TI)^2 = \frac{\left(\frac{U_{v,bias}}{\bar{V}}\right)^2 \left[1 + \left(\frac{v}{\bar{V}}\right)^2\right]}{\left(\frac{v'}{\bar{V}}\right)^2}$$

$$\left(u_{TI,bias}\right)^2 = \left(\frac{U_{v,bias}}{v'}\right)^2 \left[1 + \left(\frac{v}{\bar{V}}\right)^2\right] \tag{5.51}$$

Again, $U_{v,bias}$ is the total bias uncertainty for the omni-directional TSI probe (1%$\bar{V}$).

The relative uncertainty for the TI would be

$$u_{TI,total} = \sqrt{\left(u_{TI,bias}\right)^2 + \left(u_{TI,random}\right)^2} \tag{5.52}$$

where

$$u_{TI,random} = \frac{t_{95\%}.\sigma_{TI}}{\sqrt{N-1} < TI, readings >} \tag{5.53}$$

The relative uncertainties for TKE and TI are summarized in Table 5.11 and Table 5.12 for heated and unheated cases, respectively. The relative changes in the uncertainty for each category between heated and unheated cases are plotted in Figure 5.70 and Figure 5.71. It concluded that the uncertainties in TKE were higher with heated manikins as there were 70% of the points above zero level with 40% of the points above 20% relative change. On the other hand, the uncertainties in TI were less sensitive to the change in the environment temperature as reflected in Figure 5.71 where most of the points were scattered between -20% and 20% relative change.

Table 5.11 - Relative uncertainties for TKE and TI (Heated Manikins)

Row Index	East		Row Index	Center		Row Index	West	
	TKE	TI		TKE	TI		TKE	TI
1	31%	9%	1	17%	8%	1	26%	10%
2	21%	9%	2	20%	9%	2	17%	9%
3	19%	9%	3	14%	8%	3	16%	9%
4	21%	8%	4	18%	9%	4	15%	8%
5	26%	10%	5	16%	9%	5	16%	8%
6	20%	9%	6	20%	9%	6	24%	8%
7	25%	9%	7	24%	9%	7	28%	9%
8	27%	10%	8	15%	8%	8	15%	9%
9	21%	9%	9	39%	7%	9	64%	7%
10	22%	9%	10	22%	11%	10	33%	9%
11	30%	8%	11	42%	9%	11	24%	9%

Table 5.12 - Relative uncertainties for TKE and TI (Unheated Manikins)

Row Index	East		Row Index	Center		Row Index	West	
	TKE	TI		TKE	TI		TKE	TI
1	16%	8%	1	14%	8%	1	14%	7%
2	21%	12%	2	18%	9%	2	24%	11%
3	15%	9%	3	17%	9%	3	16%	9%
4	22%	10%	4	16%	9%	4	23%	11%
5	14%	8%	5	15%	8%	5	14%	8%
6	28%	11%	6	19%	11%	6	16%	9%
7	14%	8%	7	23%	11%	7	19%	10%
8	17%	10%	8	16%	9%	8	15%	8%
9	14%	8%	9	14%	8%	9	15%	8%
10	24%	10%	10	14%	9%	10	18%	9%
11	16%	8%	11	15%	8%	11	13%	8%

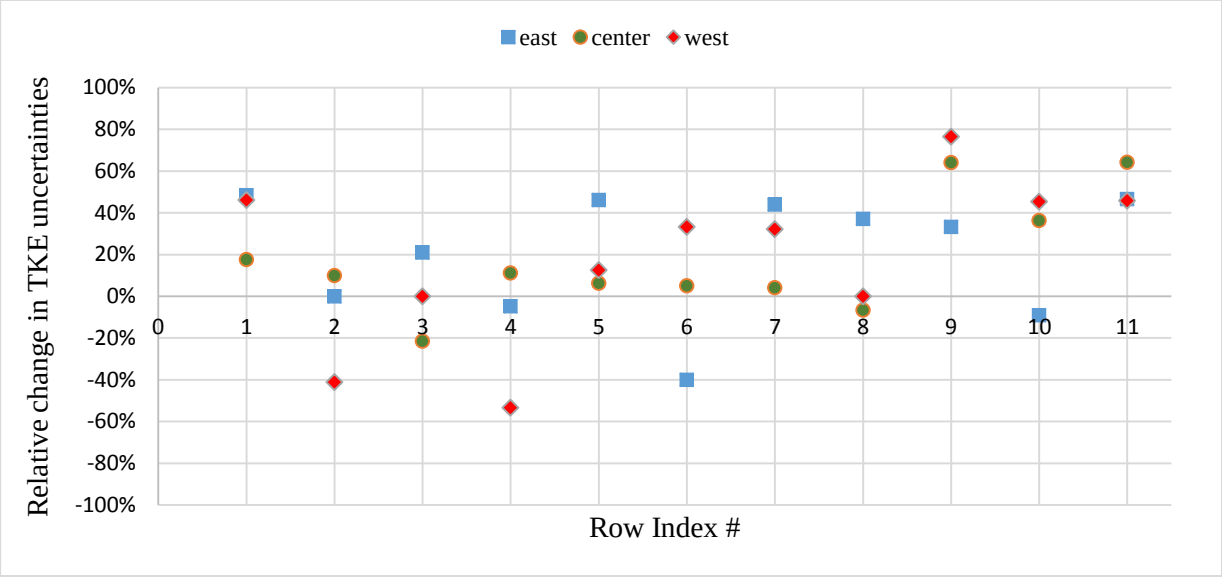

Figure 5.70 - Relative change in TKE uncertainties between heated and unheated cases using equation (5.20)

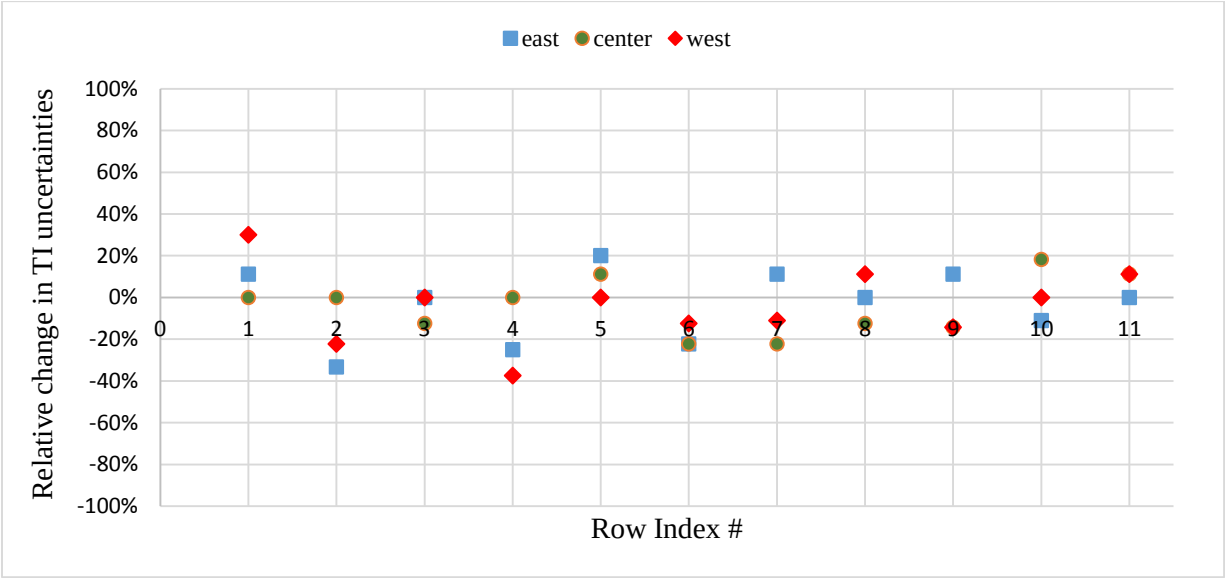

Figure 5.71 - Relative change in TI uncertainties between heated and unheated cases using equation (5.20)

5.3.5.3 Uncertainties in turbulence dissipation rates

Two speed transducers were used to evaluate the local dissipation rates inside the cabin based on Taylor's viscous dissipation model as given in equation (5.19). Thus, the bias uncertainty for the dissipation rate is

$$u_{\varepsilon,bias} = \sqrt{\left(u_{probe,1,bias}\right)^2 + \left(u_{probe,2,bias}\right)^2} \tag{5.54}$$

where $u_{probe,i}$ is similar for all probes ($u_{probe,bias}$ = ±1%). Then, the relative uncertainty would be

$$u_{\varepsilon,total} = \sqrt{{u_{\varepsilon.bias}}^2 + {u_{\varepsilon,random}}^2} \tag{5.55}$$

where

$$u_{\varepsilon,random} = \frac{t_{95\%}.\sigma_{\varepsilon}}{\sqrt{N-1}.<\varepsilon>} \tag{5.56}$$

Table 5.13 - Relative uncertainties for local dissipation "ε" with heated and unheated manikins

Row Index	Heated			Unheated		
	East	Center	West	East	Center	West
1	21%	19%	14%	30%	15%	16%
2	35%	11%	14%	12%	30%	26%
3	33%	12%	28%	11%	28%	37%
4	21%	13%	21%	35%	27%	22%
5	18%	18%	23%	40%	14%	13%
6	16%	28%	26%	16%	16%	17%
7	28%	25%	31%	18%	31%	16%
8	15%	22%	25%	17%	23%	15%
9	12%	18%	12%	18%	29%	16%
10	19%	17%	13%	29%	35%	15%
11	12%	12%	31%	22%	34%	34%

Similar to the trend followed in analyzing the effect of heat on TKE and TI, the relative change in the uncertainty of "ε" obtained for heated and unheated cases was evaluated and presented in

Figure 5.72. The uncertainties calculated for the local dissipation rates "ε" were higher with unheated manikins than with heated as reflected in the relative change chart in Figure 5.72.

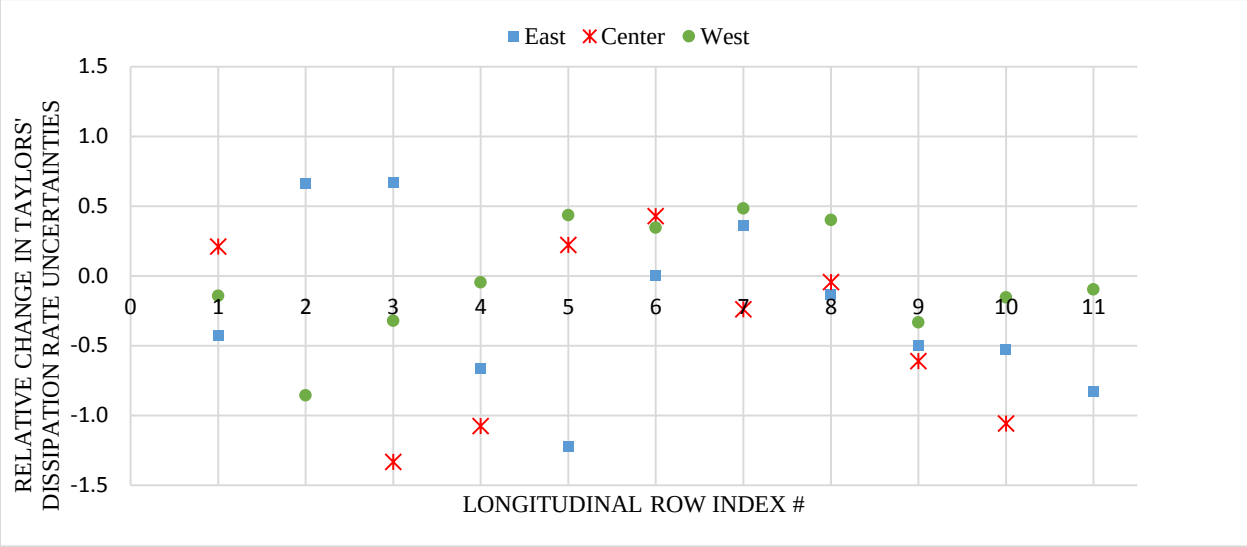

Figure 5.72 - Relative change in "ε" uncertainties between heated and unheated manikins

Chapter 6 - Summary and Conclusions

In this dissertation, three main topics affecting air quality and airflow behavior inside aircraft passenger cabin were investigated. A Boeing 767 mockup cabin was used for experimental investigations. The first topic dealt with the airflow distribution and circulation in the plan direction of the mockup cabin. The second topic investigated various turbulence parameters and their effect on airflow distribution and gaseous transport inside the cabin. The third and last topic examined the effect of heated and unheated environments on topics one and two, as described above.

Two approaches were followed in this study to understand the airflow distribution and behavior inside the mockup cabin. The first approach used theatrical smoke for visualizing the airflow while the second one used tracer gas to track gaseous dispersion. Non dispersive infrared sensors were used to sample and analyze tracer gas inside the cabin. Airflow speed, turbulence energy levels, turbulence intensities, and turbulence dissipation rates were investigated with the aid of omni-directional air speed transducers. Results from the turbulence analysis were compared to the tracer gas results as illustrated in this chapter. For all measurements, the accuracy and the uncertainty were investigated to check the validity and limitations of the results and conclusions. Tracer gas results had relative uncertainties ranging from ±14% with heated manikins to ±17% with unheated manikins. The CO_2 analyzers used for tracer gas sampling were shown to have relative uncertainties less than ±3% taking into consideration the repeatability and linearity of the units. Airflow speed measurements uncertainties were approximately ±5%.

Airflow Distribution Conclusions

Airflow visualization and tracer gas results were complimentary to each other. Airflow visualization helped in identifying potential release points for tracer gas testing. For example, smoke visualizing seemed to be vague about the behavior of the airflow in the center of row 7 where two circulations were identified that were flowing in opposite directions at the same location. The tracer gas results showed that a clockwise directed flow moved back in the mid-west seats and then circulated forwards through the mid-east side. Both approaches agreed on the general airflow behavior in the longitudinal direction inside the 11-row mockup cabin. The multiple circulations can be justified by the isotropic turbulence assumption inside the mockup cabin. The circulation size should be independent of the direction and thus should be controlled by the smallest geometrical dimension in the cabin. The height "H", which is the distance from the cabin floor to the ceiling beside the air diffusers, was found to be the integral length scale of circulations inside the cabin and thus should be the controlling parameter for the circulations. The circulations controlling the flow in the front section of the cabin were spread over the whole lateral cross section of the cabin. These circulations controlled the airflow over the region from rows 1 to 4, whereas, the middle one controlled the region from row 5 to 7. The identified circulations in the rear section of the cabin were comparatively of smaller size in the lateral and longitudinal directions. Looking into the circulation lengths in Figure 5.14, the circulation longitudinal dimensions were roughly 3.4 m in the front section, 2.6 m in the middle section, and approximately 2 m in the back section. In the front and middle sections, the circulations dominated approximately over the whole transverse cross section of the cabin, whereas in the back section it was dominating over half the cross section in both sides east and west. It might

be argued that the mid-section had two clockwise directed circulations, one in the mid-east and one in mid-west sections similar to the flows identified in the back section, but the results for release in seat 5D have shown that the gaseous transport tended to move from 5D to the east side while drifting forward and at the same time to the west back side as was shown in Figure 5.7. The forward transport from seat 5D refuted the existence of a half width clockwise circulation in the east side of the mid-section and thus a clockwise circulation over the full width of the cabin was assumed.

As the integral length scale was identified to be equal to the distance from the cabin floor to the ceiling (H2 in Table 5.3), then the dimensions of the circulations should be close to this limit. Based on this, since the back circulation had dimensions between 2-2.2 meters in both longitudinal and lateral directions, then the circulations in this section were closer to isotropic conditions than in the front and middle sections. The front section circulation had closer dimensions in the plan view of the cabin, whereas the middle section circulation had closer dimensions in the longitudinal and vertical directions. Despite this, the chaotic nature of the flow inside the cabin made the above observations reasonable taking into account the uncertainties in the measurement, which was up to ±14% for heated manikins measurements. The repeatability of the air flow in the same location inside the cabin is another piece in validating the above observations and conclusions. Appendix F - tested the repeatability of the flow inside the mockup cabin over different days and months and the flow had an uncertainty in gaseous flow repeatability varied from as low as ±3% in some locations and was up to ±9%.

Turbulence Characteristics Conclusions

The experimentally determined Taylor's length scale (λ) agreed with literature definition for the turbulence length scale which is estimated as 7% of the integral length scale of the

geometry being considered. With an average speed of 12 cm/s at a height of 1.23 m above the cabin floor, the Reynolds number based on integral length scale (L_o) was approximately 25,200. With this Reynolds number, the turbulence micro- length scale or Kolmogorov length scale was $\eta_K = 1.05\, mm$. This result agreed with literature as was reported by Lin et al. (2005) who found that the Kolmogorov length scale inside a B767-300 was around 0.9 mm.

The turbulence intensity (TI) and turbulence kinetic energy (TKE) results came into agreement with what was discussed within the speed fluctuations sections. The east side showed higher TI and higher TKE in the front section of the cabin and then all of the three transverse sides experienced the same TI and TKE levels all the way to the cabin back wall except in the west-back section that showed higher speed fluctuations and thus higher turbulence levels. However, the total uncertainty in seat 9F was approximately ±64% which would make the average TKE statistically the same as the other locations.

Regions with higher speed fluctuations were associated with higher turbulence energies and comparatively lower dissipations rates when considering local or micro-scale dimensions. The front-east side was characterized by higher turbulence energy levels than in the front-west side. Thus, it might be thought that the high energy levels served as the driving momentum pushing the flow into lower turbulence levels regions. Since the east side had almost the same level of turbulence energy along its longitudinal direction, the flow was pushed into the front centerline and west side seats. In the mid-section, the turbulence levels were almost the same in the east, center, and west sides which agrees with the two main drafts concluded in that region where one was moving forwards in the east side and one was moving backwards in the west side. The same argument could be used in the back section. It was concluded from tracer gas analysis that there were two clockwise directed circulations in the back section of the cabin. Looking into

the TKE levels in the back section of the cabin, the west and centerline seats experienced higher turbulence energy levels than in the east side. This might have caused the formulation of two circulations which was not seen in the front- and mid- sections of the cabin.

Turbulence intensity levels were lower than those reported by Lin et al. (2005). Lin's study had 50%-150% relative turbulence intensity above passengers head. The results of this study were on the range of 10%-35%, however, the positions considered by Lin et al. were closer to the diffusers which would assume higher fluctuations in the velocity and higher intensities. On the other hand, Lebbin (2006) reported turbulence intensity levels using 3D-PIV technique inside a half-generic B767 cabin and his results were between 10%-20% which agreed with the results of this study keeping in mind that the length and width of his cabin were of smaller dimensions. As mentioned earlier, the PIV measurements are more accurate than those conducted using the omni-directional speed probes due to limitations of the omni-probes.

Effect of Heated Environment on Airflow Distribution and on Turbulence Parameters

The 100-Watts generated by each of the thermal manikins affected the buoyancy of the tracer gas and caused some natural convection effects. The heat generated by the thermal manikins played a major role in the gaseous flow dispersion. With unheated manikins, the tracer gas was distributed evenly between the east and west sides of the cabin when releasing the tracer gas in the centerline seats of the cabin.

In the front section of the cabin, the results showed that the normalized tracer gas decreased to approximately 14% with unheated manikins and to 12% with heated manikins after three consecutive rows to the back of the release row in seat 2D. The flow in the middle section of the mockup cabin, as per the results concluded when releasing in seat 5D in Figure 4.22 and

Figure 5.18, showed a tendency of symmetrical distribution between east and west sides with the unheated manikins case, specially above 1 meter, as the front section of the cabin had. The average exposure in row 5, presented above, was calculated from the sampled tracer gas in all considered seats in that specific row as shown in Figure 5.15 and Figure 5.2. The unheated manikins case experienced higher exposures in the same row of release, when releasing in row 5 (seat 5D), than with heated manikins but the heated manikins case had relatively more tracer gas transported in the longitudinal direction than in the lateral direction. Table 6.1 shows that, with heated manikins, row 4 had an exposure between 16%-43%, row 3 experienced 13%-18%, row 6 had 12%-39%, and row 7 had 13%-28%, whereas, the exposure with unheated manikins ranged 12%-15%, 10%, 11%-20%, and 10-18% for row 4, row 3, row 6, and row 7, respectively. Thus, the longitudinal gaseous transport was higher with heated manikins than with unheated manikins. However, the results for release in seat 7D did not agree with the above observation where the longitudinal gaseous transport was almost the same with heated and unheated two rows to the front of the release row and one row to the back, but the unheated manikins had higher average exposures two rows and more to the back of the release location.

Table 6.1 - Lower and upper limit percent exposures with total uncertainty for respective rows when releasing in seat 5D with heated and unheated manikins

	Heated		Unheated	
Limit	Lower	Upper	Lower	Upper
Row 3	13% ± 0.3%	18% ± 0.4%	9.8% ± 0.4%	10.6% ± 0.3%
Row 4	16% ± 0.4%	43% ± 3%	12% ± 0.95%	15% ± 1%
Row 6	12% ± 0.4%	39% ± 2%	11% ± 0.4%	20% ± 0.5%
Row 7	13% ± 0.2%	28% ± 1.8%	10% ± 0.3%	18% ± 0.7%

The generated heat also affected and changed the airflow speed behavior within the cabin. The higher speeds in the front and back sections of the cabin were flipped from being almost in the

west side with heated manikins to the east side with unheated manikins. Also the mid-section speeds changed from being the highest in the east to almost the same across the transverse seats with unheated manikins case.

The speed fluctuation amplitudes were shown to increase with a heated environment and, hence, the TKE would be higher. The relative turbulence intensity appeared to be less sensitive than the kinetic energy when the cabin temperature changed. The heat affected the overall behavior of the TI but it was less significant than in the case of TKE, due to a change in both variables of the TI, speed fluctuation and average speed, as shown in equation (5.9), Figure 5.63, and Figure 5.64. Similarly, the uncertainties for TKE showed higher values with heated manikins over unheated ones, but the turbulence intensities uncertainties were less affected by a change in the environment temperature.

With respect to the turbulence dissipation rate, the large scale dissipation rates were shown to increase with a heated environment as was reflected in the relative change plot between heated and unheated cases in Figure 5.67. However, for local dissipation rates, which depend on viscosity, it was shown that the dissipation rate values did not decay as a total, but rather it showed some changes within the cabin with a change in the environment temperature. It should be noted that although the speed fluctuation amplitudes were shown to increase with heat, the relative uncertainties for the local dissipation rate decreased as the environment temperature increased.

The change in gaseous transport behavior between heated and unheated manikins in different sections of the cabin raises the importance of the buoyancy effects. With the buoyancy effects being dominating over part of the airflow behavior, then the assumption of isotropic turbulence was not quite true. An isotropic turbulence would have no directional preferences

within the cabin. The circulation dimensions should be the same in all direction, a condition that was not met perfectly except in the back section of the cabin.

In conclusion, despite the differences between the results with heated and unheated manikins, some general conclusions can be drawn that apply to both cases:

- Multiple circulations exist due to the isotropic turbulence characteristics and constraints. If the longitudinal length of the cabin is longer, more circulations are expected to exist. The minimum physical/geometrical distance is the main constraint for the size of such circulations. Hence, should the cabin be of a narrower width aircraft type, such as two or three seats per row aircraft, then the size of circulation would be controlled by the side-to-side dimension and not by the vertical dimension as was the case of this study.
- Heated environments can affect the behavior of such circulations and the gaseous dispersion.
- The increase in the cabin temperature affects buoyancy forces which can skew the isotropic turbulence characteristics.
- The multiple circulations concept could be implemented to control the quality of air by installing detection sensors in low turbulence level regions as it can be a high potential destination for the flow coming from high turbulence energy level regions and, thus, carrying particulates and contaminants, if present, with it.

References

Ahmed, S.T., Mahdi, A., Hussein, H., (2013), "A theoretical study for cold air distribution to different supply patterns," *International Journal of Engineering & Technology IJET-IJENS*, 13 (4), pp. 7-18.

Airliner Cabin Environment Research "ACER", (2012), "*Sensors and Prognostics to Mitigate Bleed Air Contamination Events*," Progress Report, Report Number RITE-ACER-CoE-2012-05

ASHRAE, (2009), "*ASHRAE Handbook-Fundamentals*," American Society of Heating, Refrigerating and Air-Conditioning Engineers, Inc., ATLANTA, GA, Chap. 9.

ASHRAE Standard 161-2007, (2007), "*Air Quality within Commercial Aircraft*," Atlanta, Georgia: American Society of Heating, Refrigerating and Air Conditioning Engineers.

American Conference for Governmental Industrial Hygienists, (2012), "*Guide to Occupational Exposure Values*," ACGIH, Cincinnati, Ohio.

Aviation Safety Reporting System (ASRS), (2012), NASA online database (http://asrs.arc.nasa.gov)

Beneke, J. M., (2010), "*Small Diameter Particle Dispersion in a Commercial Aircraft Cabin*," MS Thesis, Kansas State University, Manhattan, KS.

Bosbach, J., Pennecot, J., Wagner, C., Raffel, M., Lerche, T., and Repp, S., (2006), "Experimental and numerical simulations of turbulent ventilation in aircraft cabins," *Energy*, 31 (5), pp. 694-705.

BRE, (2003), "*Extending Cabin Air Measurements to Include Older Aircraft Types Utilized in High Volume Short Haul Operations*," BRE Report 212034, UK Building Research Establishment, Watford.

BTS, (2013), "*Airline Activity: National Summary (U.S. Flights)*," U.S. Bureau of Transportation Statistics, Research and Innovative Technology Administration, U.S. Department of Transportation, www.rita.dot.gov/bts

Buchmann, P., Riberon, J., Millet, J.R., and Lauriat, G., (1994), "Numerical predictions of airflow patterns in large enclosures with supplied air jet system," *Proceedings of Roomvent*, 1, pp. 467-480.

Coleman, H.W. and Steele, W.G., (1999), "*Experimentation and Uncertainty Analysis for Engineers*," John Wiley & Sons, Inc., pp. 47-80, Chap. 3.

Dechow, M., (1996), "Airbus cabin air quality," *FAST*, 20, pp. 24-29.

ACER, (2009), "*Draft Final Technical Report, Contaminant Transport in Airliner Cabins Project*," Institute for Environmental Research, Kansas State University, Manhattan, KS.

Eckels, S., Jones, B., Mann, G., Mohan, K., and Weisel, C., (2014), "Aircraft recirculation filter for air quality and incident assessment," *Journal of Aircraft*, 51 (1), pp. 320-326.

Emmerich, S., and McGrattan, K., (1998), "Application of a large eddy simulation model to study room airflow," *ASHRAE Transactions*, 104, pp. 1-9.

Federal Aviation Administration website, (2012) www.FAA.gov

Gilani, S., Montazeri, H., and Blocken, B., (2013), "CFD simulation of temperature stratification for a building space: Validation and sensitivity analysis," *13th Conference of International Building Performance Simulation Association*, France, pp. 504-511.

Gupta, J., Lin, C.-H., and Chen, Q., (2011), "Transport of expiratory droplets in an aircraft cabin," *Indoor Air*, 21 (1), pp. 3-11.

Guan J., Wang, C., Gao, K., Yang, X., Lin, C.H., Gao, P., and Lu, C., (2014), "Measurements of volatile organic compounds in aircraft cabins. Part I: Methodology and detected VOC species in 107 commercial flights," *Building and Environment*, 72, pp. 154-161.

Harrison, R., Murawski, J., McNeely, E., Guerriero, J., Milton, D., "*Management of Exposure To Aircraft Bleed-Air Contaminants Among Airline Workers – A Guide for Health Care Providers."*

Health Hazard Evaluation (HHE) Report, (1993), NIOSH, HETA 90-226-2281, Alaskan Airlines, Seattle, Washington.

Howard, J.S., (1966), "Ventilation measurements in houses and the influence of wall ventilators," *Bldg Sci*, 1, pp. 251-257.

Horstman, R. H., (1988), "Predicting velocity and contamination distribution in ventilated volumes using Navier-Stokes equations," *Proceedings of the ASHRAE Conference: IAQ*, Atlanta, Georgia, pp. 209-230.

IEH, (2011), "*Aircraft Cabin Air Sampling Study: Part 1 of the Final Report*," Institute of Environment and Health, Cranfield University, Cranfield, Bedfordshire, UK.

(2004), "*Jane's All the World's Aircraft*," Jane's Information Group Inc., Virginia, USA.

Johnston, J. P., Halleen, R. M., and Lazius, D. K., (1972), "Effects of span-wise rotation on the structure of two-dimensional fully developed turbulent channel flow," *J. Fluid Mech*., 56, pp. 533–557.

Kantha, L.H., (2004), "The length scale equation in turbulence models," *Nonlinear Processes in Geophysics*, 11, pp. 83-97.

Kuhn, M., Bosbach, J., and Wagner, C., (2009), "Experimental parametric study of forced and mixed convection in a passenger aircraft cabin mock-up," *Building and Environment*, pp. 961-970.

Lamb, J., McGonagle, C., Cowie, H., and Cherrie, J.W., (2012), "*Cabin Air – Surface Residue Study Report,"* Research Report TM/11/06, IOM.

Lidwell, C.M., (1960), "The evaluation of ventilation," *J. Hyg*, 58, pp. 297-305.

Lin, C.H., Horstman, R.H., Ahlers, M.F., Sedgwick, L.M., Wirogo, S., Bennett, J.S., Topmiller, J.L., and Dunn, K.H., (2005), "Numerical simulation of airflow and airborne pathogen transport in aircraft cabins - Part I: Numerical simulation of the flow field," *ASHRAE Trans 2005 Jan*; 111 (Part 1), pp. 755-763.

Lebbin, P., (2006), "*Experimental and Numerical Analysis of Air, Tracer Gas, and Particulate Movement in a Large Eddy Simulation Chamber*," PhD. Dissertation, Kansas State University, Manhattan, KS.

Lunden, M., Faulkner, D., Heredia, E., Cohn, S., Dickerhoff, D., Noris, F., Logue, J., Hotchi, T., Singer, B., and Sherman, M.H., (2012), "*Experiments to Evaluate and Implement Tracer Gas Methods to Measure Ventilation Rates in Homes*," Ernest Orlando Lawrence Berkeley National Laboratory, Environmental Energy Technologies Division.

Launder, B.E., and Spalding, D.R., (1974), "The numerical computation of turbulent flows," *Comp. Meth. Appl. Mech. Eng*., 3, pp. 269-289.

Lee, S., Poon, C., Li, X., and Luk, F., (1999), "Indoor air quality investigation on commercial aircraft," *Indoor Air*, 9, pp. 180-187.

Longnecker, M. and Ott, L., (2004), "*A First Course in Statistical Methods*," First edition, Published by Cengage, NY.

Malmfors, T., Thorburn, D., and Westlin, A., (1989), "Air quality in passenger cabins of DC-9 and MD-80 aircraft," *Environmental Technology Letters*, 10, pp. 613-628.

McKernan, L.T., Wallingford, K.M., Hein, M.J., Burge, H., Rogers, C.A., and Herrick, R., (2008), "Monitoring microbial populations on wide-body commercial passenger aircraft," *Annual Occupational Hygiene*, 52 (2), pp. 139-149.

Mellor, G. L. and Yamada, T., (1982), "Development of a turbulence closure model for geophysical fluid problems," *Rev. Geophys. Space Phys.*, 20, pp. 851–875.

Mellor, G. L. and Durbin, P. A., (1975), "The structure and dynamics of the ocean surface mixed layer," *J. Phys. Oceanogr*., 5, pp. 718–728.

Martin, P. J., (1985), "Simulation of the mixed layer at OWS November and Papa with several models," *J. Geophys. Res*., 90, pp. 903–916.

Martin, P. J., (1986), "*Testing and Comparison of Several Mixed Layer Models*," Naval Ocean Research and Development Activity (NORDA) Report143, US Navy.

Murawski, J. and Supplee, D., (2008), "An attempt to characterize the frequency, health impact, and operational costs of oil in the cabin and flight deck supply air on US commercial aircraft," *Journal of ASTM International*, 5 (5), Paper ID JAI10164

Müller, R., Scherer, T., Rotger, T., Schaumann, O., and Markwart, M., (1997), "Large body aircraft cabin a/c flow measurement by helium bubble tracking," *Journal of Flow Visualization & Image Processing*, 4, pp. 295–306.

Müller, R., Flogel, H., Scherer, T., Schaumann, O., and Buchholz, U., (2000), "Investigation of large scale low speed air condition flow using PIV," *Proceedings of 9th International Symposium on Flow Visualization*, Edinburgh, pp. 22–25.

Michaelis, S., (2007), "*Aviation Contaminated Air Reference Manual*," Published by Suzan Michaelis, CPI Antony Rowe, Eastbourne, England.

Murawski, J. and Hecker, S., (2011), "Exposure to oil fumes on aircraft: necessary to regulate?," *Occupational Health & Safety, Australian & New Zealand Journal of Health, Safety and Environment,* 27, pp. 20-34.

Murawski, J., and Michaelis, S., (2011), "A critique of recent air sampling data collected on aircraft: how much exposure to neurotoxic fumes is acceptable?," *Journal of Biological Physics and Chemistry*, 11, pp. 147-151.

Nagda, N.L., Fortmann, R.C., Koontz, M.D., et al., (1989). "*Airliner Cabin Environment: Contaminant Measurements, Health Risks, and Mitigation Options*," US Department of Transportation, Report No. DOT-P-15-89-5. Washington, DC: Government Printing Office.

Nagda, N.L., Rector, H.E., Li, Z., and Hurt, E.H., (2001), "*Determine Aircraft Supply Air Contaminants in the Engines Bleed Air Supply System on Commercial Aircraft*," Energen Report AS 20151: Energen/ ASHRAE, Germantown.

NRC, (2002), "*The Airliner Cabin Environment and the Health of Passengers and Crew*," The National Academy Press, Washington, D.C.

O'Donnell, A., Donnini, G., and Nguyen, V.H., (1991), "Air quality, ventilation, temperature and humidity in aircraft," *ASHRAE Journal*, April Issue, pp. 42-46

Pierce, W., Janczewski, J., Roethlishberger, B., and Janczewski, M., (1999), "Air quality on commercial aircraft," *ASHRAE Journal*, September Issue, pp. 26.

RAE Systems, (2005), "*Theory and Operation of NDIR Sensors*," www.raesystems.com

Rankin, W., Space, D., and Nagda, N., (2000), "*Passenger Comfort and the Effect of Air Quality*," Air Quality and Comfort in Airliner Cabins, ASTM STP 1393, N. L. Nagda Ed., American Society for Testing and Materials, West Conshohocken, PA.

SAE Aerospace Information Report (AIR) 1539, (1997) (originally issued 1981), "Environmental control system contamination," *Society of Automotive Engineers*, Warrendale, PA.

Sarkar, J., and Mandal, Soumen, (2008), "CFD modeling and validation of temperature and flow distribution in air-conditioned space," *International Refrigeration and Air Conditioning Conference*, paper 972.

Spengler, J., Burge, H., Dumyahn, T., et al., (1997), "*Environmental Survey on Aircraft and Ground-based Commercial Transportation Vehicles*," Report of May 31, 1997, Boston Ma, Harvard School of Public Health.

Shehadi, M., Hosni, M., and Jones, B.W., (2010), "Experimental investigation of optimal particulate sensor location in an aircraft cabin," *Proceedings of ASME 2010 Joint US-European Fluids Engineering Summer Meeting and 8th International Conference on Nanochannels, Microchannels, and Minichannels*, Montreal, Canada, pp. 849-859.

Shehadi, M., (2010), "*Experimental Investigation of Optimal Particulate Sensor Location inside an Aircraft Cabin*," MS Thesis, Kansas State University, Manhattan, KS.

Shehadi, M., Hosni, M., Jones, B., (2014), "Airflow distribution in the longitudinal plan of a Boeing 767 mockup cabin," *Proceedings of the ASME 2014 International Mechanical Engineering Congress & Exposition*, IMECE2014-40102, November 14-20, 2014, Montreal, Canada.

Shehadi, M., Hosni, M., and Jones, B.W., (2015), "Characterization of the frequency and nature of bleed air contamination events in commercial aircraft," *Indoor Air* (Accepted on April 4, 2015)

Sherman, M., 1990, "Tracer-gas techniques for measuring ventilation in a single zone," *Building and Environment*, 25 (4), pp. 365-374.

Shun-Cheng, L., Poon, C.S., Li, X.D., and Luk, F., (1999), "Indoor air quality investigation on commercial aircraft," *Indoor Air*, 9, pp. 180-187.

Sun, Y., Zhang, Y., Wang, A., Topmiller, J., Bennett, J., (2005), "Experimental characterization of airflows in aircraft cabins, Part 2: Results and research recommendations," *ASHRAE Transactions*, 111(2): pp. 53-59

Trupka, A.T., (2011), "*Tracer Gas Mapping of Beverage Cart Wake in a Twin Aisle Aircraft Cabin Simulation Chamber*," MS Thesis, Kansas State University, Manhattan, KS.

US CAB, (1953), "*Airplane Airworthiness Transport Categories, Ventilation, Heating, and Air Pressurization*," Section 4b.371(a) and (b). Washington, DC: United States Civil Aeronautics Board.

van Netten, C., (2000), "*Analysis of Two Jet Engine Lubricating Oils and a Hydraulic Fluid: Their Pyrolytic Breakdown Products and Their Implications on Aircraft Air Quality*," Air Quality and Comfort in Airliner Cabins, ASTM STP 1393, N. L. Nagda, Ed., ASTM International, West Conshohocken, PA, pp. 61–75.

van Netten, C., (1998), "Air quality and health effects associated with the operation of BAe146-200 aircraft," *The Journal of Applied Occupational and Environmental Hygiene*, 13 (10), pp. 733-739.

van Netten, C., and Leung, V., (2001), "Hydraulic fluids and jet engine oil: Pyrolysis and aircraft air quality," *Architecture Environment Health*, 56 (2), pp. 181–186.

Vasak, V., (1992), "*Cabin Air Contamination in BAe 146 in EastWest Airlines*," Industrial Hygiene and Environmental Service Laboratories, St. Ives.

Waters, M.A., Bloom, T.F., Grajewski, B., and Deddens, J., (2002), "Measurements of indoor air quality on commercial transport aircraft," *Proceedings: Indoor Air*, pp. 782-787.

Winder, C., (2006), "Air monitoring studies for aircraft cabin contamination," *Current Topics in Toxicology*, 3, pp. 33-48.

Wang, A., Zhang, Y., Sun, Y., and Wang, X., (2008), "Experimental study of ventilation effectiveness and air velocity distribution in an aircraft cabin mockup," *Building and Environment*, 44, pp. 337-343.

Watmuff, J. H., Witt, H. T., and Joubert, P. N., (1985), "Developing turbulent boundary layers with system rotation," *J. Fluid Mech.*, 157, pp. 405–448.

Yan W., Zhang Y., Sun Y., and Li D., (2009), "Experimental and CFD study of unsteady airborne pollutant transport within an aircraft cabin mock-up," *Building and Environment*, 44, pp. 34-43.

Zhao, L., Zhang, Y., Wang, X., Riskowski, G.L., and Christianson, L.L., (2001), "Measurement of two-dimensional air velocity in a full-scale room using particle image velocimetry," *ASHRAE Transactions*, vol. 107 (2), pp. 434-443.

Appendix A - Temperature Distribution Investigation inside the Mockup Cabin

The temperature distribution inside the mockup cabin was investigated prior to initiating any testing to ensure accurate results were obtained when conducting tracer gas, gas visualization, and speed measurement testing. Twenty four thermocouples were attached to the interior surface of the mockup cabin distributed evenly between the east and west sides (i.e. 12 in each side). In the first case, normal operating conditions were run, whereas in the second case the heat generated by the manikins was turned off. Fifty five different tests were run with the above two running conditions. The maximum and the minimum recorded temperatures in the east and west sides for heated and unheated manikins are shown in Figure A.1 and Figure A.2, respectively.

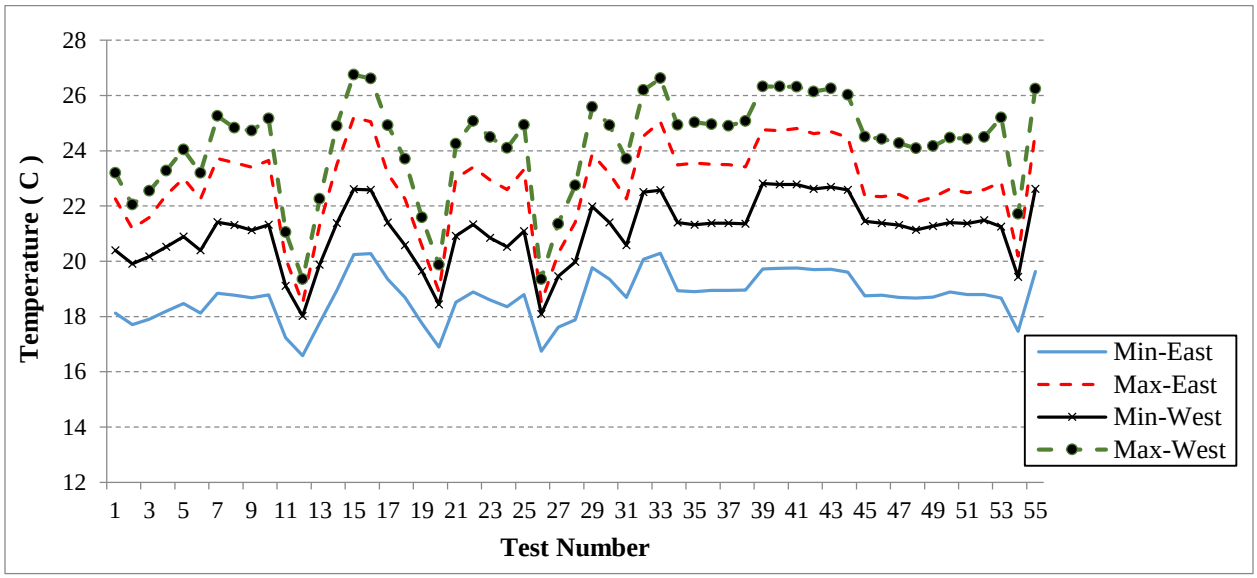

Figure A.1 - Maximum and minimum temperatures in the east and west sides of the cabin with heated manikins

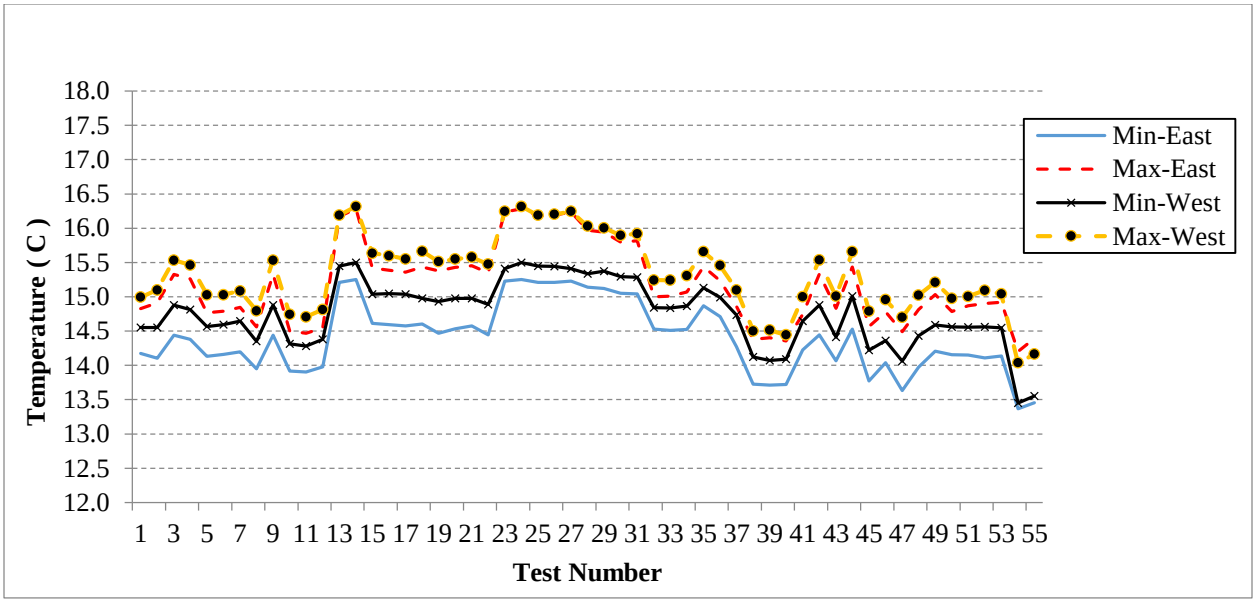

Figure A.2 - Maximum and minimum temperatures in the east and west sides of the cabin with unheated manikins

It was noticed from Figure A.1 and Figure A.2 that the west side experienced higher temperatures than the east side with or without heat being added by the manikins. However, this difference was minimal with unheated manikins. After conducting the tracer gas experiments, the high temperatures examined in the west side could be justified by the influence of the clockwise circulations. However, at the time when those validation tests were conducted, it was needed to ensure that the system was running with minimum or no flaws. Thus, to ensure that the sensors used, the cabin structural profile, and the Data Acquisition System were running with acceptable uncertainties, the air supply system was shut off and measurements were taken using the same set of sensors and the same DAQ system. To create some air circulation inside the cabin, two identical, commercial, axial fans were installed in the back section of the mockup cabin. Each fan was located on the floor of the cabin in each of the east and west aisles. Temperature measurements were taken for 45 hours. The differences between the maximum recorded temperatures, in the east and west sides, and the differences between the minimum

recorded temperatures, in the east and west sides of the cabin, are shown in Figure A.3 and Figure A.4, respectively. As can be seen, the differences were less than 1 °C. This small difference indicated that the system was running correctly with minimal errors.

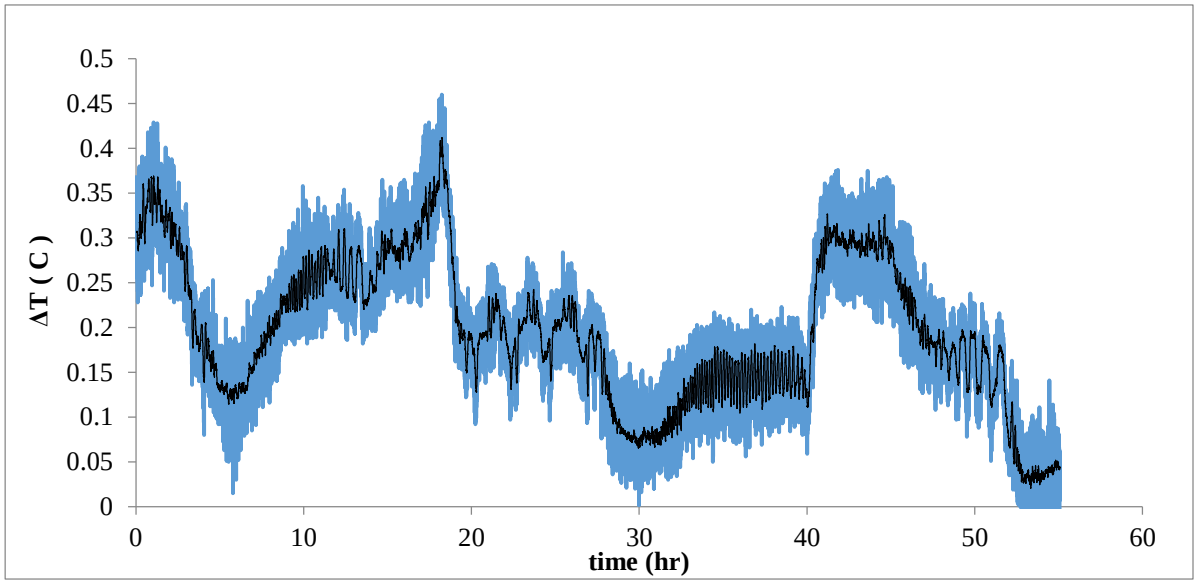

Figure A.3 - Differences between the maximum recorded temperatures in the east and west sides of the cabin with the air supply system off

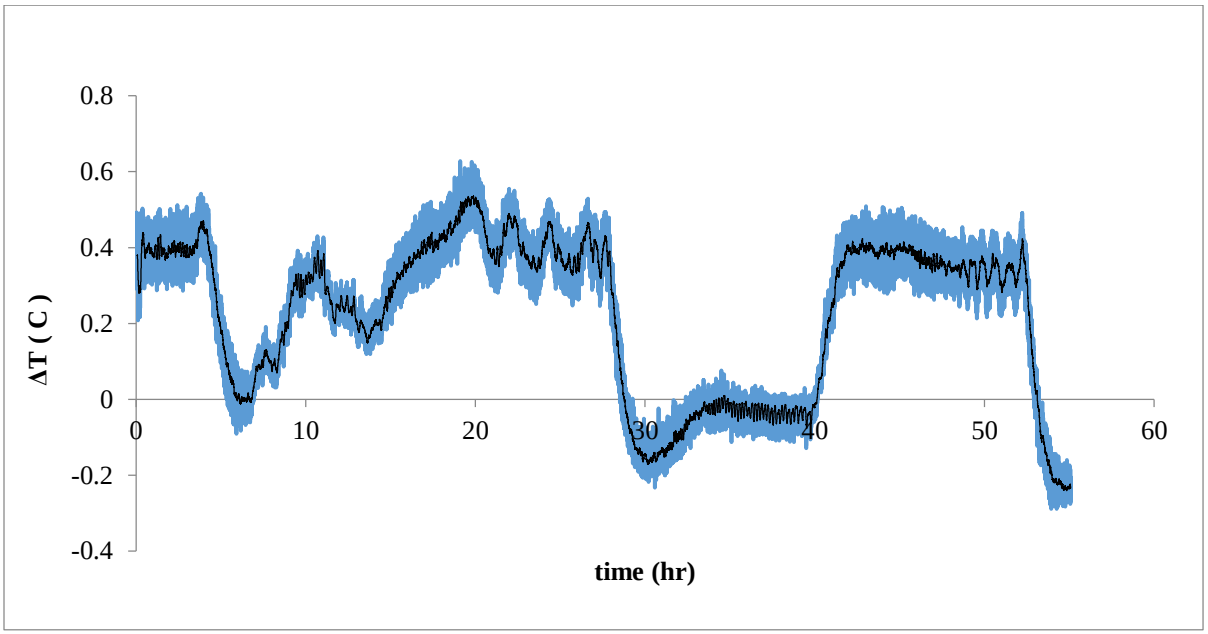

Figure A.4 - Differences between the minimum recorded temperatures in the east and west sides of the cabin with the air supply system off

Appendix B - Smoke Visualization Results

This appendix summarizes the results for smoke visualization tests. To ensure minimal intrusion disturbance was created when injecting the smoke into the cabin, the initial velocity of the smoke was set as low as possible to allow proper visualization of the smoke. Smoke was generated inside a box and compressed air was injected into the box with a pressure of approximately 1.3 bars to push the smoke out from the box to the injection port inside the cabin. The smoke flow was captured with a video camera and the flow direction was tracked by capturing consecutive pictures of the smoke movement after its release in different locations. Some locations were hard to identify by photos and the airflow patterns were concluded only by observing the recorded videos.

The figures below show the captured photos and snap shots in each corresponding location:

Release in Row 1 – Seat D

Event 1

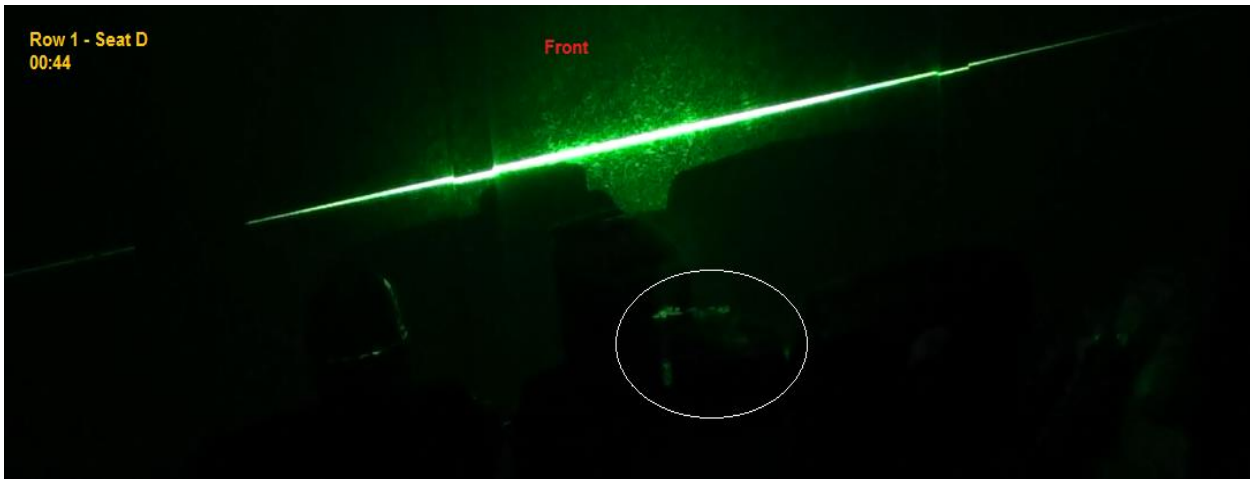

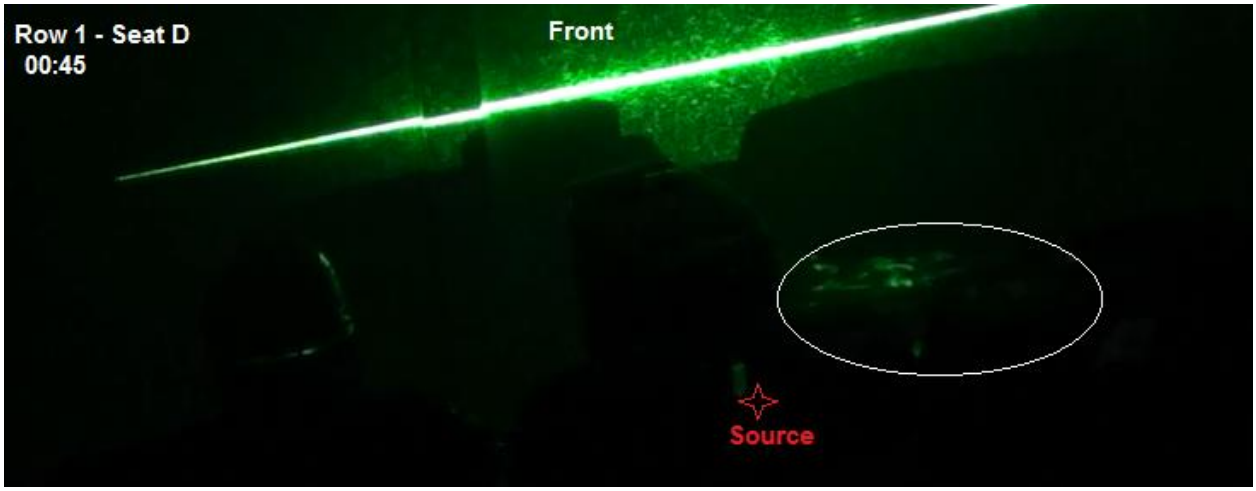

Event 2

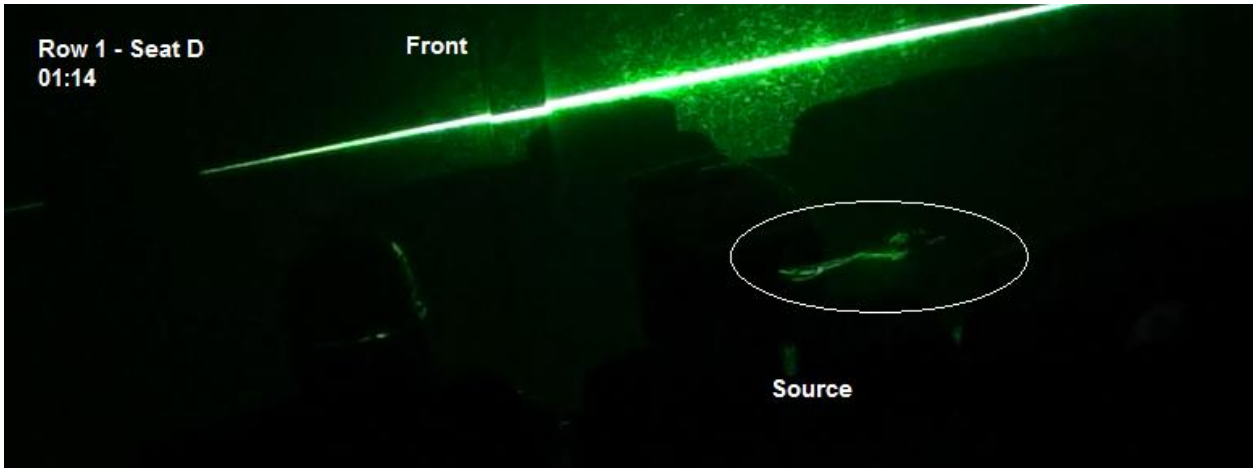

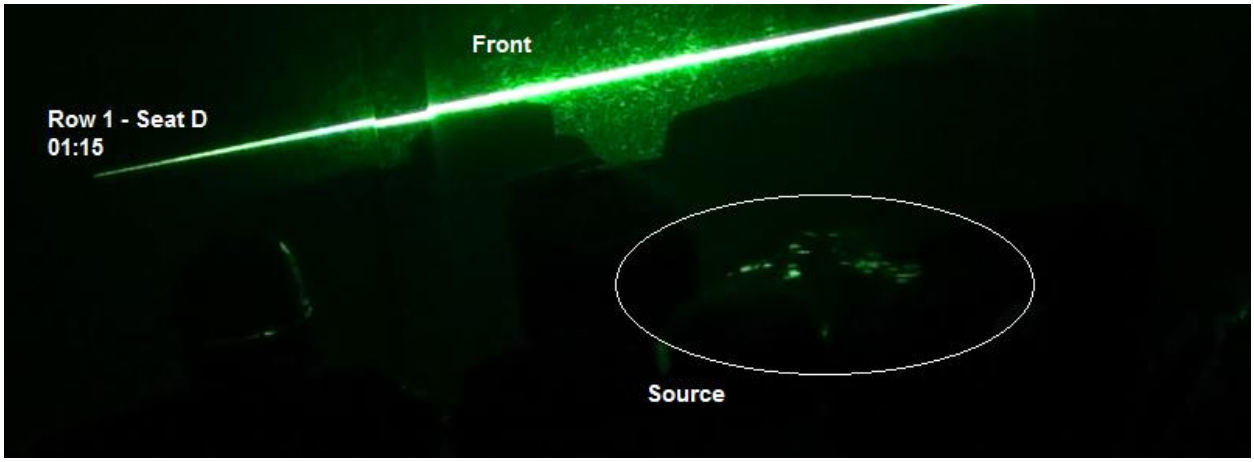
Front
Row 1 - Seat D
01:15
Source

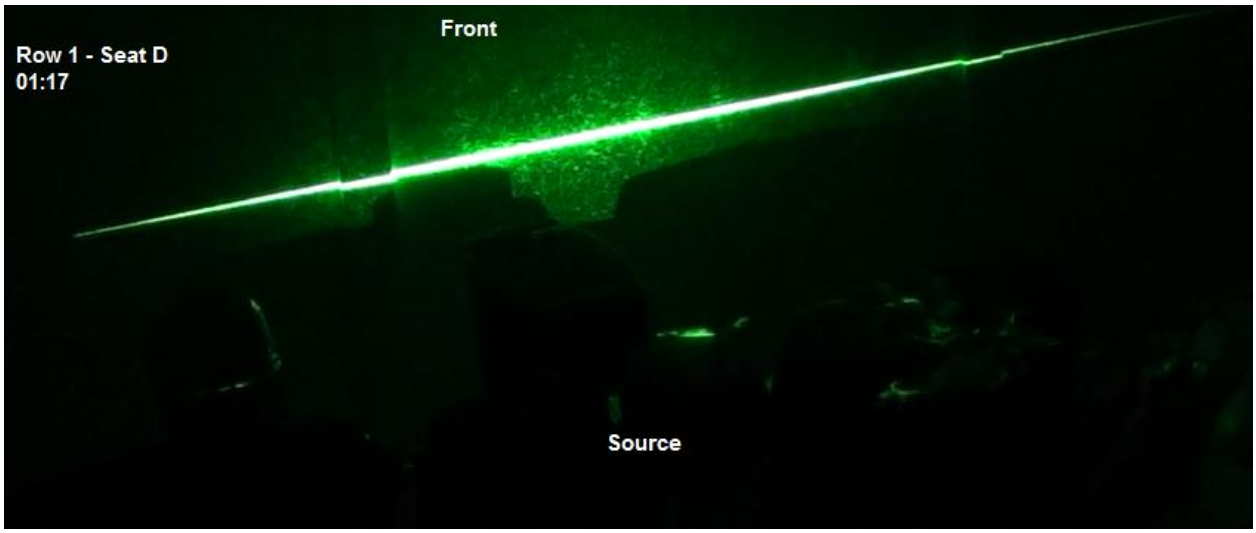
Front
Row 1 - Seat D
01:17
Source

Event 3

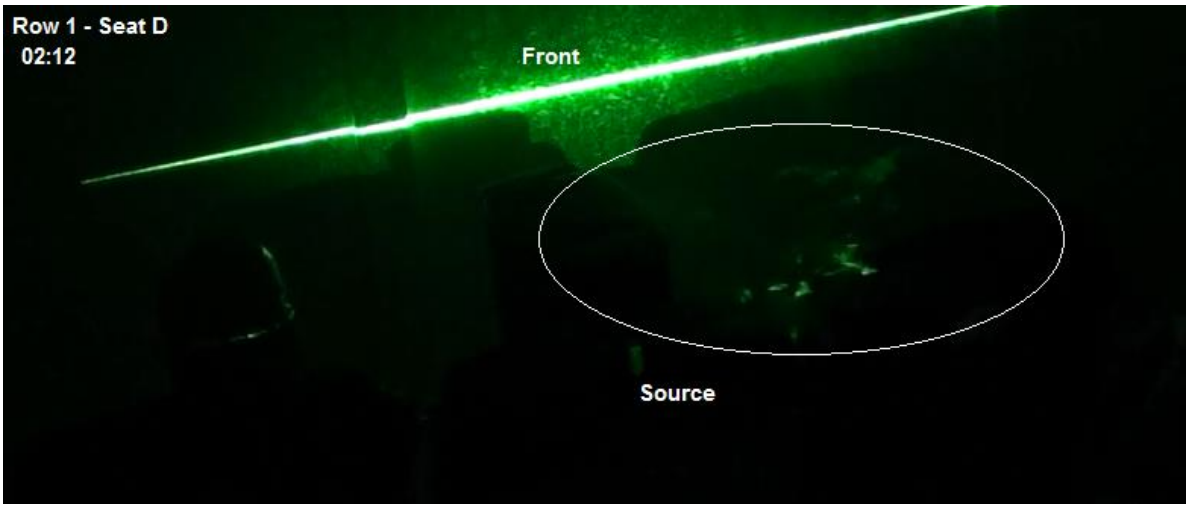

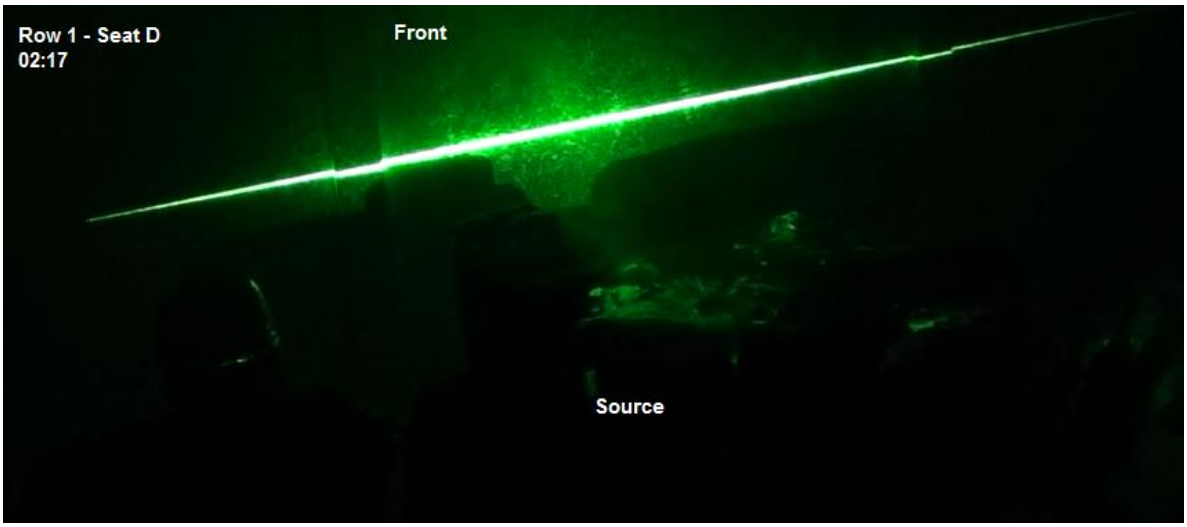

Event 4

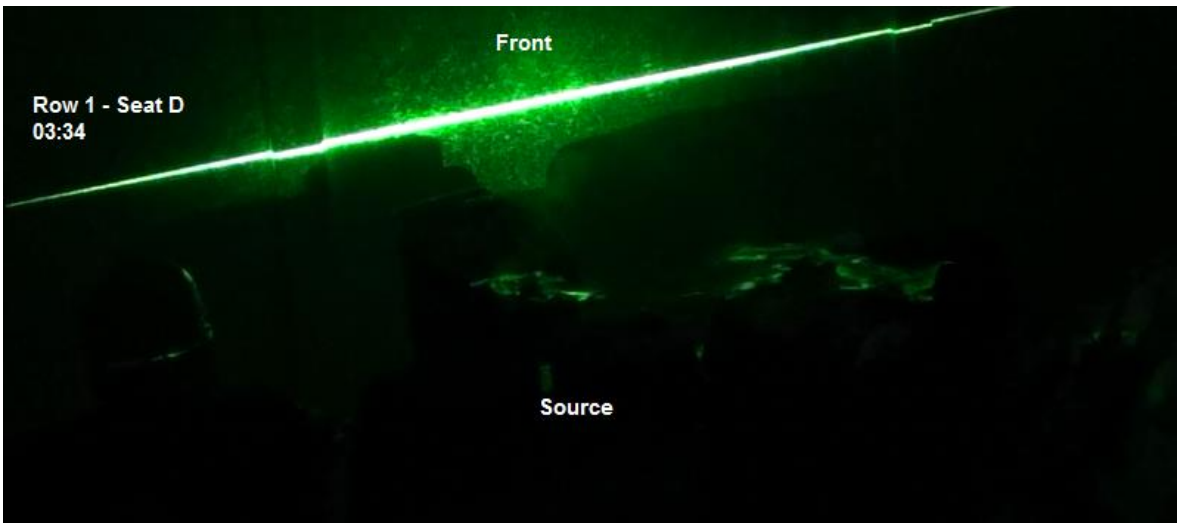

Release in Row 2 – Seat B

The smoke signal was very weak and nothing was significantly observed probably due to the fact that Seat B is close to the exhaust ports and thus the smoke was being sucked down and exhausted out quickly. Small eddies and swirls only were observed with some tendency to move around the source point in Seat B and then circulated towards seat A in the same row.

Release in Row 2 – Seat C

Event 1

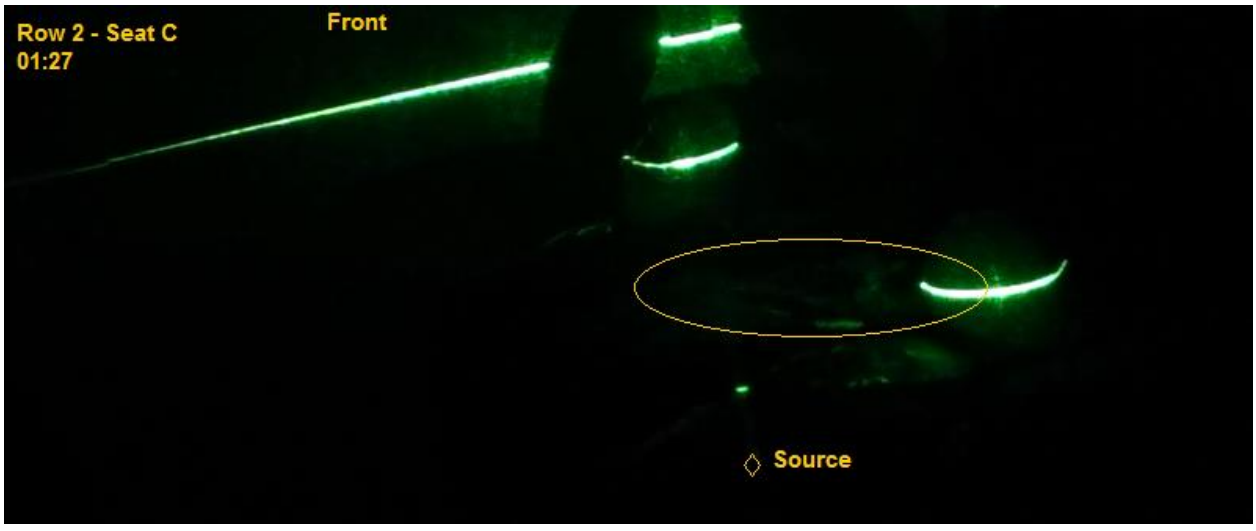

Event 2

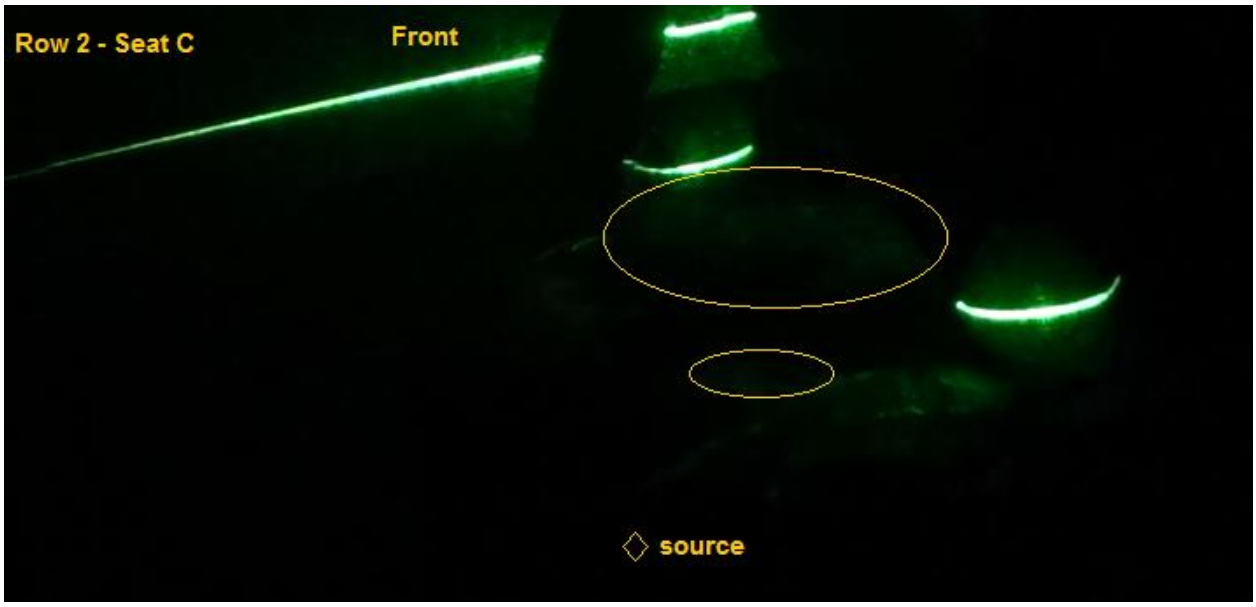

Event 3

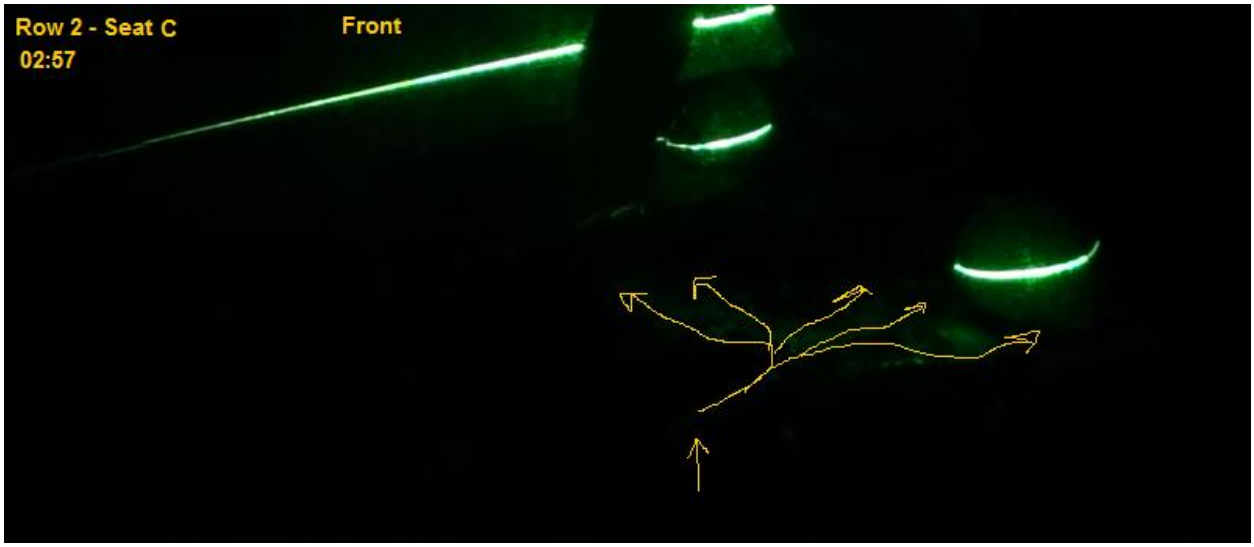

Event 4

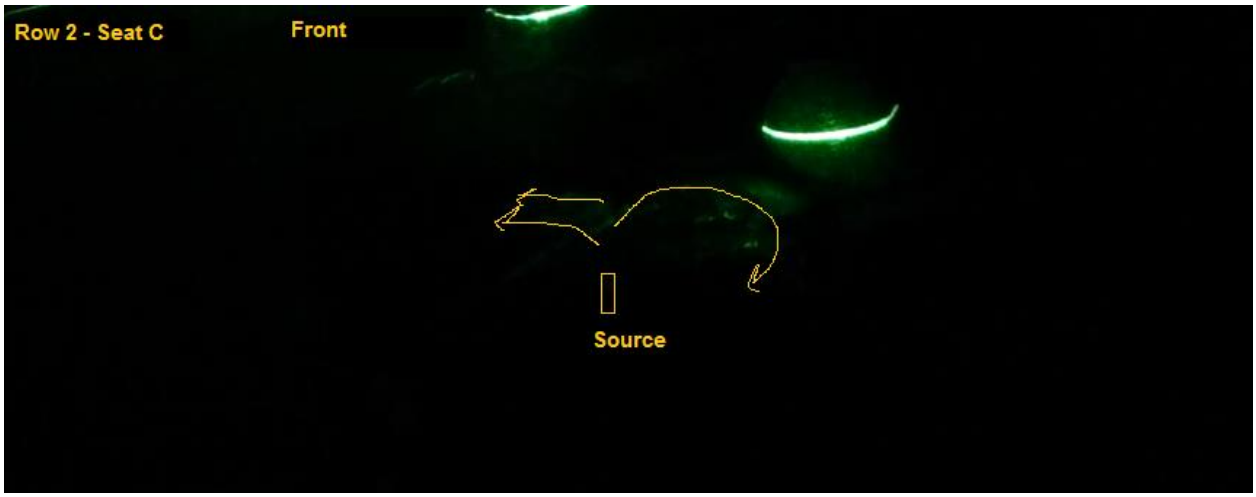

Release in Row 2 – Seat F

Event 1

Event 2

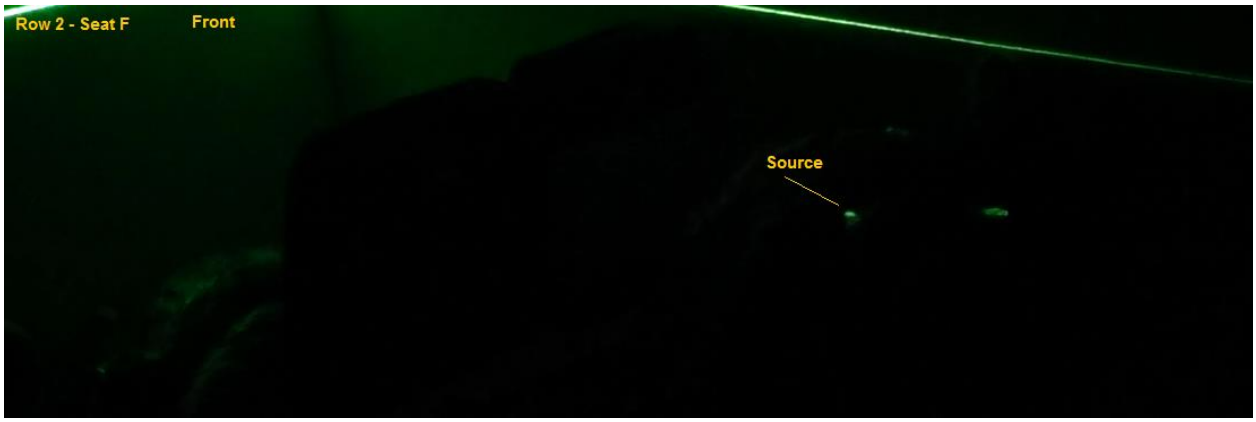

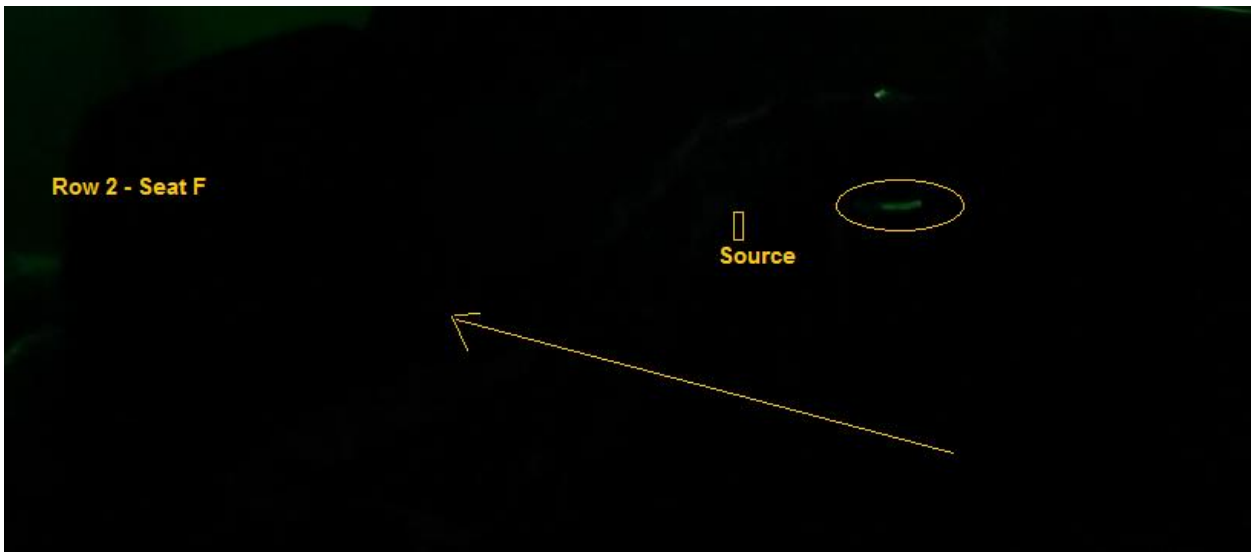

Release in Row 3 – Seat A

Event 1

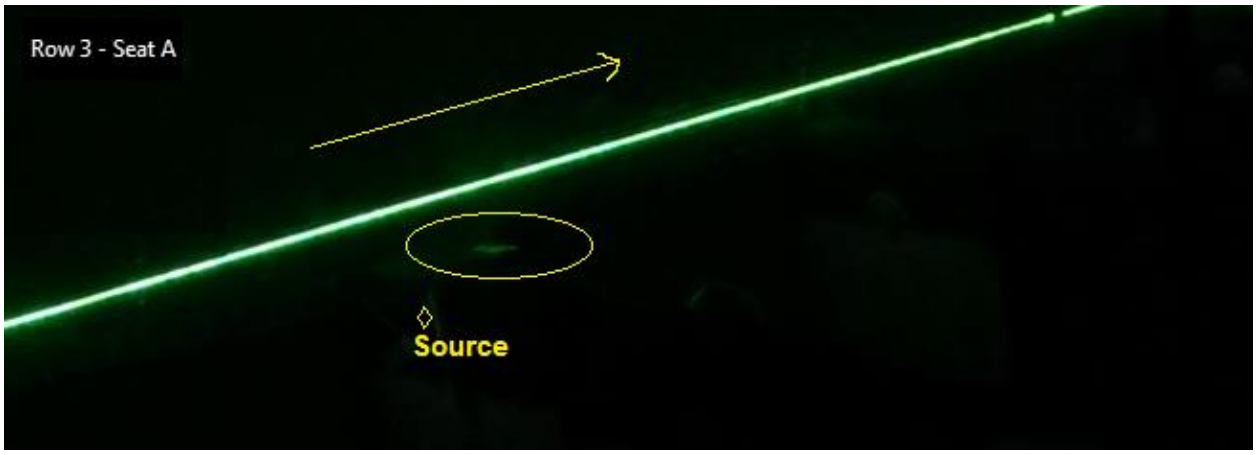

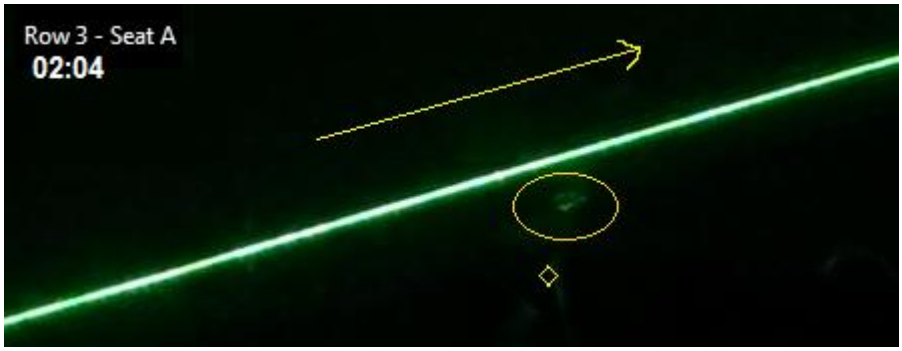

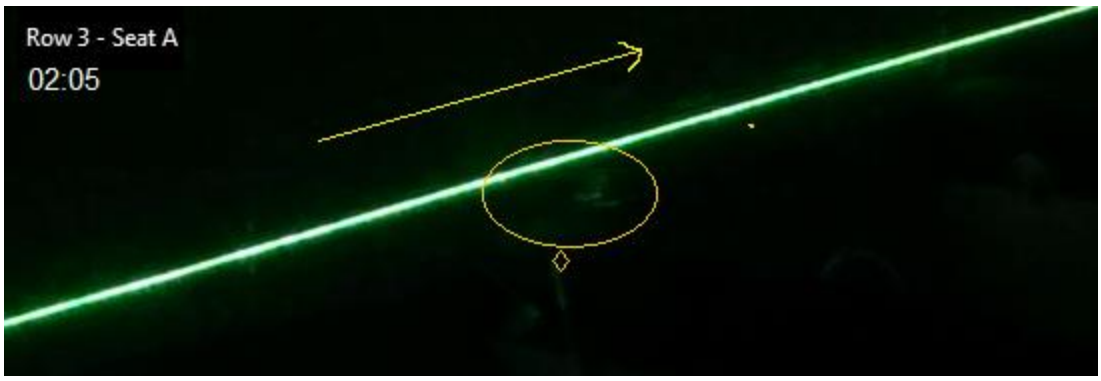

Event 2

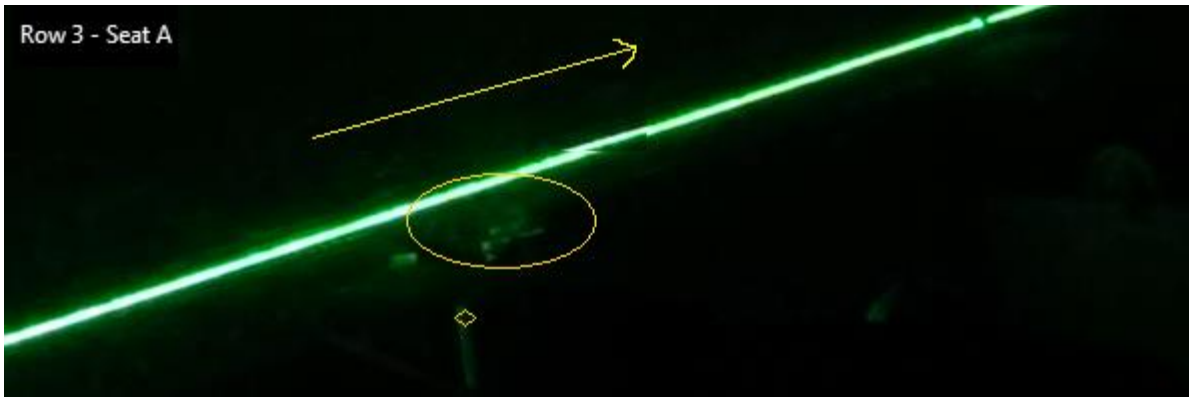

Release in Row 4 – Seat C

Event 1

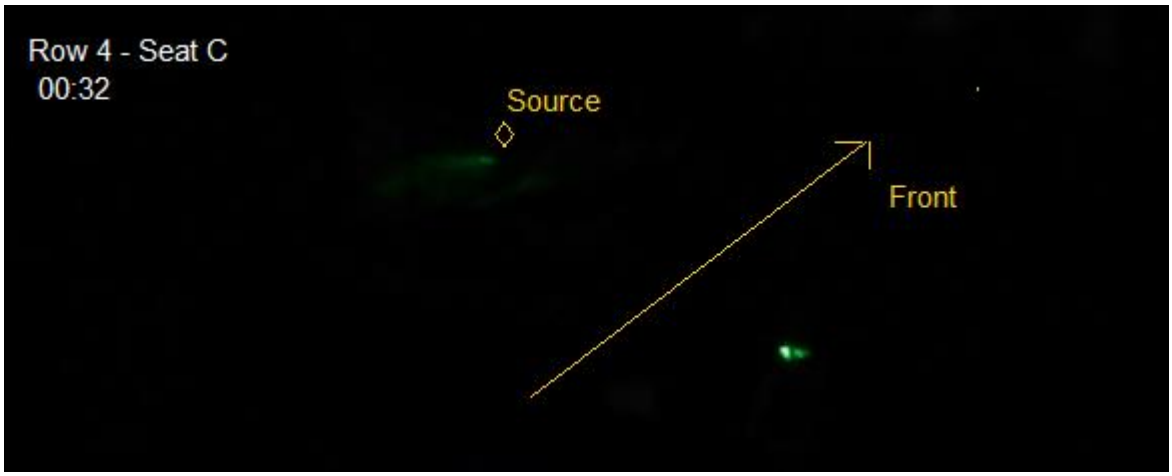

Event 2

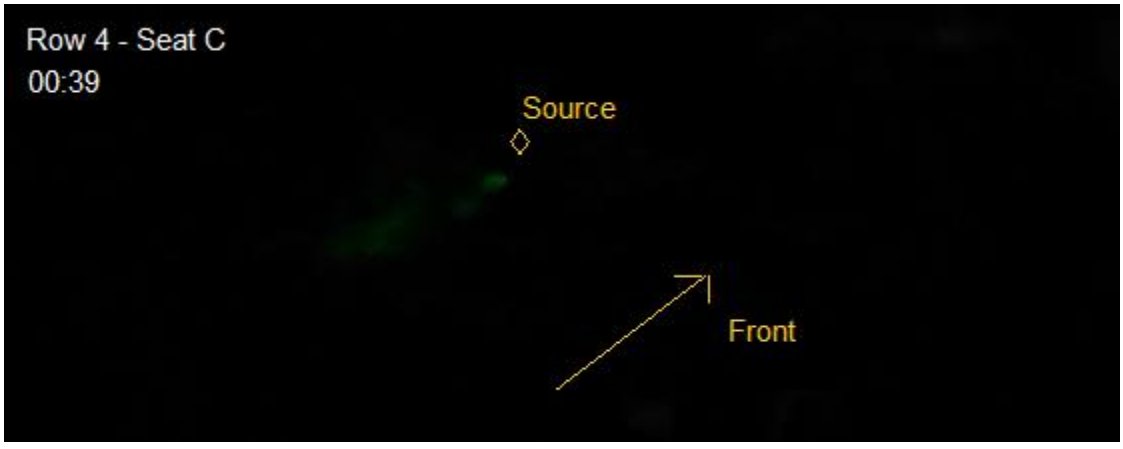

Event 3

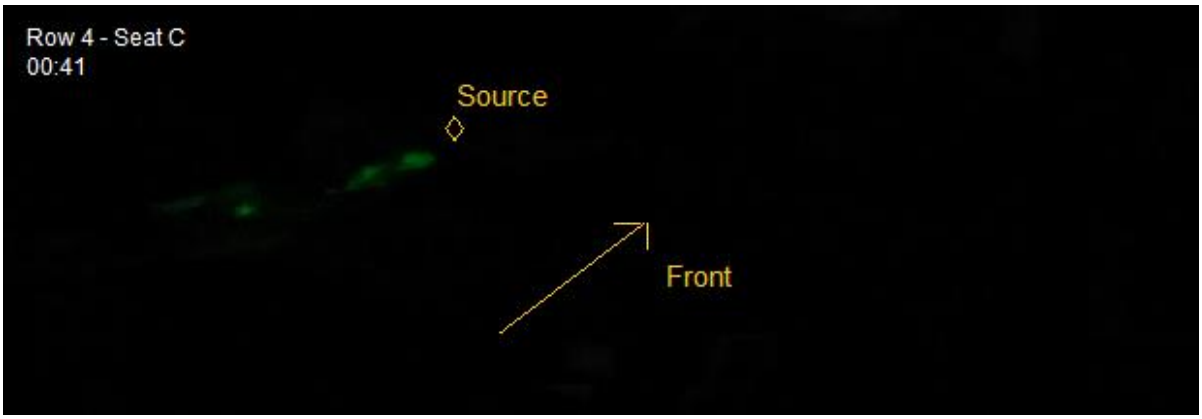

Event 4

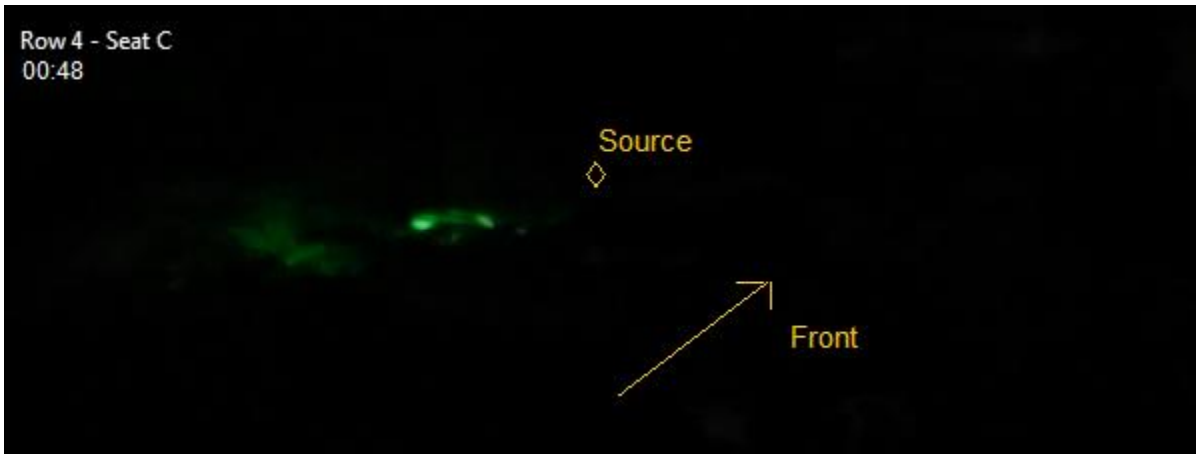

Event 5

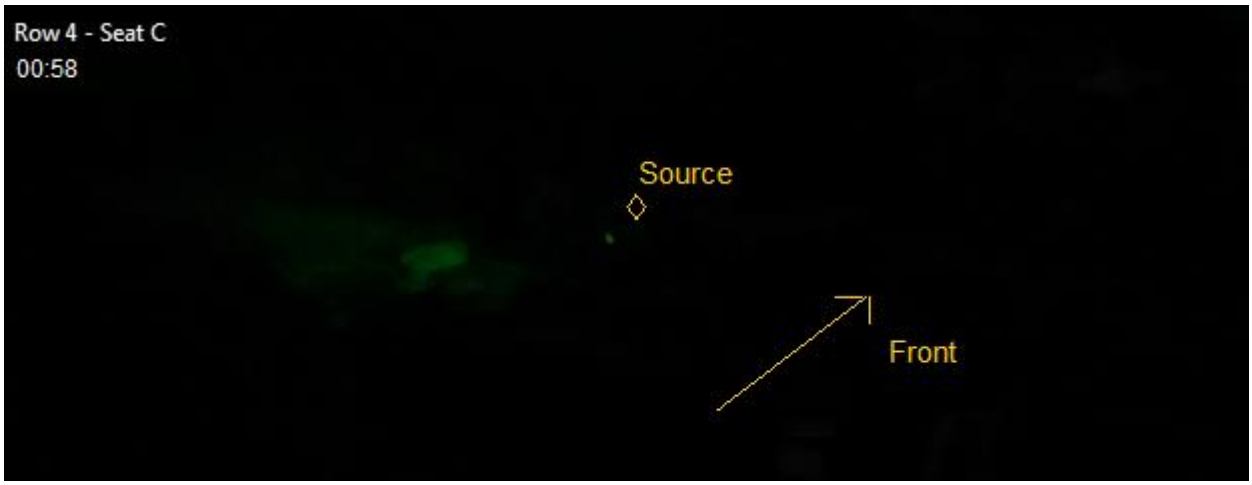

Event 6

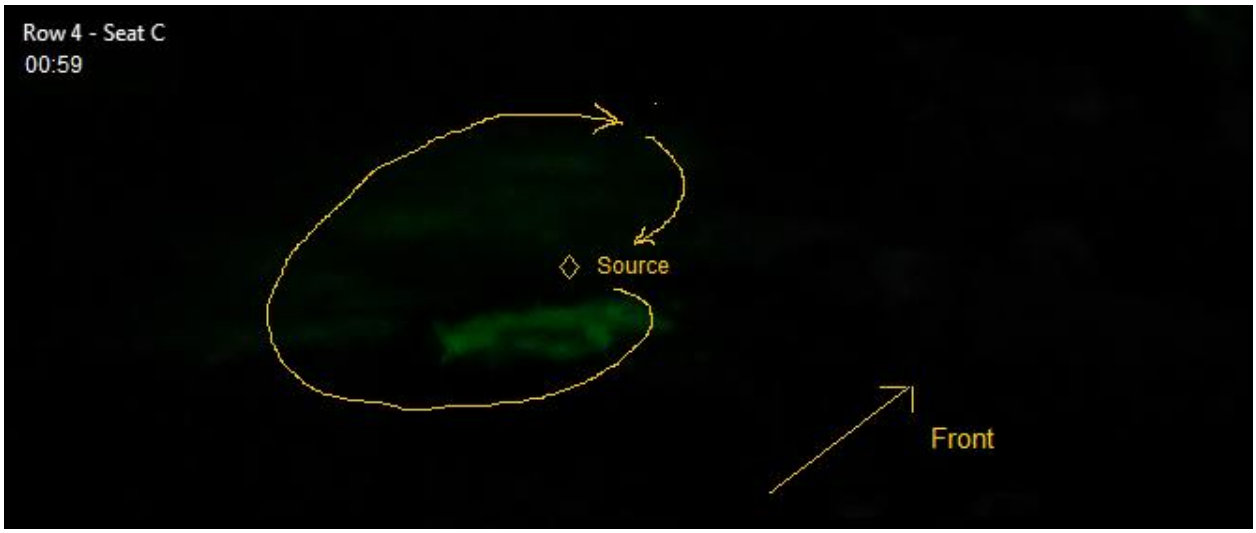

Event 7

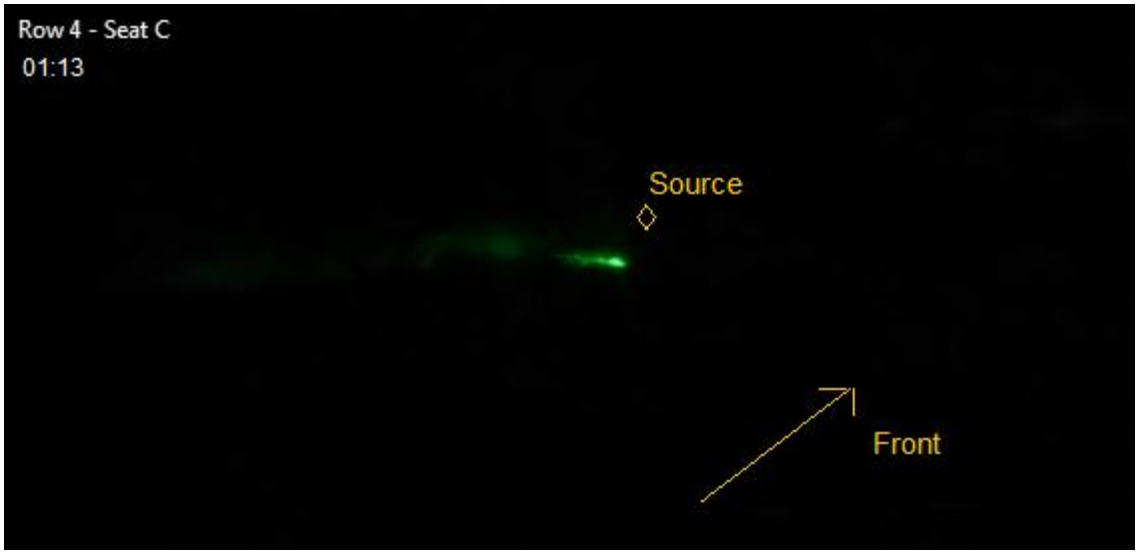

Release in Row 4 – Seat F

Event 1

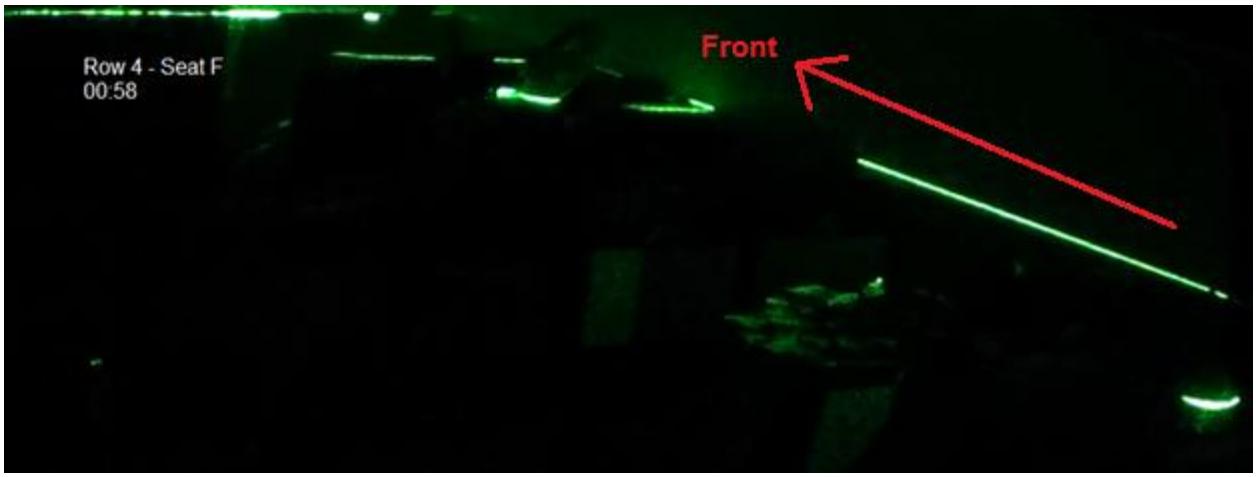

Event 2

Event 3

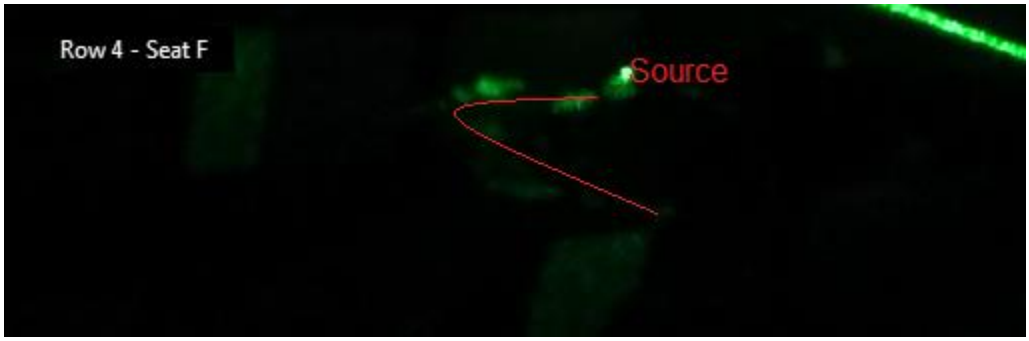

Event 4

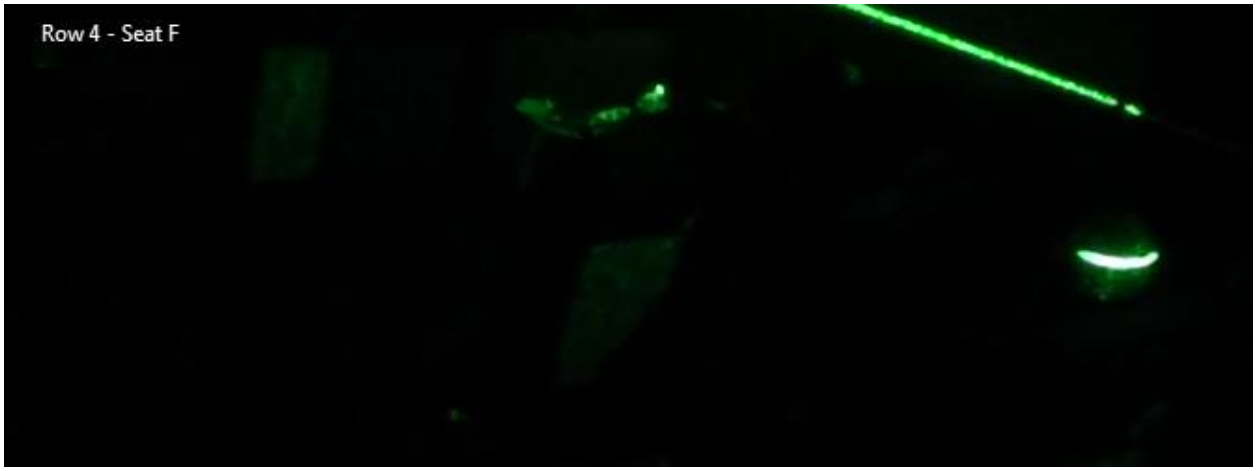

Event 5

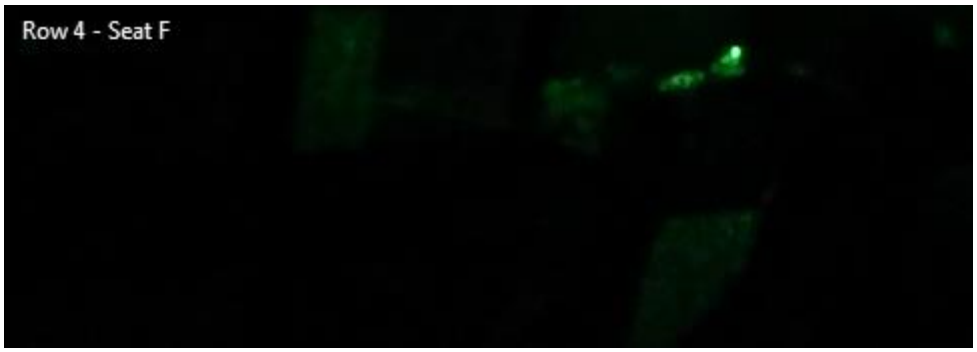

Event 6

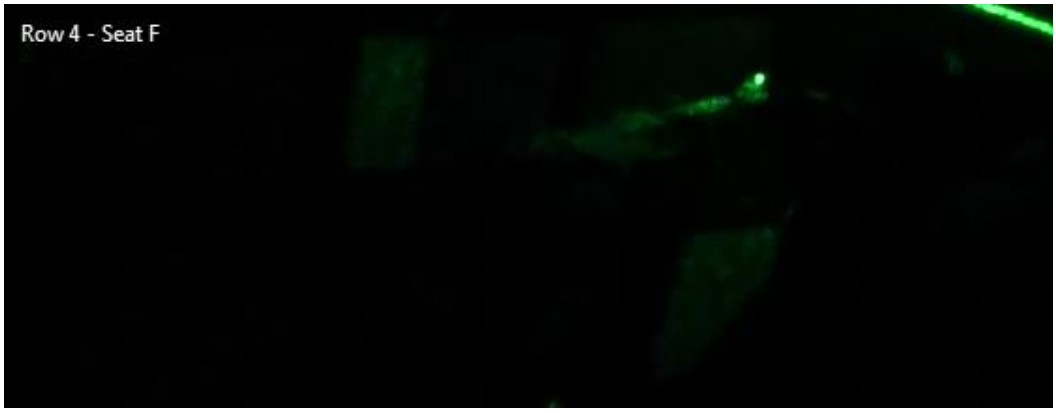

Event 7

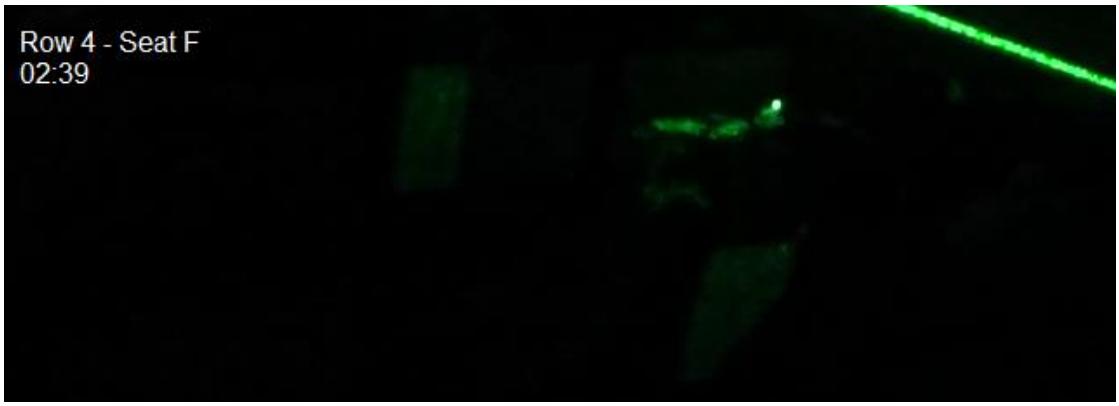

Event 8

Event 9

Release in Row 6 – Seat F

Event 1

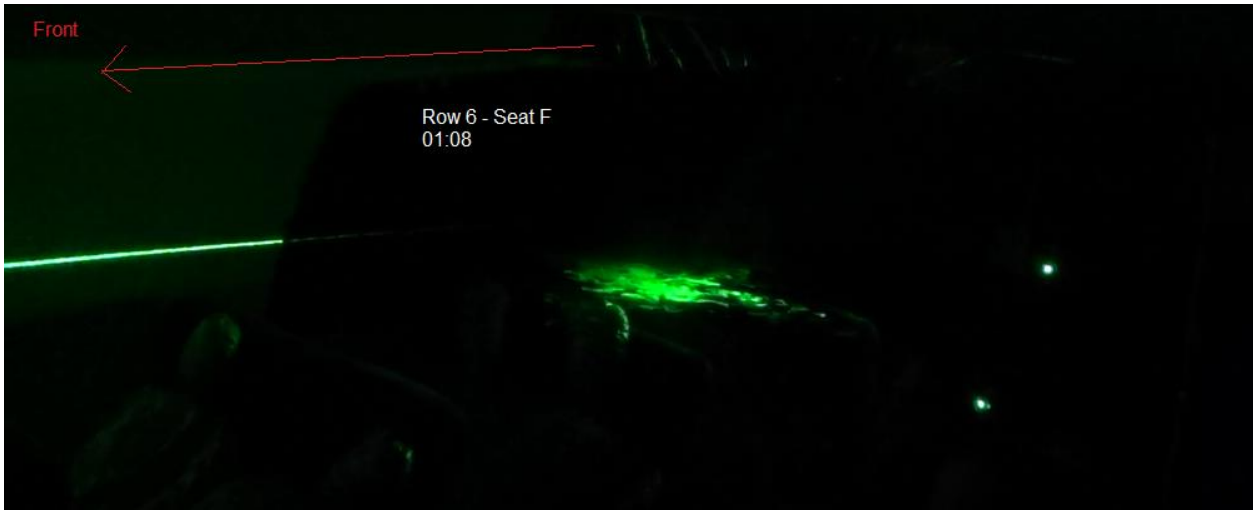

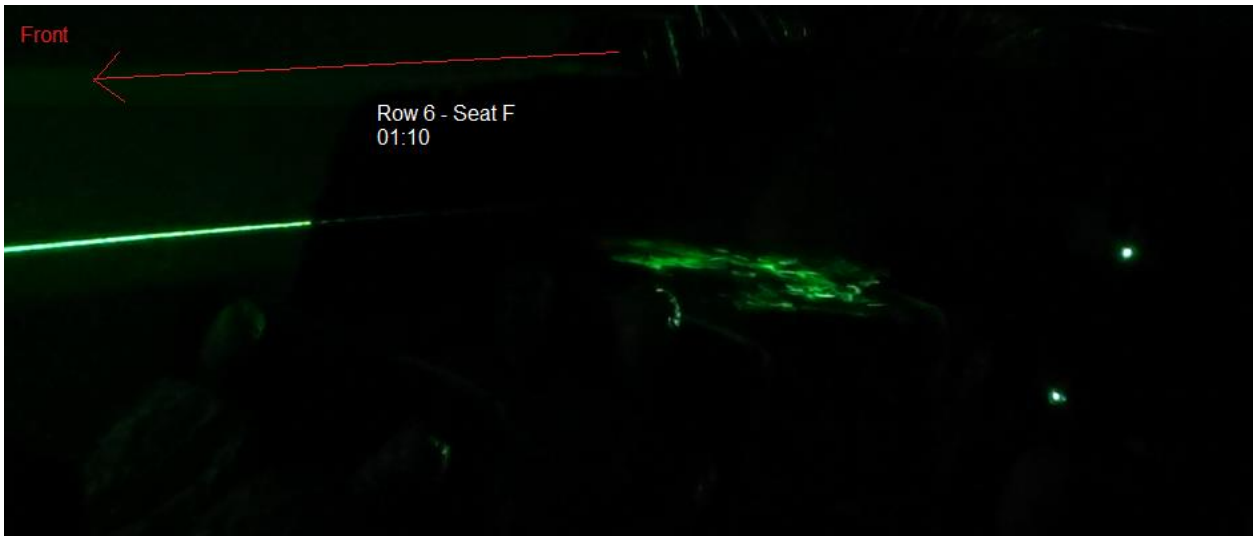
Front
Row 6 - Seat F
01:10

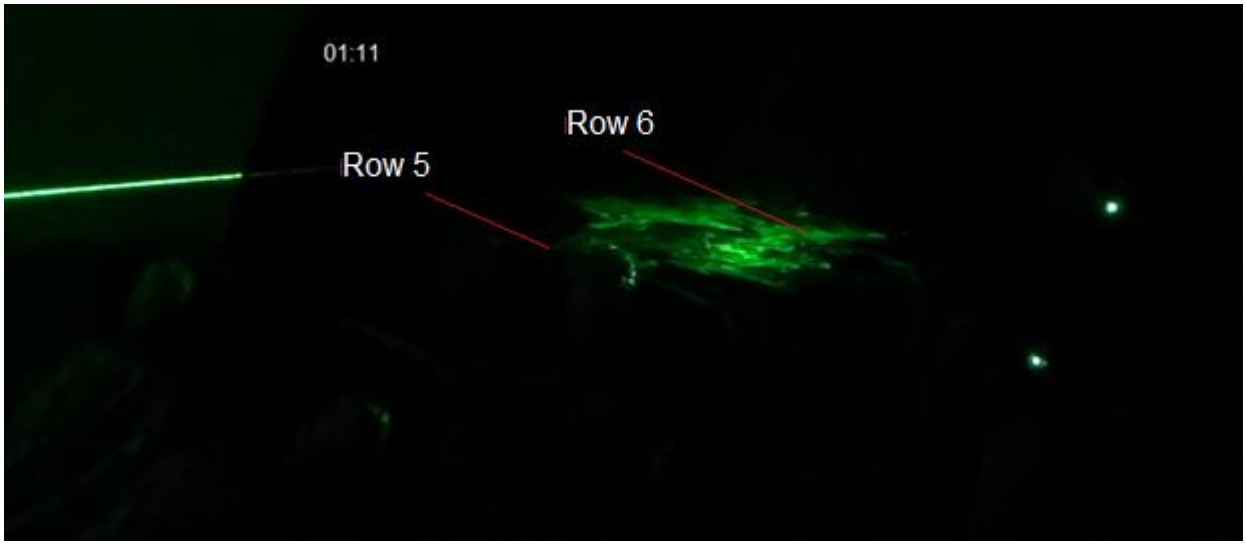
01:11
Row 6
Row 5

Event 2

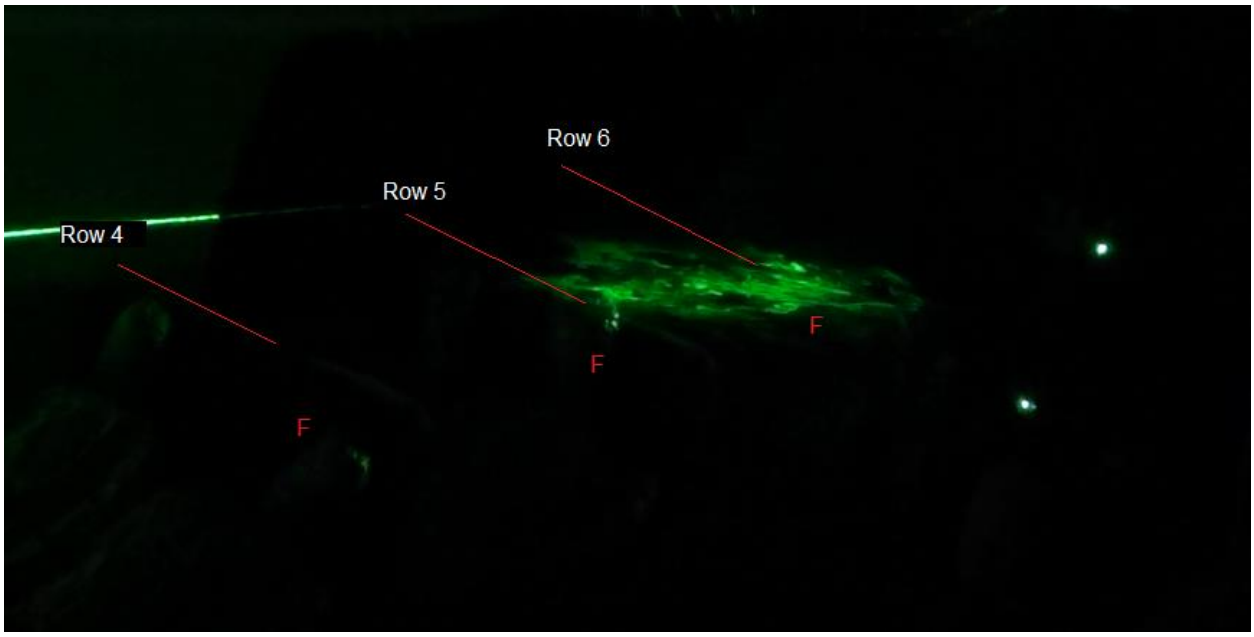

Event 3

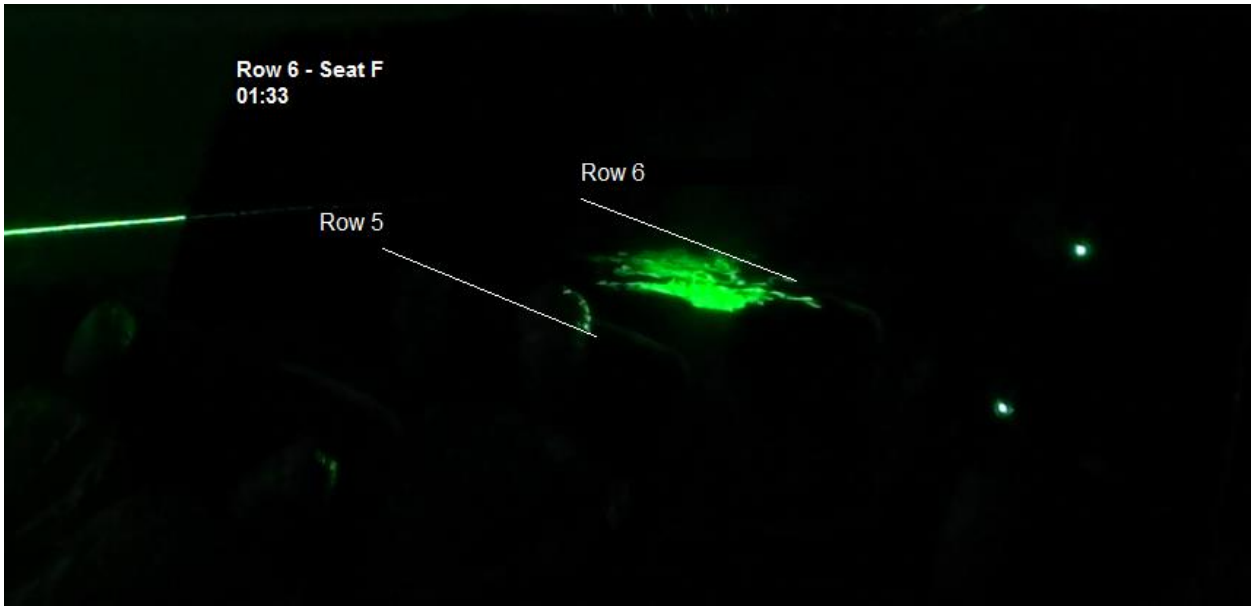

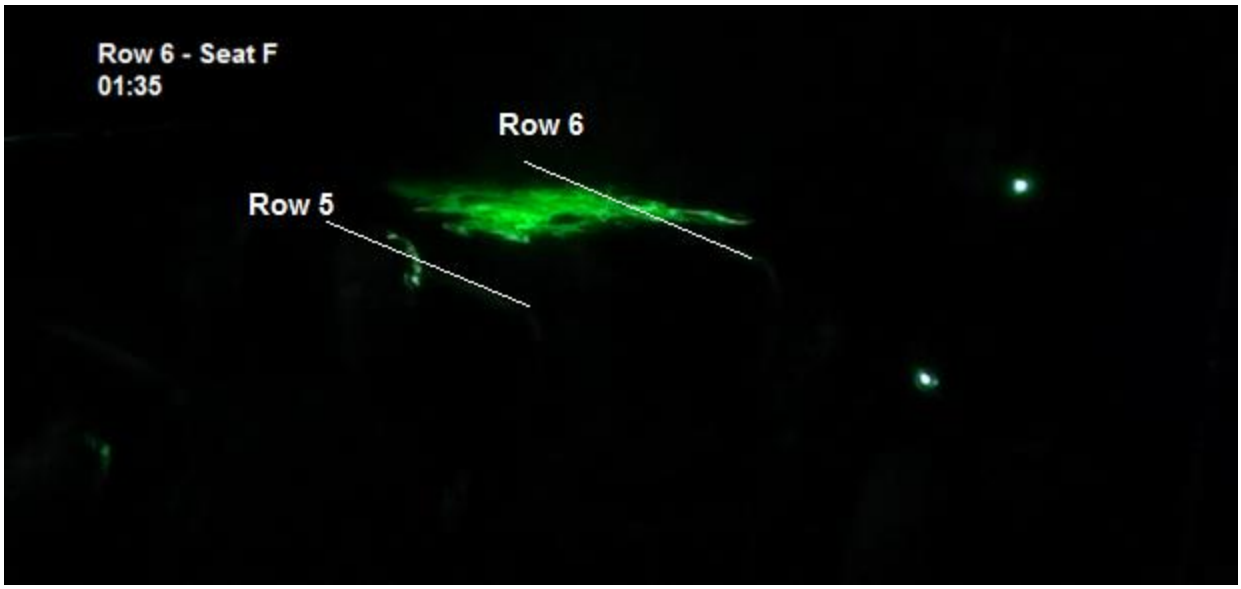
Row 6 - Seat F
01:35
Row 6
Row 5

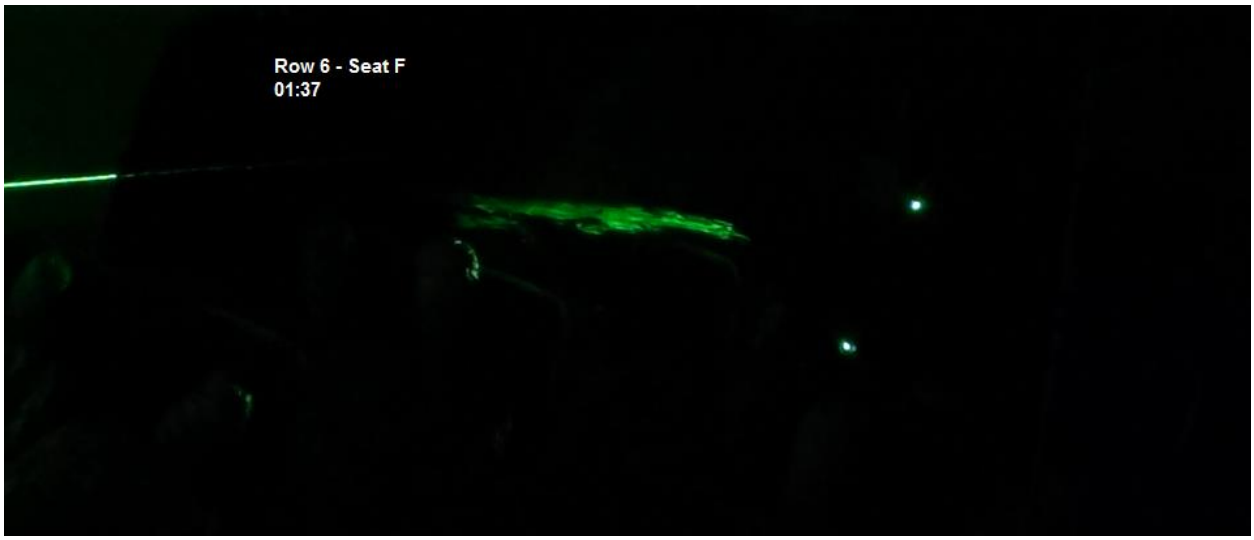
Row 6 - Seat F
01:37

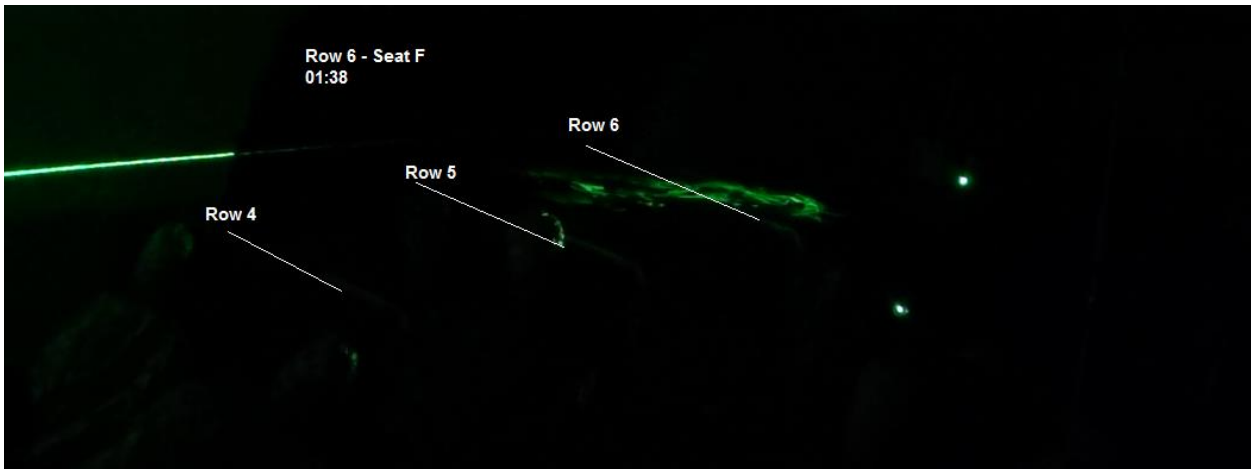
Row 6 - Seat F
01:38
Row 6
Row 5
Row 4

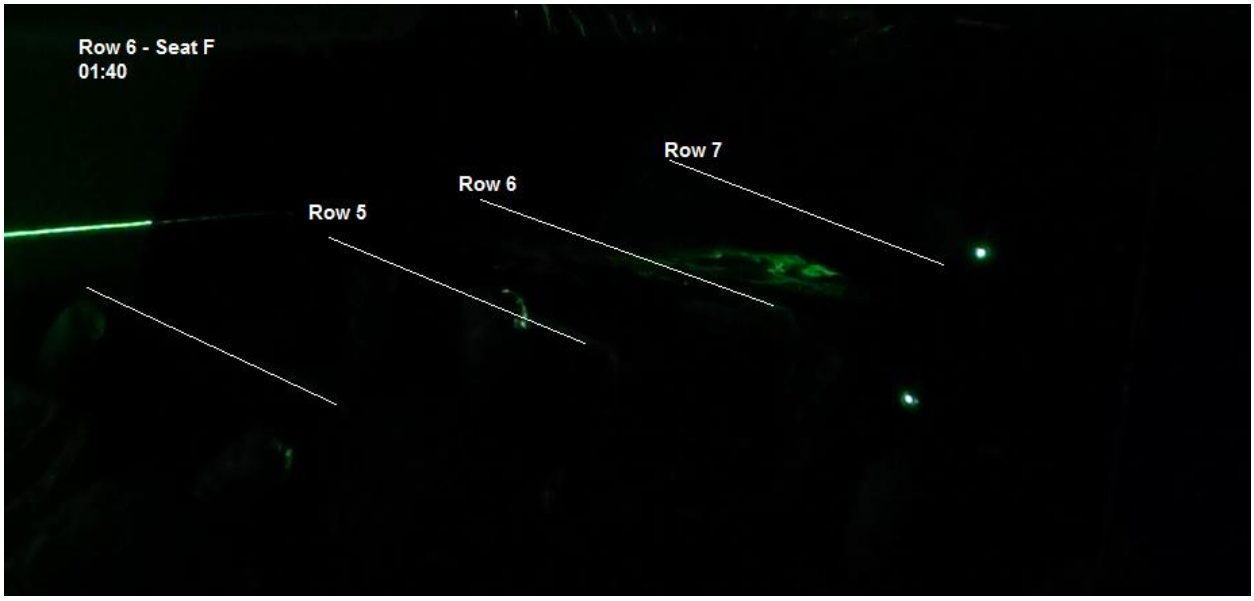
Row 6 - Seat F
01:40
Row 7
Row 6
Row 5

Release in Row 6 – Seat B

Event 1

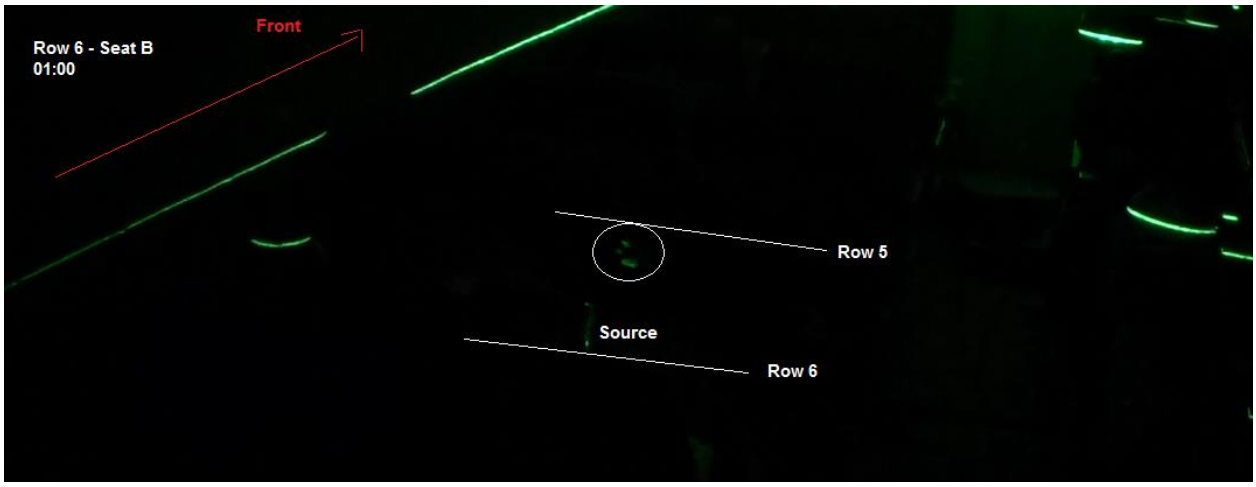

Event 2

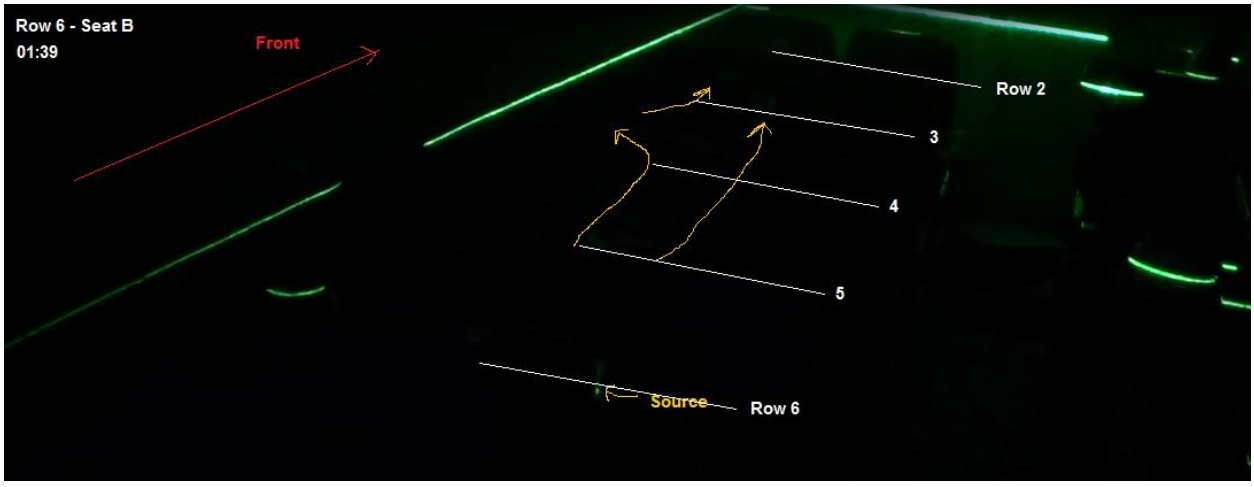

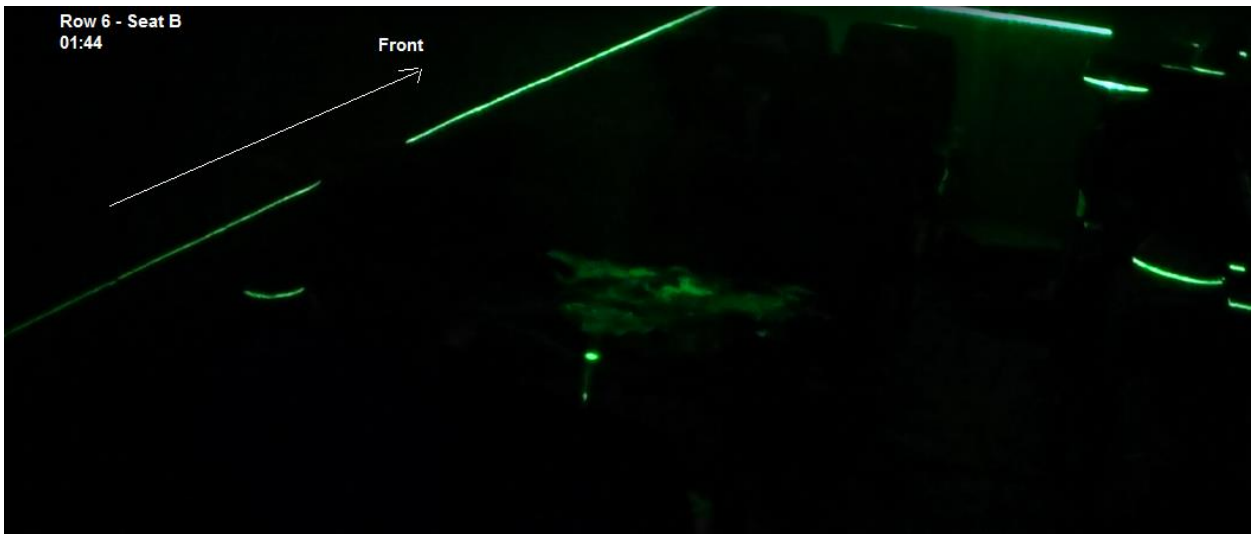

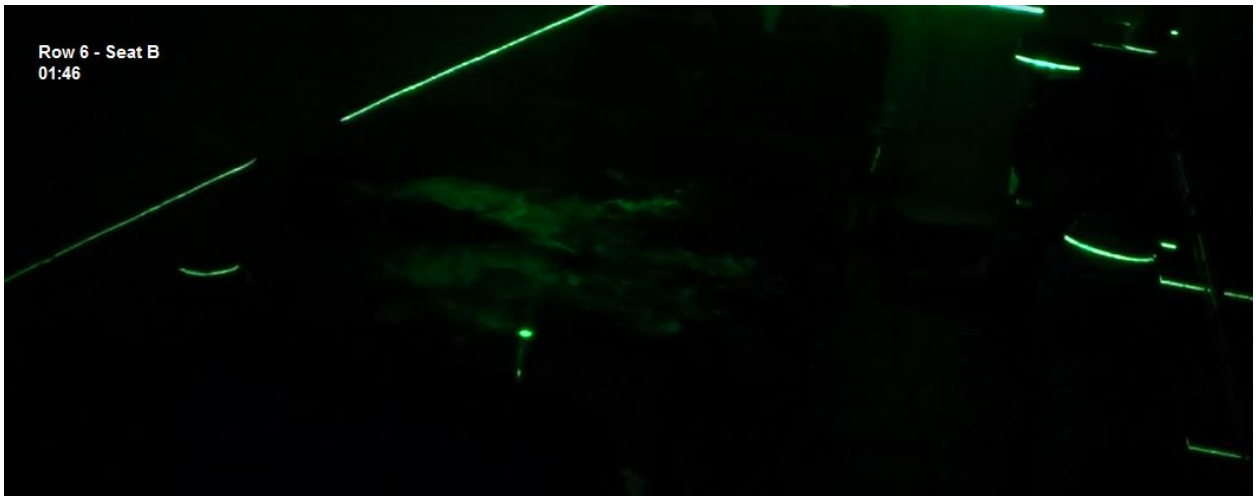
Row 6 - Seat B
01:46

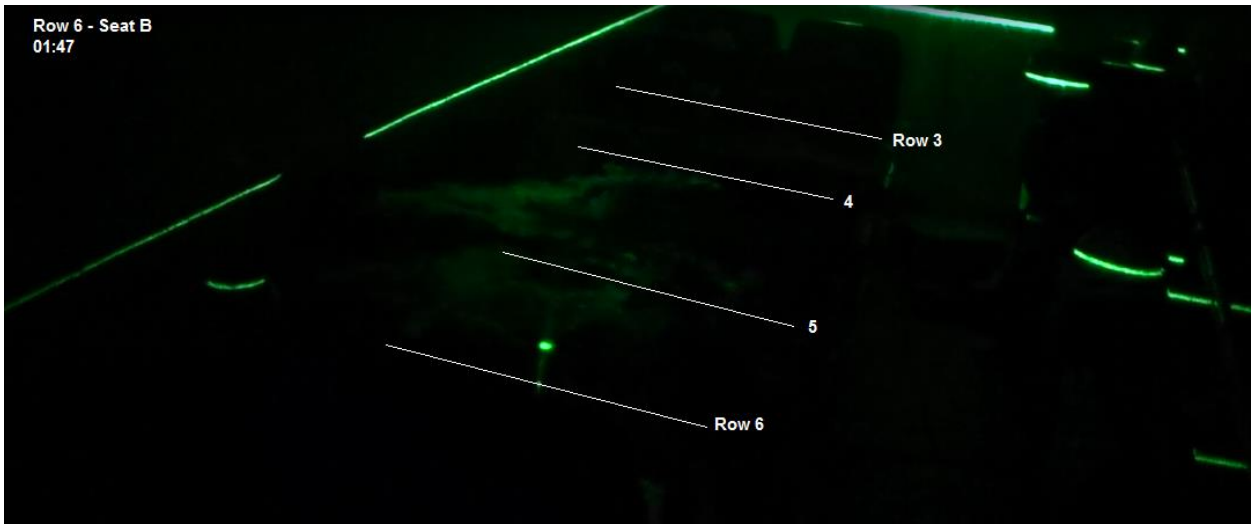
Row 6 - Seat B
01:47
Row 3
4
5
Row 6


Row 6 - Seat B
01:48

Event 3

Event 4

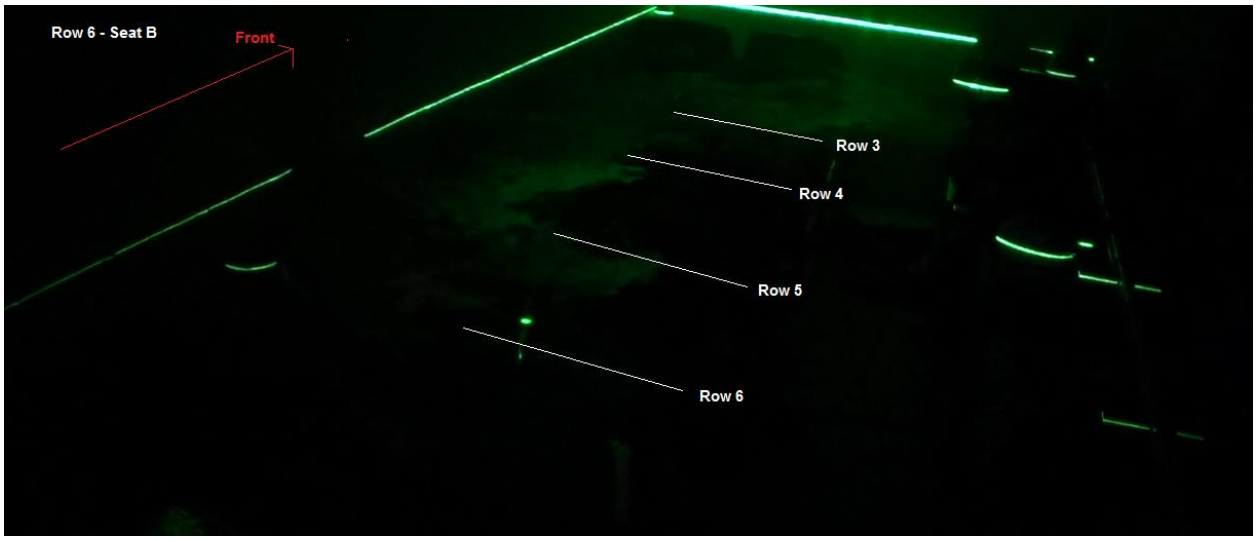

Event 5

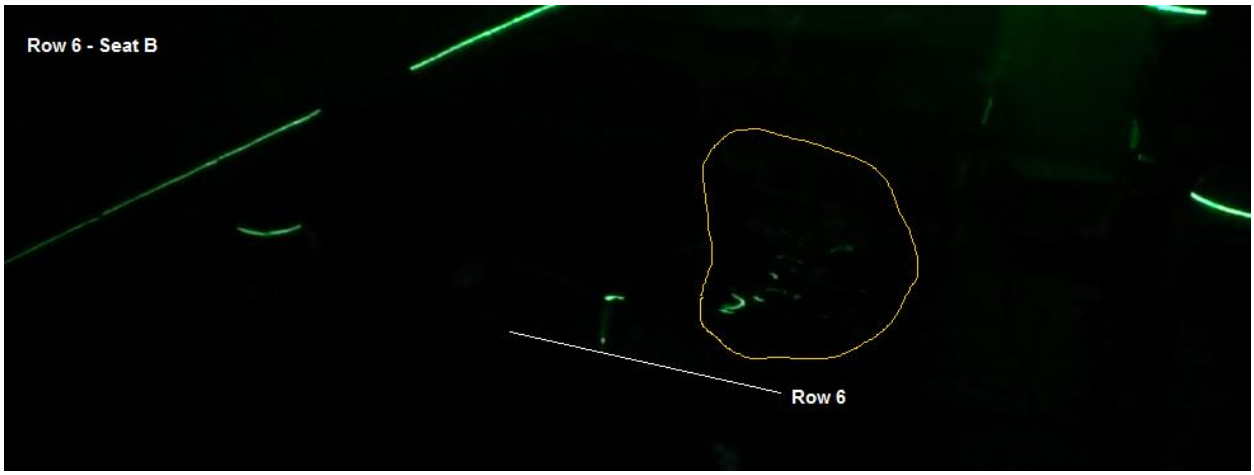

Release in Row 5 – Seat B

Event 1

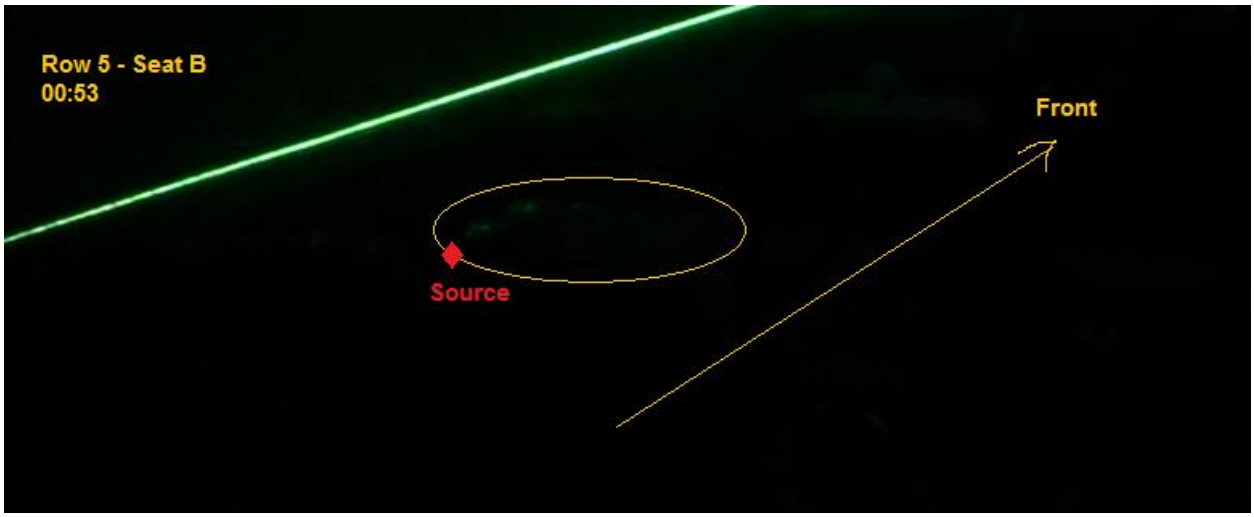

Event 2

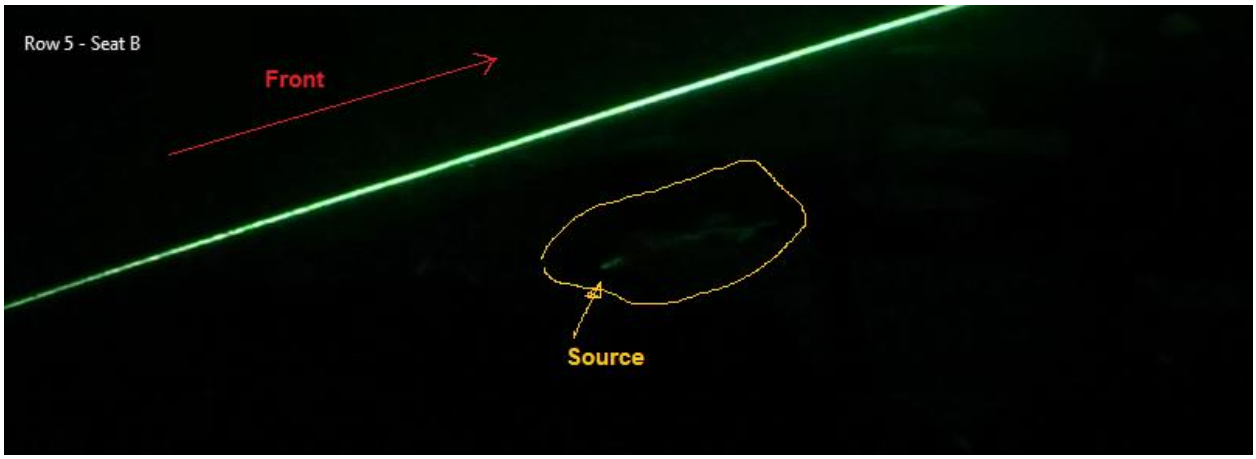

Event 3

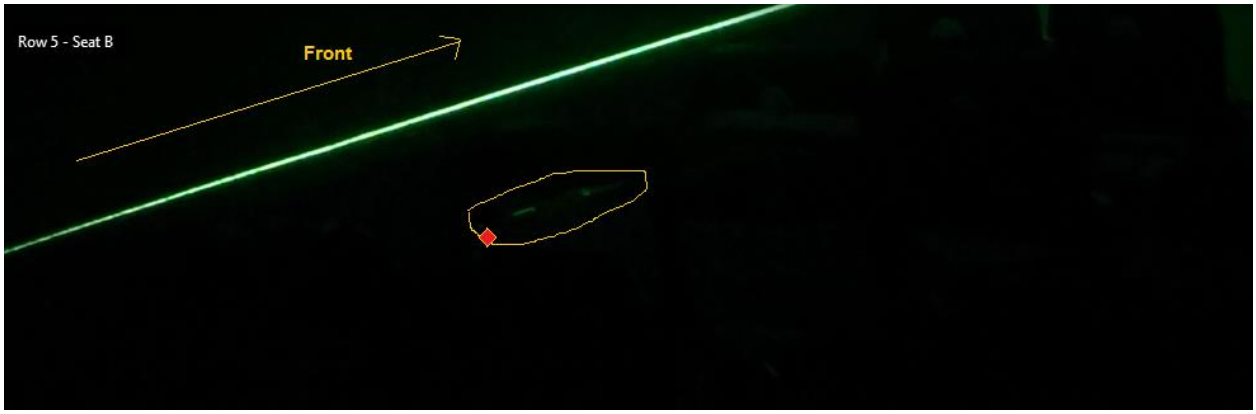

Event 4

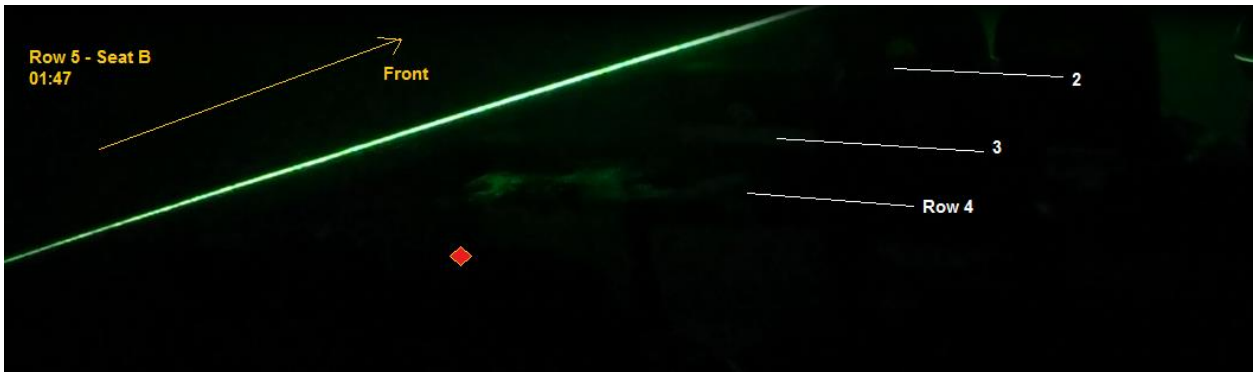
Row 5 - Seat B
01:47
Front
2
3
Row 4


Row 5 - Seat B
01:48
Row 4


Row 5 - Seat B
01:49
Row 4

Event 5

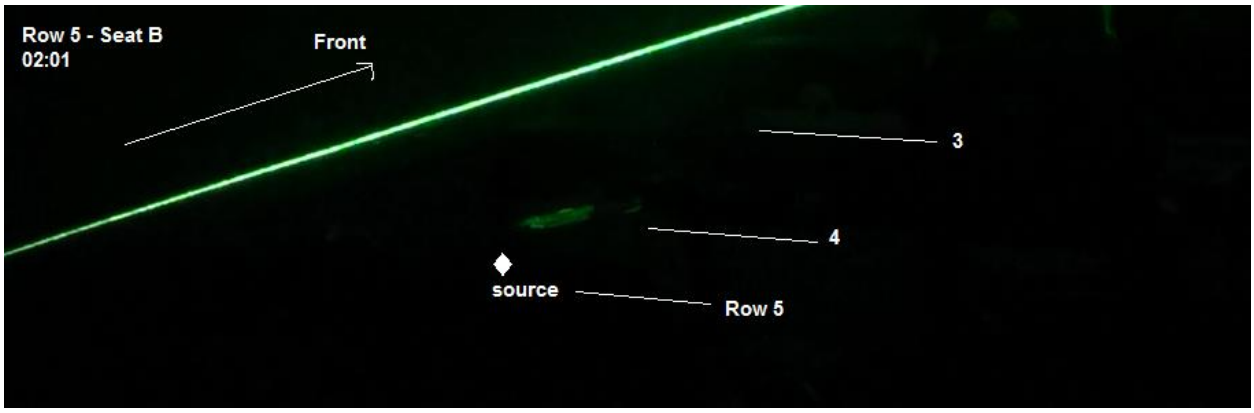

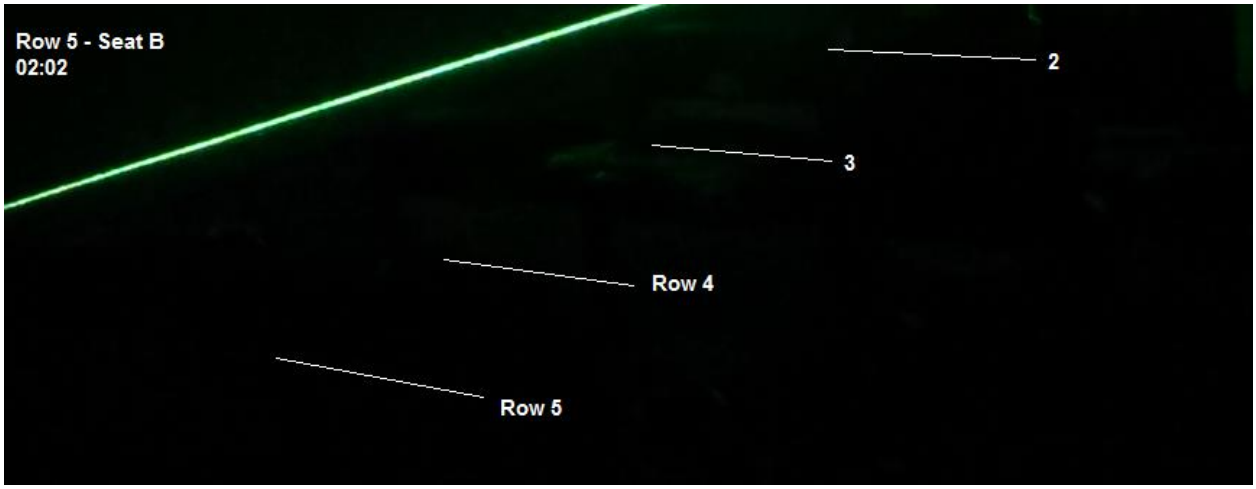

Event 6

Event 7

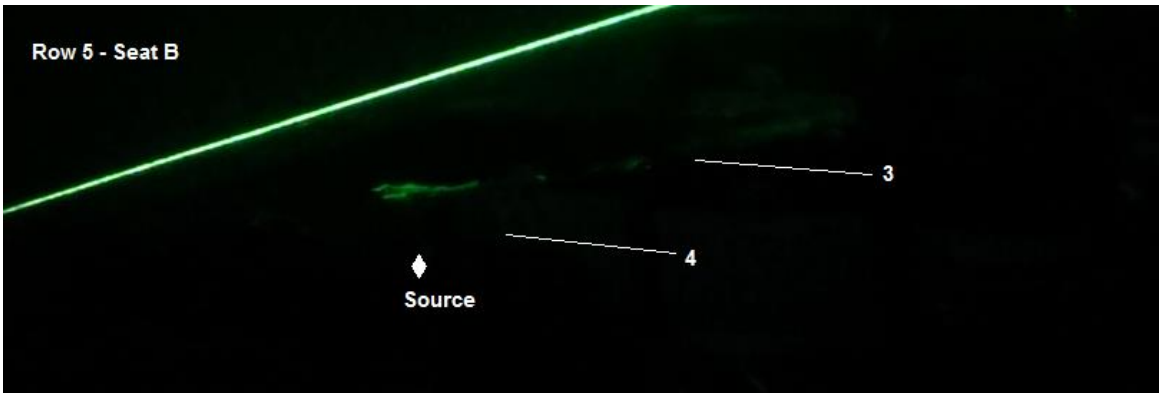

Release in Row 8 – Seat F

Event 1

Event 2

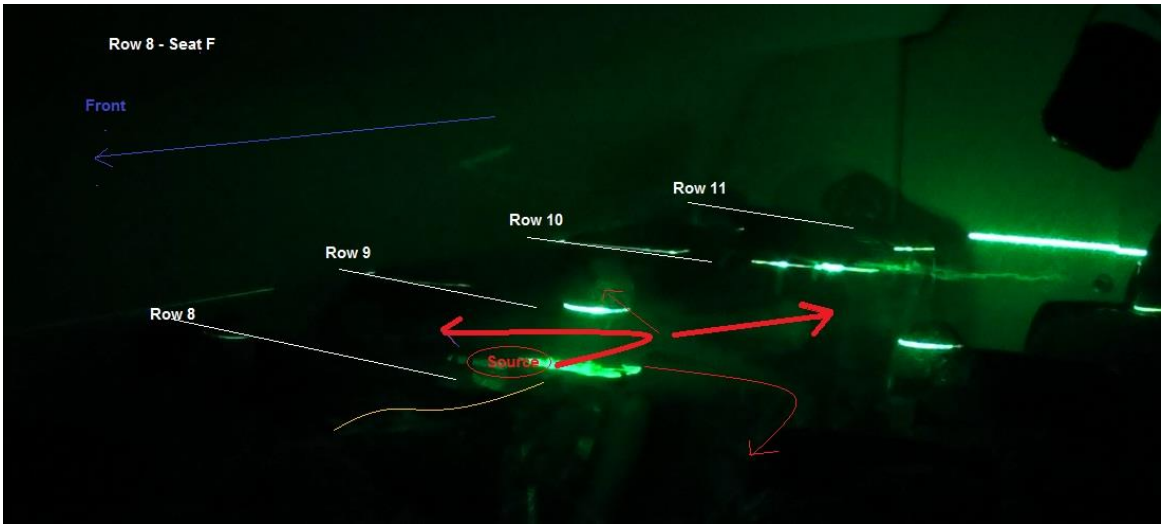

Release in Row 9 – Seat B

Event 1

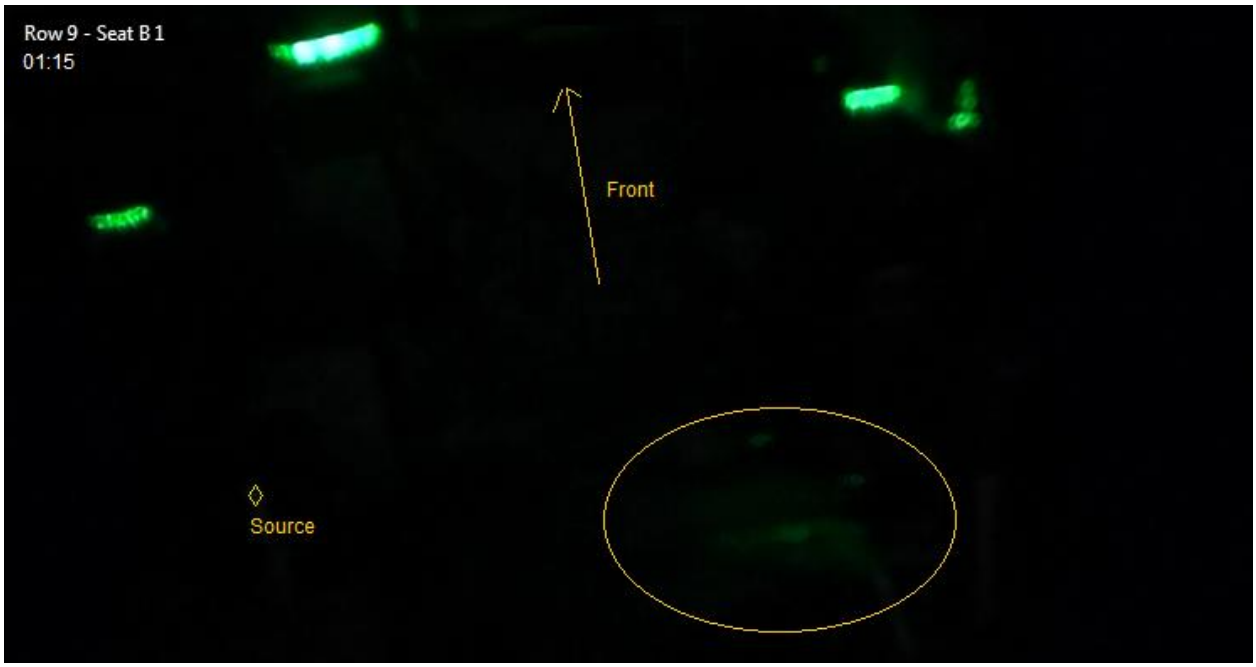

Event 2

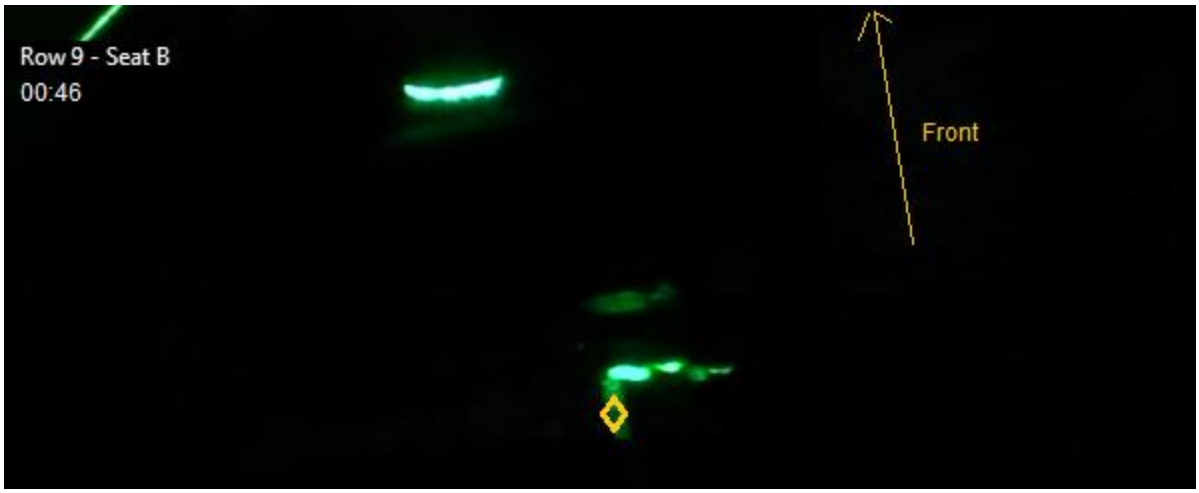

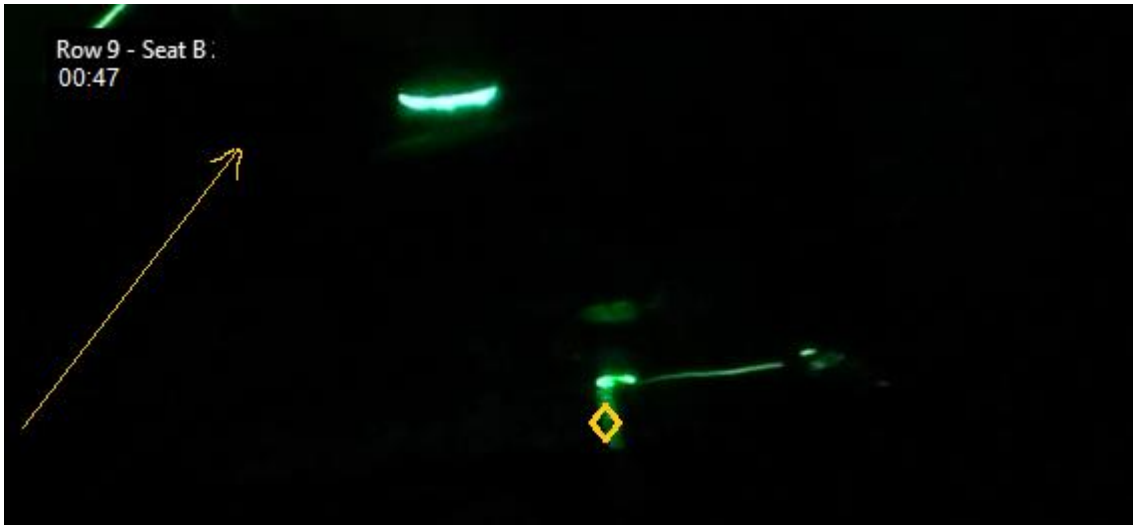

Event 3

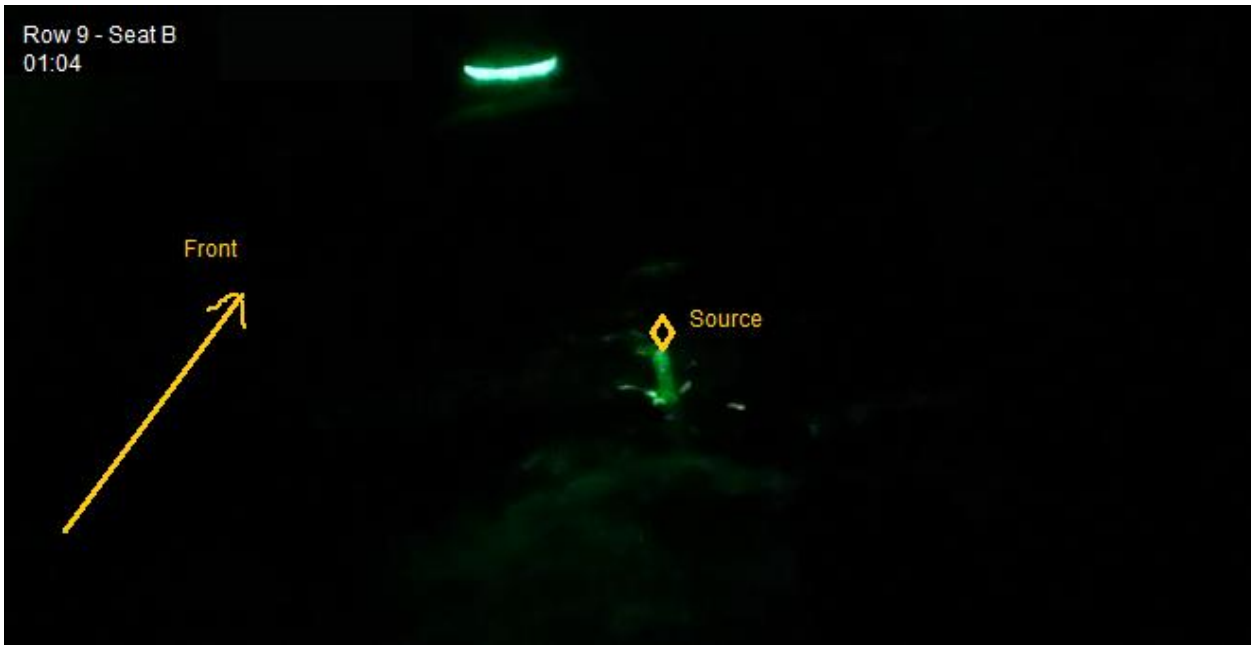

Release in Row 9 – Seat C

Event 1

Event 2

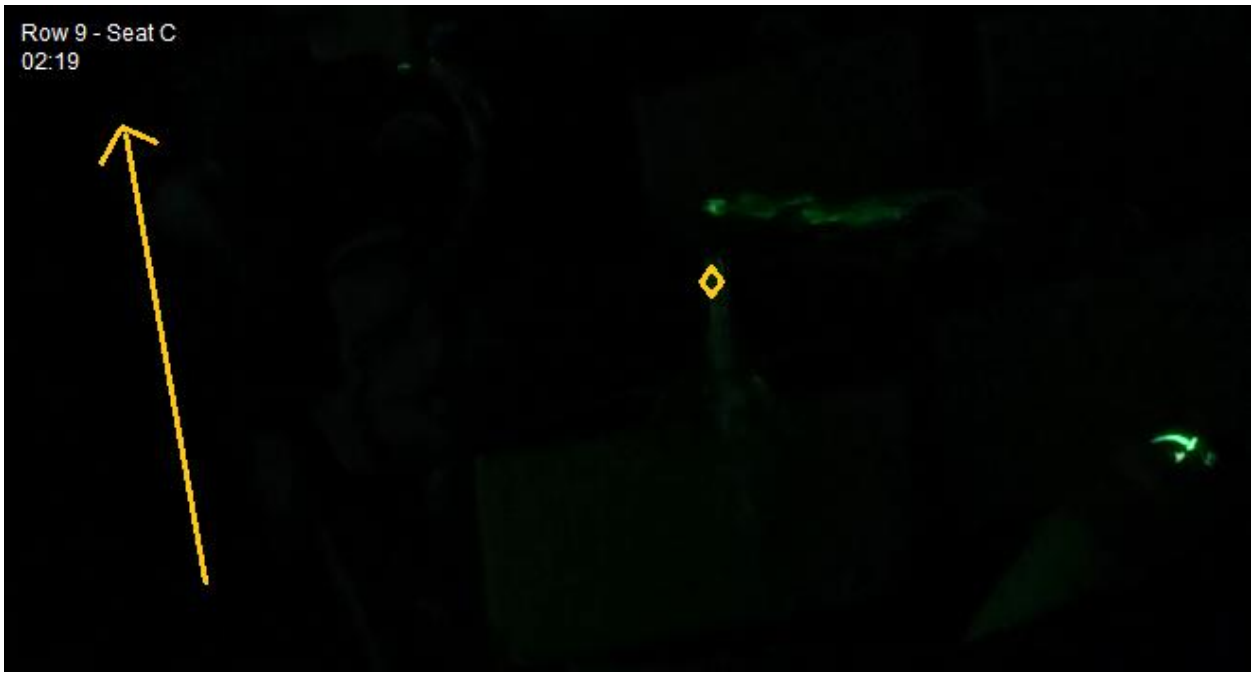

Event 3

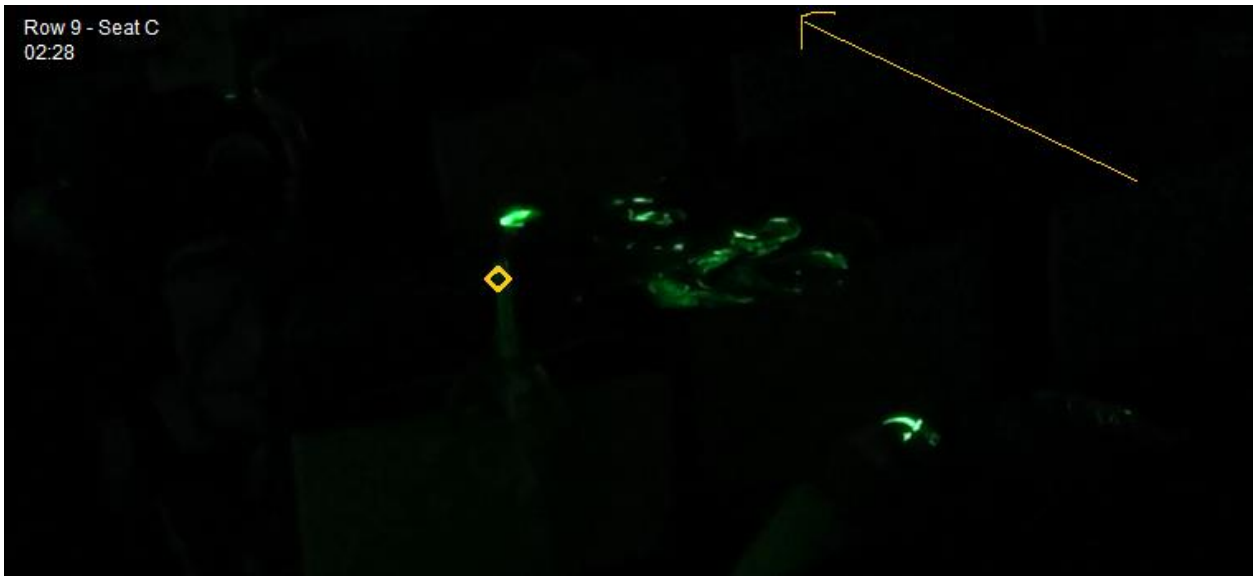

Event 4

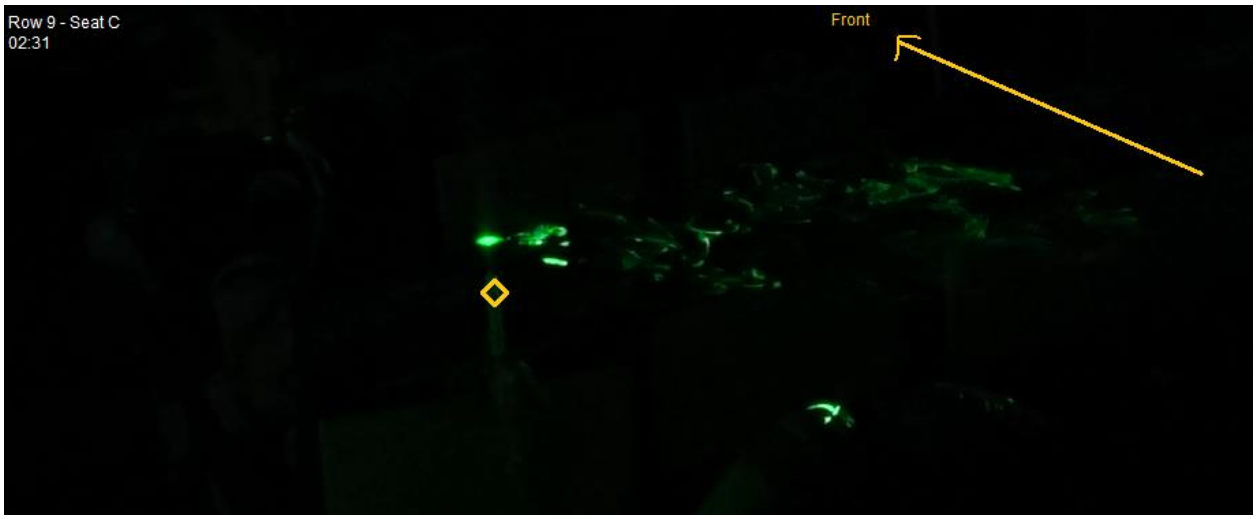

Release in Row 10 – Seat F

Event 1

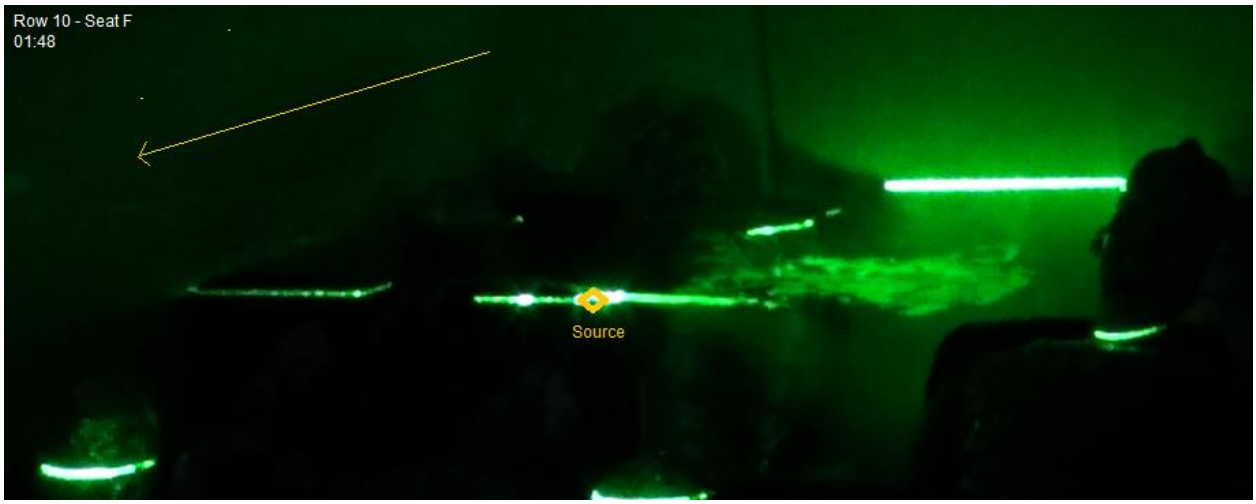

Event 2

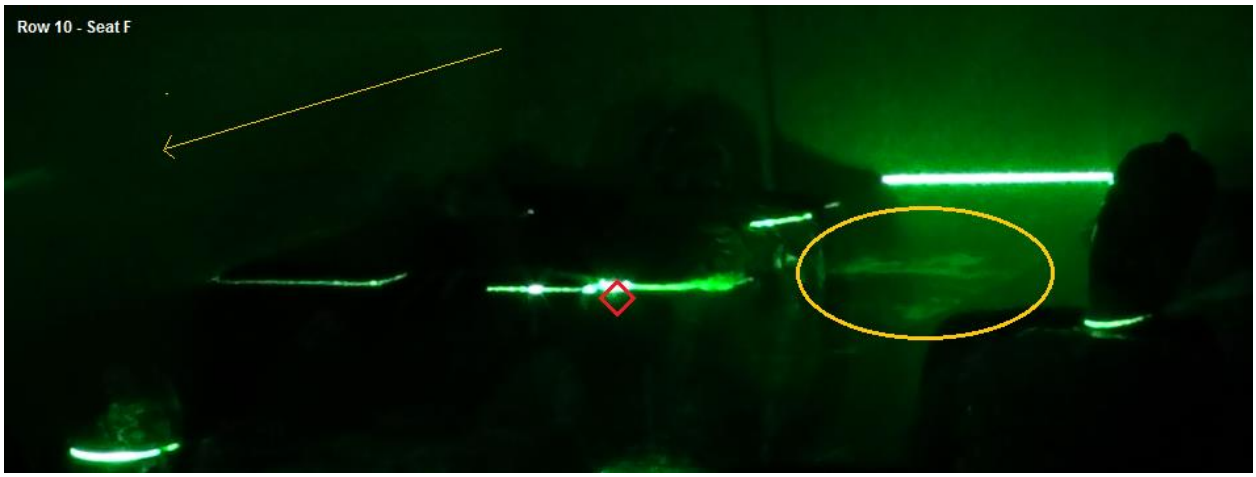

Event 3

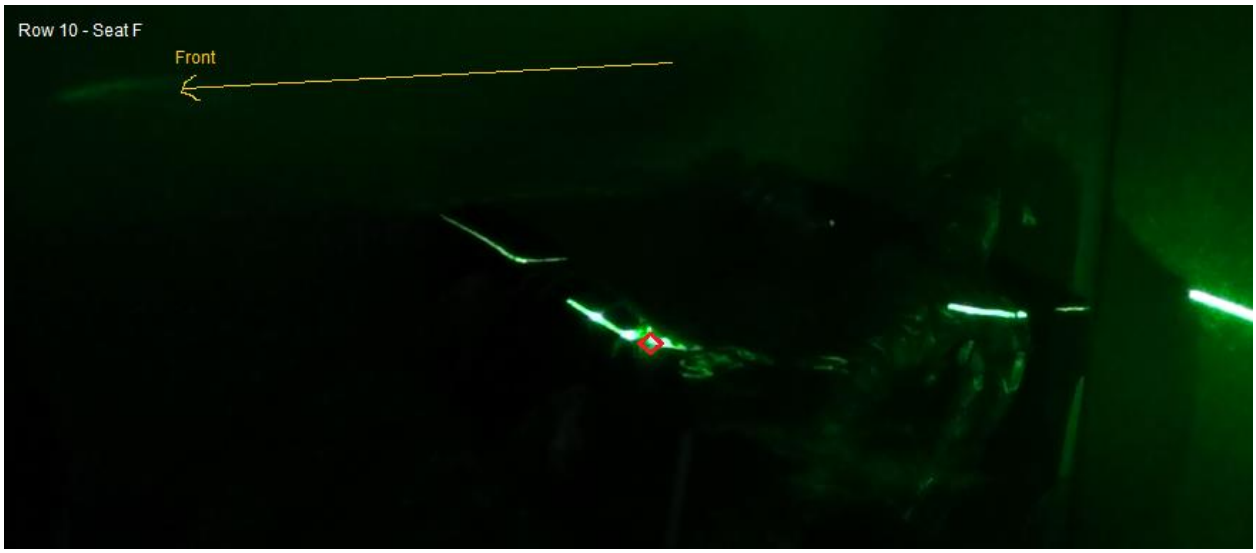

Appendix C - Normalized Tracer Gas Results with Heated Manikins

In this appendix, the normalized CO_2 in each location during each test along with the average are presented under heated running conditions.

Release in 2D

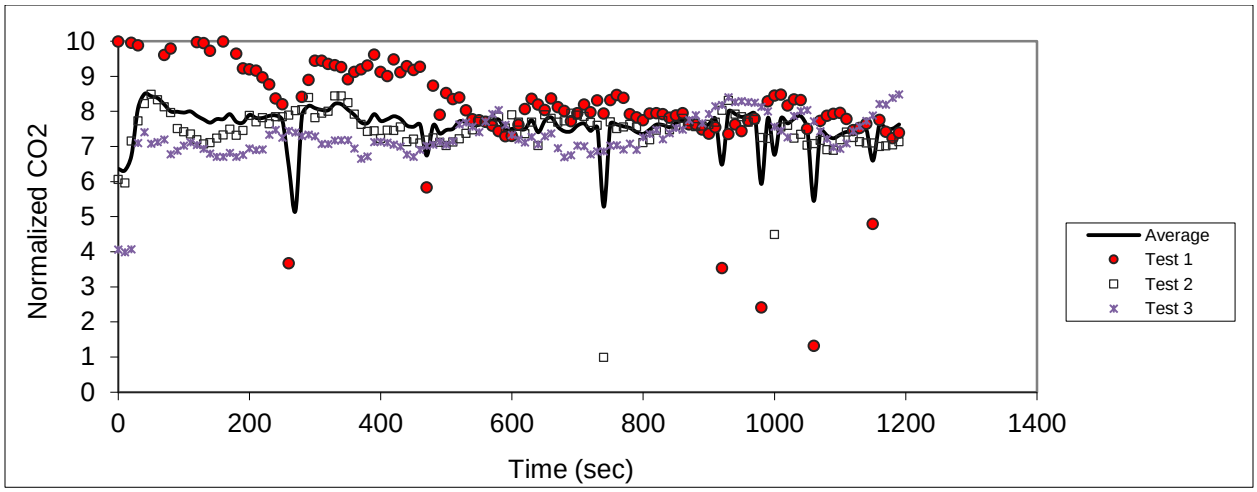

Figure C.1 - Sampling in seat 2D (release in 2D)

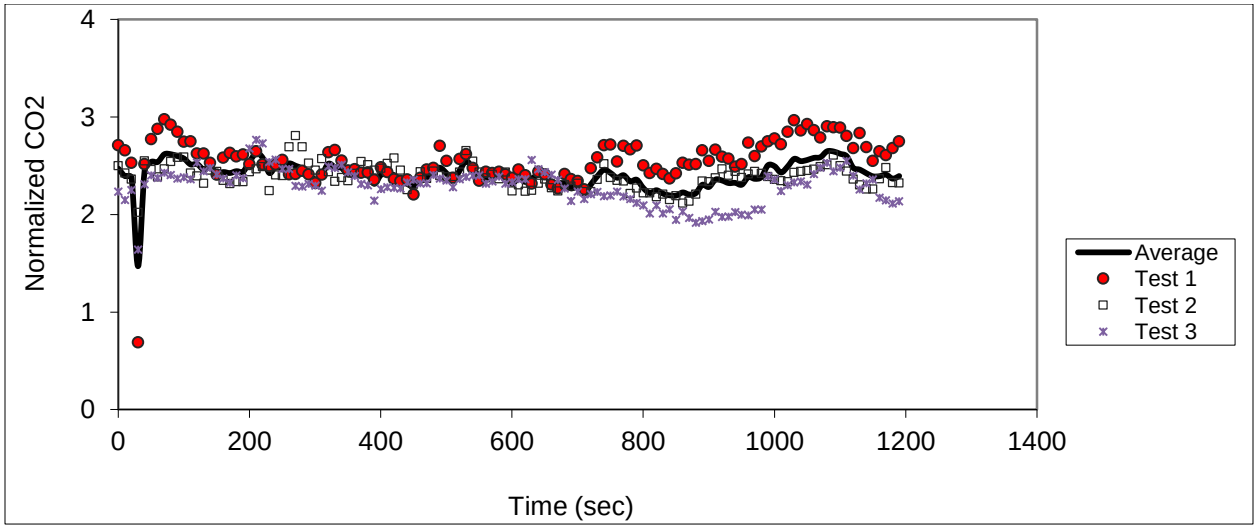

Figure C.2 – Sampling in seat 1B (release in 2D)

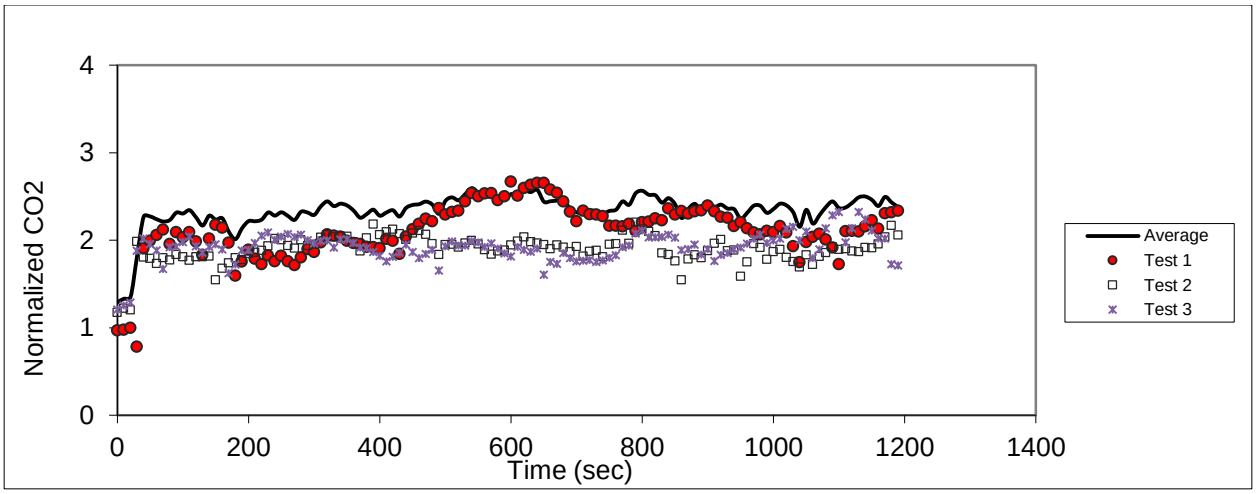

Figure C.3 – Sampling in seat 2B (release in 2D)

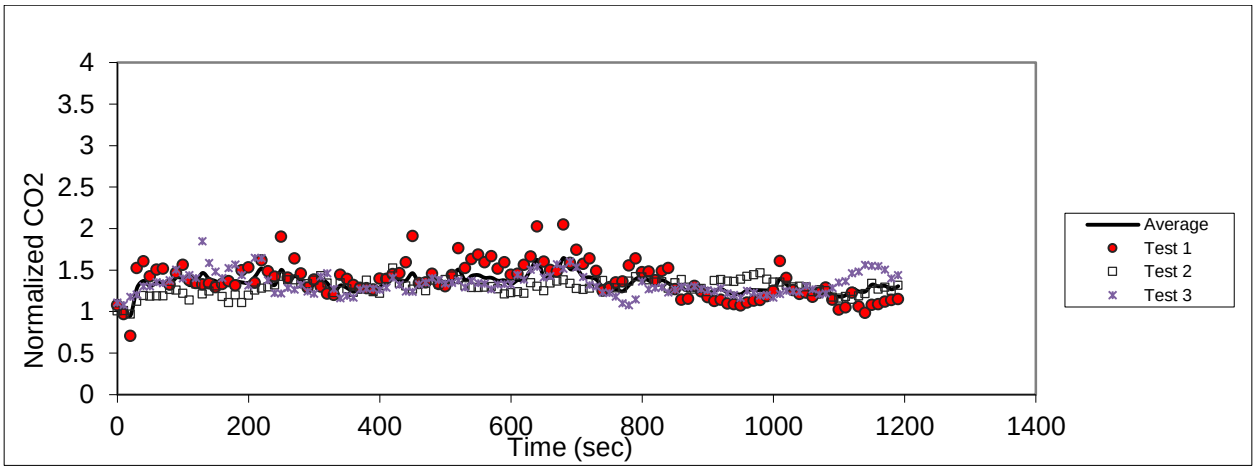

Figure C.4 – Sampling in seat 3B (release in 2D)

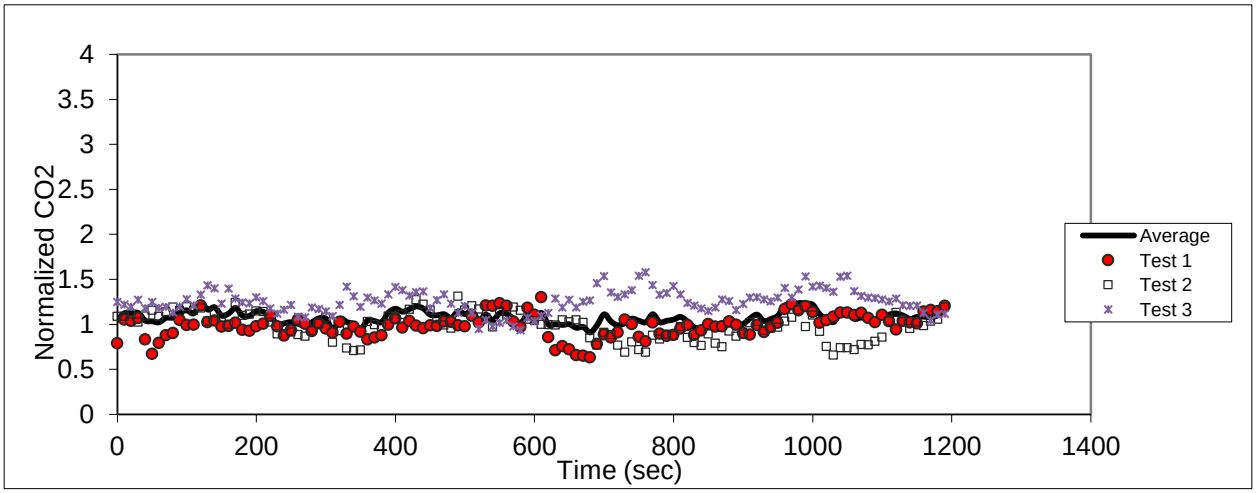

Figure C.5 - Sampling in seat 4B (release in 2D)

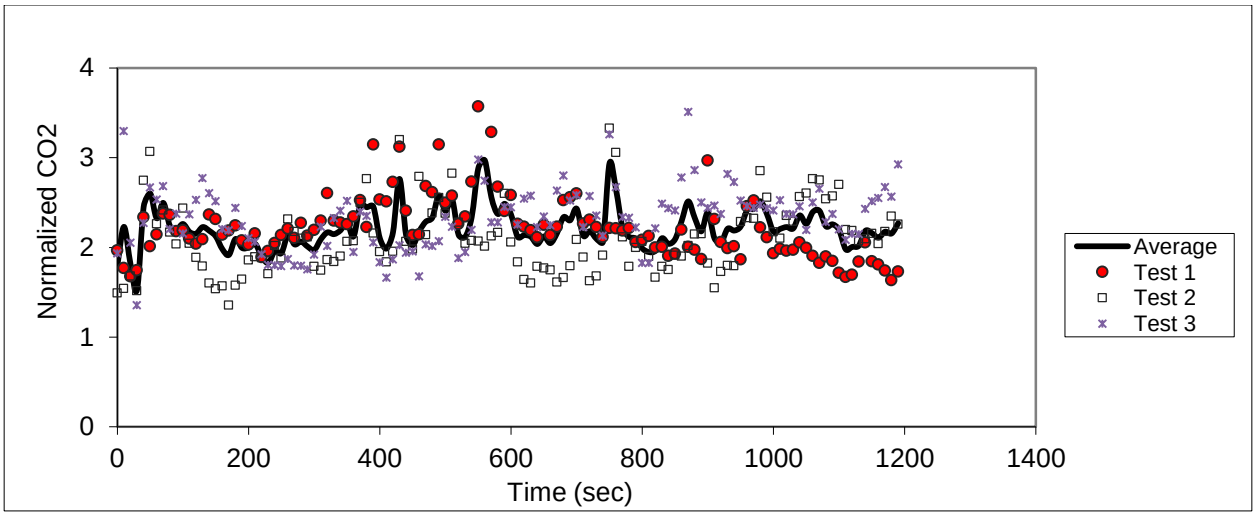

Figure C.6 – Sampling in seat 1C (release in 2D)

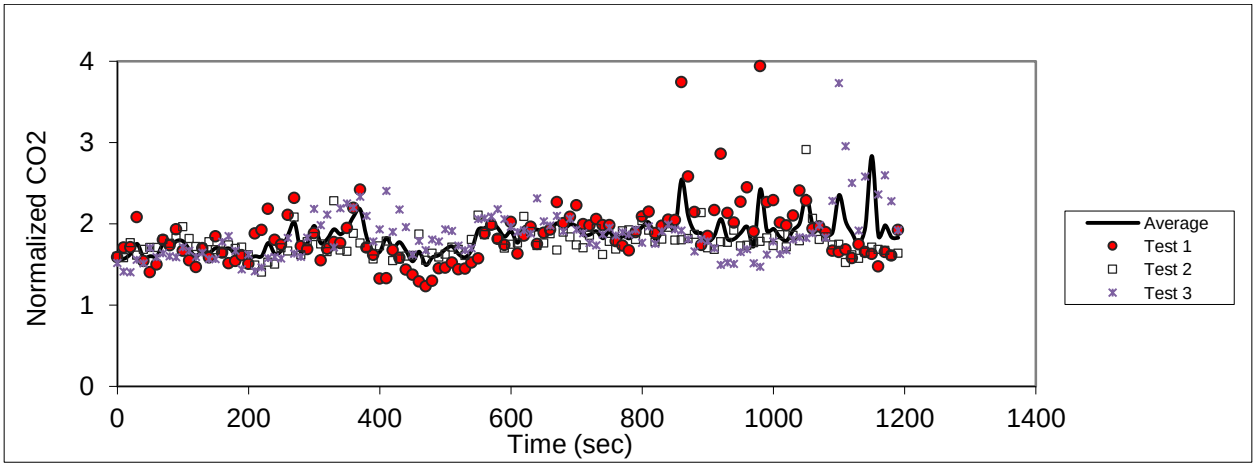

Figure C.7 – Sampling in seat 2C (release in 2D)

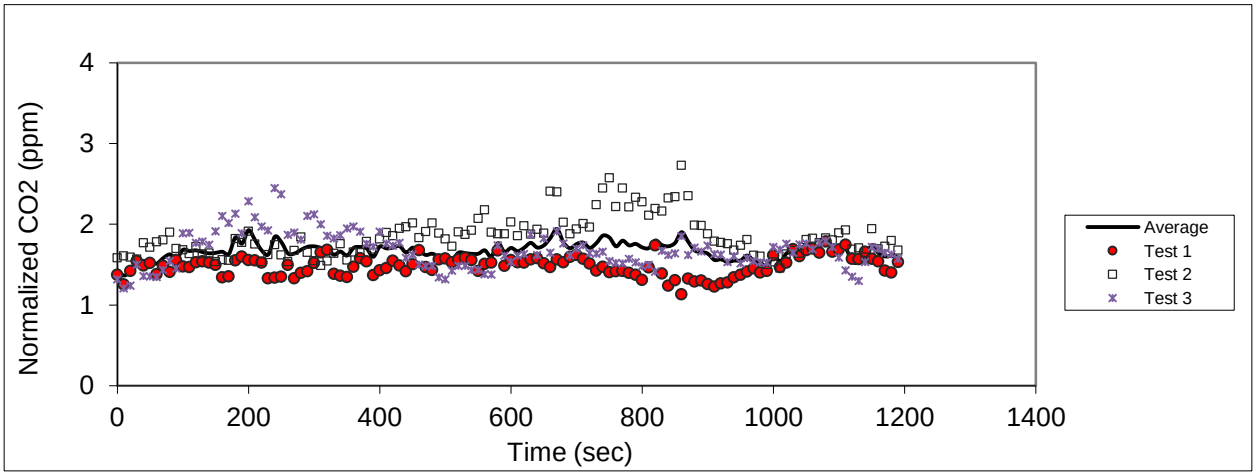

Figure C.8 – Sampling in seat 3C (release in 2D)

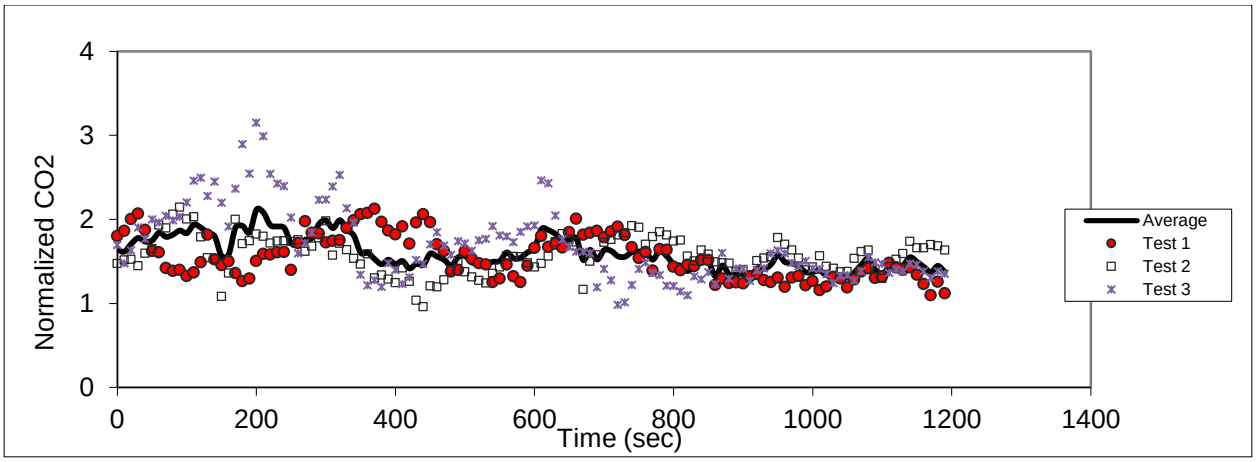

Figure C.9 – Sampling in seat 4C (release in 2D)

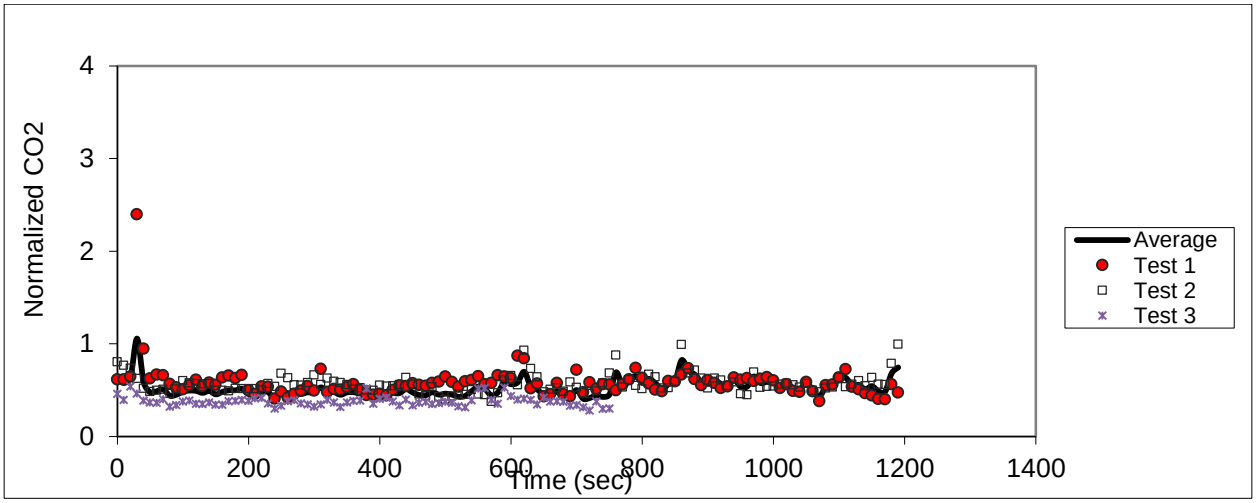

Figure C.10 – Sampling in seat 5C (release in 2D)

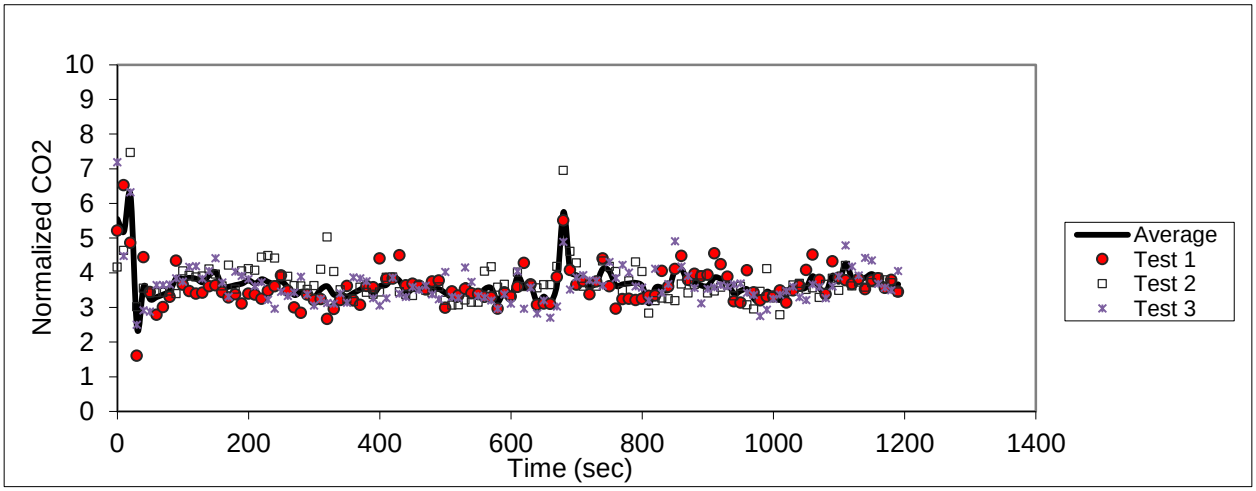

Figure C.11 – Sampling in seat 1E (release in 2D)

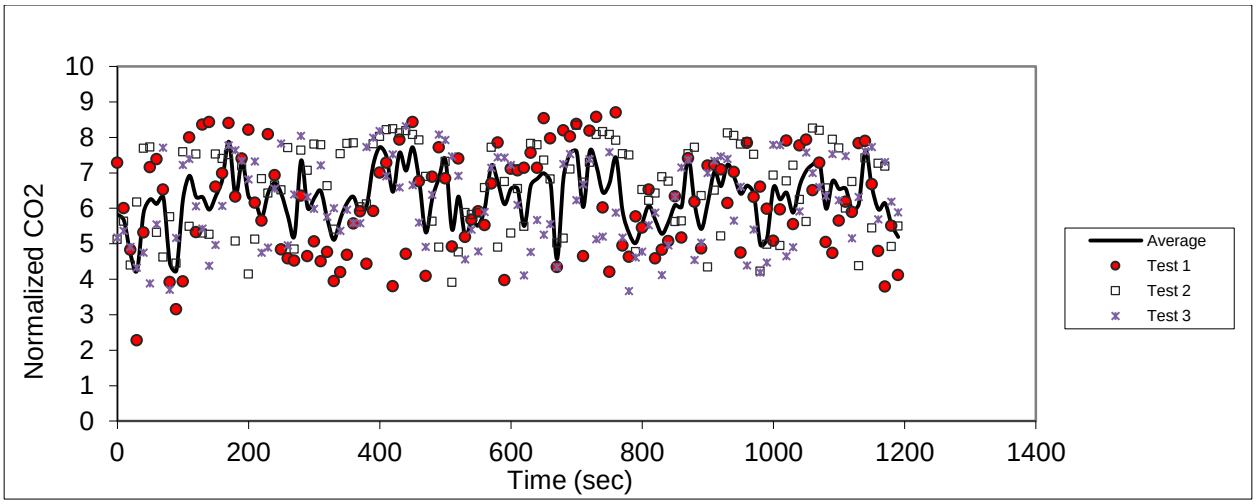

Figure C.12 – Sampling in seat 2E (release in 2D)

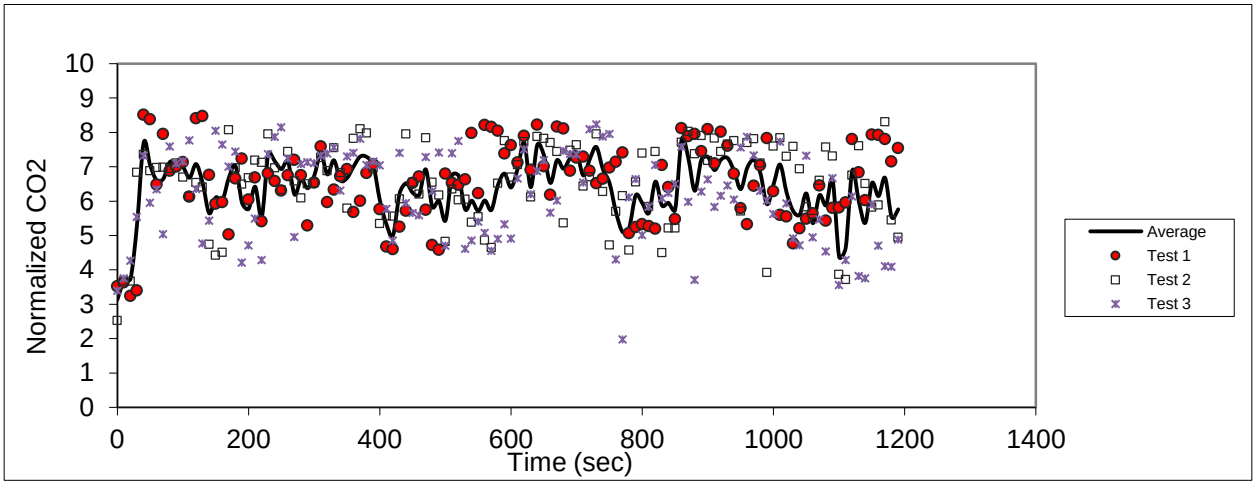

Figure C.13 – Sampling in seat 3E (release in 2D)

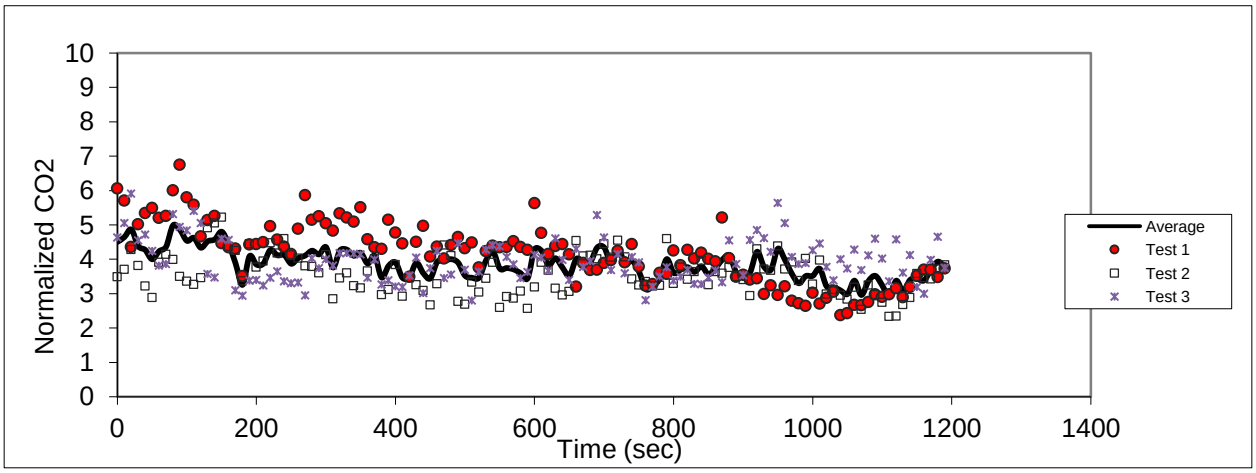

Figure C.14 - Sampling in seat 4E (release in 2D)

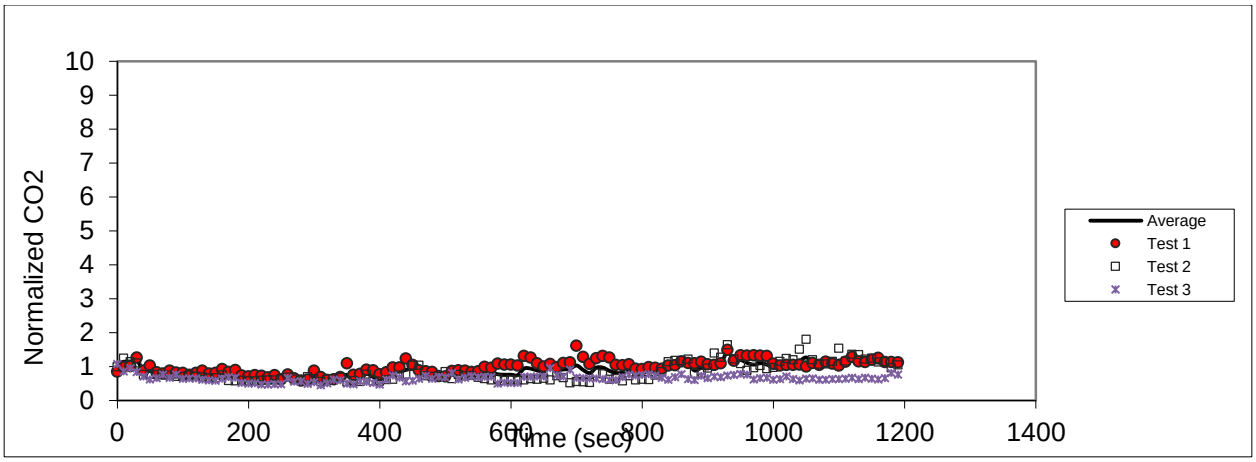

Figure C.15 - Sampling in seat 5E (release in 2D)

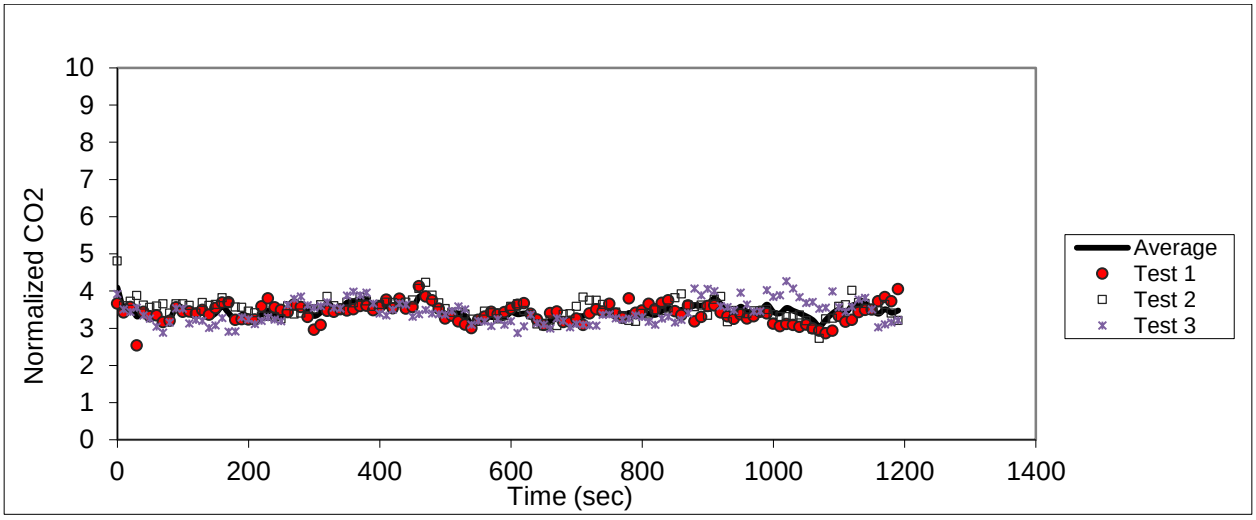

Figure C.16 – Sampling in seat 1F (release in 2D)

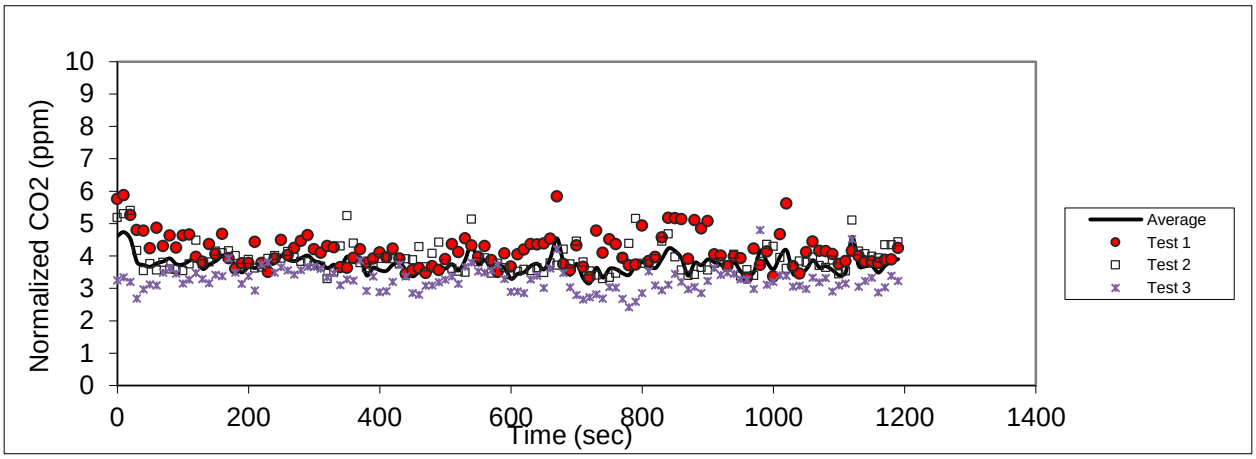

Figure C.17 – Sampling in seat 2F (release in 2D)

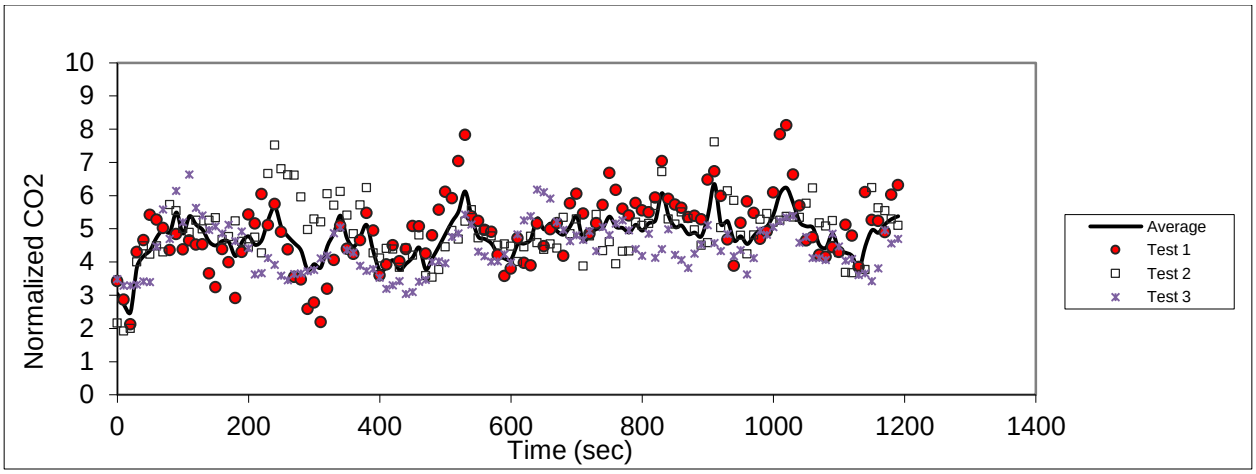

Figure C.18 – Sampling in seat 3F (release in 2D)

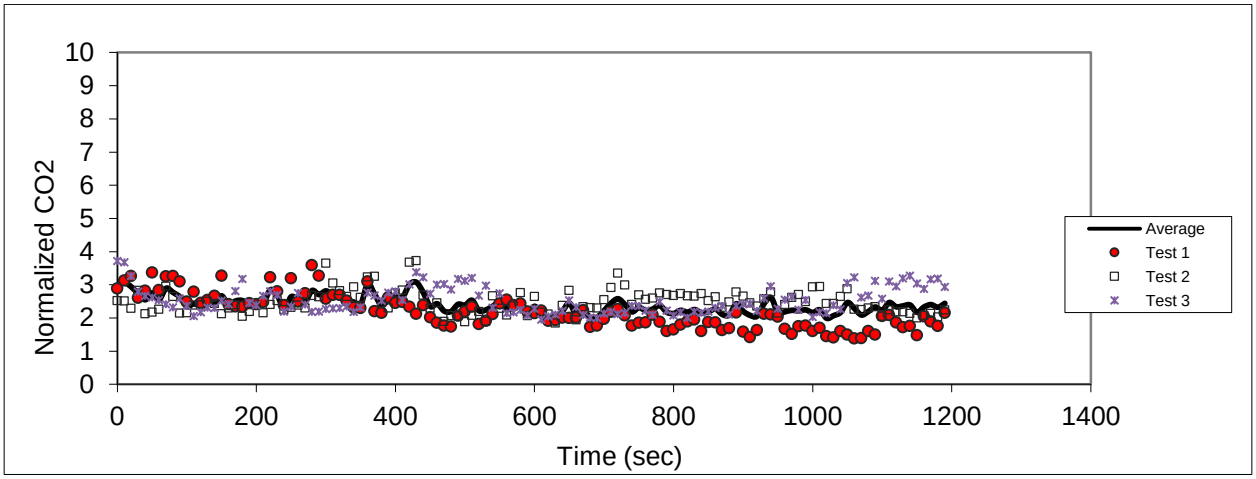

Figure C.19 – Sampling in seat 4F (release in 2D)

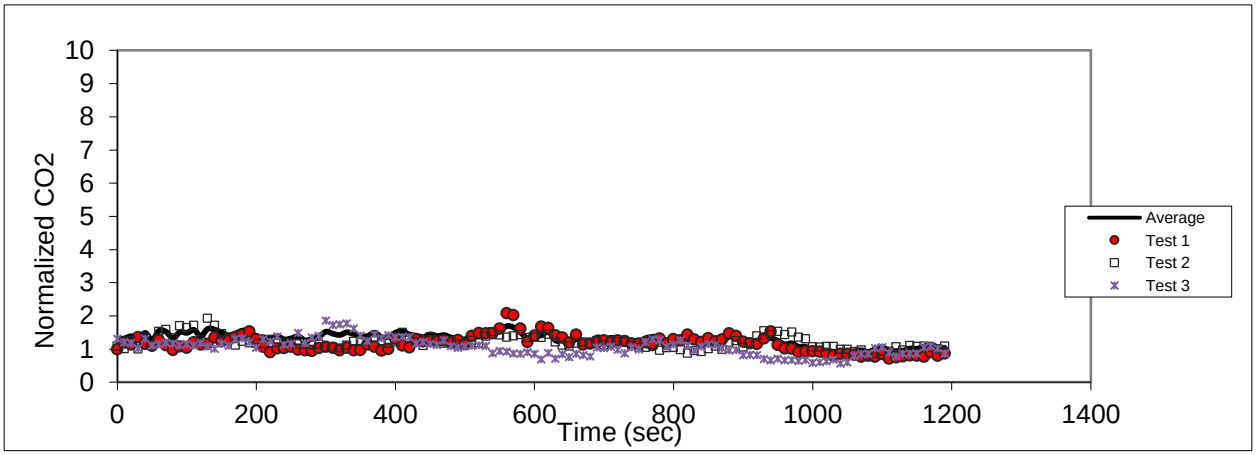

Figure C.20 – Sampling in seat 5F (release in 2D)

Release in 5D

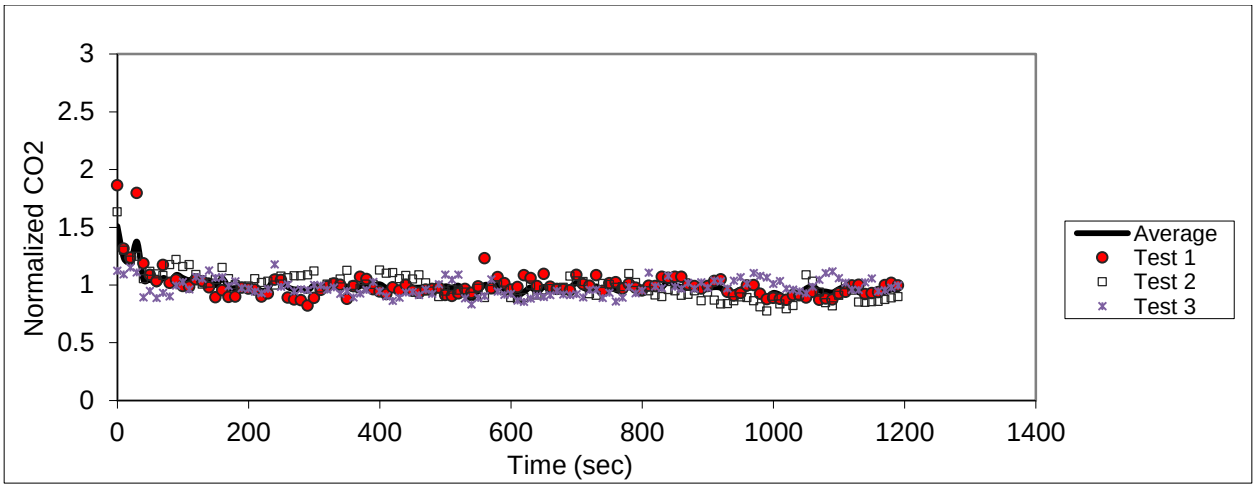

Figure C.21 – Sampling in seat 2F (release in 5D)

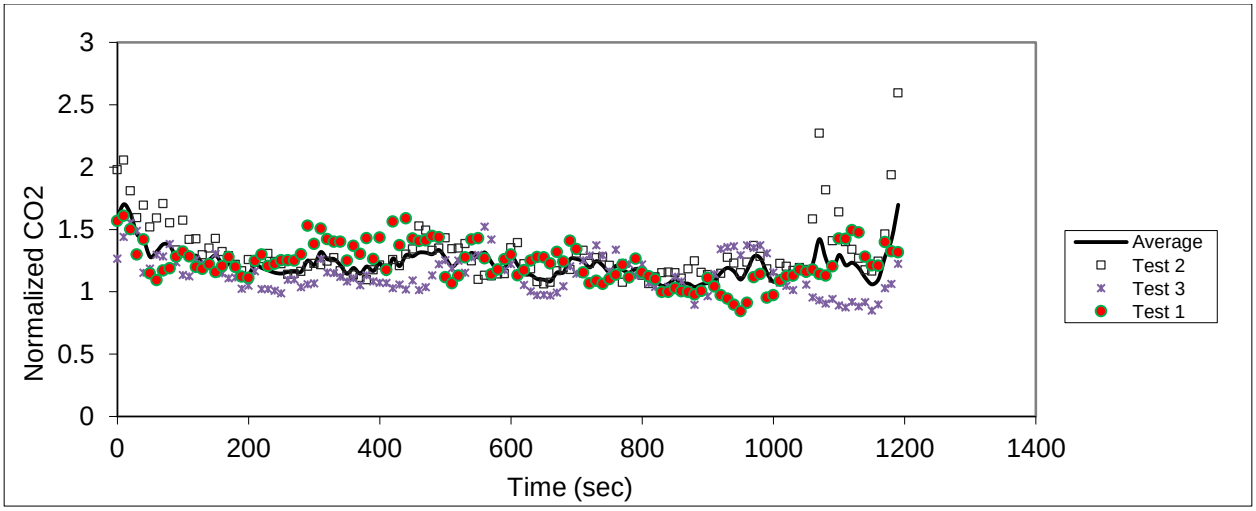

Figure C.22 – Sampling in seat 3F (release in 5D)

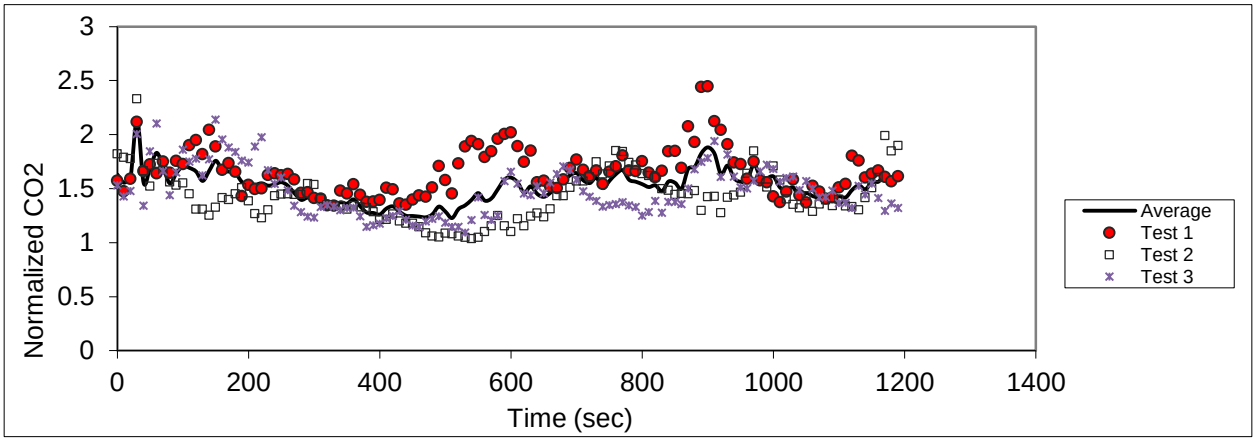

Figure C.23 – Sampling in seat 4F (release in 5D)

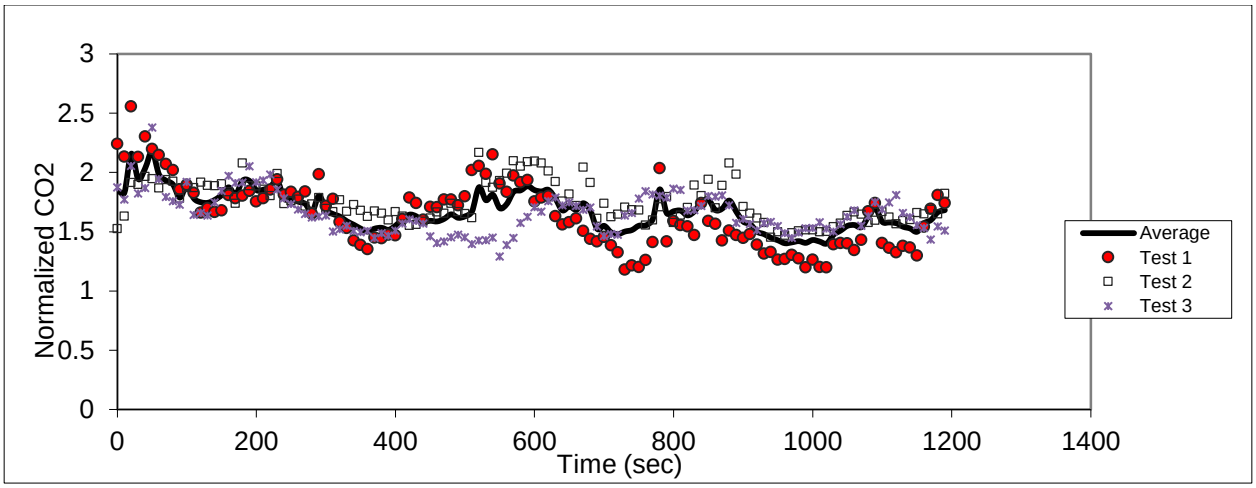

Figure C.24 - Sampling in seat 5F (release in 5D)

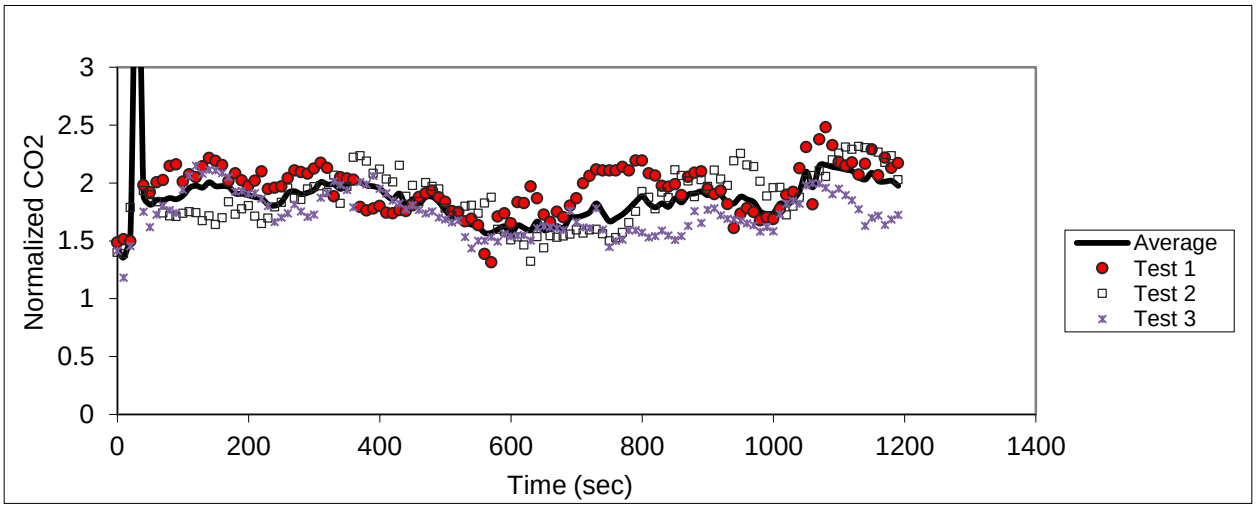

Figure C.25 – Sampling in seat 6F (release in 5D)

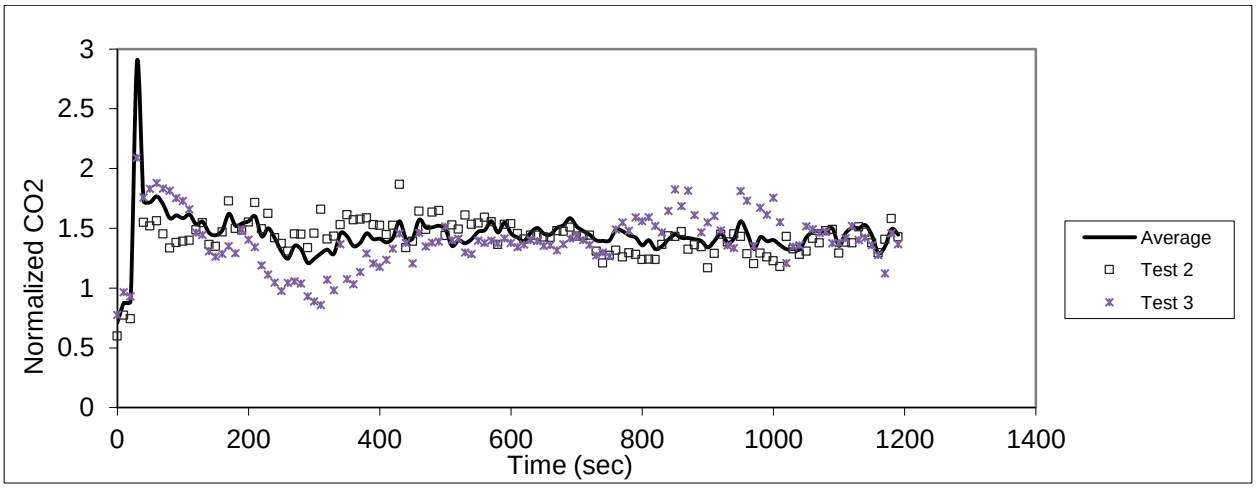

Figure C.26 – Sampling in seat 7F (release in 5D)

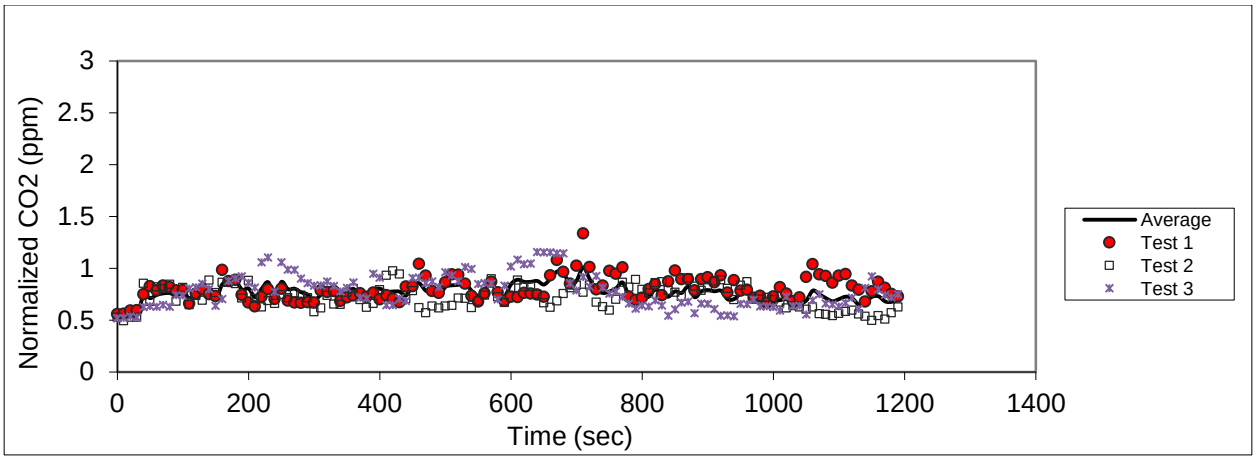

Figure C.27 – Sampling in seat 8F (release in 5D)

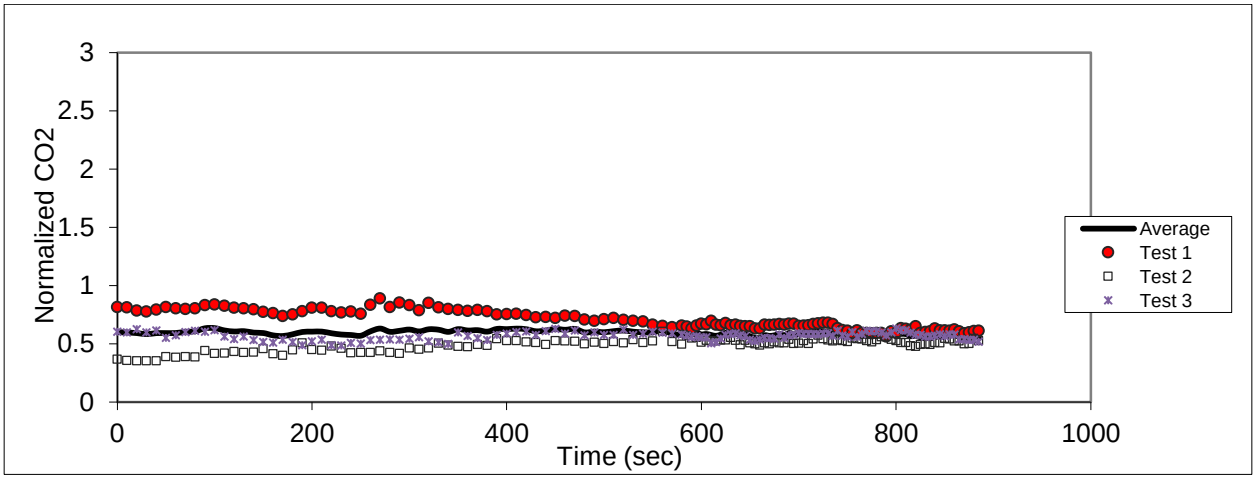

Figure C.28 – Sampling in seat 9F (release in 5D)

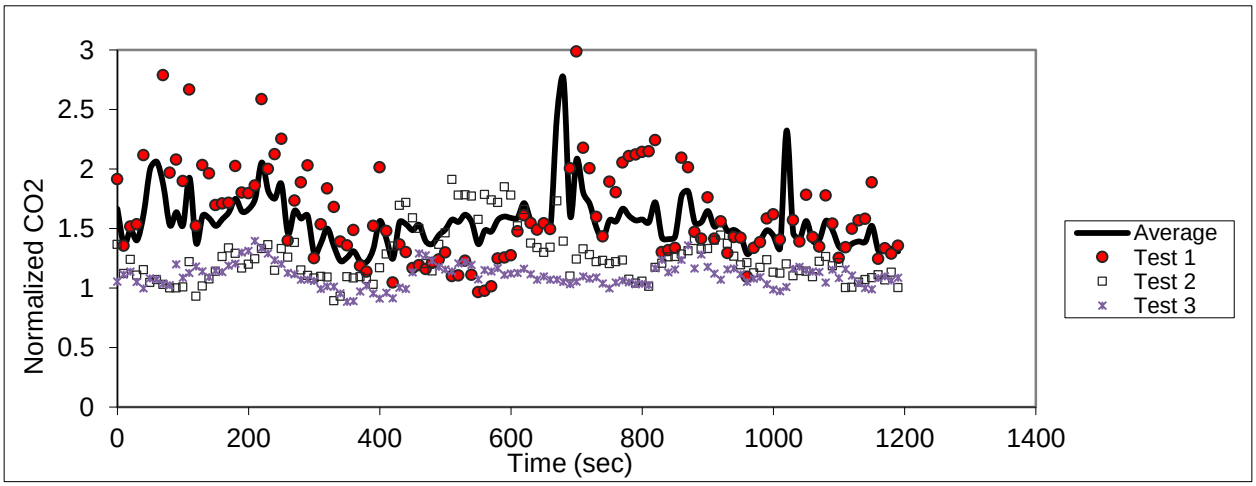

Figure C.29 – Sampling in seat 2E (release in 5D)

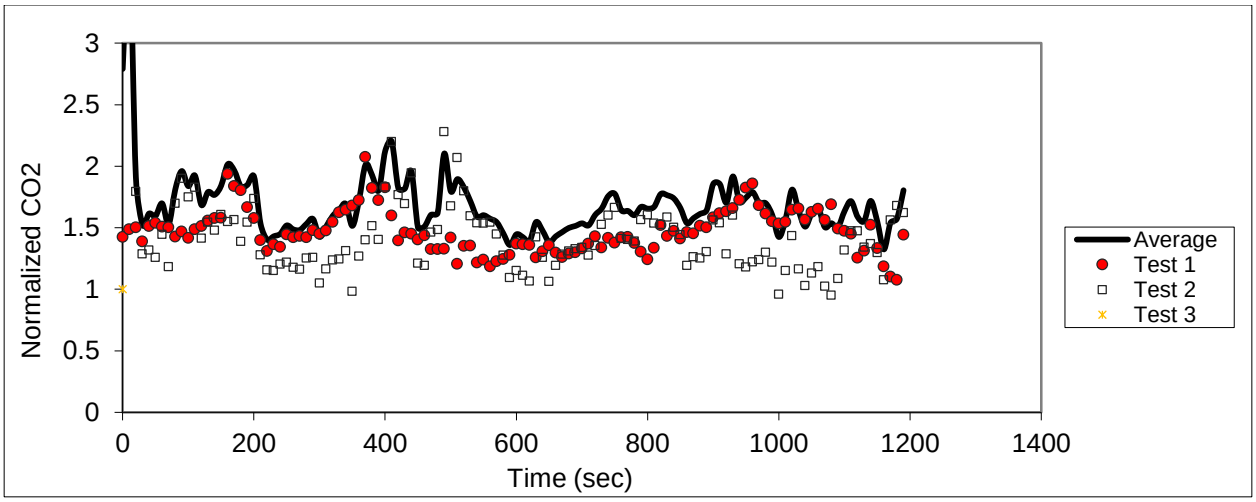

Figure C.30 – Sampling in seat 3E (release in 5D)

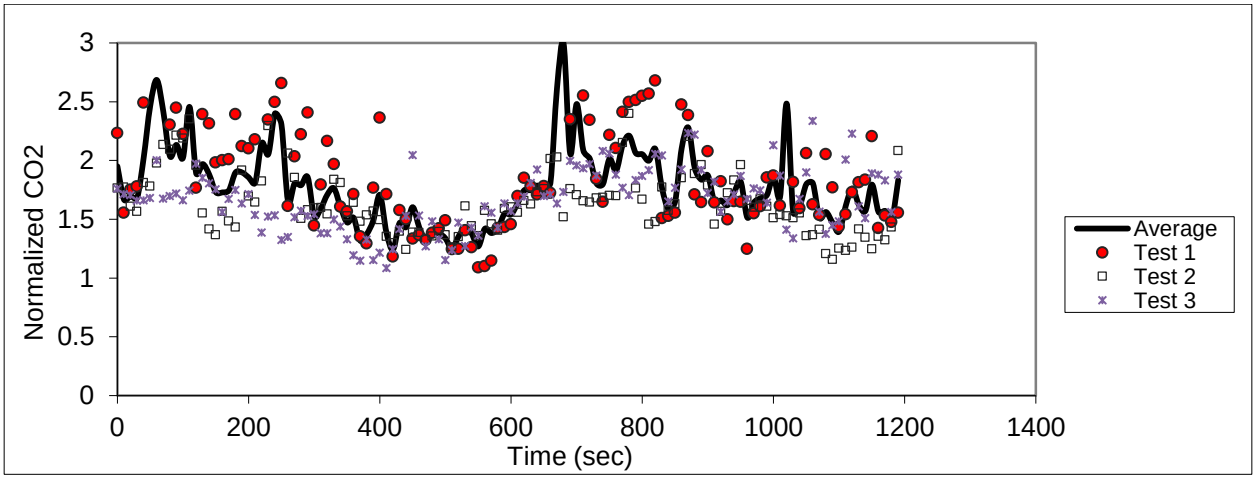

Figure C.31 – Sampling in seat 4E (release in 5D)

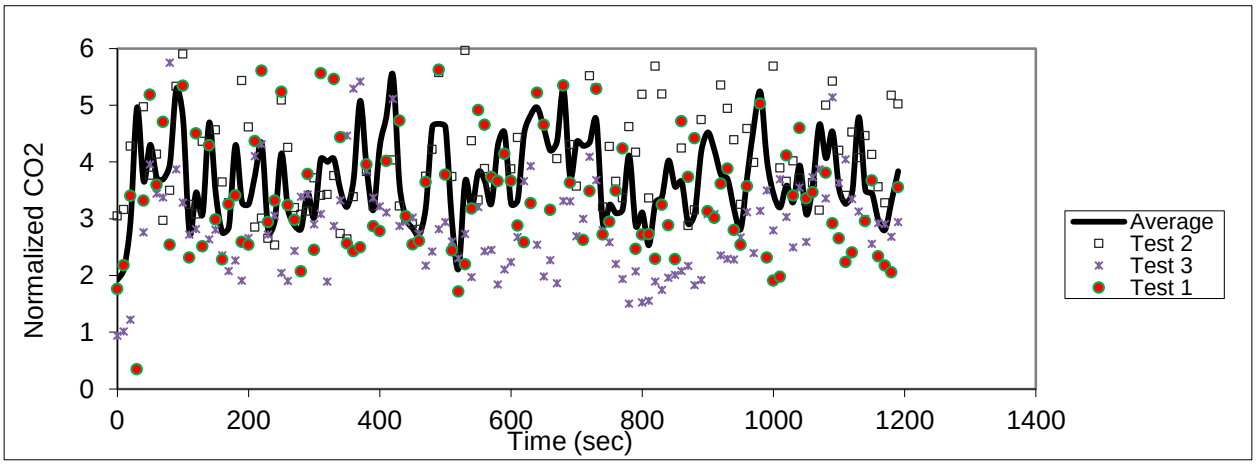

Figure C.32 – Sampling in seat 6E (release in 5D)

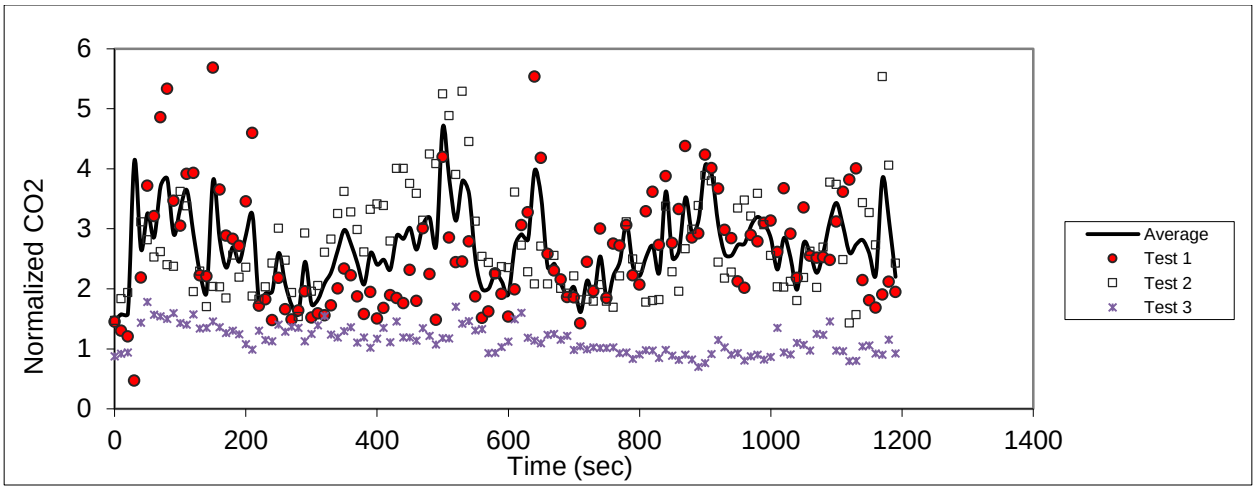

Figure C.33 – Sampling in seat 7E (release in 5D)

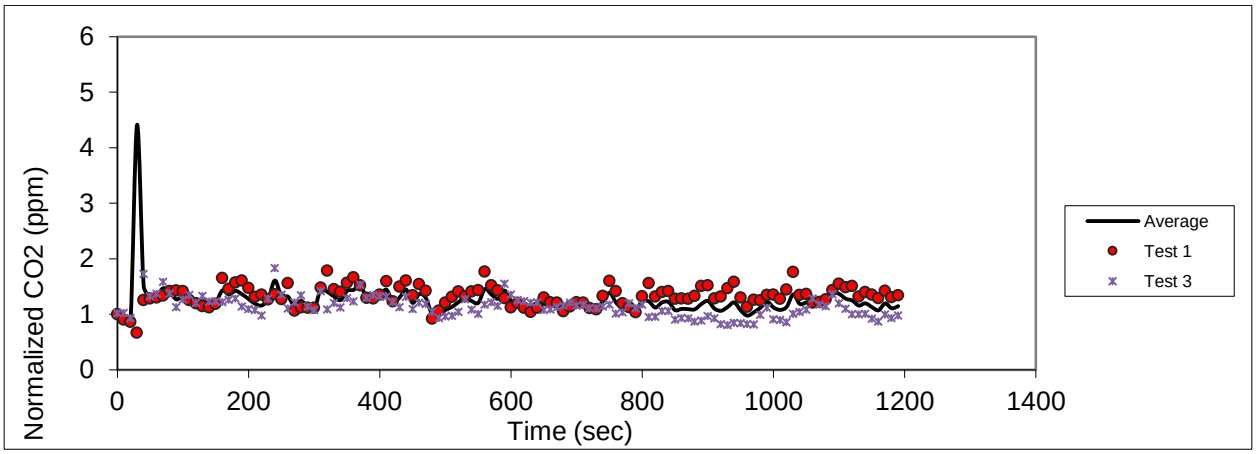

Figure C.34 – Sampling in seat 8E (release in 5D)

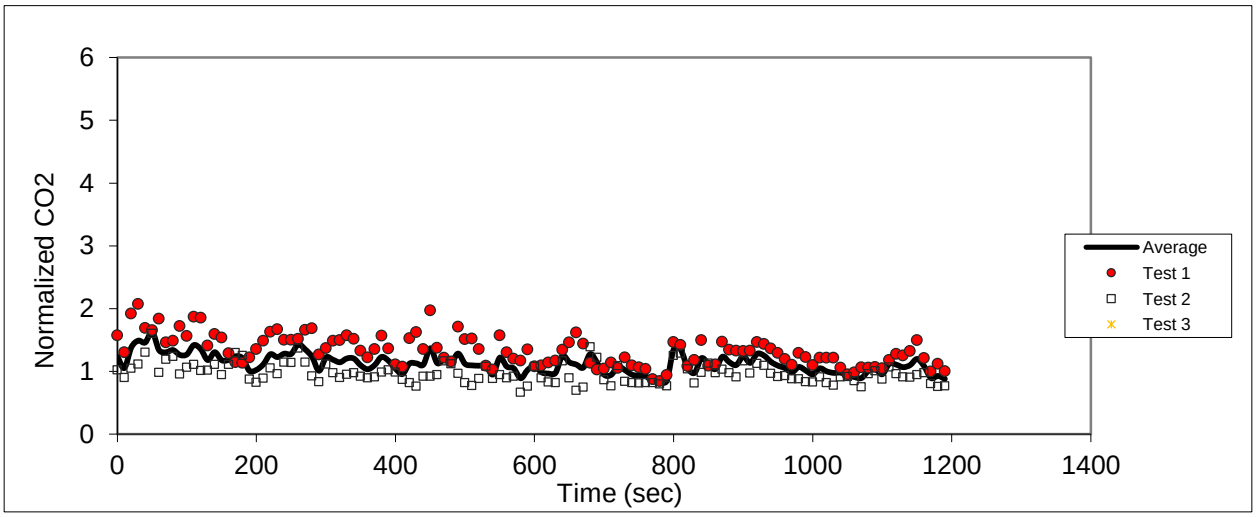

Figure C.35 – Sampling in seat 9E (release in 5D)

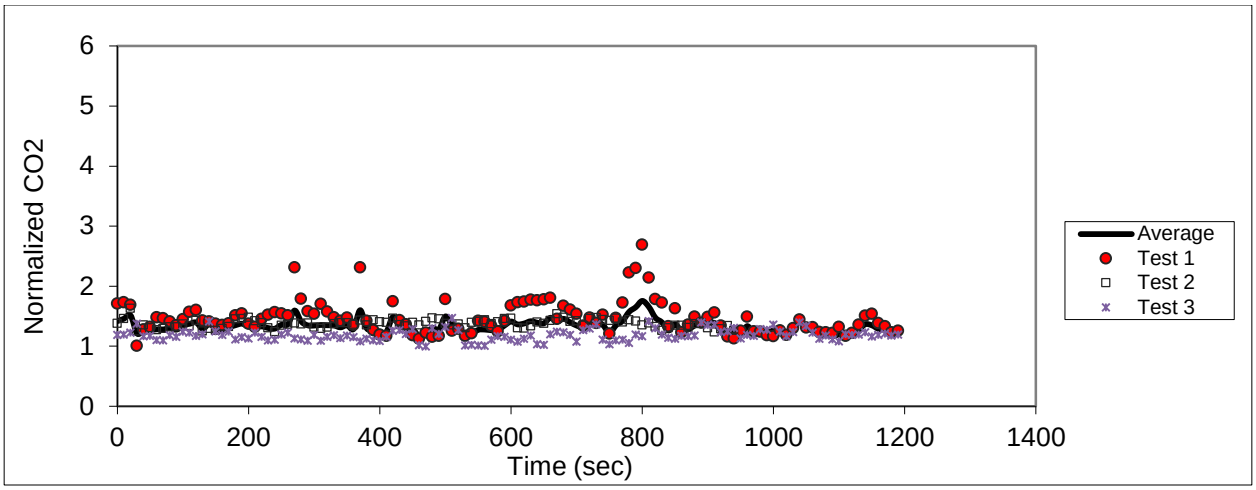

Figure C.36 – Sampling in seat 5C (release in 5D)

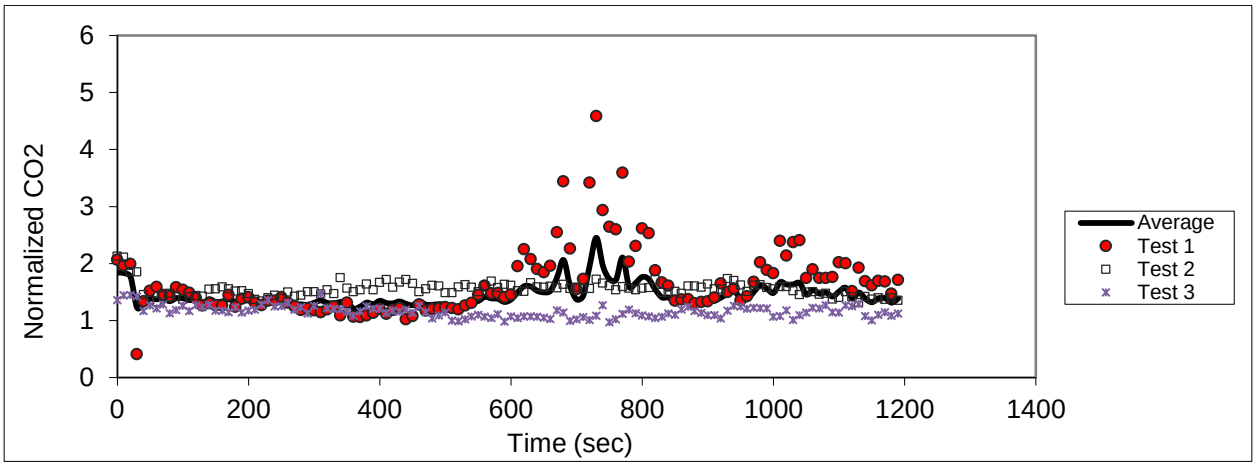

Figure C.37 – Sampling in seat 6C (release in 5D)

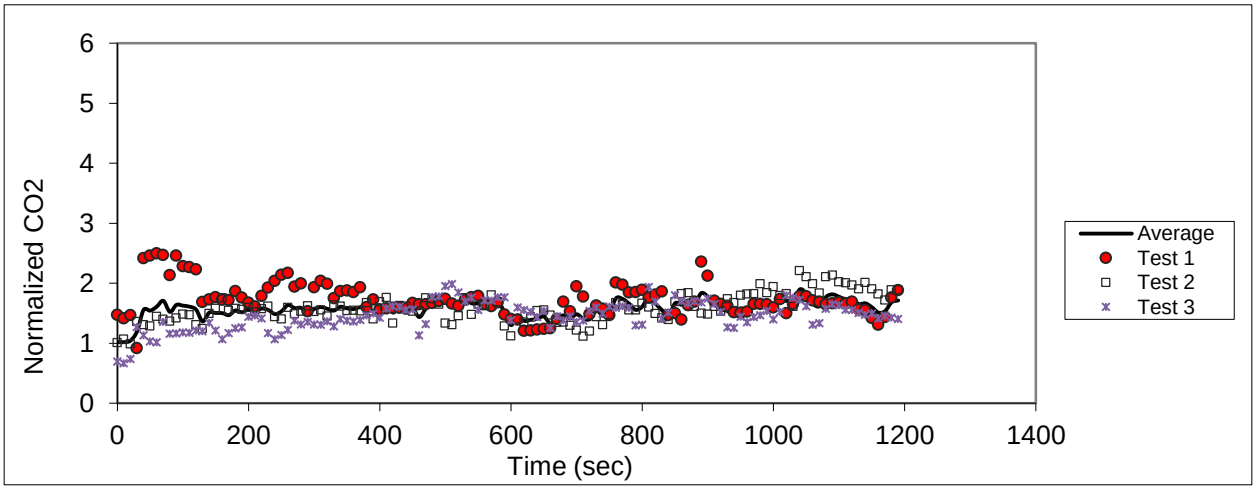

Figure C.38 – Sampling in seat 7C (release in 5D)

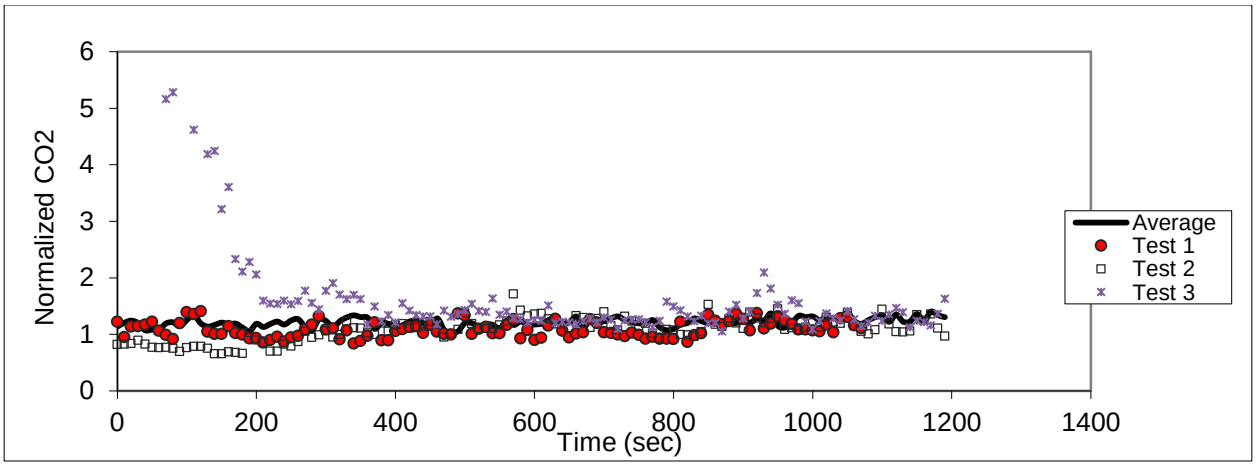

Figure C.39 – Sampling in seat 8C (release in 5D)

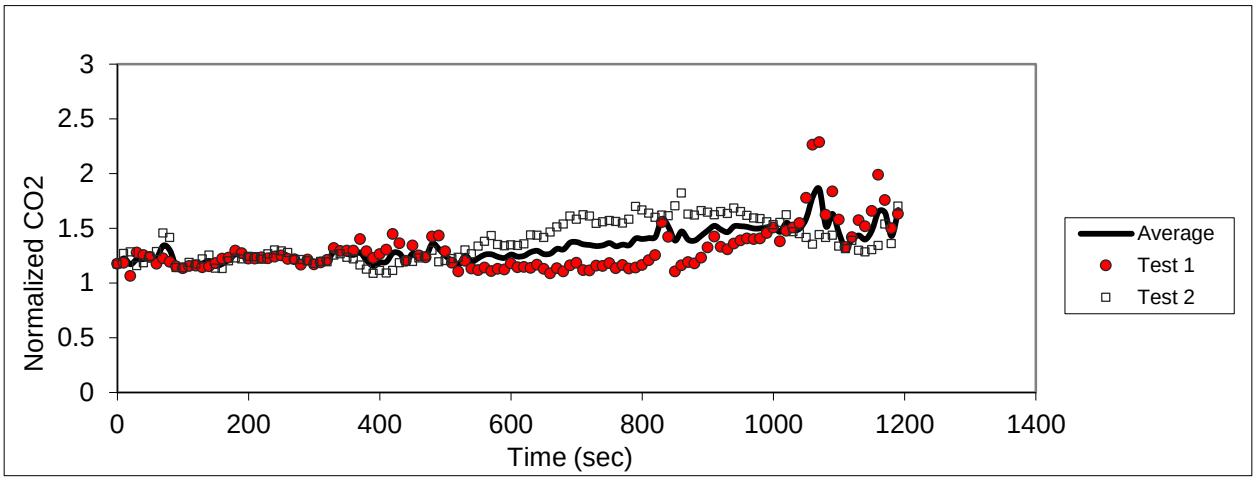

Figure C.40 – Sampling in seat 5B (release in 5D)

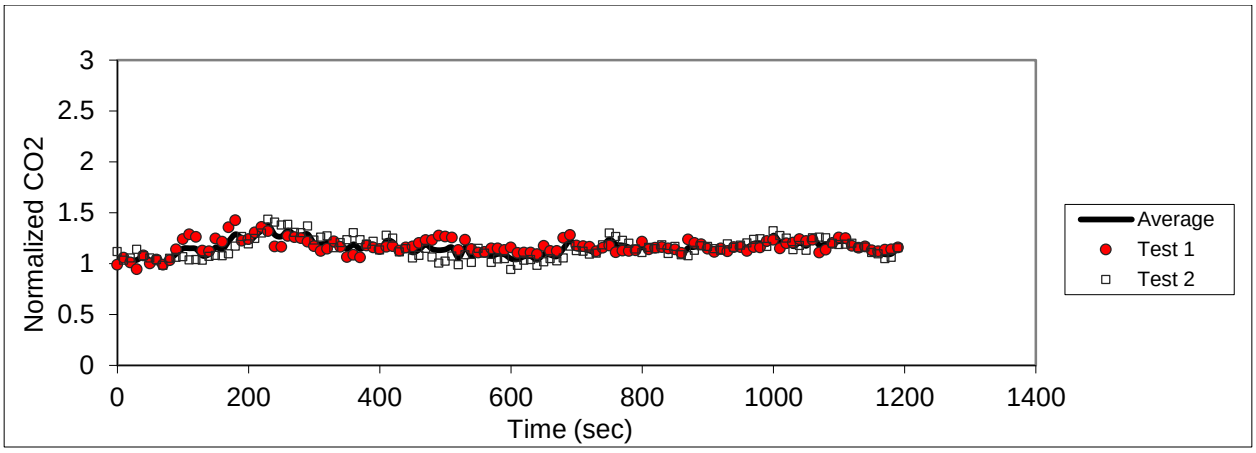

Figure C.41 – Sampling in seat 6B (release in 5D)

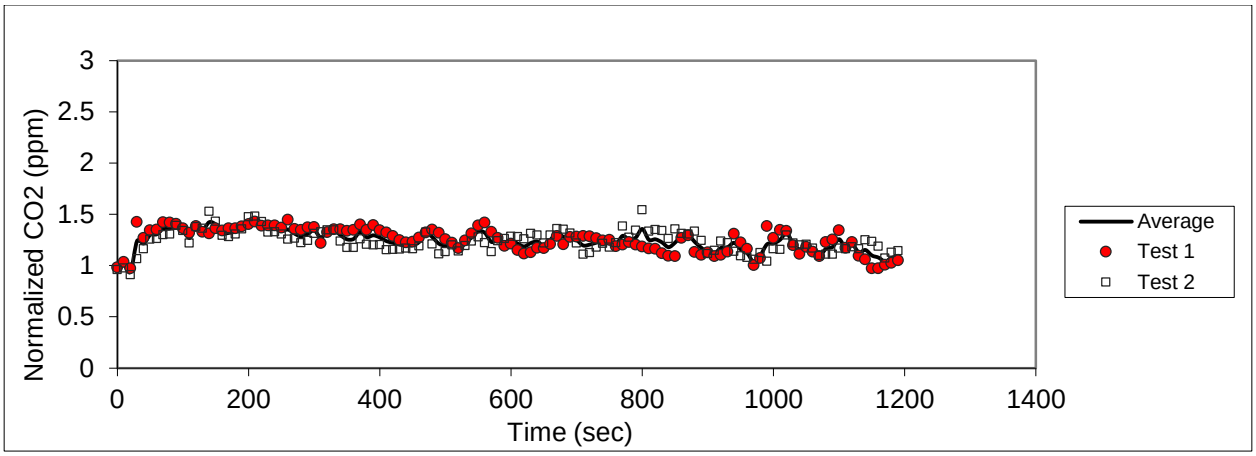

Figure C.42 – Sampling in seat 7B (release in 5D)

Release in 7D

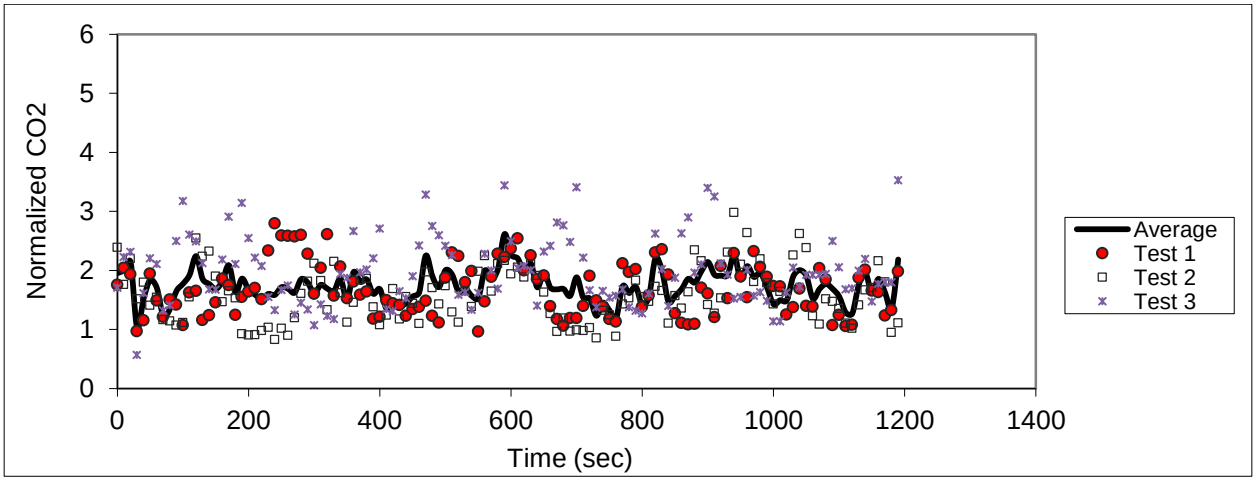

Figure C.43 – Sampling in seat 4B (release in 7D)

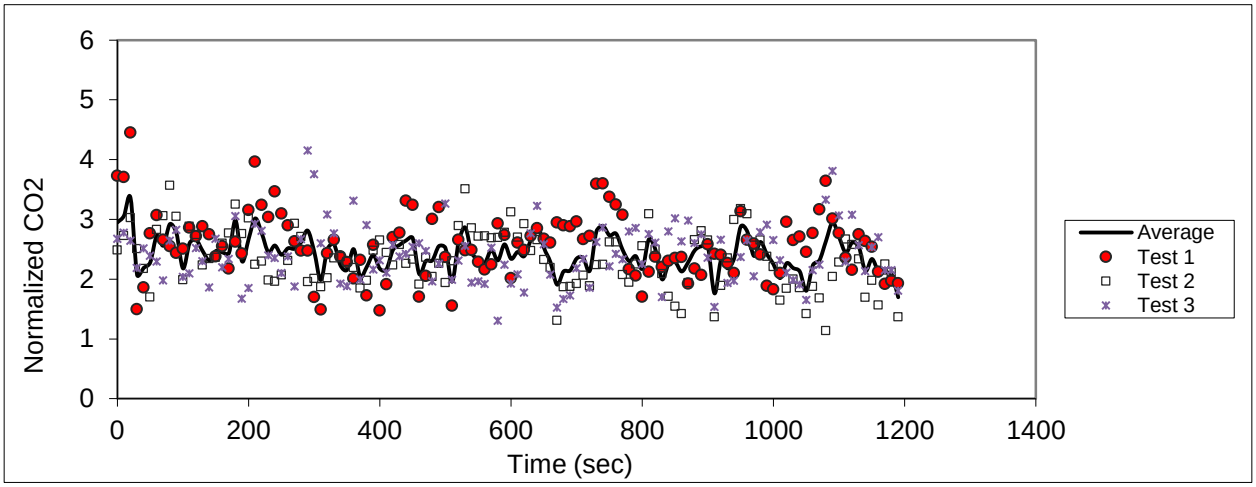

Figure C.44 – Sampling in seat 5B (release in 7D)

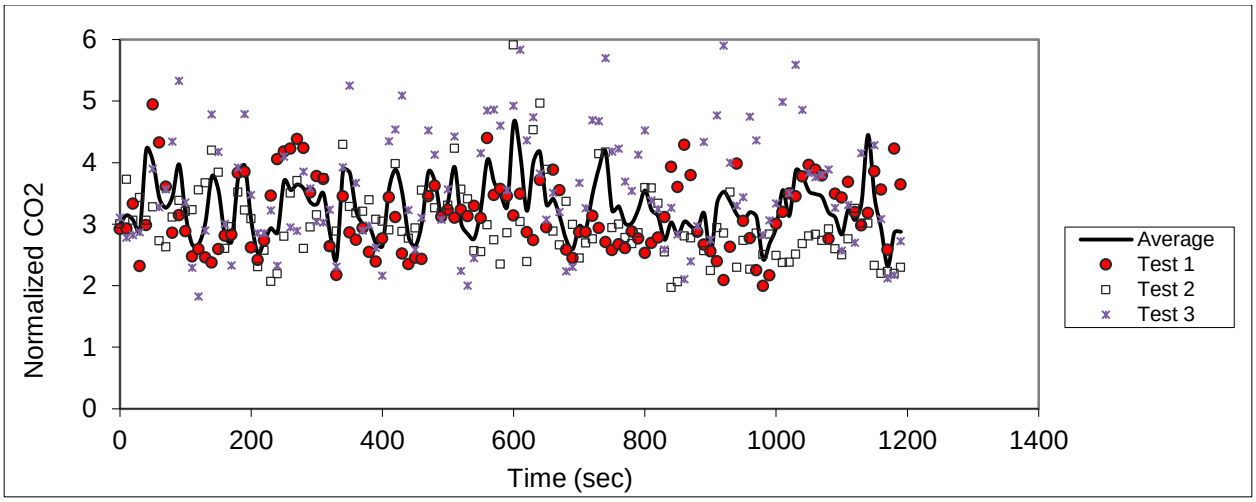

Figure C.45 – Sampling in seat 6B (release in 7D)

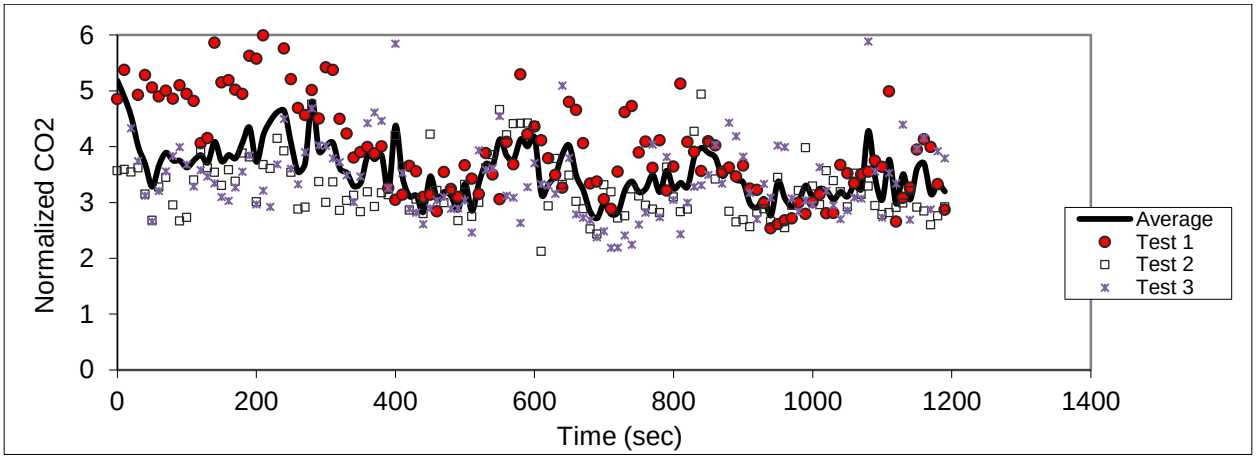

Figure C.46 – Sampling in seat 7B (release in 7D)

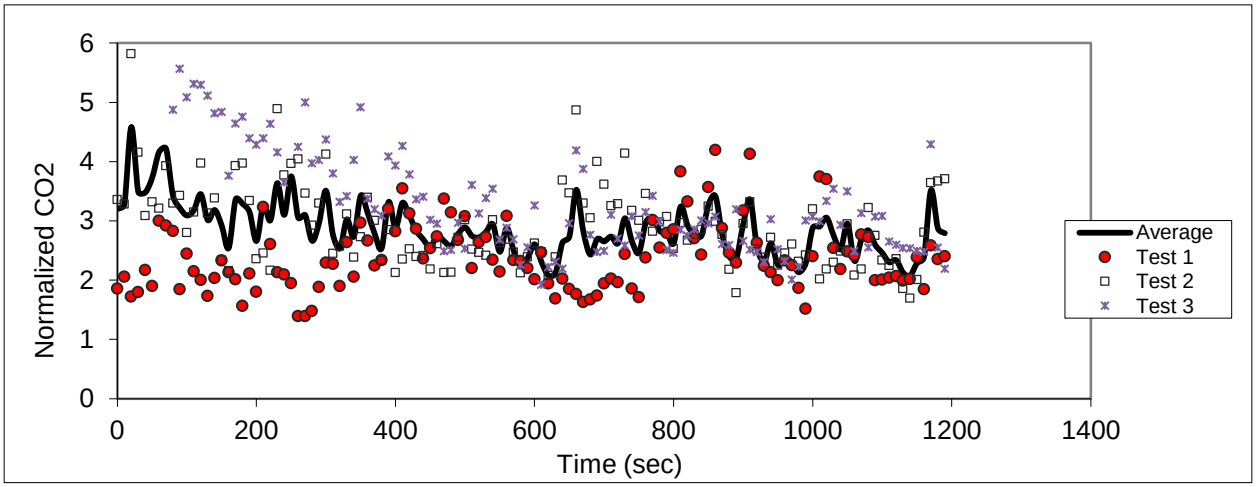

Figure C.47 – Sampling in seat 8B (release in 7D)

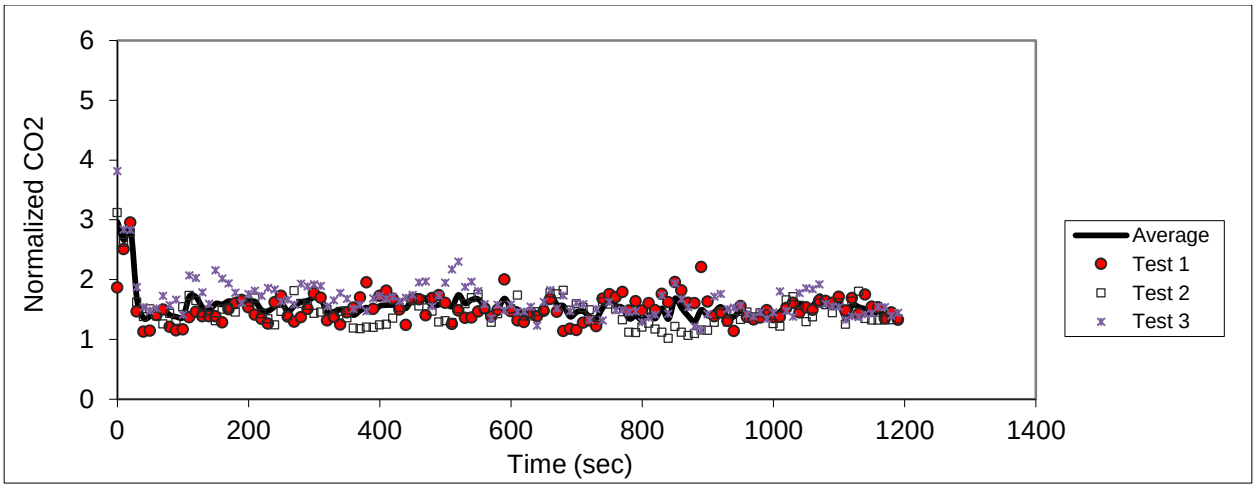

Figure C.48 – Sampling in seat 9B (release in 7D)

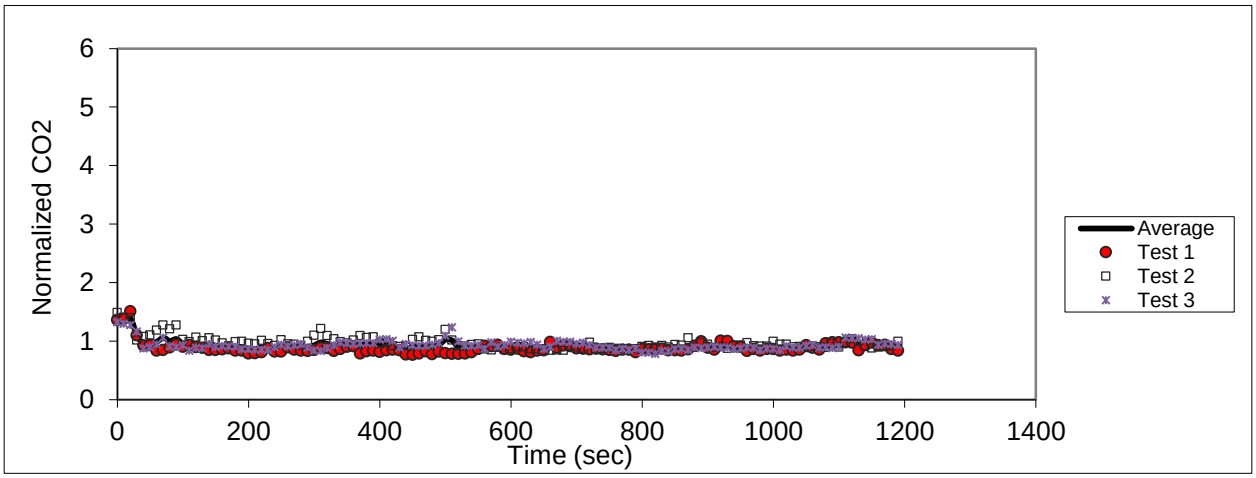

Figure C.49 – Sampling in seat 10B (release in 7D)

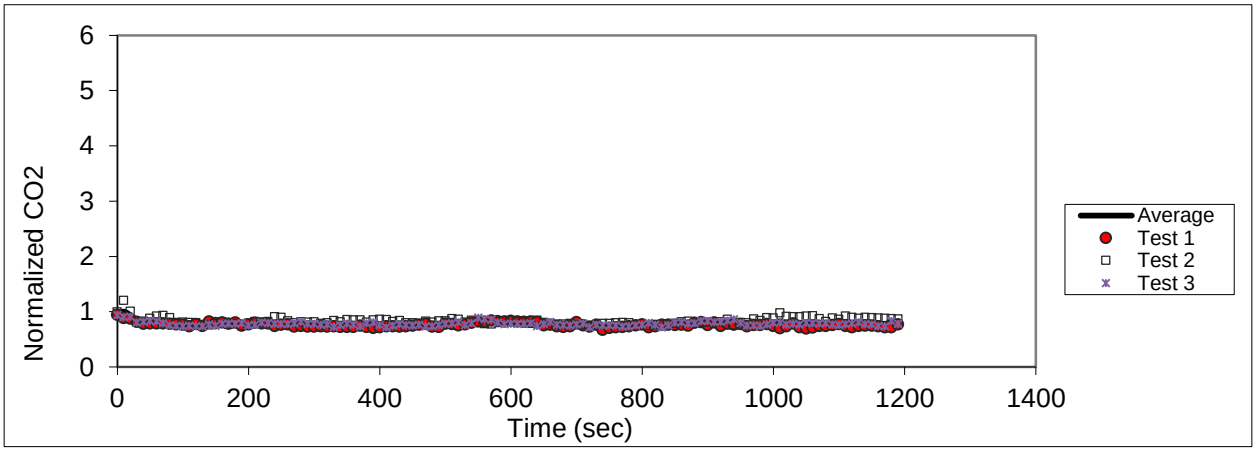

Figure C.50 – Sampling in seat 11B (release in 7D)

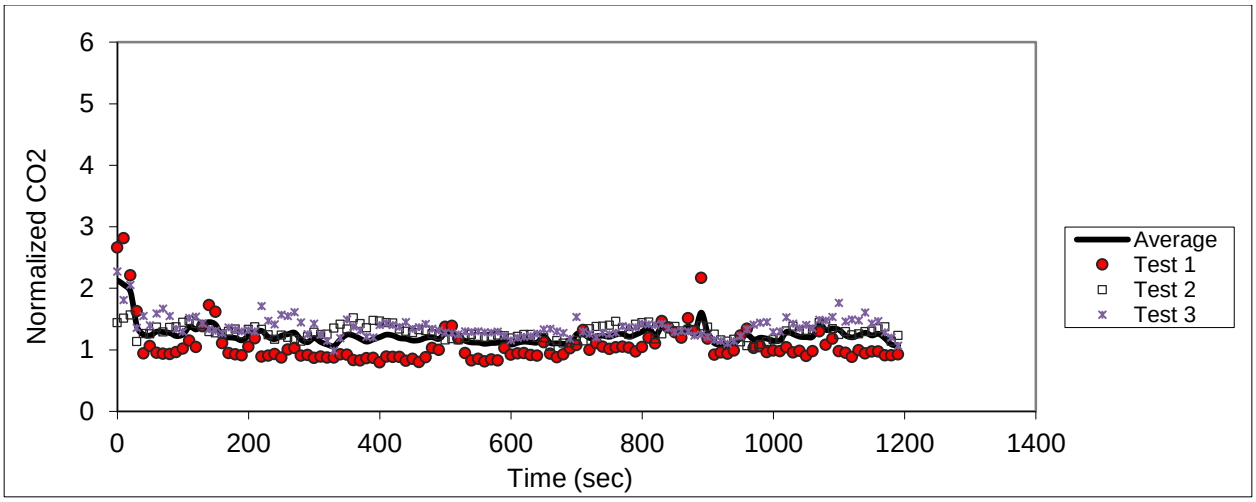

Figure C.51 - Sampling in seat 4D (release in 7D)

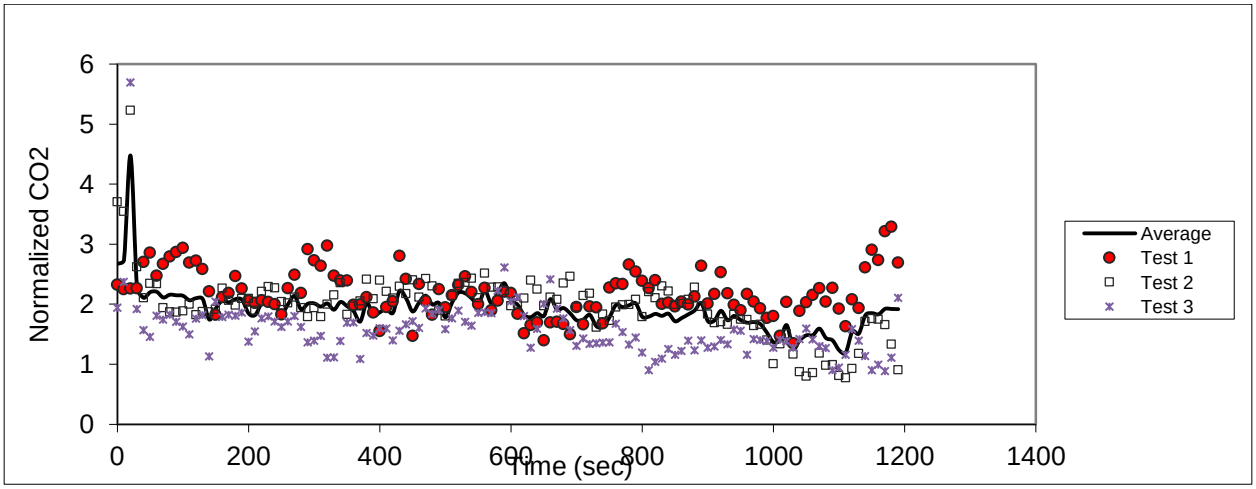

Figure C.52 – Sampling in seat 5D (release in 7D)

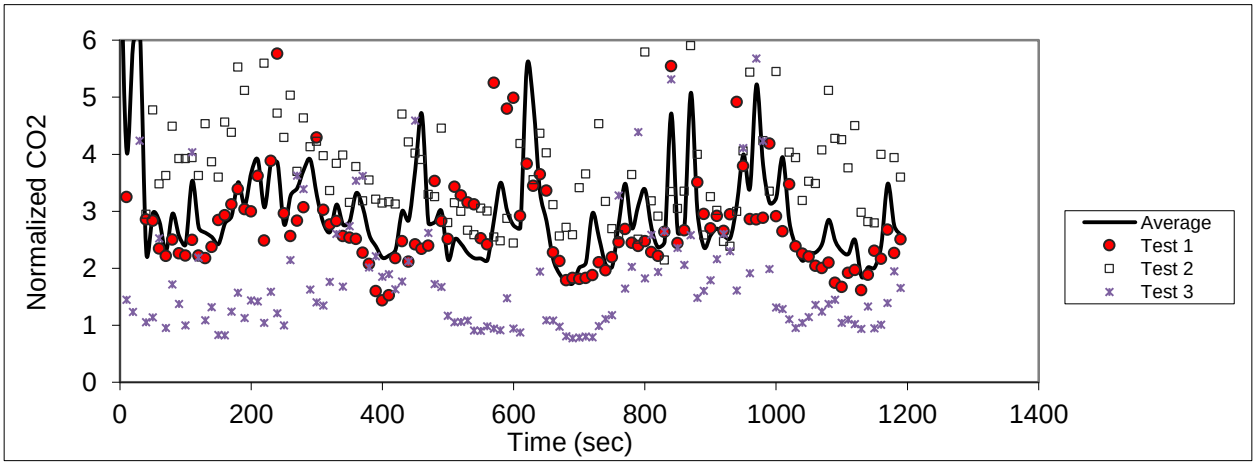

Figure C.53 – Sampling in seat 6D (release in 7D)

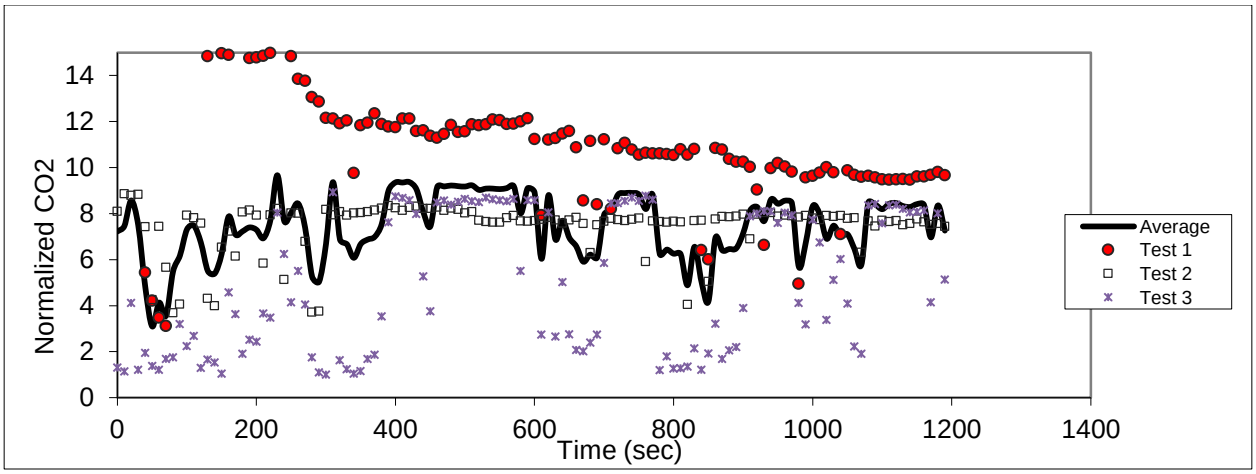

Figure C.54 - Sampling in seat 7D (release in 7D)

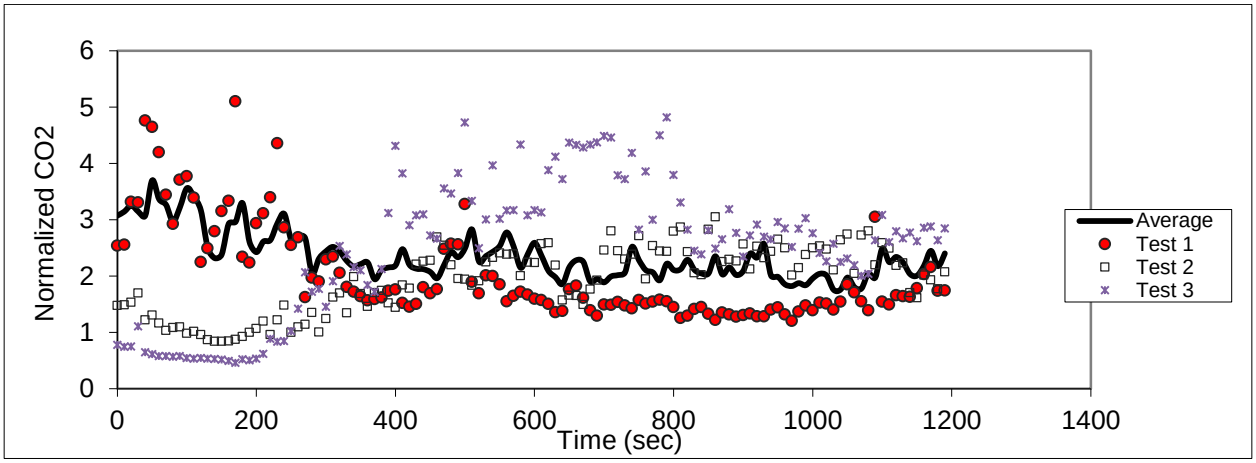

Figure C.55 – Sampling in seat 8D (release in 7D)

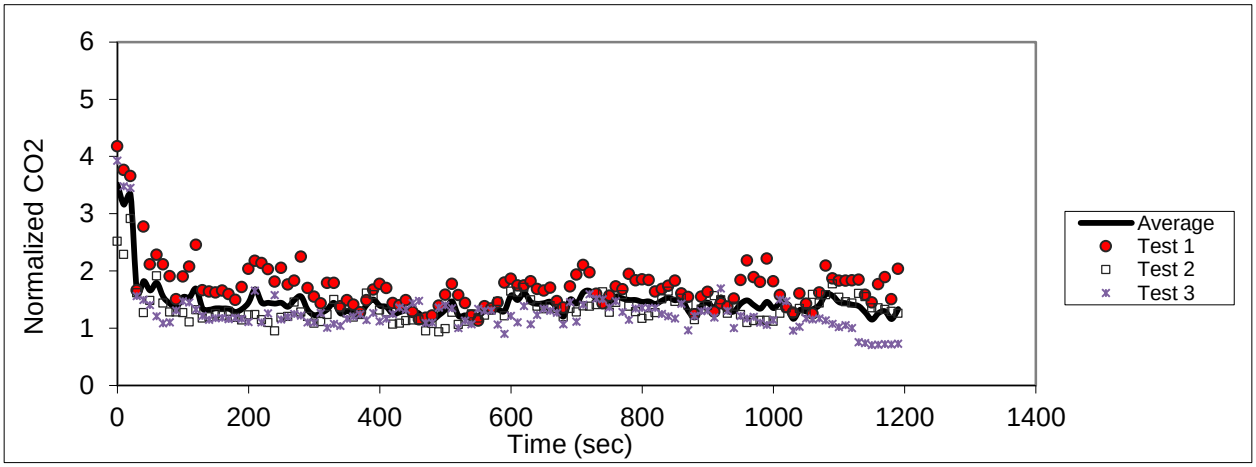

Figure C.56 – Sampling in seat 9D (release in 7D)

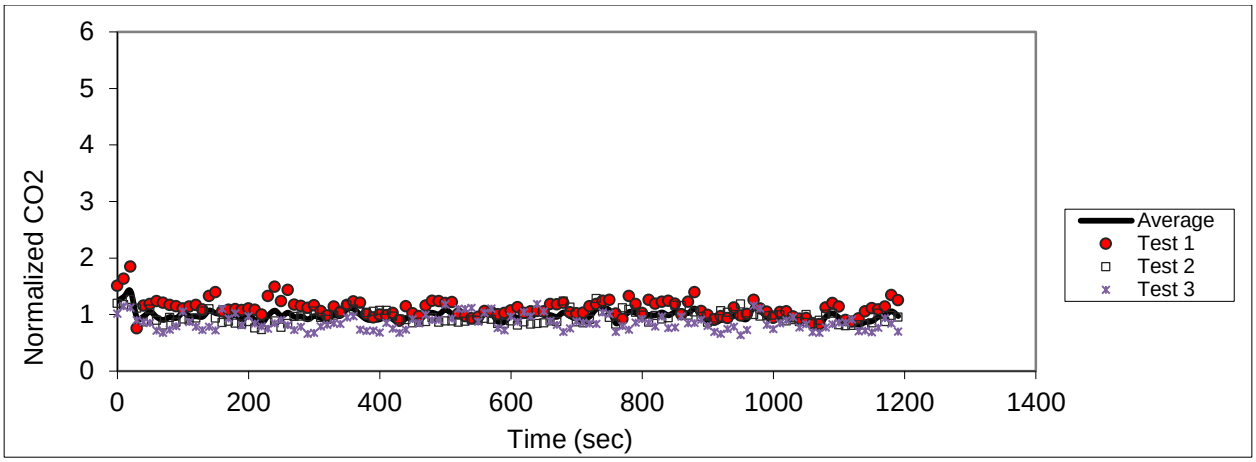

Figure C.57 – Sampling in seat 10D (release in 7D)

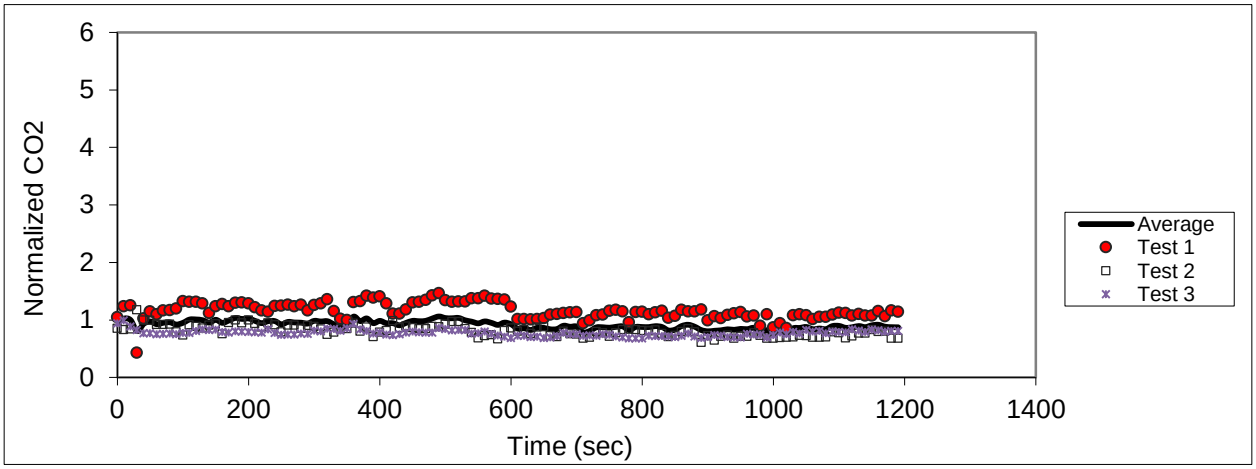

Figure C.58 – Sampling in seat 11D (release in 7D)

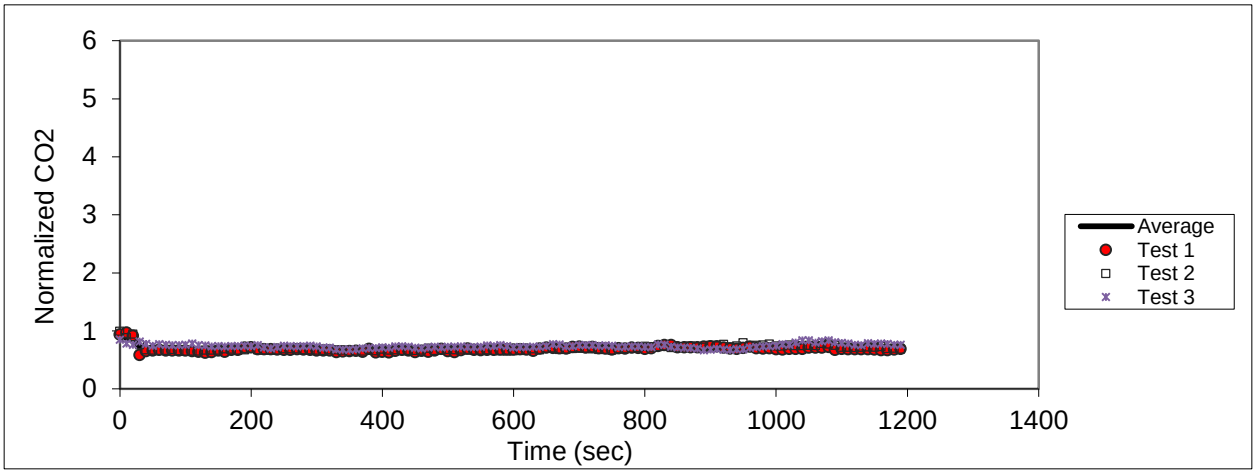

Figure C.59 – Sampling in seat 4F (release in 7D)

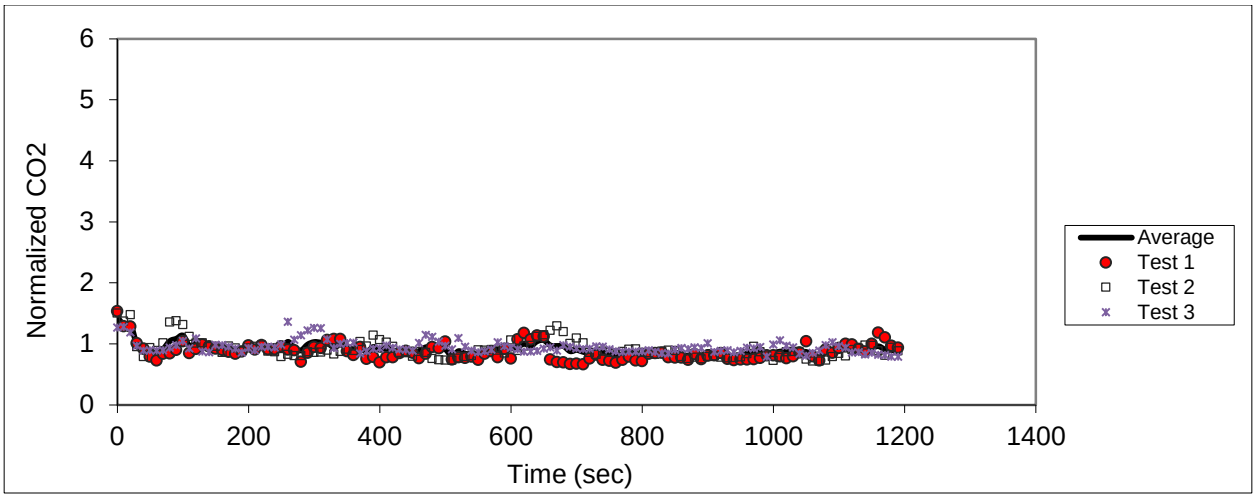

Figure C.60 – Sampling in seat 5F (release in 7D)

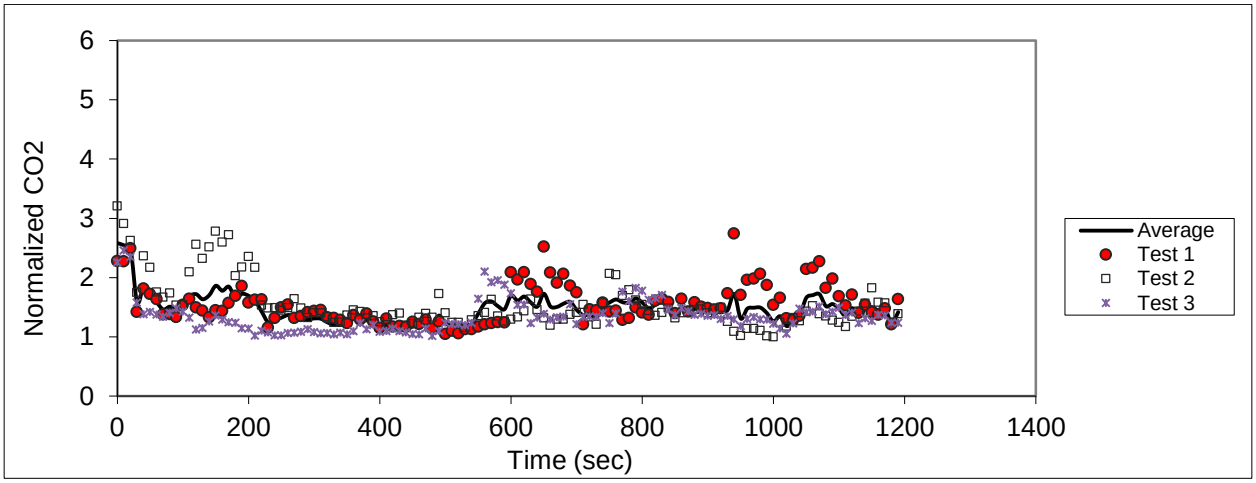

Figure C.61 – Sampling in seat 6F (release in 7D)

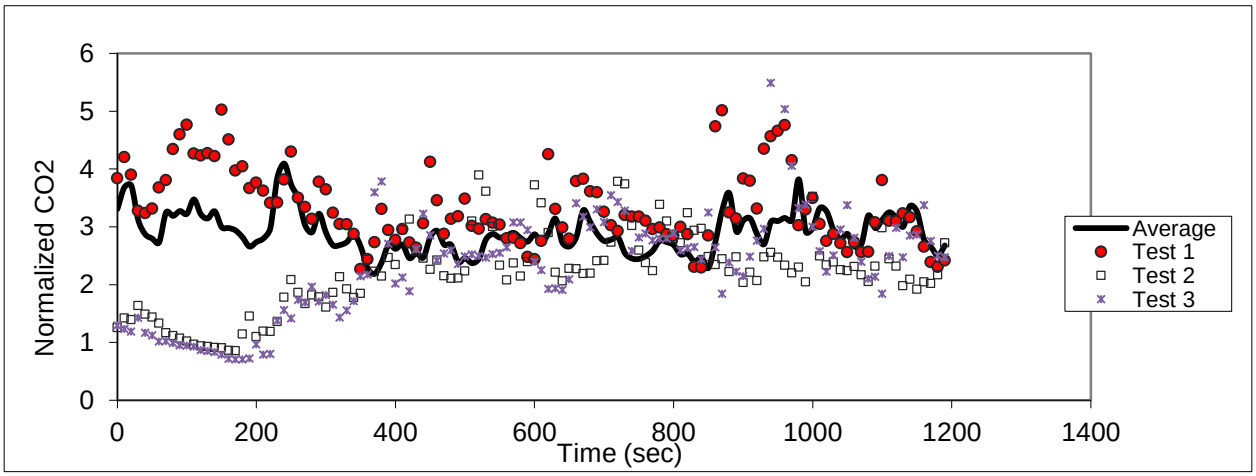

Figure C.62 – Sampling in seat 7F (release in 7D)

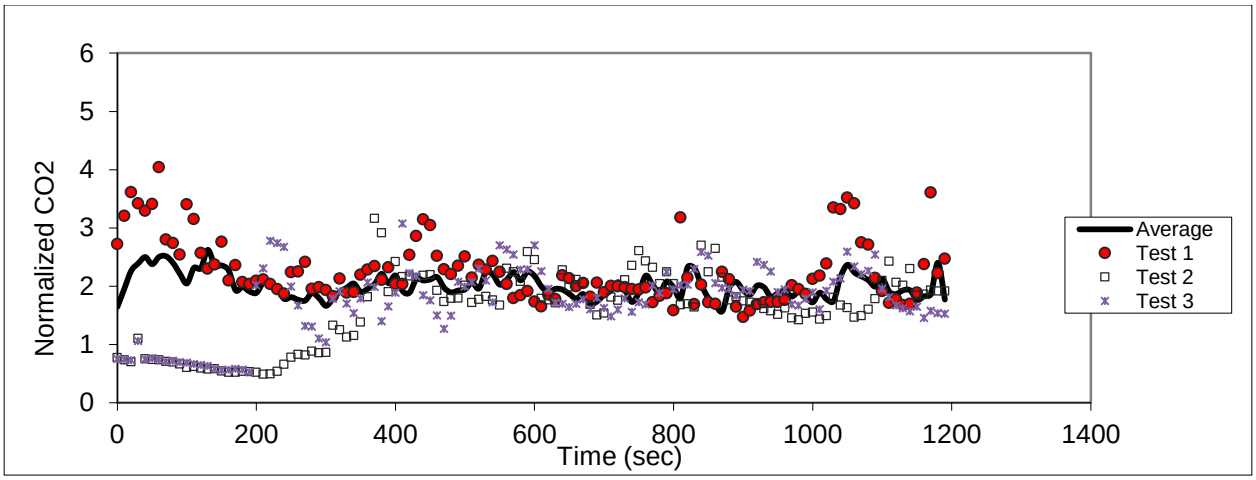

Figure C.63 – Sampling in seat 8F (release in 7D)

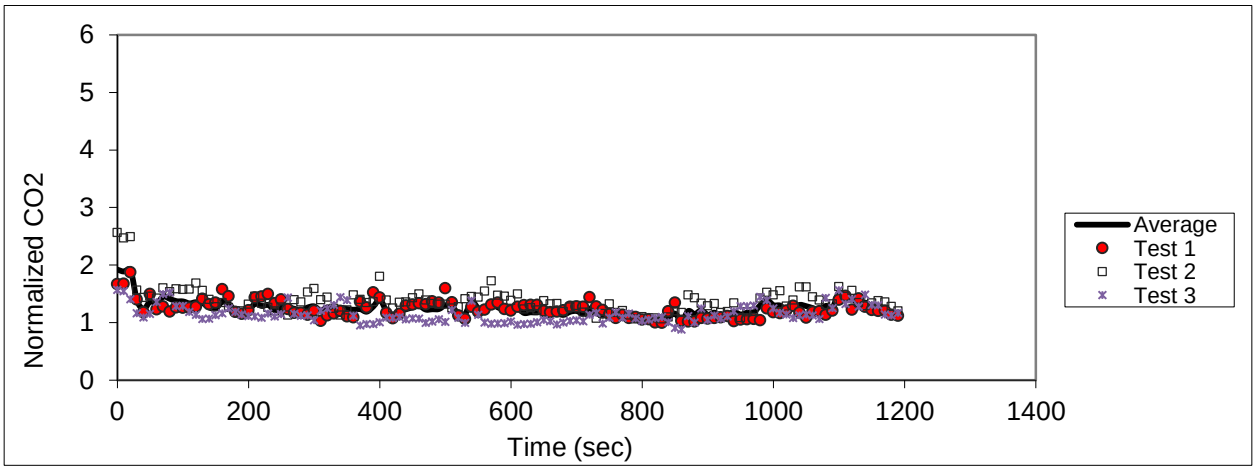

Figure C.64 – Sampling in seat 9F (release in 7D)

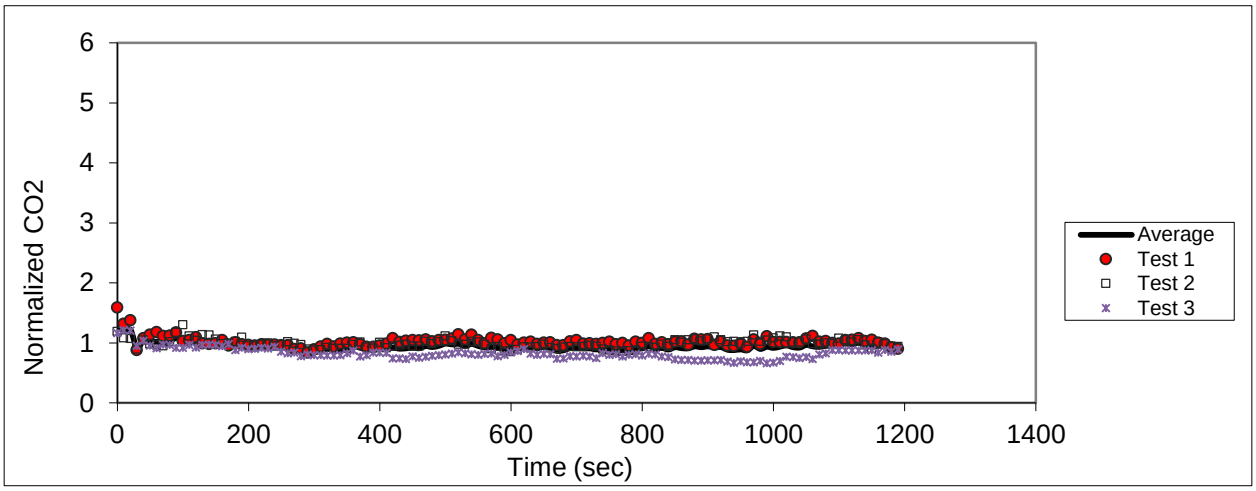

Figure C.65 - Sampling in seat 10F (release in 7D)

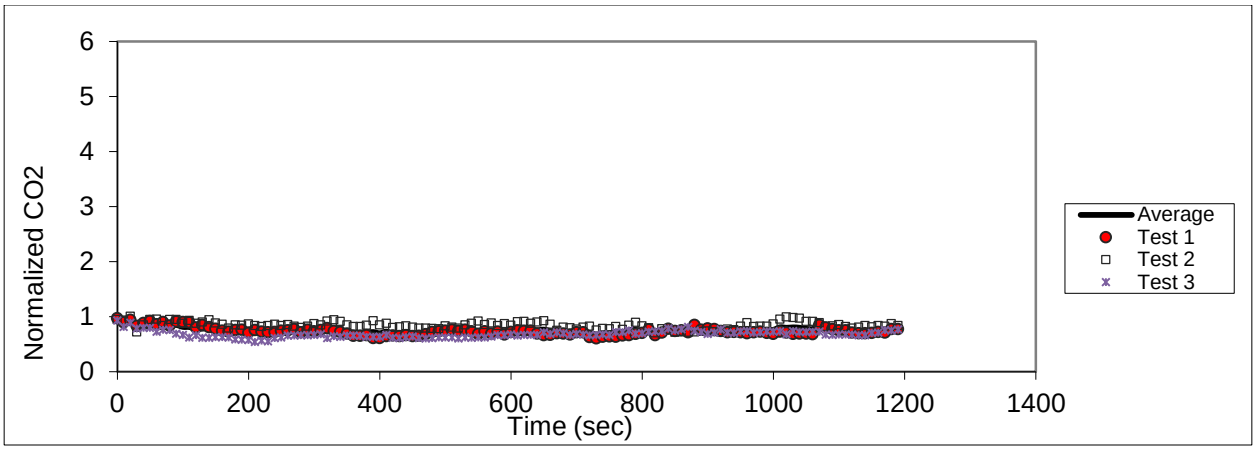

Figure C.66 – Sampling in seat 11F (release in 7D)

Release in 10D

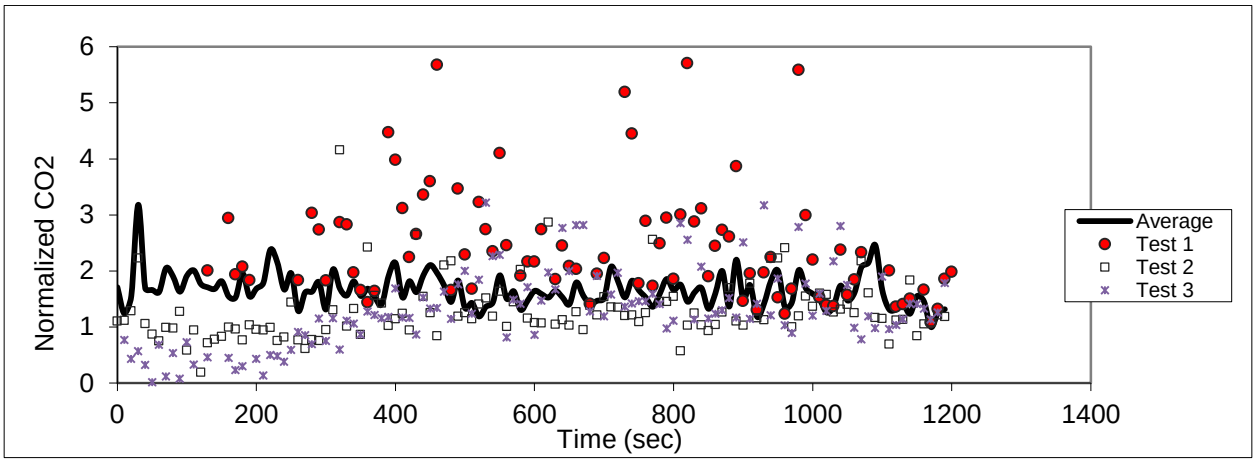

Figure C.67 – Sampling in seat 8B (release in 10D)

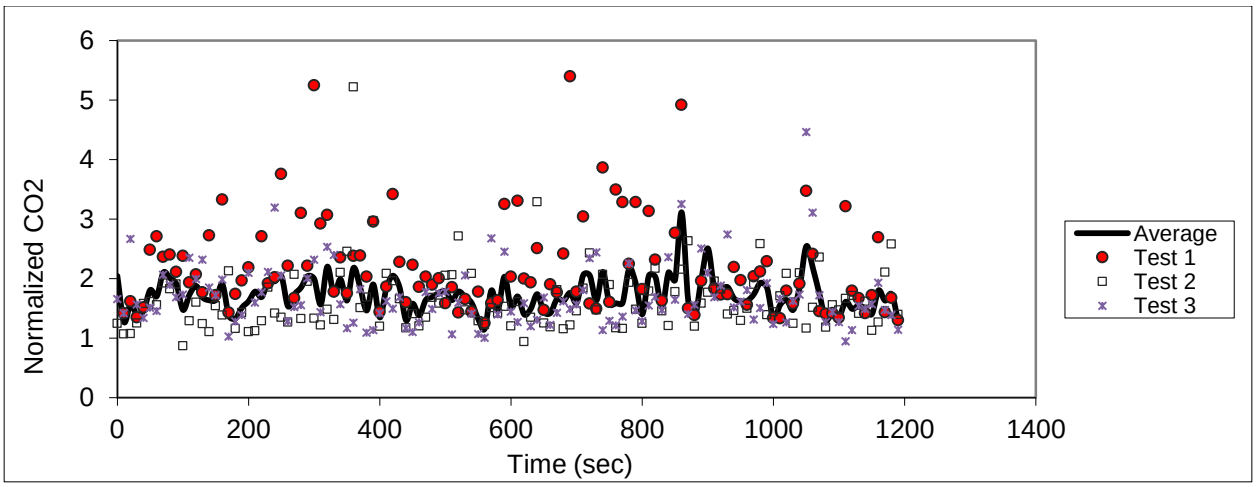

Figure C.68 – Sampling in seat 9B (release in 10D)

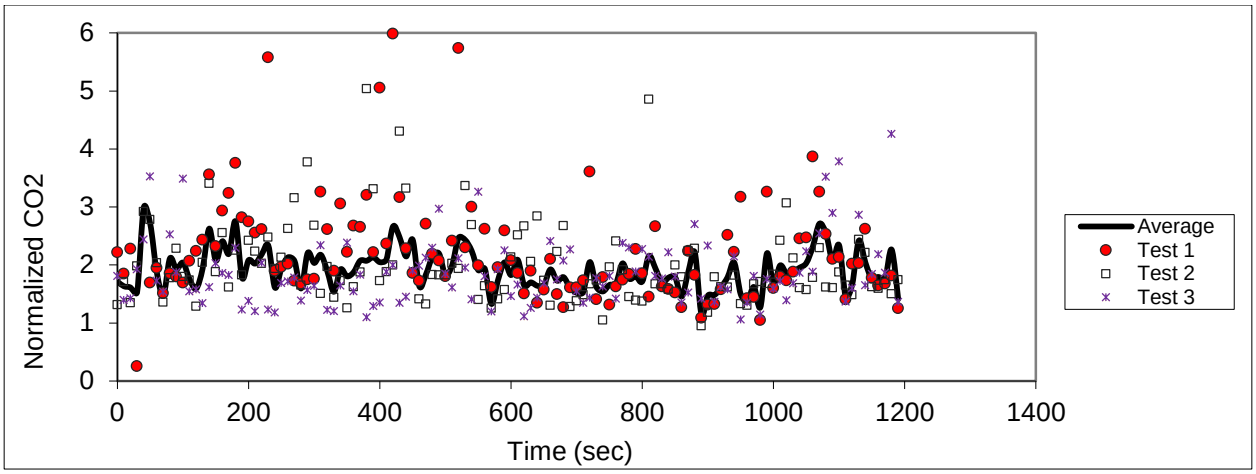

Figure C.69 – Sampling in seat 10B (release in 10D)

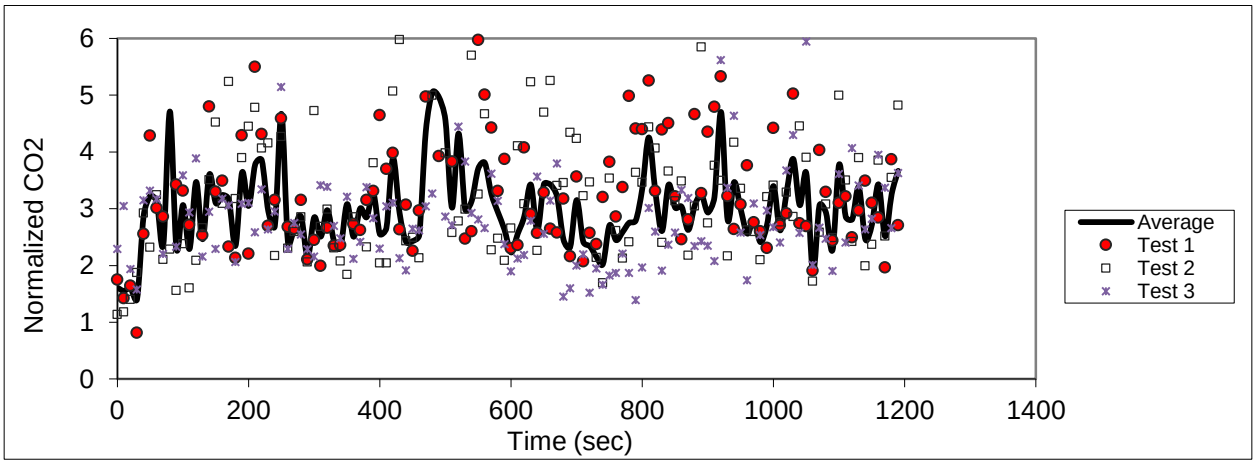

Figure C.70- Sampling in seat 11B (release in 10D)

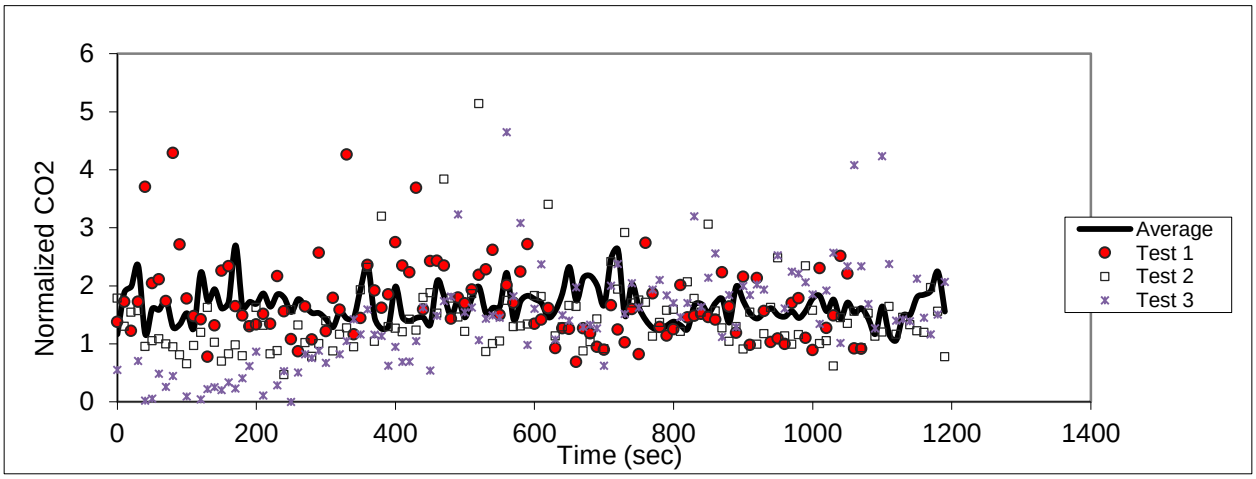

Figure C.71 - Sampling in seat 8C (release in 10D)

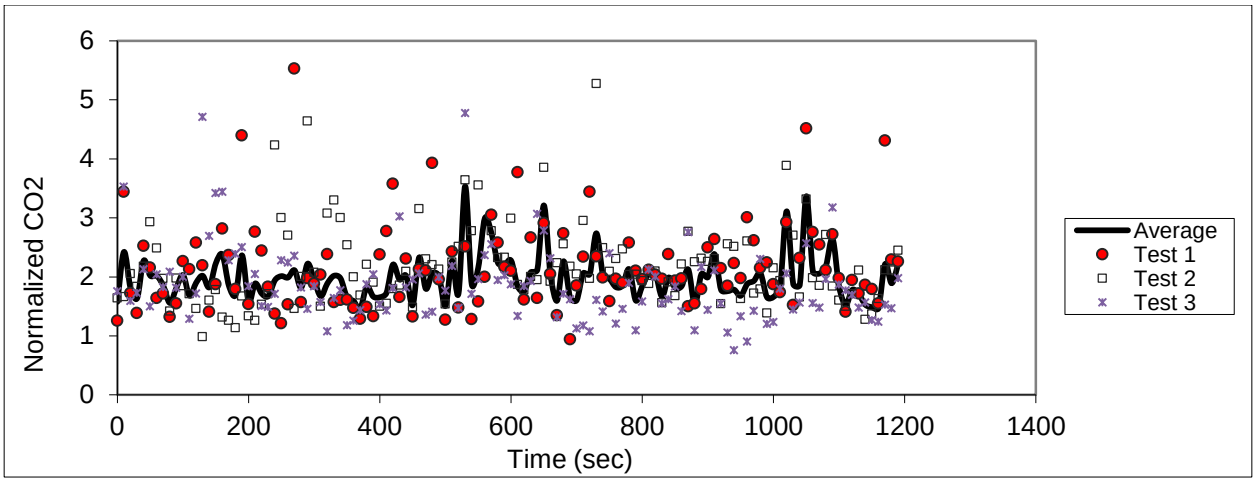

Figure C.72 – Sampling in seat 9C (release in 10D)

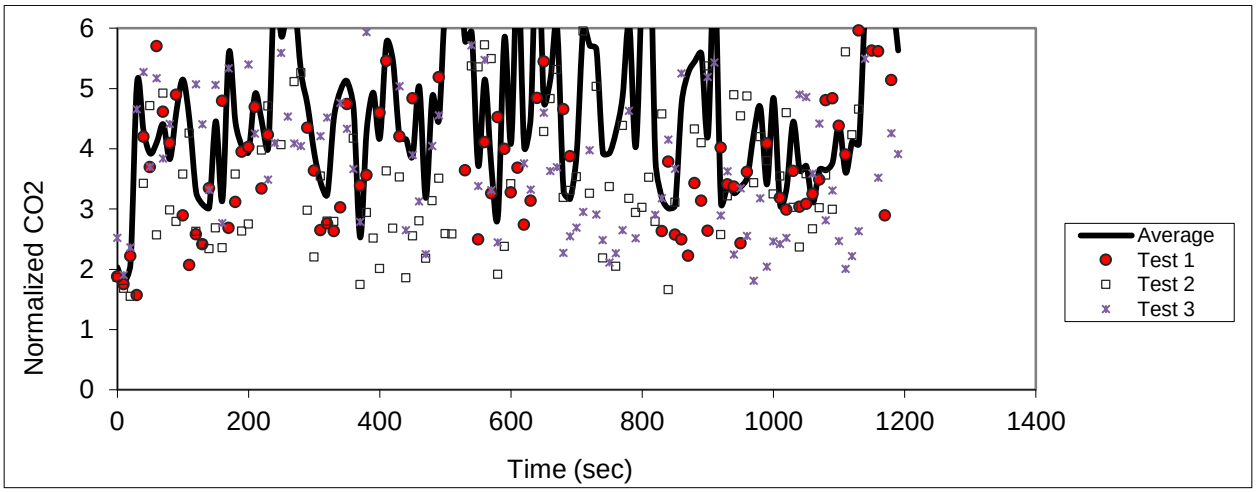

Figure C.73 – Sampling in seat 10C (release in 10D)

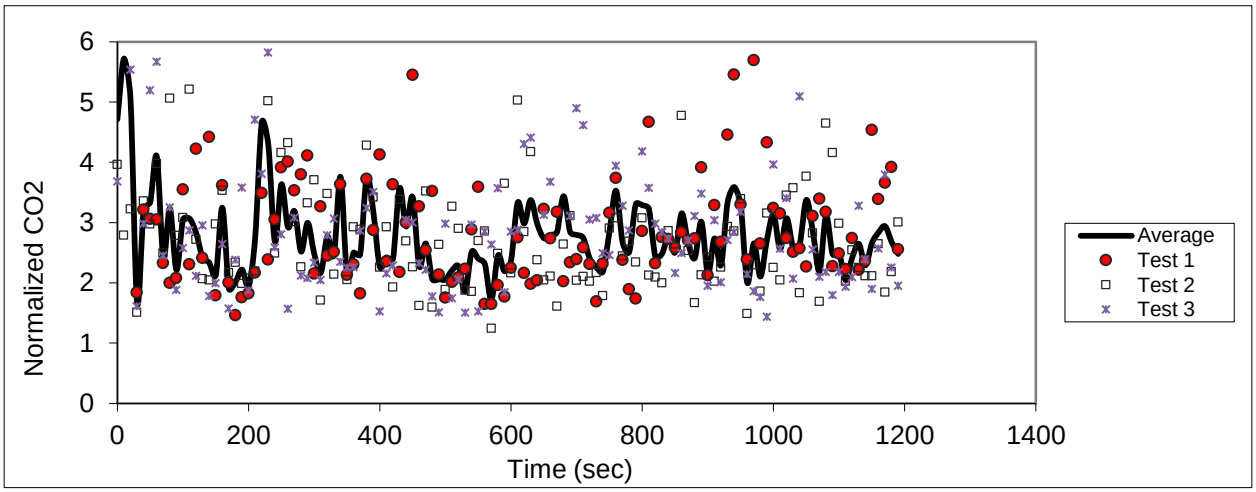

Figure C.74 – Sampling in seat 11C (release in 10D)

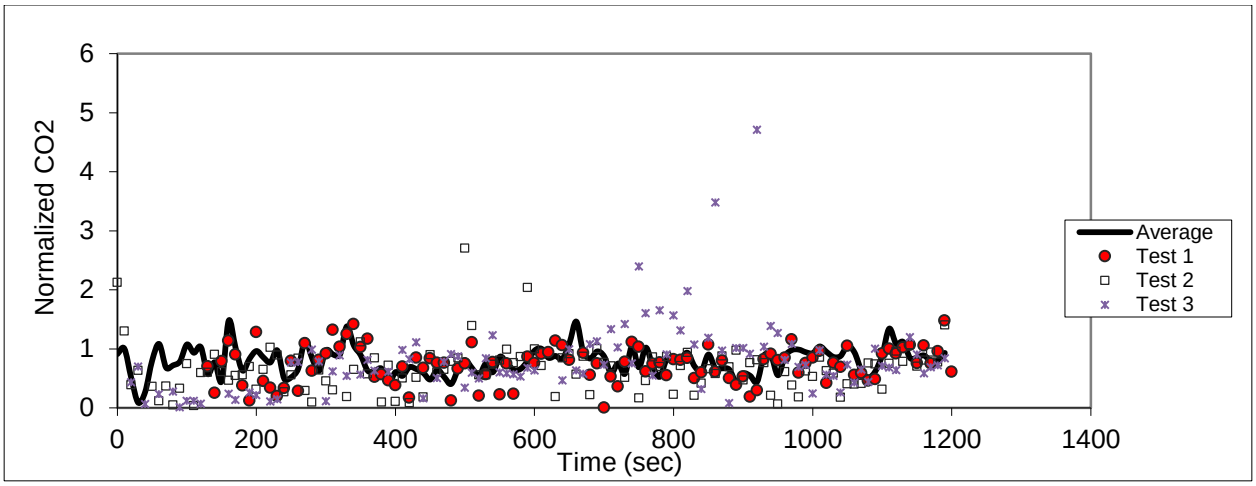

Figure C.75 – Sampling in seat 8E (release in 10D)

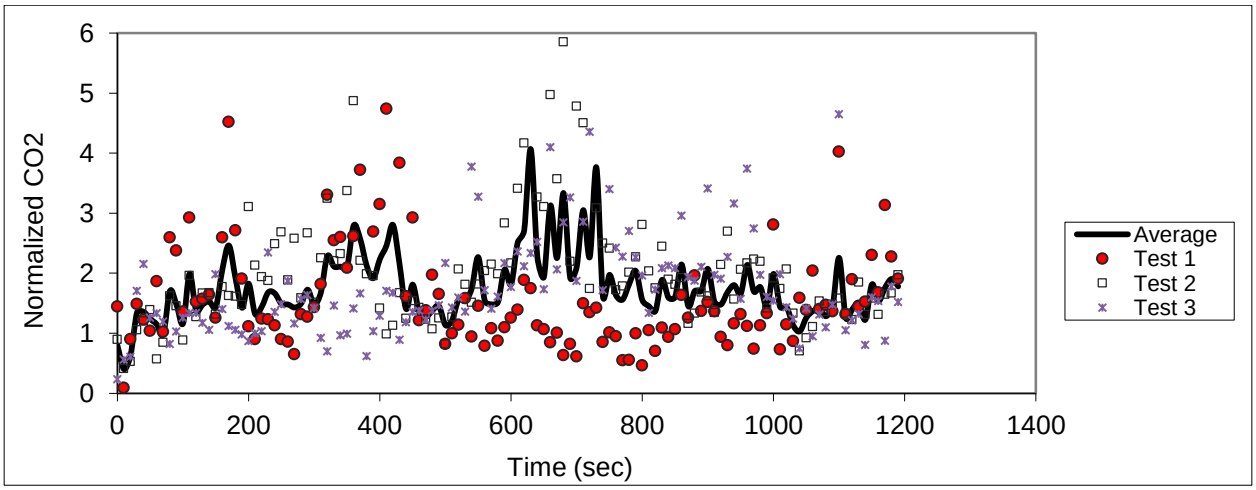

Figure C.76 – Sampling in seat 9E (release in 10D)

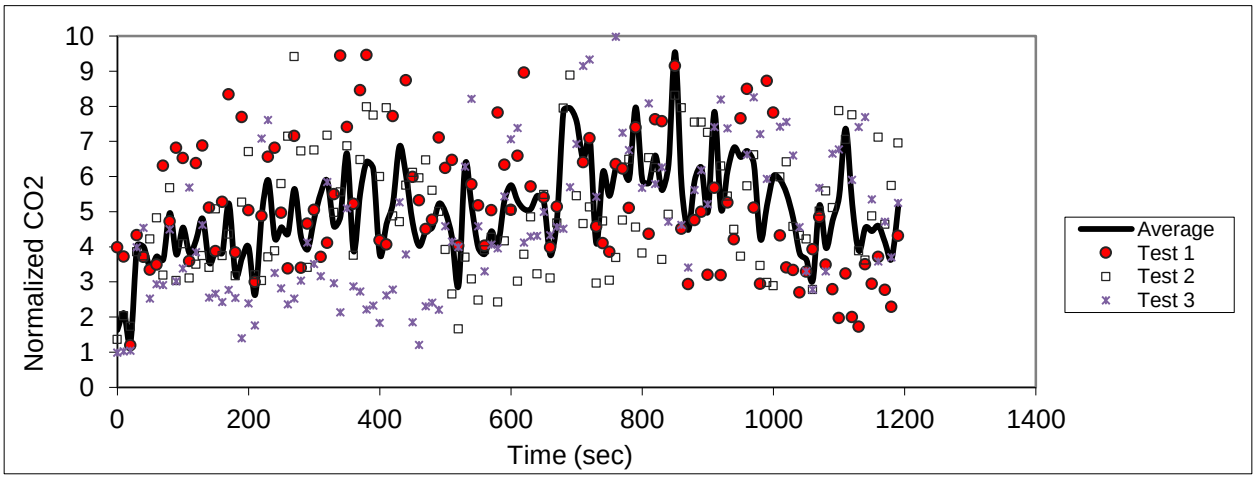

Figure C.77 - Sampling in seat 10E (release in 10D)

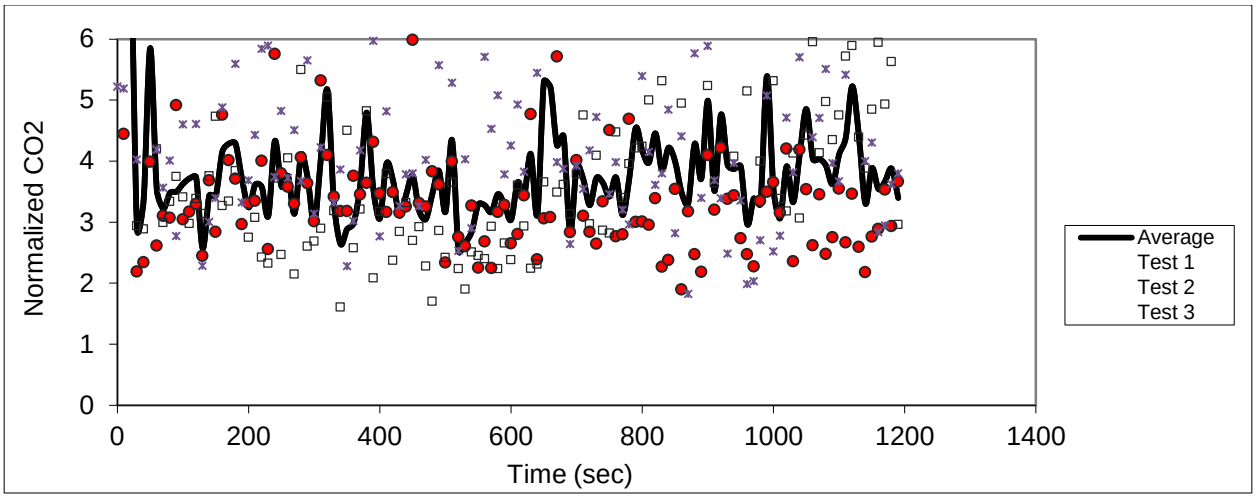

Figure C.78 – Sampling in seat 11E (release in 10D)

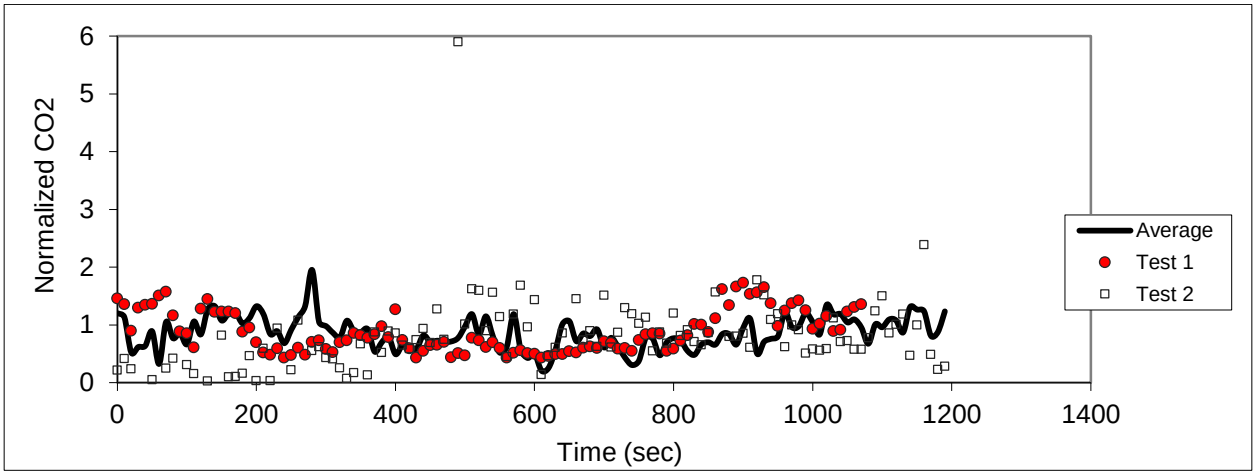

Figure C.79 – Sampling in seat 8F (release in 10D)

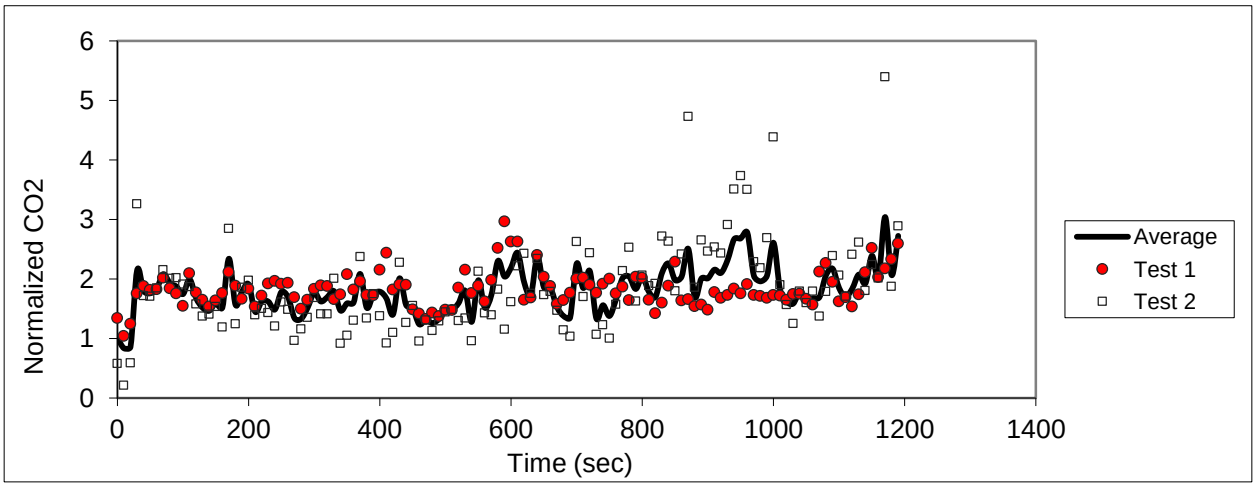

Figure C.80 – Sampling in seat 9F (release in 10D)

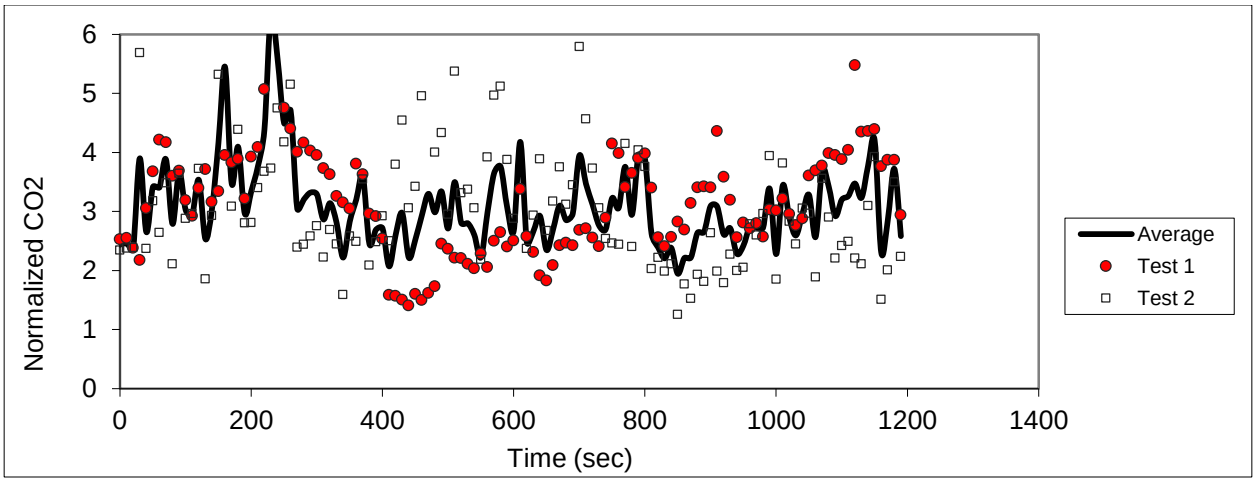

Figure C.81 – Sampling in seat 10F (release in 10D)

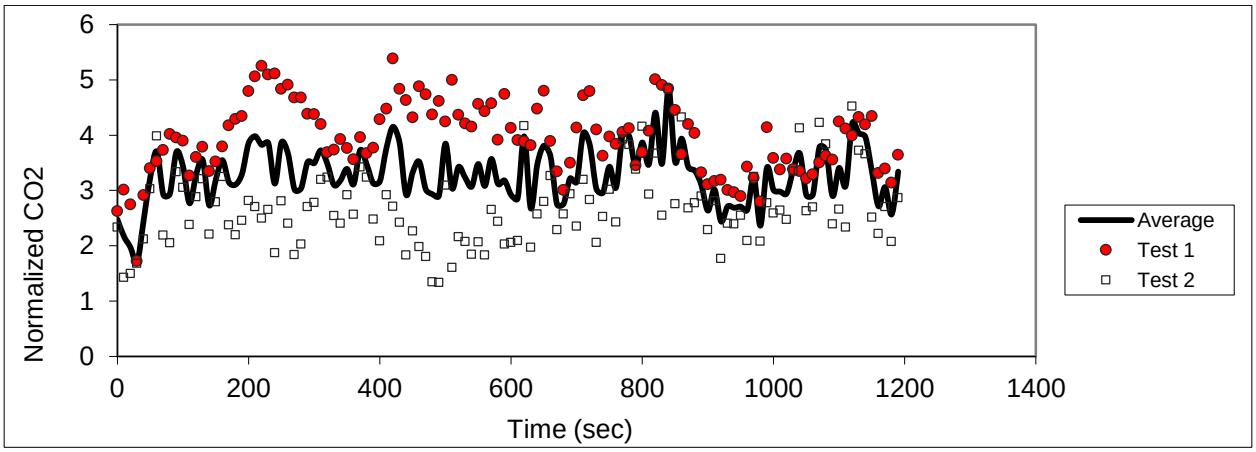

Figure C.82 - Sampling in seat 11F (release in 10D)

Release in 5B

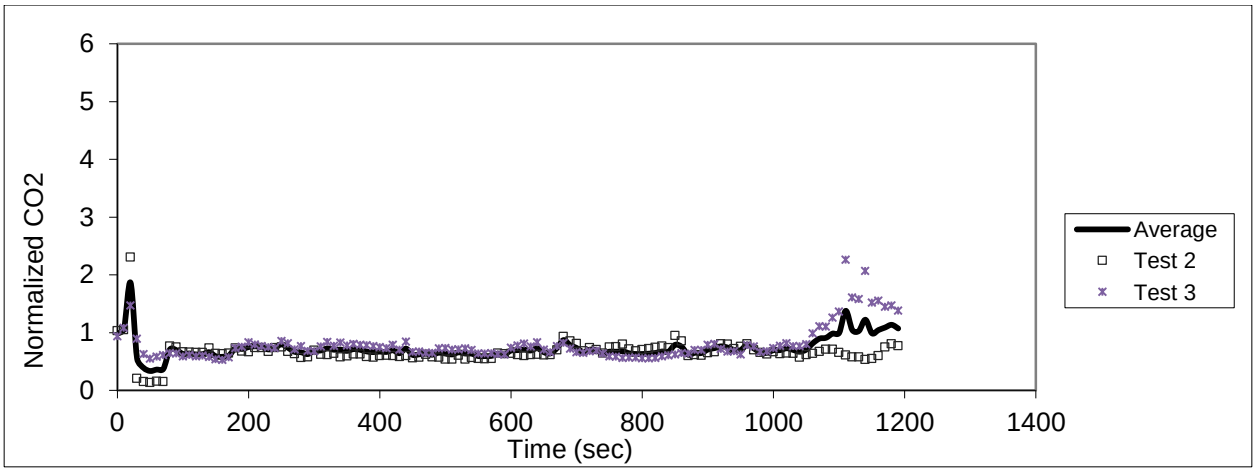

Figure C.83 - Sampling in seat 2B (release in 5B)

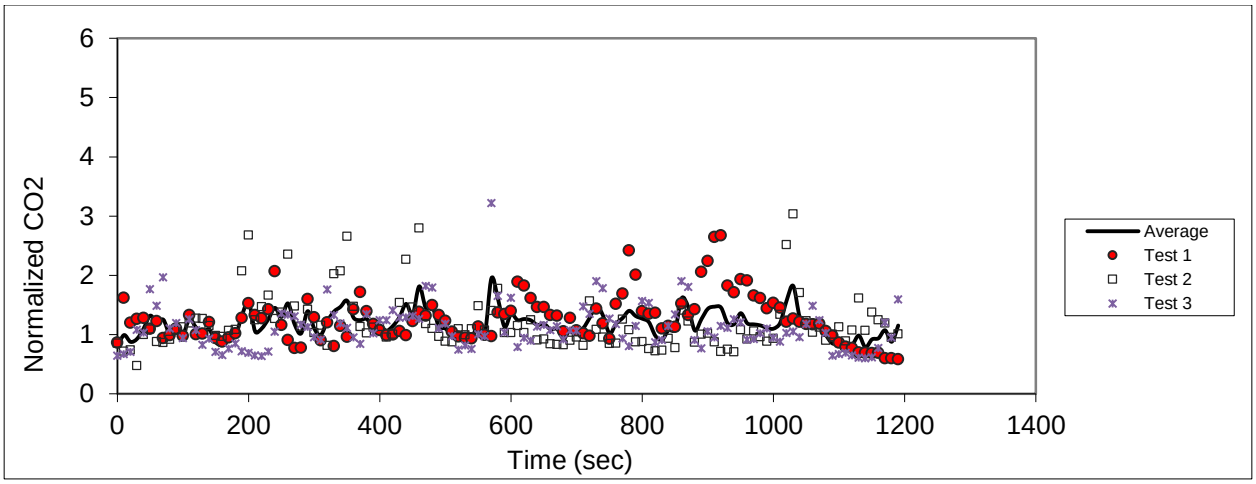

Figure C.84 – Sampling in seat 3B (release in 5B)

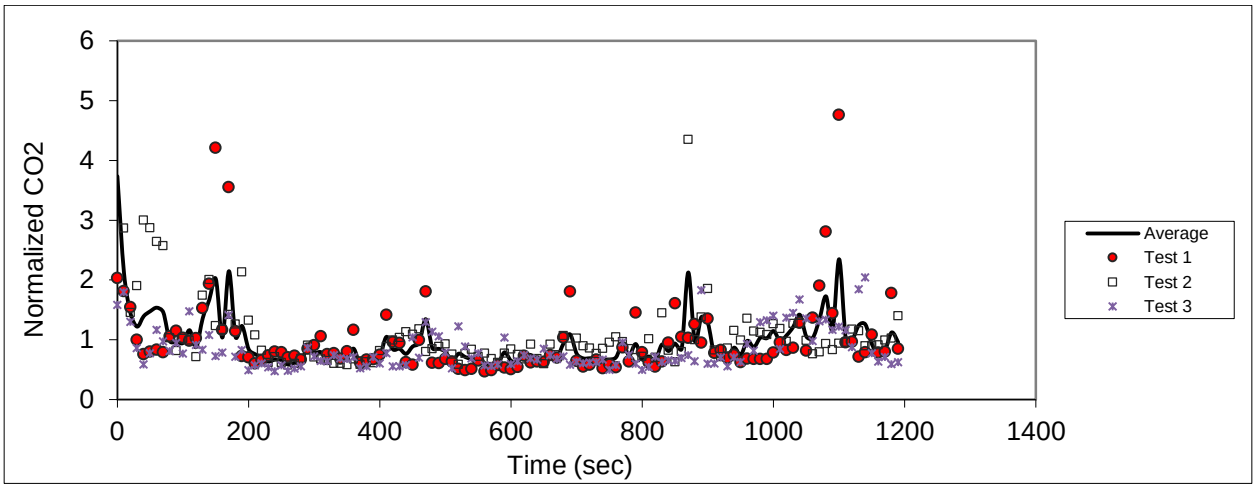

Figure C.85 – Sampling in seat 4B (release in 5B)

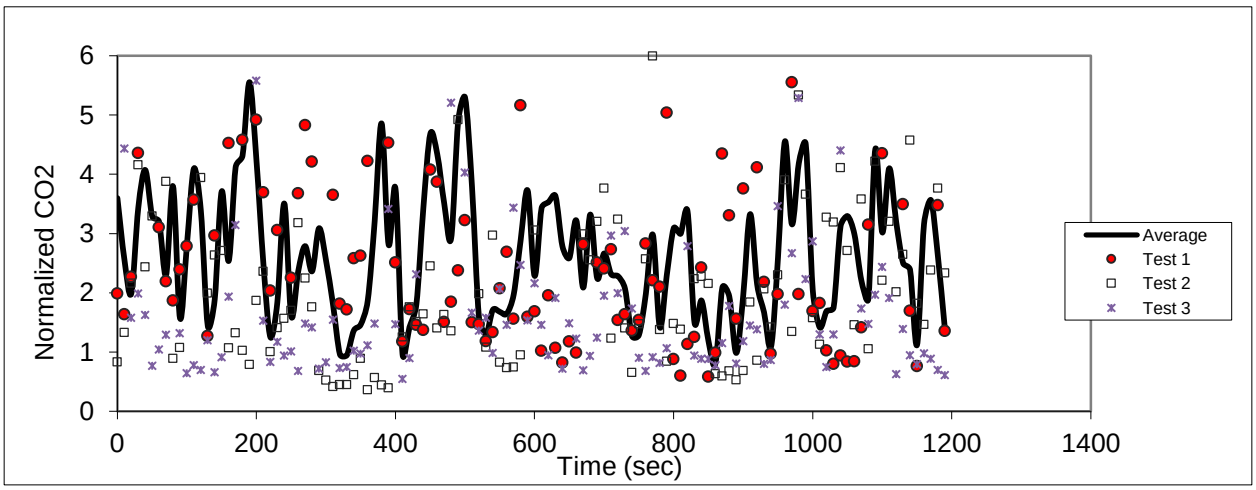

Figure C.86 - Sampling in seat 5B (release in 5B)

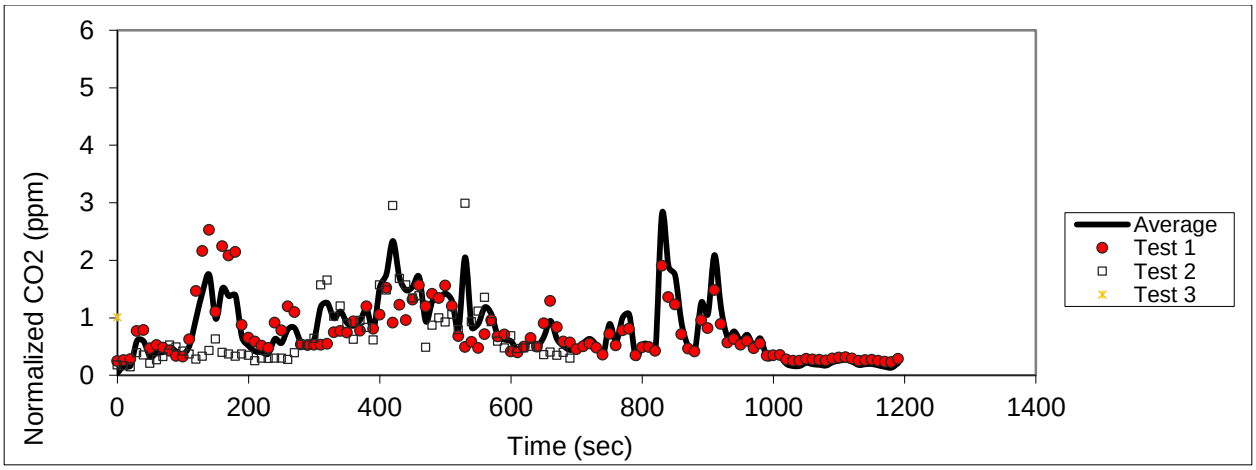

Figure C.87 – Sampling in seat 6B (release in 5B)

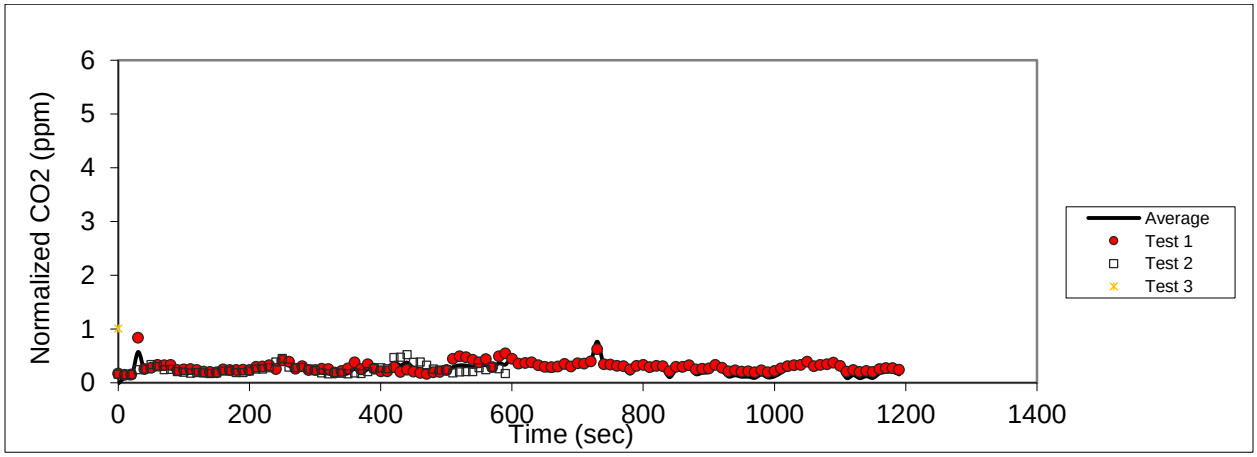

Figure C.88 – Sampling in seat 6C (release in 5B)

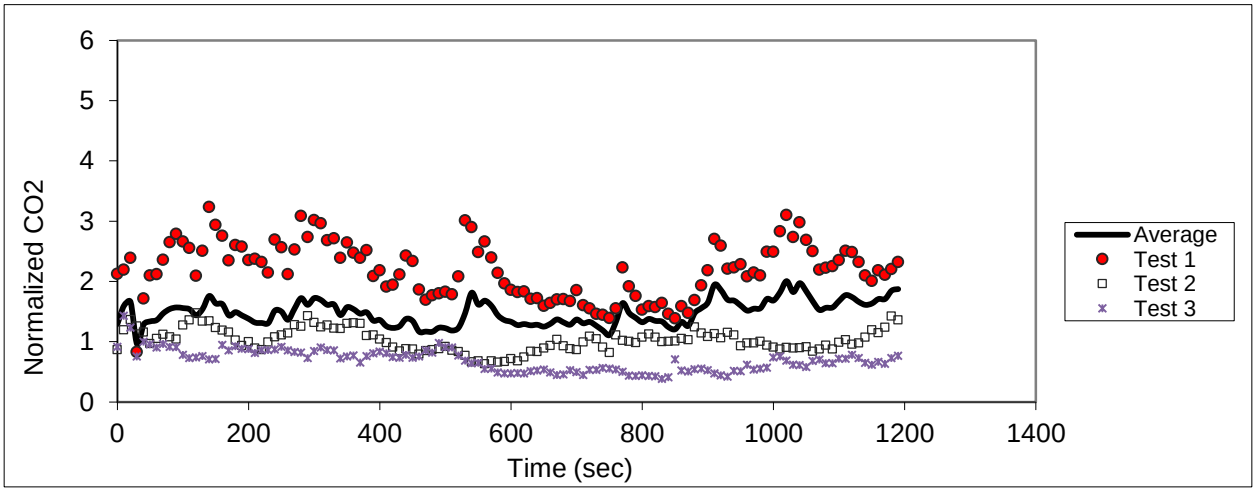

Figure C.89 – Sampling in seat 2D (release in 5B)

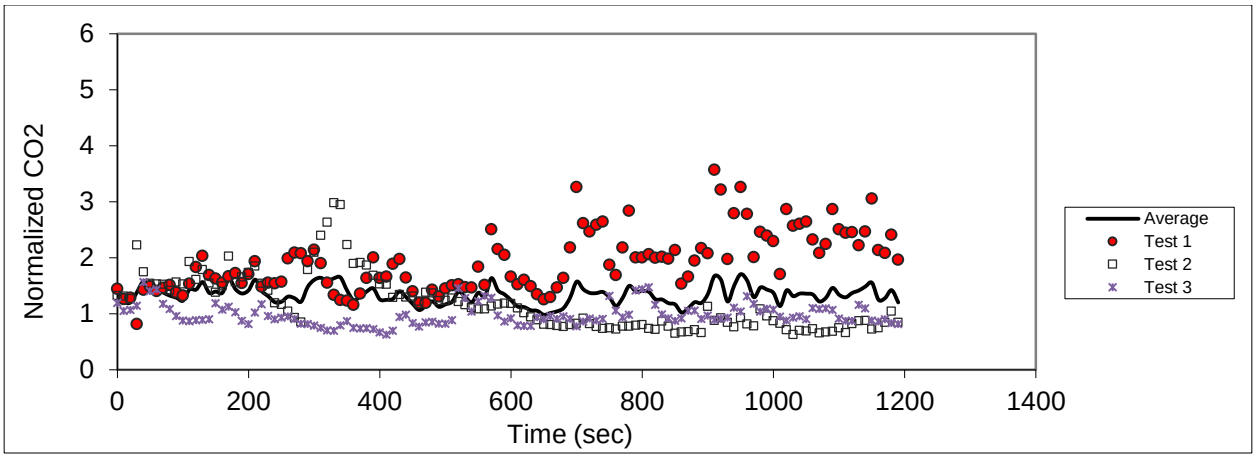

Figure C.90 – Sampling in seat 3D (release in 5B)

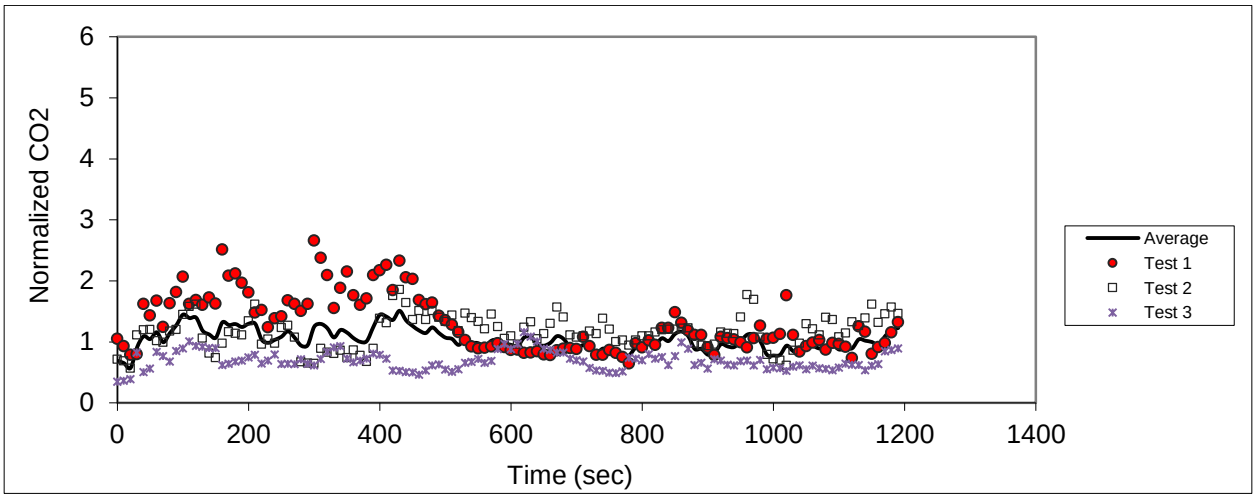

Figure C.91 – Sampling in seat 4D (release in 5B)

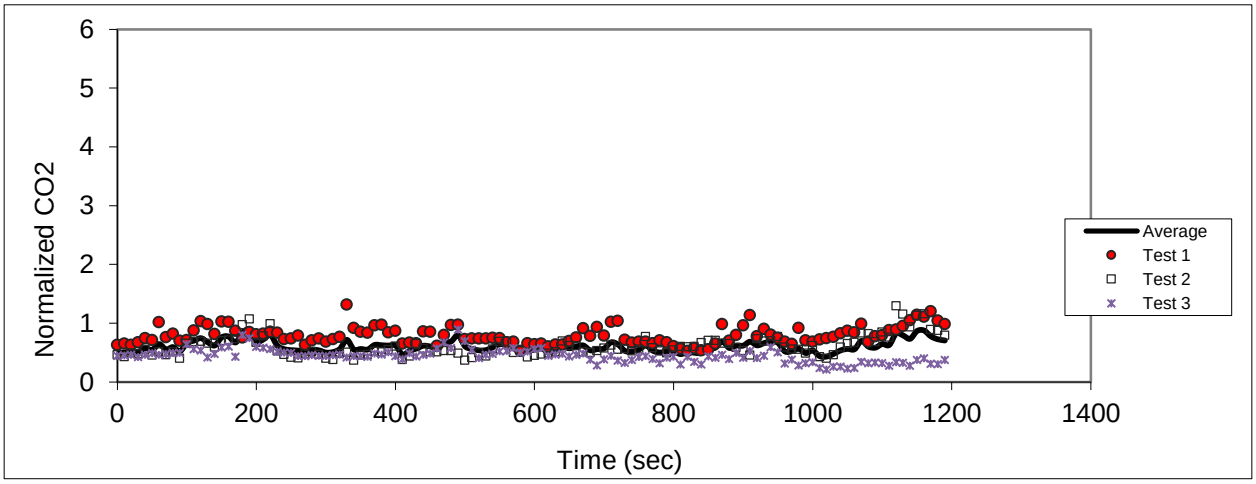

Figure C.92 – Sampling in seat 5D (release in 5B)

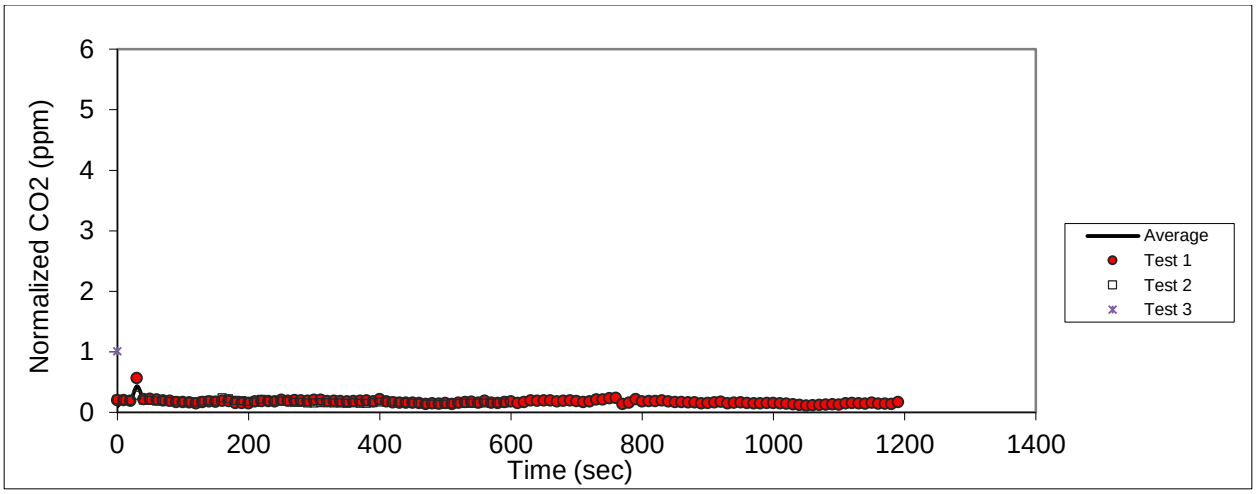

Figure C.93 – Sampling in seat 6D (release in 5B)

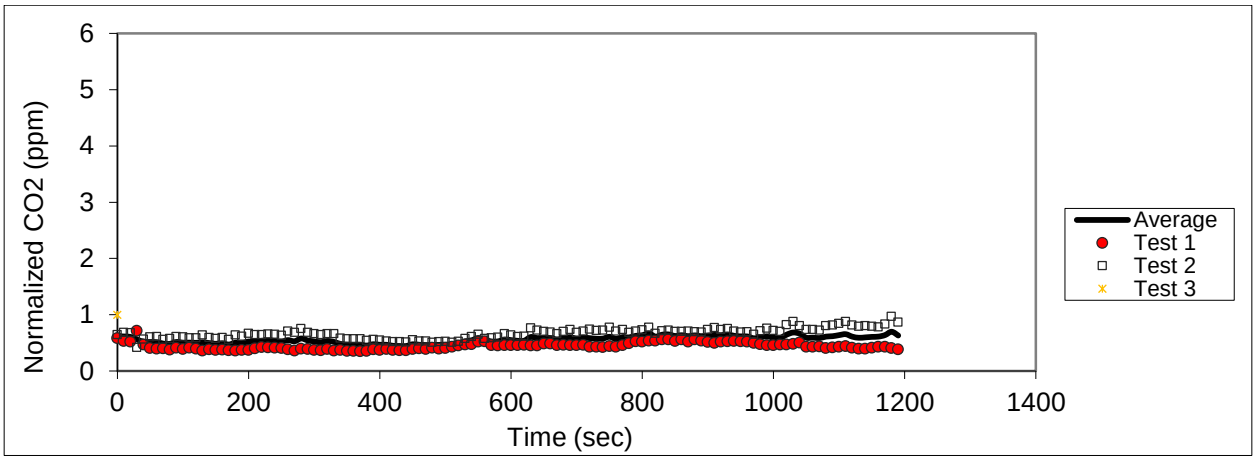

Figure C.94 – Sampling in seat 2F (release in 5B)

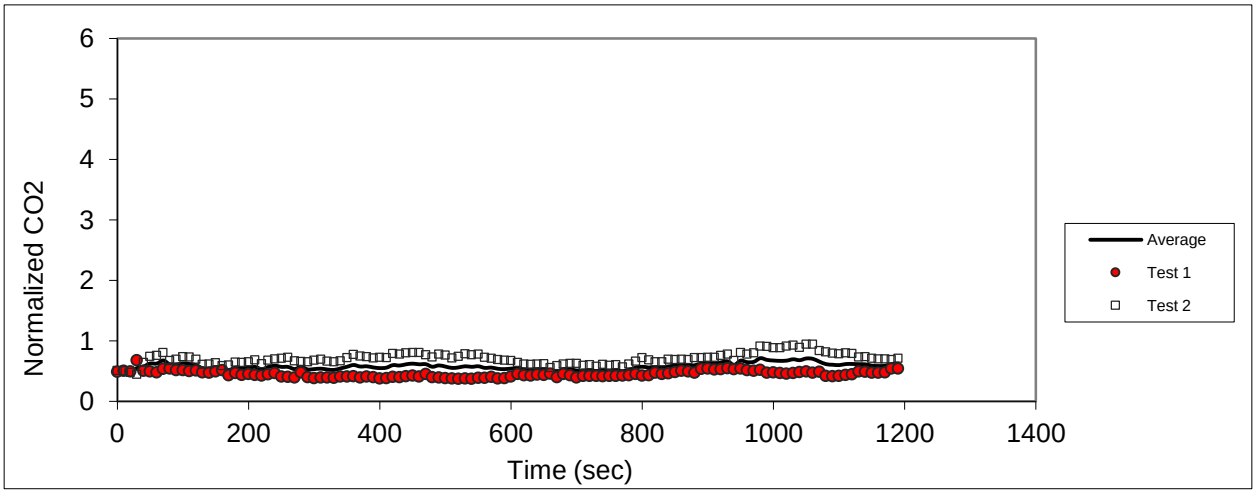

Figure C.95 – Sampling in seat 3F (release in 5B)

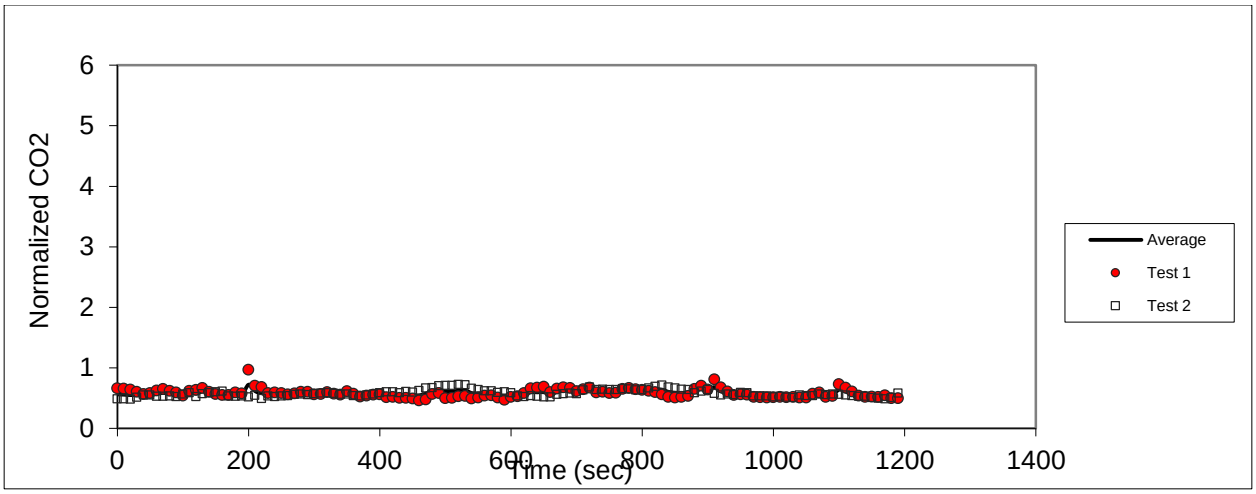

Figure C.96 – Sampling in seat 4F (release in 5B)

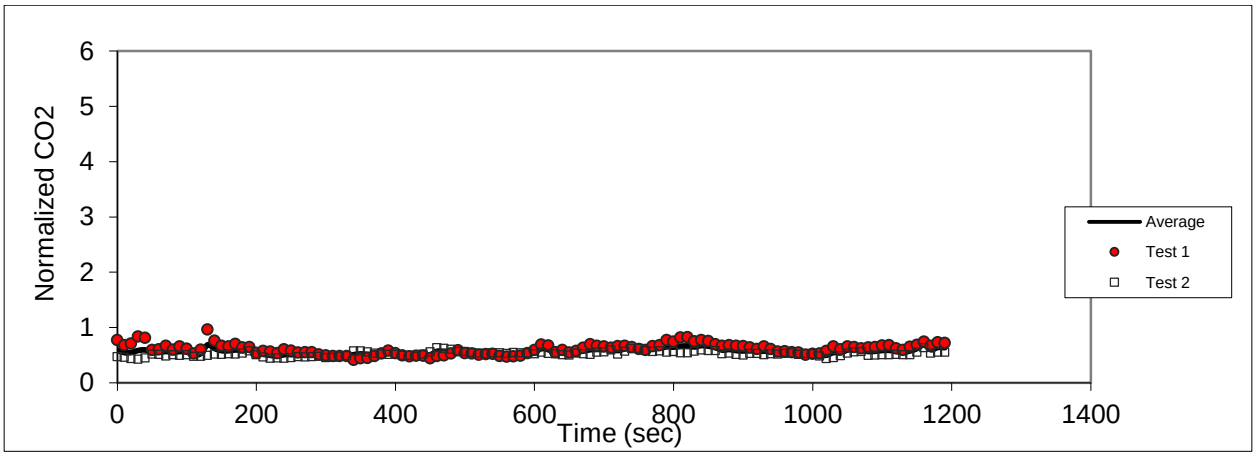

Figure C.97 – Sampling in seat 5F (release in 5B)

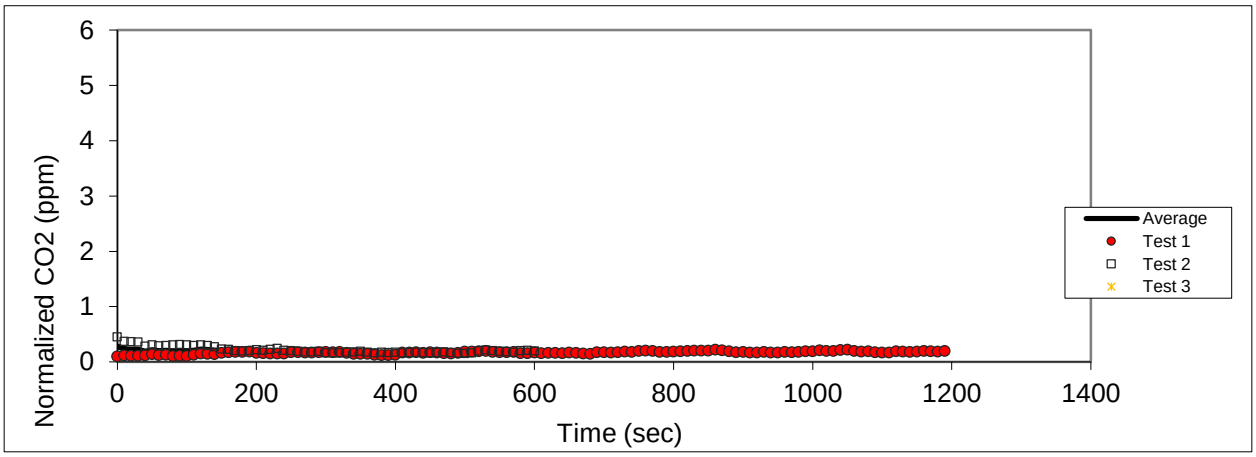

Figure C.98 - Sampling in seat 6F (release in 5B)

Release in 8B

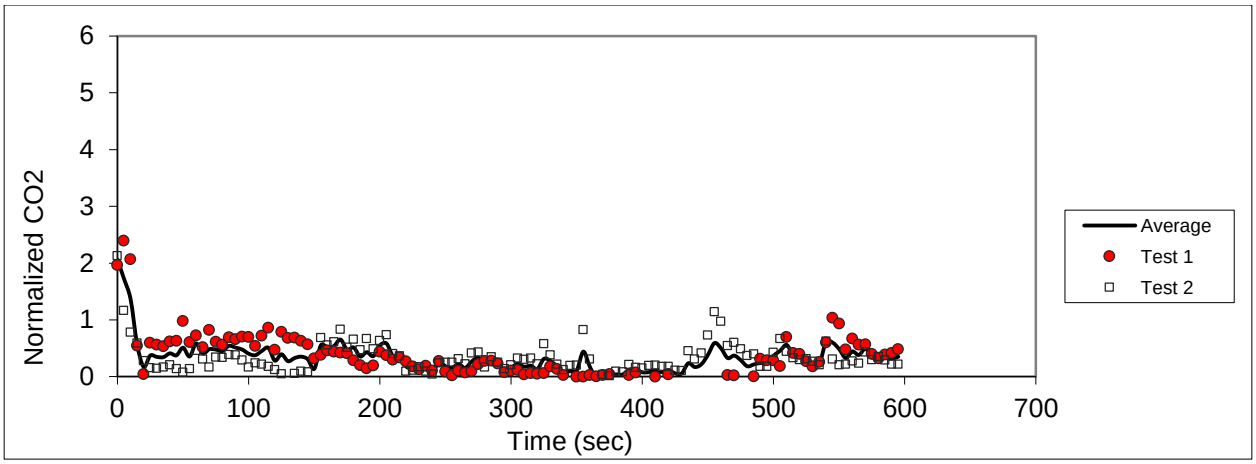

Figure C.99 – Sampling in seat 3B (release in 8B)

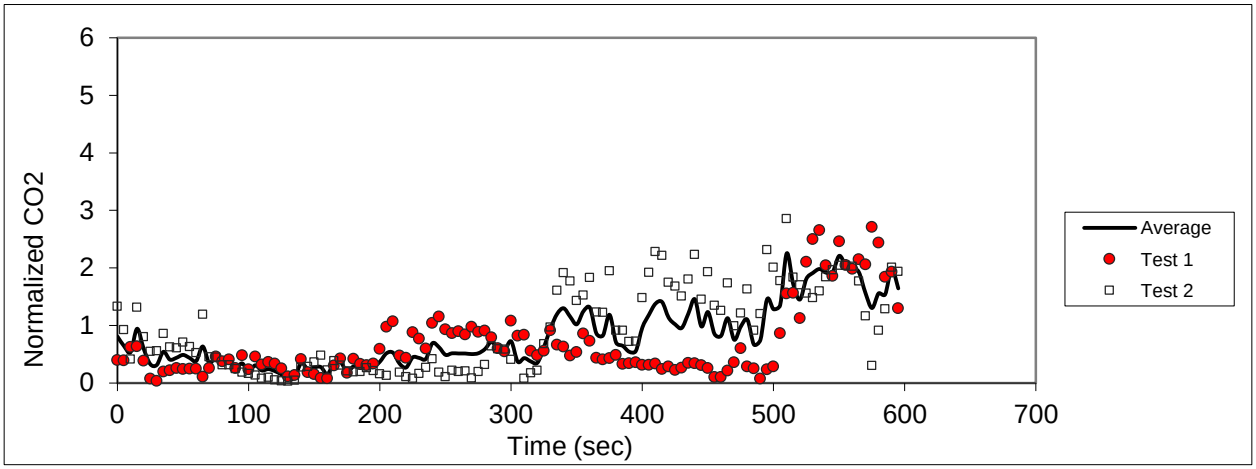

Figure C.100 – Sampling in seat 4B (release in 8B)

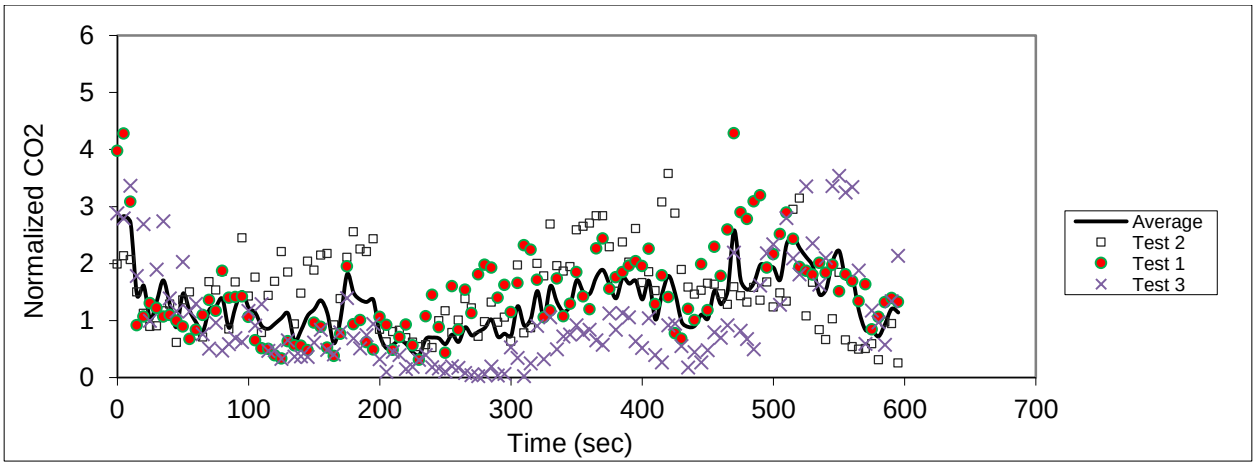

Figure C.101 – Sampling in seat 5B (release in 8B)

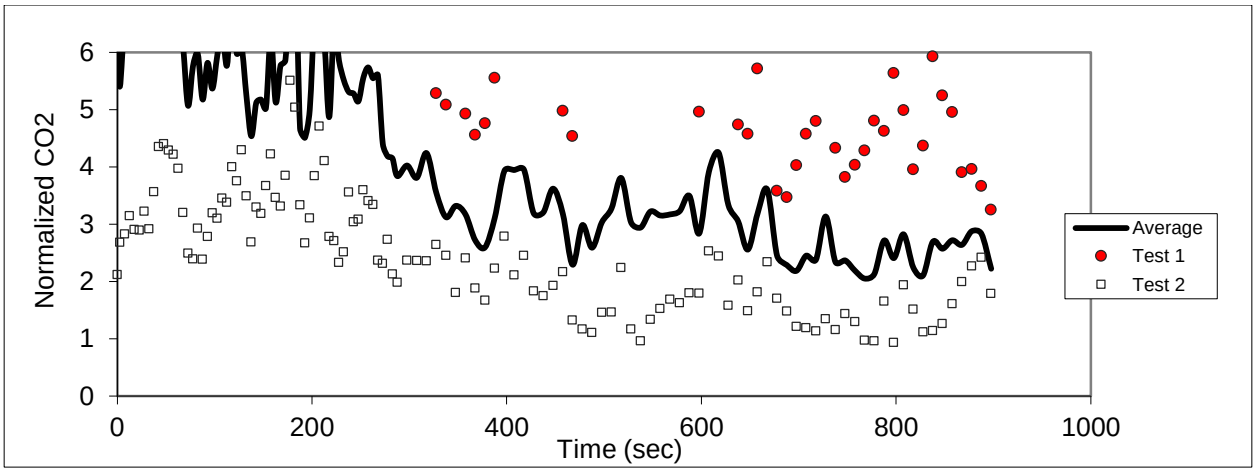

Figure C.102 – Sampling in seat 6B (release in 8B)

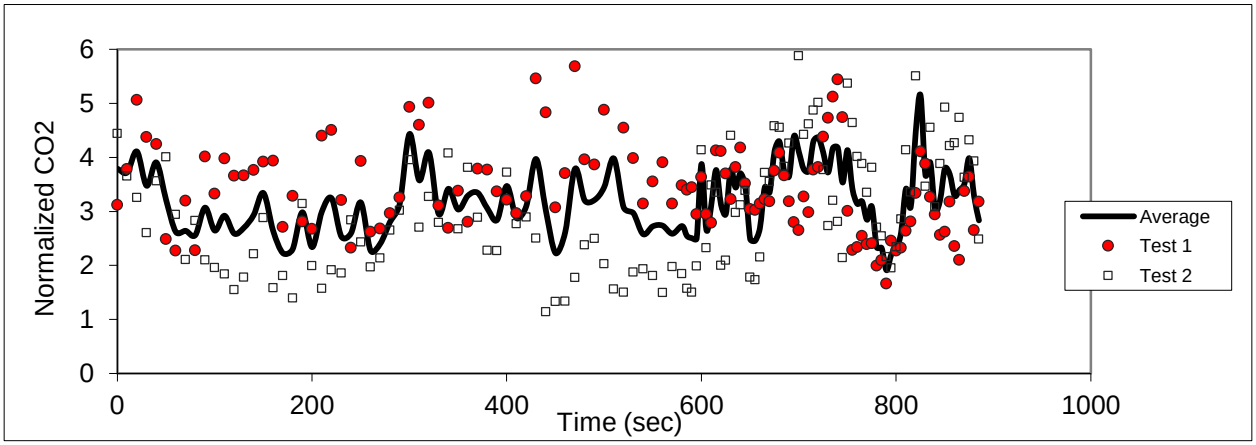

Figure C.103 – Sampling in seat 7B (release in 8B)

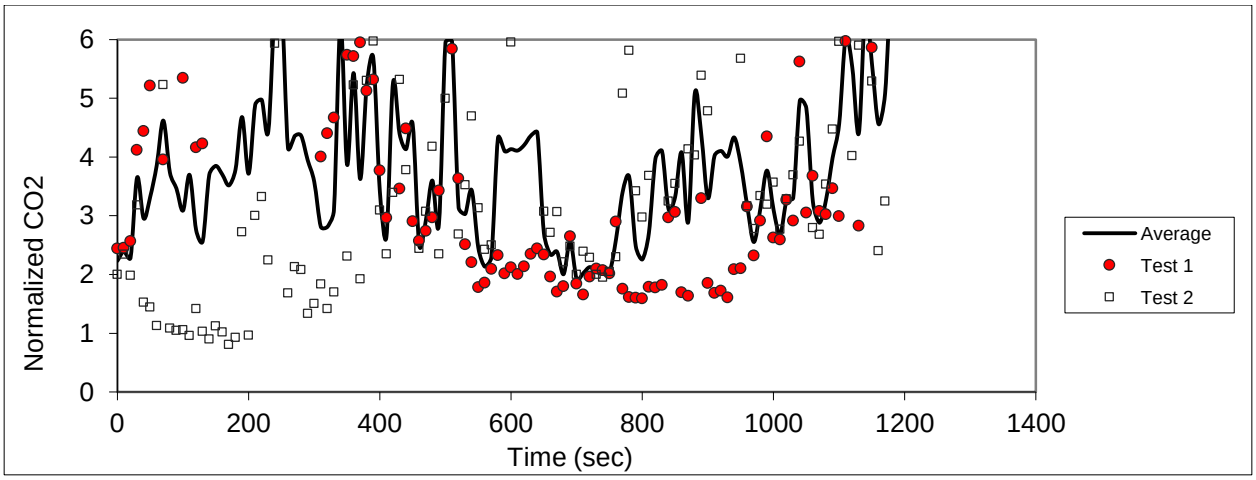

Figure C.104 – Sampling in seat 8B (release in 8B)

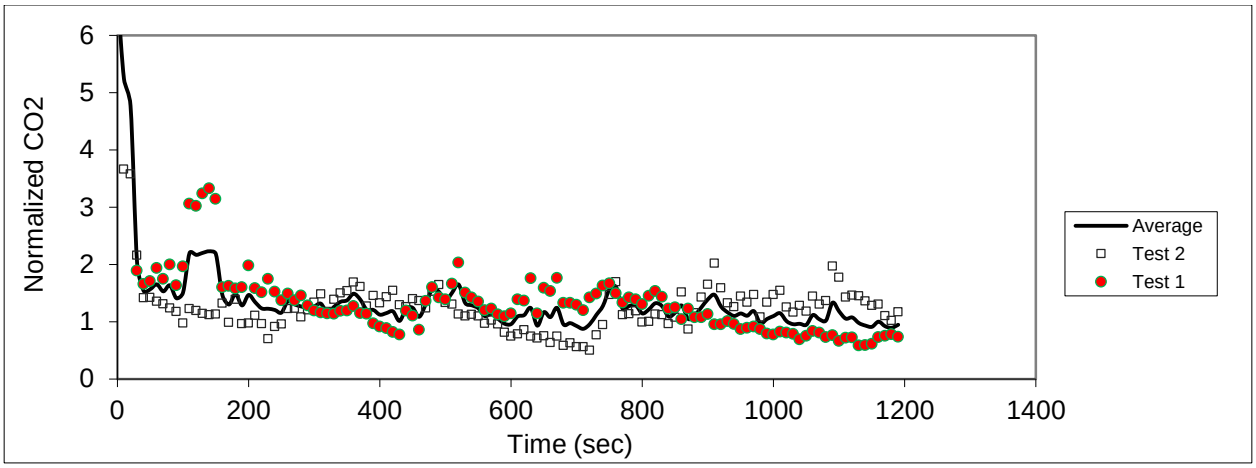

Figure C.105 – Sampling in seat 9B (release in 8B)

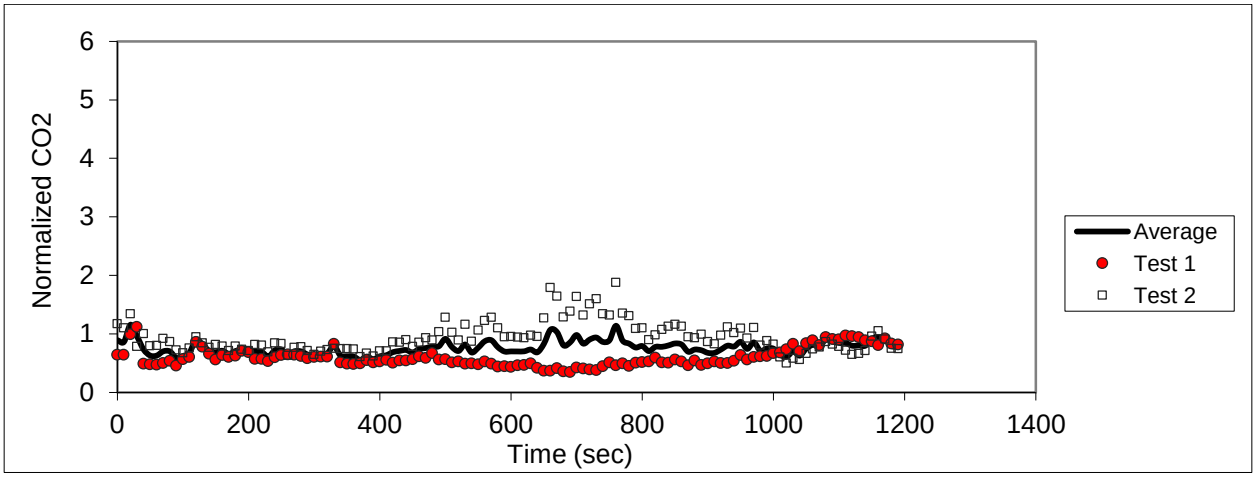

Figure C.106 – Sampling in seat 10B (release in 8B)

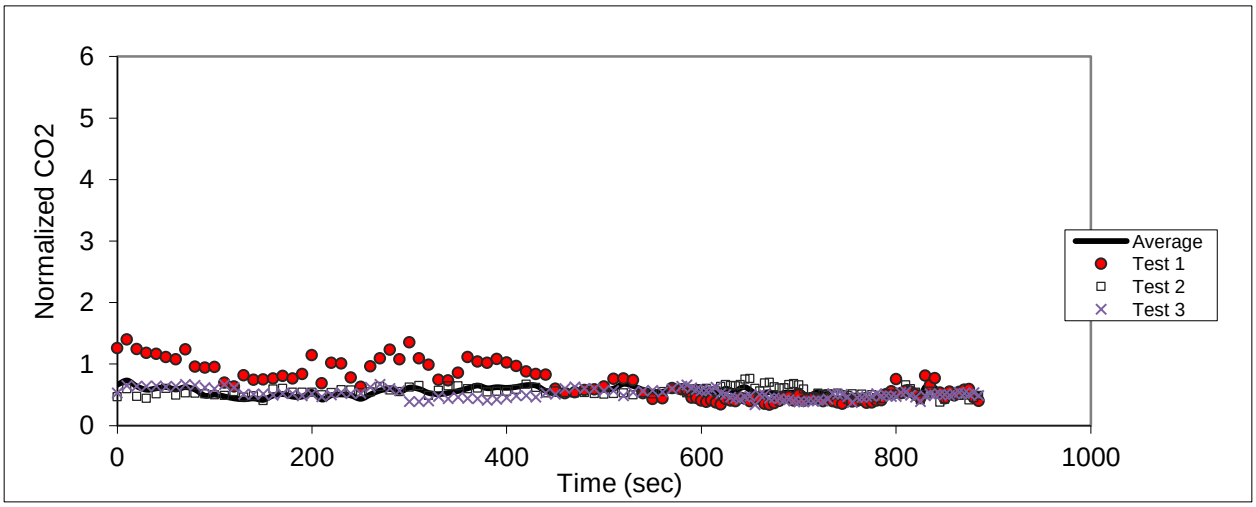

Figure C.107 – Sampling in seat 4D (release in 8B)

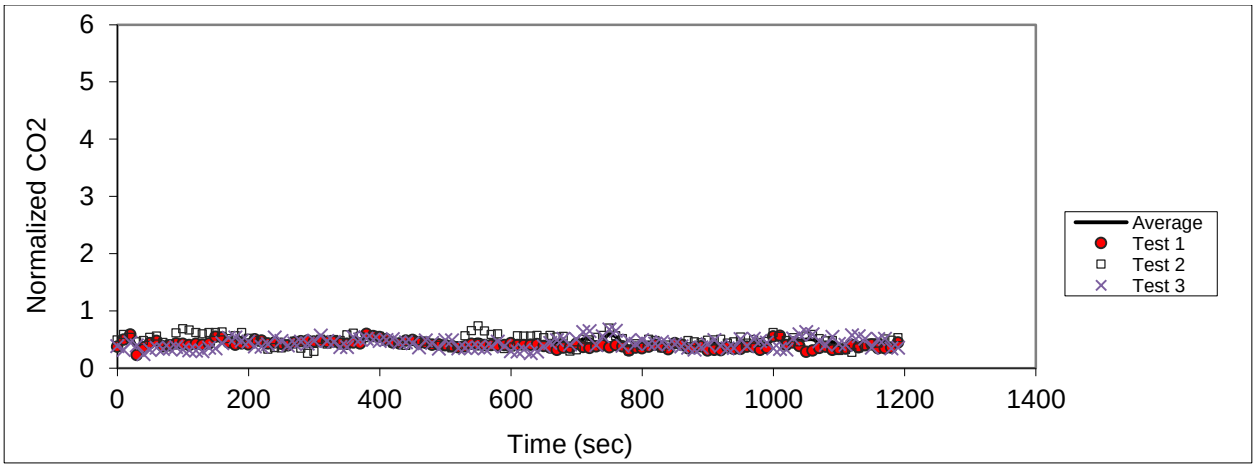

Figure C.108 – Sampling in seat 5D (release in 8B)

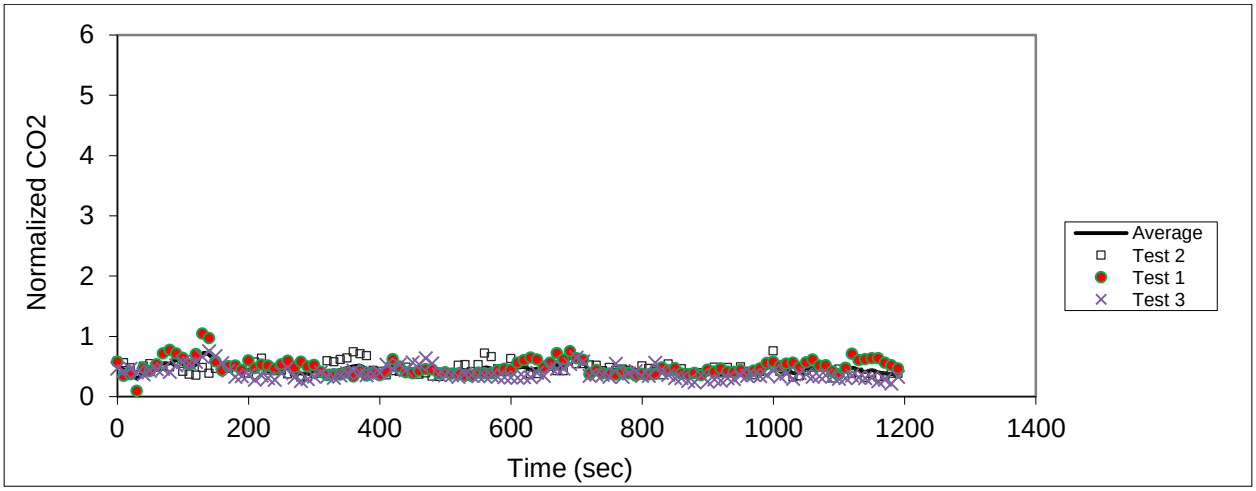

Figure C.109 – Sampling in seat 6D (release in 8B)

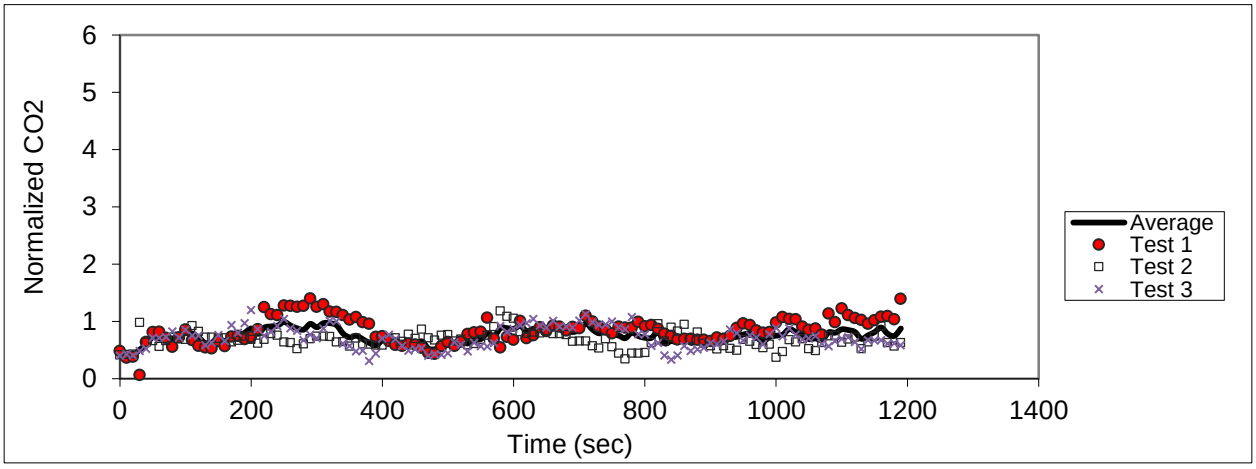

Figure C.110 – Sampling in seat 7D (release in 8B)

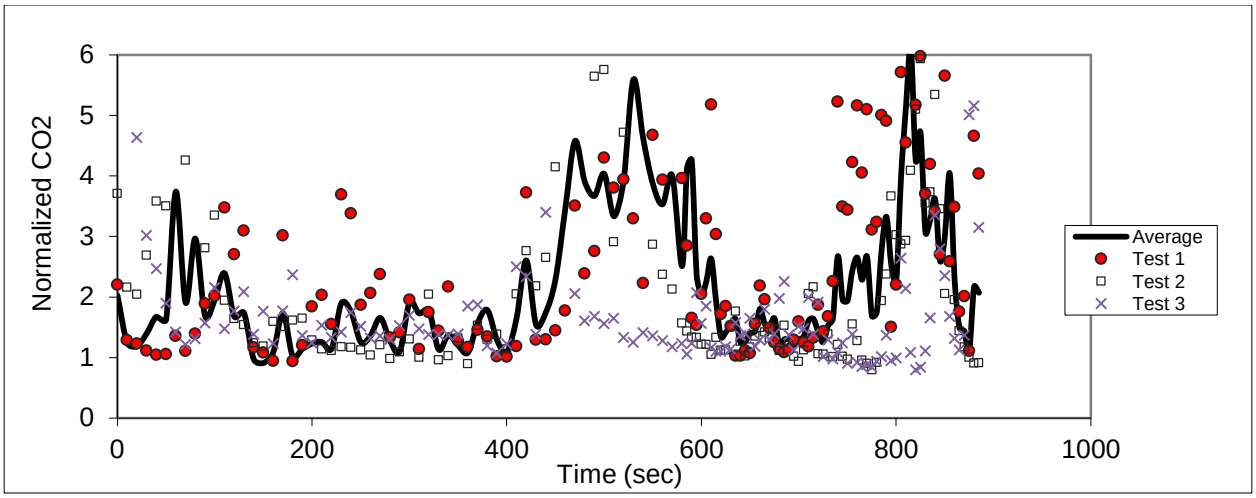

Figure C.111 – Sampling in seat 8D (release in 8B)

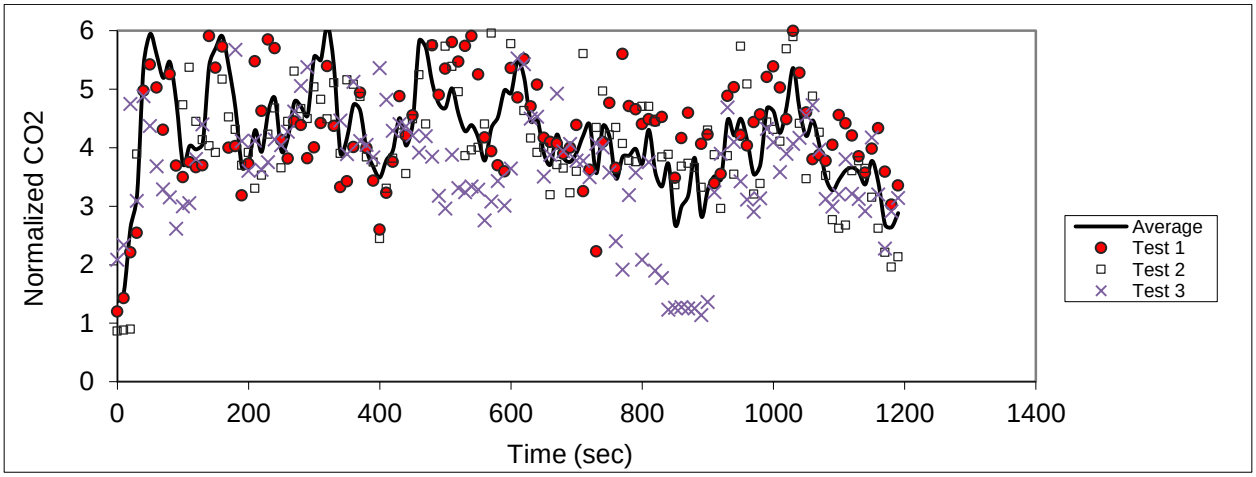

Figure C.112 – Sampling in seat 9D (release in 8B)

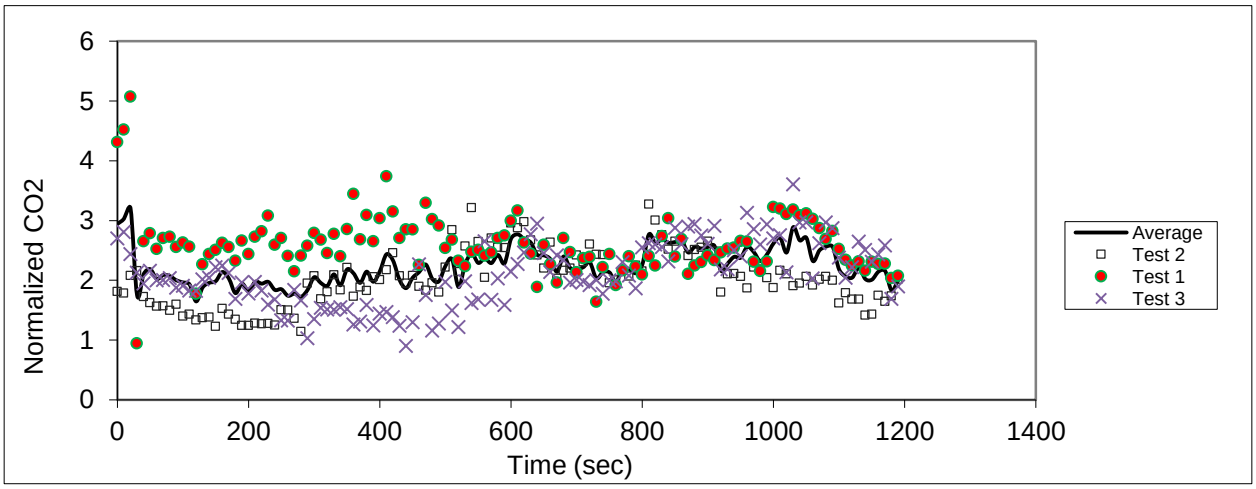

Figure C.113 - Sampling in seat 10D (release in 8B)

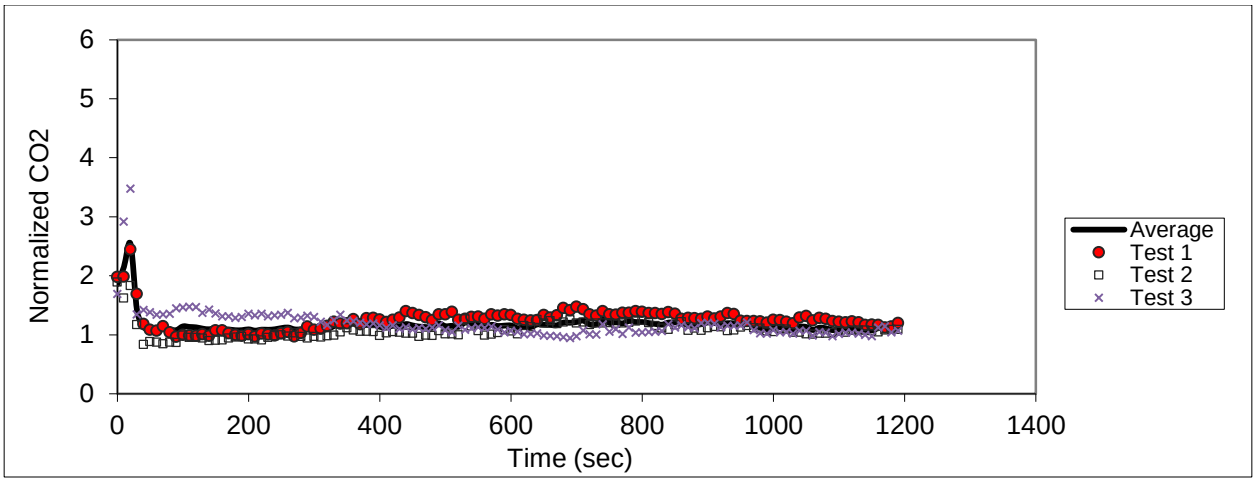

Figure C.114 – Sampling in seat 11D (release in 8B)

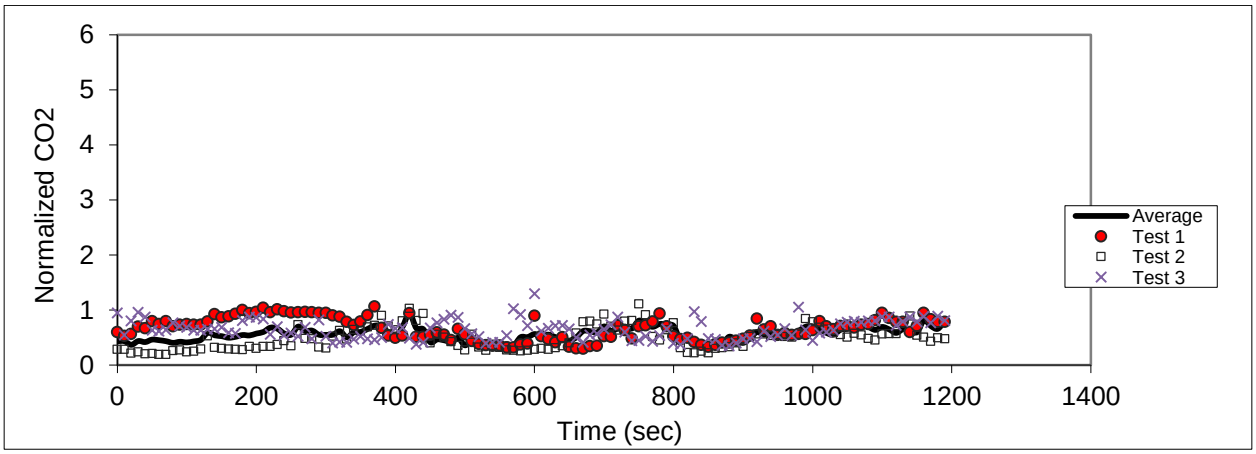

Figure C.115 – Sampling in seat 7F (release in 8B)

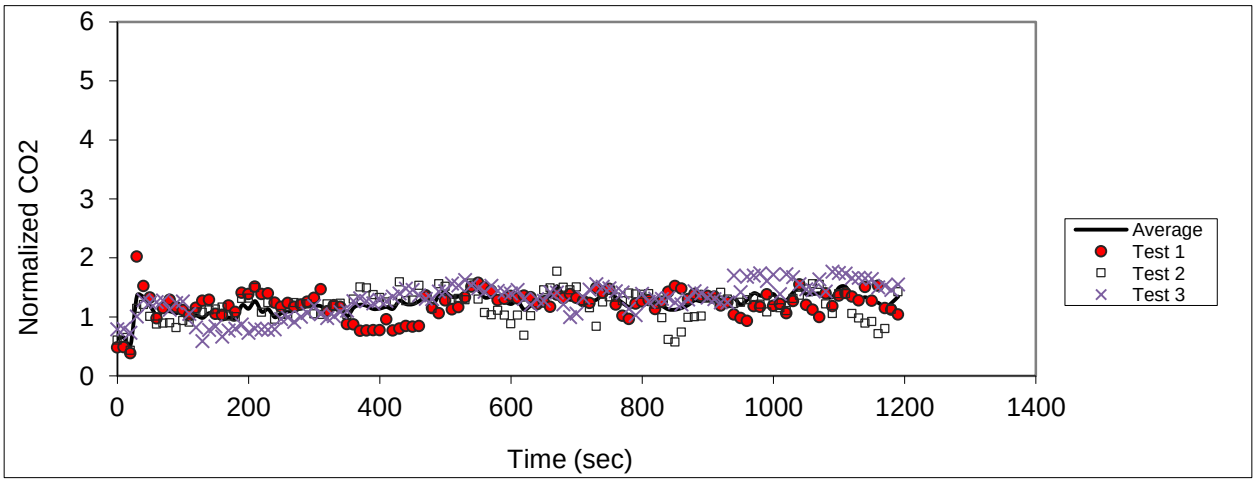

Figure C.116 – Sampling in seat 8F (release in 8B)

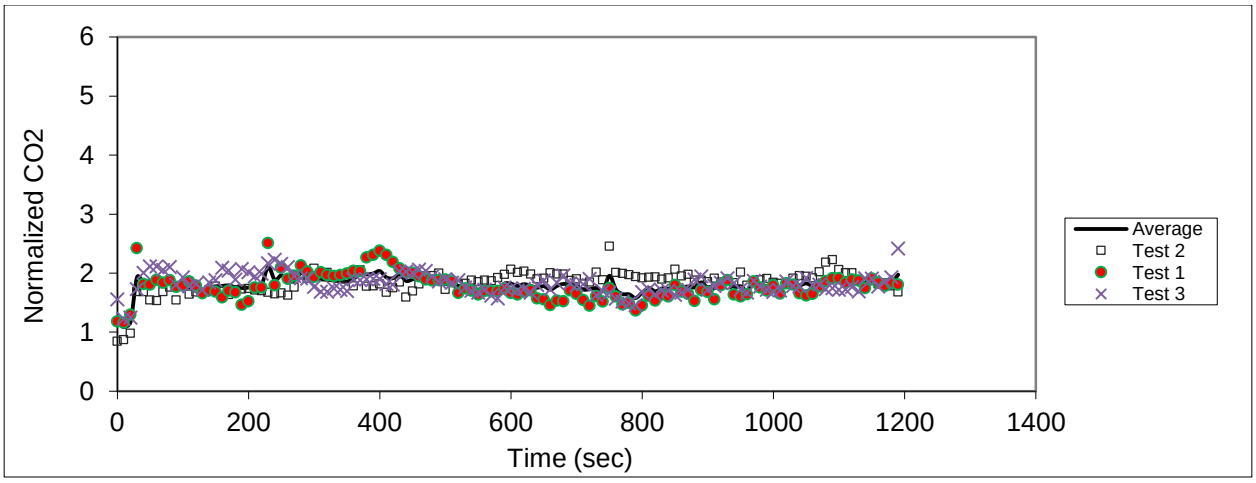

Figure C.117 – Sampling in seat 9F (release in 8B)

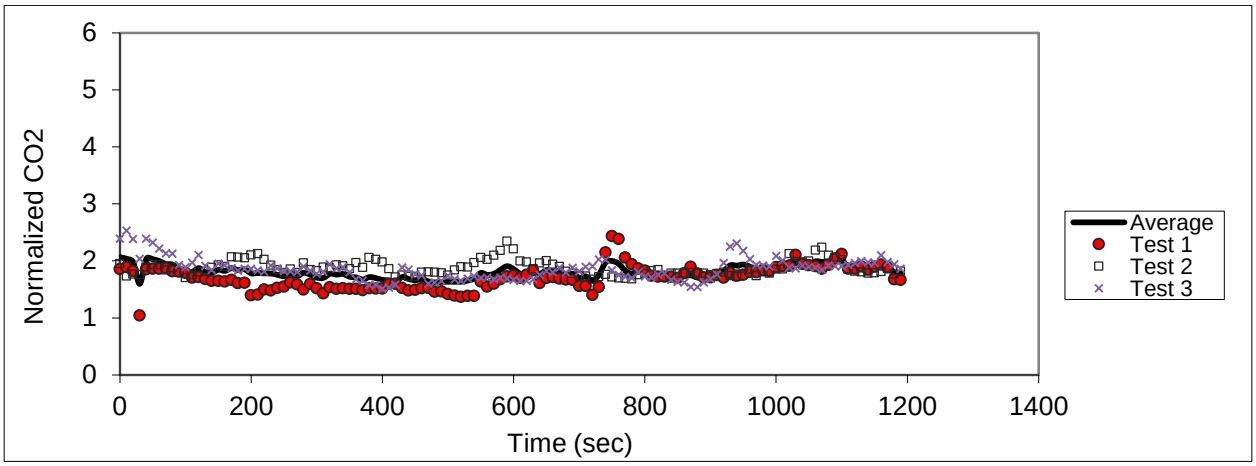

Figure C.118 – Sampling in seat 10F (release in 8B)

<u>Release in seat 4F</u>

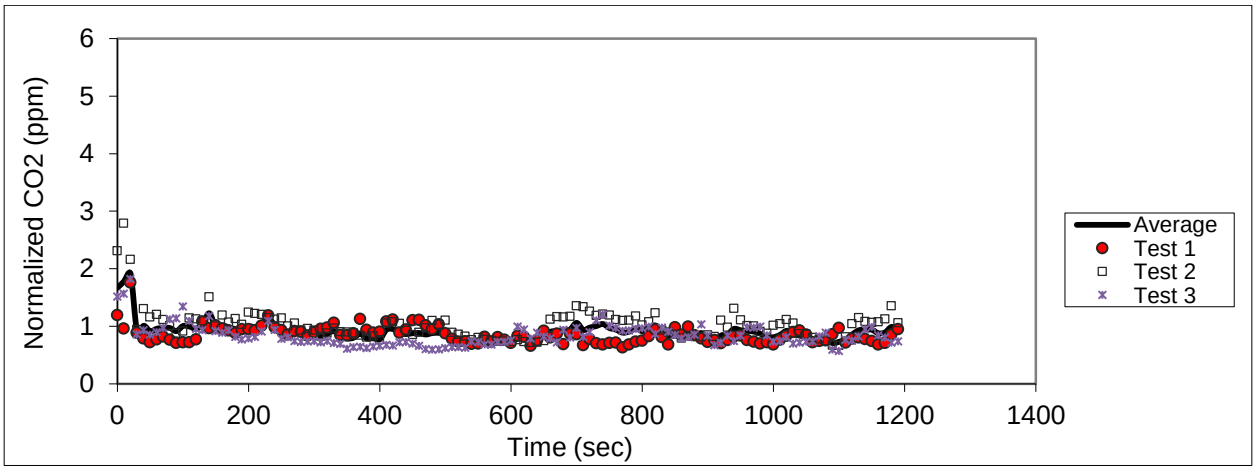

Figure C.119 - Sampling in seat 2F (release in 4F)

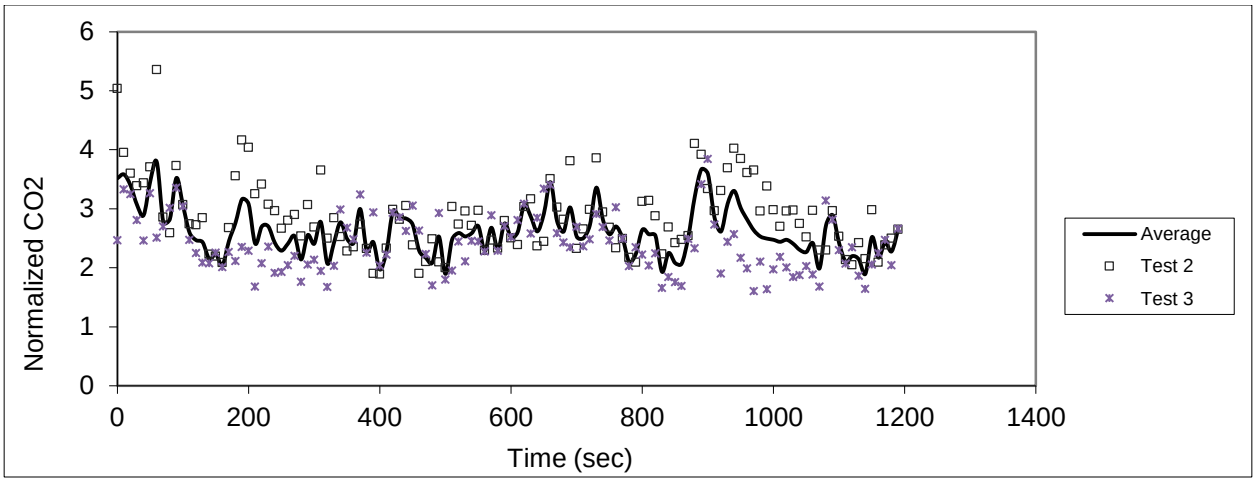

Figure C.120 – Sampling in seat 3F (release in 4F)

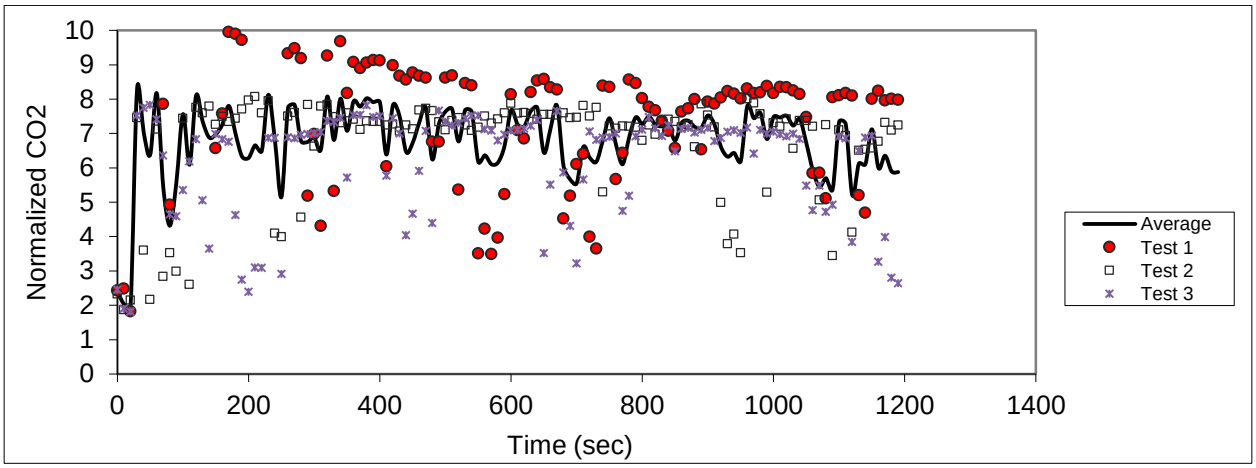

Figure C.121 – Sampling in seat 4F (release in 4F)

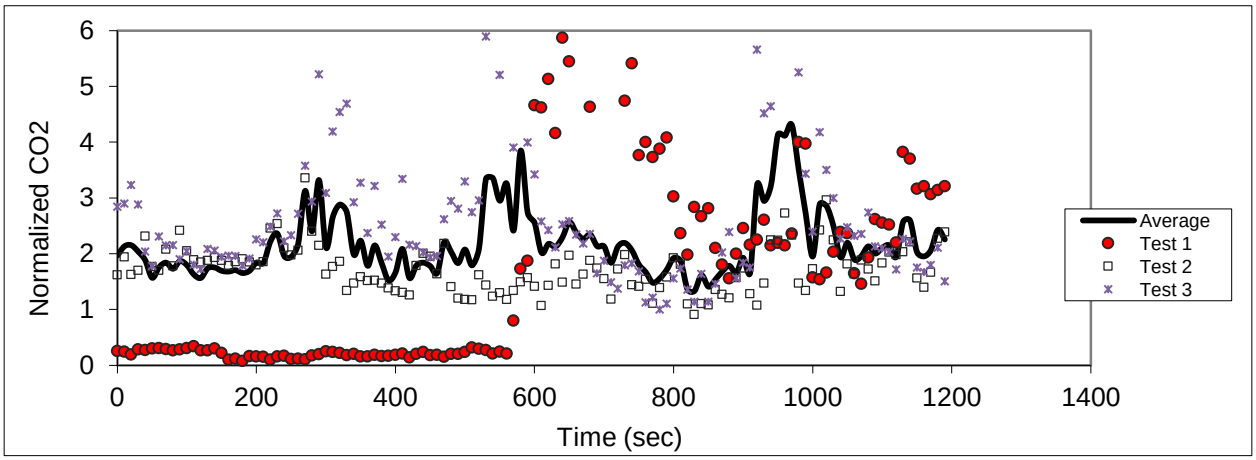

Figure C.122 - Sampling in seat 5F (release in 4F)

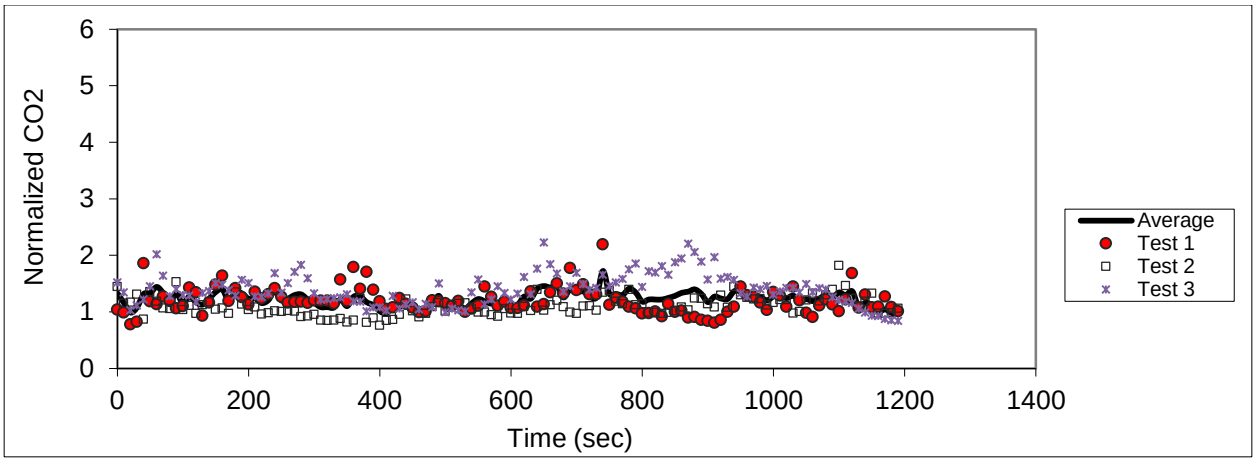

Figure C.123 – Sampling in seat 6F (release in 4F)

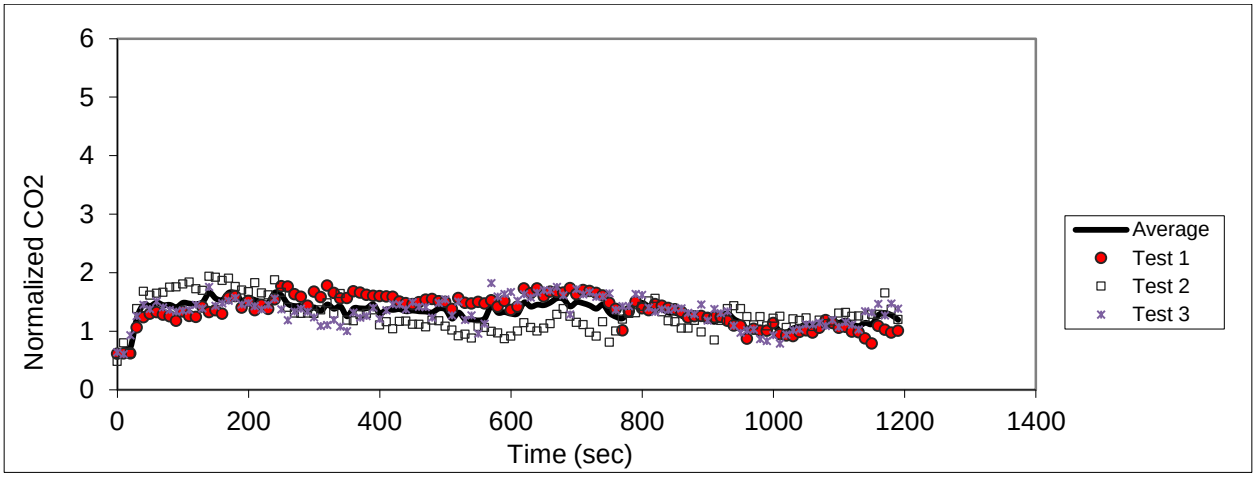

Figure C.124 – Sampling in seat 7F (release in 4F)

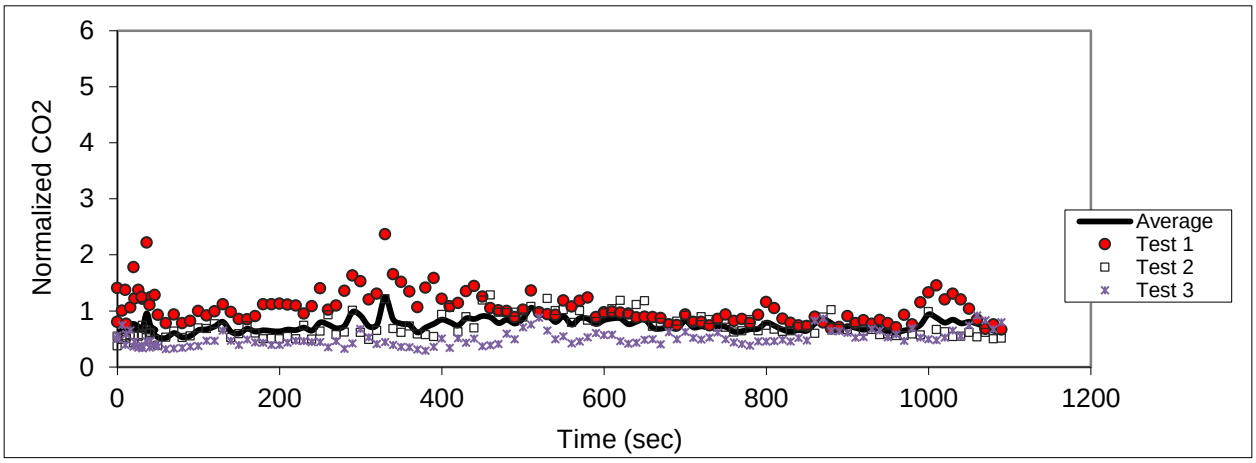

Figure C.125 – Sampling in seat 8F (release in 4F)

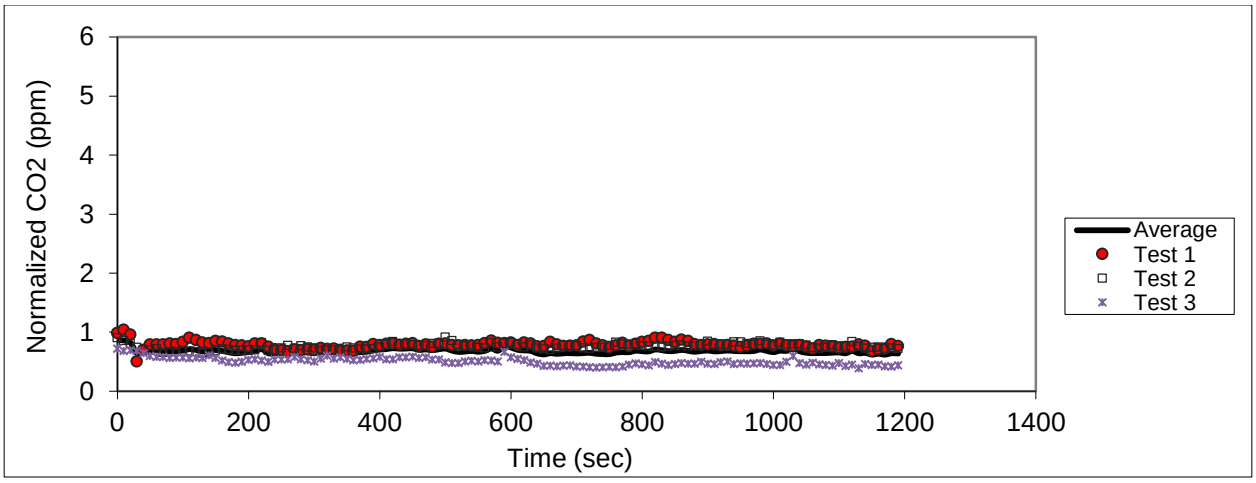

Figure C.126 – Sampling in seat 4D (release in 4F)

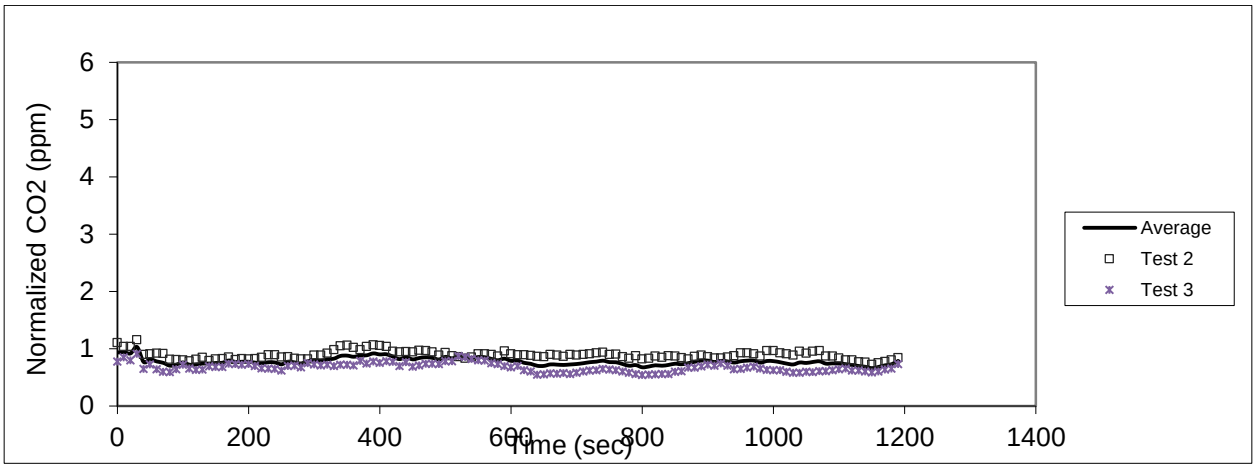

Figure C.127 – Sampling in seat 2D (release in 4F)

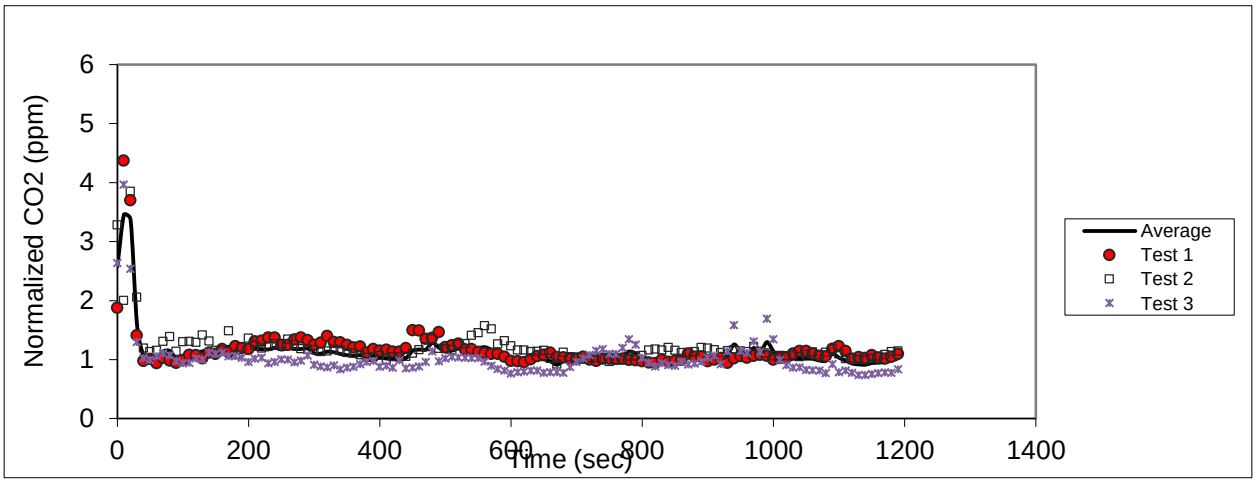

Figure C.128 – Sampling in seat 3D (release in 4F)

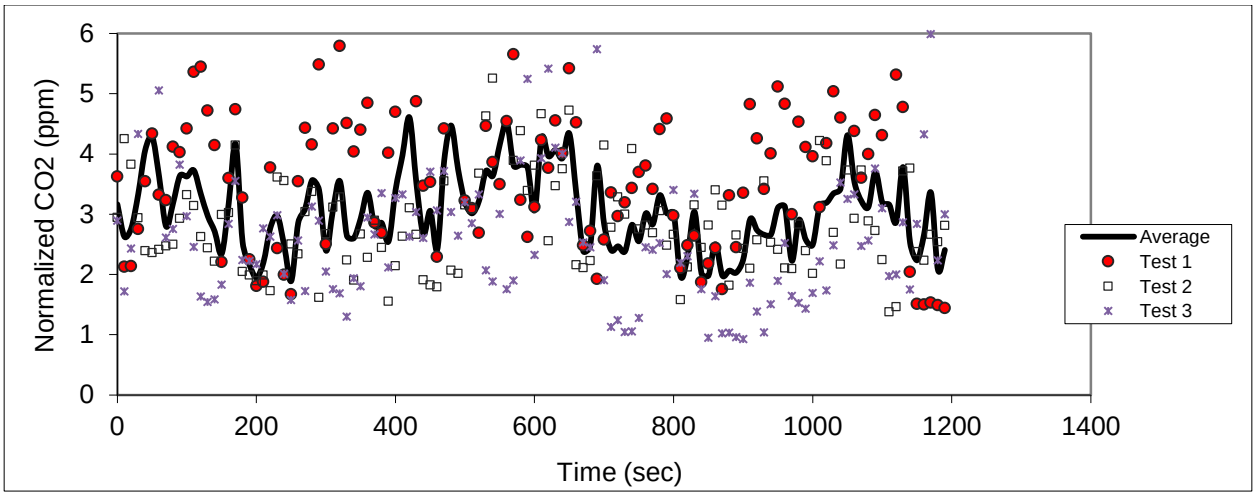

Figure C.129 - Sampling in seat 4D (release in 4F)

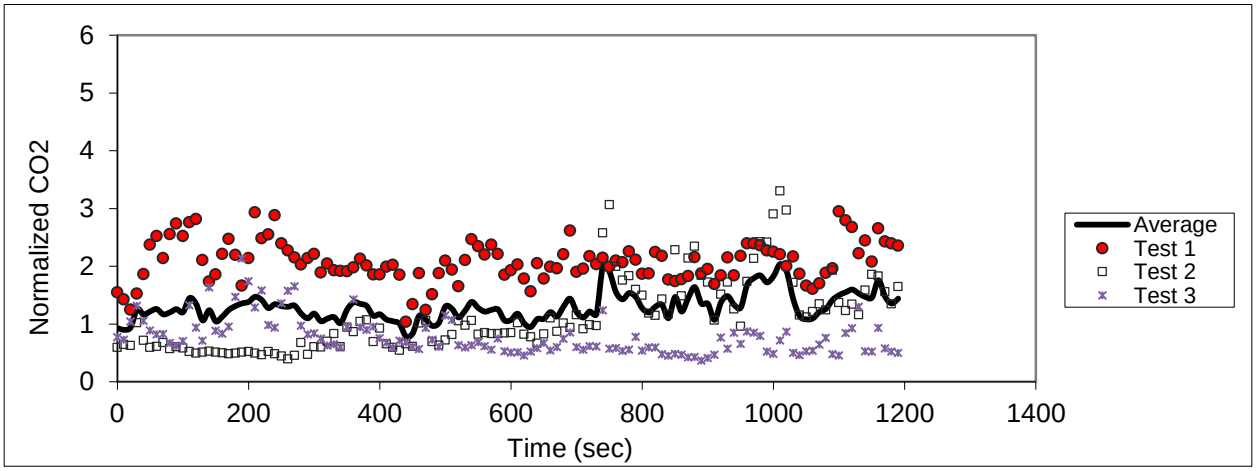

Figure C.130 – Sampling in seat 5D (release in 4F)

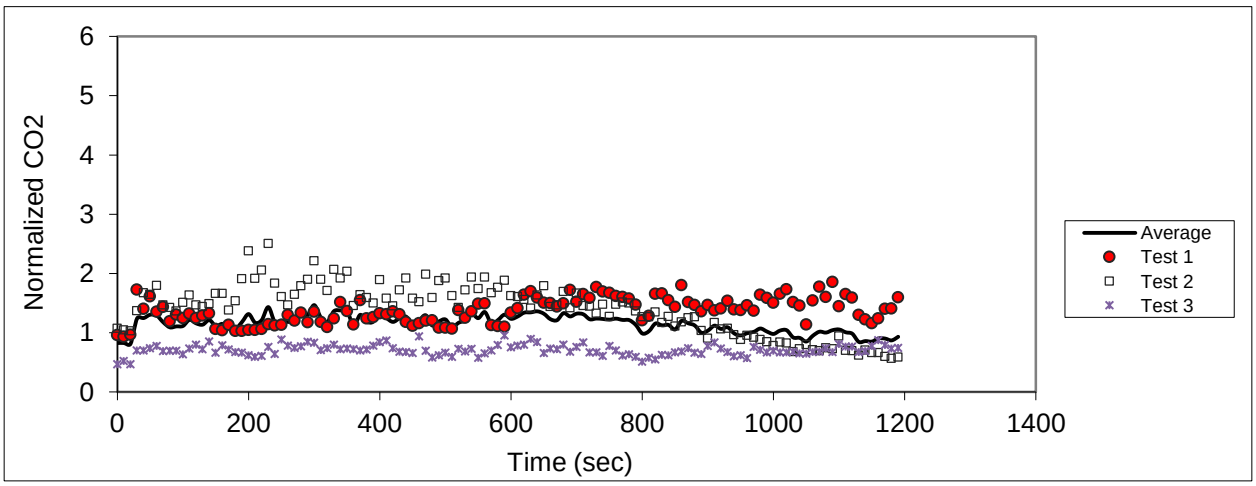

Figure C.131 – Sampling in seat 6D (release in 4F)

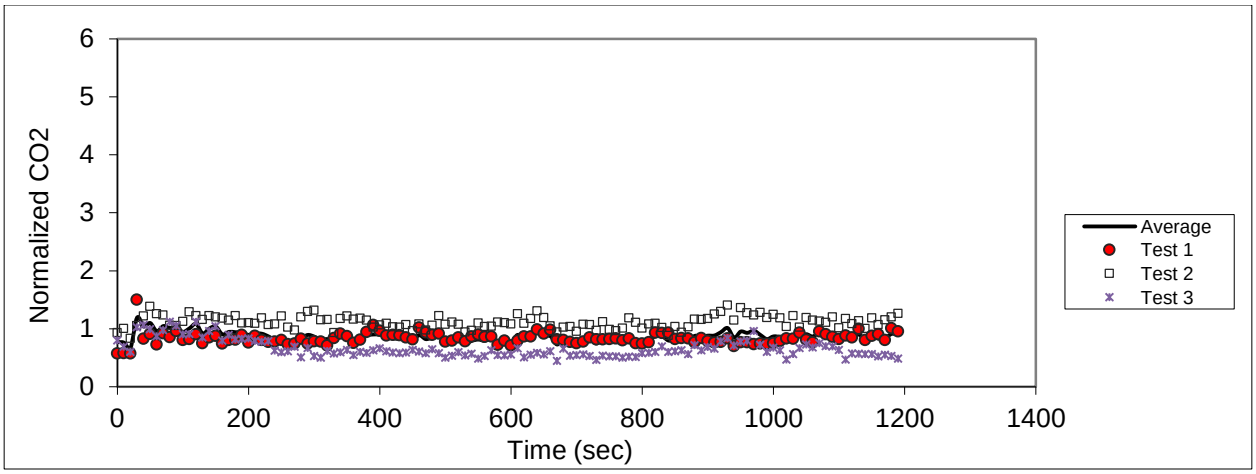

Figure C.132 – Sampling in seat 7D (release in 4F)

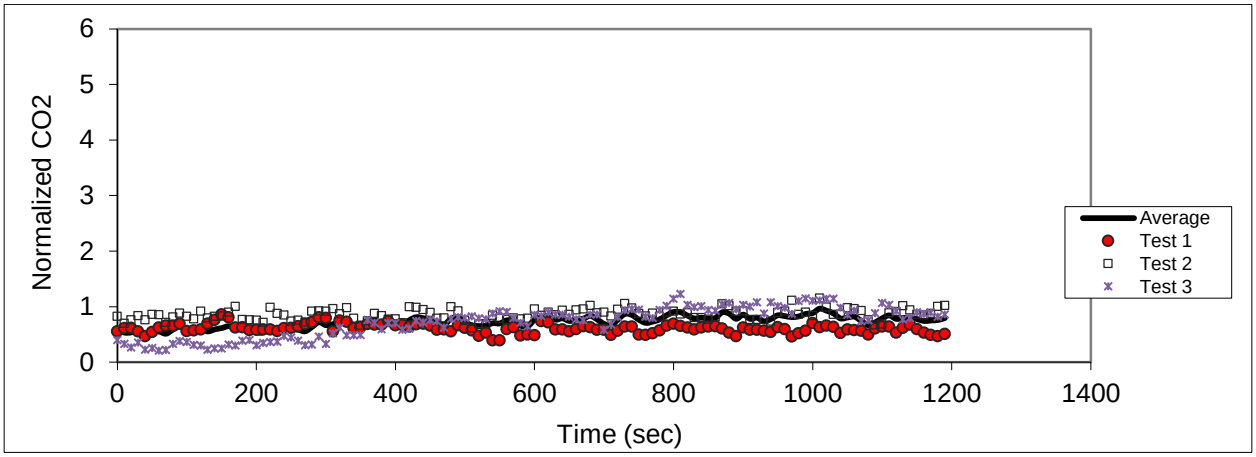

Figure C.133 - Sampling in seat 8D (release in 4F)

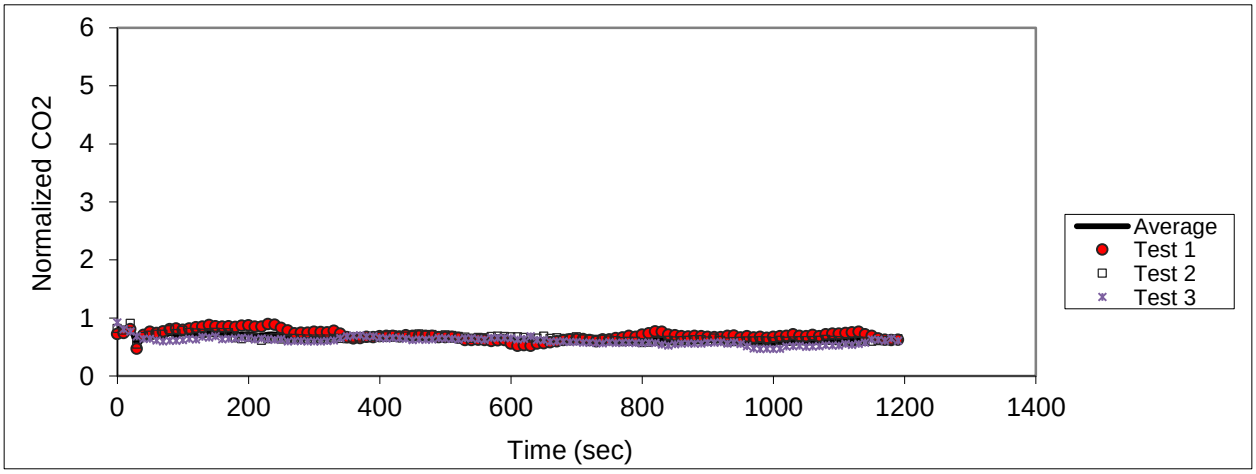

Figure C.134 – Sampling in seat 1B (release in 4F)

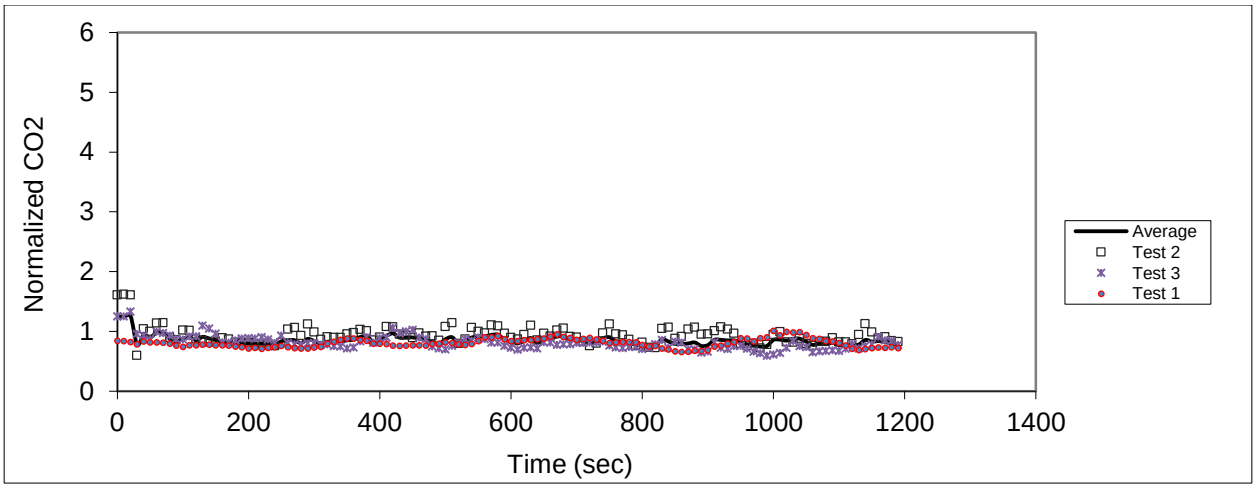

Figure C.135 – Sampling in seat 2B (release in 4F)

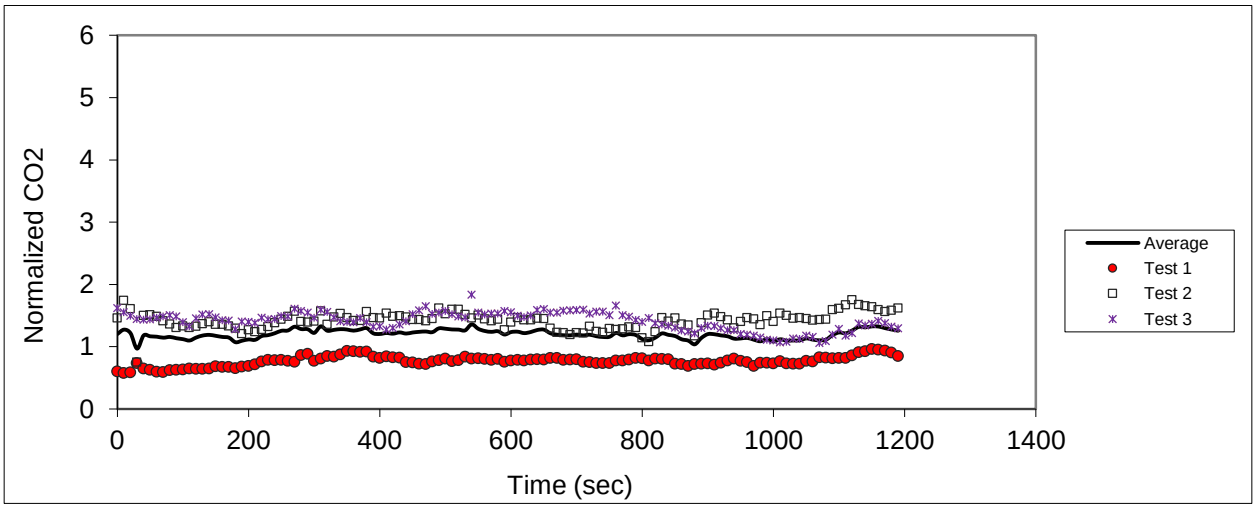

Figure C.136 - Sampling in seat 3B (release in 4F)

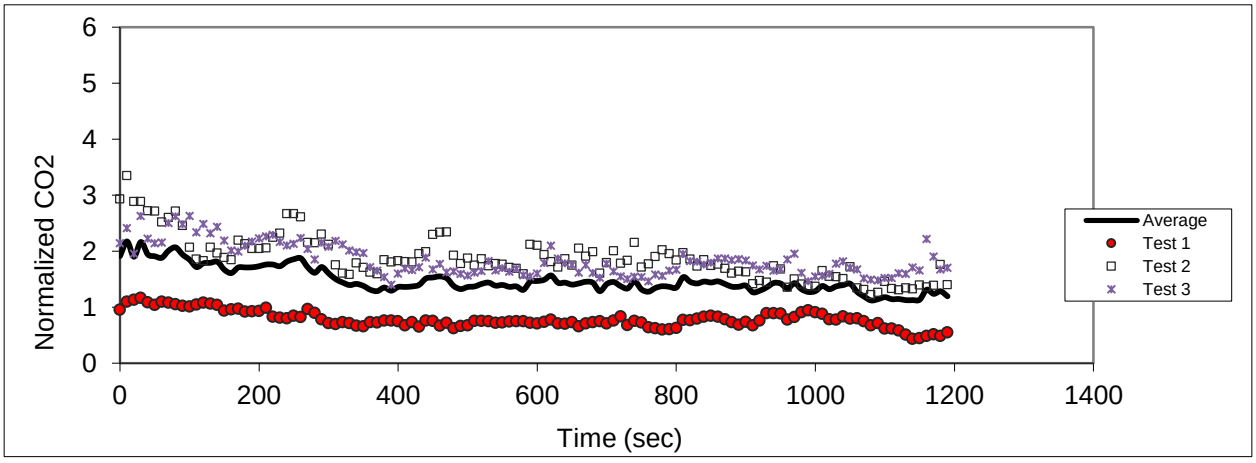

Figure C.137 – Sampling in seat 4B (release in 4F)

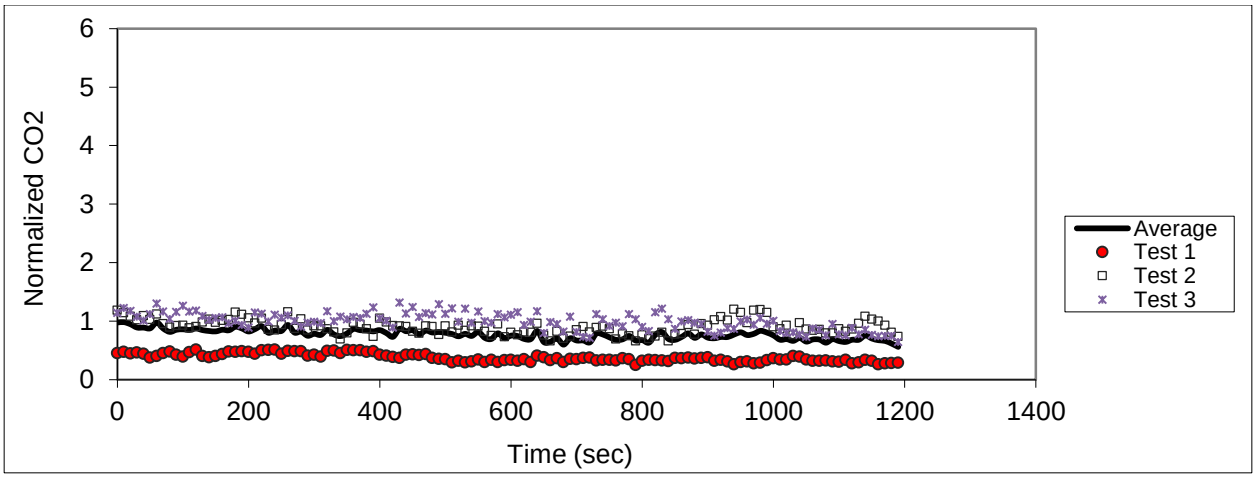

Figure C.138 – Sampling in seat 5B (release in 4F)

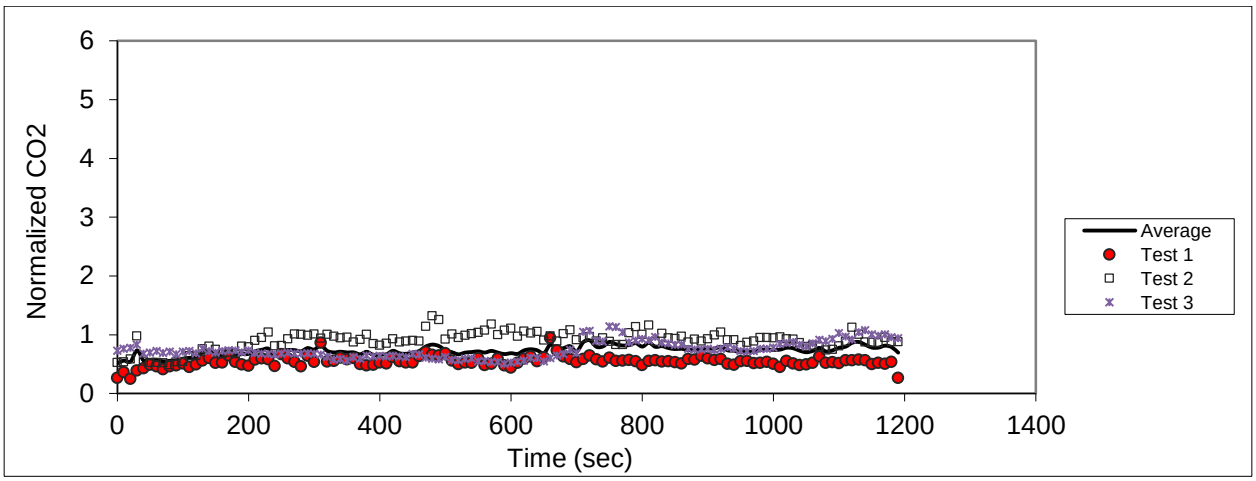

Figure C.139 – Sampling in seat 6B (release in 4F)

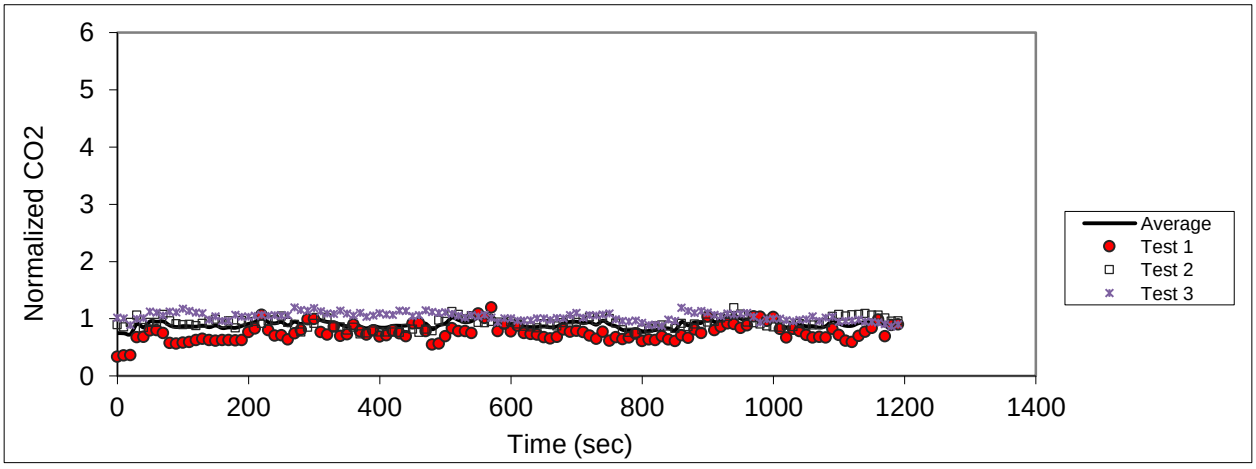

Figure C.140 – Sampling in seat 7B (release in 4F)

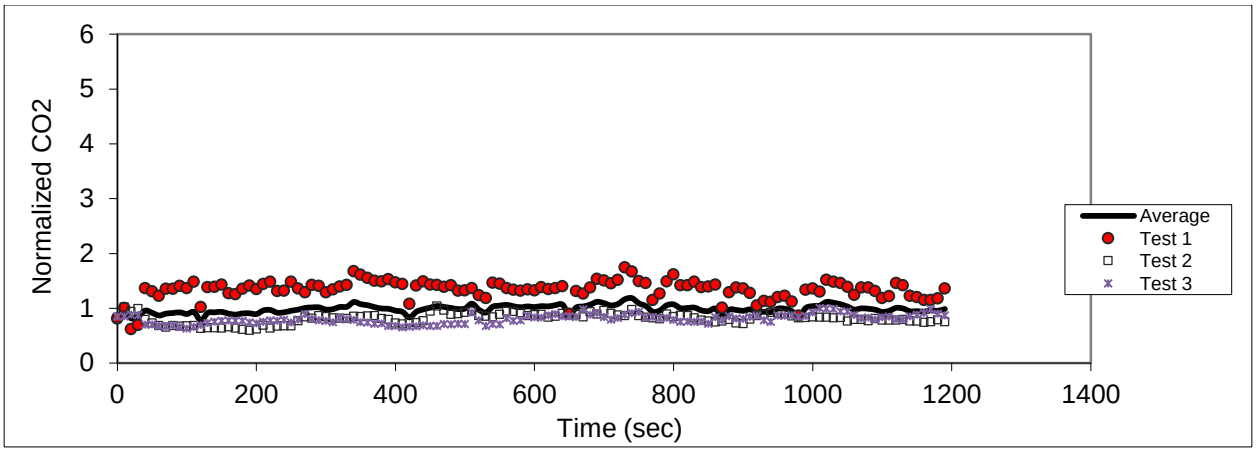

Figure C.141 - Sampling in seat 8B (release in 4F)

Release in seat 9F

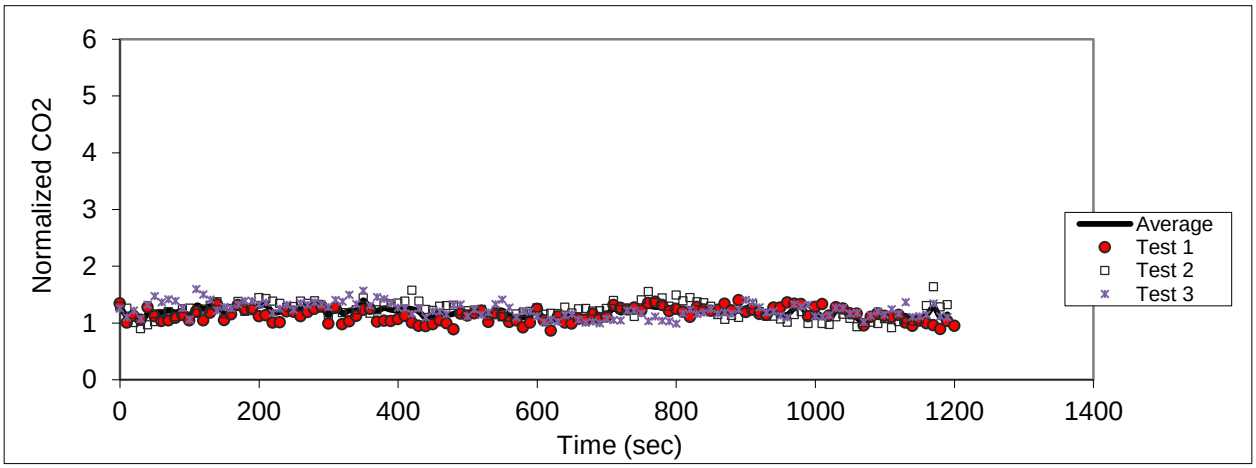

Figure C.142 – Sampling in seat 8B (release in 9F)

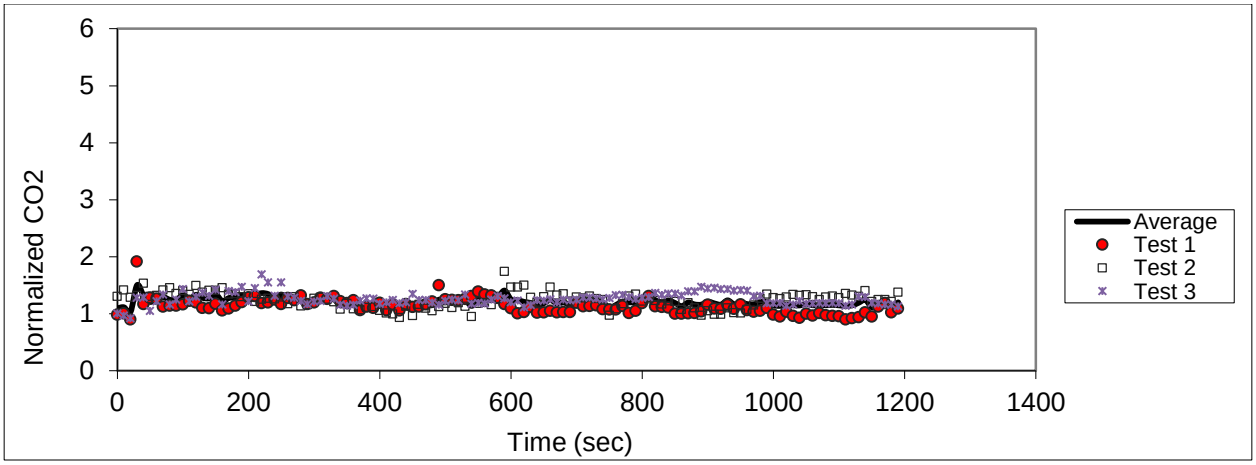

Figure C.143 – Sampling in seat 9B (release in 9F)

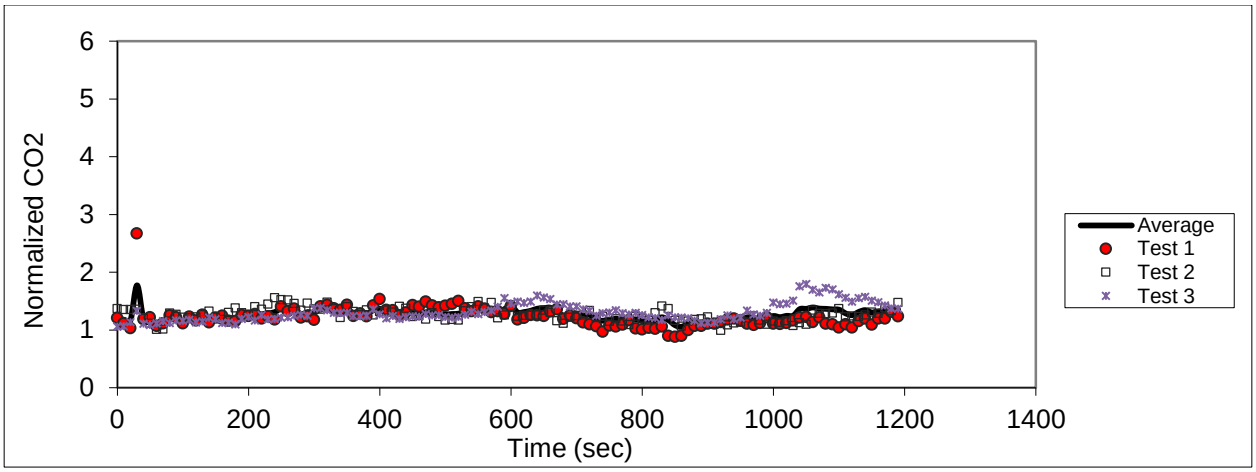

Figure C.144 – Sampling in seat 10B (release in 9F)

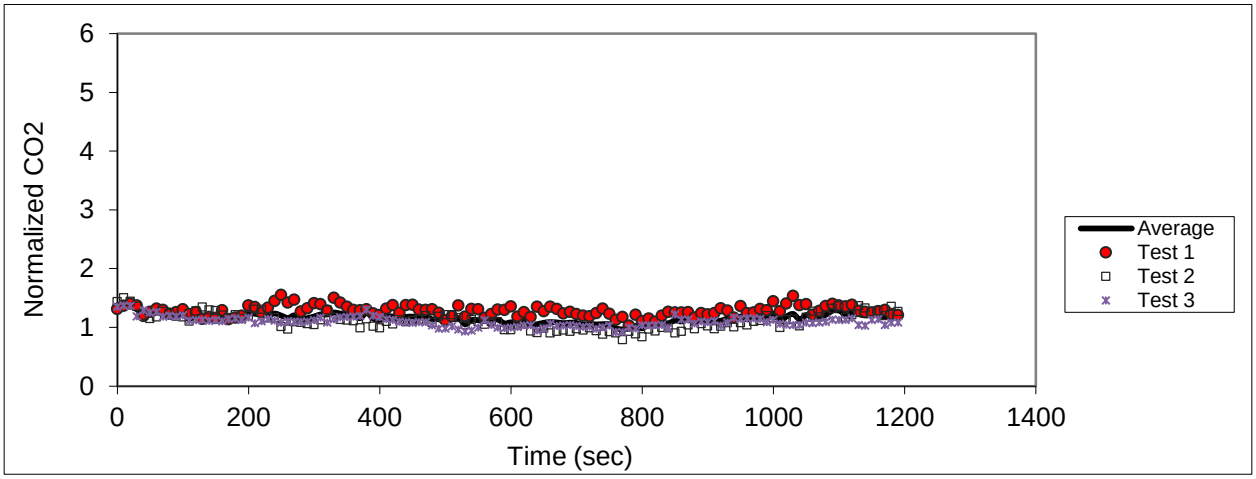

Figure C.145 - Sampling in seat 11B (release in 9F)

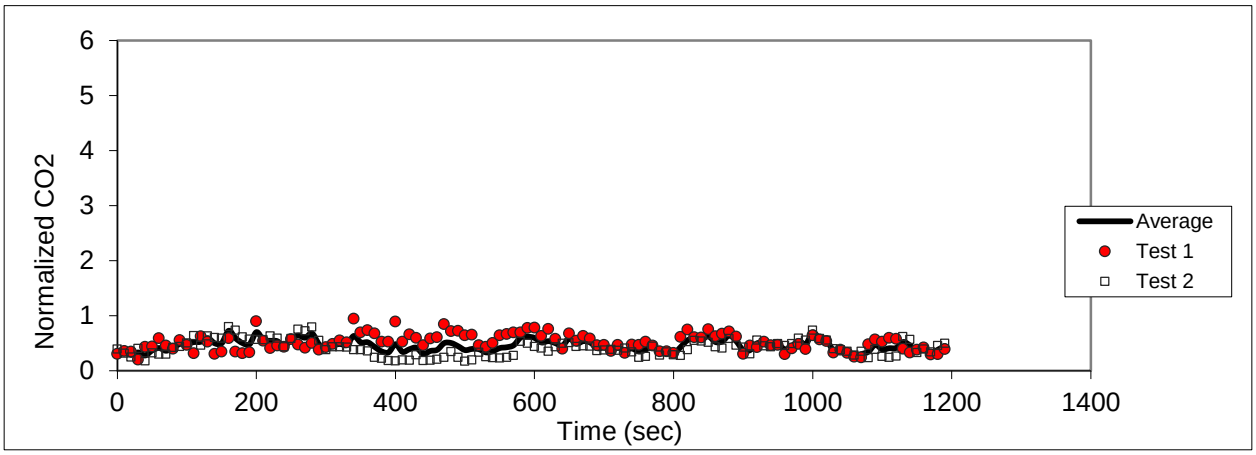

Figure C.146 - Sampling in seat 6D (release in 9F)

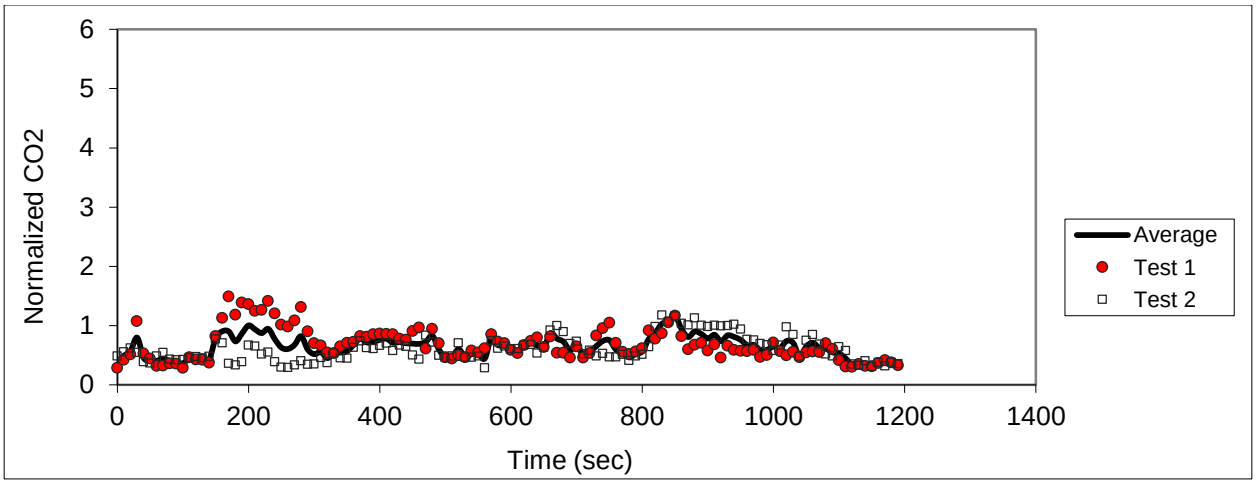

Figure C.147 – Sampling in seat 7D (release in 9F)

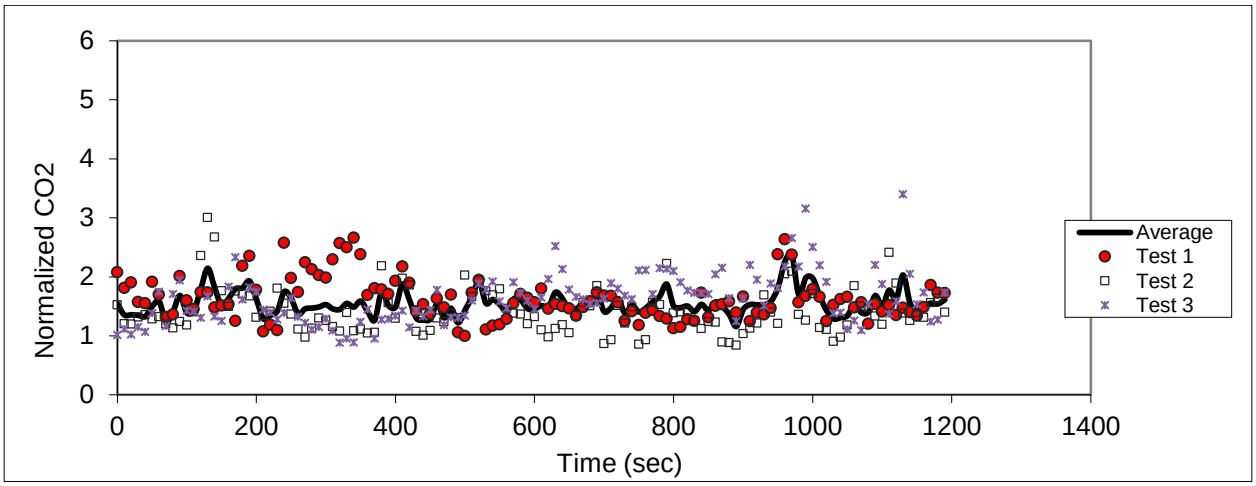

Figure C.148 – Sampling in seat 8D (release in 9F)

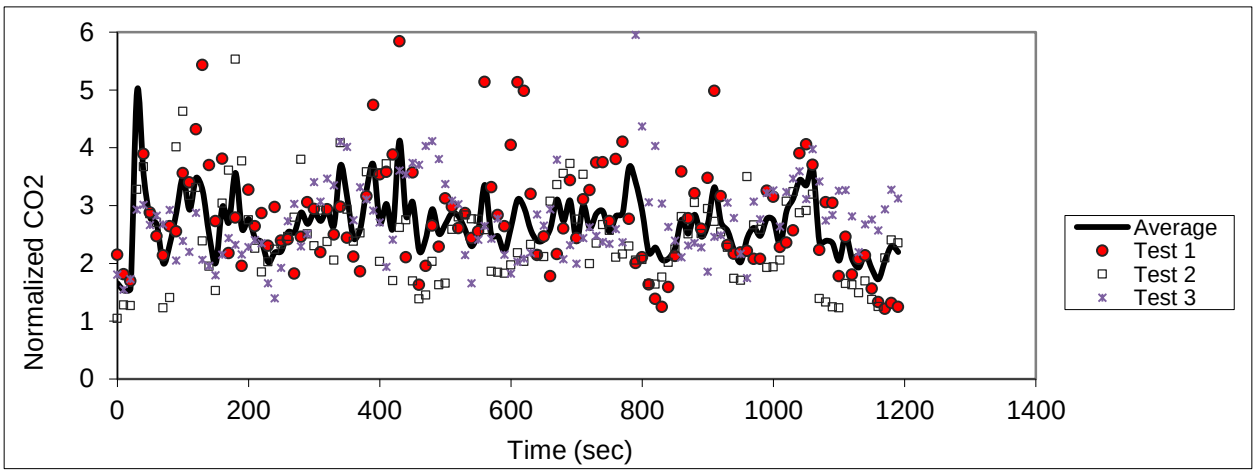

Figure C.149 – Sampling in seat 9D (release in 9F)

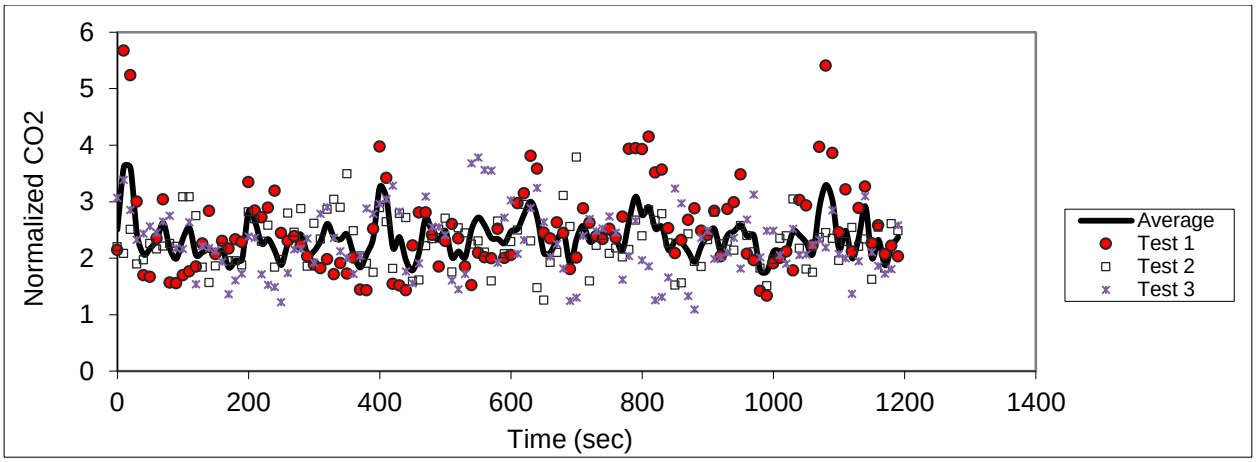

Figure C.150 – Sampling in seat 10D (release in 9F)

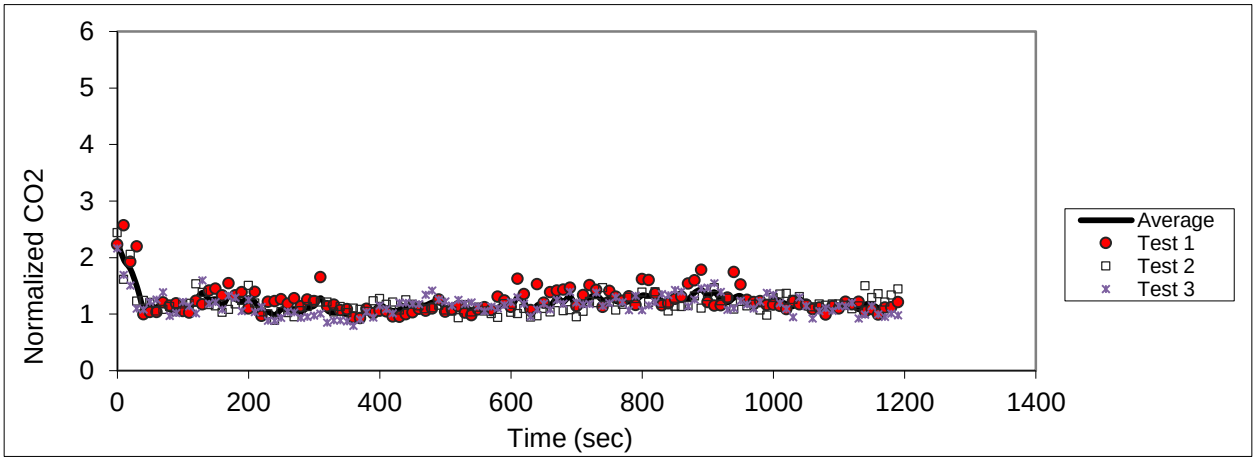

Figure C.151 – Sampling in seat 11D (release in 9F)

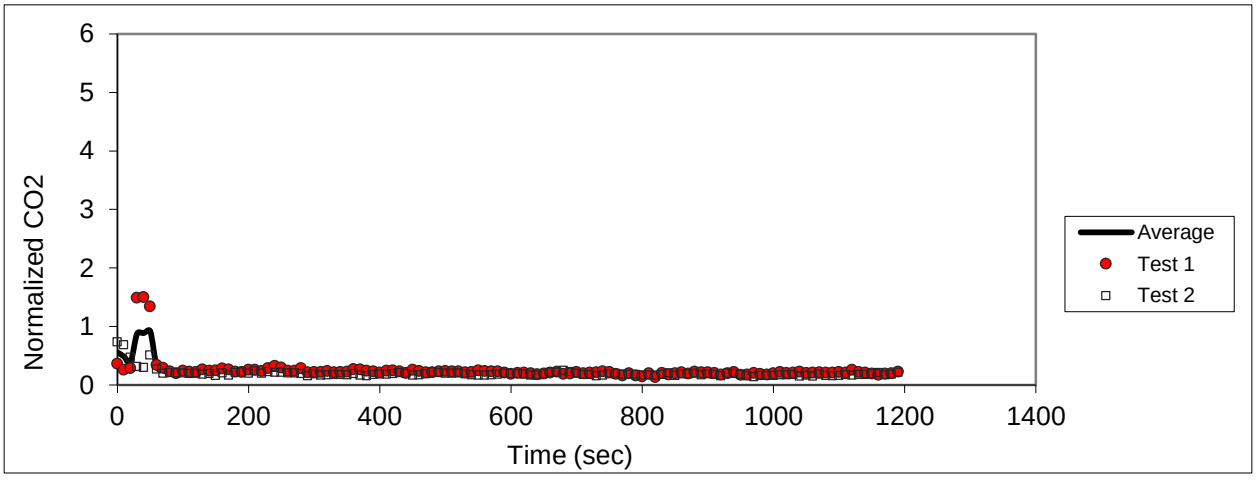

Figure C.152 - Sampling in seat 6F (release in 9F)

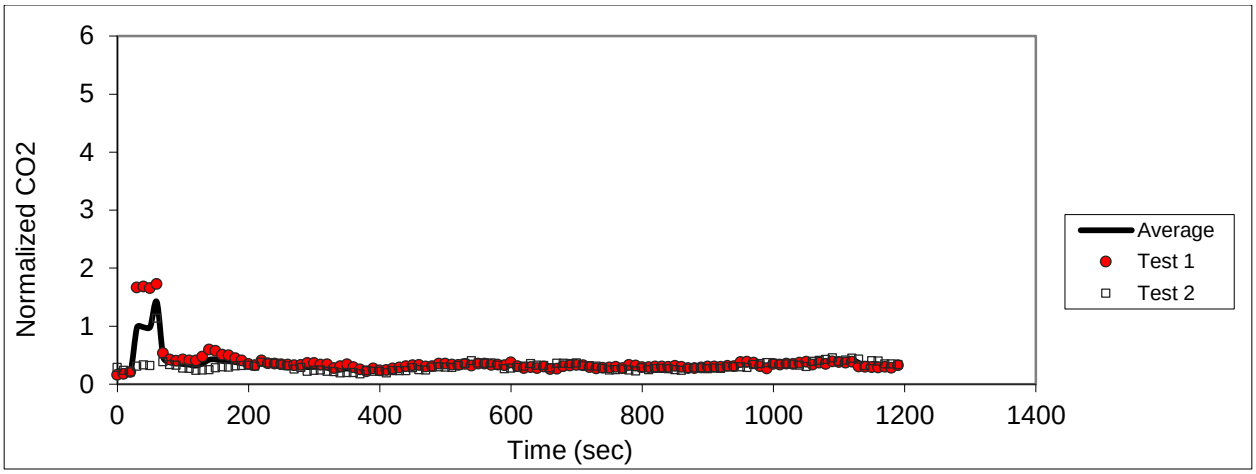

Figure C.153 – Sampling in seat 7F (release in 9F)

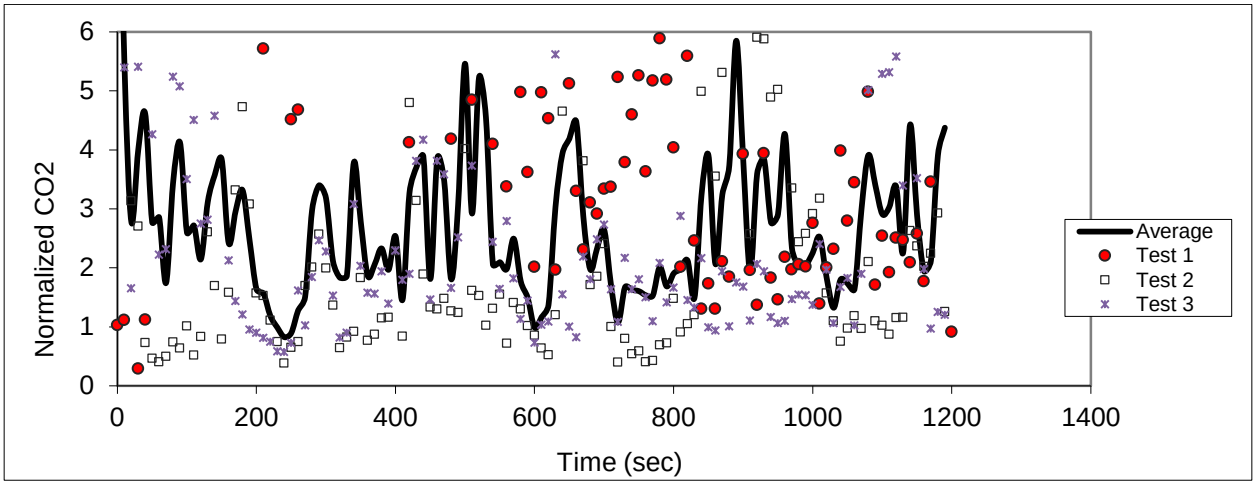

Figure C.154 – Sampling in seat 8F (release in 9F)

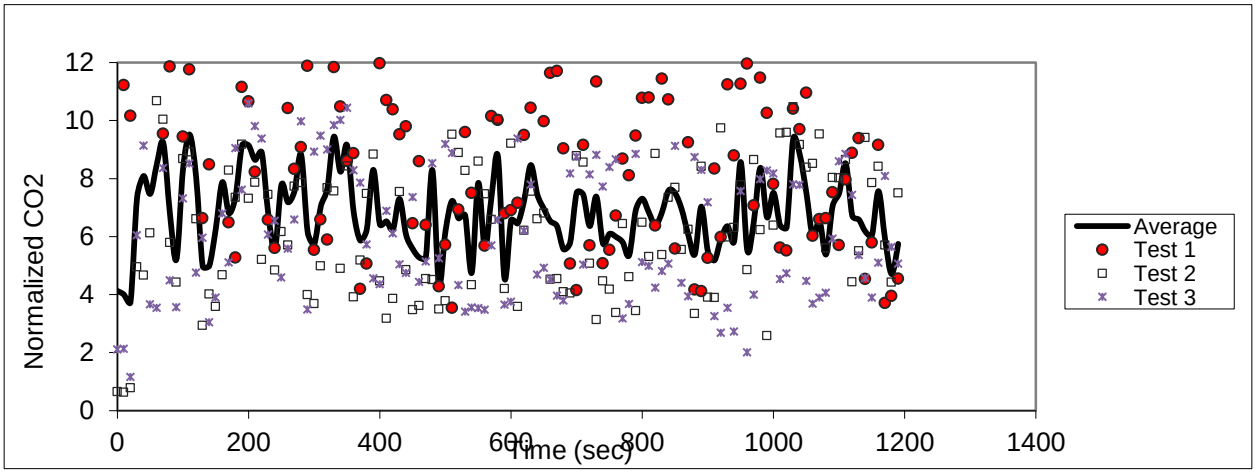

Figure C.155 – Sampling in seat 9F (release in 9F)

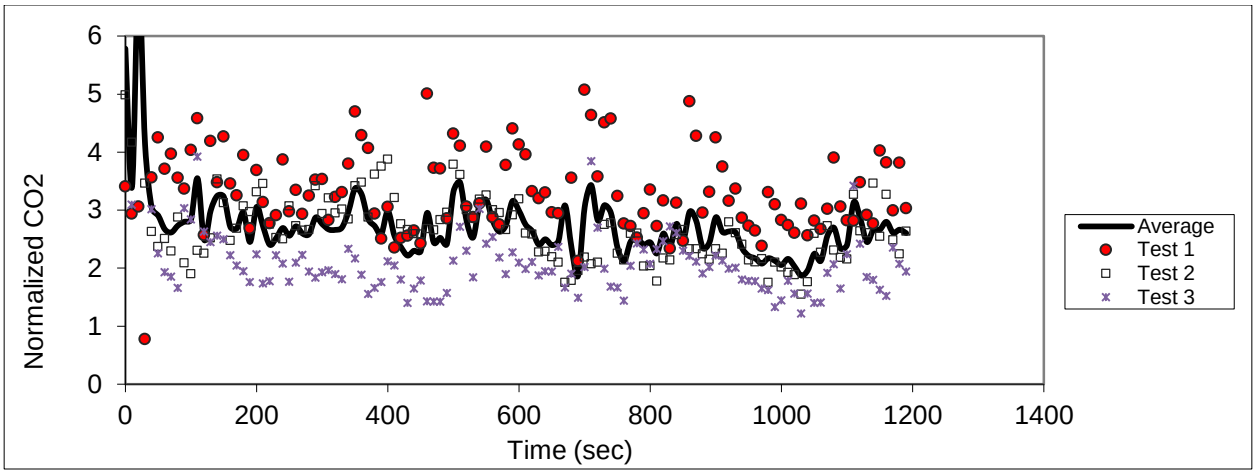

Figure C.156 – Sampling in seat 10F (release in 9F)

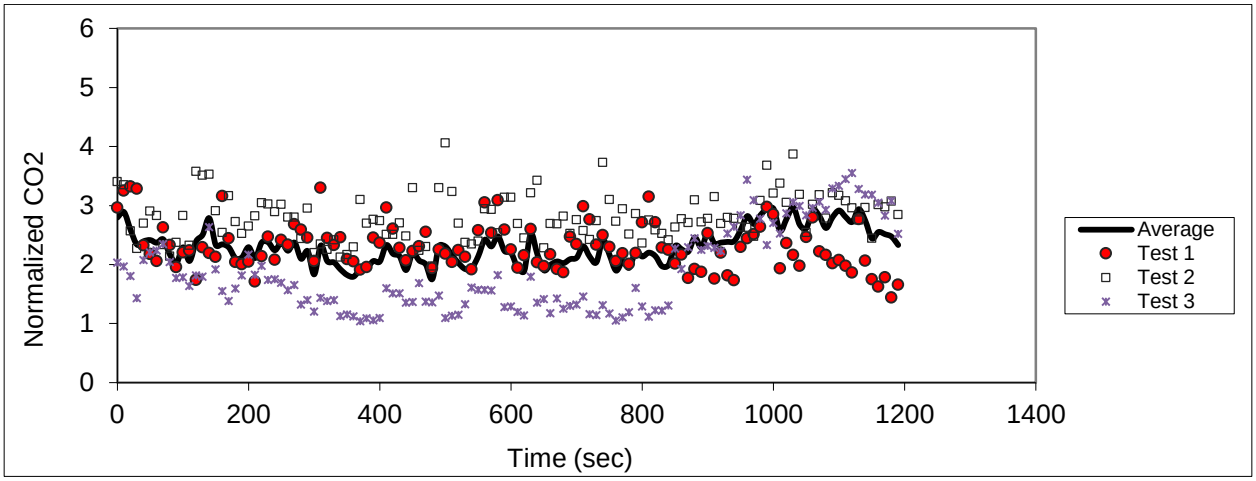

Figure C.157 - Sampling in seat 11F (release in 9F)

Appendix D - Normalized Tracer Gas Results with Unheated Manikins

In this appendix, the normalized CO_2 in each location during each test along with the average are presented under unheated running conditions.

Release in seat 2D

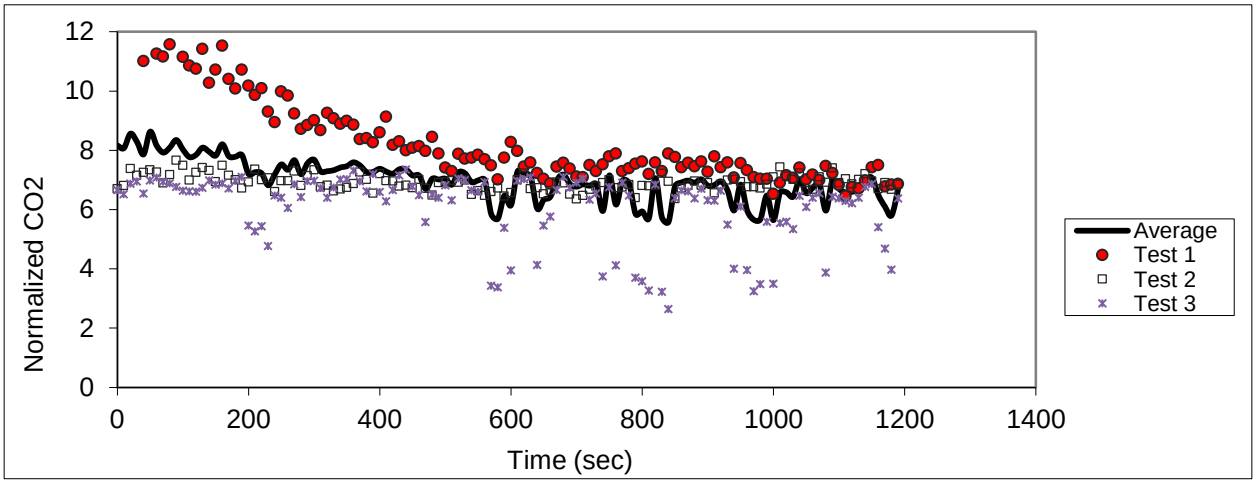

Figure D.1 – Sampling in seat 2D (release in 2D)

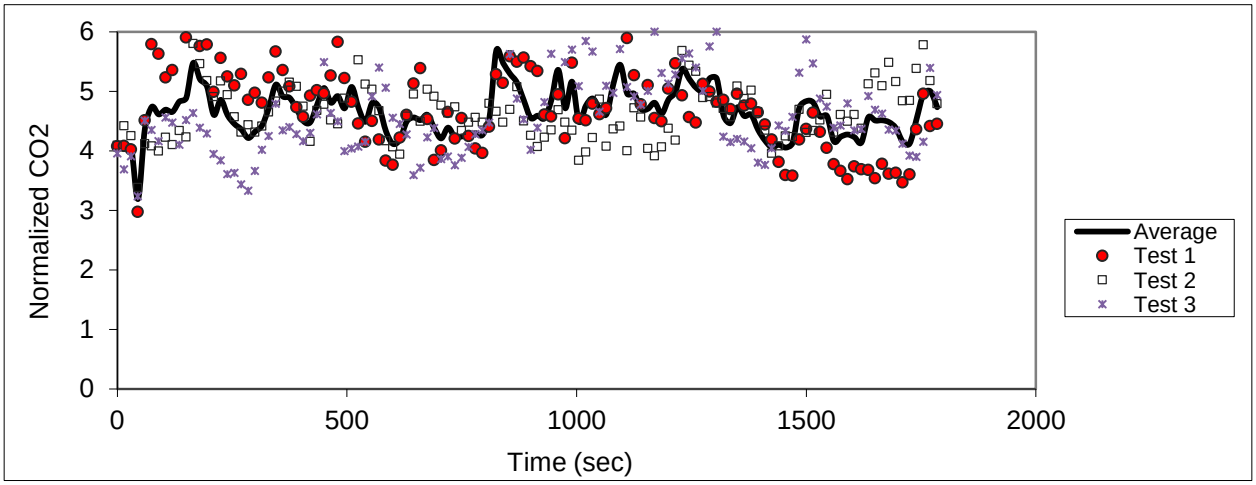

Figure D.2 – Sampling in seat 1B (release in 2D)

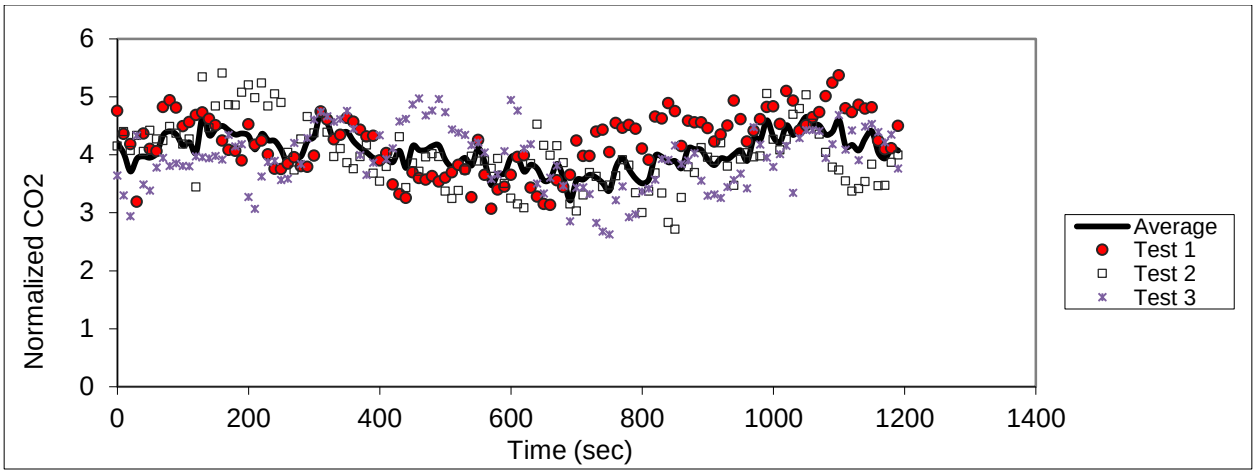

Figure D.3 – Sampling in seat 2B (release in 2D)

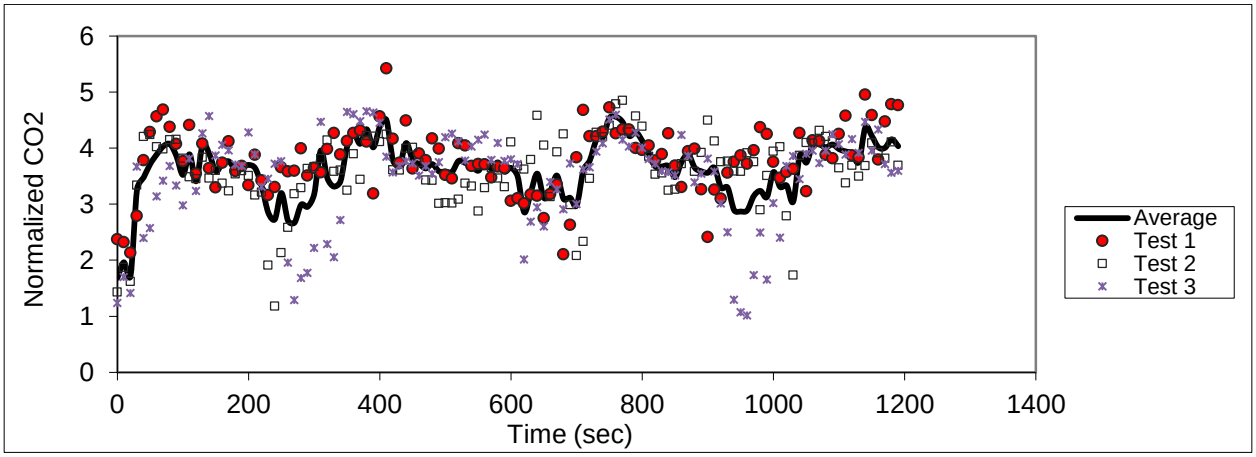

Figure D.4 – Sampling in seat 3B (release in 2D)

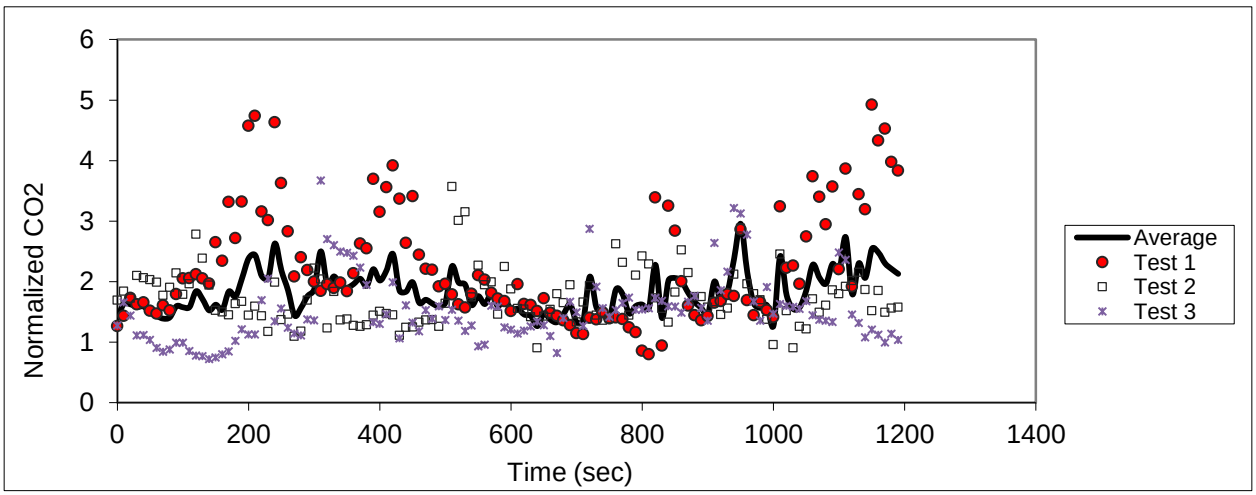

Figure D.5 – Sampling in seat 4B (release in 2D)

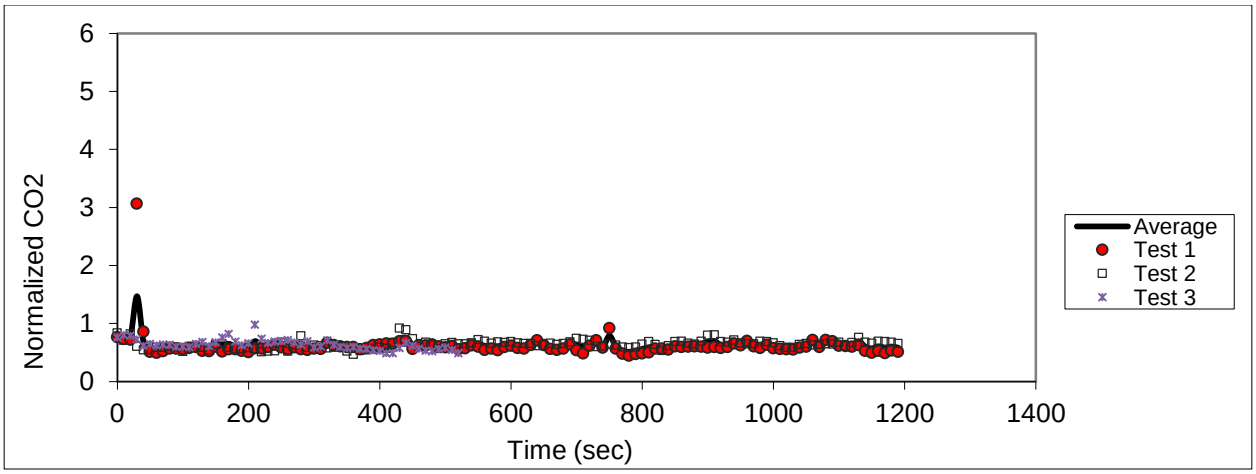

Figure D.6 - Sampling in seat 5B (release in 2D)

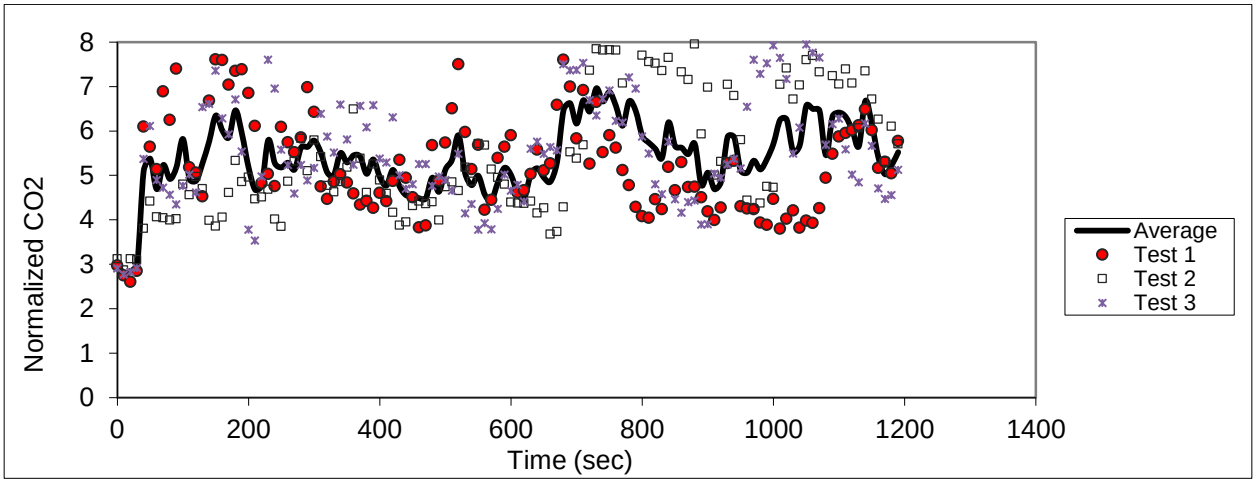

Figure D.7 – Sampling in seat 1C (release in 2D)

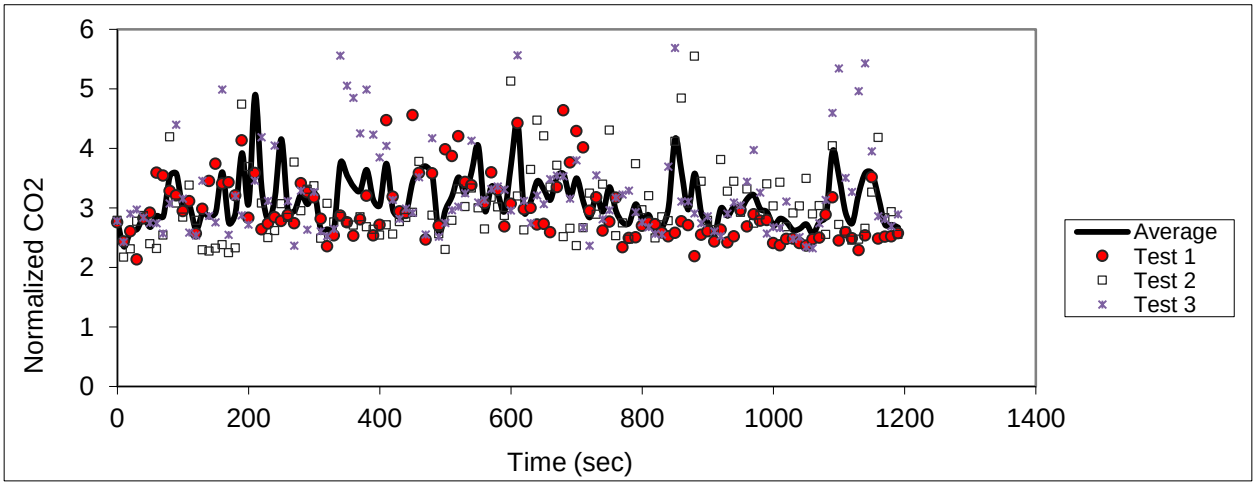

Figure D.8 – Sampling in seat 2C (release in 2D)

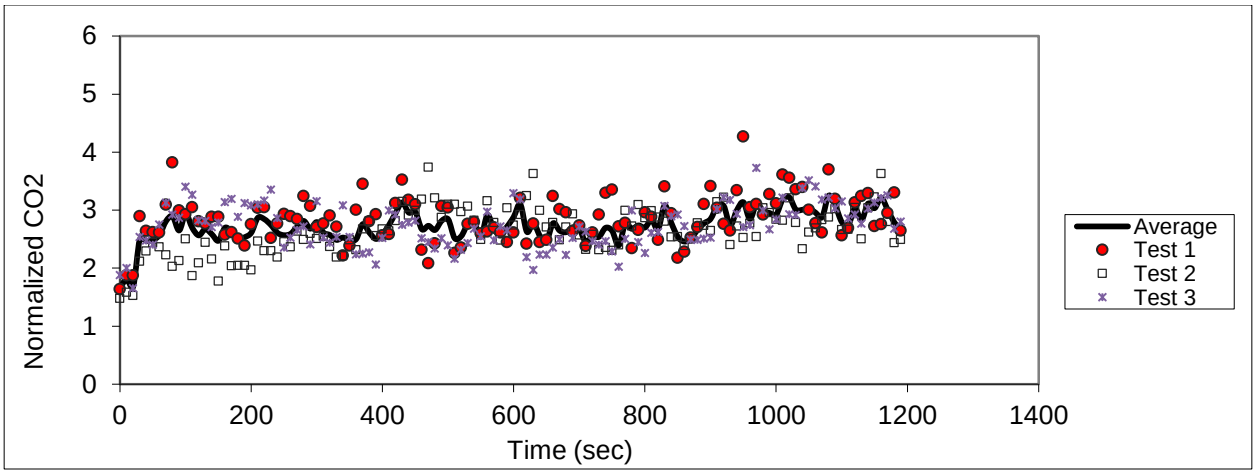

Figure D.9 – Sampling in seat 3C (release in 2D)

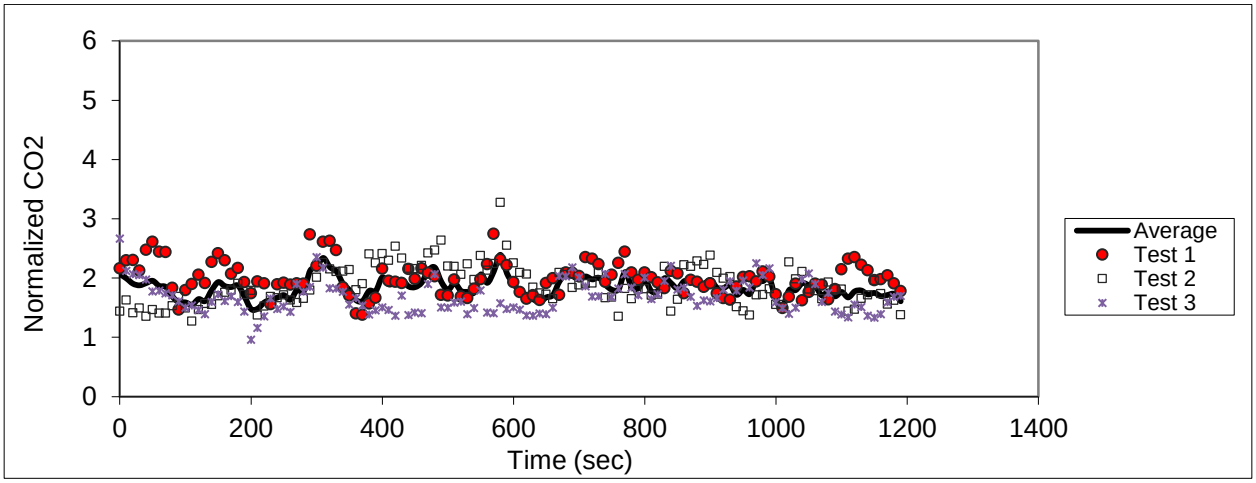

Figure D.10 – Sampling in seat 4C (release in 2D)

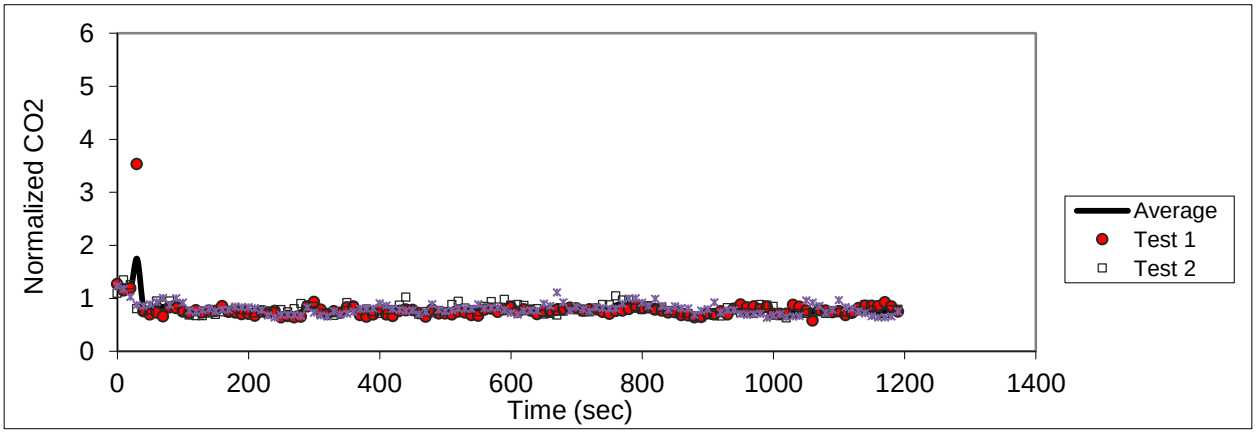

Figure D.11 - Sampling in seat 5C (release in 2D)

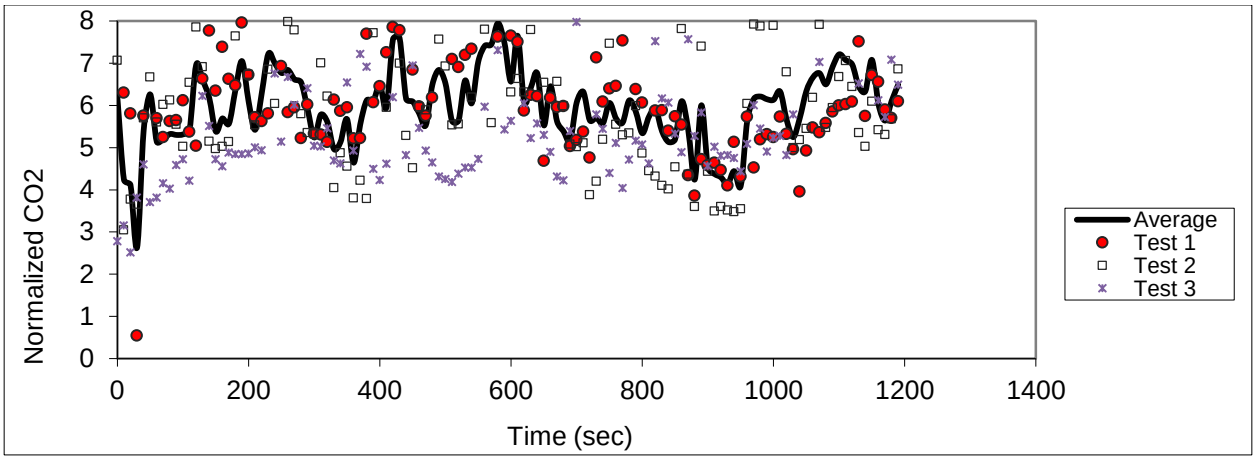

Figure D.12 – Sampling in seat 1E (release in 2D)

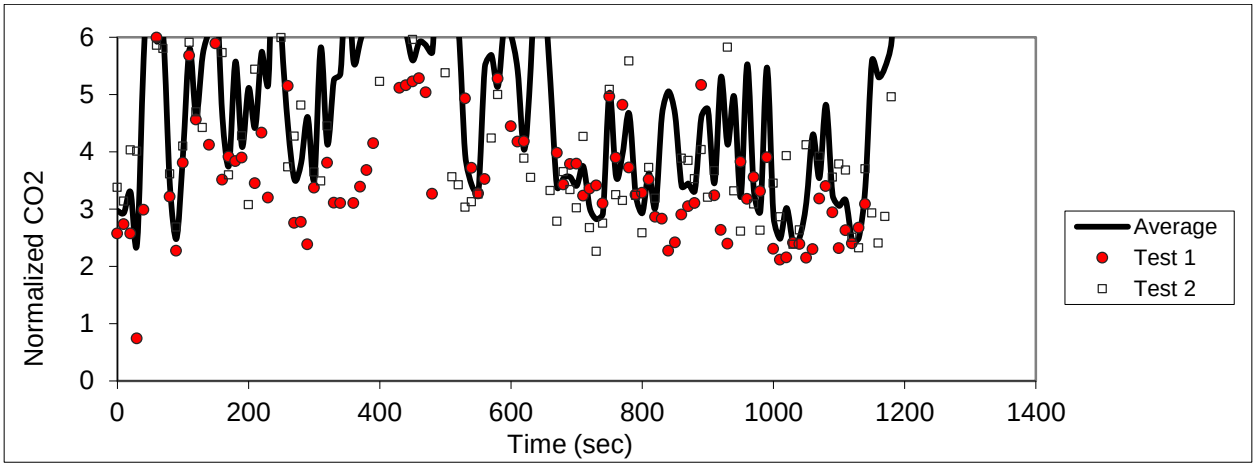

Figure D.13 – Sampling in seat 2E (release in 2D)

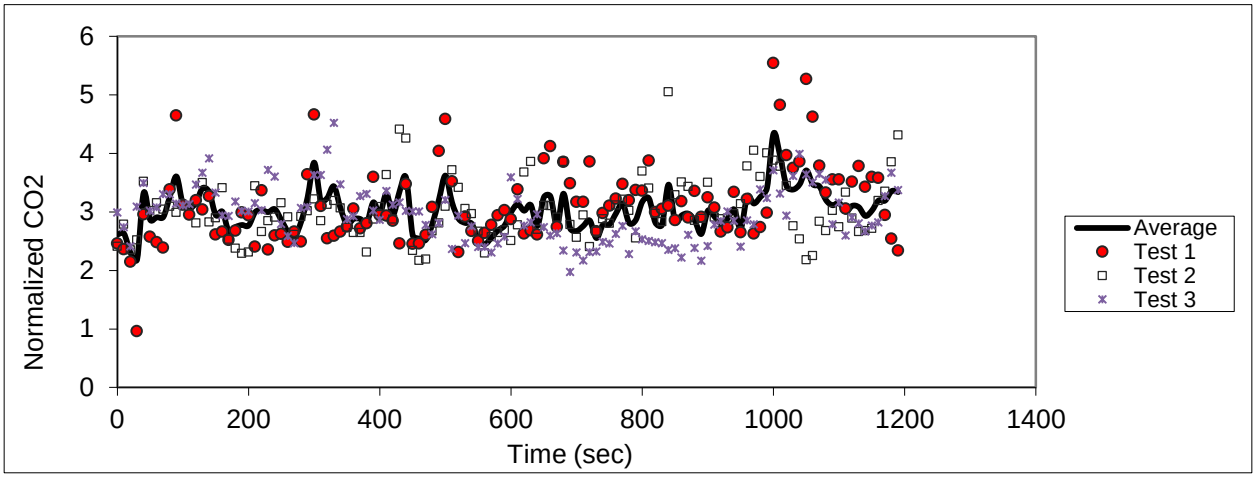

Figure D.14 – Sampling in seat 3E (release in 2D)

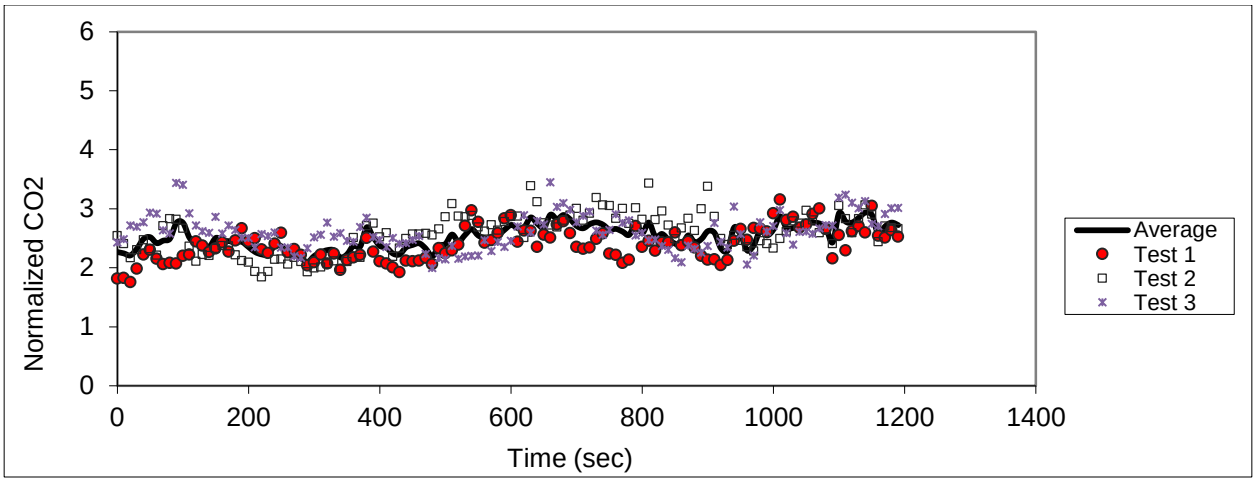

Figure D.15 – Sampling in seat 4E (release in 2D)

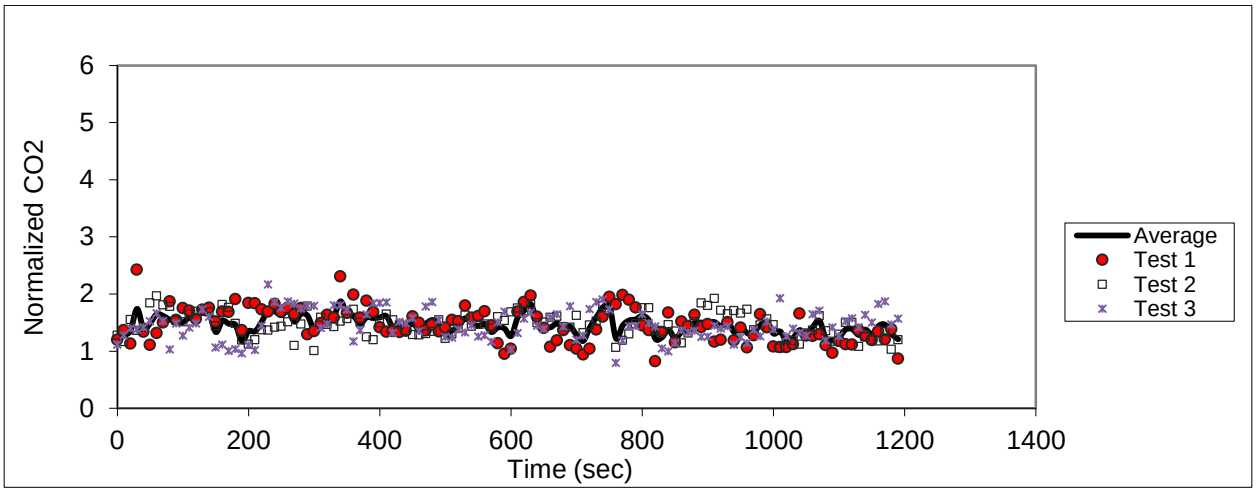

Figure D.16 – Sampling in seat 5E (release in 2D)

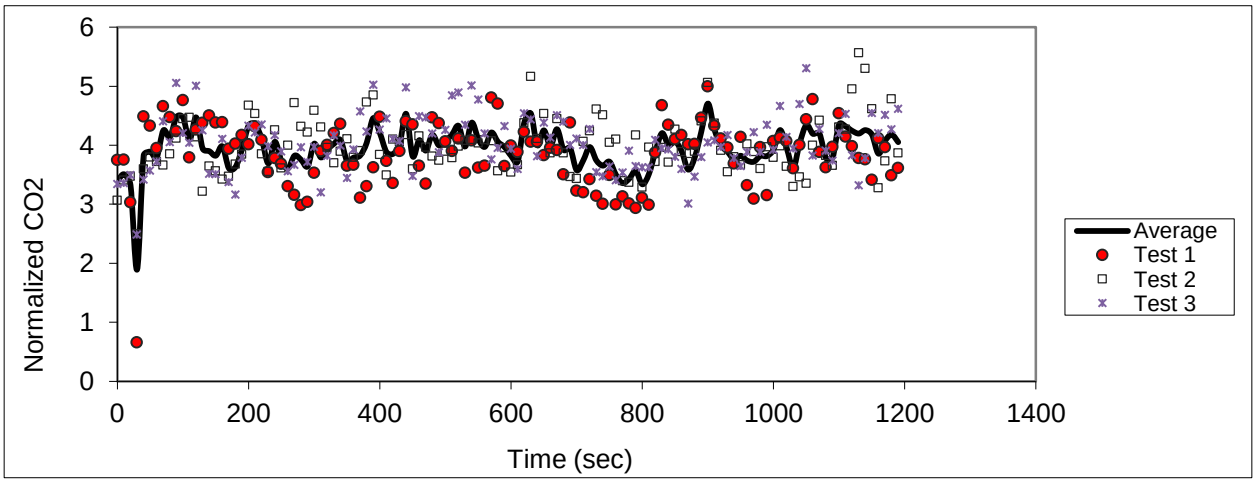

Figure D.17 - Sampling in seat 1F (release in 2D)

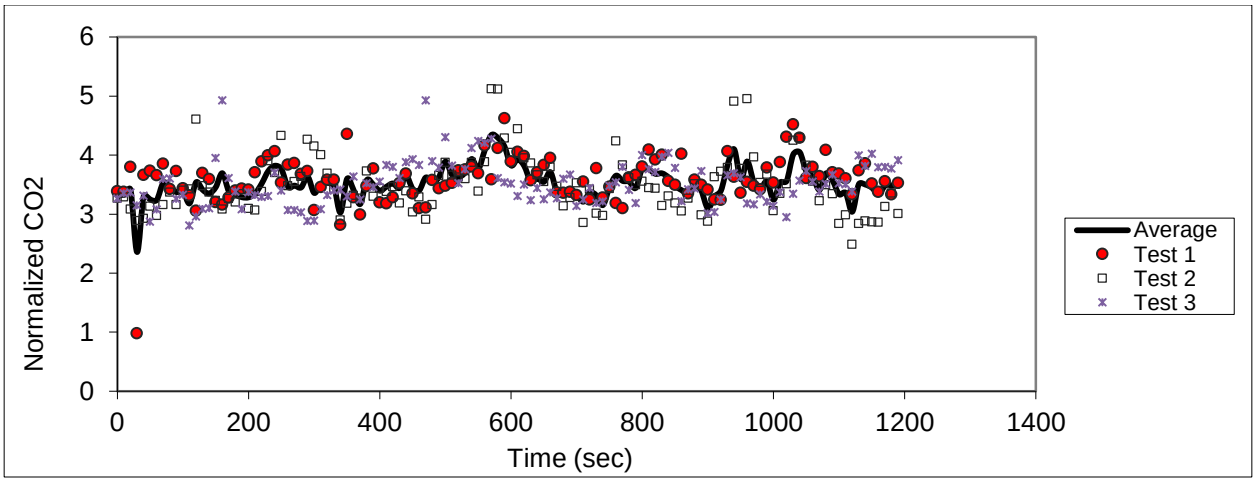

Figure D.18 – Sampling in seat 2F (release in 2D)

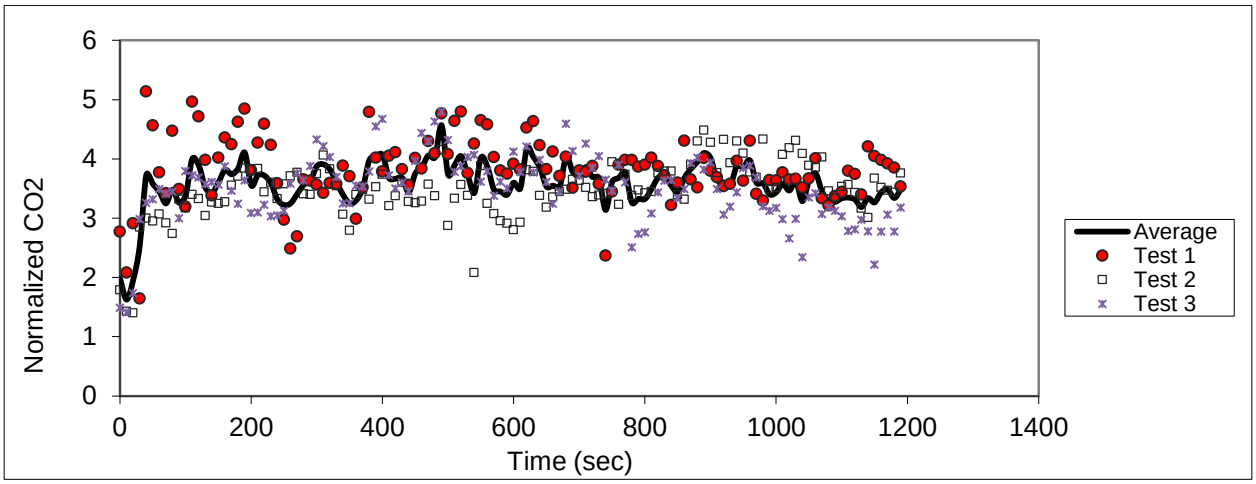

Figure D.19 – Sampling in seat 3F (release in 2D)

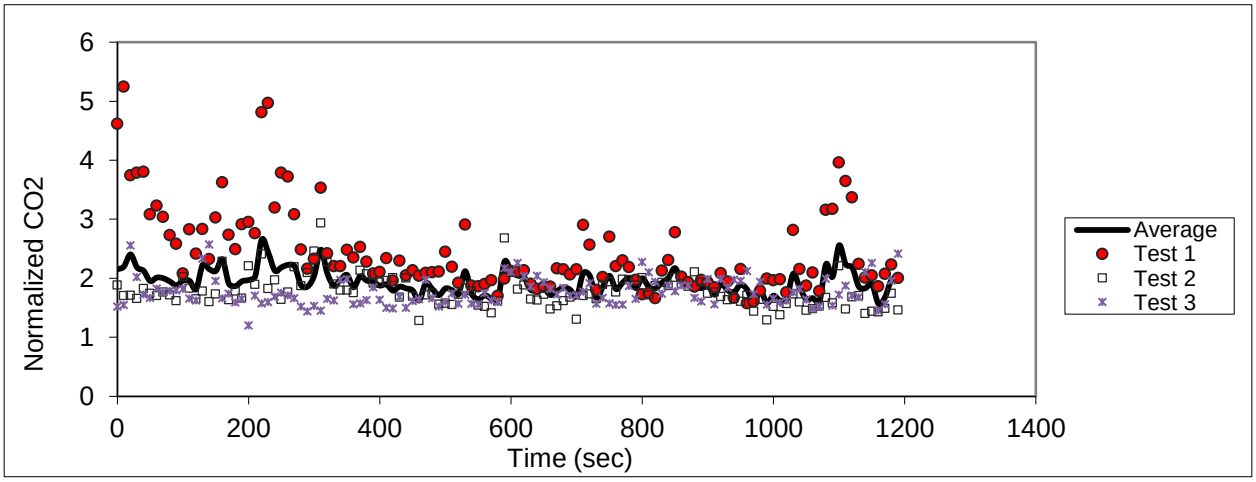

Figure D.20 – Sampling in seat 4F (release in 2D)

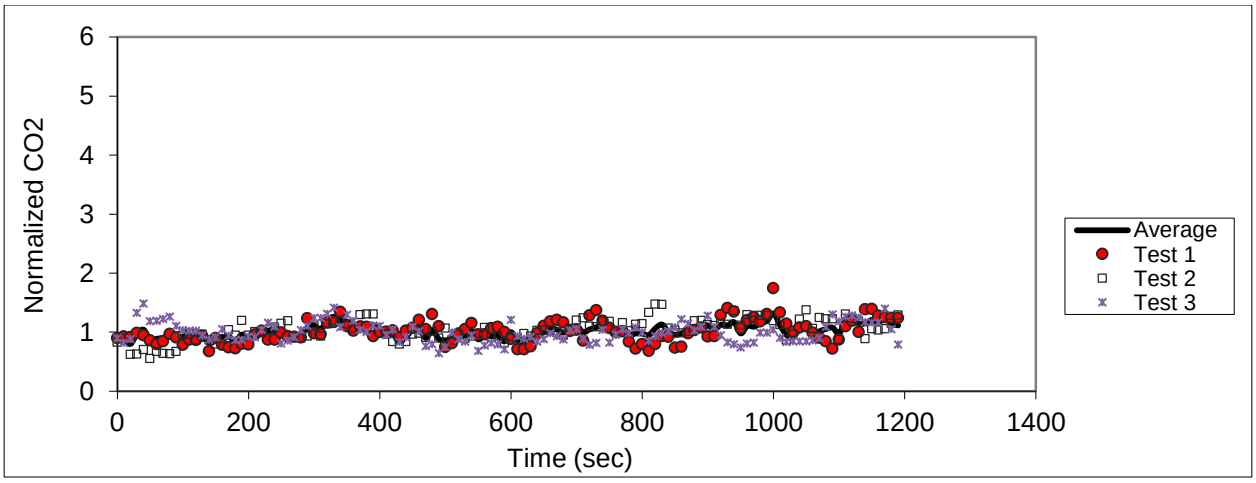

Figure D.21 – Sampling in seat 5F (release in 2D)

Release in seat 5D

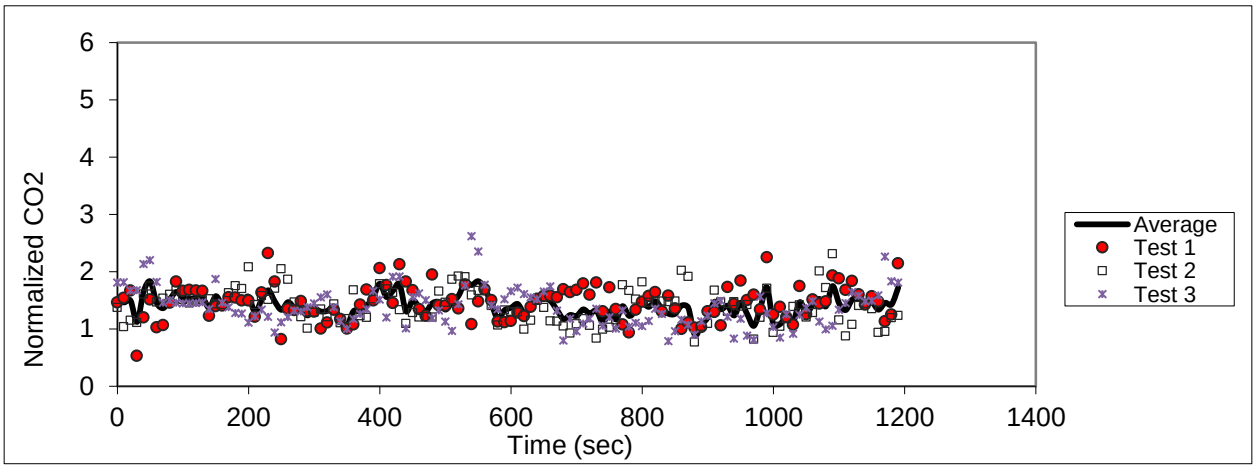

Figure D.22 – Sampling in seat 3B (release in 5D)

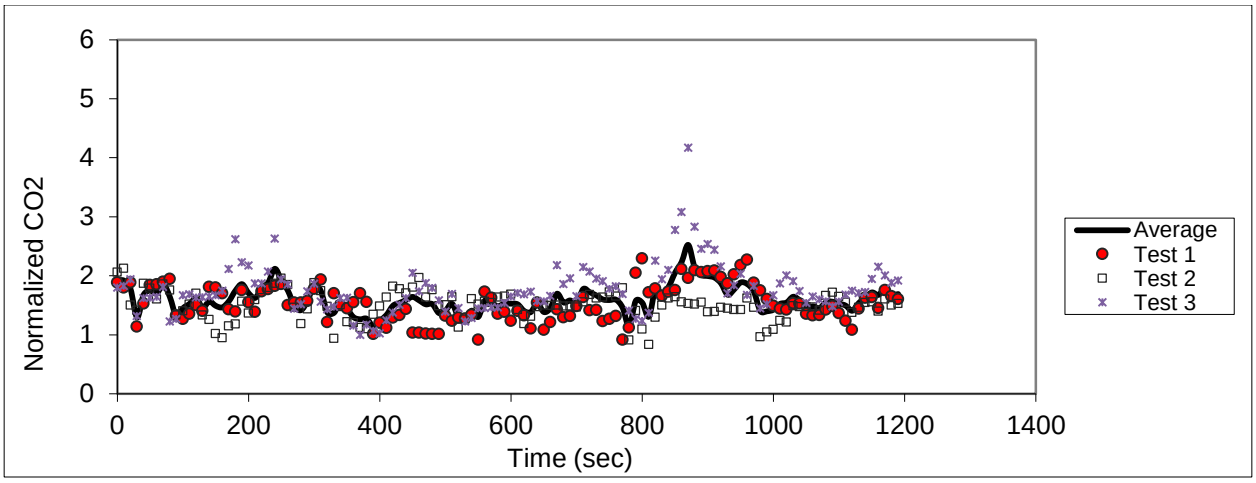

Figure D.23 – Sampling in seat 4B (release in 5D)

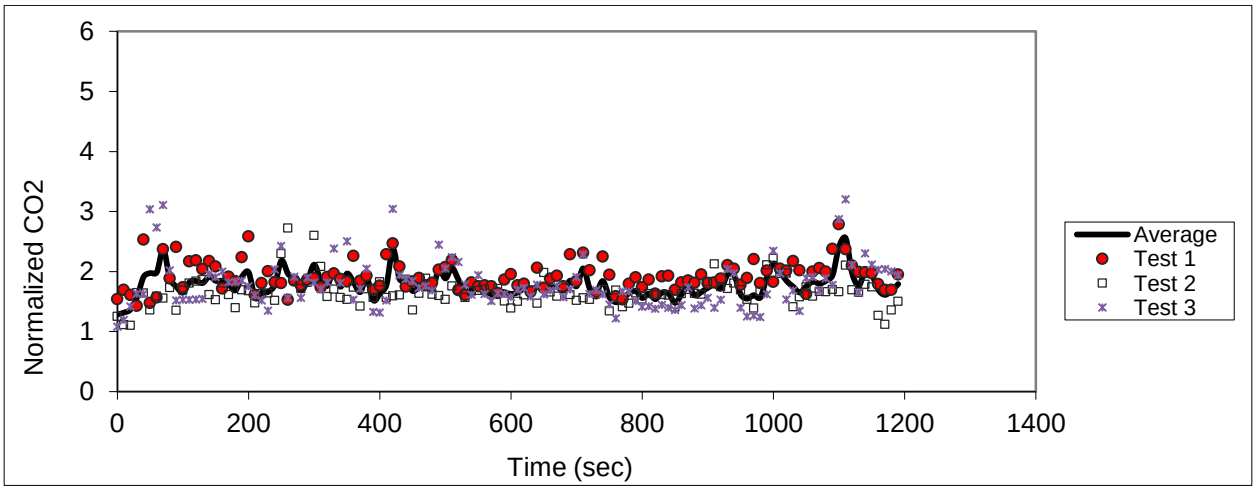

Figure D.24 – Sampling in seat 5B (release in 5D)

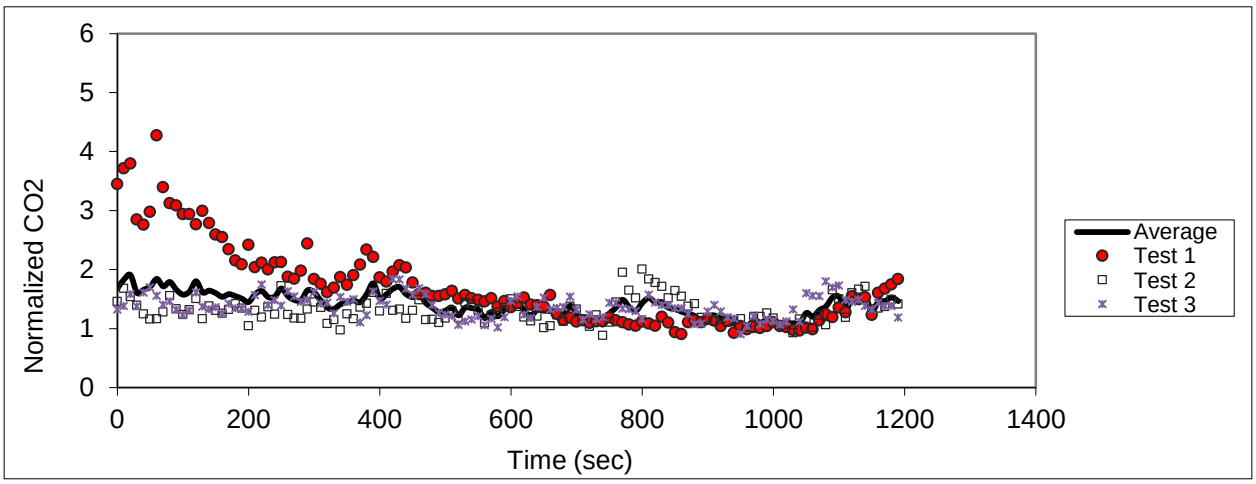

Figure D.25 – Sampling in seat 6B (release in 5D)

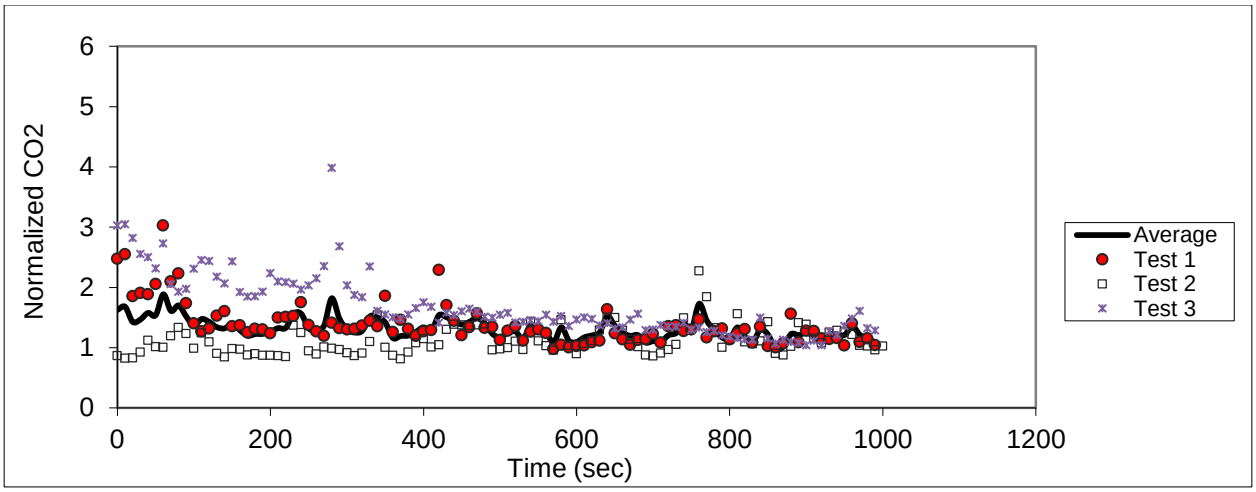

Figure D.26 – Sampling in seat 7B (release in 5D)

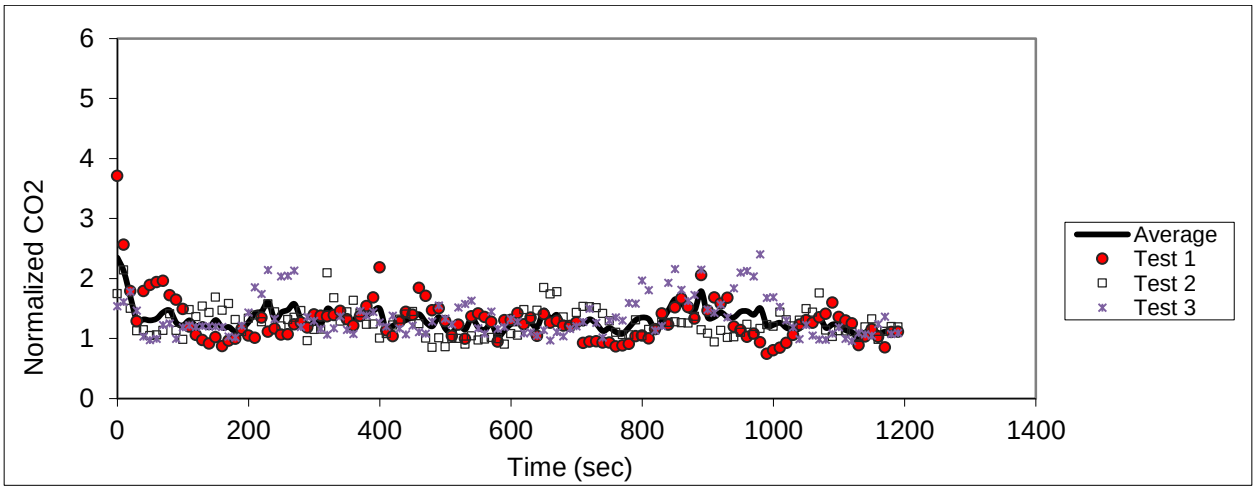

Figure D.27 – Sampling in seat 3C (release in 5D)

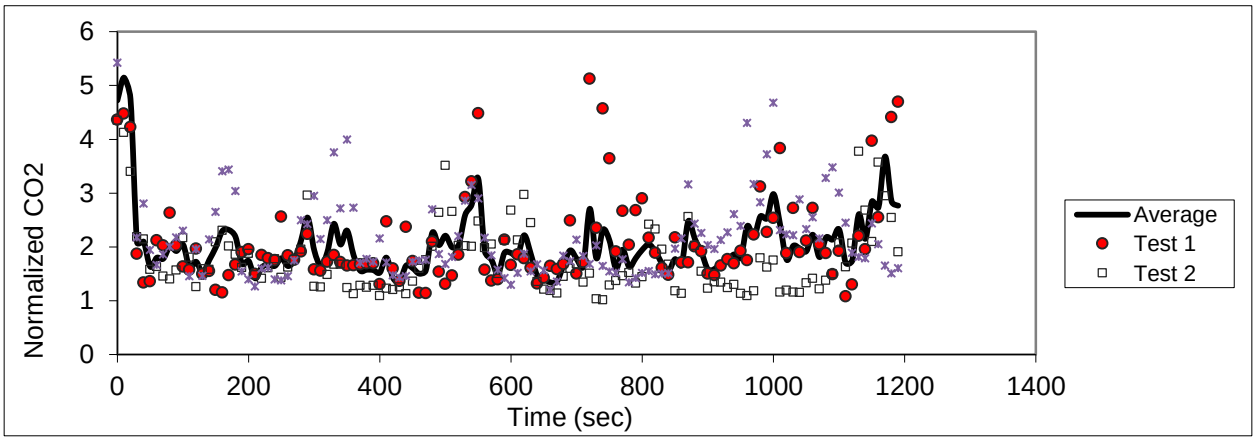

Figure D.28 – Sampling in seat 4C (release in 5D)

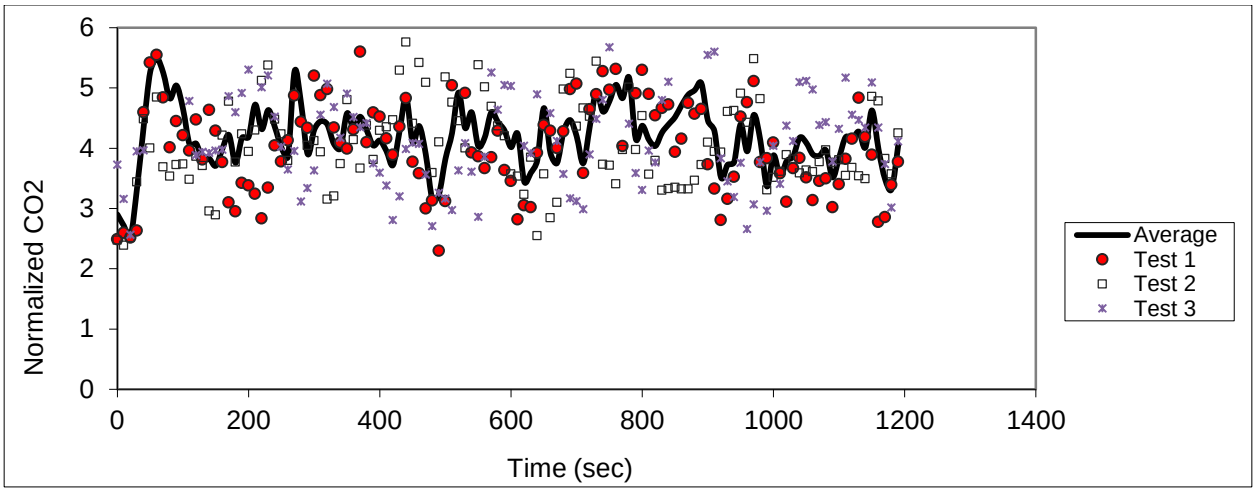

Figure D.29 – Sampling in seat 5C (release in 5D)

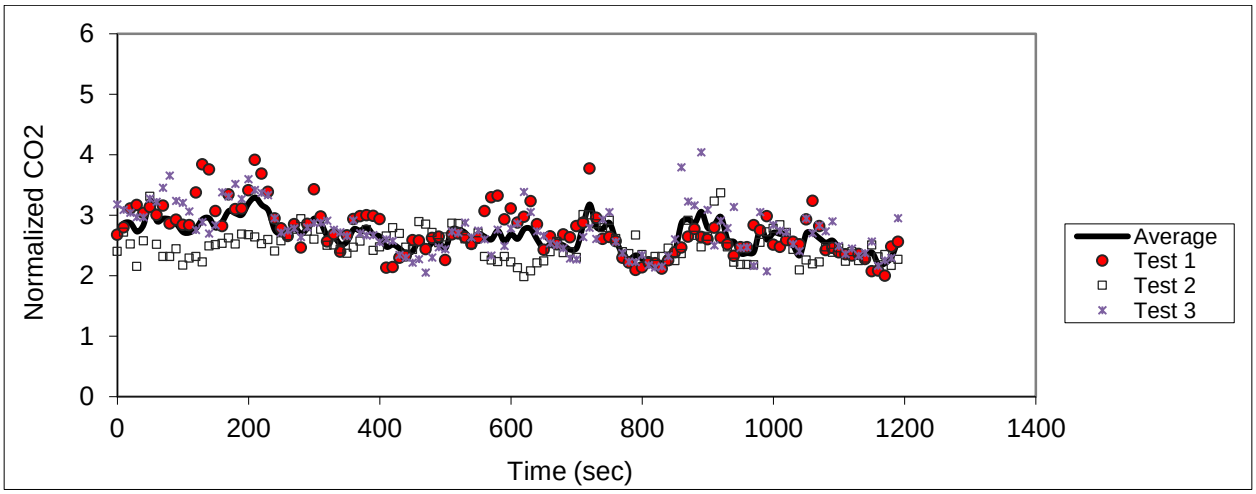

Figure D.30 – Sampling in seat 6C (release in 5D)

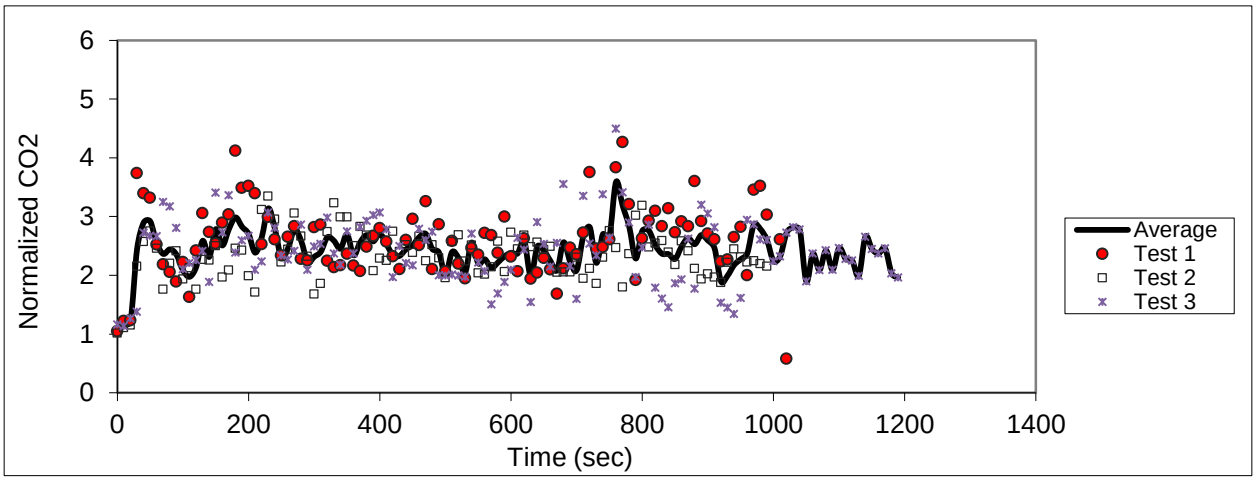

Figure D.31 – Sampling in seat 7C (release in 5D)

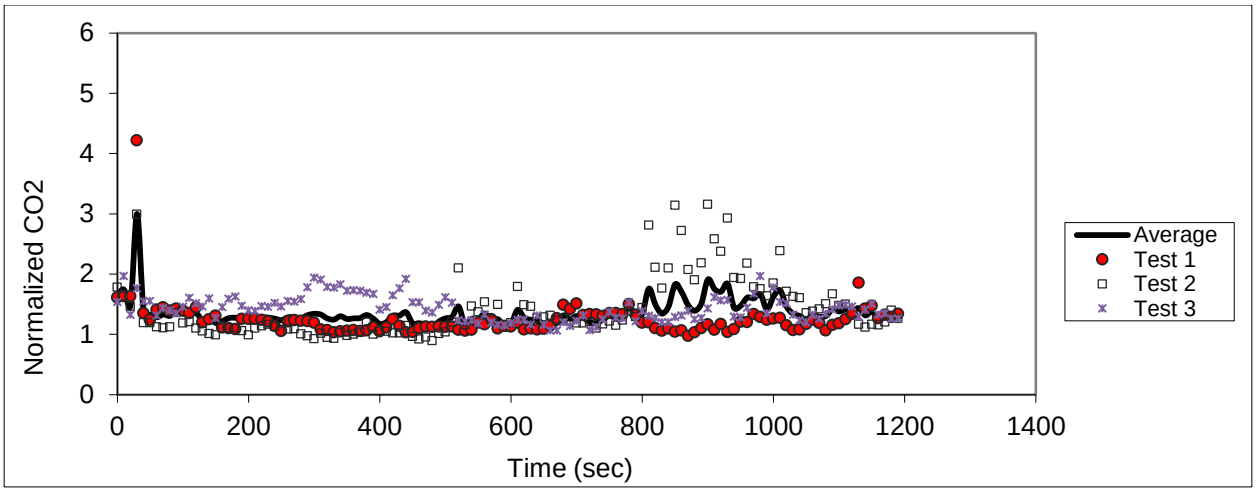

Figure D.32 – Sampling in seat 3E (release in 5D)

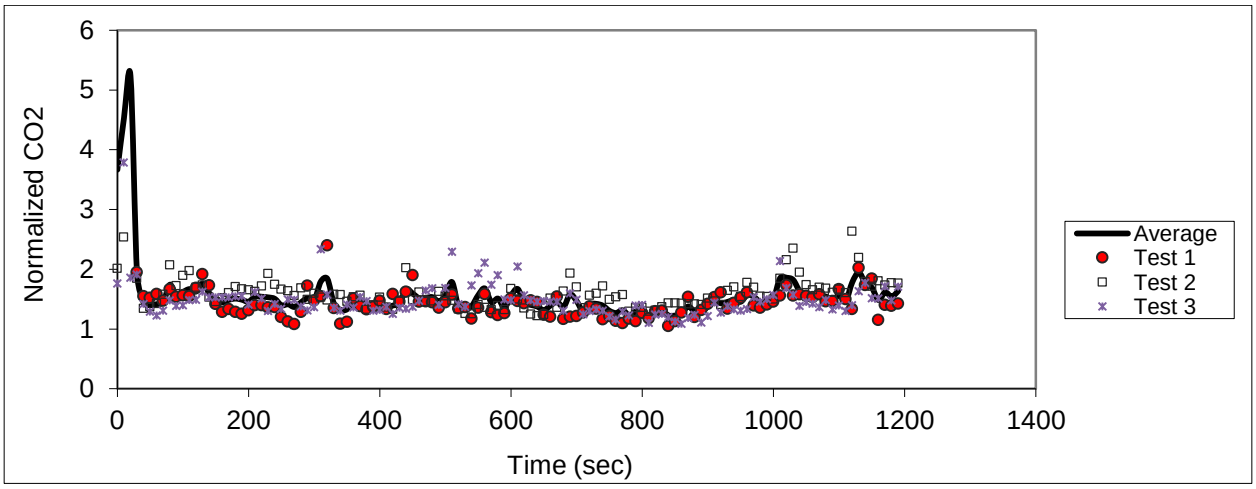

Figure D.33 – Sampling in seat 4E (release in 5D)

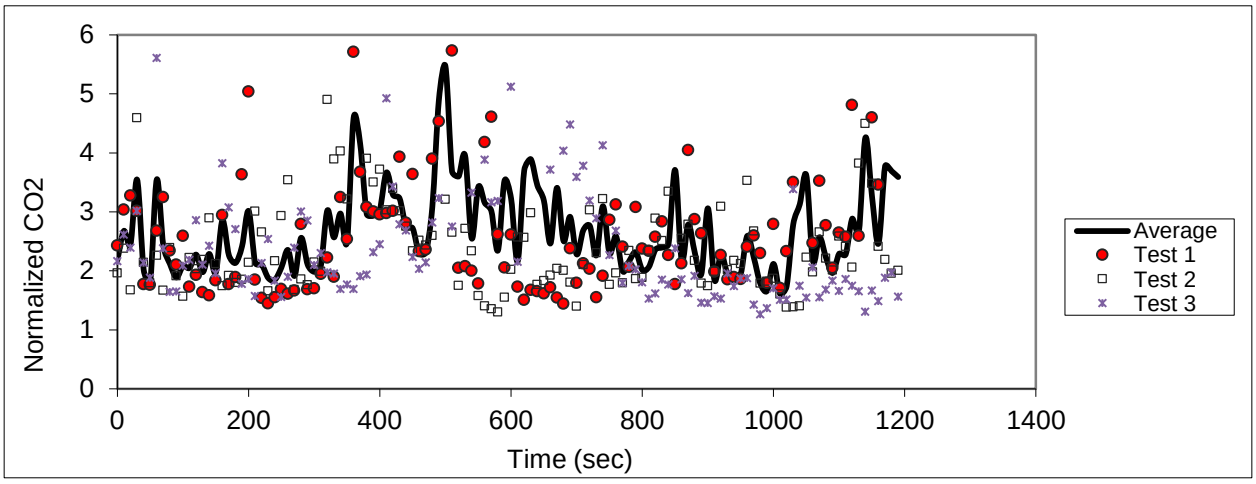

Figure D.34 – Sampling in seat 5E (release in 5D)

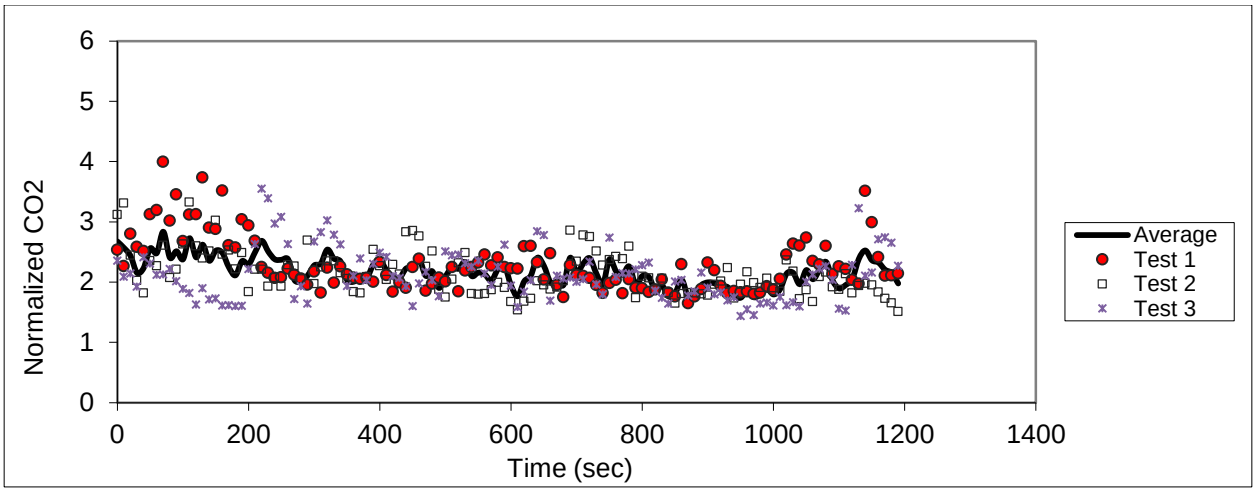

Figure D.35 – Sampling in seat 6E (release in 5D)

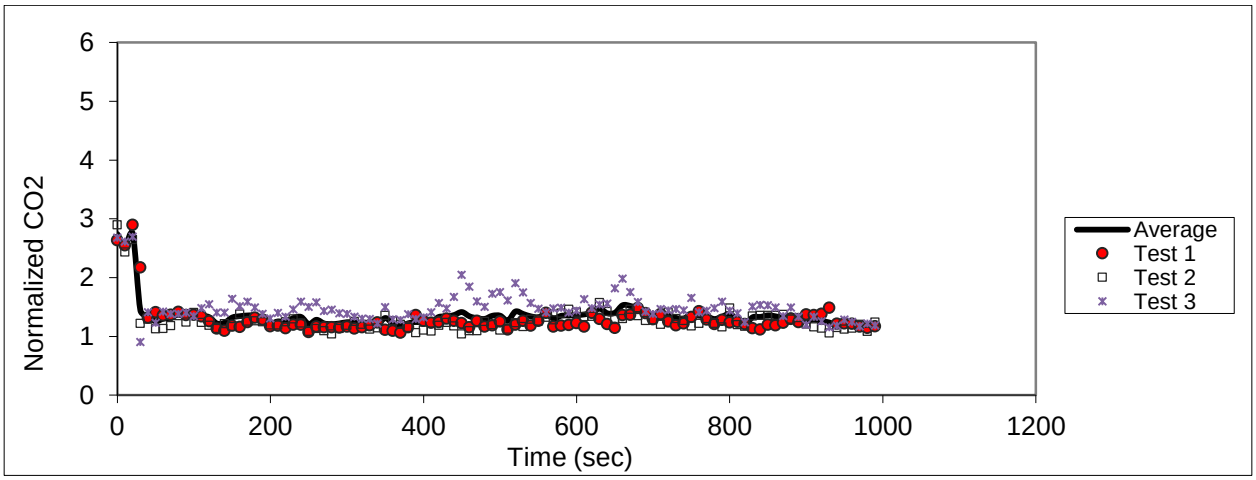

Figure D.36 - Sampling in seat 7E (release in 5D)

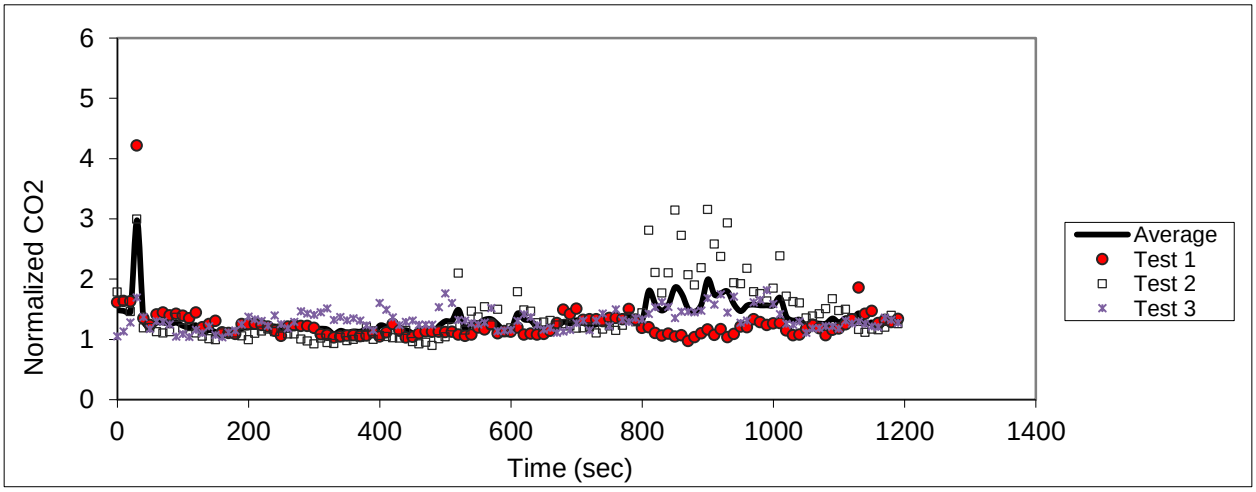

Figure D.37 – Sampling in seat 3F (release in 5D)

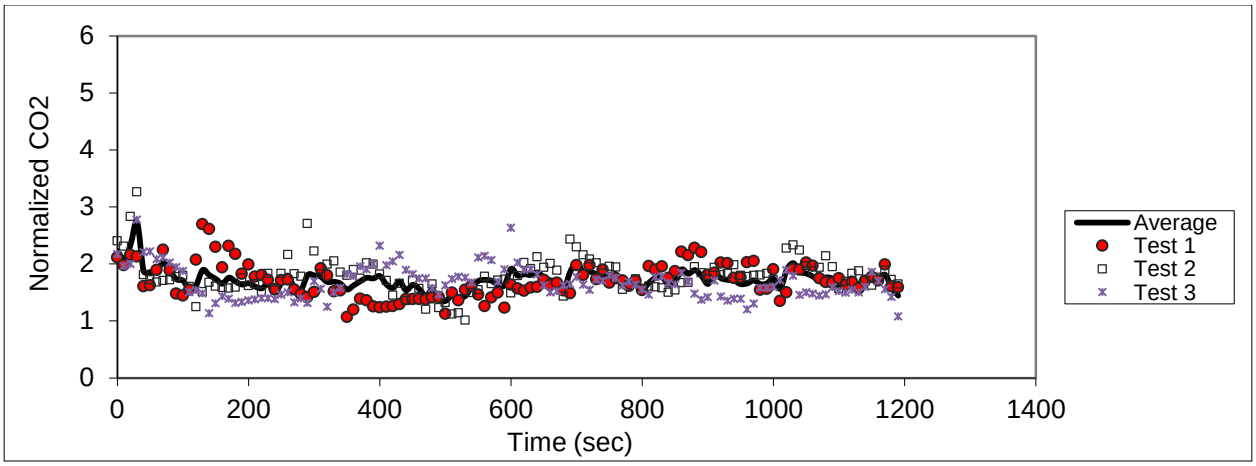

Figure D.38 – Sampling in seat 4F (release in 5D)

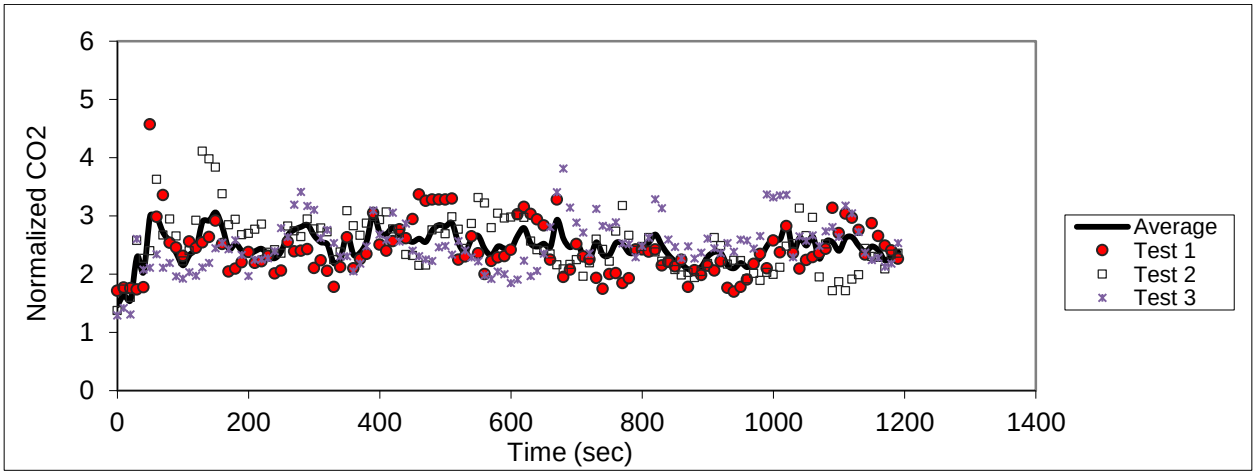

Figure D.39 – Sampling in seat 5F (release in 5D)

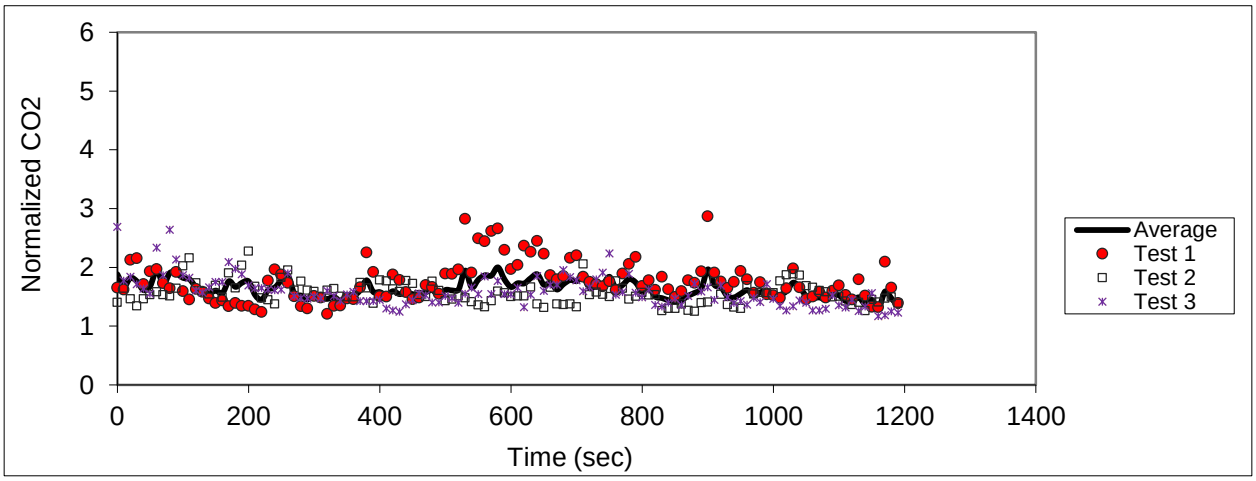

Figure D.40 – Sampling in seat 6F (release in 5D)

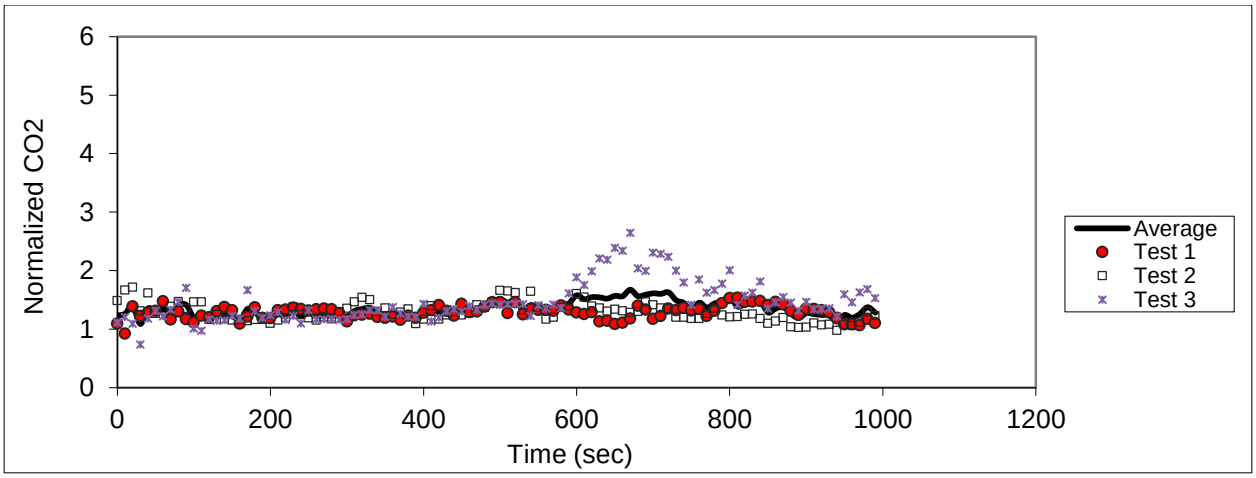

Figure D.41 - Sampling in seat 7F (release in 5D)

Release in seat 7D

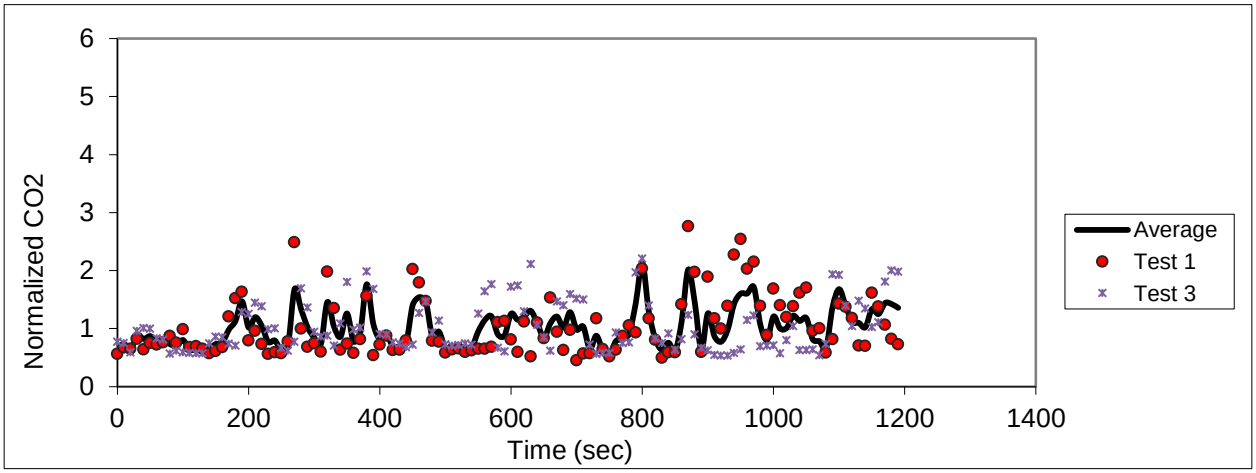

Figure D.42 – Sampling in seat 5B (release in 7D)

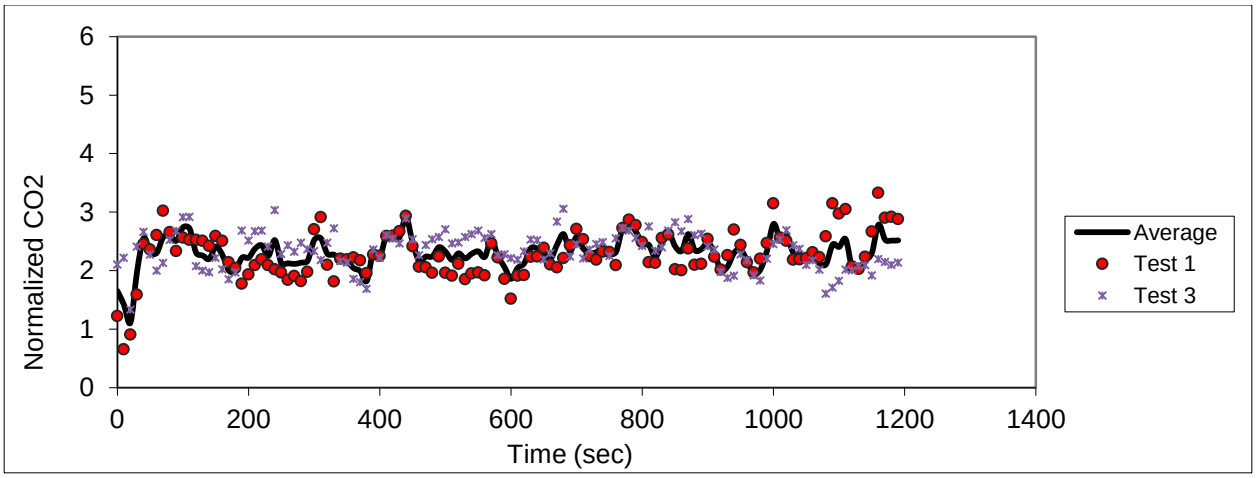

Figure D.43 - Sampling in seat 6B (release in 7D)

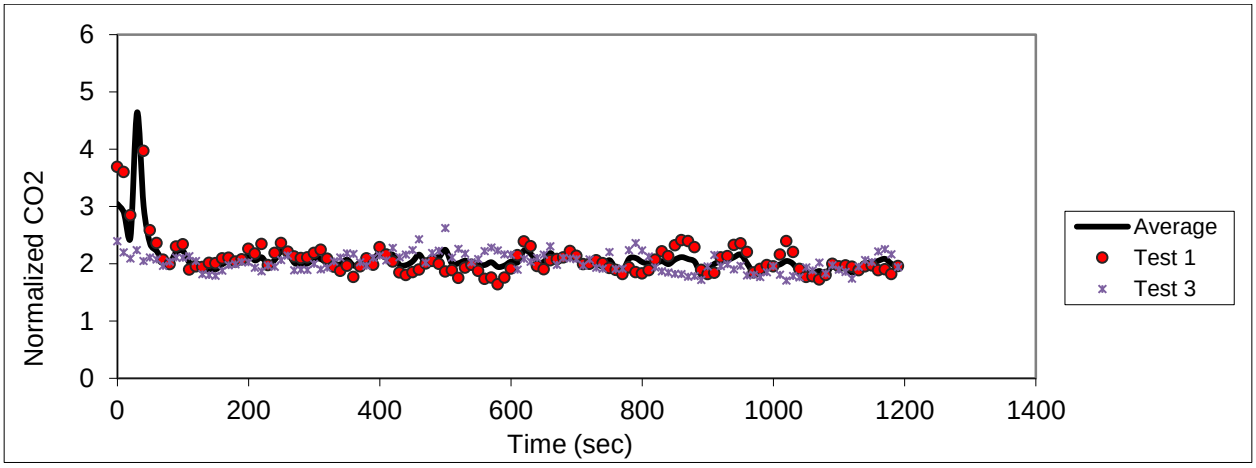

Figure D.44 – Sampling in seat 7B (release in 7D)

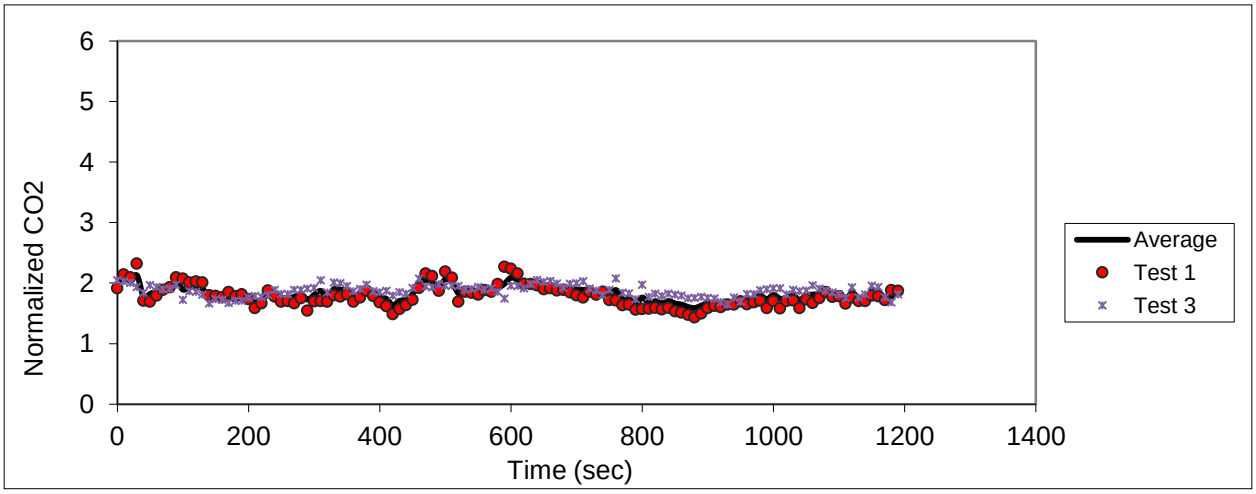

Figure D.45 – Sampling in seat 8B (release in 7D)

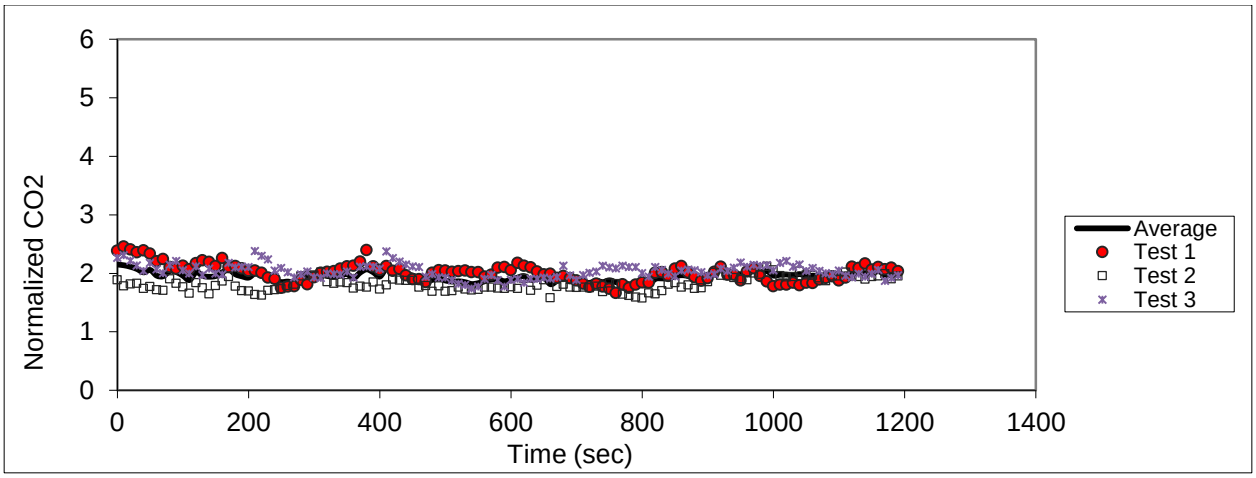

Figure D.46 – Sampling in seat 9B (release in 7D)

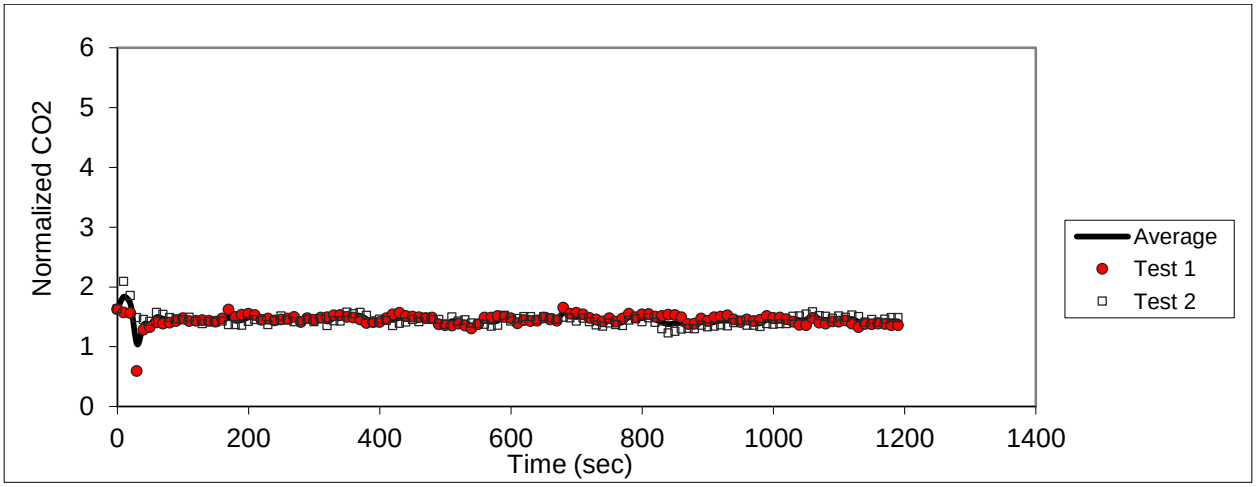

Figure D.47 - Sampling in seat 10B (release in 7D)

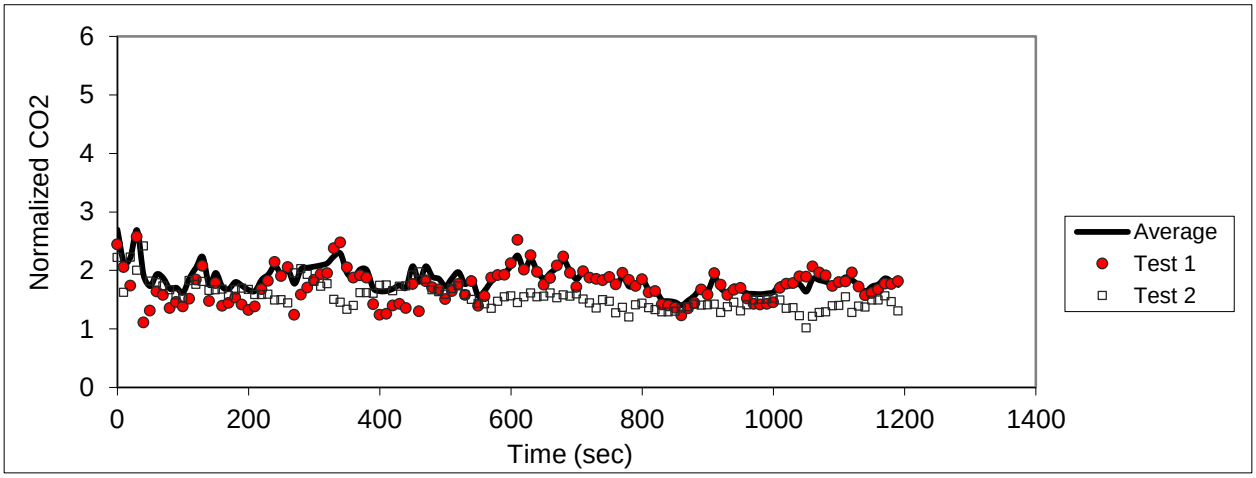

Figure D.48 – Sampling in seat 6C (release in 7D)

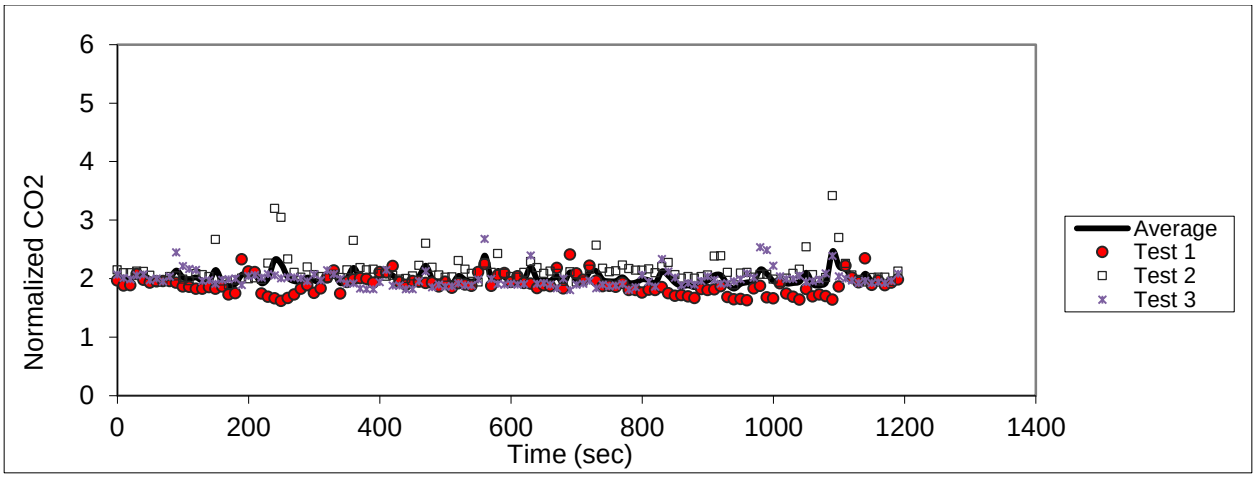

Figure D.49 - Sampling in seat 9C (release in 7D)

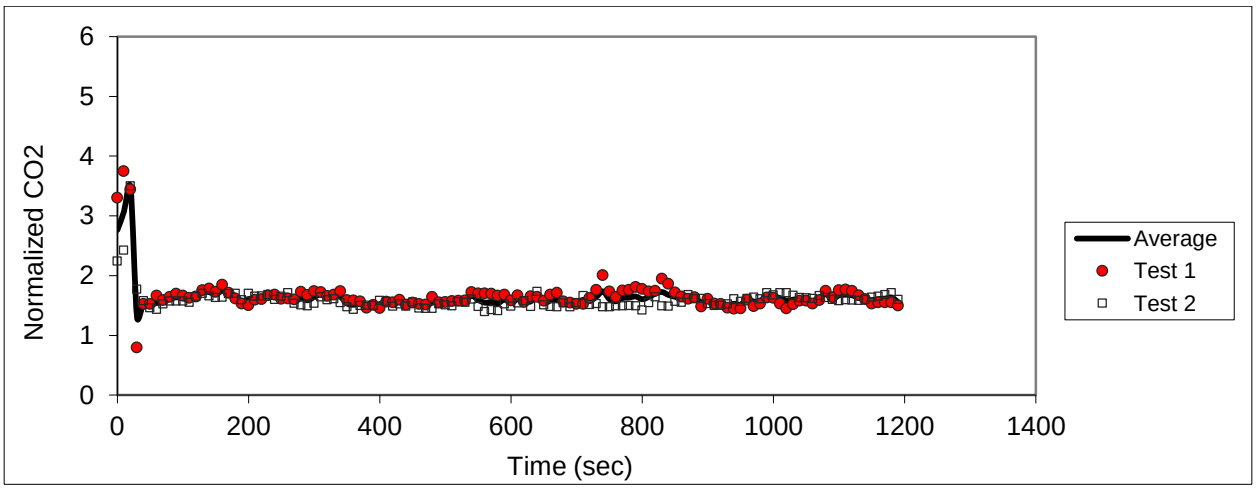

Figure D.50 - Sampling in seat 10C (release in 7D)

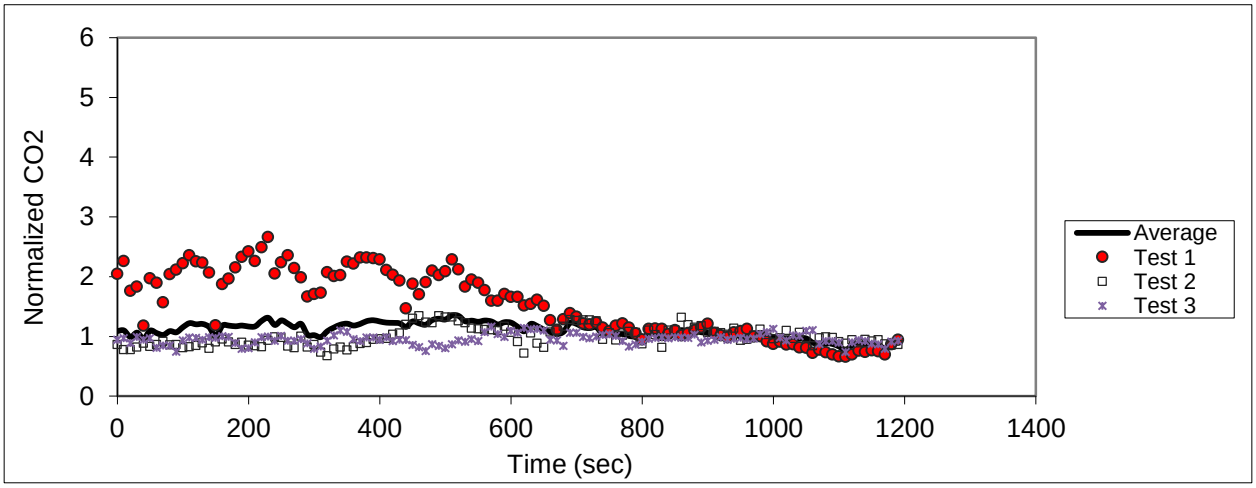

Figure D.51 – Sampling in seat 5D (release in 7D)

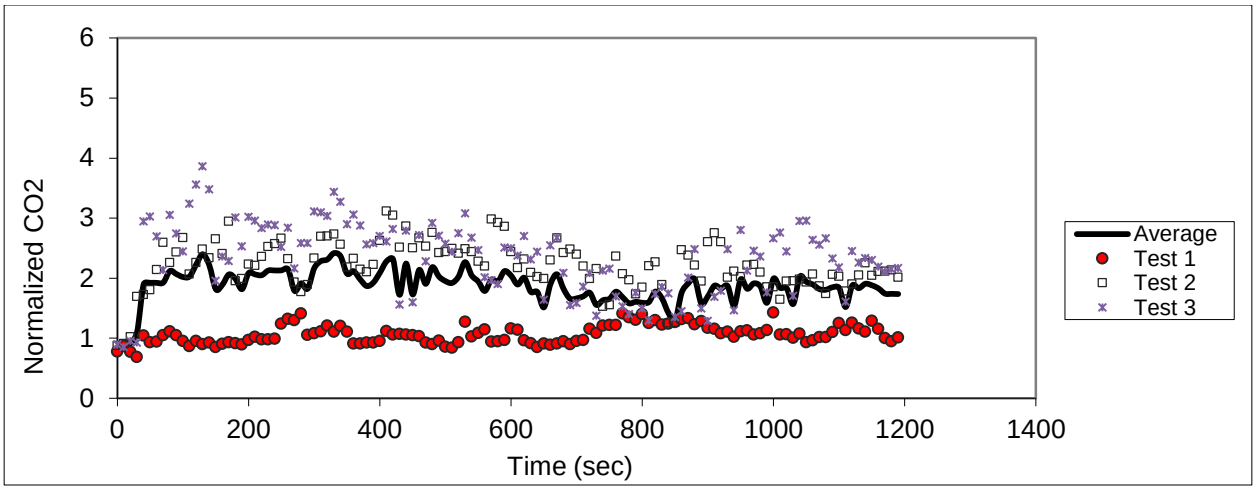

Figure D.52 – Sampling in seat 6D (release in 7D)

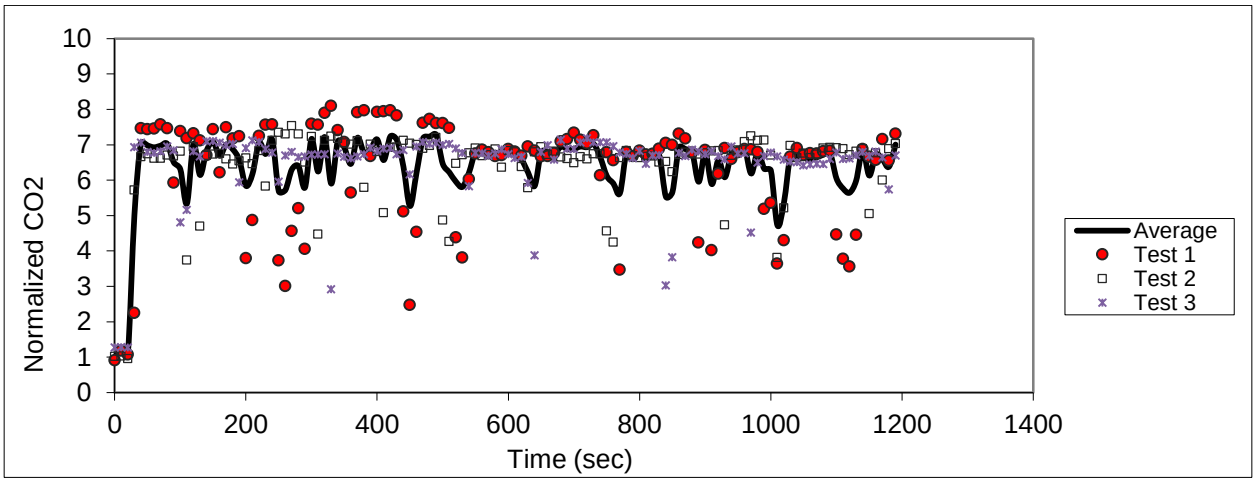

Figure D.53 - Sampling in seat 7D (release in 7D)

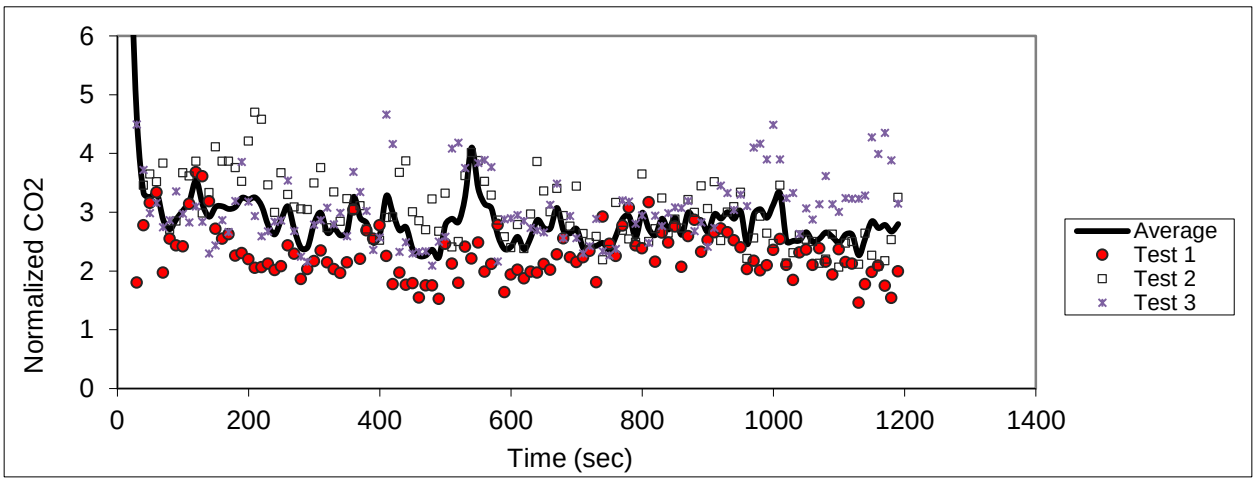

Figure D.54 – Sampling in seat 8D (release in 7D)

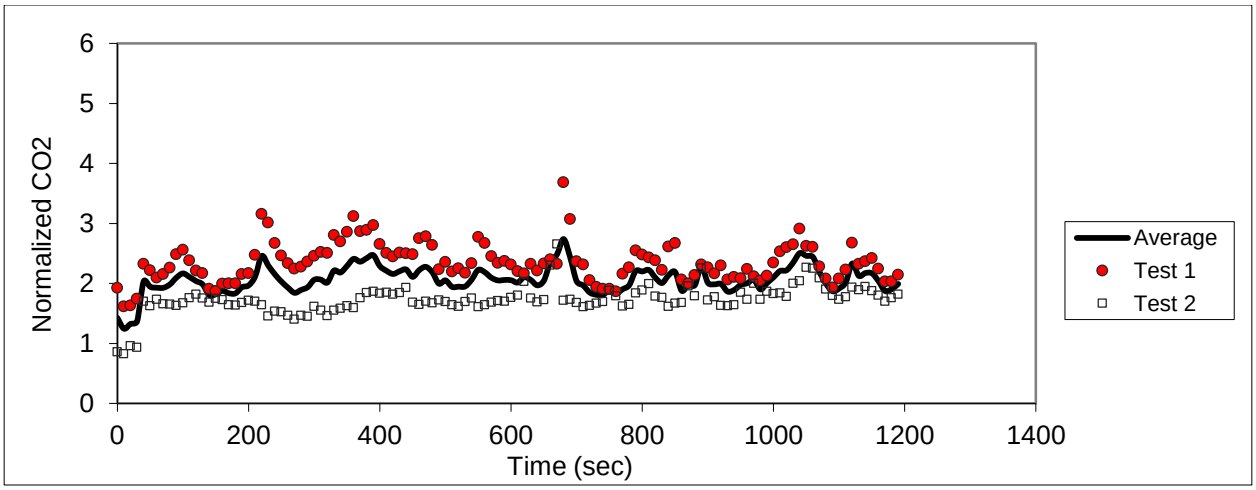

Figure D.55 – Sampling in seat 8E (release in 7D)

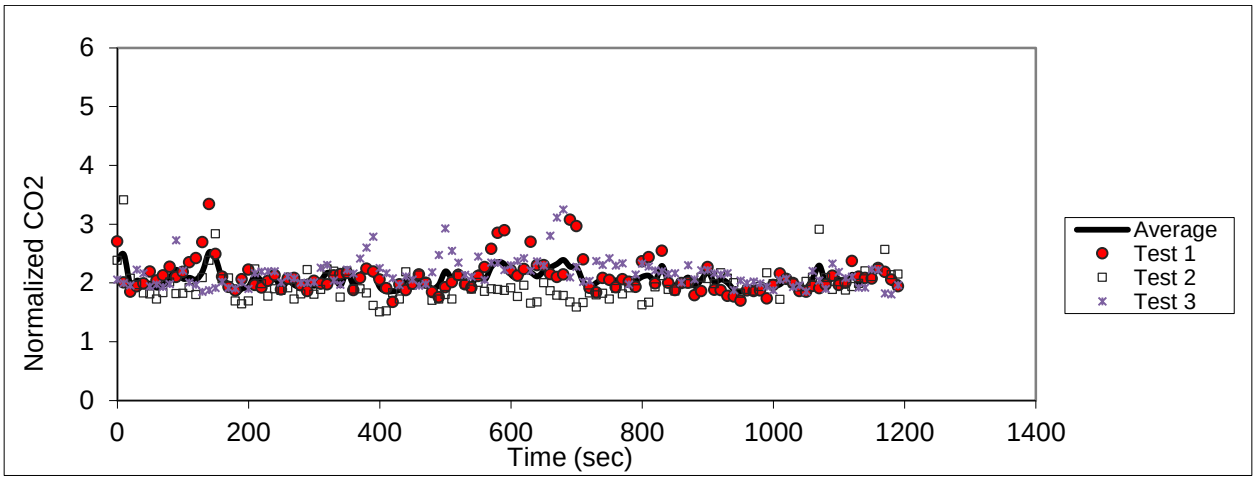

Figure D.56 – Sampling in seat 9E (release in 7D)

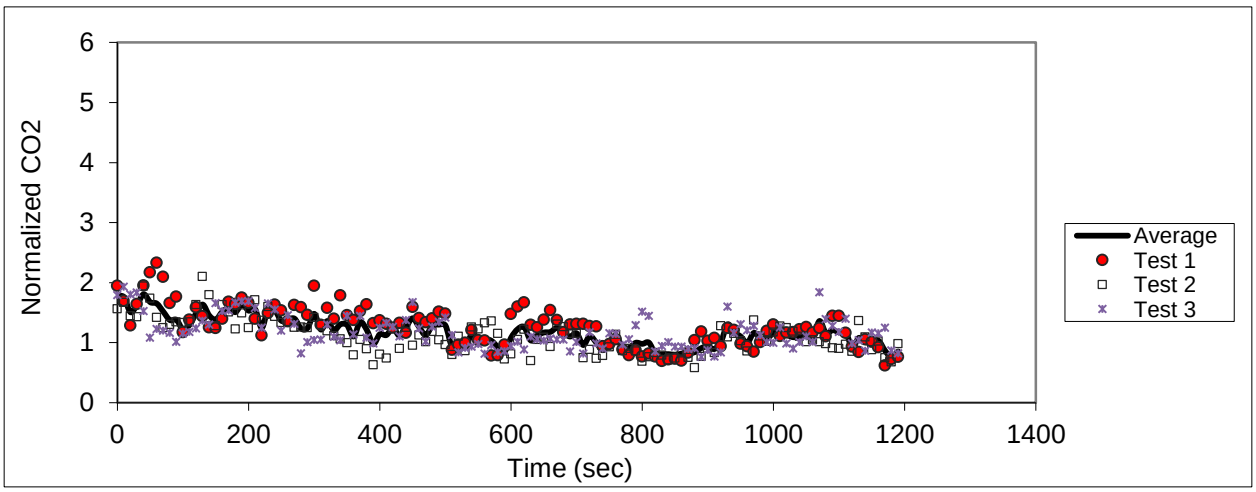

Figure D.57 – Sampling in seat 5F (release in 7D)

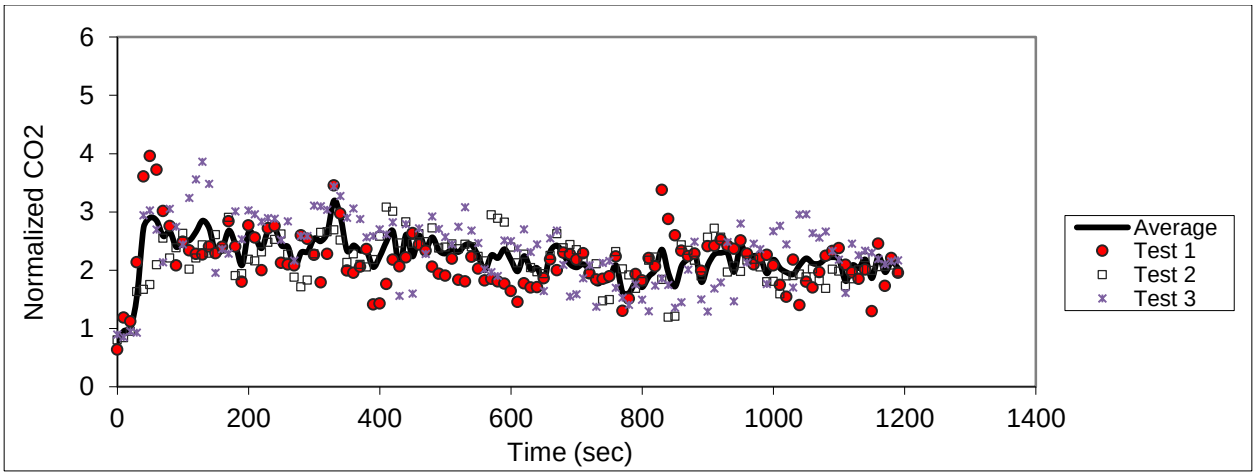

Figure D.58 – Sampling in seat 6F (release in 7D)

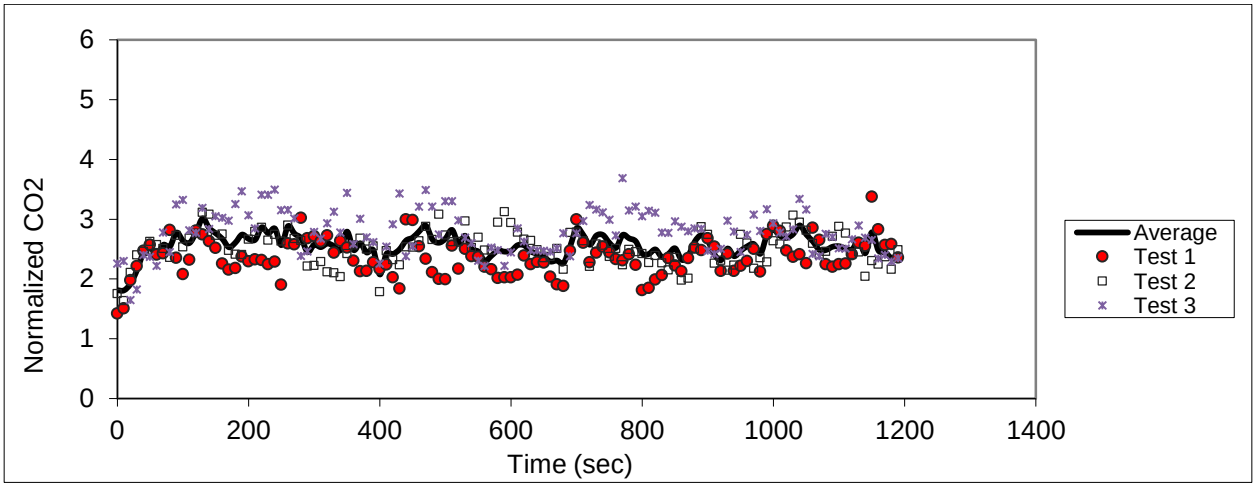

Figure D.59 – Sampling in seat 7F (release in 7D)

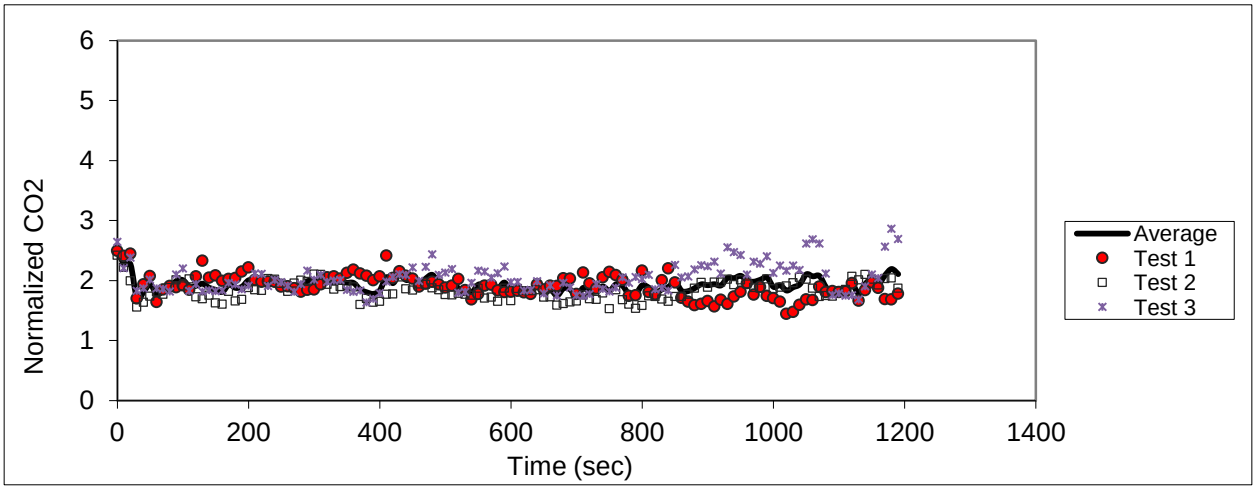

Figure D.60 – Sampling in seat 8F (release in 7D)

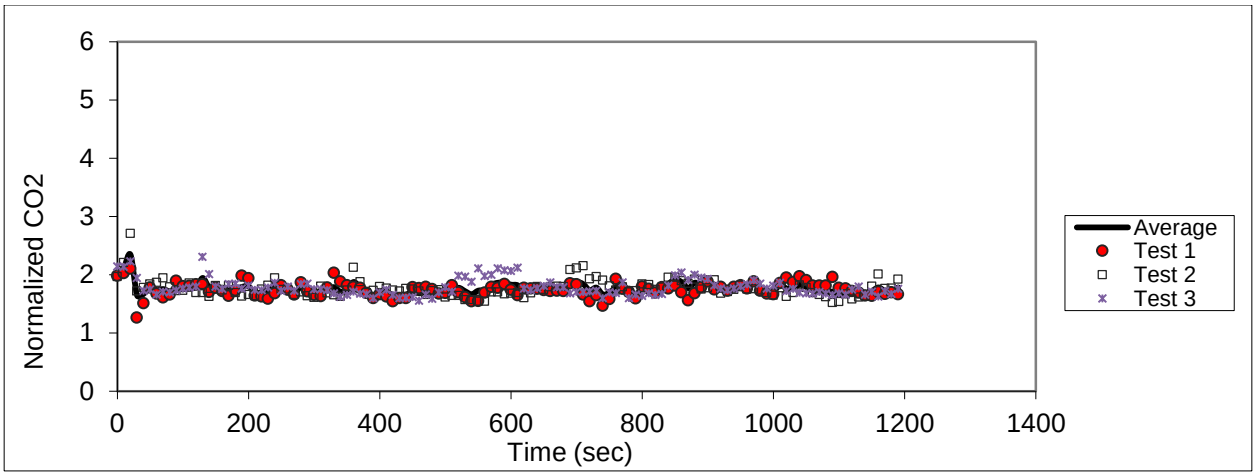

Figure D.61 – Sampling in seat 9F (release in 7D)

Release in 5B

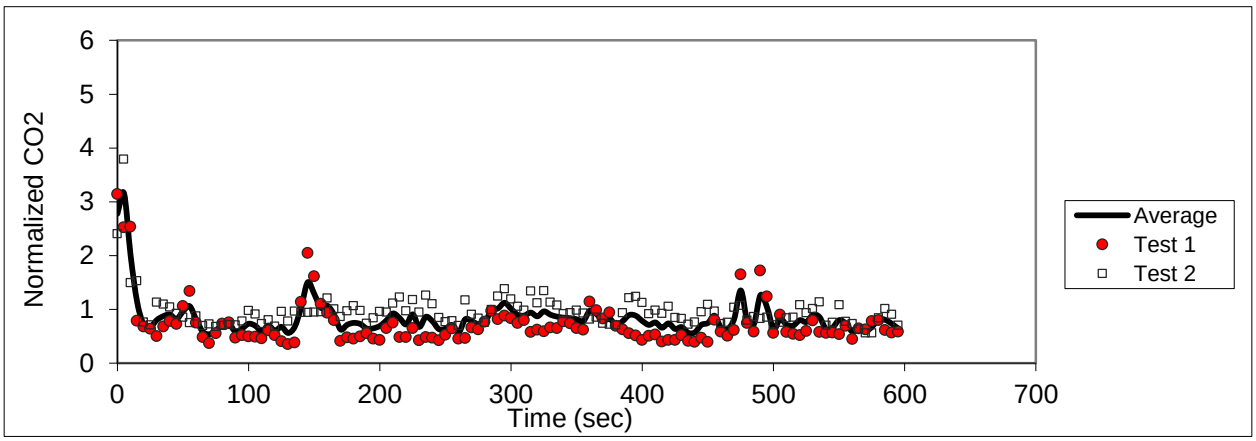

Figure D.62 – Sampling in seat 3B (release in 5B)

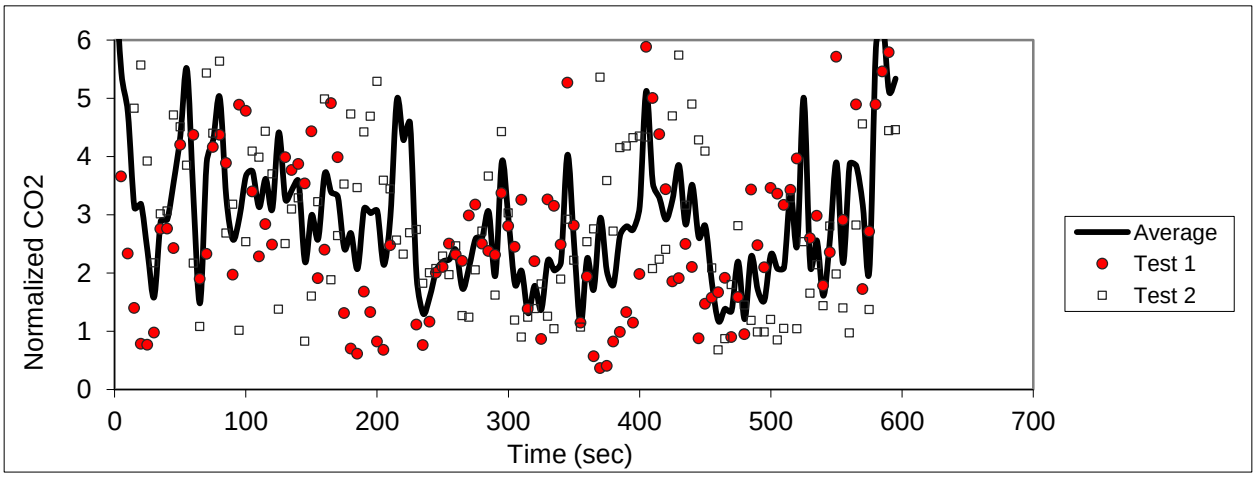

Figure D.63 - Sampling in seat 4B (release in 5B)

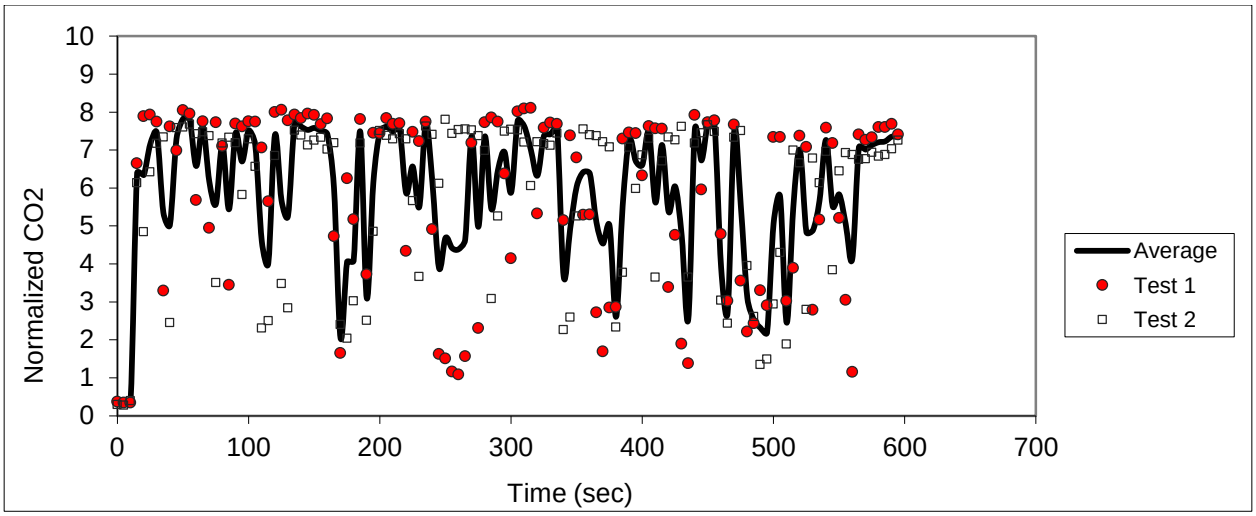

Figure D.64 – Sampling in seat 5B (release in 5B)

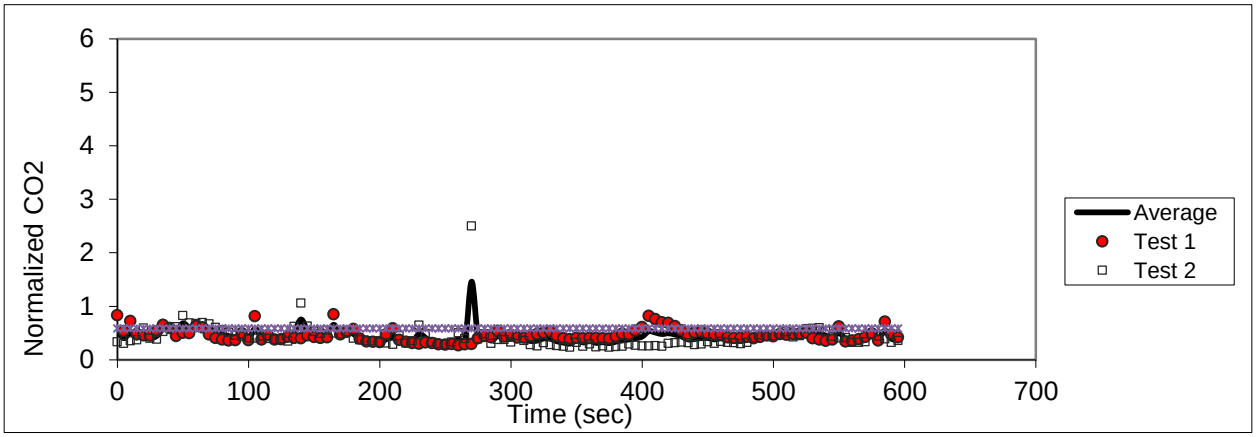

Figure D.65 – Sampling in seat 6B (release in 5B)

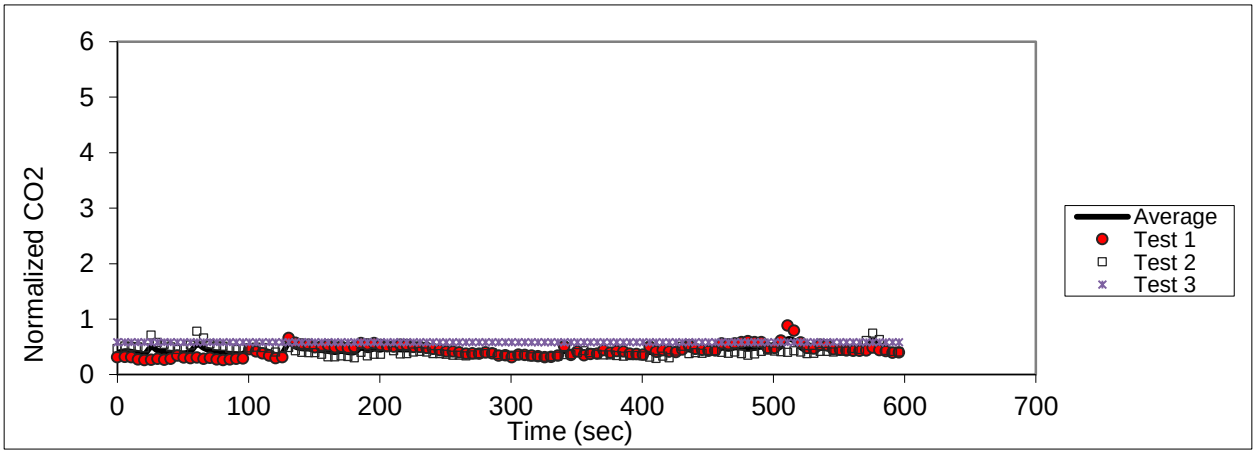

Figure D.66 - Sampling in seat 7B (release in 5B)

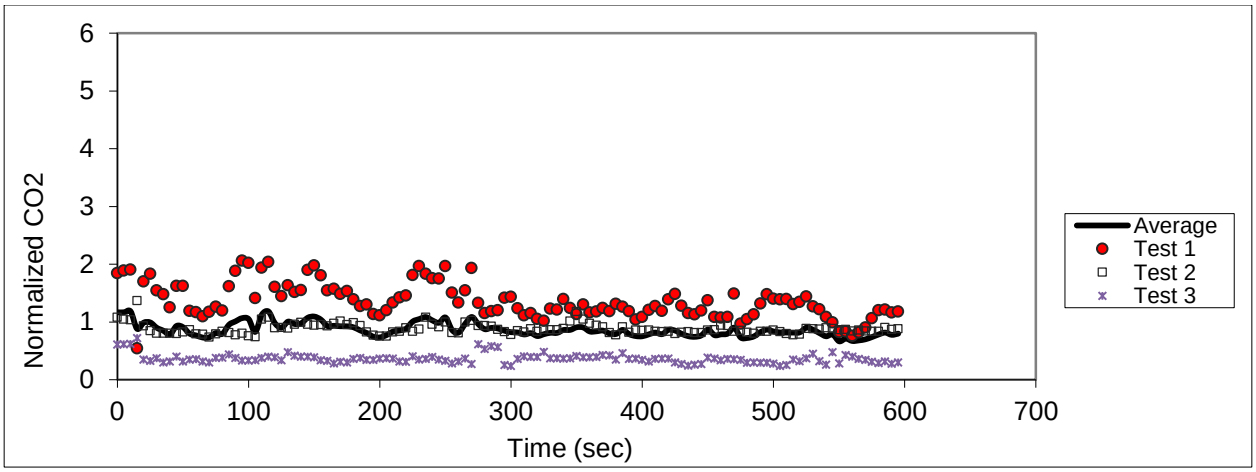

Figure D.67 – Sampling in seat 3D (release in 5B)

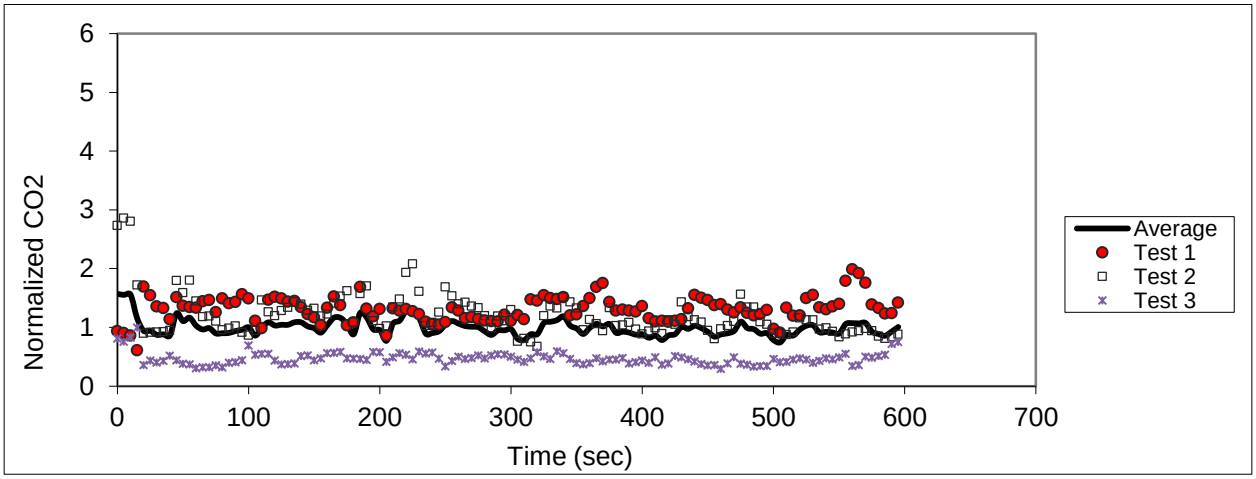

Figure D.68 – Sampling in seat 4D (release in 5B)

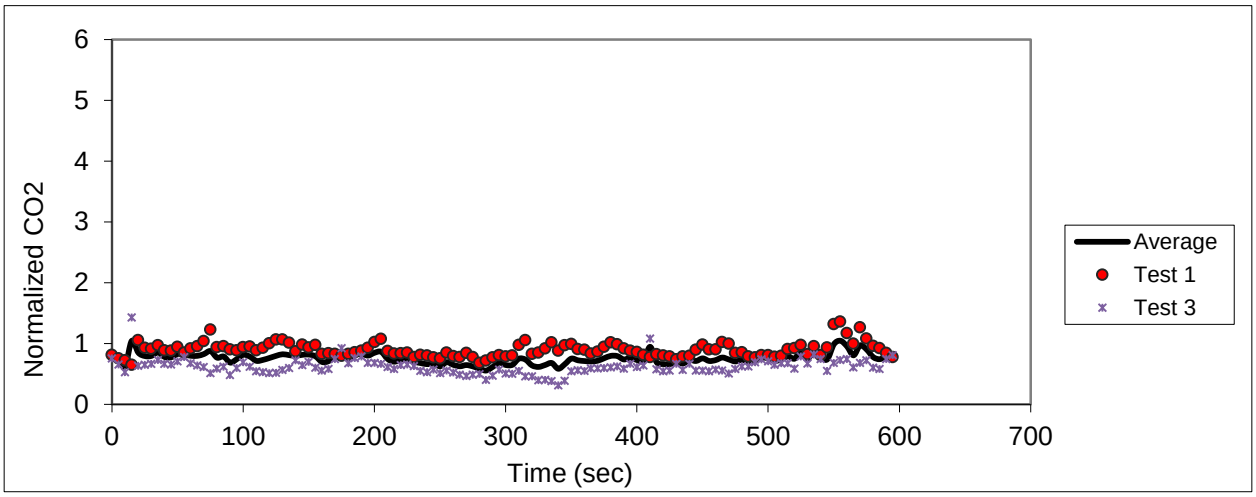

Figure D.69 – Sampling in seat 5D (release in 5B)

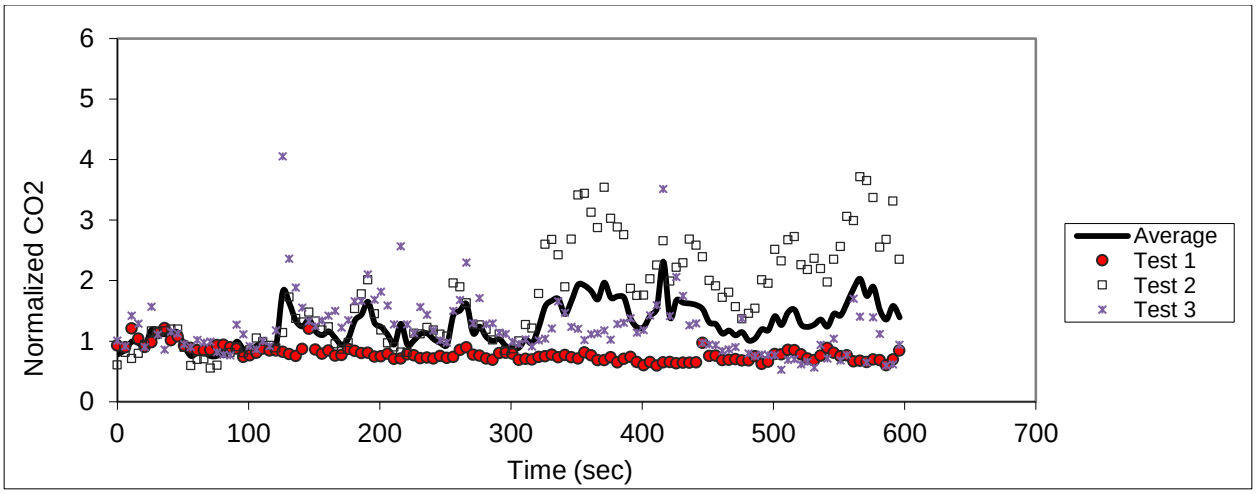

Figure D.70 – Sampling in seat 6D (release in 5B)

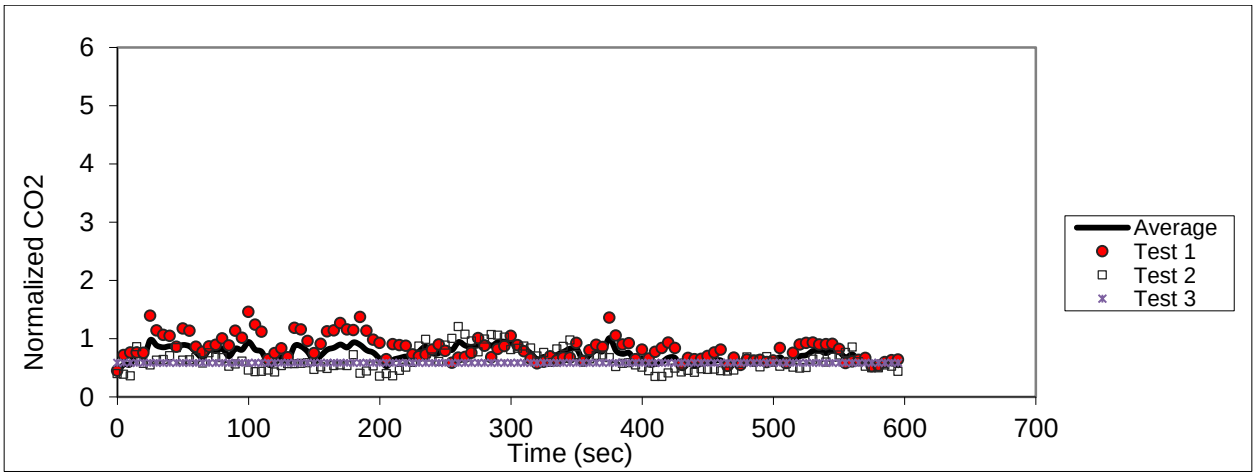

Figure D.71 - Sampling in seat 7D (release in 5B)

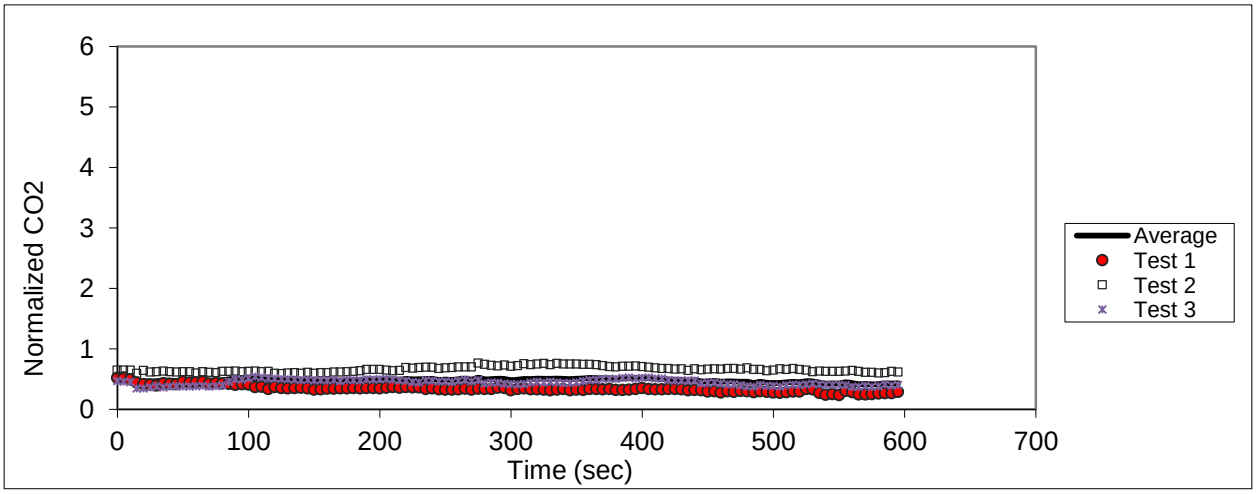

Figure D.72 – Sampling in seat 3F (release in 5B)

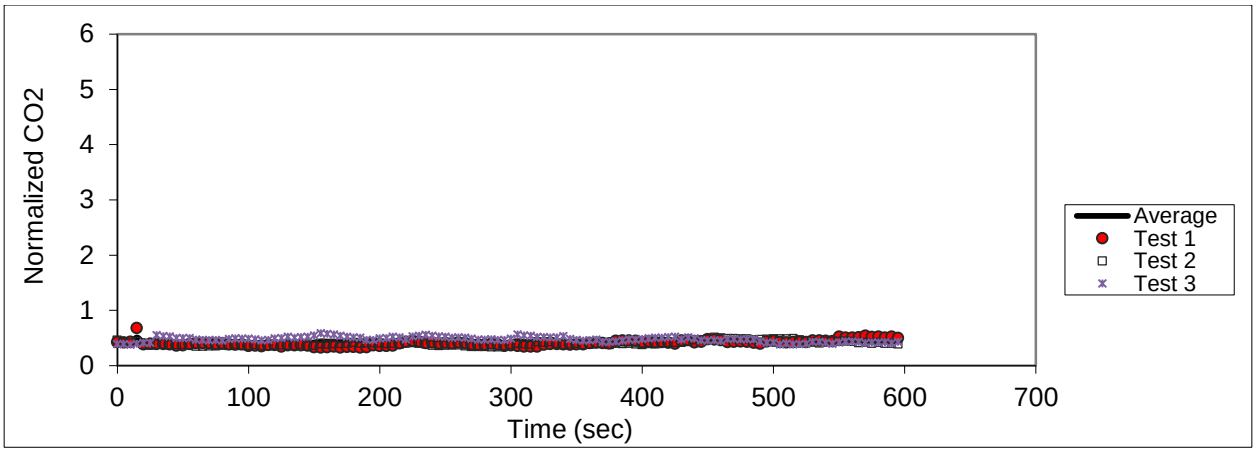

Figure D.73 – Sampling in seat 4F (release in 5B)

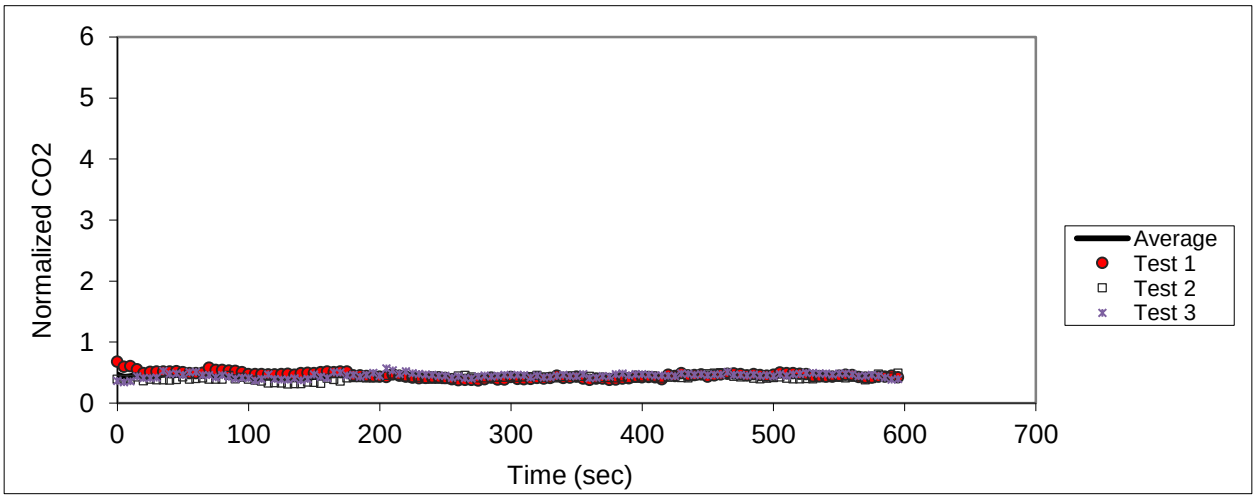

Figure D.74 – Sampling in seat 5F (release in 5B)

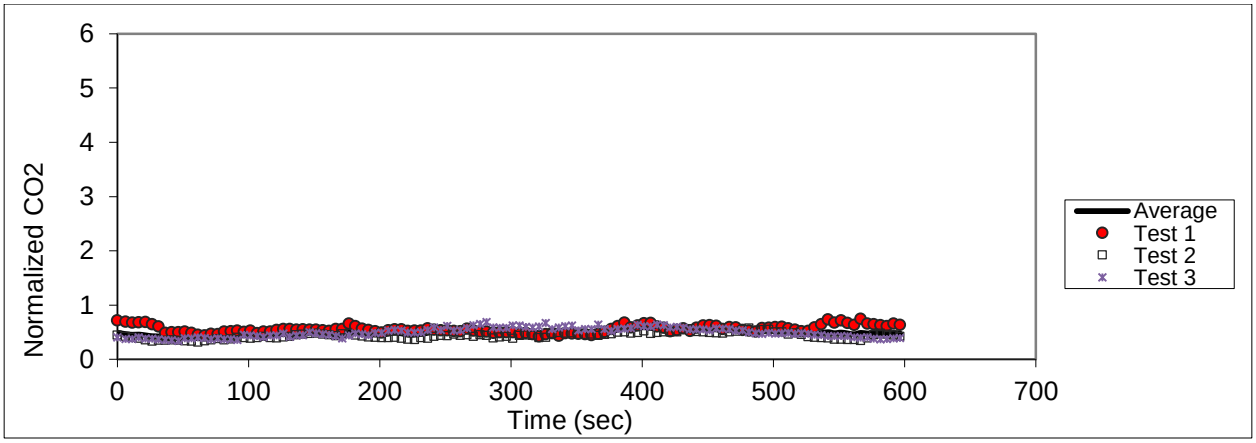

Figure D.75 – Sampling in seat 6F (release in 5B)

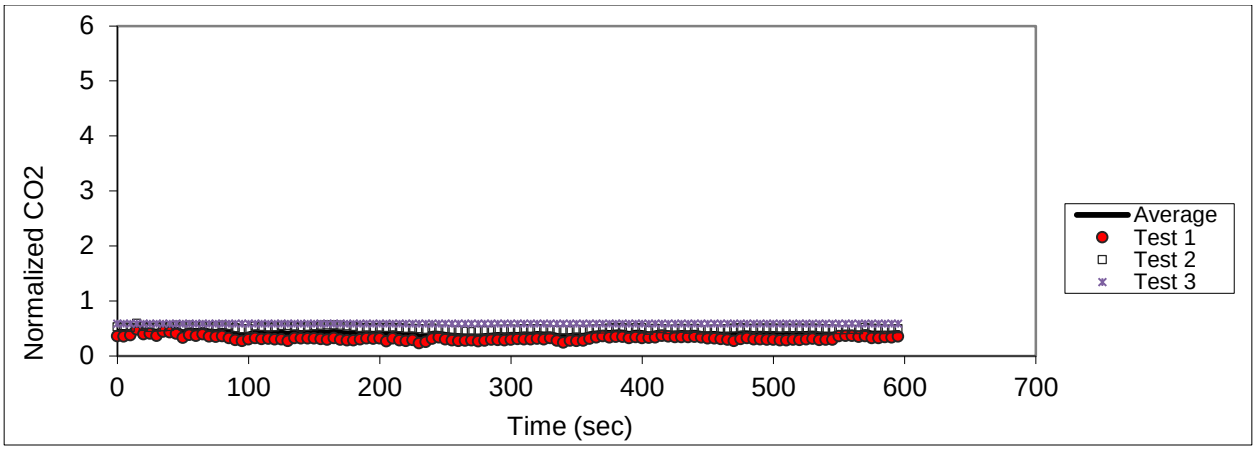

Figure D.76 - Sampling in seat 7F (release in 5B)

Release in seat 8B

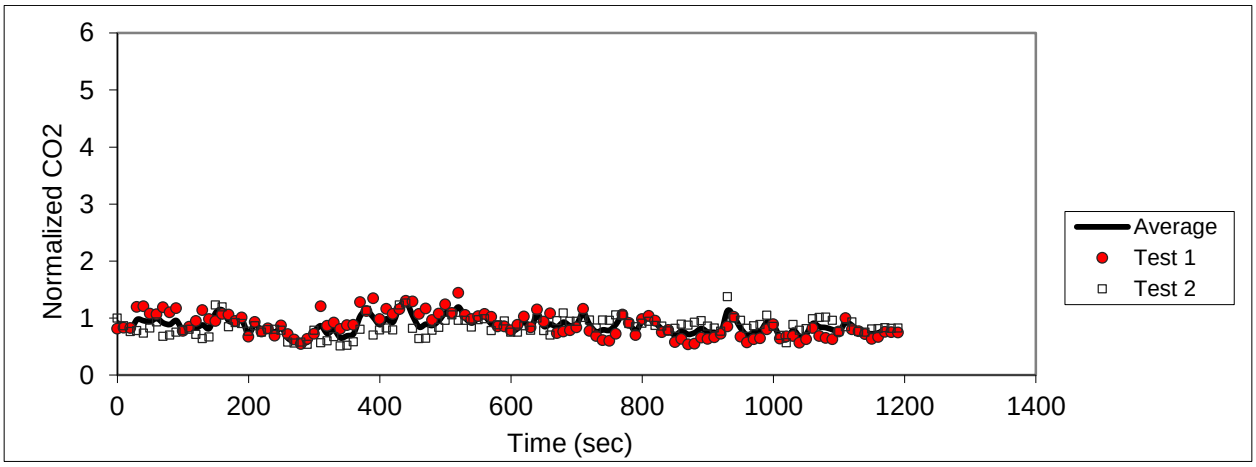

Figure D.77 – Sampling in seat 6B (release in 8B)

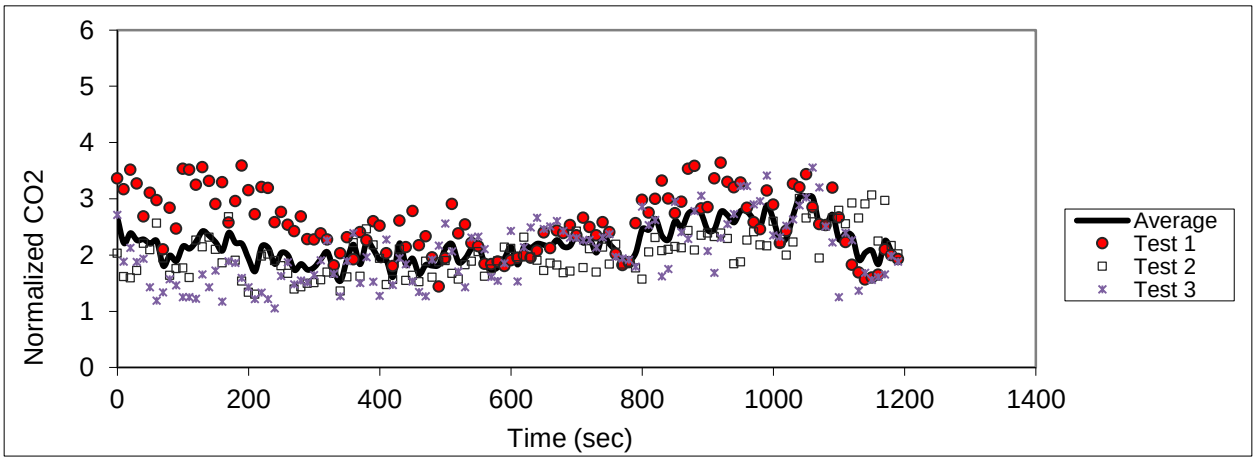

Figure D.78 – Sampling in seat 7B (release in 8B)

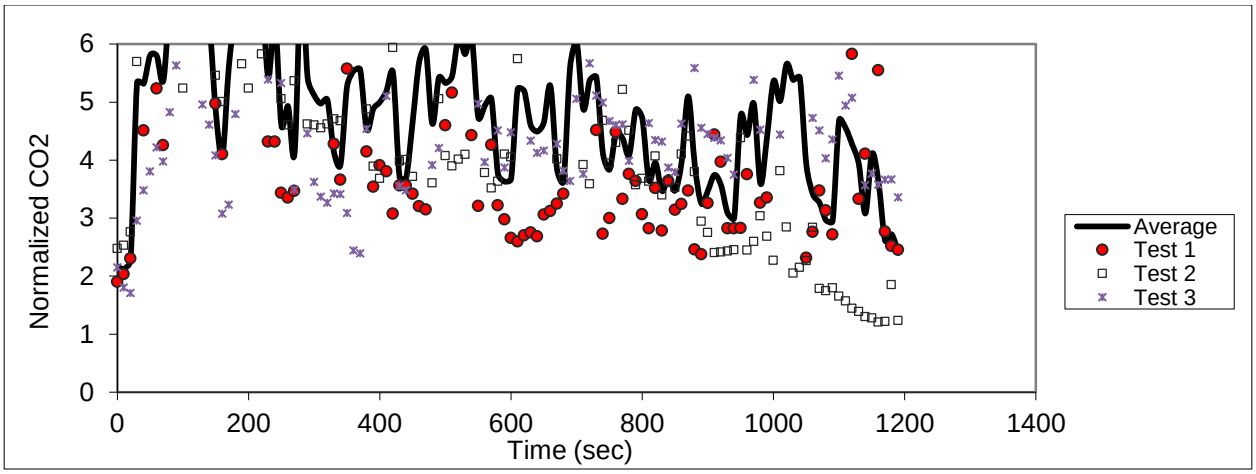

Figure D.79 – Sampling in seat 8B (release in 8B)

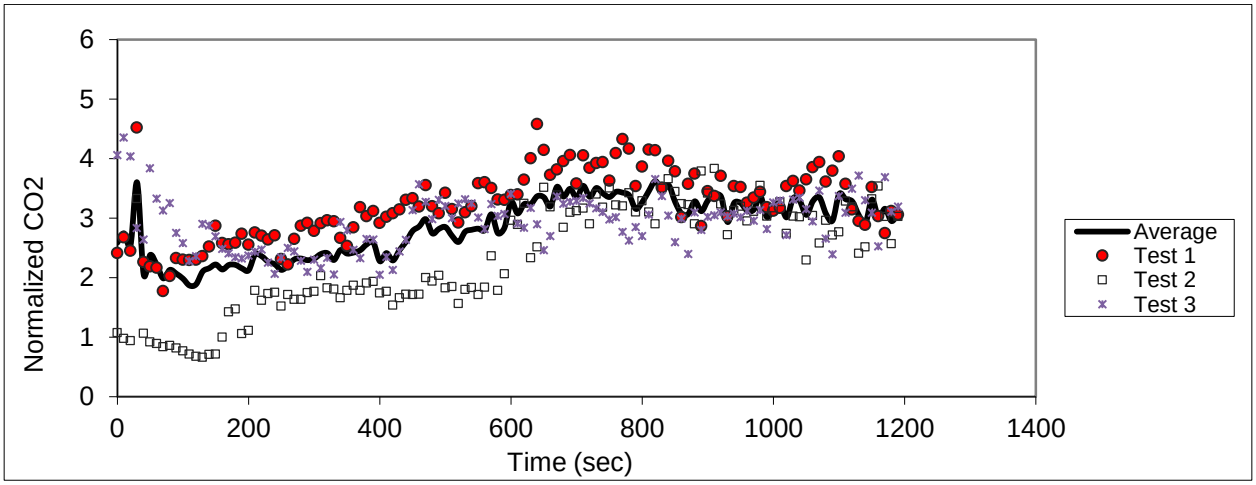

Figure D.80 – Sampling in seat 9B (release in 8B)

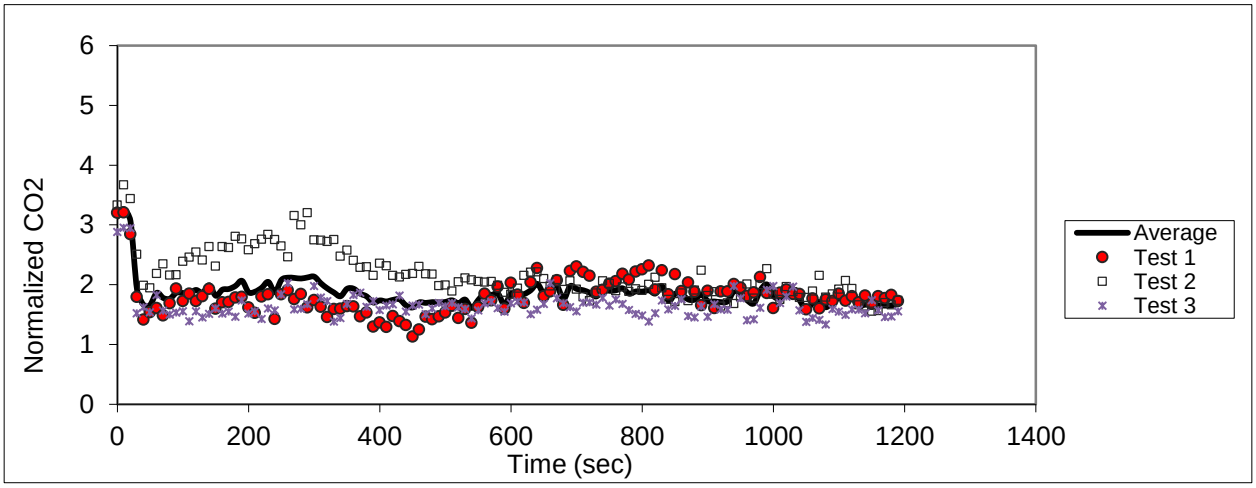

Figure D.81 – Sampling in seat 10B (release in 8B)

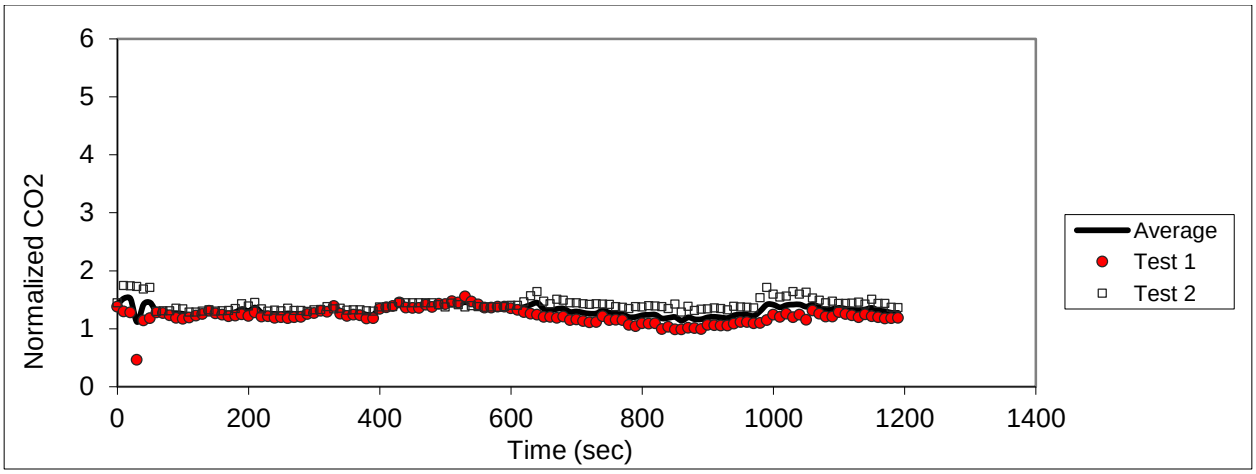

Figure D.82 - Sampling in seat 11B (release in 8B)

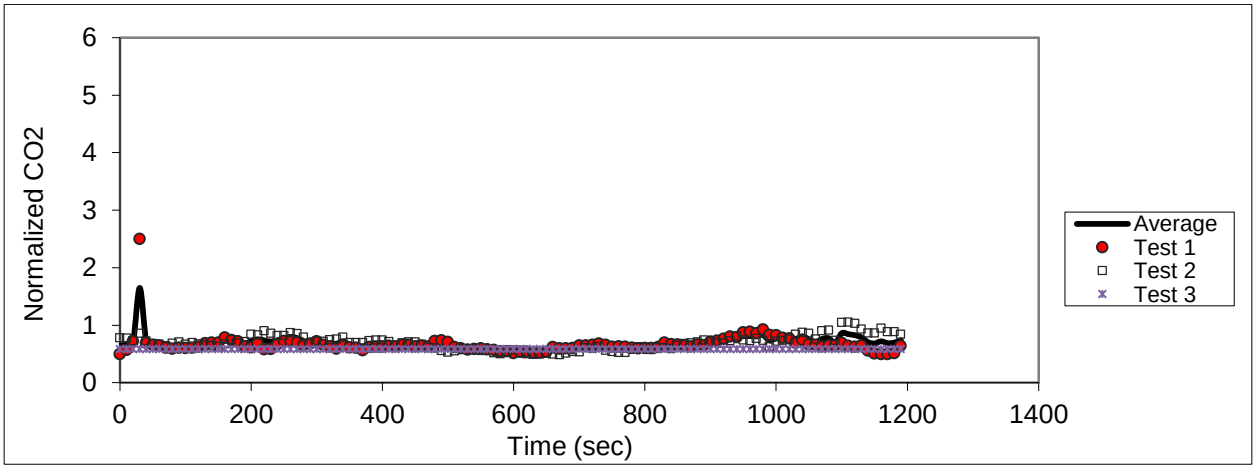

Figure D.83 - Sampling in seat 6D (release in 8B)

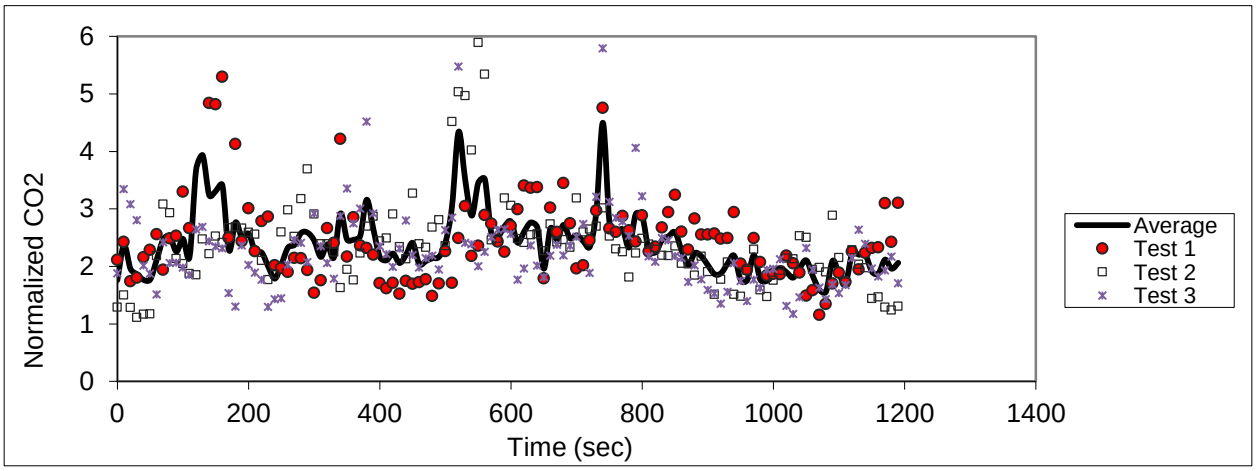

Figure D.84 - Sampling in seat 7D (release in 8B)

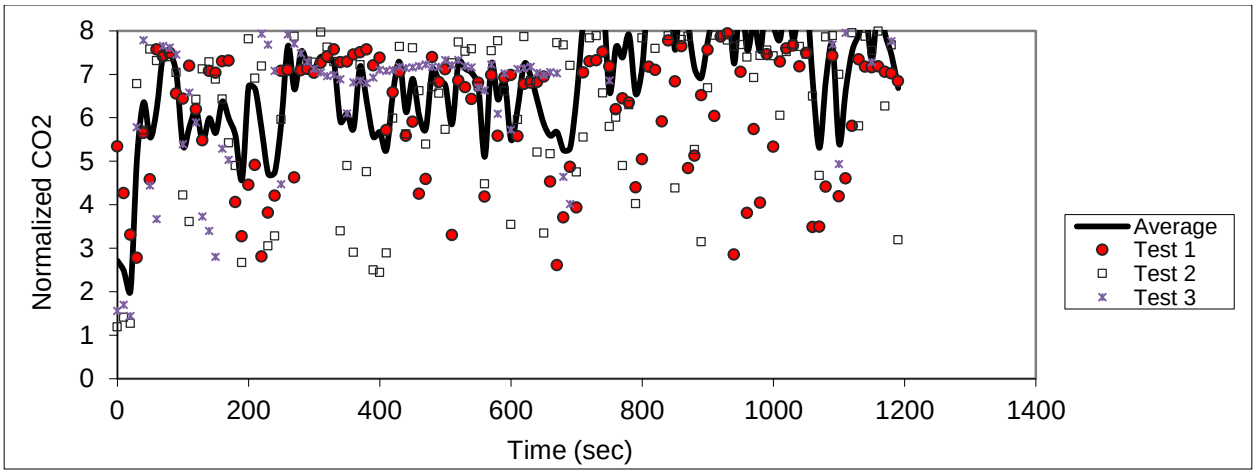

Figure D.85 – Sampling in seat 8D (release in 8B)

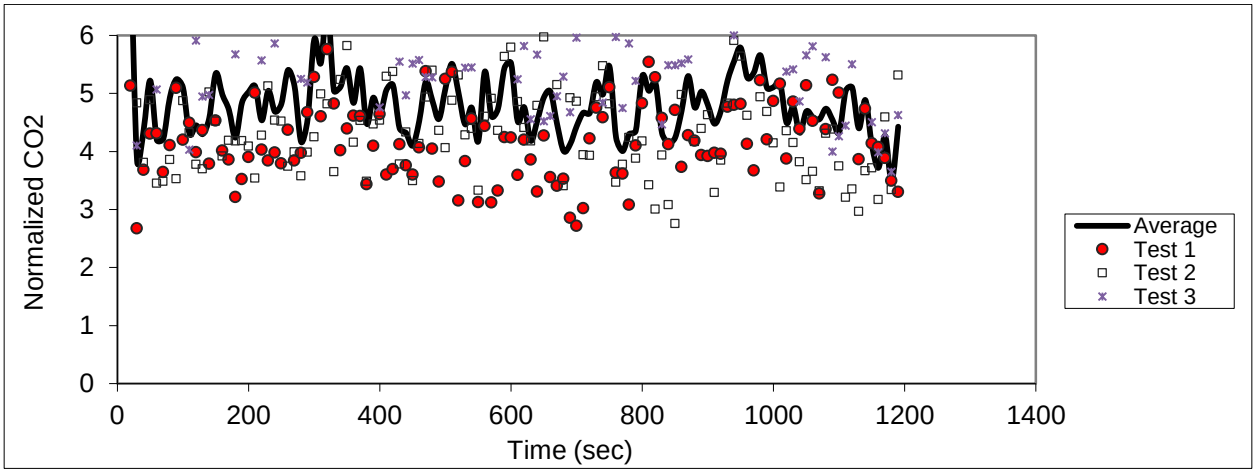

Figure D.86 – Sampling in seat 9D (release in 8B)

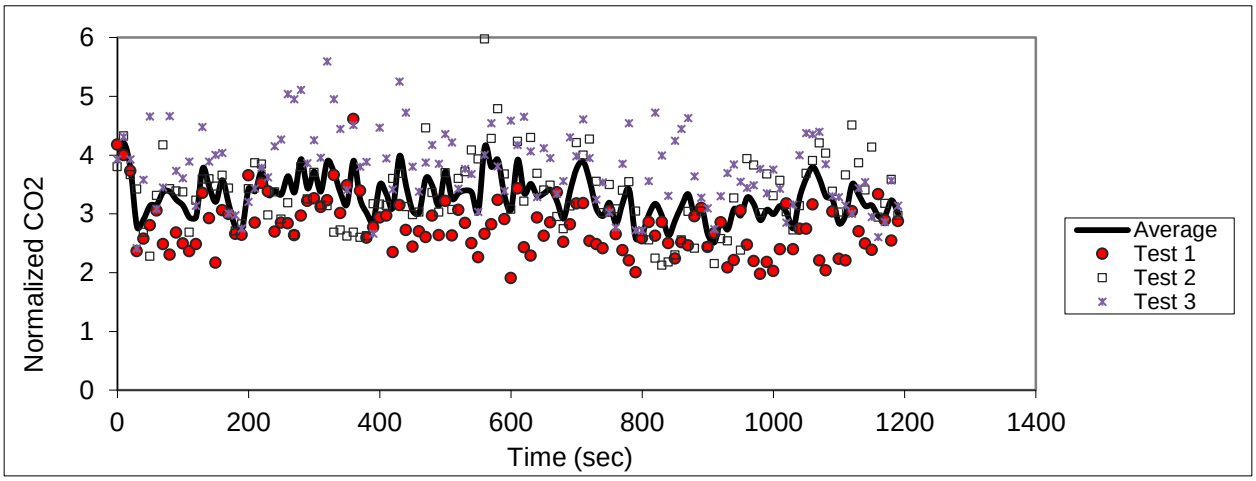

Figure D.87 – Sampling in seat 10D (release in 8B)

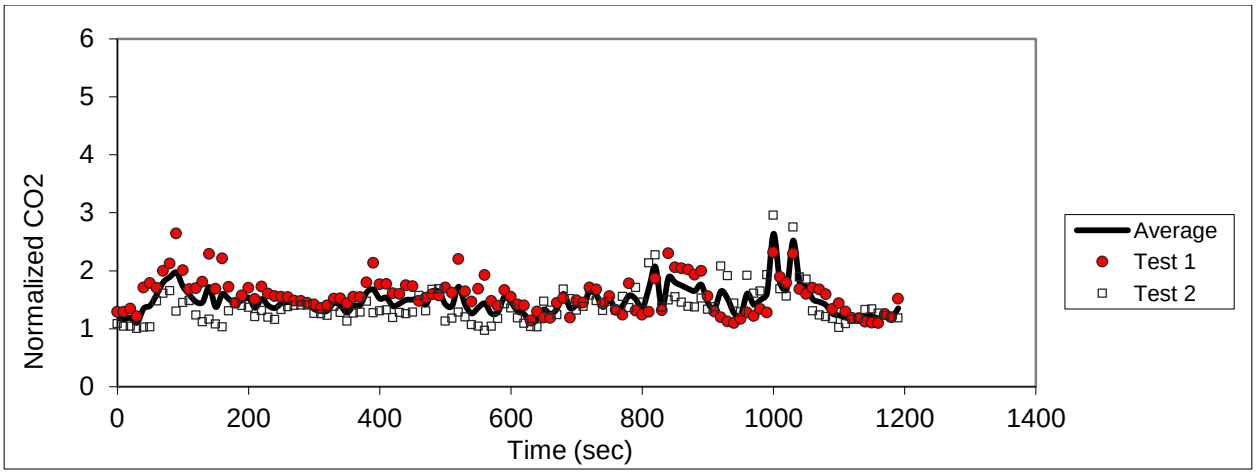

Figure D.88 - Sampling in seat 11D (release in 8B)

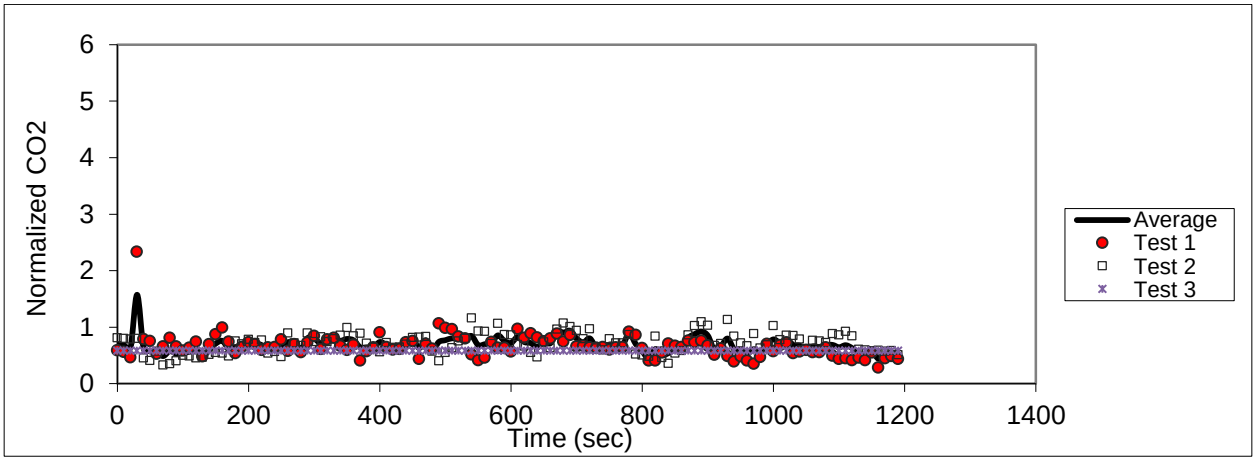

Figure D.89 – Sampling in seat 6E (release in 8B)

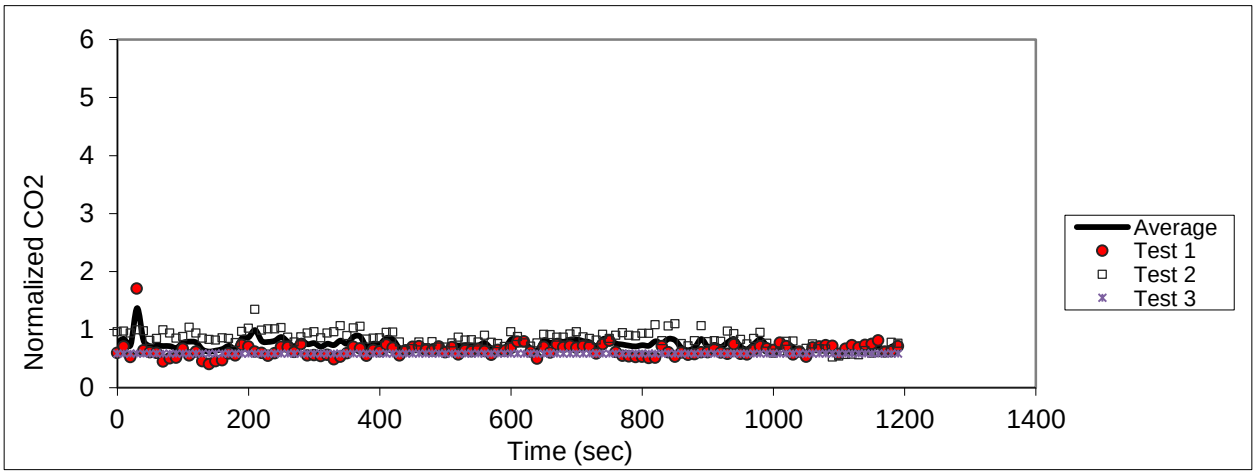

Figure D.90 - Sampling in seat 6F (release in 8B)

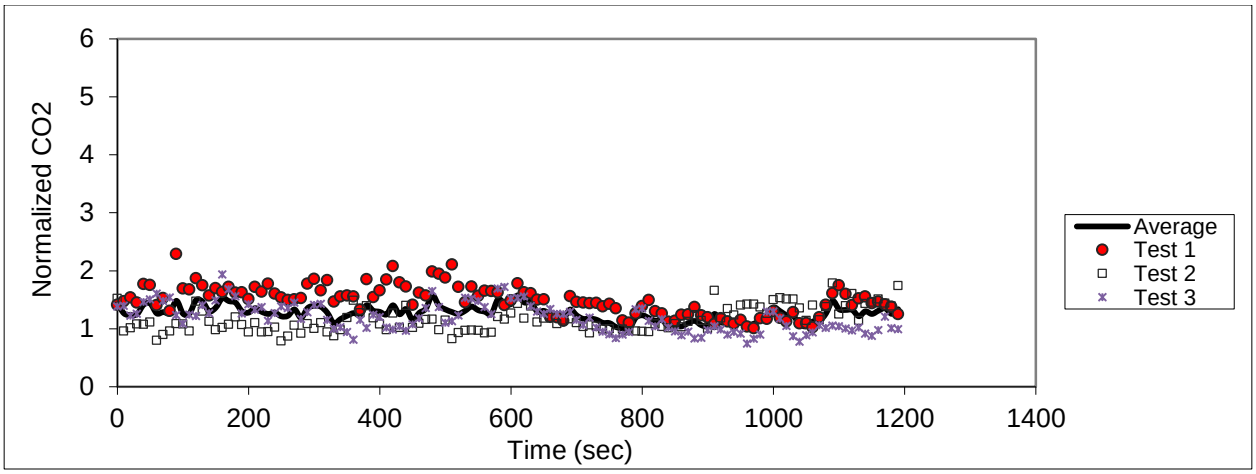

Figure D.91 – Sampling in seat 7F (release in 8B)

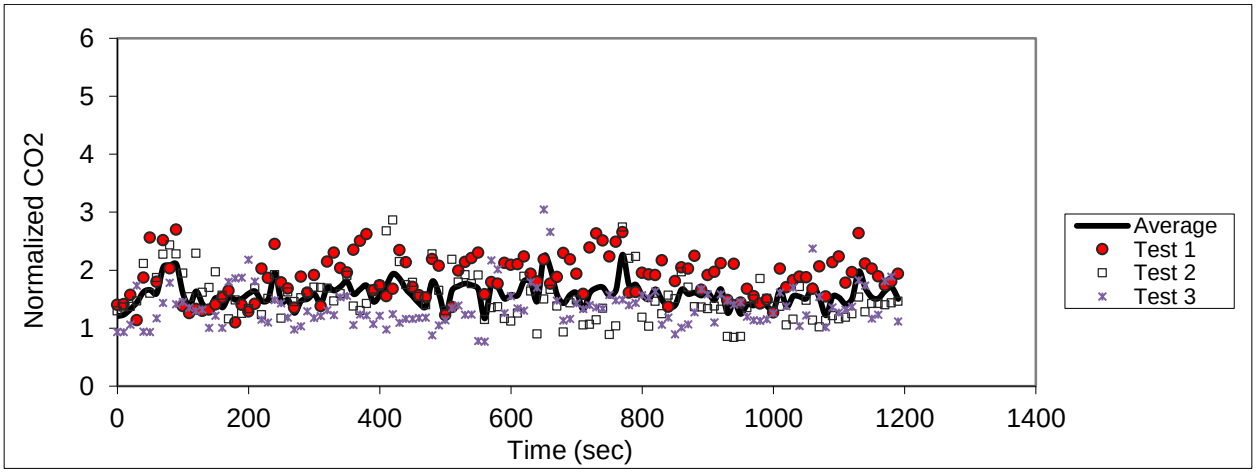

Figure D.92 – Sampling in seat 8F (release in 8B)

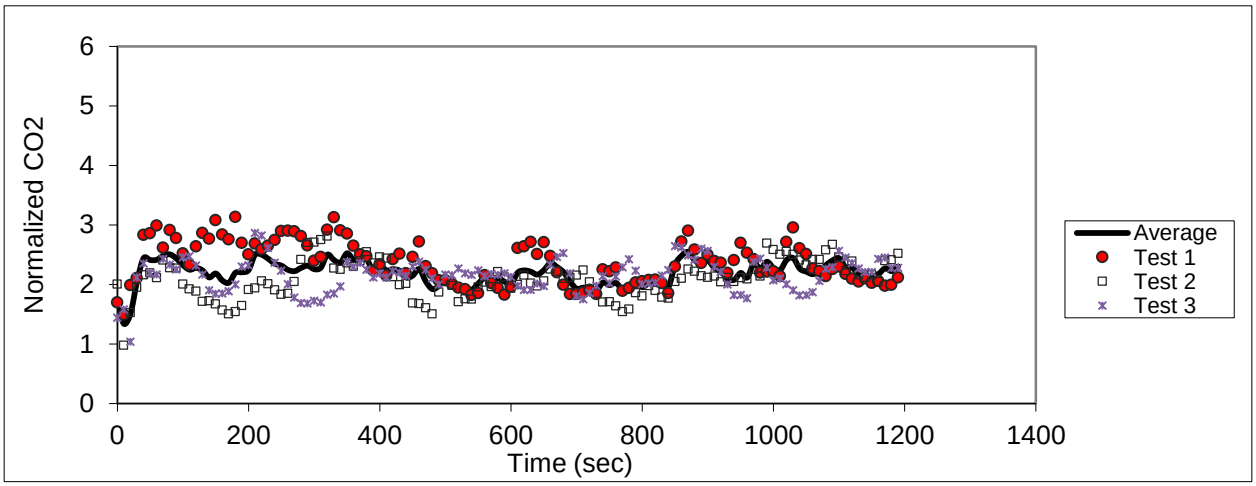

Figure D.93 – Sampling in seat 9F (release in 8B)

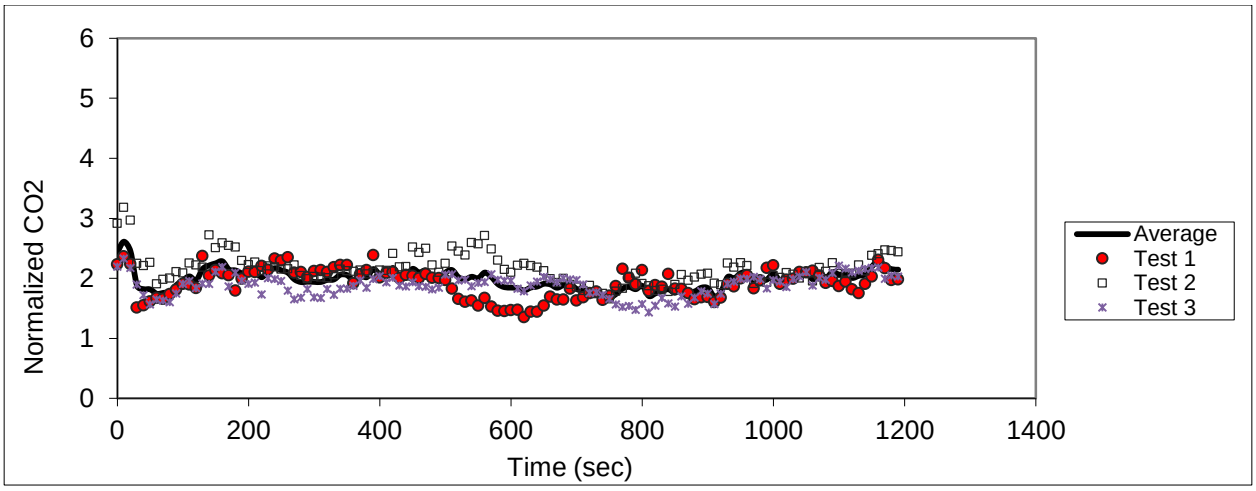

Figure D.94 – Sampling in seat 10F (release in 8B)

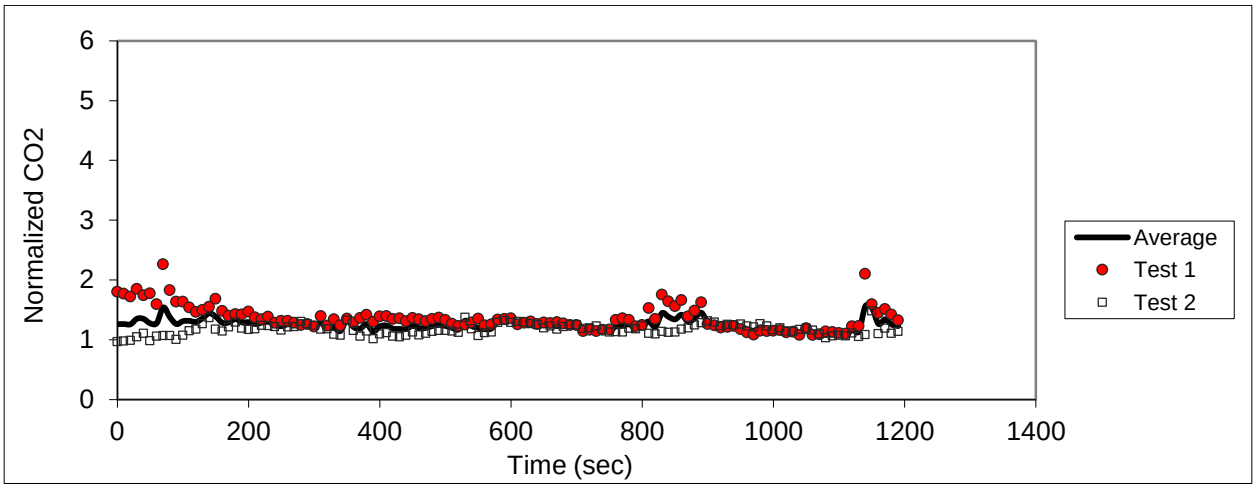

Figure D.95 - Sampling in seat 11F (release in 8B)

Release in 4F

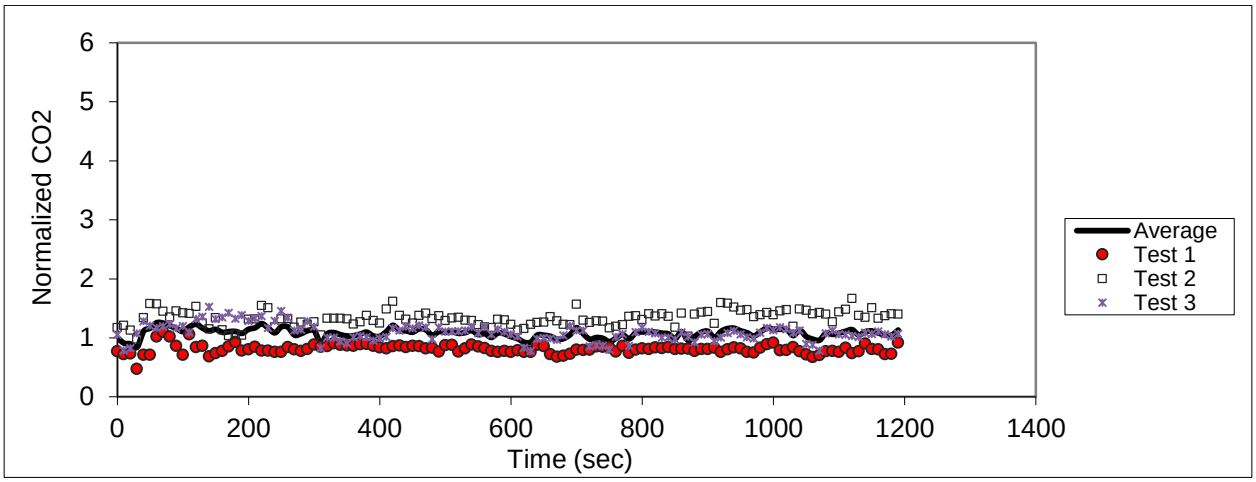

Figure D.96 – Sampling in seat 3B (release in 4F)

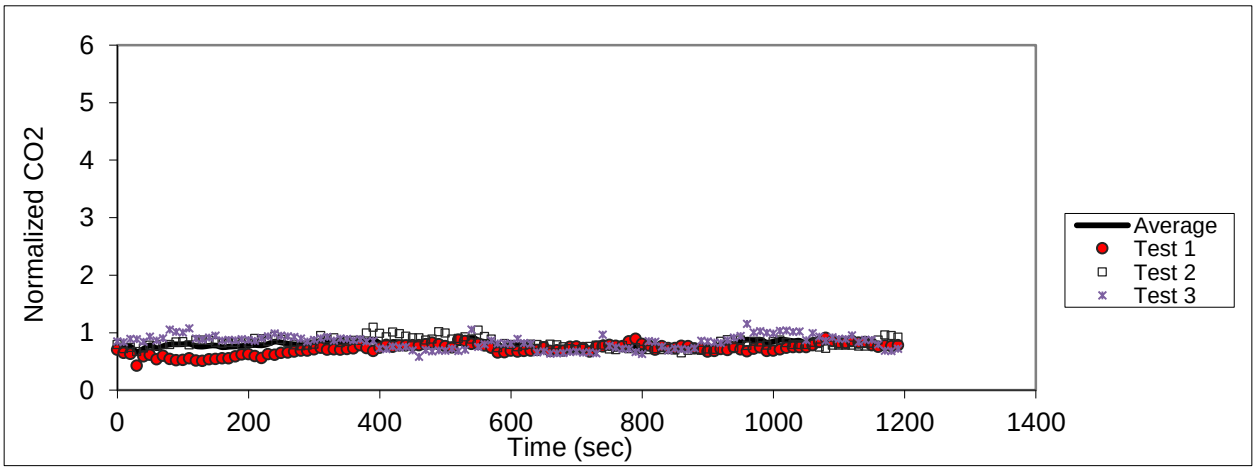

Figure D.97 – Sampling in seat 4B (release in 4F)

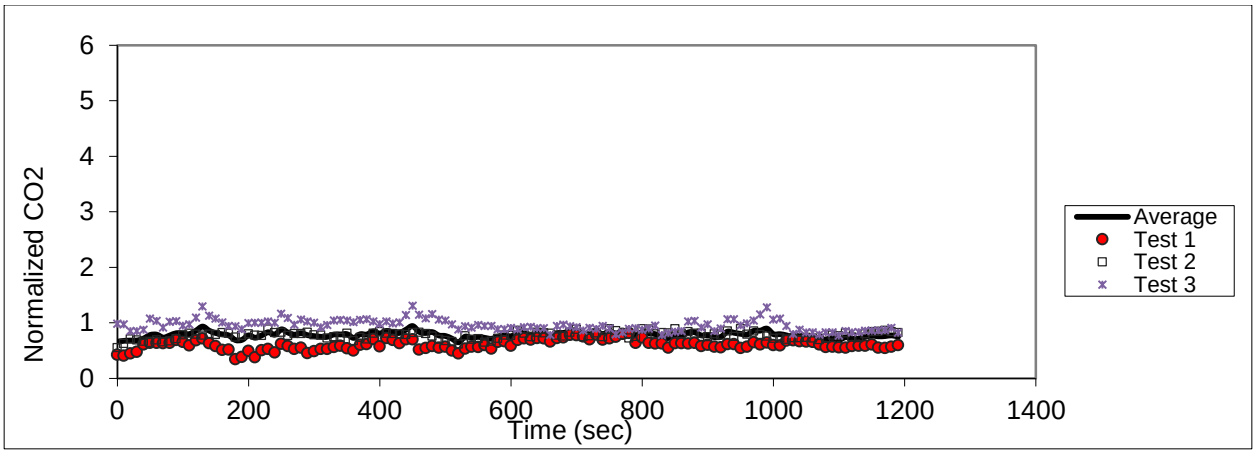

Figure D.98 – Sampling in seat 5B (release in 4F)

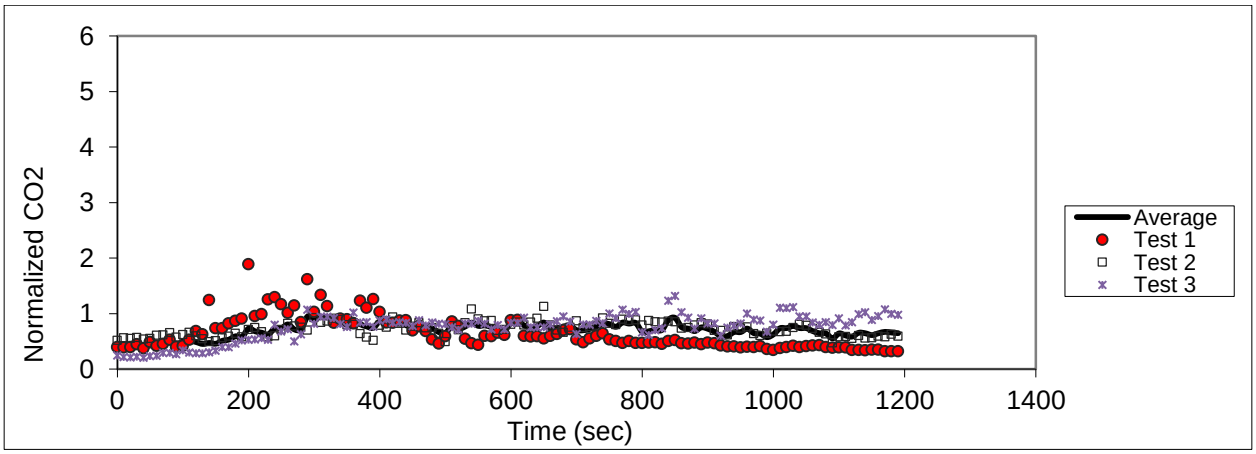

Figure D.99 – Sampling in seat 6B (release in 4F)

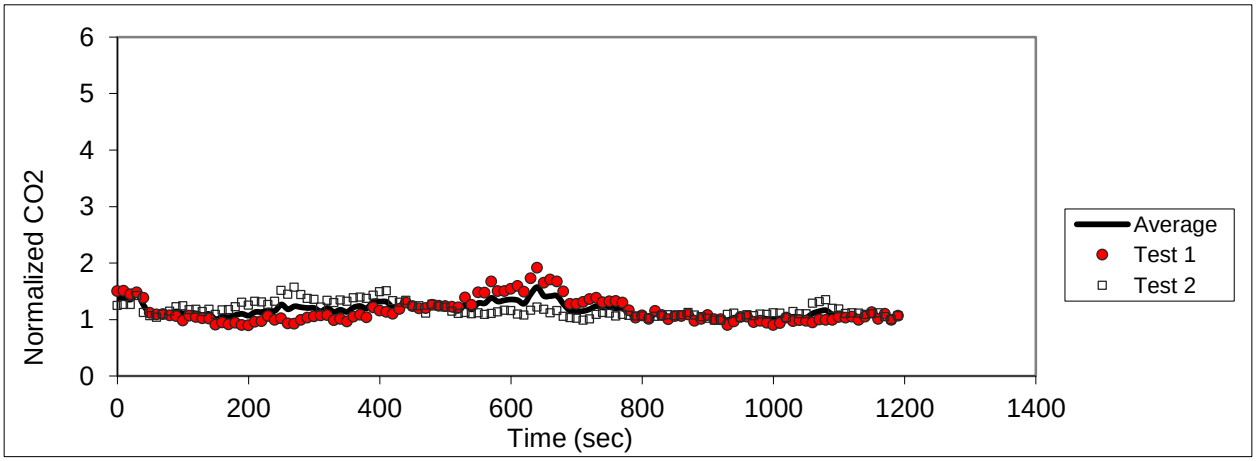

Figure D.100 - Sampling in seat 2C (release in 4F)

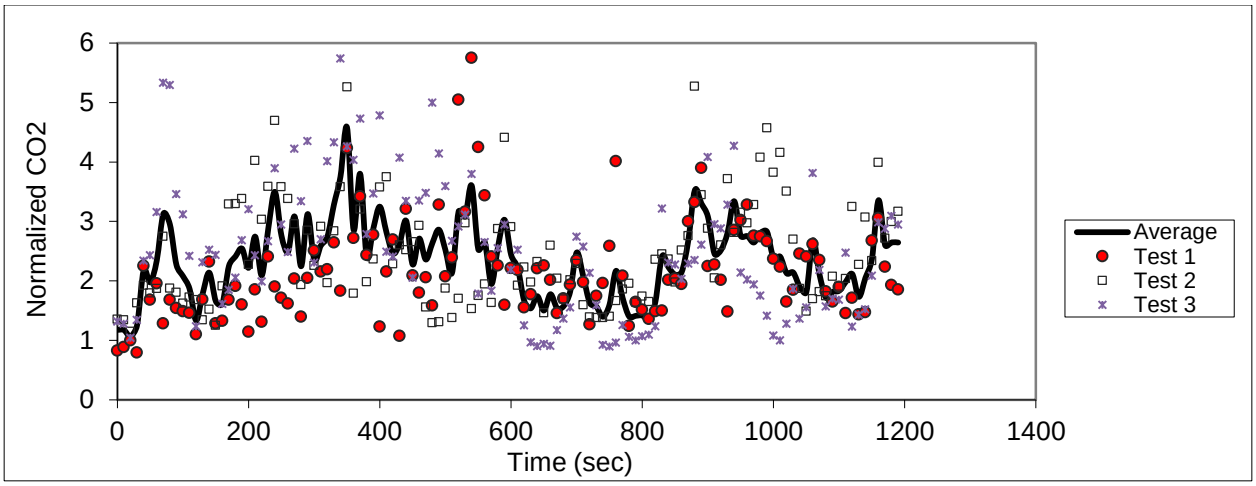

Figure D.101 – Sampling in seat 2D (release in 4F)

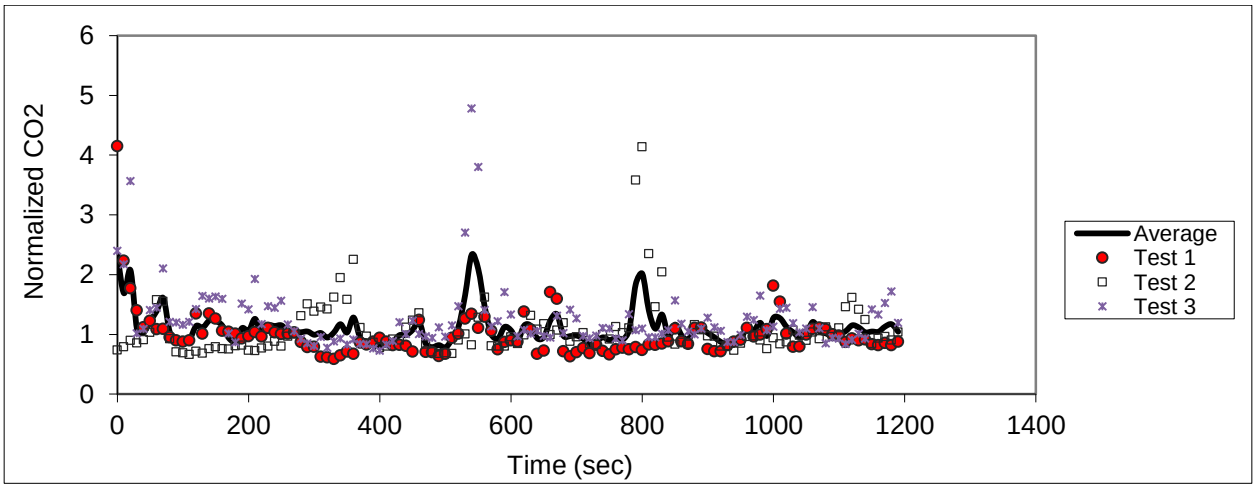

Figure D.102 – Sampling in seat 3D (release in 4F)

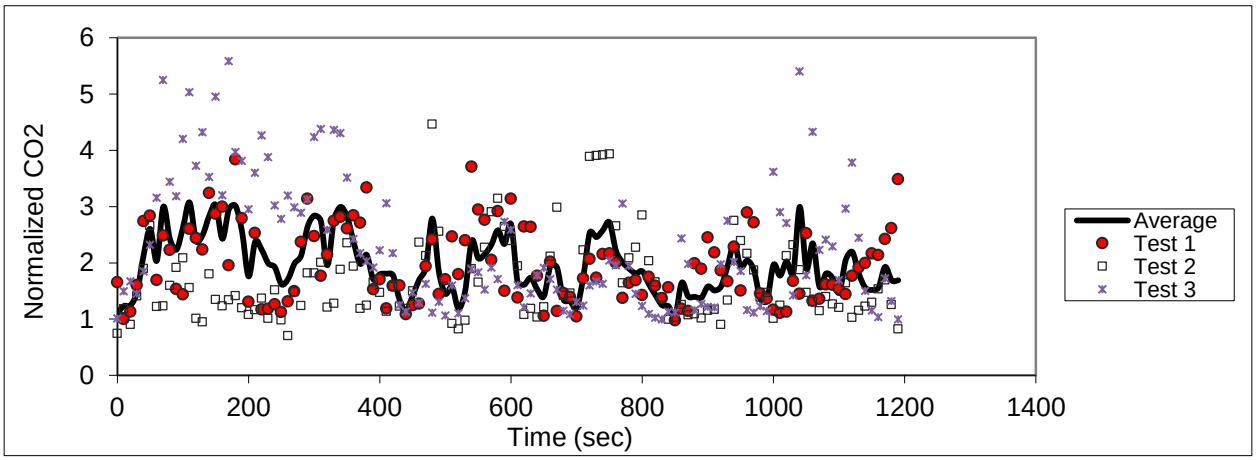

Figure D.103 – Sampling in seat 5D (release in 4F)

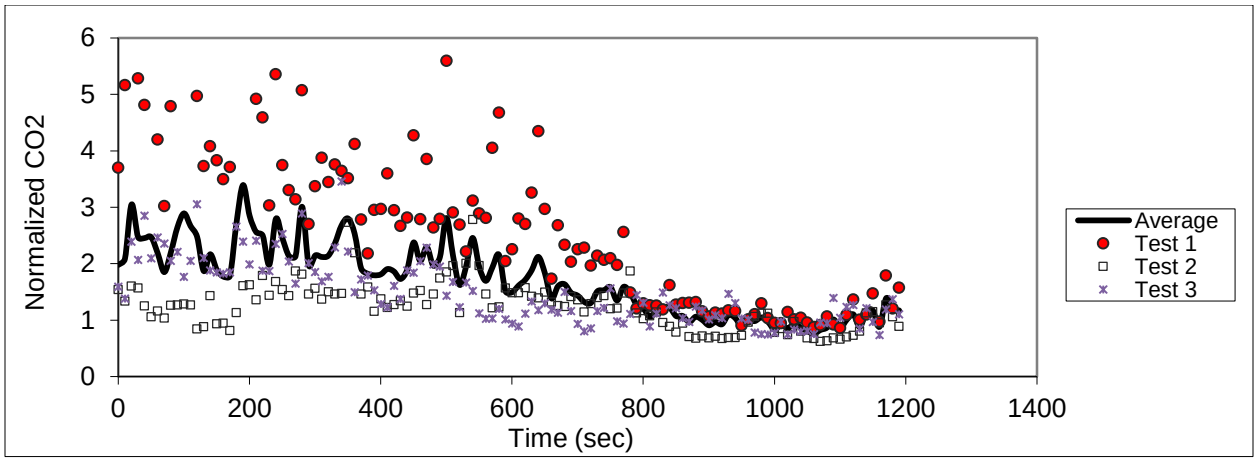

Figure D.104 – Sampling in seat 6D (release in 4F)

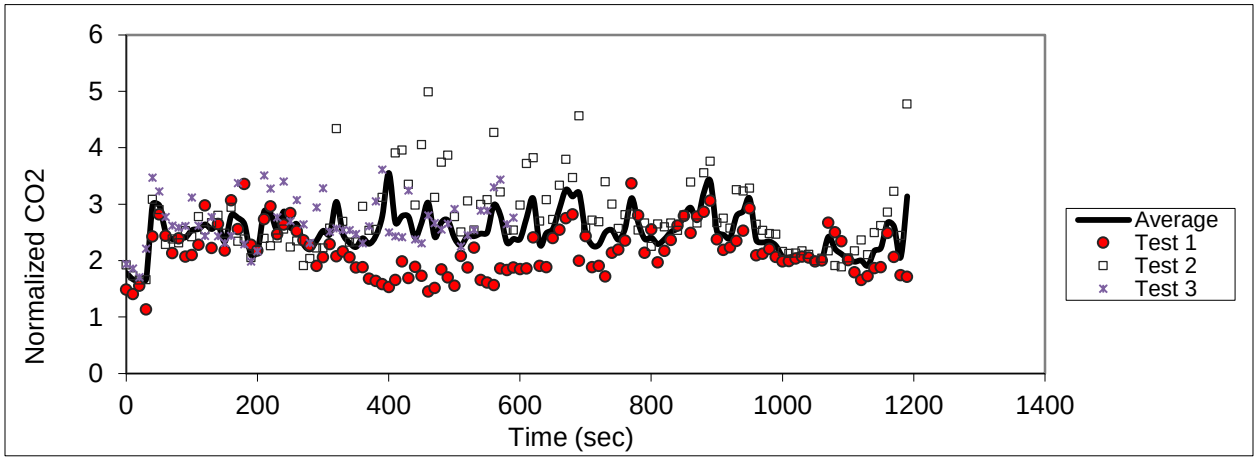

Figure D.105 – Sampling in seat 3F (release in 4F)

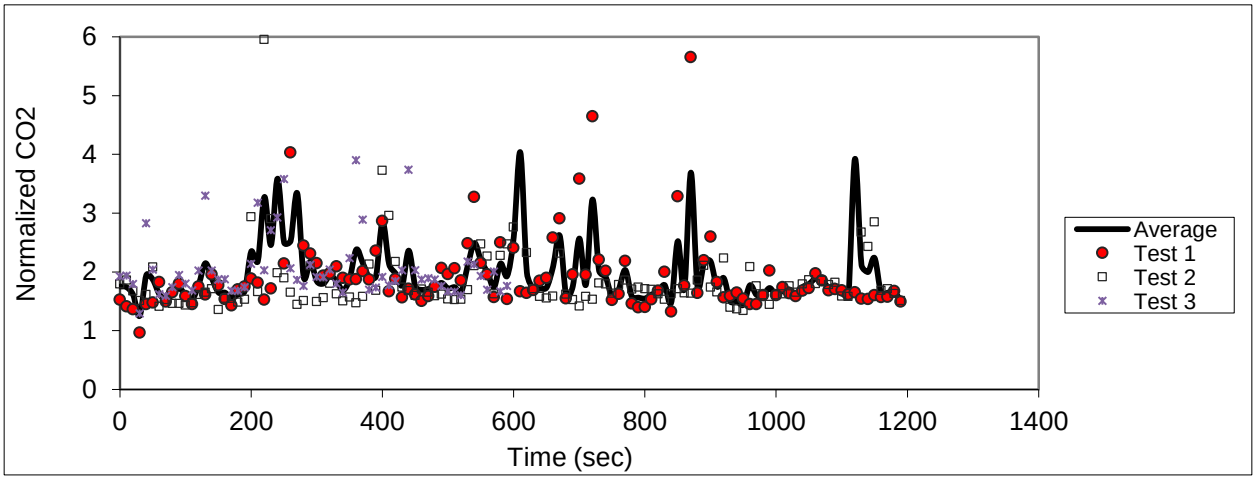

Figure D.106 – Sampling in seat 4F (release in 4F)

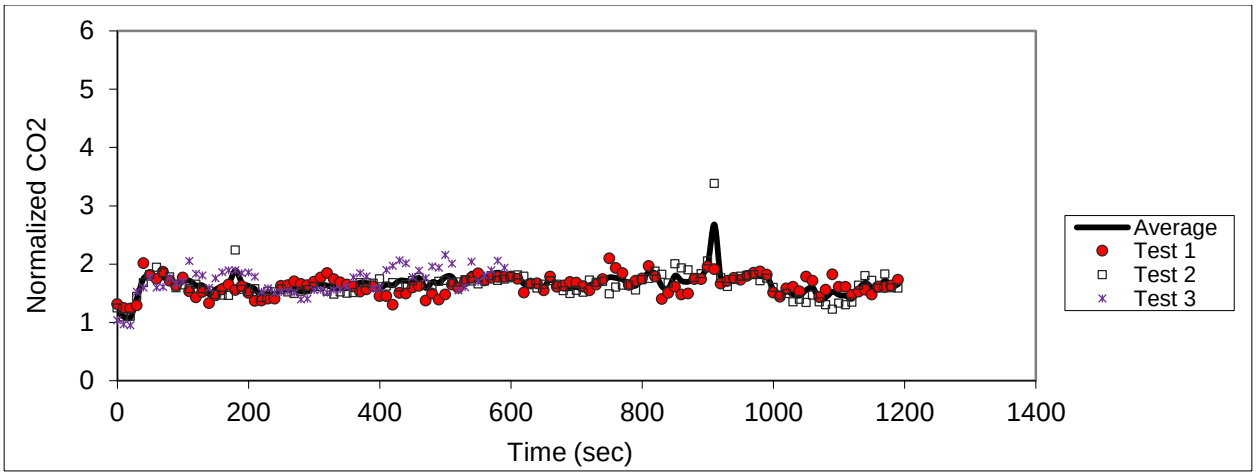

Figure D.107 – Sampling in seat 5F (release in 4F)

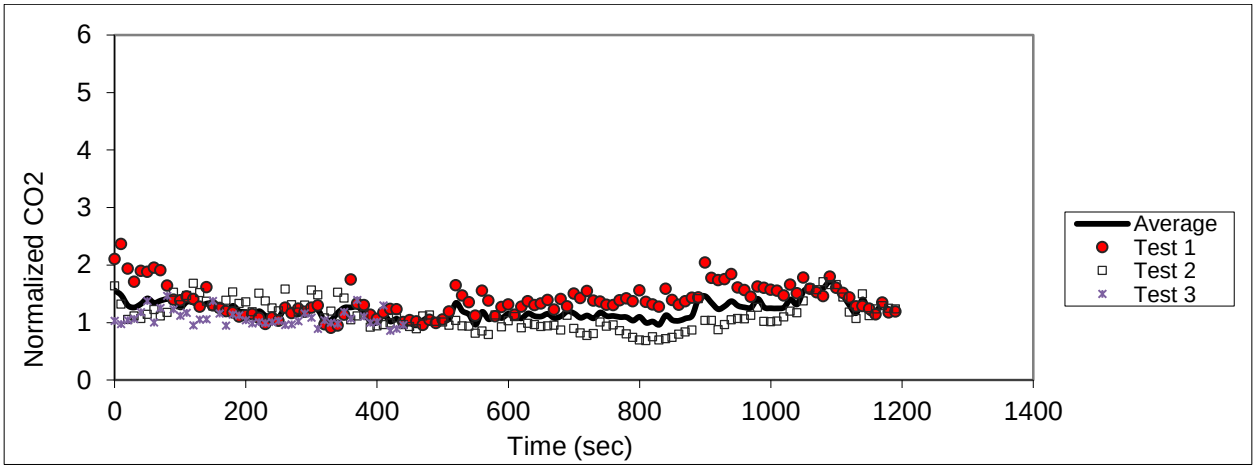

Figure D.108 - Sampling in seat 6F (release in 4F)

<u>Release in seat 9F</u>

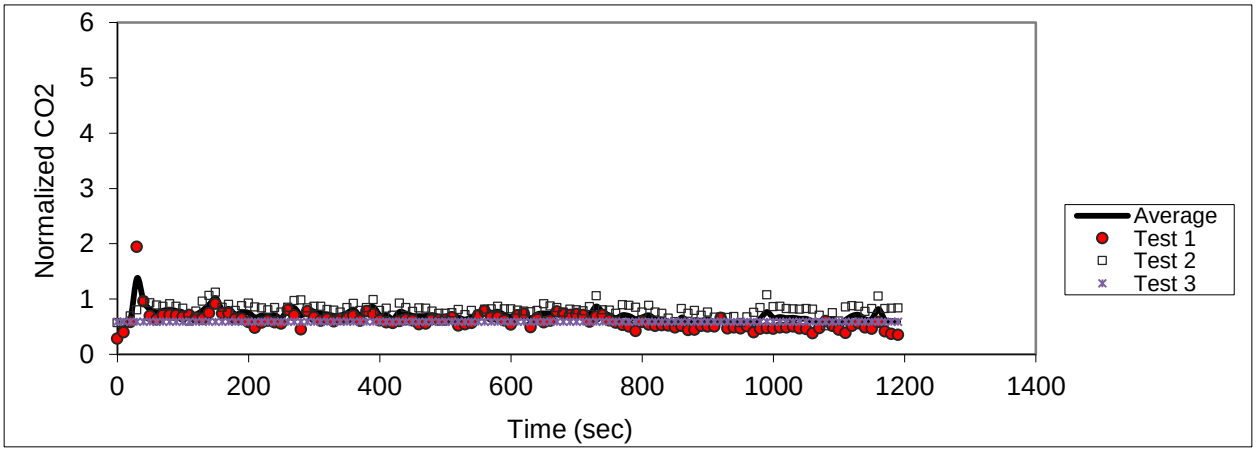

Figure D.109 - Sampling in seat 7B (release in 9F)

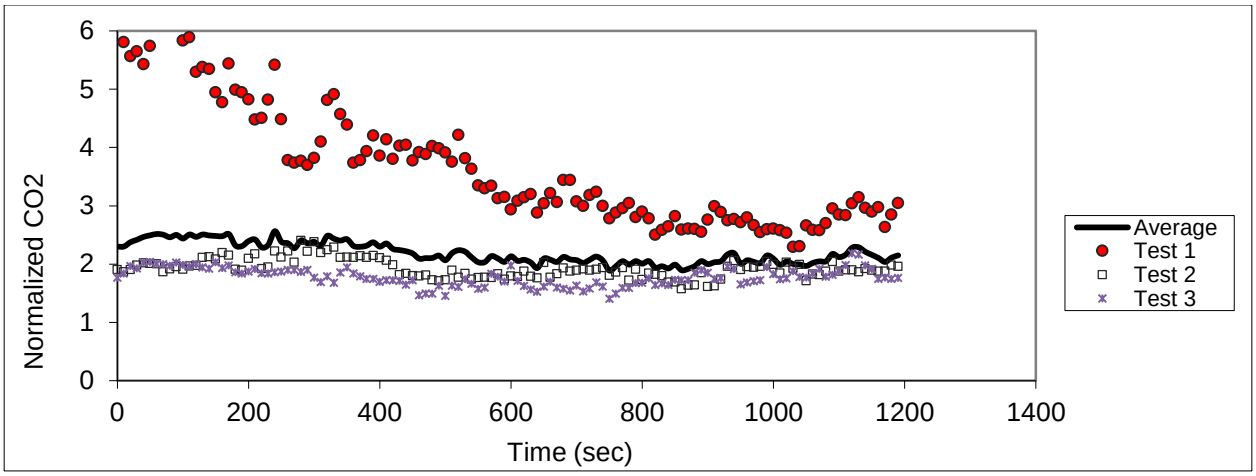

Figure D.110 – Sampling in seat 8B (release in 9F)

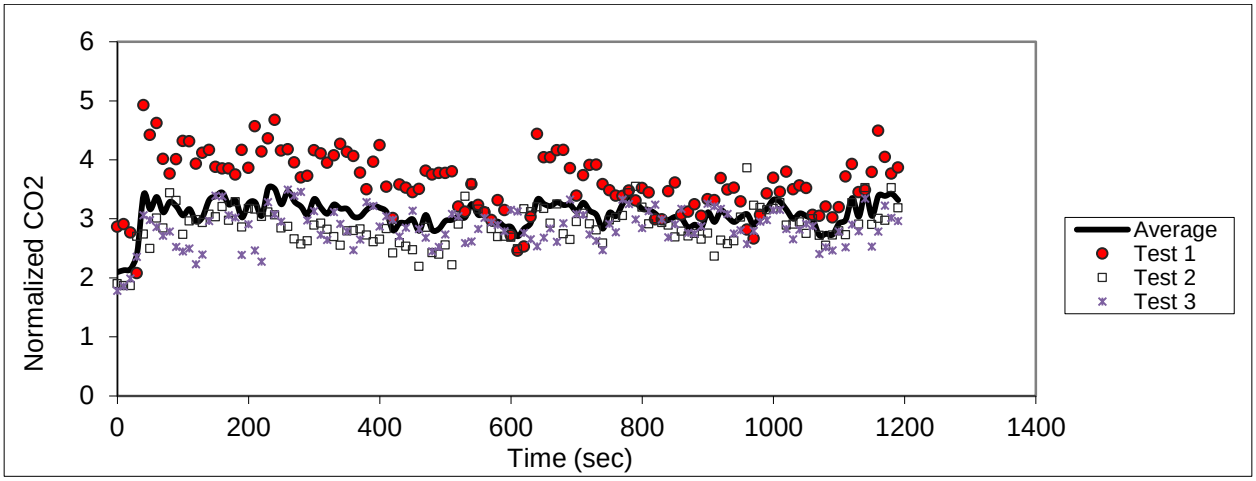

Figure D.111 – Sampling in seat 9B (release in 9F)

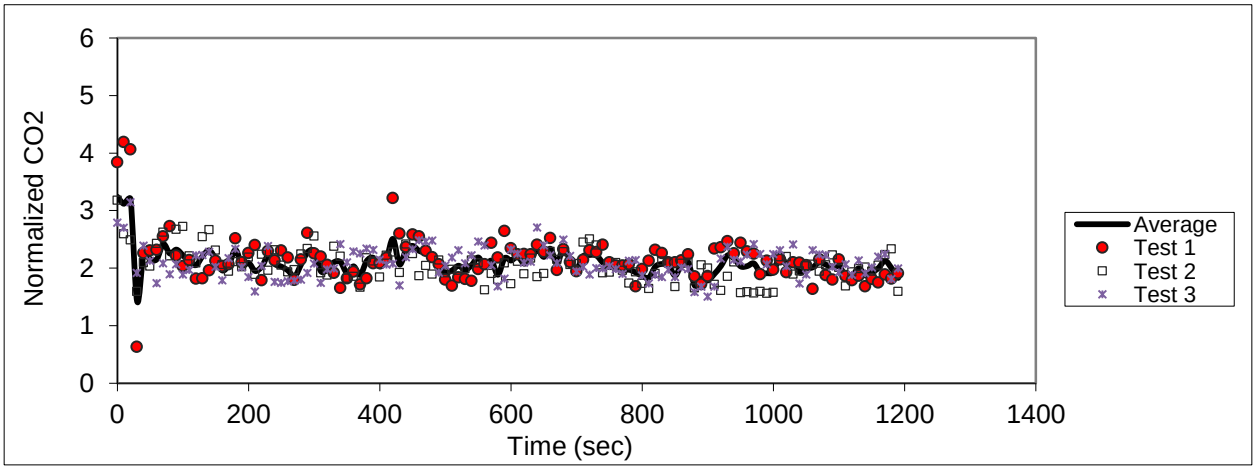

Figure D.112 – Sampling in seat 10B (release in 9F)

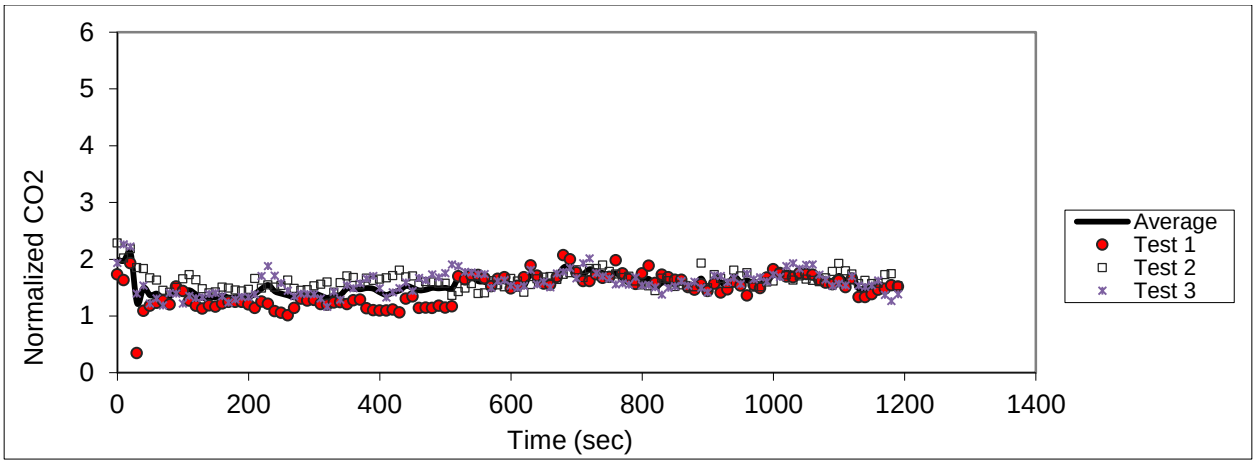

Figure D.113 - Sampling in seat 11B (release in 9F)

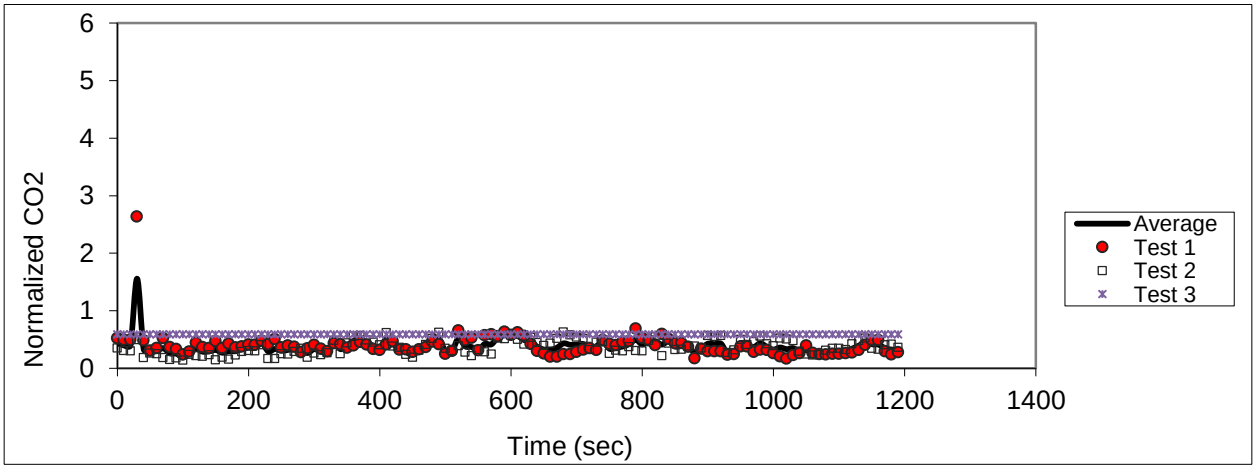

Figure D.114 – Sampling in seat 7C (release in 9F)

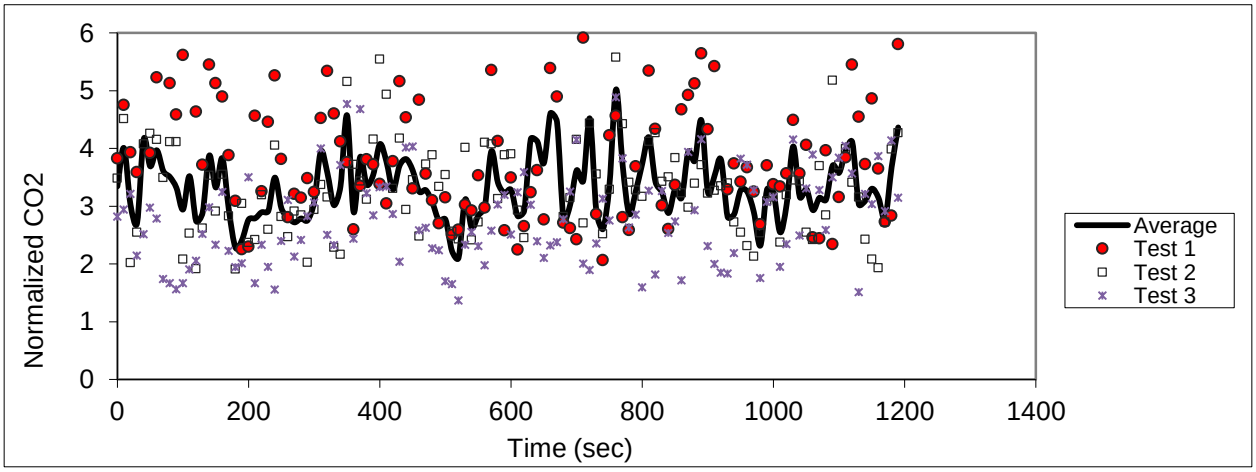

Figure D.115 – Sampling in seat 8D (release in 9F)

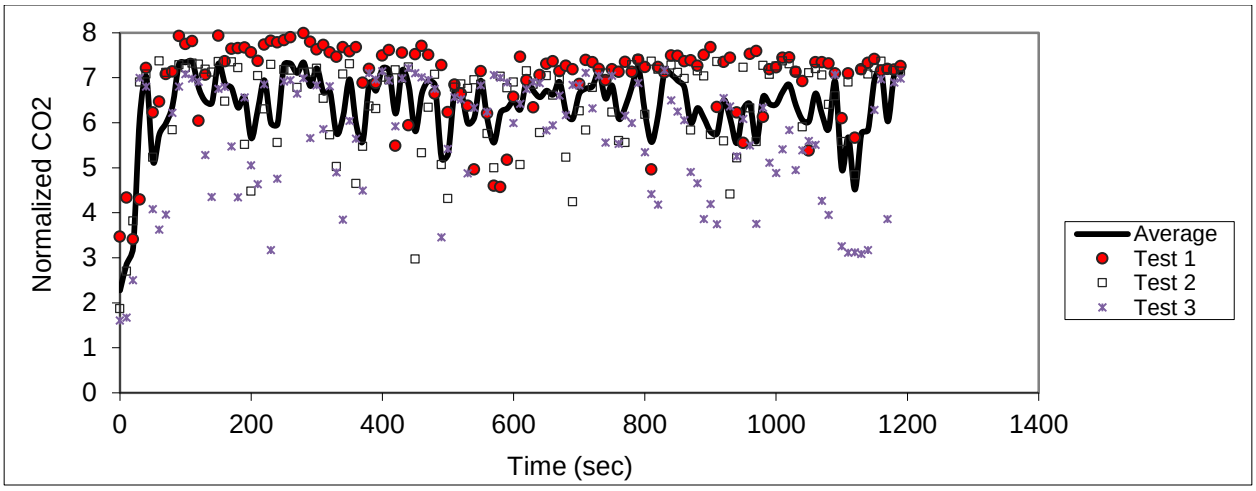

Figure D.116 – Sampling in seat 9D (release in 9F)

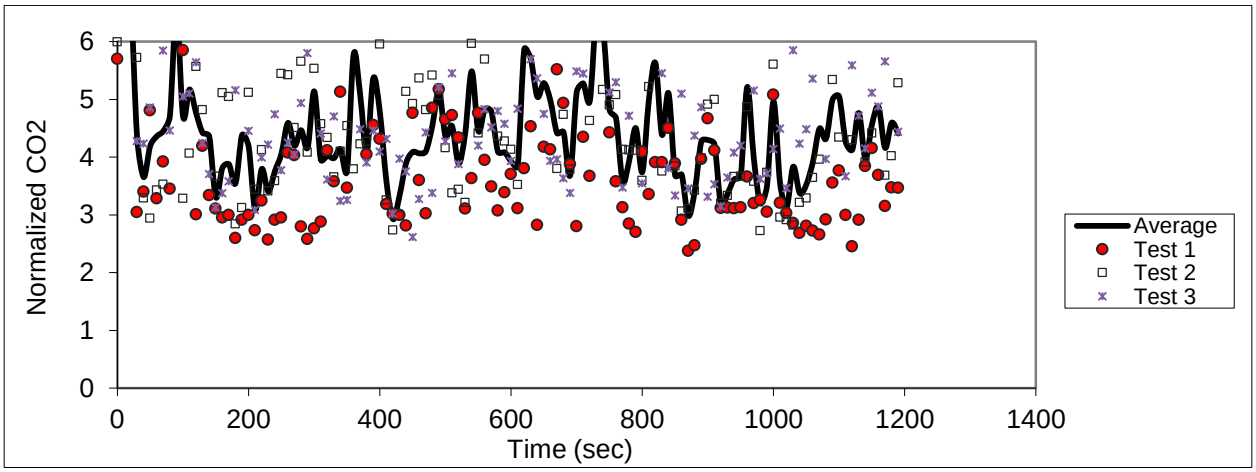

Figure D.117 – Sampling in seat 10D (release in 9F)

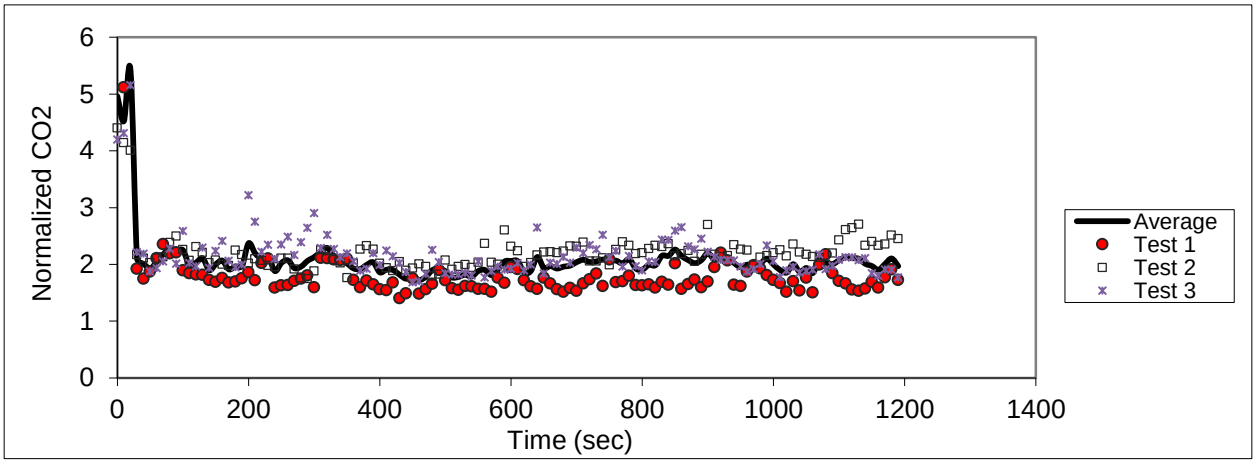

Figure D.118 - Sampling in seat 11D (release in 9F)

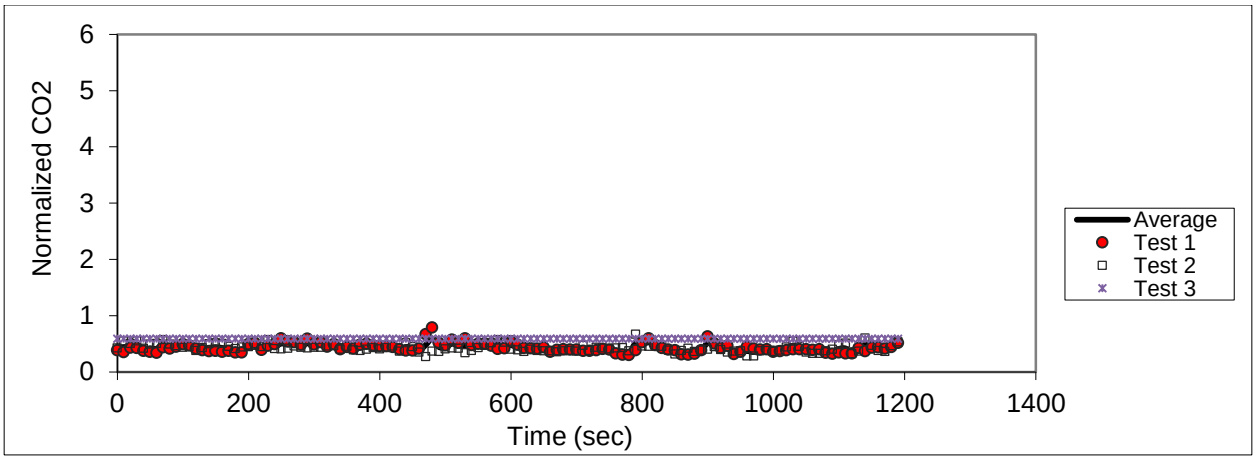

Figure D.119 – Sampling in seat 7F (release in 9F)

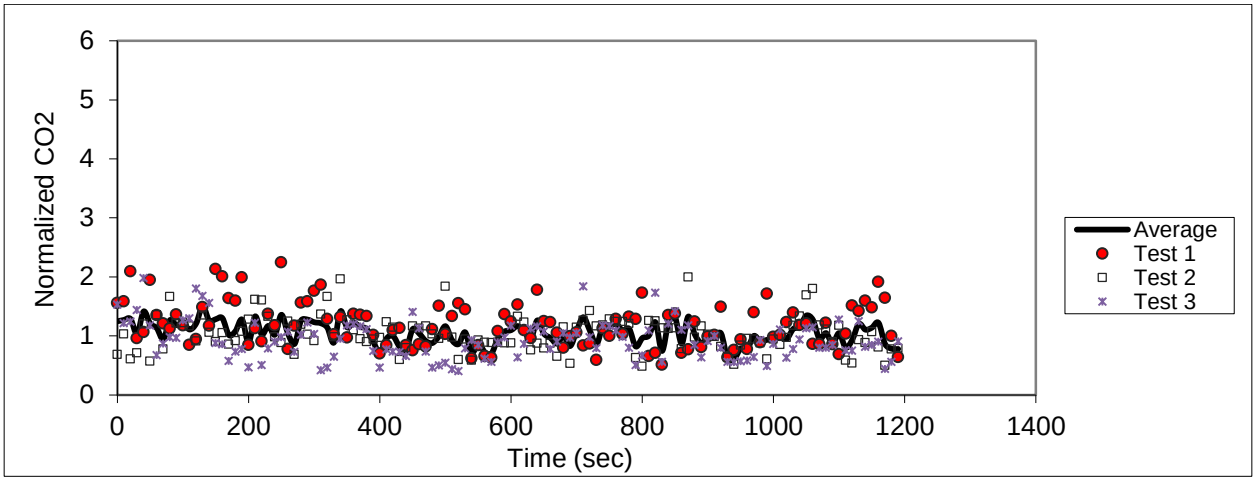

Figure D.120 – Sampling in seat 8F (release in 9F)

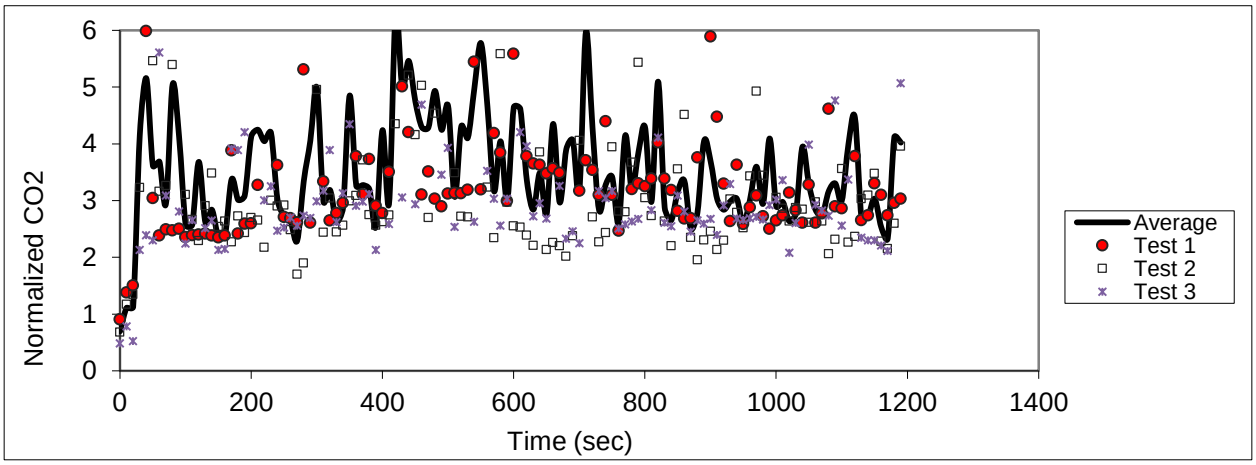

Figure D.121 – Sampling in seat 9F (release in 9F)

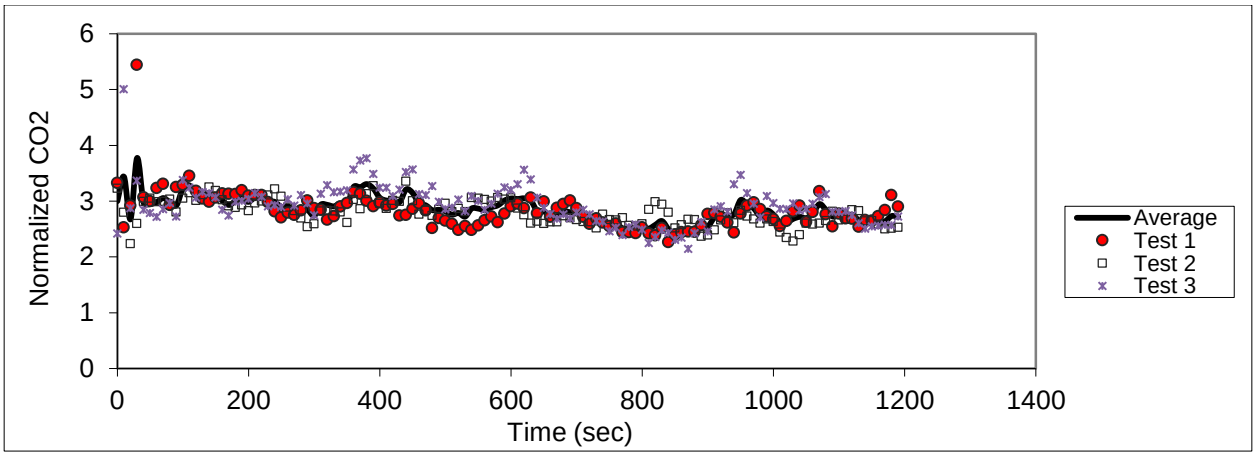

Figure D.122 – Sampling in seat 10F (release in 9F)

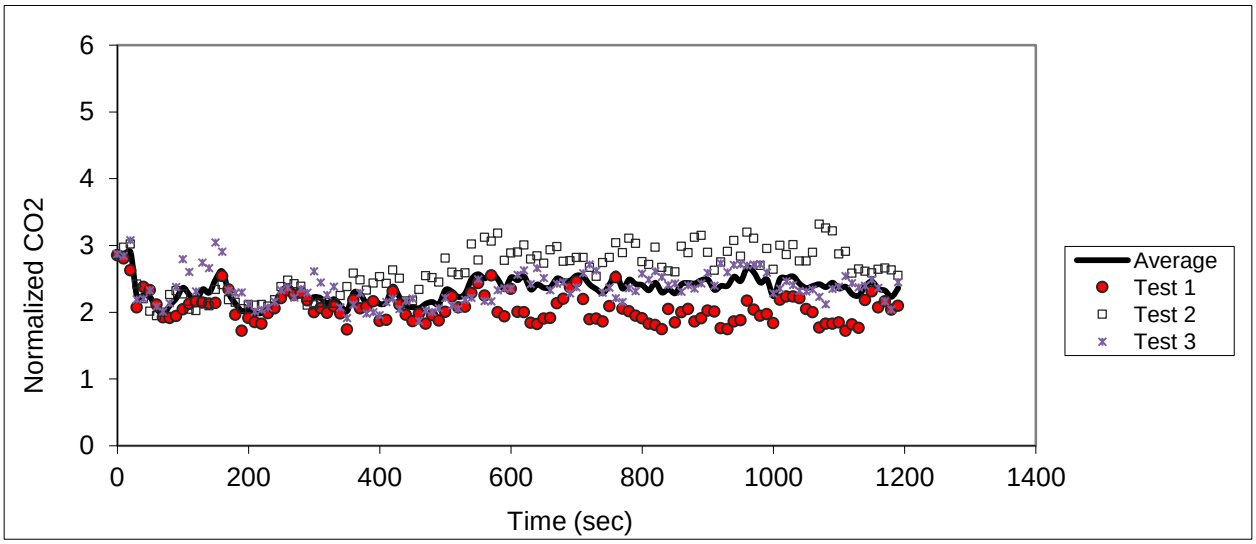

Figure D.123 – Sampling in seat 11F (release in 9F)

Appendix E - Uncertainty for Tracer Gas Results

This appendix summarizes the relative uncertainty results during tracer gas experiments for each sampling seat for each location under heated and unheated conditions. Equations used are as described in Chapter 5 in the uncertainty analysis sections.

I) Uncertainty results for CO_2 samples with heated manikins

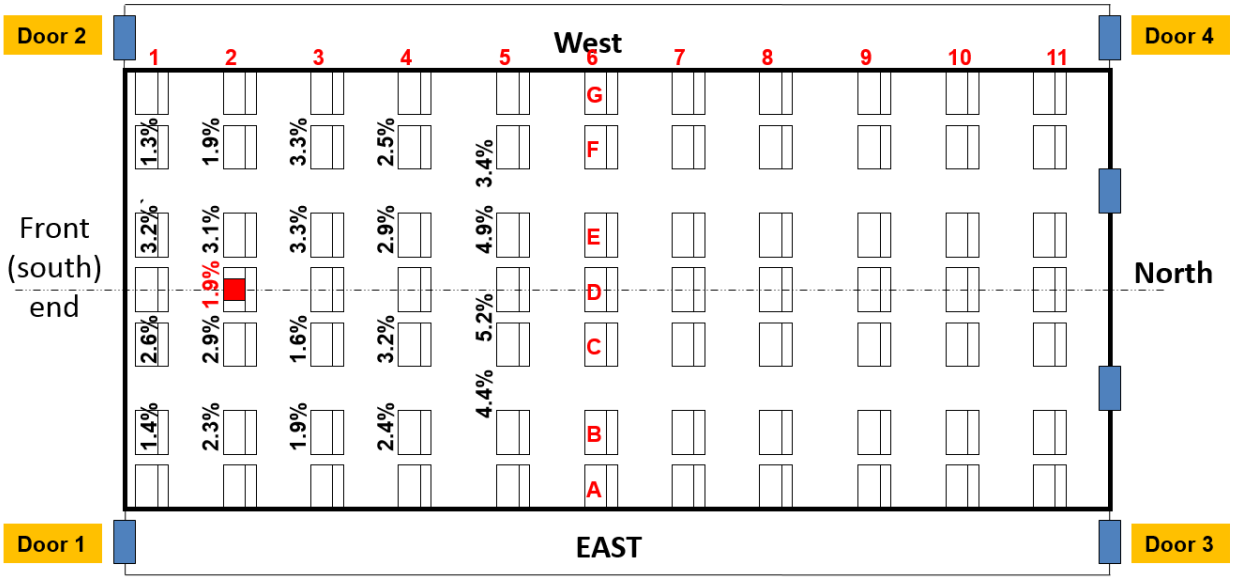

Figure E.1 – Relative uncertainty when releasing CO_2 in seat 2D (Heated Manikins)

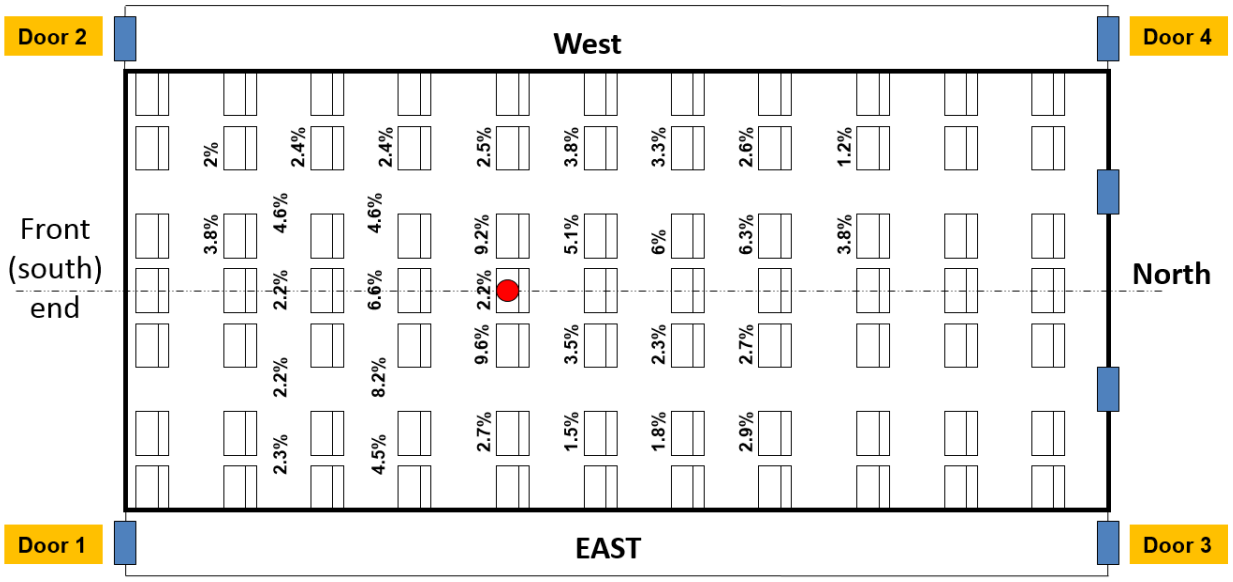

Figure E.2 - Relative uncertainty when releasing CO_2 in seat 5D (Heated Manikins)

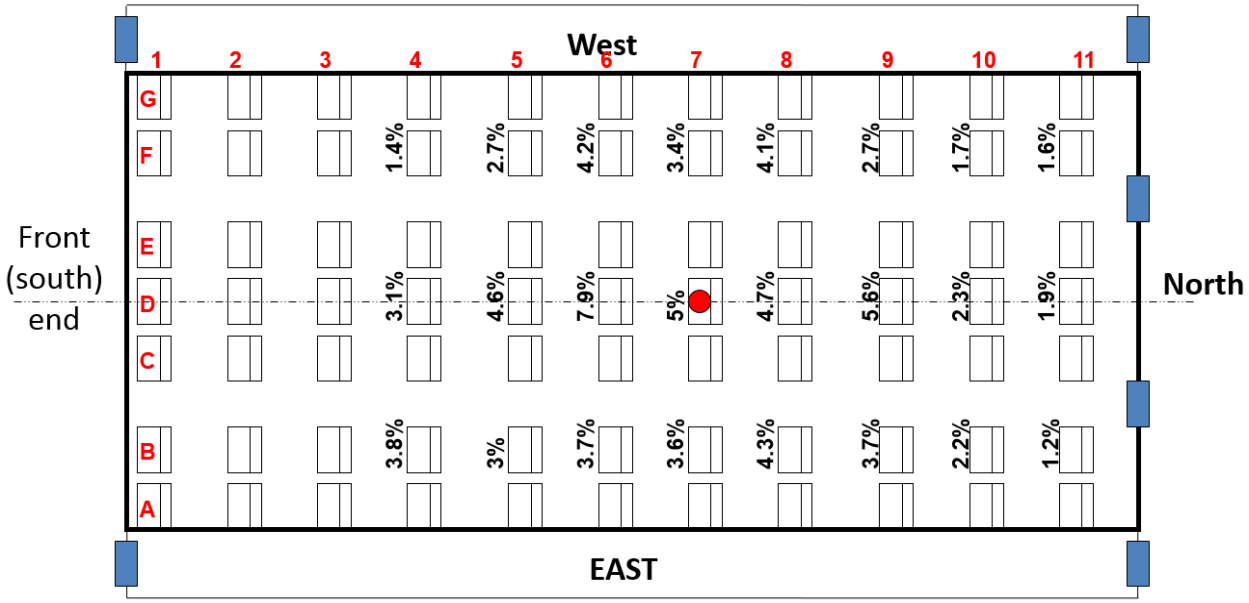

Figure E.3 - Relative uncertainty when releasing CO_2 in seat 7D (Heated Manikins)

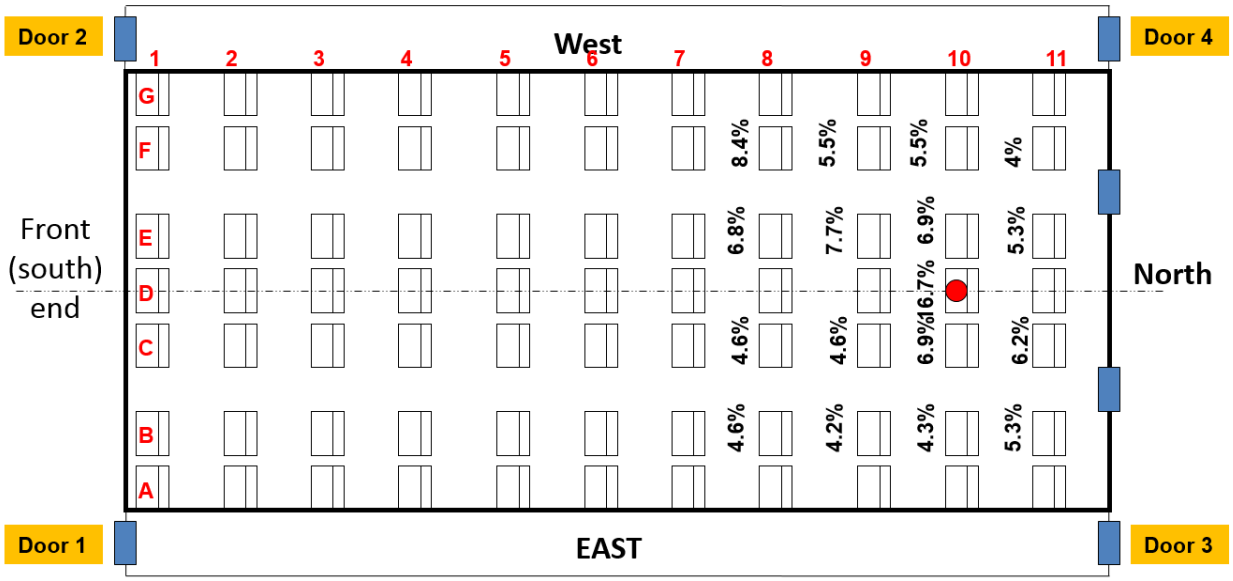

Figure E.4 - Relative uncertainty when releasing CO_2 in seat 10D (Heated Manikins)

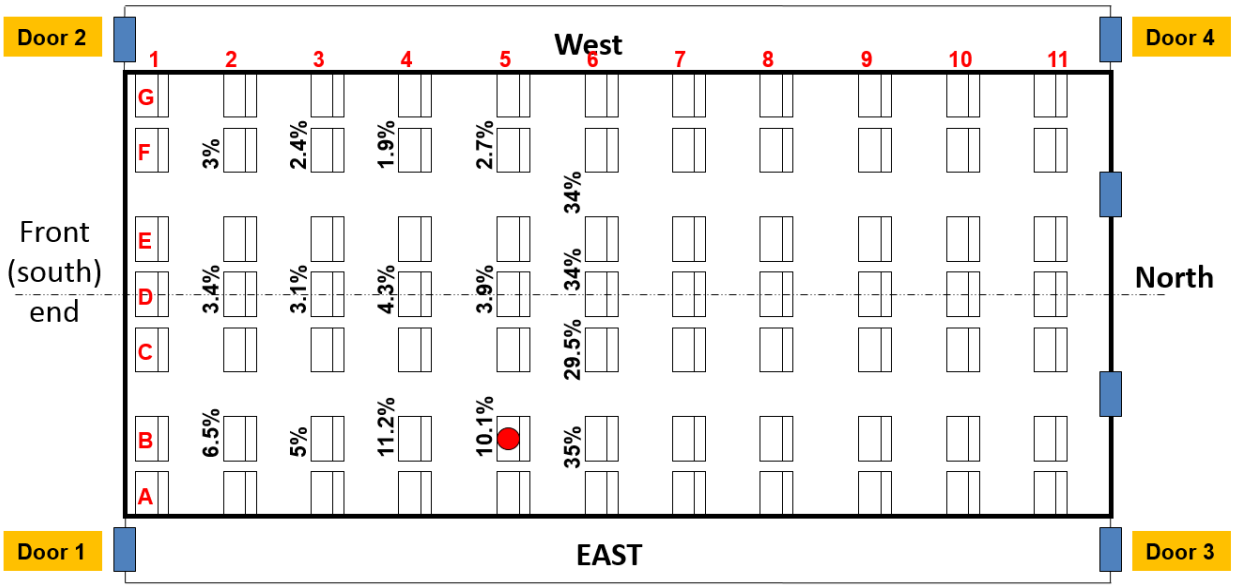

Figure E.5 – Relative uncertainty when releasing CO_2 in seat 5B (Heated Manikins)

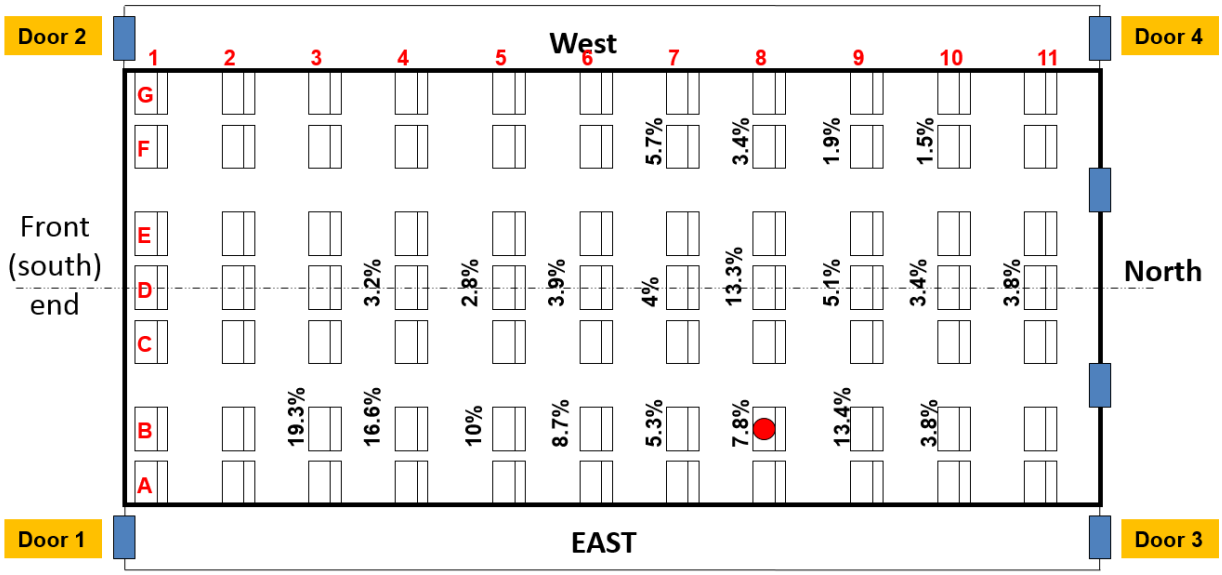

Figure E.6 – Relative uncertainty when releasing CO_2 in seat 8B (Heated Manikins)

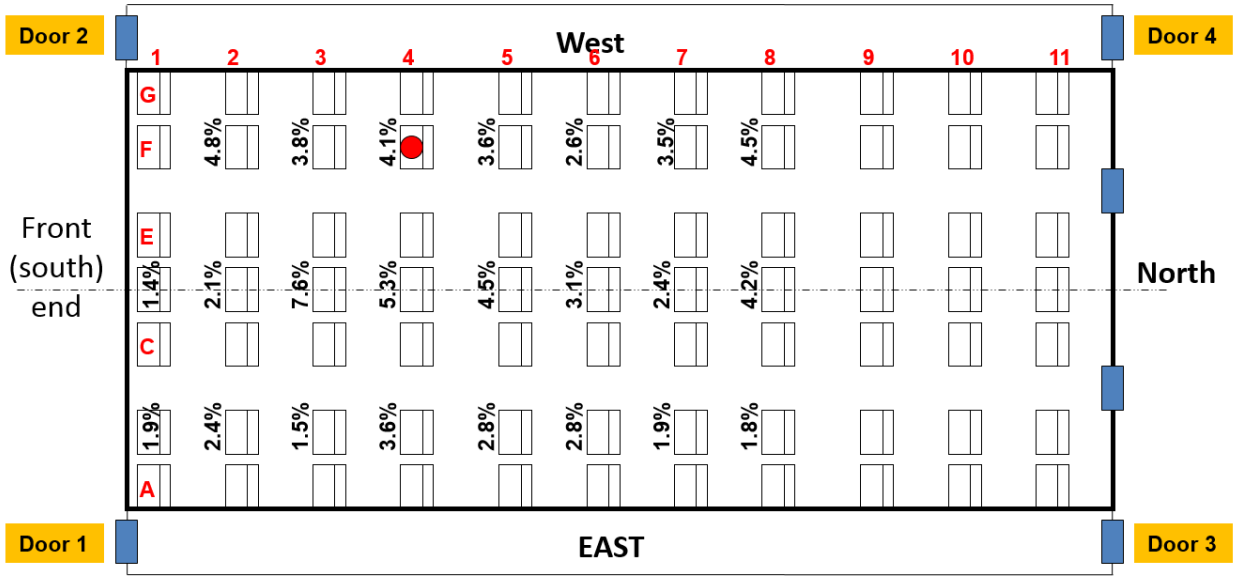

Figure E.7 - Relative uncertainty when releasing CO2 in seat 4F (Heated Manikins)

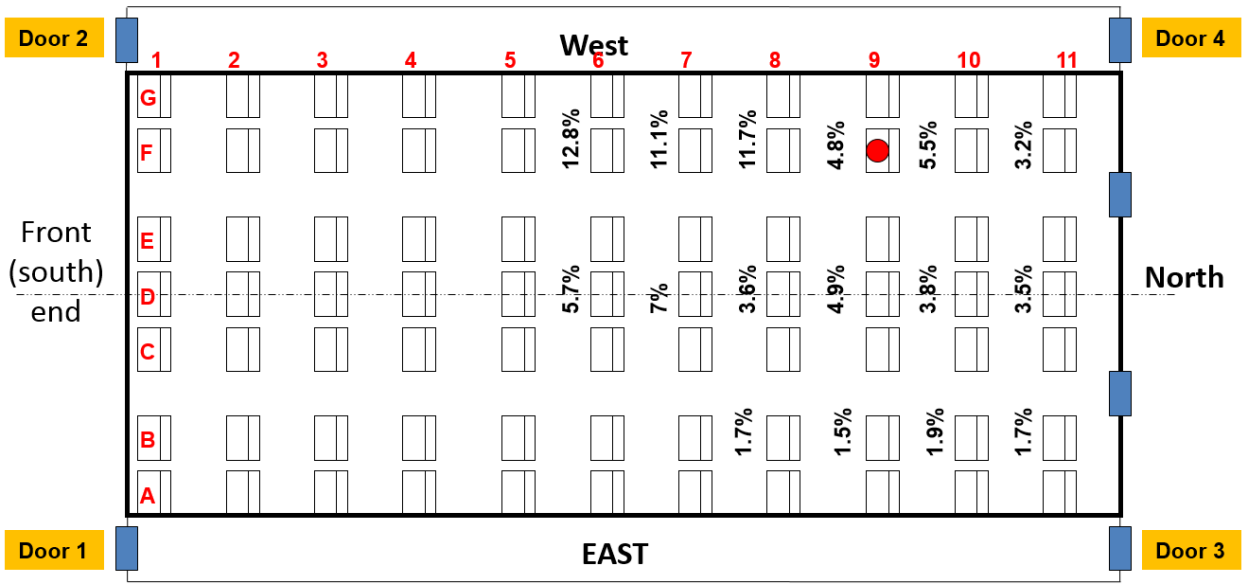

Figure E.8 - Relative uncertainty when releasing CO_2 in seat 9F (Heated Manikins)

II) Uncertainty results for CO_2 samples with unheated manikins

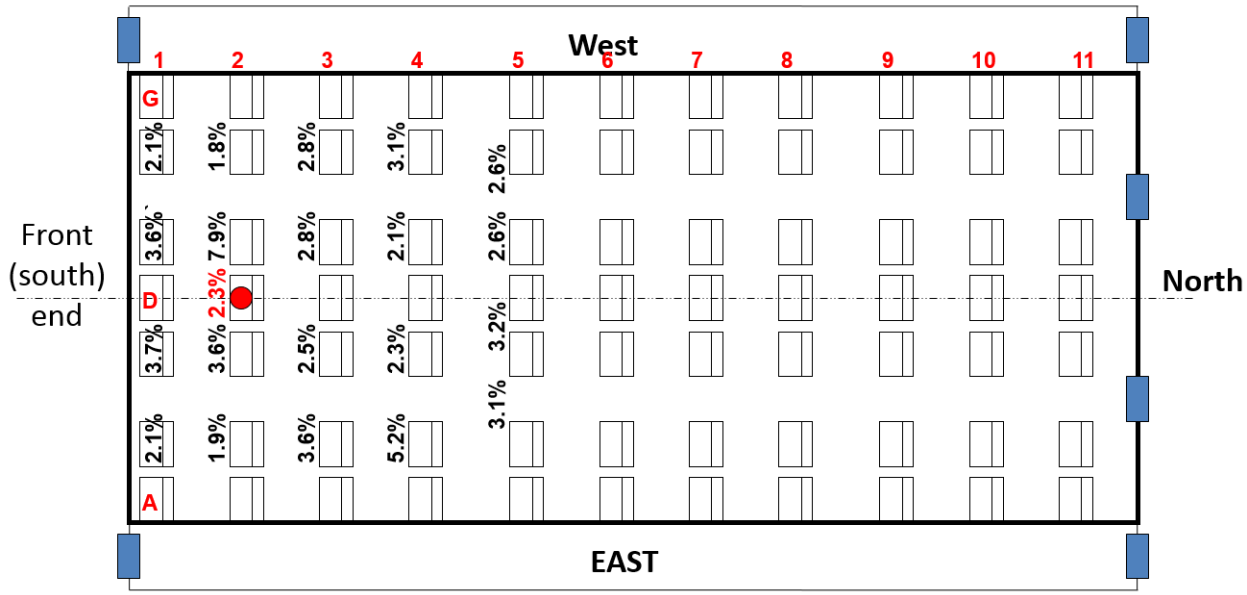

Figure E.9 – Relative uncertainty when releasing CO_2 in seat 2D (Unheated Manikins)

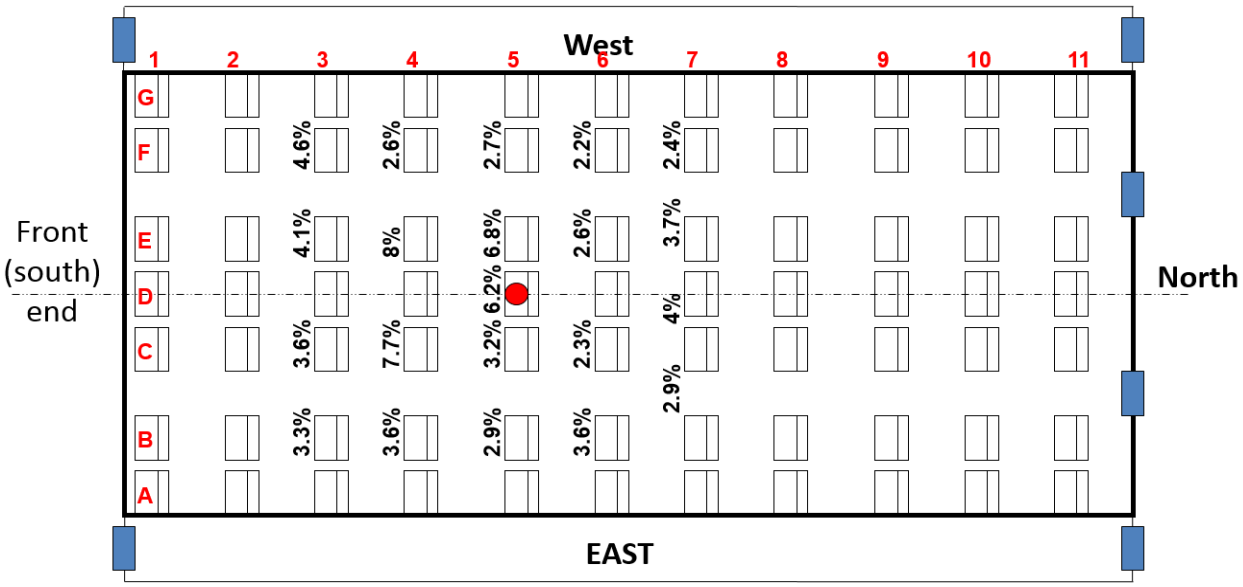

Figure E.10 – Relative uncertainty when releasing CO_2 in seat 5D (Unheated Manikins)

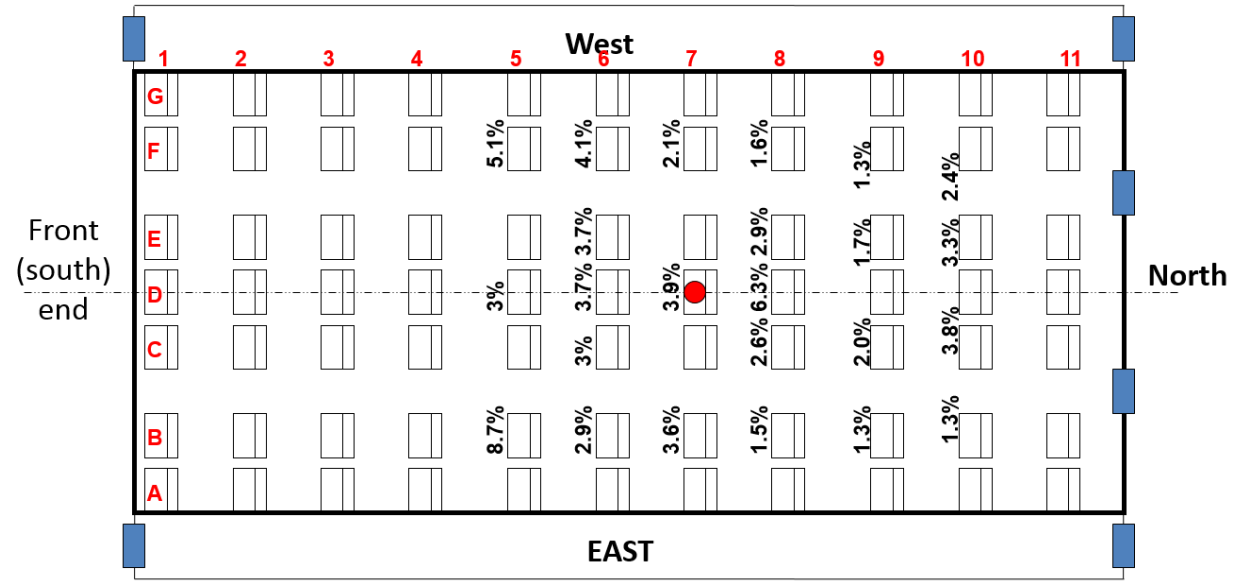

Figure E.11 – Relative uncertainty when releasing CO_2 in seat 7D (Unheated Manikins)

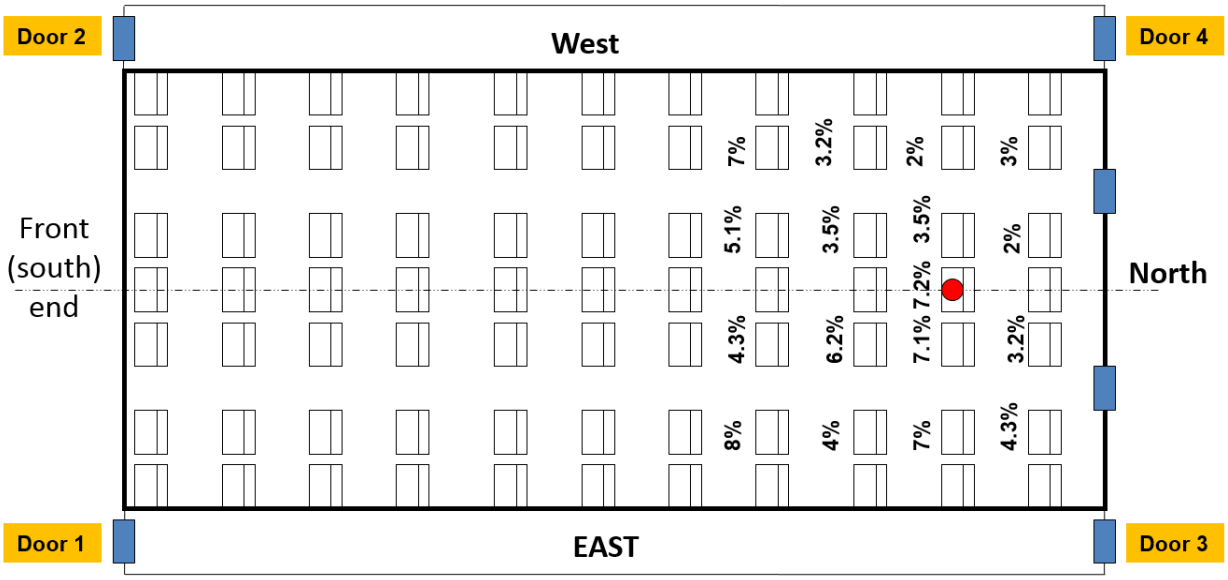

Figure E.12 - Relative uncertainty when releasing CO_2 in seat 10D (Unheated Manikins)

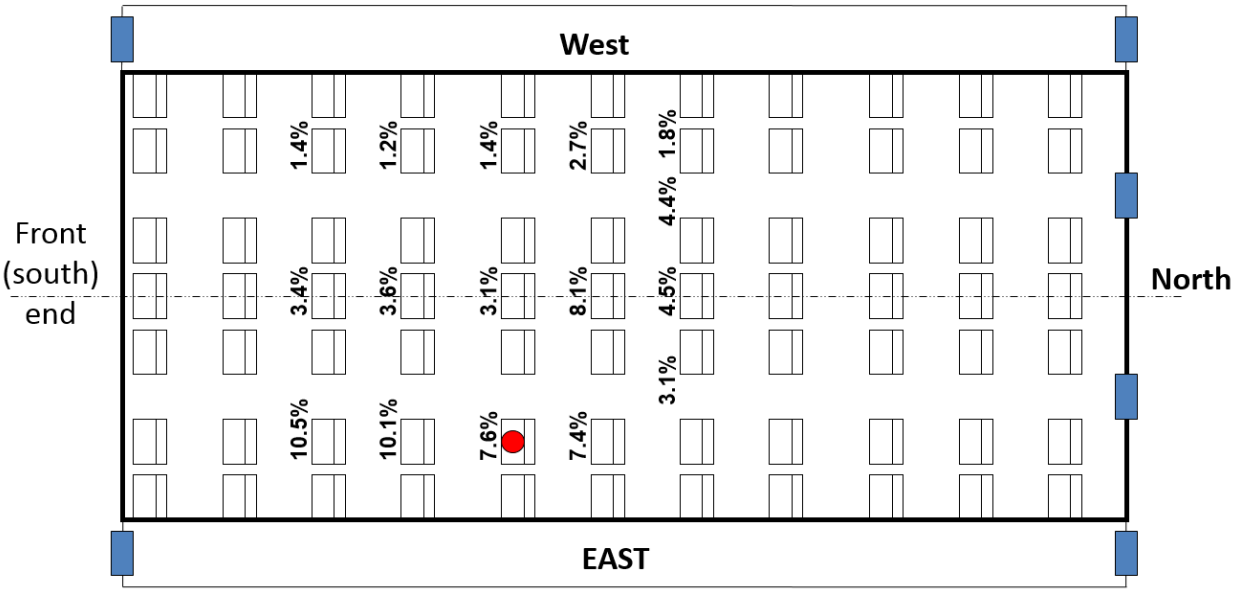

Figure E.13 – Relative uncertainty when releasing CO_2 in seat 5B (Unheated Manikins)

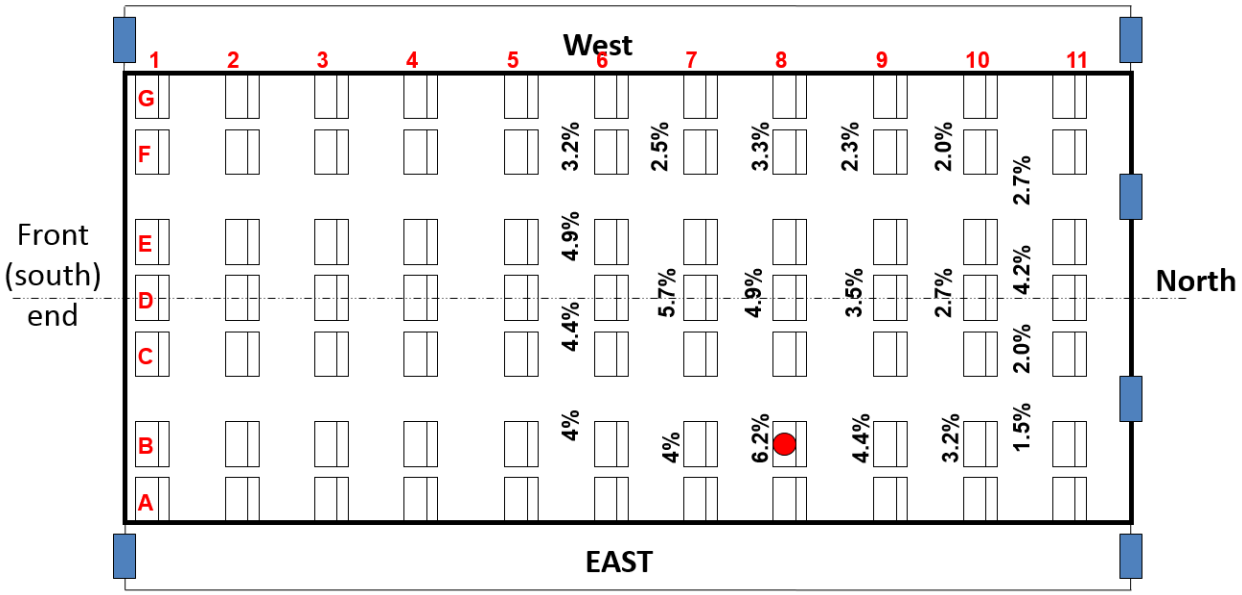

Figure E.14 – Relative uncertainty when releasing CO_2 in seat 8B (Unheated Manikins)

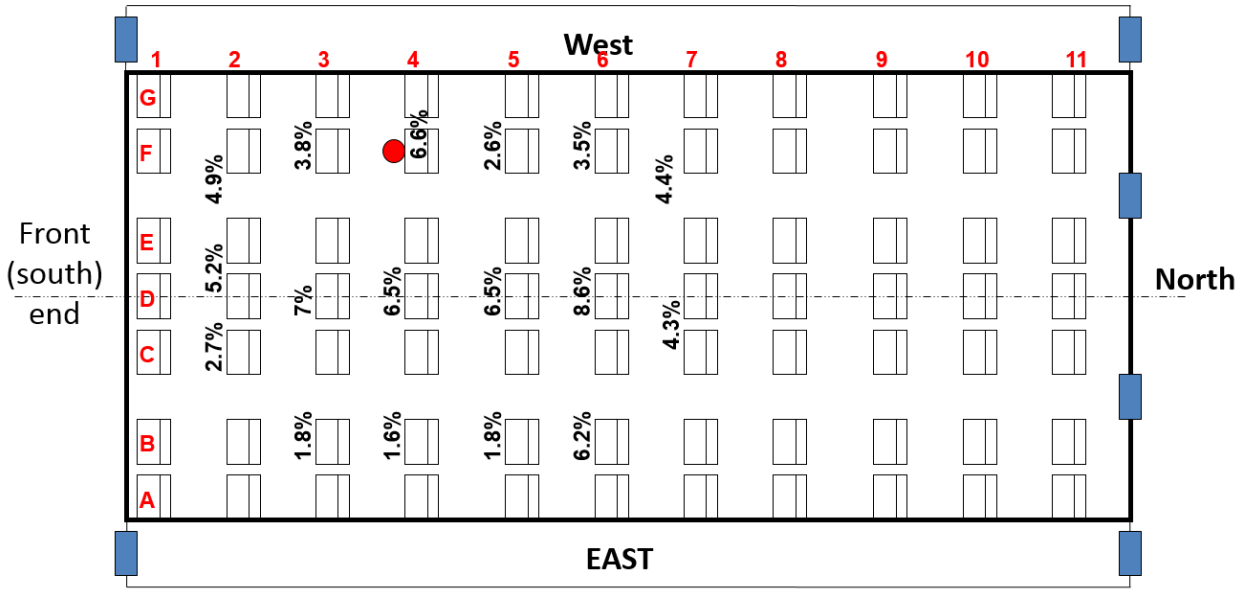

Figure E.15 – Relative uncertainty when releasing CO_2 in seat 4F (Unheated Manikins)

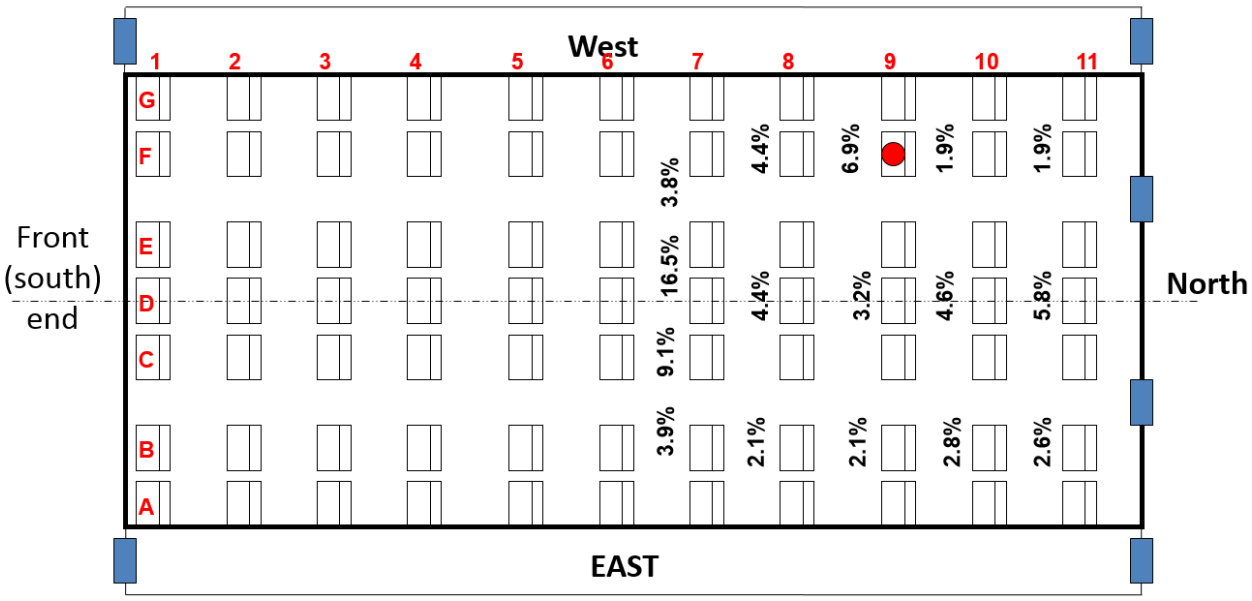

Figure E.16 - Relative uncertainty when releasing CO_2 in seat 9F (Unheated Manikins)

Appendix F - Airflow Repeatability inside the Mockup Cabin

It was important to investigate the gaseous transport and tracer gas sampling repeatability in different sections of the cabin to check on the uncertainty of the flow behavior inside the cabin over different periods of time. To do this, same procedures that were used for the CO_2 release and sampling were used here. However, the sampling was repeated at different intervals of time: after one hour, two hours or three, after one day, 3 days, 5 days, one month, and different time intervals as will be indicated in the legend of the figures.

The transient behavior of the collected samples in various locations was investigated and is shown in the following plots.

Results for Release in 6D

I) Sampling in Middle Seats (4-5-6-7 D)

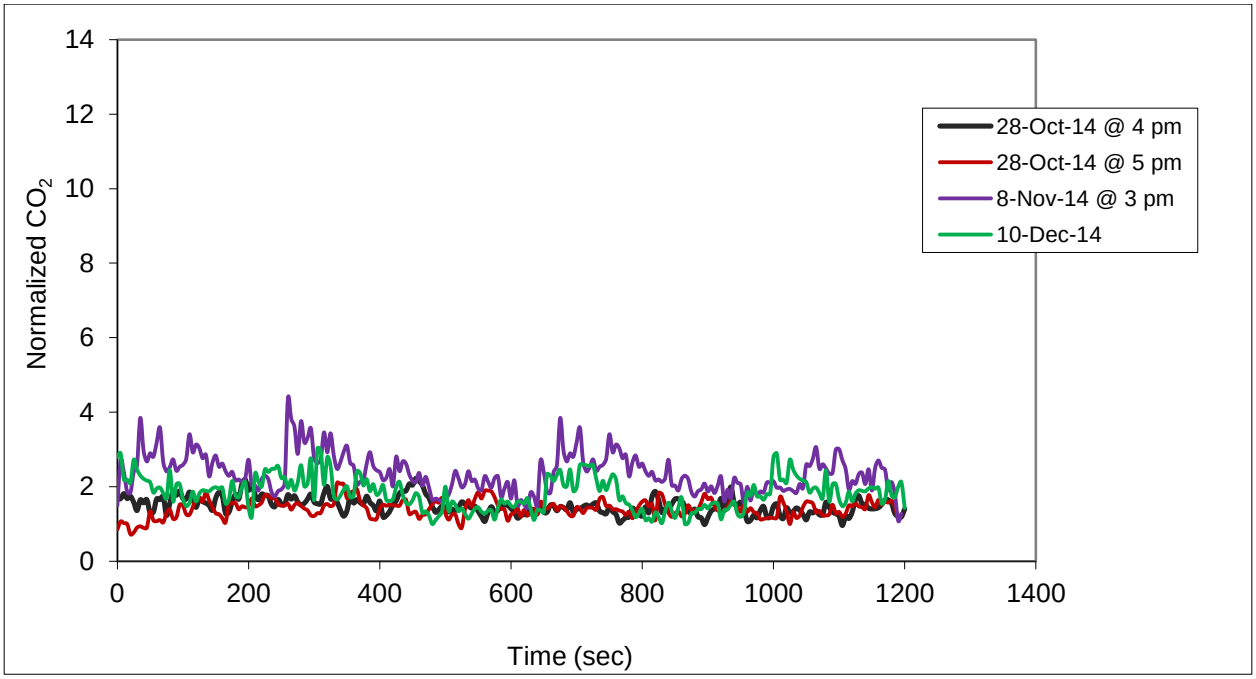

Figure F.1 - Sampling in 4D during different days (release in 6D)

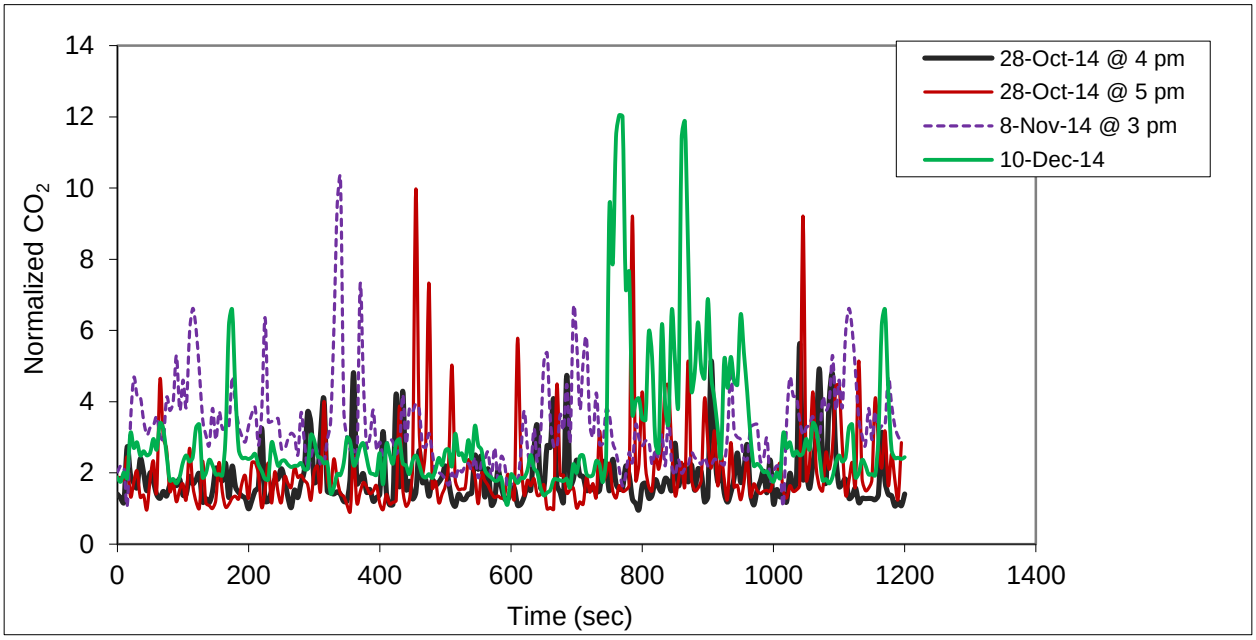

Figure F.2 - Sampling in 5D during different days (release in 6D)

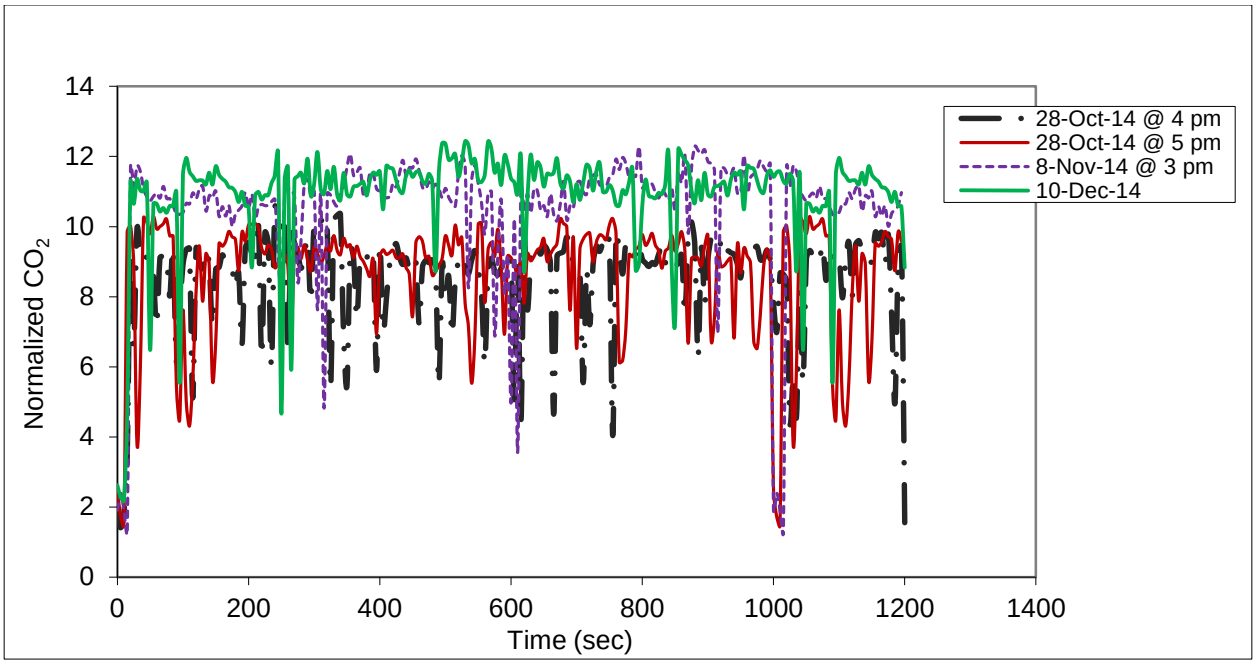

Figure F.3 - Sampling in 6D during different days (release in 6D)

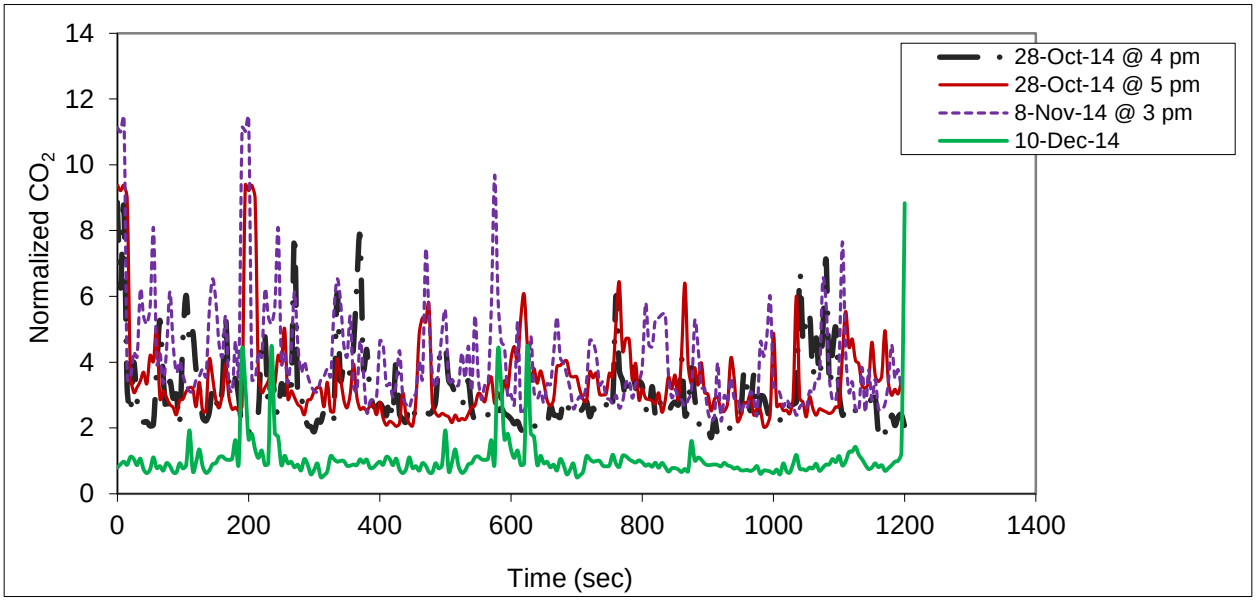

Figure F.4 - Sampling in 7D during different days (release in 6D)

Table F.1 – Average and relative uncertainty for results collected in 4D (release in 6D)

	Release in 6D	
	Sampling in seat 4D	
	Normalized	Rel. Uncertainty
Test 1	1.48	±3%
Test 2	1.40	±3%
Test 3	2.35	±4%
Test 4	1.82	±4%
Average	1.76	±4%

Table F.2 - Average and relative uncertainty for results collected in 5D (release in 6D)

	Release in seat 6D	
	Sampling in seat 5D	
	Normalized	Rel. Uncertainty
Test 1	1.82	±8%
Test 2	2.02	±11%
Test 3	3.21	±7%
Test 4	2.97	±11%
Average	2.51	±9%

Table F.3 - Average and relative uncertainty for results collected in 6D (release in 6D)

	Release in 6D	
	Sampling in seat 6D	
	Normalized	Rel. Uncertainty
Test 1	8.53	±3%
Test 2	8.59	±4%
Test 3	10.45	±3%
Test 4	10.83	±2%
Average	9.60	±3%

Table F.4 - Average and relative uncertainty for results collected in 7D (release in 6D)

	Release in 6D	
	Sampling in seat 7D	
	Normalized	Rel. Uncertainty
Test 1	3.00	±7.1%
Test 2	3.39	±7.3%
Test 3	3.99	±7.4%
Test 4	1.01	±9.8%
Average	2.85	±8%

II) Sampling in Side Wall Seats (5-6-7 G)

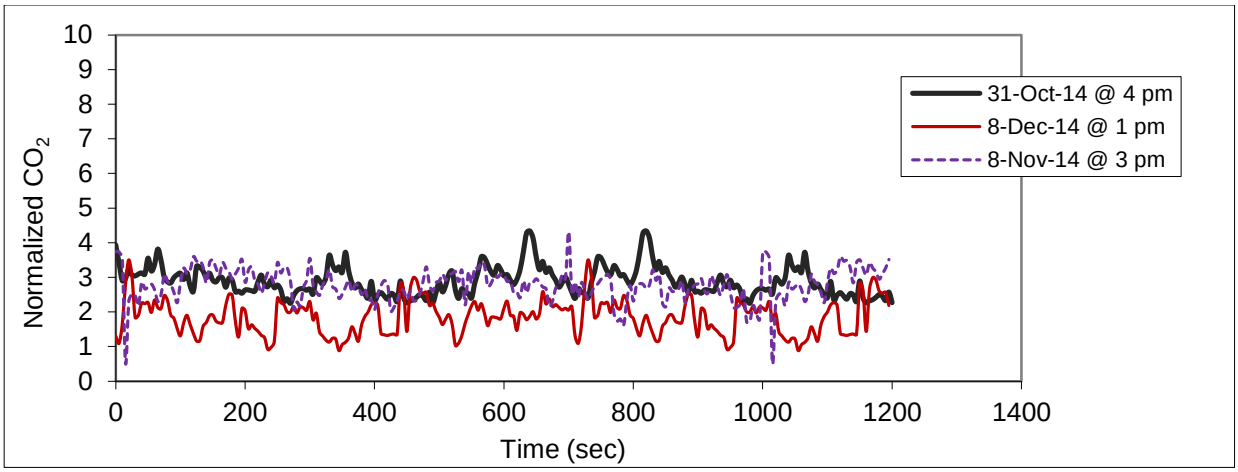

Figure F.5 - Sampling in 7G during different days (release in 6D)

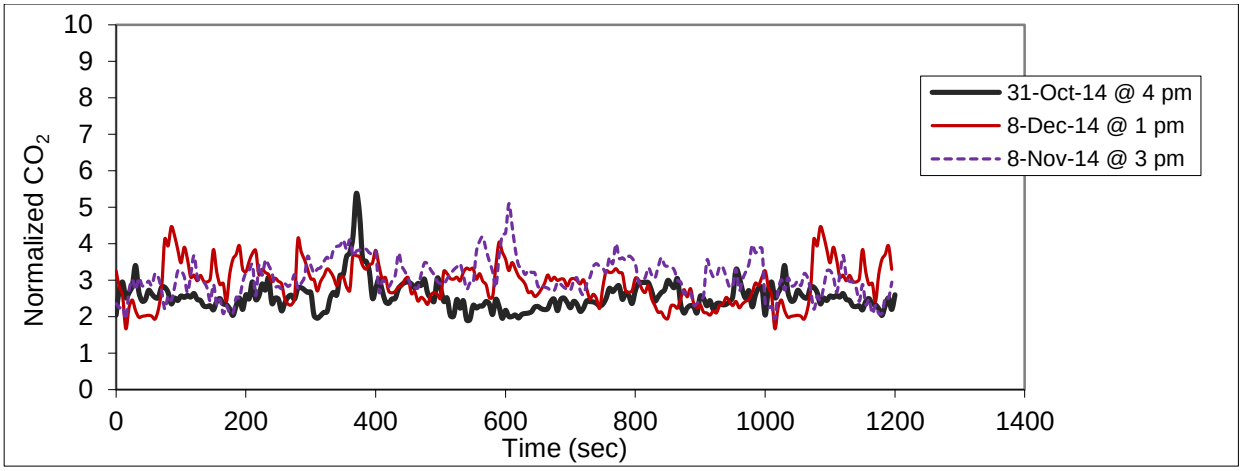

Figure F.6 - Sampling in 6G on different days (releasing in 6D)

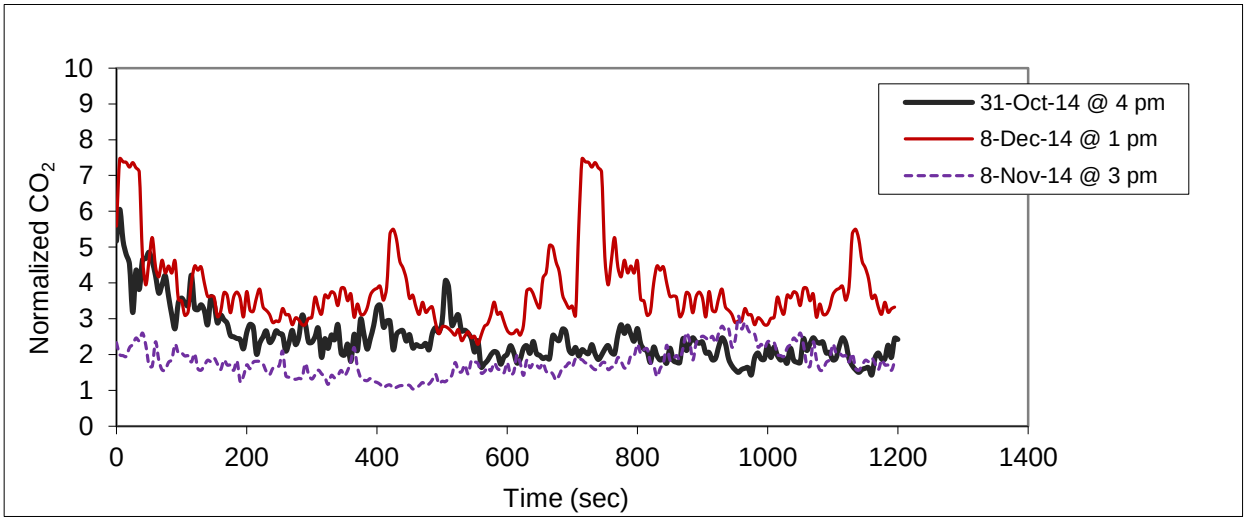

Figure F.7 - Sampling in 5G during different days (release in 6D)

Table F.5 - Average and relative uncertainty for results collected in 5G (release in 6D)

	Release in 6D	
	Sampling in seat 5G	
	Normalized	Rel. Uncertainty
Test 1	2.45	±5%
Test 2	3.76	±5%
Test 3	1.77	±6%
Average	2.66	±5%

Table F.6 - Average and relative uncertainty for results collected in 6G (release in 6D)

	Release in 6D	
	Sampling in seat 6G	
	Normalized	Rel. Uncertainty
Test 1	2.53	±2.9%
Test 2	2.90	±3.3%
Test 3	3.06	±3.2%
Average	2.83	±3%

Table F.7 - Average and relative uncertainty for results collected in 7G (release in 6D)

	Release in 6D	
	Sampling in seat 7G	
	Normalized	Rel. Uncertainty
Test 1	2.87	±2.6%
Test 2	1.84	±4.9%
Test 3	2.76	±3.1%
Average	2.49	±3.5%

Results for Release in 2D

I) Sampling in Side Wall Seats (2-3-4 B)

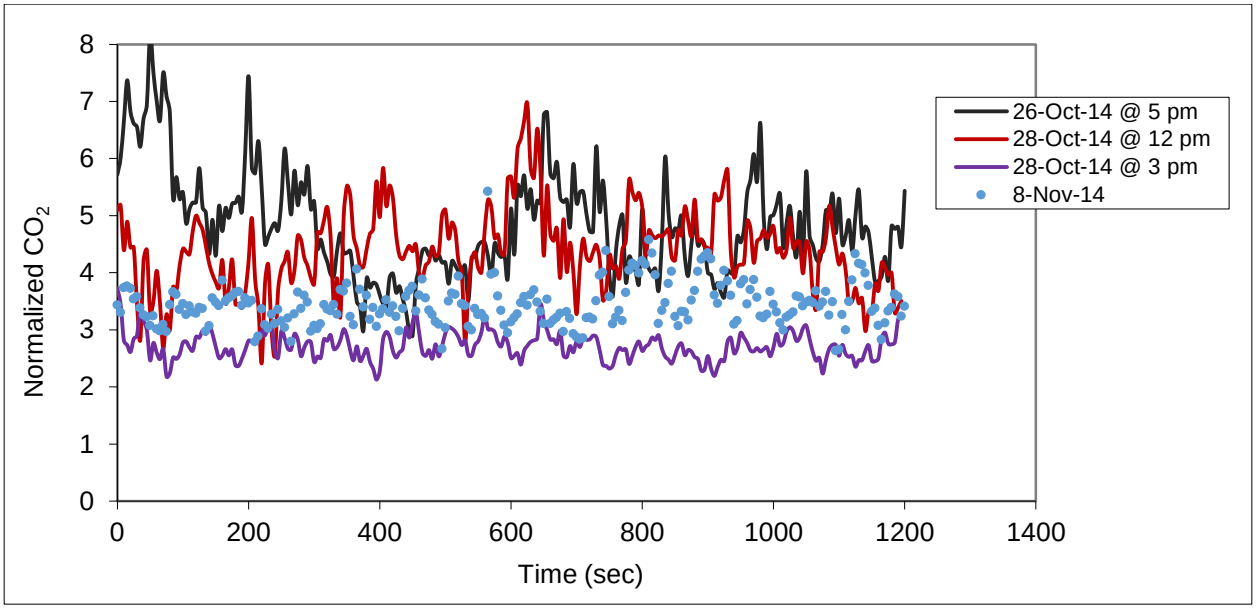

Figure F.8 - Sampling in 2B during different days (release in 2D)

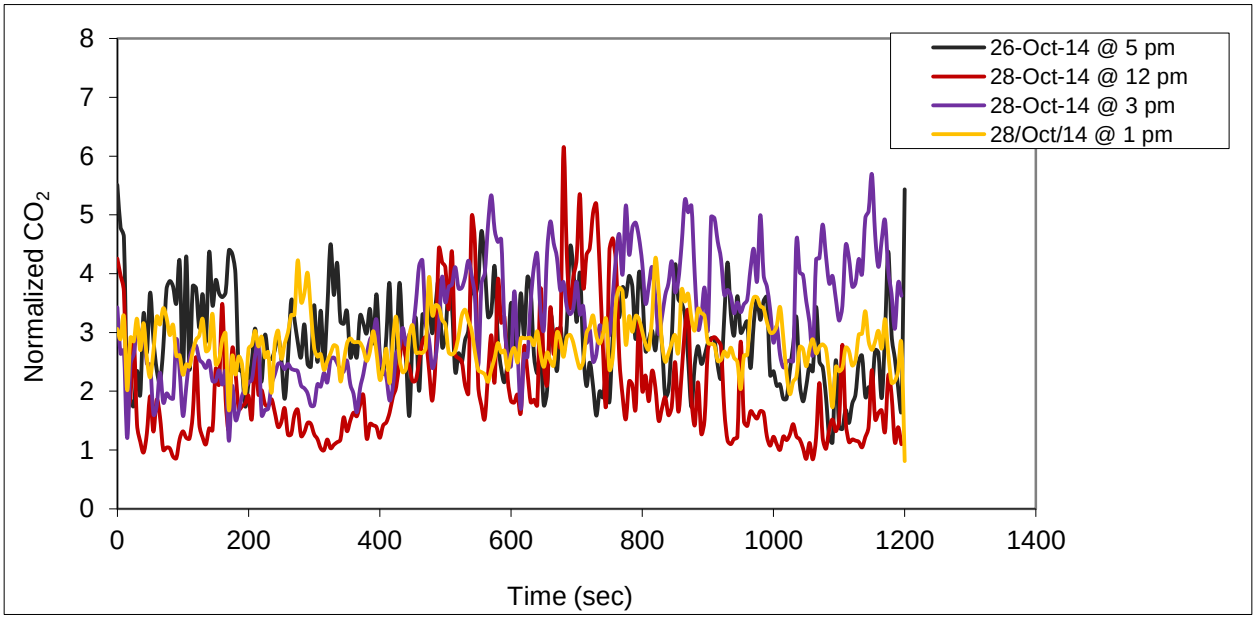

Figure F.9 - Sampling in 3B during different days (release in 2D)

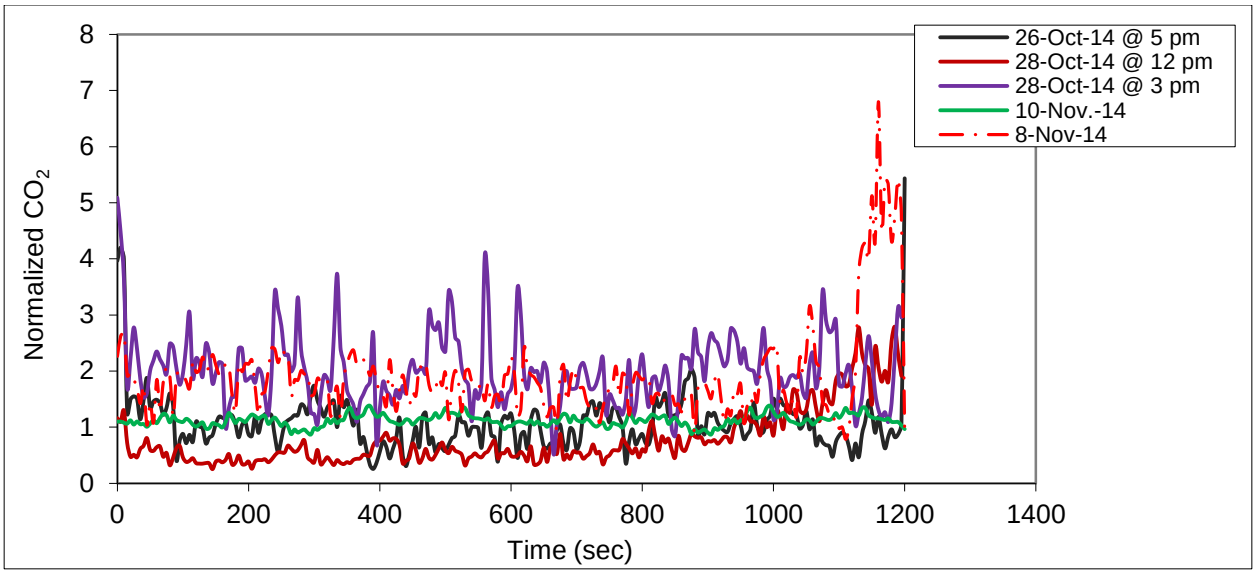

Figure F.10 - Sampling in 4B during different days (release in 2D)

Table F.8 - Average and relative uncertainty for results collected in 2B (release in 2D)

	Release in 2D	
	Sampling in seat 2B	
	Normalized	Rel. Uncertainty
Test 1	4.84	±3.4%
Test 2	4.40	±3.2%
Test 3	2.71	±1.9%
Test 4	3.45	±1.9%
Average	3.85	±3%

Table F.9 - Average and relative uncertainty for results collected in 3B (release in 2D)

	Release in 2D	
	Sampling in seat 3B	
	Normalized	Rel. Uncertainty
Test 1	2.89	±4.8%
Test 2	2.06	±8.9%
Test 3	3.19	±5.4%
Test 4	2.80	±2.7%
Average	2.73	±6%

Table F.10 - Average and relative uncertainty for results collected in 4B (release in 2D)

	Release in 2D	
	Sampling in seat 4B	
	Normalized	Rel. Uncertainty
Test 1	1.06	±8.0%
Test 2	0.78	±11.7%
Test 3	2.00	±5.6%
Test 4	1.11	±2.0%
Average	1.24	±7%

II) Sampling in Middle Seats (4-5-6 E)

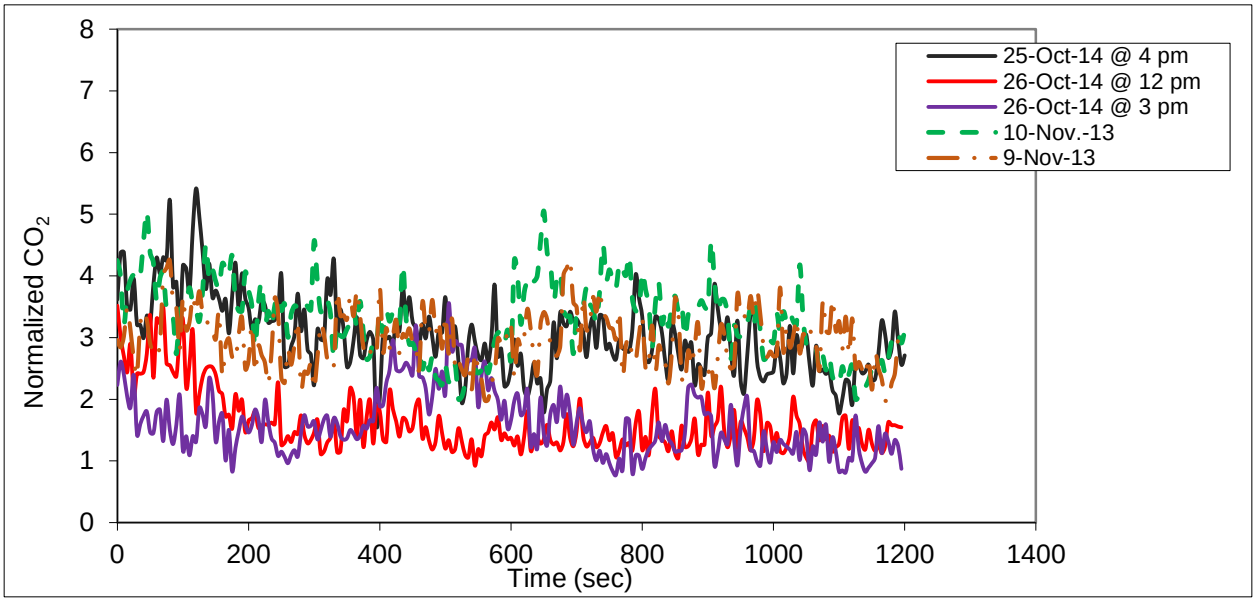

Figure F.11 - Sampling in 4E during different days (release in 2D)

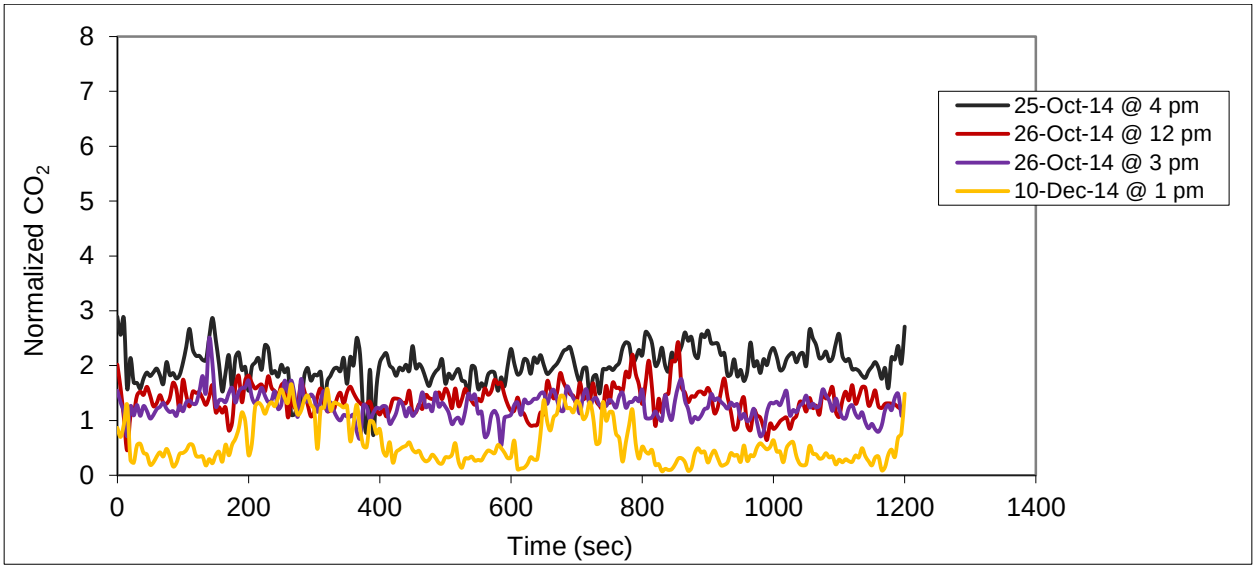

Figure F.12 - Sampling in 5E during different days (release in 2D)

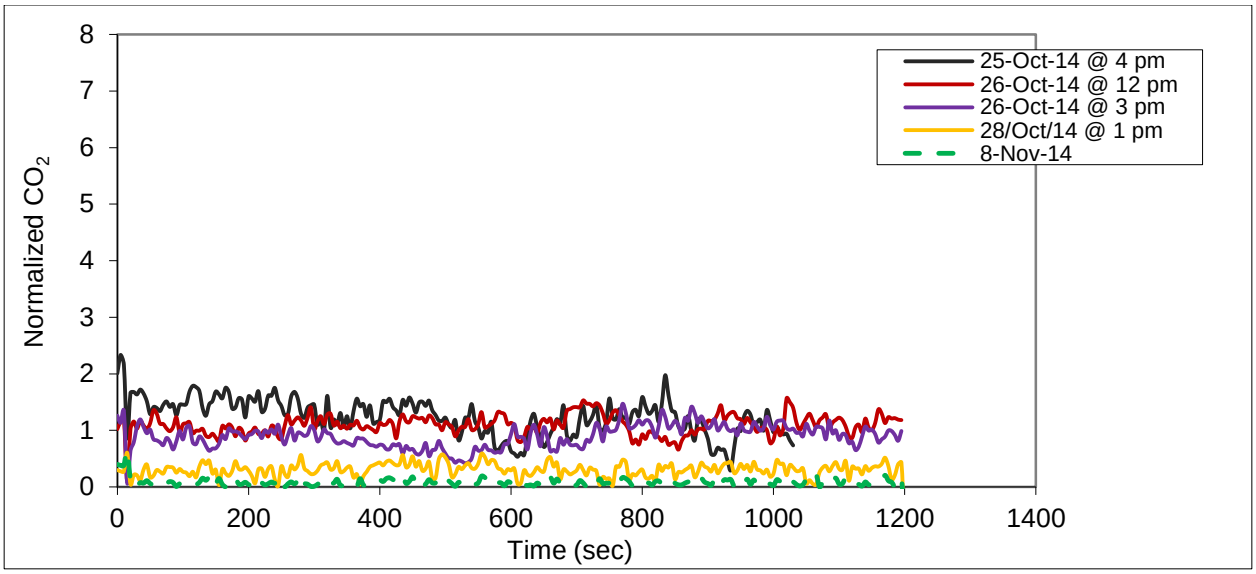

Figure F.13 - Sampling in 6E during different days (release in 2D)

Table F.11 - Average and relative uncertainty for results collected in 4E (release in 2D)

	Release in 2D	
	Sampling in seat 4E	
	Normalized	Rel. Uncertainty
Test 1	1.61	±5.0%
Test 2	1.59	±6.0%
Test 3	1.44	±6.8%
Test 4	3.29	±3.2%
Test 4	2.93	±2.8%
Average	2.17	±5%

Table F.12 - Average and relative uncertainty for results collected in 5E (release in 2D)

	Release in 2D	
	Sampling Seat 5E	
	Normalized	Rel. Uncertainty
Test 1	2.01	±2.9%
Test 2	1.37	±3.4%
Test 3	1.25	±3.2%
Test 4	0.59	±11.8%
Average	1.31	±5%

Table F.13 - Average and relative uncertainty for results collected in 6E (release in 2D)

	Release in 2D	
	Sampling Seat 6E	
	Normalized	Rel. Uncertainty
Test 1	1.18	±9%
Test 2	1.09	±3%
Test 3	0.89	±4%
Test 4	0.31	±8%
Average	0.87	±6%

Results for Release in 8B

III) Sampling in 7D, 8D, and 9D

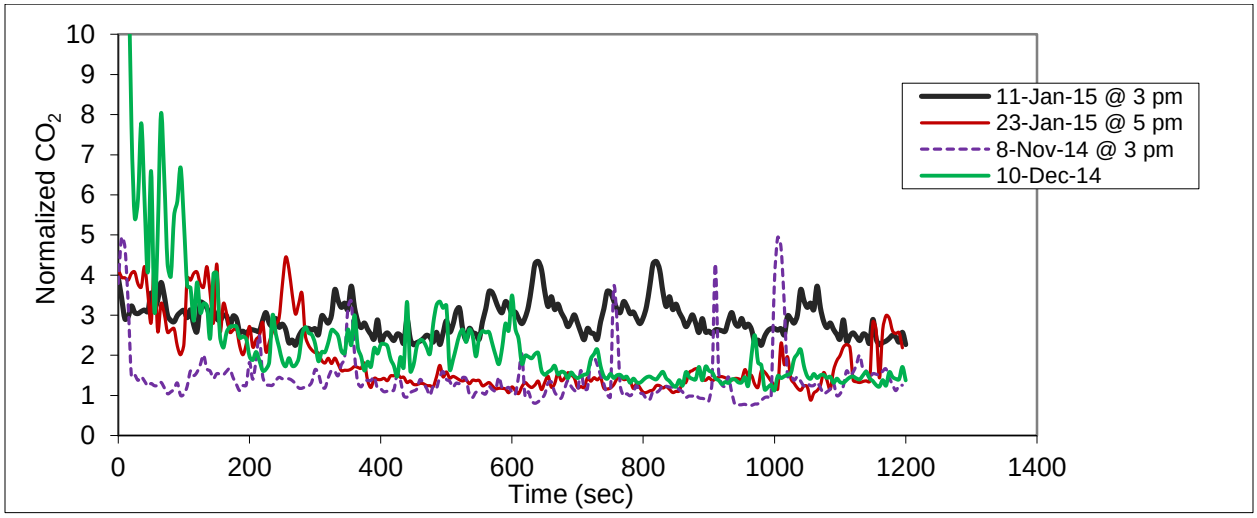

Figure F.14 - Sampling in 7D during different days (release in 8B)

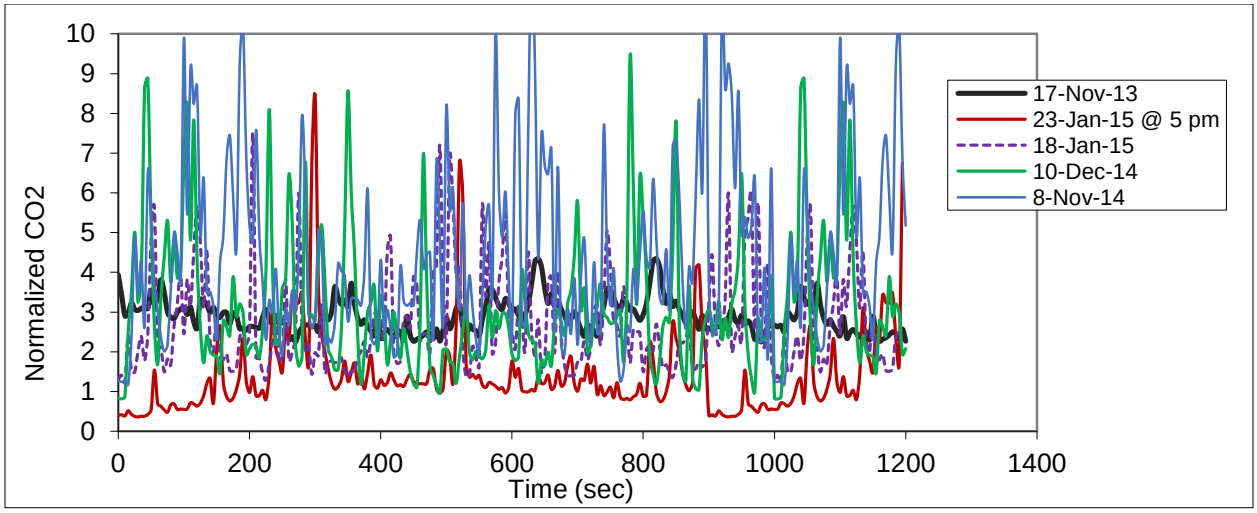

Figure F.15 - Sampling in 8D during different days (release in 8B)

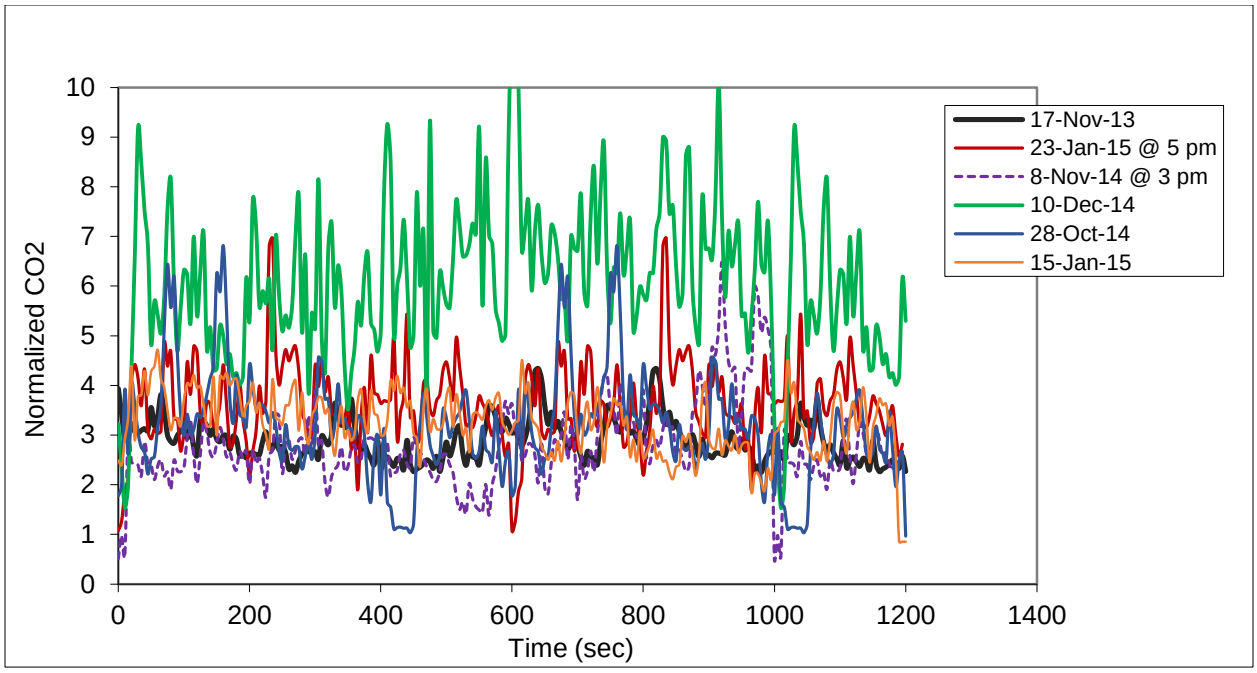

Figure F.16 - Sampling in 9D during different days (release in 8B)

Table F.14 - Average and relative uncertainty for results collected in 7D (release in 8B)

	Release in 8B	
	Sampling in seat 7D	
	Normalized	Rel. Uncertainty
Test 1	2.87	±2.6%
Test 2	1.88	±7.7%
Test 3	1.40	±8.8%
Test 4	2.39	±11.4%
Average	2.13	±8%

Table F.15 - Average and relative uncertainty for results collected in 8D (release in 8B)

	Release in 8B	
	Sampling in seat 8D	
	Normalized	Rel. Uncertainty
Test 1	2.87	±2.6%
Test 2	1.41	±13.6%
Test 3	2.65	±8.4%
Test 4	3.13	±9.9%
Average	2.51	±9%

Table F.16 - Average and relative uncertainty for results collected in 9D (release in 8B)

	Release in 8B	
	Sampling in seat 9D	
	Normalized	Rel. Uncertainty
Test 1	2.87	±2.6%
Test 2	3.61	±4.2%
Test 3	2.74	±5.0%
Test 4	6.07	±4.5%
Test 5	3.15	±6%
Test 6	3.22	±7%
Average	3.61	±5%

Some locations were repeatable over time and over days and some locations do not have a repeatable phenomenon from day to day or even from test to test within the same day. However, for all considered locations, the repeatable uncertainty was within ±10% range taking into consideration the propagation uncertainty (equation (5.35)), resulting from the terms in the CO_2 normalization in equation (3.6) and the random uncertainty encountered within the same test equation (5.36).

Appendix G - Investigating the Isotropic Assumption inside the Mockup Cabin

When measuring speed, turbulence kinetic energy, turbulence intensity, and turbulence dissipation rates for the flow inside the mockup cabin, the flow was assumed isotropic. To investigate the accuracy of the isotropic turbulence assumption, the energy dissipation rate was evaluated by measuring the airflow speed in three different arrangements: longitudinal (same direction used for evaluating the dissipation rate in sections 5.2.4.2.2 and 5.2.5 for heated and unheated), transverse, and vertical. For each configuration, the speed was measured simultaneously at three different locations with a separation distance of 127 mm (5 inches) between consecutive sensors. The longitudinal arrangement is shown in Figure G.1. For each arrangement, the middle sensor was placed in the same location as used in the longitudinal tests. The other two sensors were then located at a distance of 127 mm to the left and right sides of the sensor in the transverse direction of the cabin, and then at a distance of 127 mm above and below the sensor in the vertical direction of the cabin. For the longitudinal and transverse tests, the speed transducers were held in a vertical position , whereas during the vertical tests the transducers were held in a horizontal position to be normal to the intended measured flow.

The energy dissipation rate was evaluated by measuring the speed with the above 3 different configurations in two different locations in middle and aisle seats with heated and unheated manikins. The seats were 2E and 6D of the middle seats and 5F and 9B of the aisle seats. For each location, the test was repeated for 3 times. Each test was composed of 240 samples with 5 seconds between consecutive samples. Each set of tests was preceded with 5 minutes waiting period to allow steady state conditions to be achieved.

The results with heated and unheated manikins are shown in Figure G.4 and Figure G.5, respectively. The results represent the averages of three tests along with the random and bias uncertainty (equation (5.39)). The random uncertainty was weighted by proper confidence interval factors (1.96).

It was noticed that the vertical dissipation with heated manikins in the vertical arrangement is higher than the longitudinal and transverse except for seat 5F that showed no statistical differences between the three different arrangements with both heated and unheated manikins. The degree of isotropy was higher with unheated manikins when considering the systematic and random errors. With heated manikins the degree of isotropy was disturbed with the vertical arrangement of the probes that can be justified by the effect of the convective heat generated by the manikins.

Figure G.1 – Speed transducer arrangement in the longitudinal direction of the cabin

Figure G.2 – Speed transducer arrangement in the transverse direction of the cabin

Figure G.3 – Speed transducer arrangement in the vertical direction of the cabin

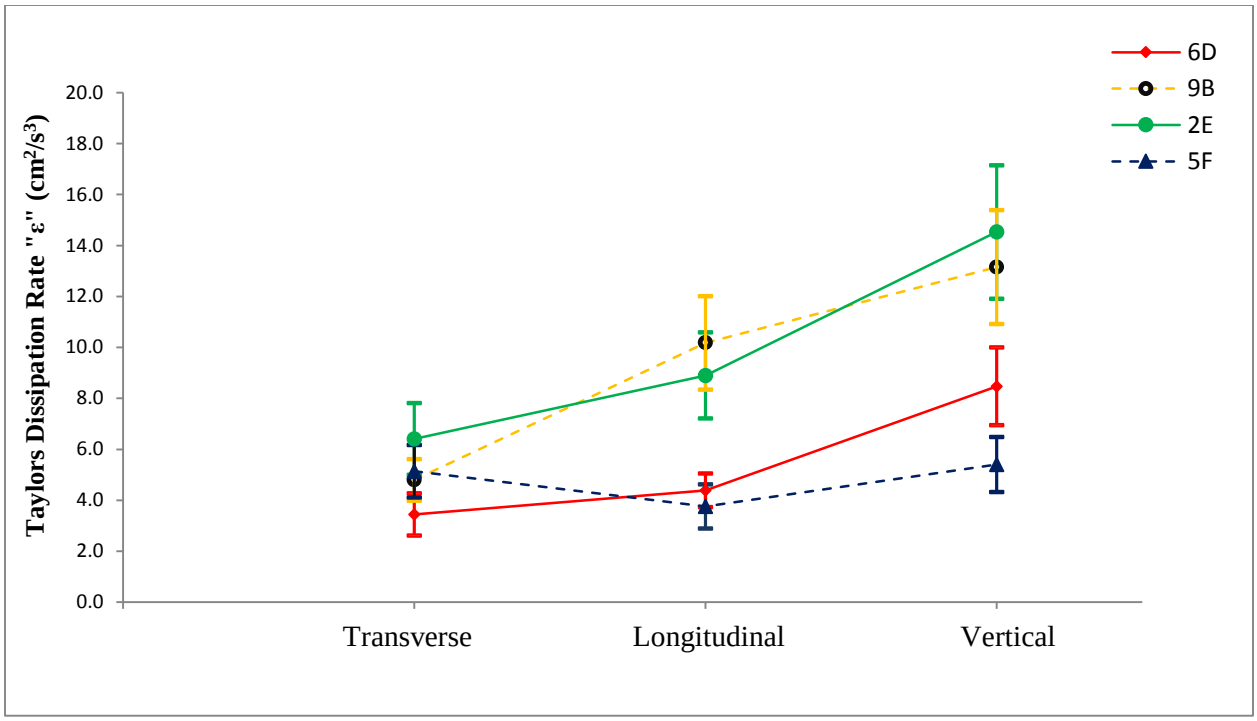

Figure G.4 – Energy dissipation rates in different seats using three different probe arrangements with heated manikins (dashed lines represent aisle seats whereas solid lines represent center seats)

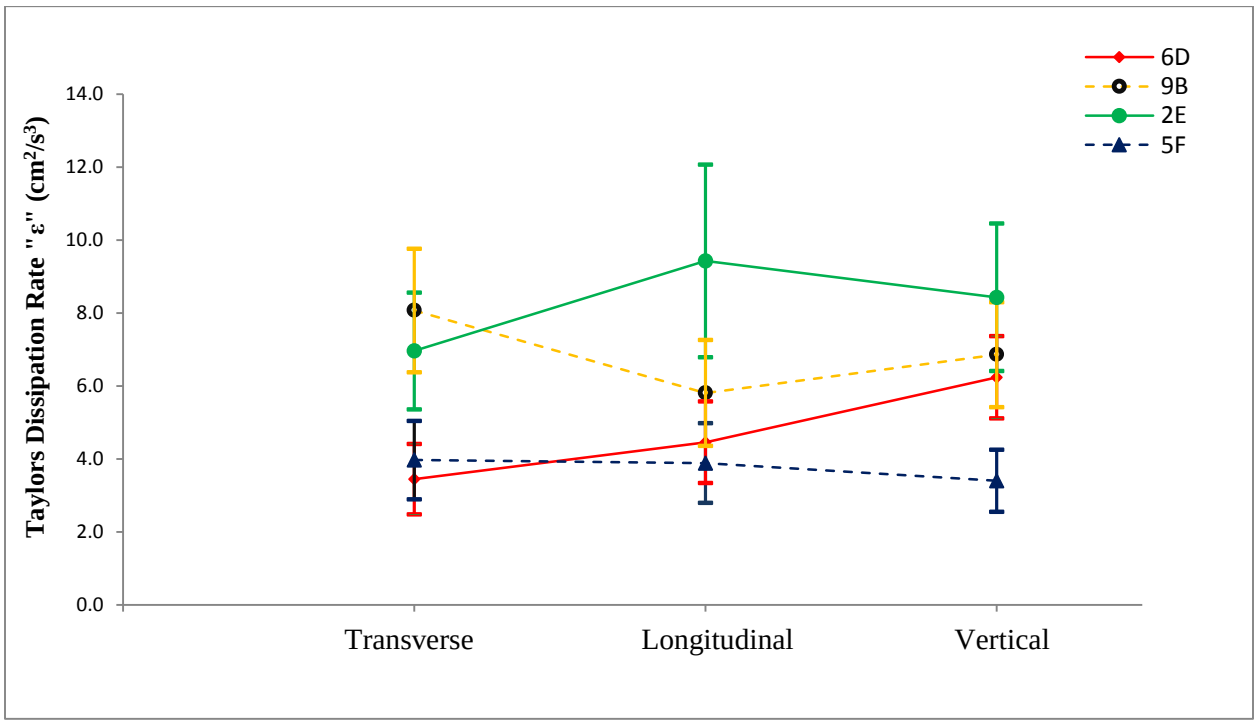

Figure G.5 – Energy dissipation rates in different seats using three different probe arrangements with unheated manikins (dashed lines represent aisle seats whereas solid lines represent center seats)

Appendix H - Tracer Gas Mass Balance inside the Mockup Cabin

This section investigates tracer gas balance for the mockup cabin. A schematic for the controlled volume of the mockup cabin is shown in Figure H.1. All possible inlets and outlets are shown in the schematic. The subscripts I, inj, lk, and o were used with different terms to represent inlet, injection, leak, and outlet, respectively. Since the cabin was pressurized to approximately 98 kPa and the surrounding environment was at atmospheric pressure, the leak flow is assumed to be into the cabin as shown in the schematic. Thus, the only outlet was through the two exhaust fans as shown in Figure 3.6.

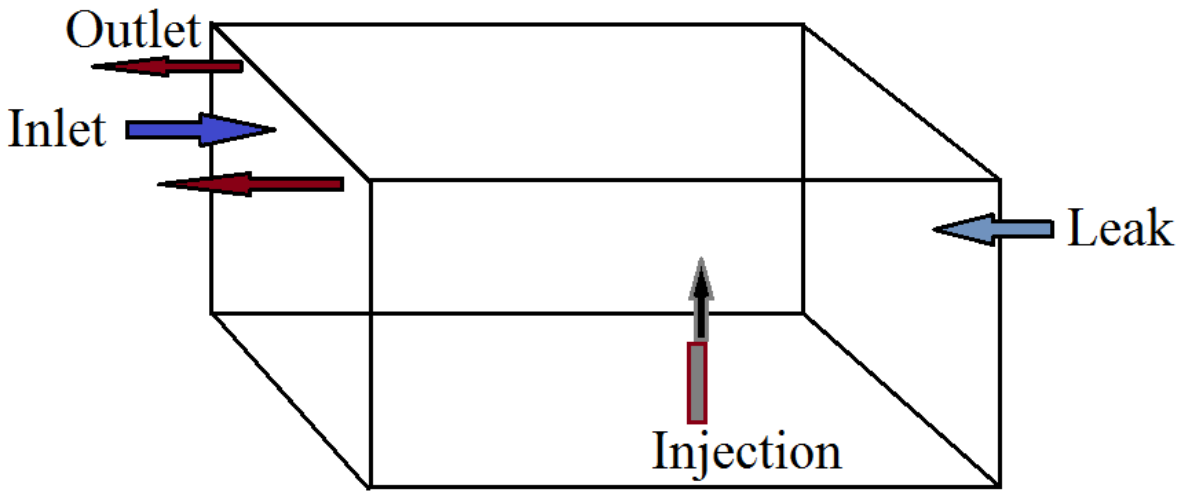

Figure H.1–- Schematic for the mockup cabin control volume with inlets and outlets flows

Conducting a mass flow balance over the defined control volume, equation (H.1) was obtained. Assuming there were no chemical reactions occurring, equation (H.2) represents the unsteady CO_2 mass balance inside the mockup cabin where ρ, $\dot{V}$, and C represent the density of CO_2,

volumetric flow rate for each flow, and the volume fraction of CO_2 in each respective flow, respectively.

$$\dot{m}_i + \dot{m_{inj}} + \dot{m}_{lk} - \dot{m}_o = \frac{dm}{dt} \tag{H.1}$$

$$\rho_i \dot{V}_i C_i + \rho_{inj} \dot{V}_{inj} C_{inj} + \rho_{lk} \dot{V}_{lk} C_{lk} - \rho_o \dot{V}_o C_o = \frac{dm_{CO2}}{dt} \tag{H.2}$$

Assuming ideal gas law can be used

$$\rho_{CO2} = \frac{PM_{CO2}}{RT} \tag{H.3}$$

where P is the pressure, M is the molar mass of CO_2, T is the temperature, and R is the universal gas constant (8314 J/kg.K). Substituting (H.3) in (H.2) and rearranging,

$$\left(\frac{P_i}{T_i}\dot{V}_i C_i + \frac{P_{inj}}{T_{inj}}\dot{V}_{inj} C_{inj} + \frac{P_{lk}}{T_{lk}}\dot{V}_{lk} C_{lk} - \frac{P_o}{T_o}\dot{V}_o C_o\right)\frac{M_{CO2}}{R} = \frac{dm_{CO2}}{dt} \tag{H.4}$$

All terms in equation (H.4) could be measured and evaluated except the leak flow rate and the stored CO_2. There are different scenarios where equation (H.4) can be implemented, such as, steady state conditions, no leakage, etc.

Assuming steady state conditions and neglecting the leakage terms, the mass balance equation becomes

$$\left(\frac{P_i}{T_i}\dot{V}_i C_i + \frac{P_{inj}}{T_{inj}}\dot{V}_{inj} C_{inj} - \frac{P_o}{T_o}\dot{V}_o C_o\right) = 0 \tag{H.5}$$

The values of the variables were extracted from the tracer gas experiments. One-thousand individual tests were used to evaluate the inlet and outlet concentrations; inlet, outlet, and injection temperatures. The margins were based on 95% confidence interval level with $t_{95\%}$ = ±1.96. To simplify the calculation

- P_i = 98.9 kPa, T_i= (14.72 ± 1) ˚C, $\dot{V}_i$ = 0.66 m^3/s (1400 cfm), C_i = (408 ± 12) ppm
- P_{inj} = 101 kPa, T_{inj}= T_i , $\dot{V}_{inj}$ = 0.00019 m^3/s (11.4 lit/min), C_{inj} = (62.4%)
- P_o = 101 kPa, T_o= (24.88 ± 1) ˚C, $\dot{V}_o = \dot{V}_i$, **$C_{o,measured}$ = (602 ± 18) ppm**

From equation (H.5), the calculated concentration at the outlet was defined as

$$C_o = \left(\frac{\frac{P_i}{T_i}\dot{V}_i C_i + \frac{P_{inj}}{T_{inj}}\dot{V}_{inj} C_{inj}}{\frac{P_o}{T_o}\dot{V}_o} \right) \tag{H.6}$$

The calculated outlet CO_2 concentration was found to be 600 ppm. As can be seen, the calculated and measured ports CO_2 concentrations at the outlet ports agreed within the given margins of uncertainty with insignificant differences. Thus, it was concluded that leakage into or out of the cabin was minimal. The above results also confirms that the rate of deposition of tracer gas on the walls and floor of the cabin, seats, and other structures reached to saturation and steady state assumptions were met with reasonable uncertainties.

Appendix I - Spectral Power Distribution for the Normalized CO_2 with Heated Manikins

Fourier transformation technique was used to investigate the spectral power density of the normalized CO_2 inside the cabin to check whether there were any significant peaks in the spectrum obtained. Also, the intent of this appendix was to check on the repeatability of such peaks. Below are the results for heated manikins case only.

If $\rho(\tau)$ is the transient correlation coefficient between the sampled CO_2 concentration, as defined by equation (I.1),

$$\rho(\tau) = \frac{\overline{C'(t).C'(t+\tau)}}{[C'(t)]^2} \quad \text{(I1)}$$

where C'(t) is the instantaneous fluctuation in the sampled concentration (instantaneous difference in the sampled CO_2 with respect to the average CO_2)

the spectral density power is defined as

$$S(\omega)=\frac{1}{\pi}\int_0^{\infty} e^{-i\tau\omega}\,.\,\rho(\tau).\,d\tau \quad \text{(I2)}$$

where ω is the radial angular frequency

but $e^{-i\tau\omega} = \cos(-\tau\omega) + i\sin(-\tau\omega)$ (I3)

since $\rho(\tau)$ is an even function, thus, $\sin(-\tau\omega) = 0$

therefore, $S(\omega)=\frac{1}{\pi}\int_0^{\infty} \cos(\tau\omega)\,.\,\rho(\tau).\,d\tau$ (I4)

There were no significant peaks identified for measurements in all locations that were unique, as shown in the below . Thus, it was not possible to determine the time period to observe two consecutive or repeatable peaks in the sampled CO_2 using this approach.

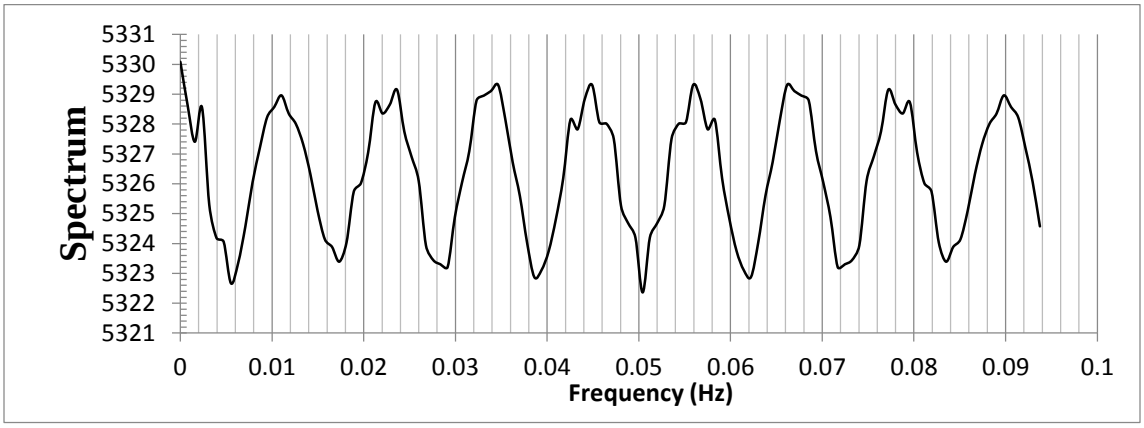

Figure I.1 - Spectral density for sampling in 1F (release in 2D)

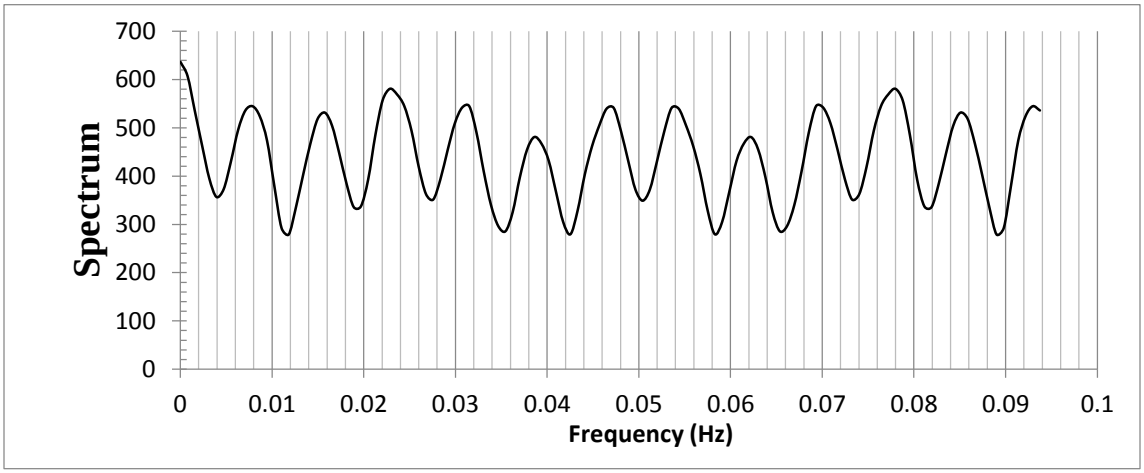

Figure I.2 – Spectral density for sampling in 2F (release in 2D)

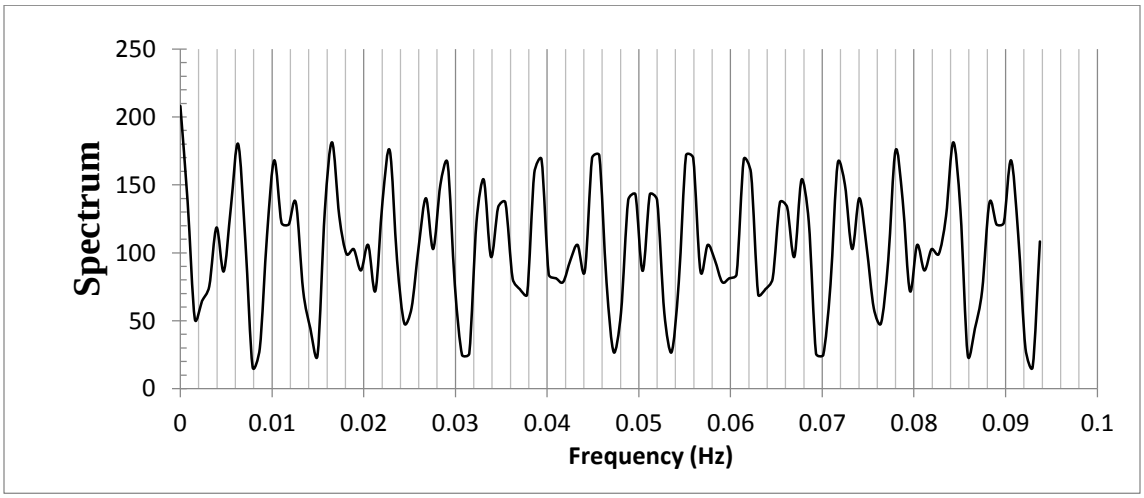

Figure I.3 - Spectral density for sampling in 3F (release in 2D)

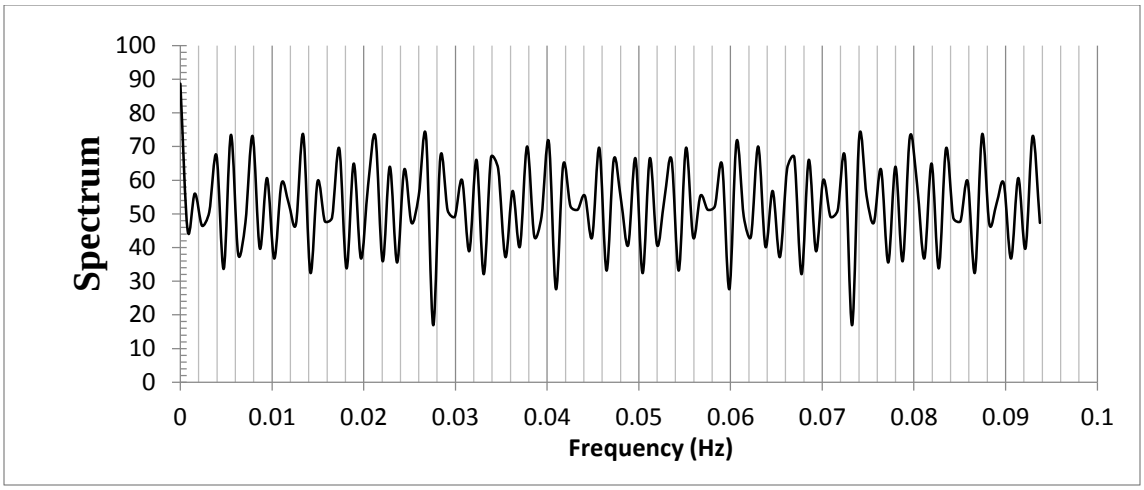

Figure I.4 - Spectral density for sampling in 4F (release in 2D)

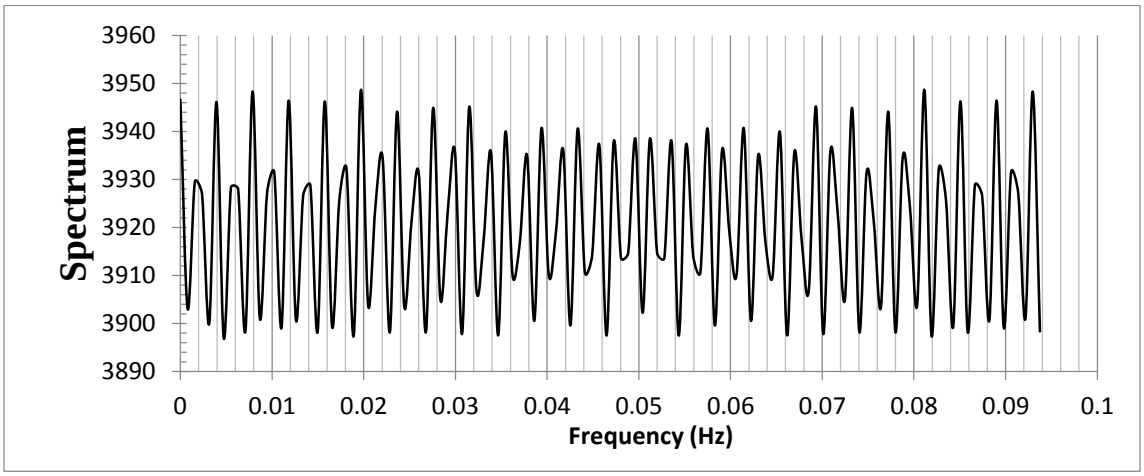

Figure I.5 – Spectral density for sampling in 1E (release in 2D)

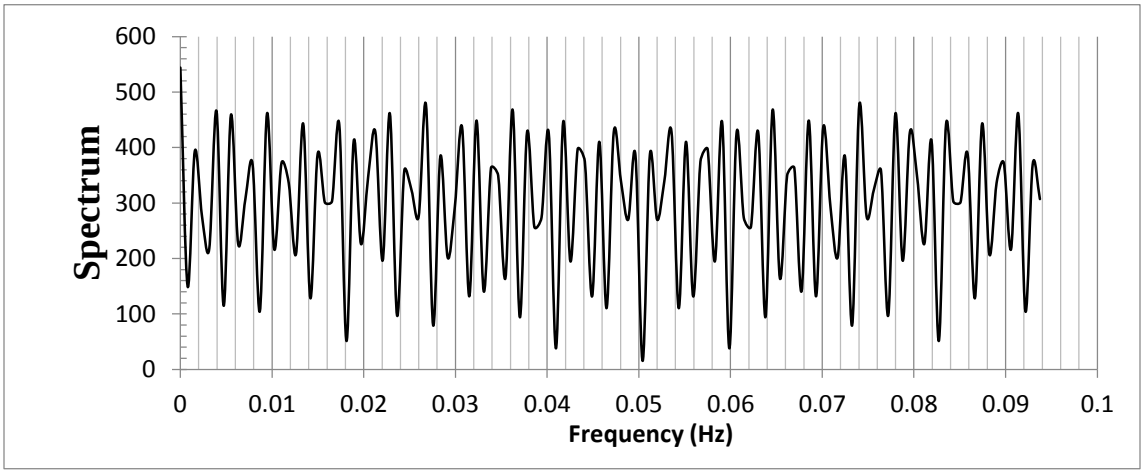

Figure I.6 – Sampling in 8B (release in 10D)

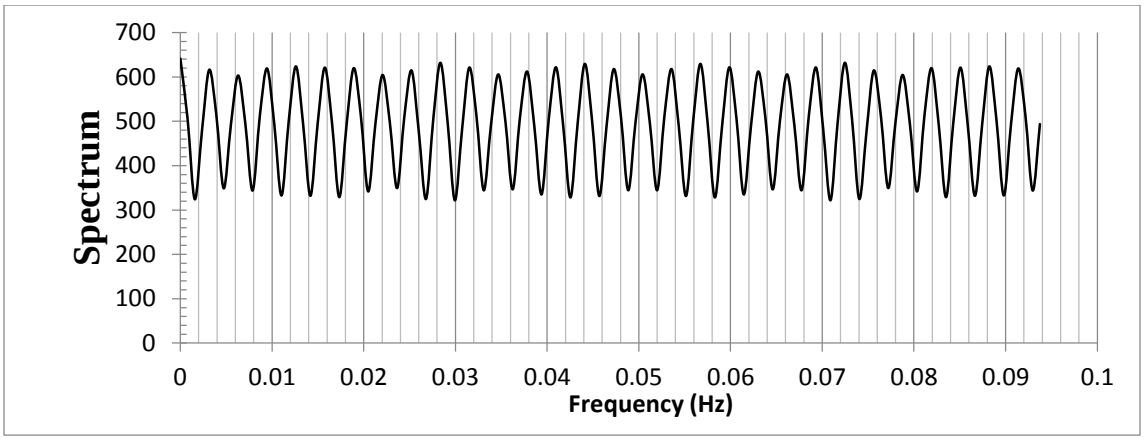

Figure I.7 – Sampling in 10B (release in 10D)

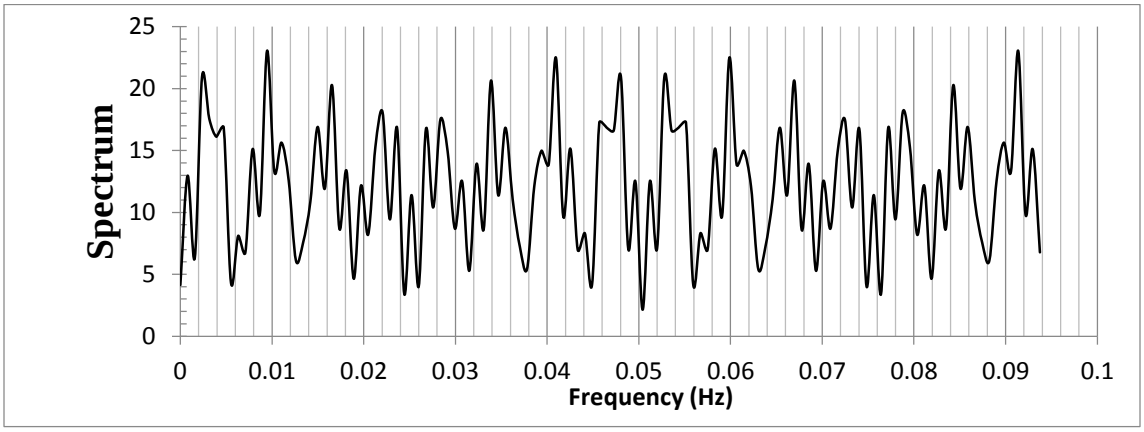

Figure I.8 – Sampling in 11B (release in 10D)

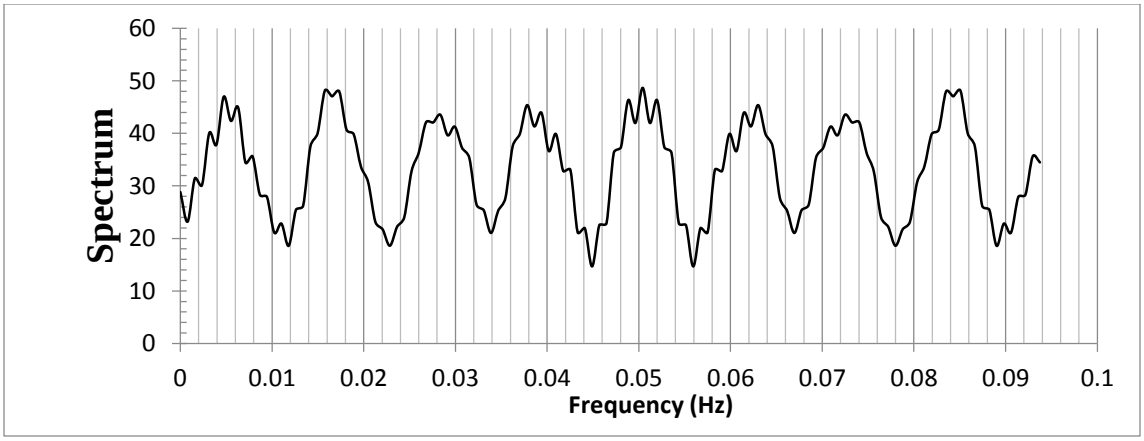

Figure I.9 – Sampling in 9F (release in 9F)

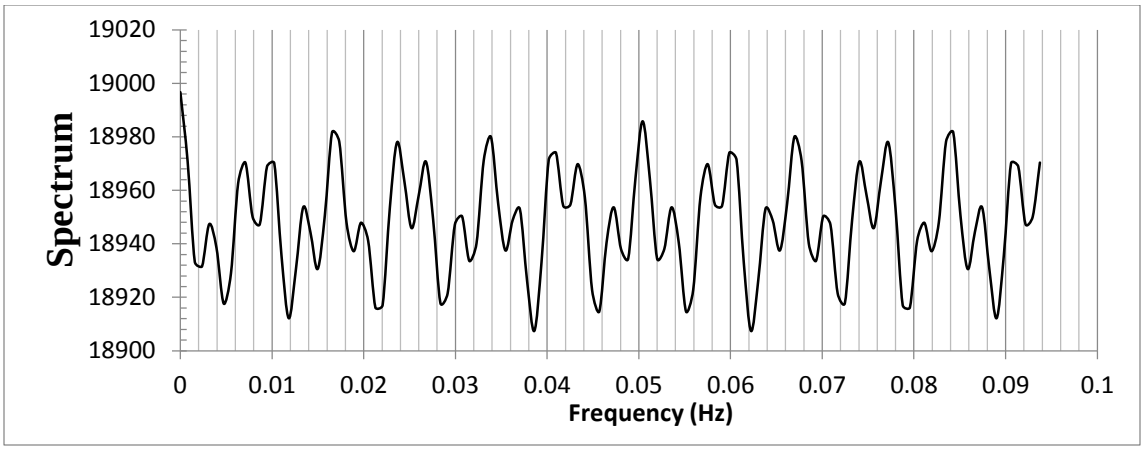

Figure I.10 – Sampling in 10F (release in 9F)

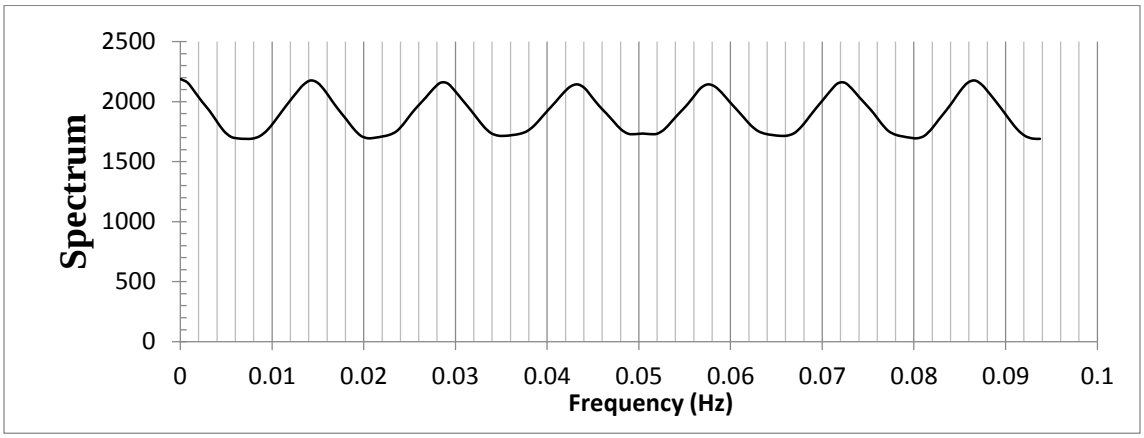

Figure I.11 – Sampling in 11F (release in 9F)

Appendix J - List of Publications

The following is a list of publications resulted from this research:

JOURNAL PUBLICATIONS:

- Shehadi, M., Jones, B., and Hosni, M., 2015, "Characterization of the frequency and nature of bleed air contamination events in commercial aircraft," *Indoor Air*, DOI: 10.1111/ina.12211

Pending Publications

- Shehadi, M., Jones, B., and Hosni, M., 2015, "Bleed air contamination financial related costs on board commercial flights," (submitted to SAE International – Journal of Aerospace)
- Shehadi, M., Hosni, M., and Jones, B., "Airflow distribution and turbulence analysis inside aircraft passengers cabins," (**under review for submission**)

CONFERENCE PROCEEDINGS PUBLICATIONS:

- Shehadi, M., Hosni, M., and Jones, B., 2014, "Airflow distribution in the longitudinal plan of a Boeing 767 mockup cabin," *Proceedings of the ASME 2014 International Mechanical Engineering Congress & Exposition*, IMECE2014-40102, November 14-20, 2014, Montreal, Canada, Montreal, Canada
- Shehadi M., Hosni M., and Jones B. W., 2010, "Experimental investigation of optimal particulate sensor location in an aircraft cabin," *Proceedings of the ASME 2010 3rd Joint US-European Fluids Engineering Summer Meeting collocated with 8th International Conference on Nanochannels, Microchannels, and Minichannels*, Montreal, Canada, Volume 1, pp. 849:859

CONFERENCE ORAL PRESENTATIONS & POSTERS:

- ASME, 2014. International Mechanical Engineering Congress & Exposition (IMECE), Montreal, CA, Oral Presentation and Poster
- ISES, 2014. International Society of Exposure Science 24th Annual Meeting, Cincinnati, OH, Oral Presentation
- ASME, 2010. 3rd Joint US-European Fluids Engineering Summer Meeting, Montreal, CA, Oral Presentation